

Advances in Polymer Science 276

Finizia Auriemma  
Giovanni Carlo Alfonso  
Claudio De Rosa *Editors*

# Polymer Crystallization I

From Chain Microstructure to Processing

 Springer

**Editorial Board:**

- A. Abe, Yokohama, Kanagawa, Japan
- A.-C. Albertsson, Stockholm, Sweden
- G.W. Coates, Ithaca, NY, USA
- J. Genzer, Raleigh, NC, USA
- S. Kobayashi, Kyoto, Japan
- K.-S. Lee, Daejeon, South Korea
- L. Leibler, Paris, France
- T.E. Long, Blacksburg, VA, USA
- M. Möller, Aachen, Germany
- O. Okay, Istanbul, Turkey
- V. Percec, Philadelphia, PA, USA
- B.Z. Tang, Hong Kong, China
- E.M. Terentjev, Cambridge, UK
- P. Theato, Hamburg, Germany
- M.J. Vicent, Valencia, Spain
- B. Voit, Dresden, Germany
- U. Wiesner, Ithaca, NY, USA
- X. Zhang, Beijing, China

## **Aims and Scope**

The series *Advances in Polymer Science* presents critical reviews of the present and future trends in polymer and biopolymer science. It covers all areas of research in polymer and biopolymer science including chemistry, physical chemistry, physics, material science.

The thematic volumes are addressed to scientists, whether at universities or in industry, who wish to keep abreast of the important advances in the covered topics.

*Advances in Polymer Science* enjoys a longstanding tradition and good reputation in its community. Each volume is dedicated to a current topic, and each review critically surveys one aspect of that topic, to place it within the context of the volume. The volumes typically summarize the significant developments of the last 5 to 10 years and discuss them critically, presenting selected examples, explaining and illustrating the important principles, and bringing together many important references of primary literature. On that basis, future research directions in the area can be discussed. *Advances in Polymer Science* volumes thus are important references for every polymer scientist, as well as for other scientists interested in polymer science - as an introduction to a neighboring field, or as a compilation of detailed information for the specialist.

Review articles for the individual volumes are invited by the volume editors. Single contributions can be specially commissioned.

Readership: Polymer scientists, or scientists in related fields interested in polymer and biopolymer science, at universities or in industry, graduate students.

Special offer:

For all clients with a standing order we offer the electronic form of *Advances in Polymer Science* free of charge.

More information about this series at <http://www.springer.com/series/12>

Finizia Auriemma • Giovanni Carlo Alfonso •  
Claudio De Rosa

Editors

# Polymer Crystallization I

From Chain Microstructure to Processing

With contributions by

R.G. Alamo • R. Androsch • F. Auriemma • X. Chen •  
S.Z.D. Cheng • C. Cioce • X.-H. Dong • H. Gao •  
R. Di Girolamo • C.-H. Hsu • M. Huang • W. Hu • Y. Li •  
H. Liu • B. Lotz • A. Malafrente • V.B.F. Mathot •  
R.M. Michell • A. Mugica • A.J. Müller • R.A. Pérez-Camargo •  
C. De Rosa • L. Santonja-Blasco • C. Schick • M. Scoti •  
H.-J. Sun • J. Wang • C.-L. Wang • X. Yu • K. Yue • X. Zhang •  
W.-B. Zhang • M. Zubitur

 Springer

*Editors*

Finizia Auriemma  
Department of Chemical Sciences  
University of Naples Federico II  
Napoli, Italy

Giovanni Carlo Alfonso  
Department of Chemistry and Industrial  
Chemistry  
University of Genova  
Genova, Italy

Claudio De Rosa  
Department of Chemical Sciences  
University of Naples Federico II  
Napoli, Italy

ISSN 0065-3195

Advances in Polymer Science

ISBN 978-3-319-49201-8

DOI 10.1007/978-3-319-49203-2

ISSN 1436-5030 (electronic)

ISBN 978-3-319-49203-2 (eBook)

Library of Congress Control Number: 2016961289

© Springer International Publishing AG 2017

This work is subject to copyright. All rights are reserved by the Publisher, whether the whole or part of the material is concerned, specifically the rights of translation, reprinting, reuse of illustrations, recitation, broadcasting, reproduction on microfilms or in any other physical way, and transmission or information storage and retrieval, electronic adaptation, computer software, or by similar or dissimilar methodology now known or hereafter developed.

The use of general descriptive names, registered names, trademarks, service marks, etc. in this publication does not imply, even in the absence of a specific statement, that such names are exempt from the relevant protective laws and regulations and therefore free for general use.

The publisher, the authors and the editors are safe to assume that the advice and information in this book are believed to be true and accurate at the date of publication. Neither the publisher nor the authors or the editors give a warranty, express or implied, with respect to the material contained herein or for any errors or omissions that may have been made.

Printed on acid-free paper

This Springer imprint is published by Springer Nature

The registered company is Springer International Publishing AG

The registered company address is: Gewerbestrasse 11, 6330 Cham, Switzerland

# Preface

The APS volumes “Polymer Crystallization: From Chain Microstructure to Processing” appear about 10 years after the three APS volumes (180, 181, and 191) “Interphases and Mesophases in Polymer Crystallization” edited by Giuseppe Allegra. The volumes follow a series of workshops on polymer crystallization held in Genova in 2010, 2012, and 2014, which were triggered by the need to stimulate debate and share new ideas among leading scientists from academia and industry on emerging topics related to the crystallization of polymers. We decided to collect some of these contributions into two APS volumes, eventually including the contributions of additional authors to fix the new concepts, ideas, and findings into a unified project reflecting the state of art.

With the development of new theoretical and experimental tools for investigating matter at the atomic level, significant advances in the understanding of phenomena associated with polymer crystallization have been achieved. However, elucidating the fundamental physical and chemical issues that govern the crystallization process in a polymer, by which chain molecules move from the melt state to a semicrystalline state with formation of lamellar crystals, is still a challenge.

The volumes include a wide range of different topics. The first section of Volume I is related to molecular aspects of polymer crystallization, with chapters on polymorphism (“Crystallization of Statistical Copolymers”), properties of statistical copolymers (“Molecular View of Properties of Random Copolymers of Isotactic Polypropylene”), the crystallization of cyclic polymers (“Crystallization of Cyclic Polymers”), and precision ethylene copolymers (“Crystallization of Precision Ethylene Copolymers”). This section ends with a chapter devoted to the crystallization of giant molecules (“Supramolecular Crystals and Crystallization with Nanosized Motifs of Giant Molecules”). The second section of Volume I deals with two different basic aspects of the nucleation process that are also important in industrial processes: self-nucleation (“Self-nucleation of Crystalline Phases Within Homopolymers, Polymer Blends, Copolymers and Nanocomposites”) and nucleation at high supercooling (“Crystal Nucleation of Polymers at High Supercooling of the Melt”).

Volume II begins with a section concerning aspects of polymer crystallization that have often been overlooked in the literature and are related to concomitant crystallization and cross-nucleation (“Concomitant Crystallization and Cross-Nucleation in Polymorphic Polymers”), surface-induced epitaxial crystallization (“Epitaxial Effects on Polymer Crystallization”), and study of the origin of banded spherulites with nanofocus X-ray diffraction (“Microstructure of Banded Polymer Spherulites: New Insights from Synchrotron Nanofocus X-Ray Scattering”). The two latter chapters are illustrative examples of modern investigation of crystal morphology at the molecular level. The second section of Volume II collects important issues in industrial application and processing. Topics includes the use of synchrotron light for studying phase transformation during processing or deformation in real time (“Real-Time Fast Structuring of Polymers Using Synchrotron WAXD/SAXS Techniques”), the role of amorphous phase in stress-induced crystallization of natural rubber (“Strain-Induced Crystallization in Natural Rubber”), the influence of cooling rate and pressure on polymer crystallization (“Non-isothermal Crystallization of Semicrystalline Polymers: The Influence of Cooling Rate and Pressure”), and the modeling of flow-induced crystallization (“Modeling Flow-Induced Crystallization”).

We are thankful to all contributors to the project for their high quality work.

These two volumes cover only a few aspects of polymer crystallization, and final solutions to the big problems in the field have not been assessed. Several topics covered in the volumes are still under development and need additional in-depth analyses, checks, and improvements. Nonetheless we hope that the selected topics will stimulate new discussions, inspire new theories and experiments, intrigue new followers, and initiate new research in this fascinating world.

Napoli, Italy

Genova, Italy  
04 July 2016

Finizia Auriemma  
Claudio De Rosa  
Giovanni Carlo Alfonso

# Contents

<b>Crystallization of Statistical Copolymers . . . . .</b>	<b>1</b>
Wenbing Hu, Vincent B.F. Mathot, Rufina G. Alamo, Huanhuan Gao, and Xuejian Chen	
<b>Molecular View of Properties of Random Copolymers of Isotactic Polypropylene . . . . .</b>	<b>45</b>
Finizia Auriemma, Claudio De Rosa, Rocco Di Girolamo, Anna Malafronte, Miriam Scoti, and Claudia Cioce	
<b>Crystallization of Cyclic Polymers . . . . .</b>	<b>93</b>
Ricardo A. Pérez-Camargo, Agurtzane Mugica, Manuela Zubitur, and Alejandro J. Müller	
<b>Crystallization of Precision Ethylene Copolymers . . . . .</b>	<b>133</b>
Laura Santonja-Blasco, Xiaoshi Zhang, and Rufina G. Alamo	
<b>Supramolecular Crystals and Crystallization with Nanosized Motifs of Giant Molecules . . . . .</b>	<b>183</b>
Xue-Hui Dong, Chih-Hao Hsu, Yiwen Li, Hao Liu, Jing Wang, Mingjun Huang, Kan Yue, Hao-Jan Sun, Chien-Lung Wang, Xinfei Yu, Wen-Bin Zhang, Bernard Lotz, and Stephen Z.D. Cheng	
<b>Self-Nucleation of Crystalline Phases Within Homopolymers, Polymer Blends, Copolymers, and Nanocomposites . . . . .</b>	<b>215</b>
R.M. Michell, A. Mugica, M. Zubitur, and A.J. Müller	
<b>Crystal Nucleation of Polymers at High Supercooling of the Melt . . . .</b>	<b>257</b>
René Androsch and Christoph Schick	
<b>Index . . . . .</b>	<b>289</b>



# Crystallization of Statistical Copolymers

**Wenbing Hu, Vincent B.F. Mathot, Rufina G. Alamo, Huanhuan Gao, and Xuejian Chen**

**Abstract** Conventional polymers contain various chemical, geometrical, and stereo-optical sequence irregularities along the backbone chain, which can be treated as noncrystallizable comonomers in statistical copolymers. For statistical copolymers, the link between chemistry (copolymerization to characterize statistical copolymers) and physics (crystallization to determine structures and properties) has recently been enhanced. This review discusses how the crystallization behavior and resulting semicrystalline structure of statistical copolymers are affected by the various microstructure parameters of their comonomers, such as content, distribution along or even among polymer chains, and size (determining their inclusion in or exclusion from the crystallites). The discussion of crystallization is focused on its interplay with component segregation at three different length scales: monomer, monomer sequence, and macromolecule. The first two mainly occur in homogeneous copolymers, whereas the last one is only operative for heterogeneous copolymers. In addition, some unique phenomena such as strong memory effects and (cross)fractionation are discussed briefly.

**Keywords** Component segregation • Crystallization • Heterogeneous • Homogeneous • Statistical copolymers

---

W. Hu (✉) and H. Gao

Department of Polymer Science and Engineering, State Key Lab of Coordination Chemistry, School of Chemistry and Chemical Engineering, Nanjing University, 210023 Nanjing, P.R. China

e-mail: [wbhu@nju.edu.cn](mailto:wbhu@nju.edu.cn)

V.B.F. Mathot

SciTe B.V., Ridder Vosstraat 6, 6162 AX Geleen, The Netherlands

R.G. Alamo and X. Chen

Department of Chemical and Biomedical Engineering, FAMU-FSU College of Engineering, 2525 Pottsdamer St., Tallahassee, FL 32310-6046, USA

## Contents

1	Introduction .....	2
2	Chain Microstructure of Statistical Copolymers: The (Missing) Link to Crystallization Behavior .....	4
2.1	Markov Modeling of Copolymerization .....	4
2.2	Determination of Chain-Growth Parameters .....	8
2.3	Homogeneous and Heterogeneous Copolymers .....	9
3	Crystallization with Monomer Segregation .....	13
4	Crystallization with Monomer-Sequence Segregation .....	25
5	Crystallization with Macromolecular Segregation .....	33
6	Summary .....	39
	References .....	40

## 1 Introduction

Synthetic chemistry provides an economic way to produce polymers with the same monomer units and regular sequence structures, both of which favor crystallization. However, a polymer with fully crystalline structure has only hard and brittle properties, which limit its practical application. Introducing intramolecular defects, mainly on the backbone chain, is the conventional path for obtaining a useful semicrystalline product. Sequence irregularities on the backbone can be classified according to three sources in the detailed polymerization processes: chemical modifications, geometric isomers, and stereoisomers. For instance, various kinds of chemical modifications on the backbone have led to important new classes of commercial polyolefins, such as high impact polypropylene (HIPP), high density polyethylene (HDPE), low density polyethylene (LDPE), heterogeneous and homogeneous linear low density polyethylene (LLDPE), and very low density polyethylene (VLDPE).

Over the years, every part of the ‘chain of knowledge’ for polymer crystallization (meaning the successive steps from polymerization via processing to properties) has been well studied, but the links between these parts are still weak or even absent [1]. For instance, studies of the connection between chain microstructure and crystallization behavior often stopped at the content of sequence defects and overlooked their detailed distribution, probably as a result of technical difficulties in obtaining a clear characterization of sequence distribution. However, defect distribution has a huge impact on the crystallization behavior of polymers, which is why determination of the distribution should have the full attention of researchers studying the crystallizability of polymers, especially because crystallization has appreciable effects on the end properties of the product. During crystallization, the sequence segments containing defects do not usually match the geometric or spatial requirements of compact packing in the crystalline ordered regions composed of crystallizable units. Thus, they behave like noncrystallizable entities and hinder the development of crystallinity by the polymer main chains. In this sense, they bring

an intramolecular chemical confinement, being inclusion in the case of mobile defects or exclusion in the case of immobile defects in the crystalline phase, which depends on the size and rigidity of the defect-containing segments relative to the crystallizable units. The sequence defects, on the one hand, bring more chain connections between crystallites to improve the durability of plastic products, but, on the other hand, suppress crystallinity and in extreme cases give rise to an amorphous polymer such as atactic polystyrene or atactic poly(methyl methacrylate) (PMMA). Driven by strong industrial interests, along with modern developments in the use of well-designed catalysts, NMR characterization, and molecular simulations, research has stepped forward to examine how the detailed distribution of sequence defects affects crystallization behavior and the resulting semicrystalline structure of synthetic polymers.

Many synthetic polymers show sequence defect distributions that resemble some statistical features; therefore, their crystallization behaviors can be discussed by treating them as statistical copolymers produced by typical addition polymerization following a statistical mechanism. Statistical homogeneous and heterogeneous copolymers, although distinguished by their differing homogeneity of comonomer distribution among macromolecules, both exhibit an intramolecular multicomponent behavior. Upon crystallization, two levels of component microphase segregation (from small to large scale) may be of relevance: monomer segregation (according to different chemical species of the chain units) and monomer-sequence segregation (according to different consecutive lengths of monomer units along the chain). Heterogeneous copolymers have, in addition, an intermolecular multicomponent phase-separation behavior (caused by different comonomer contents and distributions between macromolecules), which could lead to macromolecular segregation. Various levels of liquid-liquid phase separation are likely to occur prior to liquid-solid crystallization and, thus, change the course of the latter. Therefore, the interplay between crystallization and component segregation is an interesting issue [2] and of importance in understanding better the complex phase transition behavior of statistical copolymers.

In this review, we survey current understanding of different levels of component segregation and the resulting crystallization phenomena of statistical copolymers. After a description of statistical copolymers, the discussion focuses on the occurrence of monomer segregation, monomer-sequence segregation, and macromolecular segregation during the process of crystallization of statistical copolymers. For each type of segregation, we discuss factors of chemical structure such as comonomer content, comonomer distribution, and molar mass, as well as the thermodynamic conditions (mainly temperature). More specifically, we compare various copolymers of different comonomer mobility in the crystalline phase, which represent different extents of intramolecular confinement in the crystallization of statistical copolymers. We hope that with this strategy, the complex crystallization behavior of statistical copolymers can clearly unfold in front of the reader's eyes.

## 2 Chain Microstructure of Statistical Copolymers: The (Missing) Link to Crystallization Behavior

### 2.1 Markov Modeling of Copolymerization

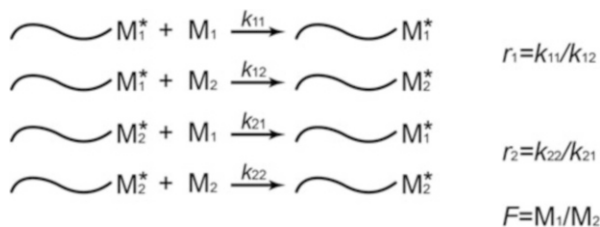
We have taken commercial polyethylene-based linear statistical copolymers as typical examples for our discussion. Figure 1 provides an overview of the classification of polyethylene products [3–6]. These are not just grades of polyethylene, but intrinsically new polymers because of their unique properties. Thus, polymer chemistry plays a crucial starting role, leading to additional large-scale production for globally demanding markets. In addition, the chain of knowledge from polymer microstructure to macroscopic properties is continuously being improved by the sophisticated, state-of-the-art techniques of polymer characterization. The weakest (and in fact often the ‘missing’) link is usually the relation between the detailed sequence distribution and its influence on crystallization. In the case of copolymers, the missing link is knowledge of comonomer distribution in and between chains and its translation to crystallization behavior, morphology, and so on.

Chemical modifications of polymer chains are often realized through addition or condensation copolymerizations. A typical example of addition copolymerization

		LINEAR	SHORT CHAIN BRANCHED			
			HOMOGENEOUS	HETEROGENEOUS		
Crystalline	1000	 LPE UHMWPE	 Ethylene Copolymers EP EB EO EPDM	 UHMWPE HDPE	 LLDPE VLDPE (ULDPE)	 Molar Mass Distribution Sample History
	Semi-crystalline					
Amorphous	855					
State at 25°C	$D^{25^\circ\text{C}}$ (kg/m <sup>3</sup> )		DSC Curve Shape		Influencing Thermal Properties	
			Single Peaked		Multiple Peaked	

**Fig. 1** Classification of polyethylene products. *LPE* linear polyethylene, *UHMWPE* ultra-high molecular weight polyethylene, *HDPE* high density polyethylene, *LDPE* low density polyethylene, *SCB* short chain branching, *LCB* long chain branching, *LLDPE* linear low density polyethylene, *VLDPE* very low density polyethylene, *EP* ethylene–propylene, *EB* ethylene–1-butene, *EO* ethylene–1-octene, *EPDM* ethylene propylene diene monomer. Adapted from [3]. SciTe ©. Courtesy of VBF Mathot

**Fig. 2** Schematics of homo- and cross-propagation reactions in addition copolymerization



resulting in a product of large market share is LLDPE ('linear' indicates the absence of long-chain branching). Historically, although production started with heterogeneous types of LLDPE (resulting, for example, from Ziegler–Natta polymerization), homogeneous types of LLDPE were later produced by means of single-site catalysts, including metallocene-based catalysts. By varying the type of comonomer and the number and distribution of noncrystallizable short-branched comonomers, LLDPEs can show behaviors ranging from thermoplastic elastomers to hard plastics [3, 4, 7].

In principle, the sequence distributions of the (co)monomers of LLDPE as produced by one (or each) catalytic site can be fairly described by a statistical model on the basis of a simplified stochastic mechanism of addition copolymerization, which provides a unified classification of copolymers under the name of statistical copolymers [8]. In addition to copolymerization, linear polymer chains can be produced by stepwise addition of free monomers or comonomers, while the choice made depends upon the type of unit at the chain end, the concentrations of free monomers and comonomers, and their relative reactivity. In such a case, the chain-propagation process can be treated as a stochastic Markov process. If propagation at polymer chain ends quickly loses the memory of previously added units, only short-range interactions with the active chain ends are relevant. A first-order Markov process (called the terminal model) corresponds to the case where the active ends can be characterized by the last added (co)monomer. A second-order Markov process (called the penultimate model) corresponds to the case where the last two (co)monomers have influence, which in specific cases gives a more accurate description of the complex kinetic process [9], as discussed in more detail below.

First, we look at the terminal model of copolymerization of monomers and comonomers on a single-site catalyst. The chain propagation process can be modeled as shown in Fig. 2, where monomers and comonomers are separately marked as  $M_1$  and  $M_2$ , and the reaction rate constants are  $k_{ij}$  (with  $i, j$  elements of  $\{1, 2\}$  to characterize the preference of reaction of monomers and comonomers, respectively). The asterisks marked at the ends of propagating chains represent the active unit of polymerization. Then, the propagating probabilities for the formation of the two successive units are:

$$P_{11} = \frac{k_{11}[M_1][M_1^*]}{k_{11}[M_1][M_1^*] + k_{12}[M_2][M_1^*]} = \frac{r_1 F}{r_1 F + 1}, \quad (1)$$

$$P_{12} = 1 - P_{11}, \quad (2)$$

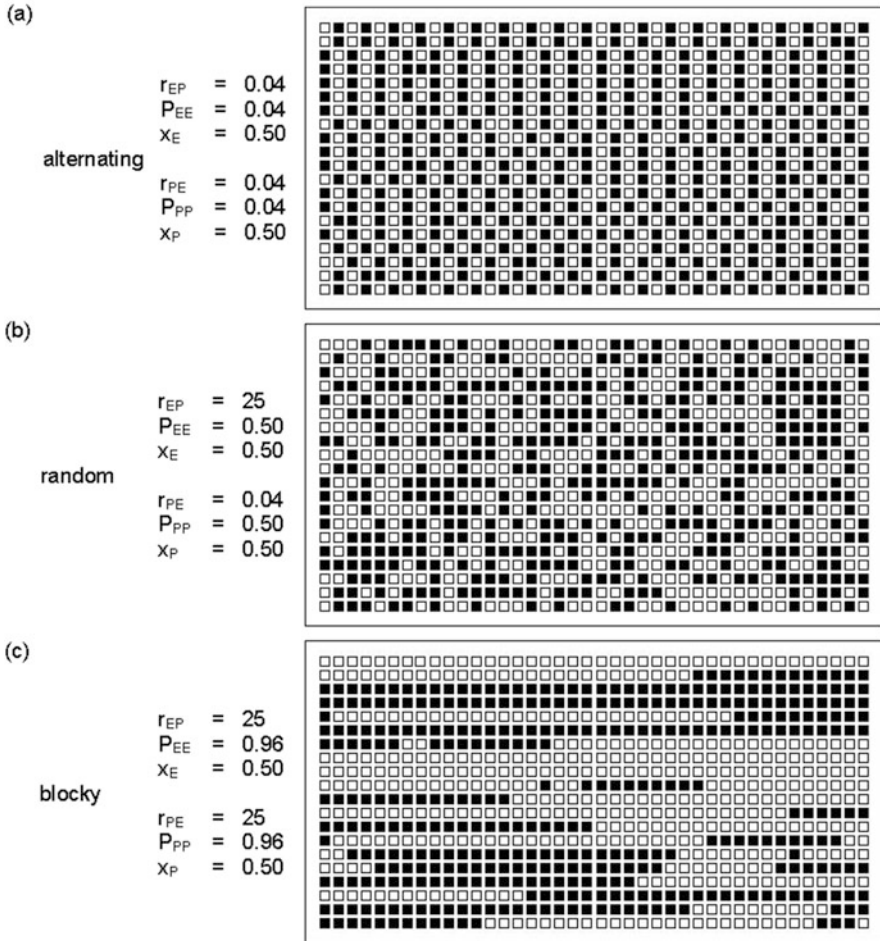
$$P_{22} = \frac{k_{22}[M_2][M_2^*]}{k_{22}[M_2][M_2^*] + k_{21}[M_1][M_2^*]} = \frac{r_2}{r_2 + F}, \quad (3)$$

$$P_{21} = 1 - P_{22}, \quad (4)$$

where  $r_1 \equiv k_{11}/k_{12}$  and  $r_2 \equiv k_{22}/k_{21}$  are the reactivity ratios related to monomer and comonomer incorporation at the chain ends, and  $F \equiv [M_1]/[M_2]$  is the ratio of mole fractions of monomer and comonomer as representative of the feed composition in the reaction mixture. In this sense, the probability of adding the consecutive sequences of monomers with length  $n$  ( $n > 0$ ) is given by  $P_{21}P_{11}^{n-1}P_{12}$ . When  $n = 0$ , the probability of having two successive comonomers is given by  $P_{22}$ .

One could wonder whether the chain-growth preferences can also be described by the reactivity ratios, as well as by the probabilities, especially when conversion between the two is simple. Indeed, expressions regarding content and distribution in a statistical copolymer sample can be described by either using a specific  $P$ -set and the specific mole fraction of monomer  $x_1$  (or comonomer  $x_2 = 1 - x_1$ ) or, alternatively, using a specific  $r$ -set and specific  $F$ , and the one can be calculated from the other. The advantage of the  $P$  description is that it can be done on a sample without any additional information and is thus very useful for analysis of a competitor sample. For a series of homogeneous copolymers (well-polymerized under constant external conditions and with knowledge of the feeds used), the advantage of the description with an  $r$ -set is that it is a constant, intrinsic property of the catalyst, implying that is useful for describing the whole series by one common  $r$ -set, in addition to characterizing specific samples by a specific  $r$ -set and a specific  $F$ . In practice, this turns out to be feasible and very useful information becomes available.

The product of two reactivity ratios,  $r_1 r_2$ , is decisive for the type of sequence length distribution of both monomer and comonomer. Values of  $r_1 r_2$  approaching zero (the alternative description is  $P_{11} \ll x_1$ ) and infinity (the alternative is  $P_{11} \gg x_1$ ) correspond to the two extreme situations of forming alternating copolymers and blocky copolymers, respectively. Between these extremes, a characteristic value for the  $r$ -set is achieved in the case of statistically random copolymers for which different  $r_1$  and  $r_2$  values give the product  $r_1 r_2 = 1$  (since  $r_1 \neq 1$ , according to Eq. (1),  $P_{11} \neq x_1$ ). Usually, in a first-order Markov (terminal model) process,  $r_1$  and  $r_2$  have quite different values that lead to intramolecular heterogeneity during chain growth. However, in the special case of a zero-order Markov (Bernoullian-like) process, random copolymers also result for the reason that  $r_1 r_2 = 1$  because  $r_1 = 1$  and  $r_2 = 1$ , and  $P_{11} = x_1$ . In the latter case, the distribution of (co)monomer units in the chains is the same random distribution as the (co)monomer distribution in the reactor before the copolymerization. Figure 3 shows the distribution of monomer and comonomer units for a fictive copolymer [1]. One can see that at the same



**Fig. 3** Schematics (*to be read like a book*) of (fictive) ethylene (E)–propylene (P) copolymers with (a) alternating ( $r_{EP} \times r_{PE} < 1$ ), (b) random ( $r_{EP} \times r_{PE} = 1$ ), and (c) blocky ( $r_{EP} \times r_{PE} > 1$ ) distributions of the monomer (*open squares*) and comonomer (*filled squares*) units. The values  $r_{ij}$ ,  $P_{ij}$ , and  $x_i$  are the reactivity ratios, the propagation probabilities, and mole fractions of (co) monomer incorporated in the chain, respectively. Note that the propylene content is 50% for each of the three copolymers. Also note that  $P_{EE}$  is lower than  $x_E$  for alternating, equal to  $x_E$  for random, and higher than  $x_E$  for blocky copolymers. Schematics taken from [1]. SciTe\_TU/e-F.G. Karssenber ©. Courtesy of VBF Mathot

comonomer mole fractions of 50%, the chain structure can be quite different depending upon whether distribution is alternating, random, or blocky. Clearly, knowledge of the comonomer content alone is not enough for a copolymer description nor for evaluation of its crystallization behavior. This implies that if the copolymerization process is not random, one has to use  $P_{11}$  rather than  $x_1$ , because the latter could lead to totally wrong results.

In Fig. 3, it is assumed that the feed composition  $F$  is constant during the copolymerization process of a specific grade, similar to the steady-state continuous reaction processes used in industry. In such a case, the sequence distributions are homogeneous among all the copolymer chains. This leads to a definition of a homogeneous copolymer [10]: for each sample polymerized, all chains have the same average (co)monomer content and have the same statistics with regard to the (co)monomer distribution. To this end, the statistics in each sample are characterized by one specific set of chain propagation probabilities during (co)monomer incorporation in the chains (a  $P$ -set) in combination with one mole fraction of the monomer or comonomer actually incorporated in the chains,  $x_i$ . Alternatively, a specific sample can also be characterized by the combination of one specific set of reactivity ratios (an  $r$ -set) and one specific monomer/comonomer ratio  $F$  during copolymerization. For a series of samples, a common set of reactivity ratios should be applied and then various samples are characterized by various values of  $F$ . All other copolymers, by definition, are heterogeneous, and some possibilities are discussed later.

## 2.2 Determination of Chain-Growth Parameters

Before discussing the crucial influence of the statistics of (co)monomer incorporation on the crystallization and melting behavior, we need to explain how the reactivity ratios (and propagation probabilities) can be determined from experimental data [11–14].

In early studies of copolymerization, the determination of (co)monomer distribution lacked rigorous treatment. There were three main reasons for this: First, the best technique available, NMR, was not good enough at the time to provide the information needed. Second, the limited information (mainly from signals related to the copolymer) available from NMR (comonomer content, diads, triads, methylene sequences) was not fully used. These two items frustrated determination not only of the short sequences but also of longer sequences [15]. Third, the lack of well-copolymerized and characterized series of homogeneous copolymers led to comparison of copolymers of different origins [16], in which copolymers were not homogeneous or had different statistics such as random, blocky, or alternating. The result could be best described as restricted to information concerning the smallest sequences and was therefore not good enough to serve as an input for realistic crystallization studies.

To improve this situation, the direct  $^{13}\text{C}$ -NMR peak method (DPM) [11–13] was developed to analyze the results of high field, quantitative  $^{13}\text{C}$ -NMR [17]. This method makes use of the total information available in the NMR spectrum. All relevant peaks are calculated using a Markovian model of the relevant order, an  $r$ -set, and an  $F$ . After minimization of the differences between the experimental and calculated intensities, the chi-square value determines the reliability of the fit. The Markovian order of the system is also found in this way. An important aspect of



DPM is that it is possible to model a series of samples as a whole. For copolymers of ethylene and a higher  $\alpha$ -olefin with long relaxation times of the atoms of the short chain branches (e.g., ethylene–1-octene copolymers), quantitative, high signal-to-noise  $^{13}\text{C}$ -NMR spectra were acquired by adding an optimized amount of chromium(III)-triacetylacetonate as relaxation agent [17] in order to enable DPM. So far, DPM has been applied successfully to various series of homogenous copolymers from ethylene–propylene (EP) copolymers to ethylene–1-octene (EO) copolymers, as polymerized by vanadium and different metallocene catalysts. This method is not limited to ethylene–1-alkene copolymers but can be used for all olefin copolymers (e.g., propylene–1-pentene copolymer) [1, 18]. With adjustments, DPM could be generalized for other types of copolymers. It was also found that DPM is able to unravel chain structures resulting from a mixture of two homogeneous catalysts [19]. This has opened the way towards understanding and modeling the chain microstructures of heterogeneous copolymers having bimodal (co)monomer distributions.

Next, examples are given of detailed and realistic chain microstructures of copolymers that have been analyzed by using the methods discussed above.

### 2.3 *Homogeneous and Heterogeneous Copolymers*

As the first example of the application of DPM in the determination of the structure of a mainstream commercial polymer, EPDM (ethylene propylene diene monomer) rubber is discussed (the minor diene is tentatively not included in the following consideration). For the purpose of mimicking the essence of the molecular structure of the terpolymer EPDM, a series of 19 EP copolymers with propylene content ( $x_p$ ) ranging from 0 (linear polyethylene) to 35.3% were prepared using the same promoted catalyst system, consisting of an aluminum alkyl combined with a vanadium component. This system has been known to act as a single-site catalyst, and the copolymers were produced under steady-state conditions and by stepwise changing of the feed in the reactor. In this case, the occurrence of inversion of the comonomer complicates the modeling. Normally, a propene unit is incorporated via 1,2 (or primary) insertion. With some catalysts of industrial importance (e.g., constraint geometry catalysts), inverted 2,1 (or secondary) insertion is also possible, which is relatively slow. Thus, in fact, one deals with a ‘degenerated’ terpolymer. In this case, a first-order Markov description was successfully used [11–13], based on the methylene sequence length method (MSLM), even though only part of the  $^{13}\text{C}$  NMR data was used. As a result, the following parameters were found (where subscript 1 stands for ethylene, 2 for inverted propylene, and 3 for normal propylene):

$r_{12} = 19.6$ ;  $r_{13} = 120$ ;  $r_{21} = 0.032$ ;  $r_{23} = 2.8$ ;  $r_{31} = 0.005$ ;  $r_{32} = \infty$  (meaning that head–head linking of propylenes did not occur:  $P_{32} = 0$ ). The reliability was <90.0%.

In this model, if the difference between ‘normal’ and ‘inverted’ propylenes is removed and everywhere is changed into ‘propylenes’ a kind of product of reactivity ratio,  $r_E r_P$ , can be calculated for  $x_P$  between 15 and 40% [11, 12]:

$$r_E = 17; r_P \sim 0.029; r_E r_P \sim 0.50$$

The value of  $r_E r_P$  characterizes the copolymer as slightly alternating.

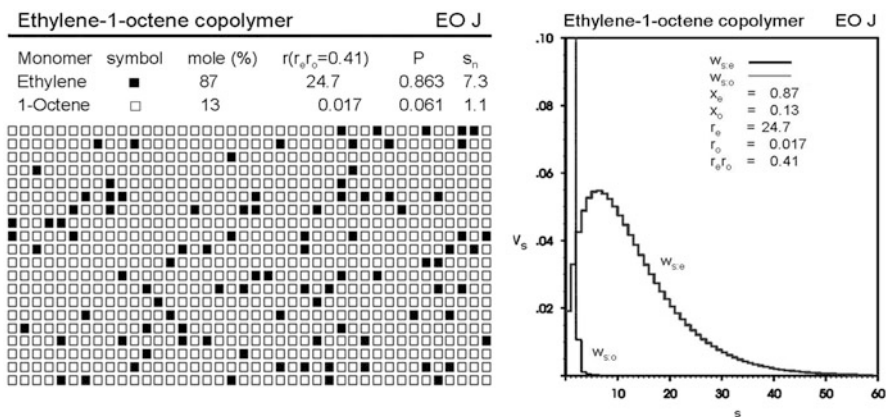
Later, the analysis using DPM was improved [20] such that all relevant data were utilized, leading to the following reactivity ratios:

$$r_{12} = 20.0 (\pm 2.0\%); r_{13} = 162 (\pm 16.2\%); r_{21} = 0.015 (\pm 6.7\%); r_{23} = 1.3 (\pm 7.7\%); \\ r_{31} = 0.060 (\pm 5.0\%); r_{32} = \infty.$$

The reliability was  $> 99.5\%$ , illustrating the improvement obtained using DPM.

The second example is a series of EO copolymers, produced using the same vanadium-based catalyst system with concomitant occurrence of inversion. The crystallization and melting behavior by simulation are discussed later (see, for example, Fig. 12). Extensive experimental research results on both EP and EO series are found in the literature ([4, 6] and related publications). To facilitate a better understanding of the interaction between chain microstructure and the crystallization behavior of samples of the EO copolymer series, the crystallization and melting behaviors of one of these (EO-J) were studied using differential scanning calorimetry (DSC) and were discussed in detail with respect to chain microstructure.

Figure 4 shows the structure of part of a chain of the homogeneous EO copolymer EO-J, as determined using MSLM for first-order Markov modeling of  $^{13}\text{C}$  NMR data [4, 11], taking inversion into account (which is needed to get the full

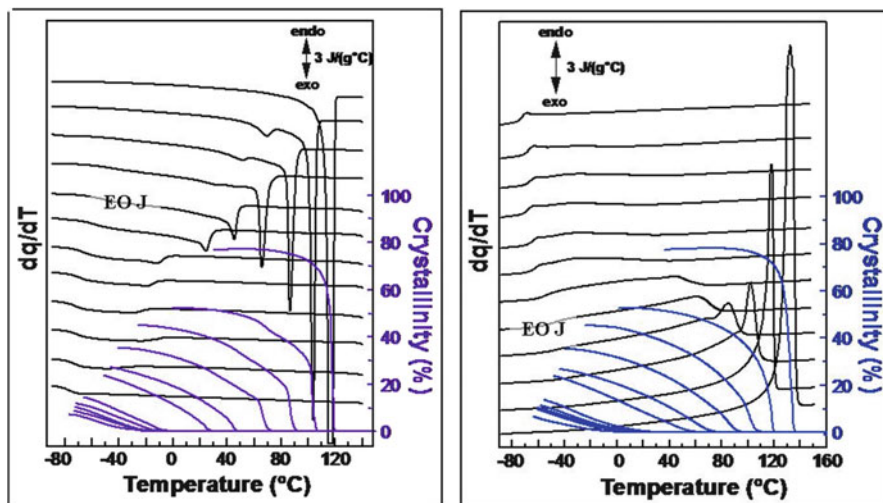


**Fig. 4** Left: Schematics (to be read like a book) of the EO-J (vanadium-based) ethylene-1-octene copolymer with the same types of comonomer units (either normal or inverted 1-octene; filled squares). Symbols as in Fig. 3.  $s_n$  is the number-average sequence length. Right: Normalized sequence length distributions of EO-J for ethylene and 1-octene on the basis of a degenerated terpolymer model. There is a wide distribution in the case of ethylene, up to approximately 50 units, and a very narrow distribution for 1-octene, up to sequences of approximately 4 units. SciTe\_DSM ©. Courtesy of VBF Mathot

picture). Subsequently, the difference between ‘normal’ and ‘inverted’ 1-octenes can be removed and everywhere is changed into ‘1-octenes’, because EO-J has long sequences and inversion does not influence the crystallization behavior. The value of  $r_{E/O}$  is 0.41, so the ‘copolymer’ is between alternating and random. The inversion percentage is approximately 19%, which is not constant but varies with the fraction of 1-octene, reaching 100% for poly(1-octene) alone. Figure 5 gives an overview of DSC cooling and heating curves and the corresponding crystallinity curves [6].

EO-J clearly shows broad crystallization and melting peaks (see Fig. 5), caused by the broadness of the ethylene-sequence-length distribution, as calculated by Monte Carlo simulation (see Sect. 3). DSC studies of a series of 11 samples show cooling and heating (see Fig. 5) results for samples ranging from amorphous to highly crystalline. In Sect. 3, Fig. 11 shows the crystallinity curves for both a series consisting of EO-A with  $x_O = 0.44$  to EO-J with  $x_O = 0.115$  and the series JW-1121 with  $x_O = 0.80$  to the linear polyethylene JW-1114 with  $x_O = 0$ .

Several more examples on EP copolymers can be found in the literature [21–23]. As mentioned before, metallocene-catalyst-based propylene–1-pentene copolymers have also been studied successfully, showing that the statistics of the copolymerization process could be denoted as random because the products  $r_{Pr/Pc}$  of the first-order Markov reactivity ratios were found to be 1.06 and 1.09 for two different metallocene catalysts denoted EI and MBI, respectively [18]. In conclusion, the modeling discussed here, including the application of DPM, can be generalized for all the crystallizable copolymers of interest.



**Fig. 5** *Left*: DSC cooling curves at  $-10^{\circ}\text{C}/\text{min}$  and related crystallinity curves of ethylene-1-octene copolymers. The curves of EO-J are indicated [6]. *Right*: Ditto in subsequent heating at  $10^{\circ}\text{C}/\text{min}$  [6]. SciTe\_KU Leuven-Sofie Vanden Eynde ©. Courtesy of VBF Mathot

In contrast to copolymerization at constant feed, in the case of a batch reaction process when the monomer reactivity ratios are usually not the same, one component is used up more quickly than the other and, thus, the feed composition  $F$  drifts with time. In this case, the comonomer content differs from one chain to another. Such a product is not homogeneous but is an example of a so-called heterogeneous copolymer.

Most commercially available heterogeneous copolymers are produced with multisite Ziegler–Natta catalysts in continuous steady-state processes. The multiple reaction sites of the catalyst produce copolymers of different comonomer contents and different sequence length distributions [7–10, 24–26]. It is also characteristic that the comonomers can influence chain length by increasing the chance of ending the polymerization process, such that the higher the comonomer content, the shorter the chain. For example, two different catalytic sites could lead to two (very) different distributions and, as a result, such heterogeneous copolymers can be regarded as binary blends. This situation was mimicked by a 1:5 mixture of metallocene catalysts 1 and 2, resulting from a semibatch polymerization during which interaction between the two metallocenes was prohibited [19]. Thus, the two catalysts operate independently and simultaneously in dual-site experiments, creating the same copolymers as in single-site experiments. Values of 2.02 and 0.03, respectively, were found for the classical  $r_{E/P}$  products, demonstrating that catalyst 1 produces an almost random sequence of copolymers and catalyst 2 alternating copolymers. Melting temperatures of ethylene-type and propylene-type crystallinity could be attributed to one of the two catalysts, indicating the use of this kind of calculation for analysis of properties.

Comonomer distributions can still be regarded as heterogeneous inside each chain, even for homogeneous copolymers, except for truly random copolymers (zero-order Markov statistics) or alternating copolymers. The extreme cases are gradient copolymers and block copolymers. Their crystallization behaviors combine some features from both random copolymers and heterogeneous copolymers.

Besides the chemical modifications described above, other defects may also be generated during monomer addition, such as regio- and stereo-defects that confer geometric or stereo-isomerism to the copolymer chains. For example, a few head–head additions may join the chain propagation of the dominant head–tail additions of propene units during polymerization, as in the inversion case of EPDMs (vanadium-based). Other causes of sequence defects in polypropylene are stereoisomers, leading to isotactic, syndiotactic, or atactic polypropylenes having totally different crystallizabilities that range from high to zero and result in different properties. Both isotactic and syndiotactic sequences can be regarded as crystallizable, depending on the temperature range and time provided for their crystallization. The hydrogenated polybutadienes (HPBDs) can be regarded as a random copolymer of ethylene and 1-butene, because a few 1,2 additions accompany the dominant 1,4 addition during the polymerization of polybutadienes. In the next sections, the outcomes obtained by applying DPM are used as a key input for the simulations of crystallization and morphology.

### 3 Crystallization with Monomer Segregation

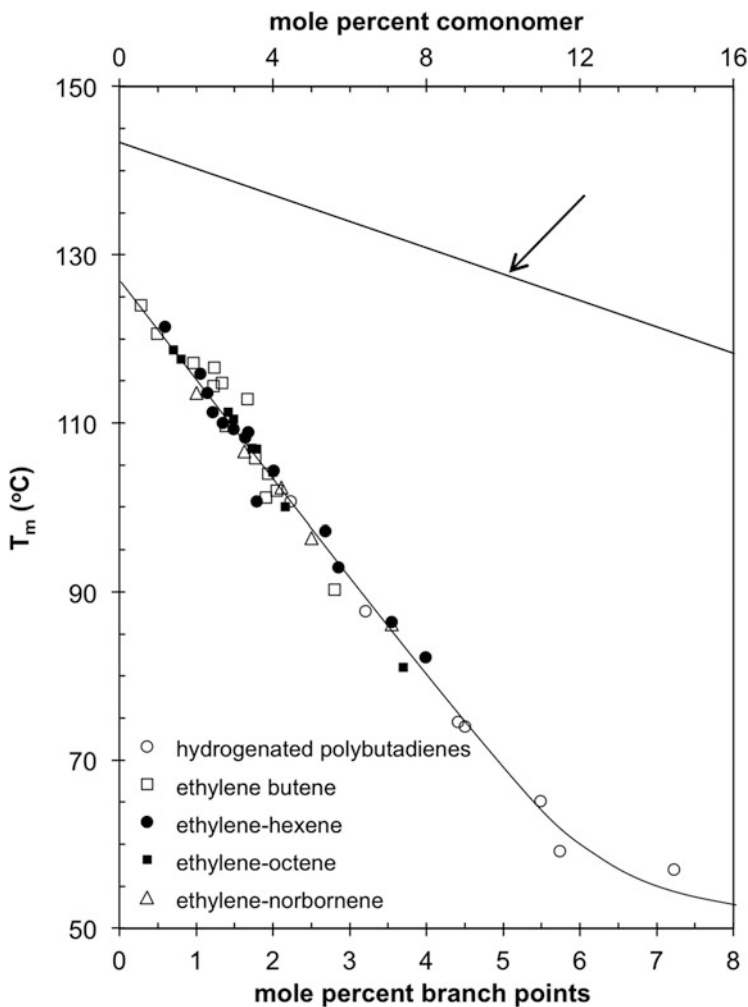
The phase transition from the liquid state to the crystalline state of copolymers can be thermodynamically described on the basis of a two-component system composed of crystallizable A and noncrystallizable B building units of the copolymer. Any theoretical approach to formulation of the equilibrium line as a function of comonomer composition must assume, a priori, the distribution of the components between the two phases. The best-known equilibrium theory is Flory's classical approach, dating back to 1947. In his consideration, comonomer B was completely excluded from the crystalline phase of monomer A. In other words, comonomers are completely segregated from monomers upon crystallization. He treated the crystalline phase of random copolymers as limited by the monomer sequence lengths [27–29]. A terminal-type (first-order Markovian type) of chain growth was considered, and the monomer sequence length was characterized by the crystallizable sequence propagation probability  $P_{AA}$ . For this type of chain, when the crystalline phase remains pure, the equivalence of chemical potentials between the crystalline phase and the amorphous phase gives an equilibrium melting temperature of the copolymer,  $T_m$ , expressed as:

$$\frac{1}{T_m} - \frac{1}{T_m^0} = -\frac{R}{\Delta H_u} \ln P_{AA}, \quad (5)$$

where  $T_m^0$  is the melting temperature of the pure parent homopolymer,  $R$  is the gas constant, and  $\Delta H_u$  is the enthalpy of fusion per repeating unit. This equation gives the very interesting result that the melting temperature of a copolymer does not depend directly on its composition, but rather on the nature of the sequence distribution. The reason for this unique result lies in the chain-like character of polymers. The chemical potential of a unit in the chain, in either state, depends on the sequence distribution rather than on the composition [28–30]. Copolymers are more complex and cannot be treated as simple monomer molecules that contain isolated impurities. We can analyze three different types of sequence distributions in terms of  $x_A$ , the mole fraction of crystallizable units. For an ordered or block copolymer,  $P_{AA} \gg x_A$ . For such copolymers, there is at most a slight decrease in the melting temperature compared with that of the corresponding homopolymer. For an alternating copolymer,  $P_{AA} \ll x_A$  and a drastic reduction in the melting temperature occurs. The prediction that copolymers having the same composition, but constituted in different ways (see Fig. 3), will have drastically different melting temperatures has been amply demonstrated by experimental observation of a wide variety of copolymer types [31–34]. For a truly random copolymer (following zero-order Markov statistics),  $P_{AA} = x_A$  and Eq. (5) becomes:

$$\frac{1}{T_m} - \frac{1}{T_m^0} = -\frac{R}{\Delta H_u} \ln x_A, \quad (6)$$

Coleman found that this treatment for random copolymers is also applicable to stereoisomer-based copolymers [35], and Allegra et al. re-examined this treatment based on conditional probabilities [36]. Many experimental observations follow Eq. (6), without recognition of chemical differences between comonomers, as seen in Fig. 6 for data extracted from early work on ethylene-1-alkene copolymers



**Fig. 6** Melting peak temperatures for rapidly crystallized hydrogenated polybutadienes and metallocene random ethylene copolymers as a function of branching composition. The weight-average molar mass for all is  $90,000 \pm 20,000$  g/mol. Data extracted from similar plots in [7, 37]. The arrow indicates the line calculated on the basis of  $T_m^0 = 418.5$  K and  $\Delta H_u = 970$  cal/mol in Eq. (6). Courtesy of RG Alamo

[7, 37, 38]. When the comonomer content is small, Eq. (6) applies and  $\ln(x_A) = \ln(1-x_B) \approx x_B$ . In Fig. 6, the melting temperatures of rapidly crystallized samples are plotted versus branching content (half comonomer content) for HPBDs. These are models for random ethylene–1-butene copolymers as their synthesis ensures very narrow molar mass, random distribution of ethyl branches, and uniform intermolecular branching composition. Also plotted are copolymers synthesized with a metallocene catalyst, having the most probable molar mass distribution, random sequence distribution, and very narrow comonomer composition distribution. The equilibrium line is also plotted as reference using  $T_m^0 = 418.5$  K and  $\Delta H_u = 970$  cal/mol ( $\Delta H_u = 290$  J/g), drawn from the homopolymer. The deviation of this line from the data points implies the nonideality (for instance, the surface tension) of ethylene-sequence crystals. Fortunately, the data points at small comonomer fractions maintain the linear relationship as expected from Eq. (6). Clearly, there is no significant deviation in the experimental melting temperatures between the different types of copolymers. Even ethylene–norbornenes with a very bulky side group fall on the melting versus composition line of the HPBDs. The conclusion can be made that both types of copolymers must display the same behavior with respect to branch partitioning between crystalline and noncrystalline regions. If the norbornene cannot be accommodated into the crystalline lattice, the ethyl branch must also be rejected from the crystal.

Thus, Flory’s treatment is reasonable for those ethylene-based copolymers with relatively ‘large’ short-chain branches (1-butene, 1-hexene, 1-heptene, 1-octene, etc.) that cannot enter the compact-packing region composed of crystallizable ethylene monomers (denoted as ‘exclusion’). This phenomenon is not only substantiated experimentally in many other works [3, 38–43] but also recently via molecular simulations [44]. An example of the latter is given in Fig. 7, where  $T_m$  values for different copolymers were obtained from the onset of template crystallization on cooling, and the parameter  $E_p/kT_m$  is plotted versus  $\ln x_A$ . A linear relation is obtained, as predicted by Eq. (6).

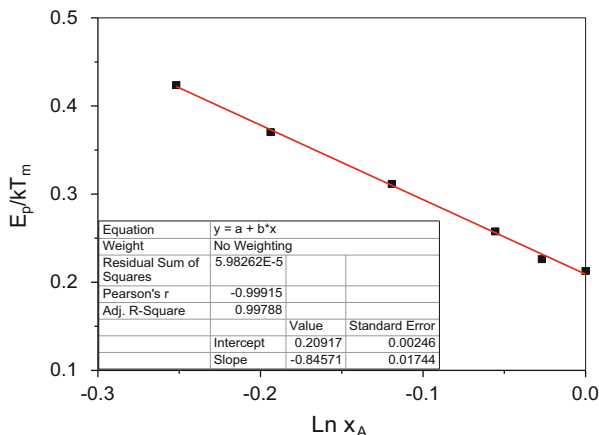
Industrial processing often orients semicrystalline polymers via a strain-induced crystallization process, such as plastic molding, thin-film stretching, or fiber spinning, in order to gain a high mechanical performance. Flory derived the melting point of strained polymers [45], which can be combined with Eq. (6) to predict the melting point of strained random copolymers [46], as given by:

$$\frac{1}{T_{\text{msco}}} = \frac{1}{T_m^0} - \frac{R}{\Delta H_u} [\ln x_A + f(s)], \quad (7)$$

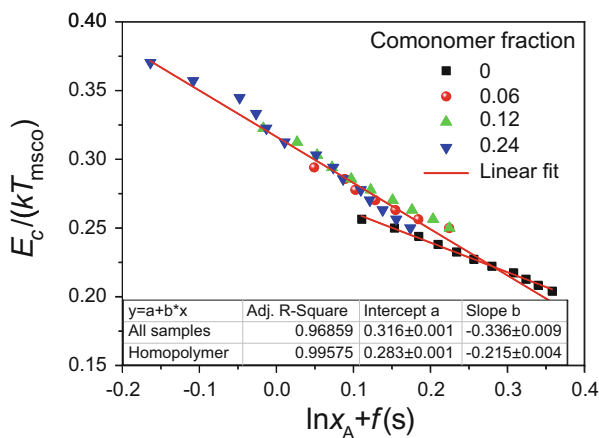
where

$$f(s) = \left(\frac{6}{\pi N}\right)^{1/2} (s+1) - \frac{1}{N} \left(\frac{s^2 + 2s + 1}{2} + \frac{1}{s+1}\right),$$

and  $s$  is the strain of polymers, and  $N$  is the chain length. The combination has been validated by the onset strains in the simulations of strain-induced copolymer crystallization, as demonstrated in Fig. 8 [46].



**Fig. 7** Reciprocal of melting points versus logarithmic mole fraction of monomers, with the data points adopted from the equilibrium melting points in dynamic Monte Carlo simulations of random copolymers [44]. Comonomers were not allowed to slide into the crystalline regions made up of crystallizable monomers. *Straight line* is linear fitting of the data points according to Eq. (6). Courtesy of W-B Hu



**Fig. 8** Inverse melting points ( $E_c$  is the bending energy of bond connection on the chain) versus the sum of logarithmic monomer fraction and strain function for homopolymer and random copolymers with various comonomer mole fractions, as labeled, according to Eq. (7). The *long straight line* results from linear regression with the fitting parameters shown in the *inset table*. The homopolymer data were also fitted for comparison [46]. Courtesy of W-B Hu

Conversely, the methyl branch in ethylene-propylene copolymers can be partially accommodated in the crystallites, as found in early works [47–50]. If comonomers can be included in the crystalline ordered regions composed of crystallizable monomers (denoted as ‘inclusion’), Colson and Eby suggested that



the comonomers homogeneously distributed in the ordered region can be regarded as crystalline lattice defects with excess free energy  $\varepsilon$  [51]. They derived the expression:

$$T_m = T_m^0 \left( 1 - \frac{\varepsilon}{\Delta H_u} x_B \right). \quad (8)$$

Following the initial derivations of Helfand and Lauritzen [52], a more elaborated equation was derived by Sanchez and Eby [53, 54]. The melting temperature of an infinitely thick crystal of a copolymer with an overall mole fraction of B units,  $x_B$ , and a mole fraction of B units in the crystal  $x_C$ , is given as:

$$\frac{1}{T_m^0} - \frac{1}{T_m} = -\frac{R}{\Delta H_u} \left[ \varepsilon \frac{x_C}{RT_m} + (1 - x_C) \ln \left[ \frac{(1 - x_C)}{(1 - x_B)} \right] + x_C \ln \left( \frac{x_C}{x_B} \right) \right]. \quad (9)$$

When  $x_C$  reaches the equilibrium value, it becomes:

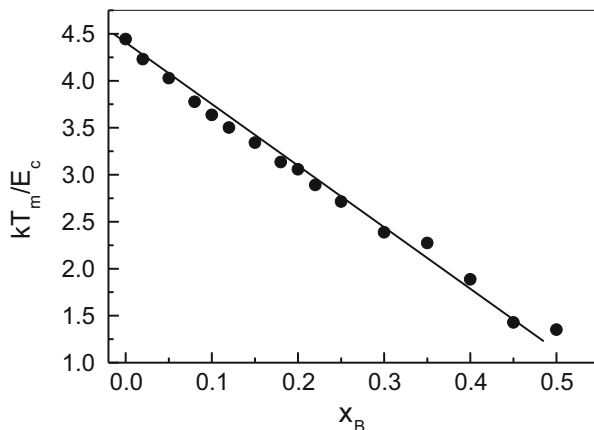
$$x_{\text{eq}} = \frac{x_B e^{-\varepsilon/RT}}{1 - x_B + x_B e^{-\varepsilon/RT}}. \quad (10)$$

For these conditions, the equilibrium melting point of the copolymer becomes:

$$\frac{1}{T_m^0} - \frac{1}{T_m} = \frac{R}{\Delta H_u} \ln \left( 1 - x_B + x_B e^{-\varepsilon/RT} \right). \quad (11)$$

For the case of exclusion, when  $\varepsilon = \infty$ , Eq. (11) reverts to Eq. (6). For uniform inclusion, when  $x_B = x_C$ , Eq. (10) reverts to Eq. (8). This situation implies that the concentration of comonomer inside the crystallites is identical to the comonomer concentration in the copolymer chain, which is a case rarely encountered in ethylene-based random copolymers. The results of Monte Carlo simulations of a hypothetical case of uniform inclusion are consistent with the linearity of Eq. (8) and are shown in Fig. 9 [55]. Moreover, we need to consider that both equilibrium approaches [Eqs. (6) and (8)] predict a linear correlation between  $T_m$  and  $x_B$  for relatively low total  $x_B$ , as those of interest for LLDPE. Therefore, from experimental data showing a decrease in  $T_m$  with an increase in comonomer content, one cannot predict whether the B units are included or rejected from the crystallites. Additional data are required to make a conclusion regarding comonomer partitioning [56–58].

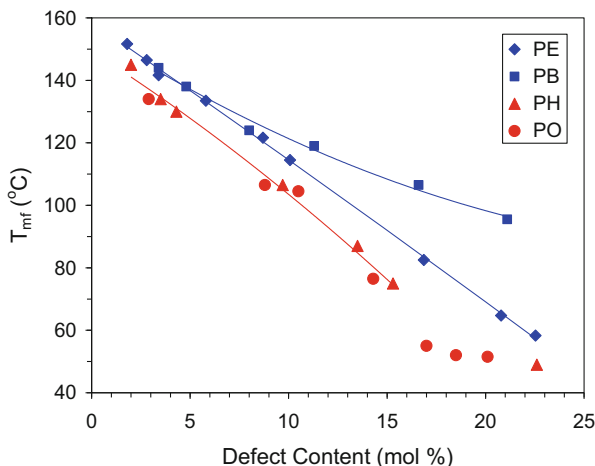
The melting behaviors of a series of random propylene–1-alkene copolymers, synthesized with a single-site metallocene catalyst to ensure narrow intermolecular composition distributions, are also excellent examples of the effect of branch partitioning and of correspondence with the premise of thermodynamic derivations based on exclusion or inclusion of the comonomer units.



**Fig. 9** Reduced melting point versus the mole fraction of comonomer B obtained from dynamic Monte Carlo simulations of bulk random copolymers of 16-mers in a  $16^3$  cubic lattice box. Comonomers are mobile in the crystalline region of monomers.  $E_p/E_c=1$ , where  $E_p$  is the compact-packing energy for two parallel-packed bonds, and  $E_c$  is the bending energy for two consecutively connected bonds on the chain;  $k$  is the Boltzmann constant. The *straight line* is drawn according to Eq. (8) to guide the eye [55]. Courtesy of W-B Hu

A plot of melting temperature versus defect composition is shown in Fig. 10 for sets of propylene-based copolymers with ethylene (PE), 1-butene (PB), 1-hexene (PH) or 1-octene (PO) as co-units [59]. Defects for these copolymers are the comonomers and other stereo- and regio-irregularities in the chain. The groups of both Baer and Galeski investigated the structure–property relationship of homogeneous PH copolymers [60]. De Rosa et al. systematically investigated the influence of chemical and stereo- and regio-defects on the physical properties of propylene-based copolymers [61–63]. For these data, the final melting temperature of the endotherm ( $T_{mf}$ ) was plotted instead of the melting peak because the composition of the melt at  $T_{mf}$  most closely resembles the defect chain composition for any copolymer. Furthermore, plotting  $T_{mf}$  for copolymers with <15 mol% defects also ensures that the melting behavior of the same alpha crystals is comparatively analyzed for these copolymers. The relationship between melting temperature and composition of these copolymers falls into three groups. For participation of the 1-butene comonomer in the crystalline regions at the highest level [64], their crystallizable sequence lengths are the longest among the series for any given comonomer content; hence, they display the highest melting temperatures. The ethylene comonomer also participates in the crystallization [56–58] but at a lesser extent than 1-butene; consequently, lower melting temperatures are observed. PH and PO copolymers with up to ~13 mol% comonomer that are rejected from the crystallites display the lowest melting temperatures, with no difference between these two comonomers [59, 65].

The trends in melting points of propylene–1-alkene copolymers are explained on the basis of phase equilibrium between crystallites of the same crystallographic

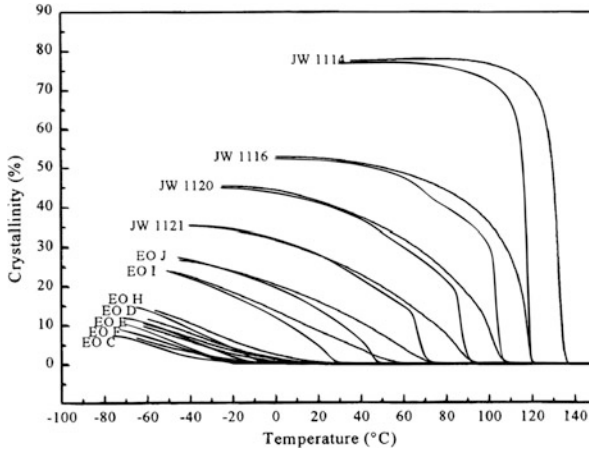


**Fig. 10** Final melting temperature ( $T_{mf}$ ), as determined by DSC for propylene–ethylene (PE), propylene–1-butene (PB), propylene–1-hexene (PH), and propylene–1-octene (PO) copolymers melt-crystallized at 23°C and kept at room temperature for 2 weeks. Lines are drawn to guide interpretation of the experimental data. Re-plotted from published data [59]. Courtesy of RG Alamo

nature and a composition-dependent melt. As a result of rejection from the crystalline lattice, the comonomer composition of the melt coexisting with crystals of PH or PO is richer than the corresponding compositions of PE or PB. Therefore, on equilibrium basis, and in reference to the homopolymer, the melting of PO and PH crystallites is more depressed than the melting of PE or PB.

Thus, DSC measurements are regularly used to observe the crystallization and melting behaviors of statistical copolymers. Figures 5 [6] and 11 [66] demonstrate the experimental observations of cooling and heating curves for the crystallinity of EO copolymers with various comonomer contents. Higher comonomer content results in lower crystallinity as well as lower crystallization and melting temperatures, demonstrating the depression of crystallization as a result of intramolecular chemical confinement of sequence defects.

Dynamic Monte Carlo simulations of lattice-model polymers have reproduced the phenomena above [67]. Three series of statistical copolymers separately representing random copolymers, slightly alternating copolymers, and heterogeneous copolymers with various comonomer contents were considered. In analogy to the copolymerization of ethylene and 1-octene with a vanadium-based Ziegler–Natta catalyst ( $r_1 = 24.7$  and  $r_2 = 0.017$ ) [68], sequence distributions of homogeneous alternating-to-random copolymers resulted from copolymerization via a continuous reaction with constant feed compositions, whereas that of heterogeneous copolymers resulted from a batch reaction with shifting feed compositions. The crystallinity curves upon cooling and heating of random copolymers with

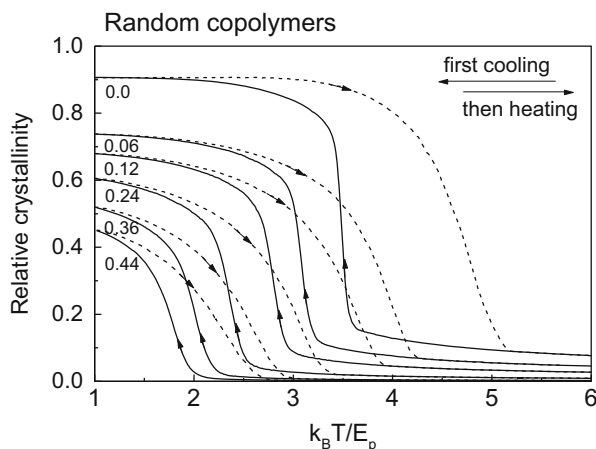


**Fig. 11** Crystallinity curves of a set of ethylene-based copolymers with different comonomer contents from low (JW series) to high (EO series) during cooling and heating processes of DSC scanning at  $10^{\circ}\text{C}/\text{min}$ . Re-plotted from published data [66]. SciTe\_KU Leuven-Sofie Vanden Eynde ©. Courtesy of VBF Mathot

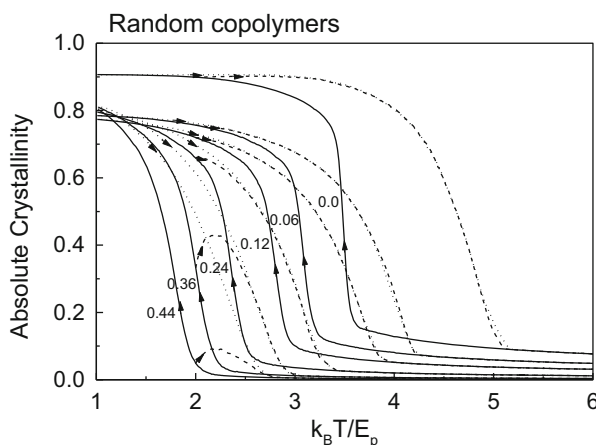
various comonomer contents are shown in Fig. 12, demonstrating the reproduction of experimental observations.

In the temperature-scanning curves shown in Fig. 12, the crystallinity is relative to the fraction of crystalline bonds (characterized by the release of latent heat during melting) in the total amount of monomers (characterized by the monomer mole fractions multiplied by the total sample mass). In principle, the estimation of crystallinity should be based on the total amount of crystallizable bonds of monomers, which is different from the total amount of monomers because of their connections with comonomers. However, the former cannot be accurately estimated experimentally. Thus, in simulations, the absolutely crystallinity was defined by the fraction of crystalline bonds in the total amount of crystallizable monomer bonds. Figure 13 shows the parallel simulation results of absolute crystallinity for comparison with Figs. 11 and 12. An interesting observation is that, although the experimentally defined crystallinity is suppressed by comonomers present, the absolute crystallinity of the copolymers is hardly influenced by the comonomer content. Nearly 80% of crystallizable bonds are eventually transferred into crystalline states at low temperatures. This result implies that crystallization exhausts the local crystallizable bonds, and that the observed depression of crystallinity is mainly a result of our improper but pragmatic definition of relative crystallinity.

The significant hysteresis between heating and cooling curves reflects the nucleation-controlled process of crystallization. If the copolymers are reheated directly from a middle temperature of the cooling process, as demonstrated in Fig. 13, a temporally continuing increase in crystallinity is observed at the beginning of reheating. This is because the crystals can still grow once the nucleation process has been initiated. The homogeneous slightly alternating copolymers



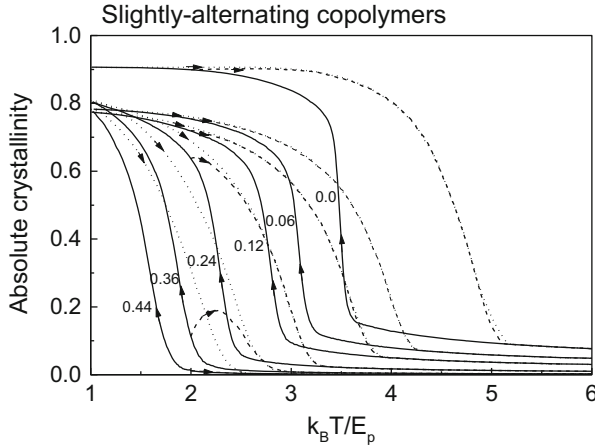
**Fig. 12** Crystallinity curves of a set of homogeneous random copolymers during cooling (*solid lines*) and reheating (*dashed lines*) processes of molecular simulations. The crystalline bonds were defined as those monomer bonds containing more than five parallel neighbors of the same species (which also occurs in the melt, giving positive responses). The comonomer mole fractions are marked below the corresponding curves. The *arrows* show the direction of temperature evolution [67]. Courtesy of W-B Hu



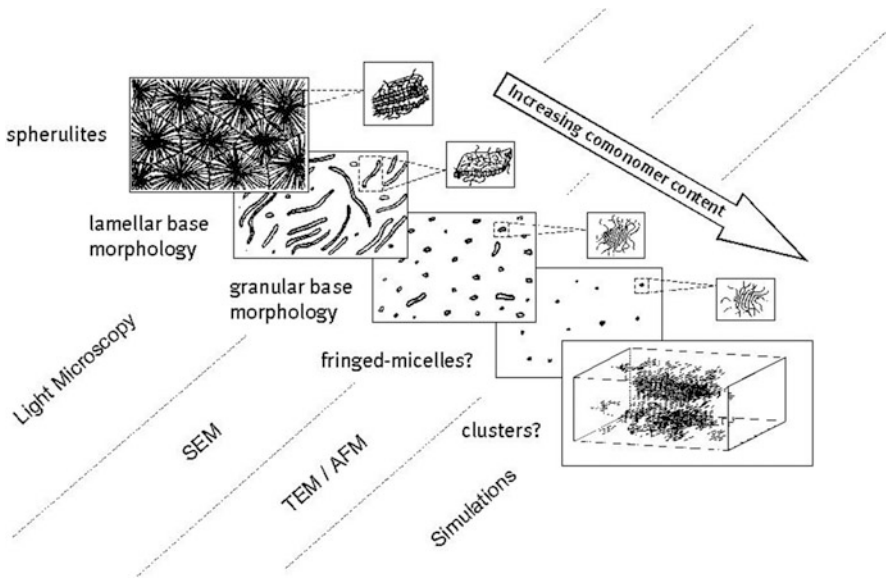
**Fig. 13** Absolute crystallinity curves of a set of homogeneous random copolymers during cooling (*solid lines*) and reheating (*dashed lines*) processes in molecular simulations. The comonomer mole fractions are marked below the corresponding curves. The *arrows* show the direction of temperature evolution [67]. Courtesy of W-B Hu

exhibit similar behaviors to random copolymers (as shown in Fig. 14), indicating the common features of homogeneous copolymers.

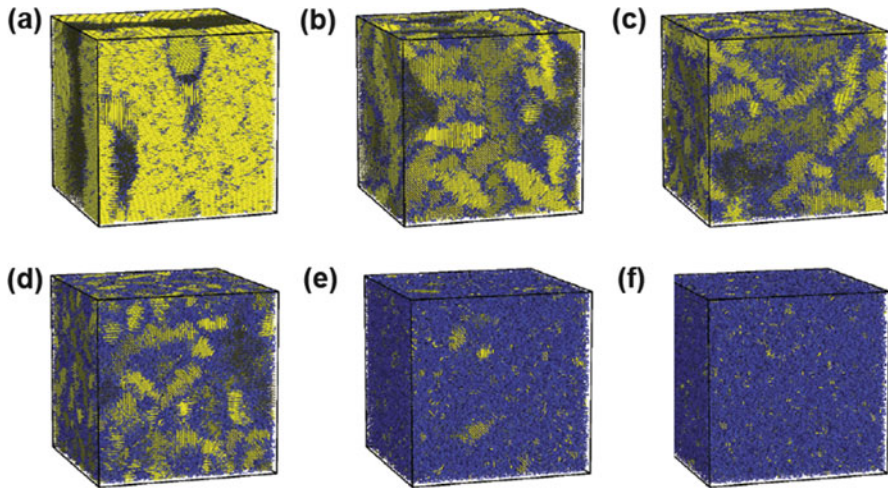
With an increase in comonomer content, crystallite morphologies of homogeneous copolymers fade out dramatically, as schematically illustrated in Fig. 15 [1, 6]. The crystallites decay from spherulites in homopolymers to random stacking



**Fig. 14** Absolute crystallinity curves of a set of slightly alternating copolymers during cooling (*solid lines*) and heating (*dashed and dotted lines*) processes in molecular simulations. The comonomer mole fractions are marked below the corresponding curves. The *arrows* show the direction of temperature evolution [67]. Courtesy of W-B Hu



**Fig. 15** Morphological degeneration of polymer crystals in statistical copolymers with the increase in comonomer content [69]. SciTe\_TU/e-F.G. Karssenberg\_KU Leuven-S. Vanden Eynde ©. Courtesy of VBF Mathot

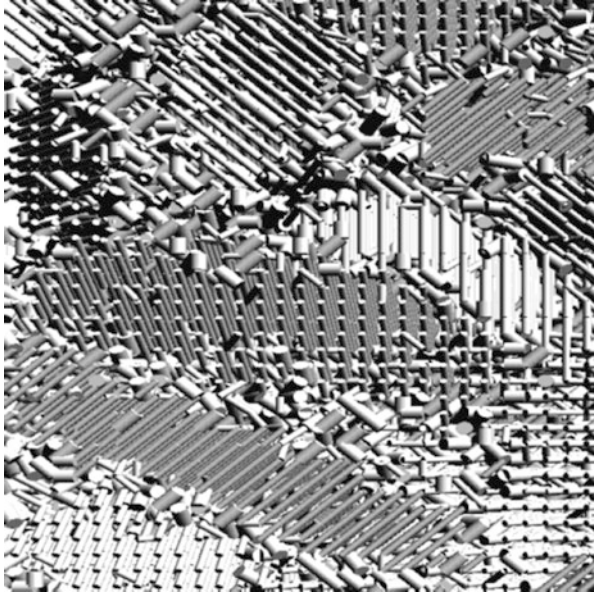


**Fig. 16** Snapshots of a set of homogeneous random copolymers when cooled to a low temperature, as shown in Fig. 12 in molecular simulations. The comonomer mole fractions are (a) 0, (b) 0.06, (c) 0.12, (d) 0.24, (e) 0.36, and (f) 0.44. The amorphous bonds are represented by *blue cylinders*, and the crystalline bonds are represented by *yellow cylinders* [67]. Courtesy of W-B Hu

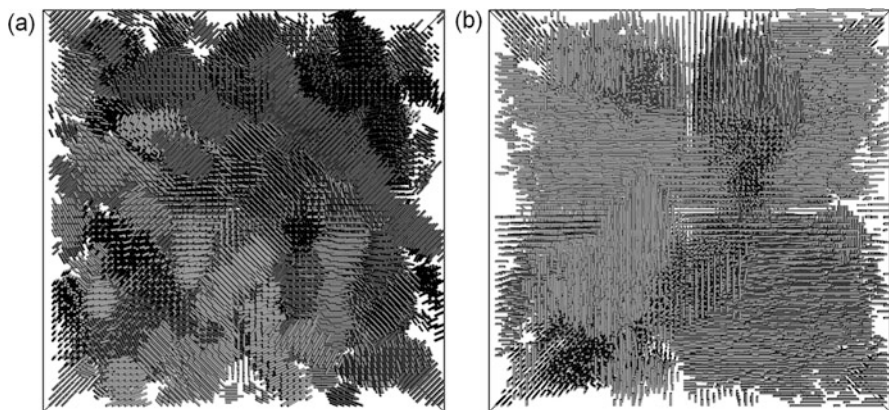
of lamellar crystals, granular crystals (probably progressing to fringed micelles), and eventually unstable clusters of crystalline bonds in an amorphous matrix.

Figure 16 shows snapshots of homogeneous random copolymers obtained after cooling to  $T=1.0$  in the unit of  $E_p/k_B$ , where the crystallization has been saturated in molecular simulations [67]. Even with a comonomer content as low as 0.06, the lamellar thickness of polymer crystals is significantly depressed, demonstrating the effects of chemical confinement of comonomers along the direction of polymer chains. Similar observations also exist for the series of homogeneous slightly alternating copolymers with various comonomer contents. Closer observation of the comonomer distribution in the copolymer matrix reveals comonomers preferring to accumulate at the peripheries of crystals, as demonstrated in Fig. 17. With an increase in comonomer content, the morphology of polymer crystals decays from lamella to granular crystallites. Because the crystallizable bonds are almost completely used by the crystallites at low temperatures, polymer chains trespass several crystallites to make a network in 3D space. In this sense, the crystallites act as physical crosslinking points, which enables homogeneous LLDPE samples with high enough comonomer content to perform as thermoplastic elastomers [70].

In ethylene-based homogeneous copolymers, relatively small comonomers such as propylene residues still have the possibility of entering the crystalline region of ethylene sequences [50]. The ability of comonomer units to slide into the crystalline region determines the effect of chemical confinement along polymer chains, and thus influences the crystallization behaviors as well as crystal morphologies of homogeneous copolymers. In molecular simulations, a comparison of the crystallization morphology of homogeneous random copolymers with or without



**Fig. 17** Zoom-in snapshot of the semicrystalline texture of a slightly alternating copolymer with comonomer content of 0.12 at  $T = 1$ , as shown in Fig. 18. The monomer bonds are drawn as *thin cylinders*, and those bonds containing comonomers are drawn as *double thicker cylinders* [67]. Courtesy of W-B Hu



**Fig. 18** Snapshots of crystallites in homogeneous random copolymers (a) with and (b) without comonomer sliding restrictions in the crystalline regions of monomers prepared by cooling to  $T = 1$ . Only the crystalline bonds are drawn as *small cylinders*. The amorphous part is omitted for clarity. More details can be found in [71]. Courtesy of W-B Hu

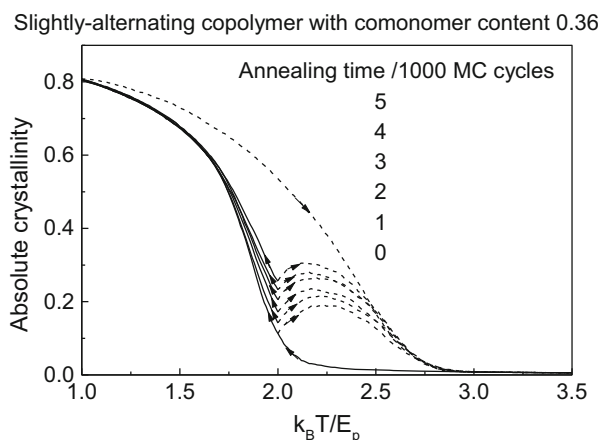
comonomer sliding diffusion restrictions has been made, as shown in Fig. 18 [71]. As a result of removal of chain-sliding restrictions, which weaken the chemical confinement along polymer chains, lamellar crystals can be well developed in



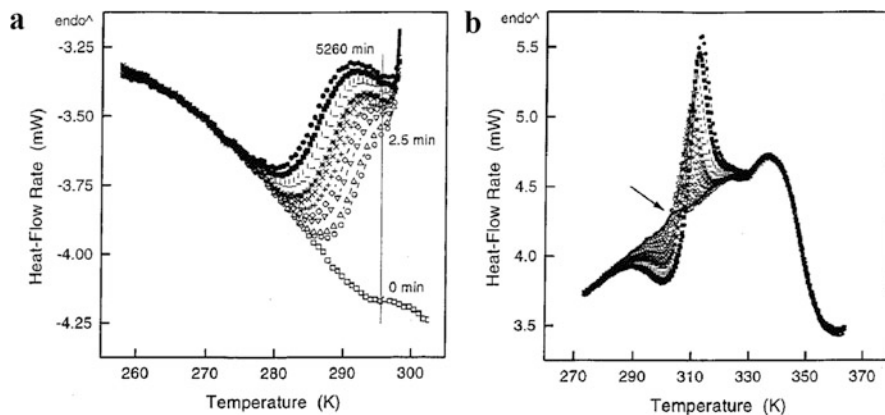
the vertical directions, but crystal growth in lateral directions appears less dominant, as demonstrated in Fig. 18b. If comonomers are able to slide into monomer crystals, the morphology change appears mainly on the thicker lamellar crystals, although not reaching fully extended sequences. The extended-chain crystals of polyethylene can mainly be prepared by crystallization via the hexagonal phase under high pressures [72, 73].

## 4 Crystallization with Monomer-Sequence Segregation

As shown in Figs. 11, 12, 13, and 14, homogeneous copolymers with higher comonomer contents exhibit broader temperature ranges of crystallization and melting. An interesting phenomenon in Figs. 13 and 14 is that, irrespective of the temperature chosen to stop cooling and start the reheating process, the crystallinity curves soon converge to the heating curves starting from the lower temperatures. Similar behavior also exists in the cooling curves for various periods of annealing at a certain crystallization temperature, as demonstrated in Fig. 19. The annealing process raises the crystallinity, the extent depending upon the annealing period (Fig. 19). However, the annealing process disturbs the crystallinity curves on both cooling and heating in the local temperature range. The crystallinity curves merge into each other away from the annealing temperature. Similar annealing experiments were performed by Androsch and Wunderlich in their DSC measurements of EO copolymers, as demonstrated in Fig. 20 [74]. The observations imply that there exists a pair of master curves separately for crystallization on cooling and for



**Fig. 19** Crystallinity curves of slightly alternating copolymers with comonomer content of 0.36 upon cooling and reheating after they had been cooled to  $T = 2.0$  and then annealed at various time periods, as denoted. The arrows show the direction of temperature evolution [67]. Courtesy of W-B Hu

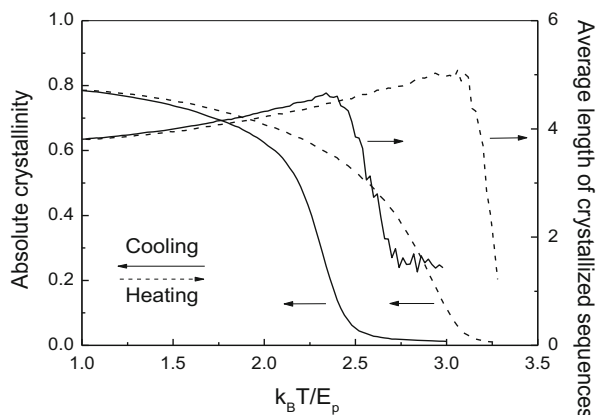


**Fig. 20** DSC scanning curves of (a) cooling and (b) reheating of ethylene-1-octene copolymers after annealing at 296 K for different time periods, as labeled in (a) [74]. Reprinted with the permission of ACS Publisher

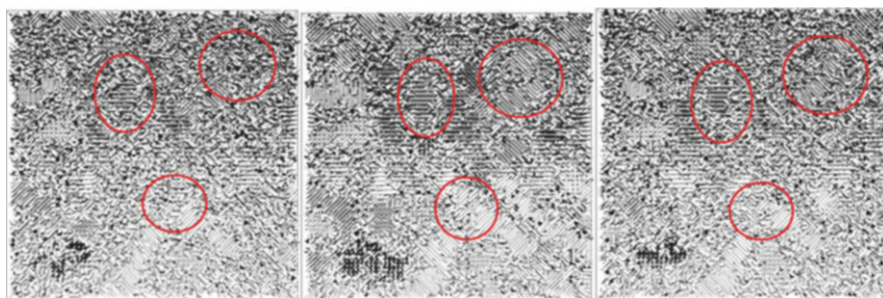
melting on reheating of homogeneous copolymers. In a given temperature range, crystallization of homogeneous copolymers generates crystals with corresponding thermal stability. The amount of generated crystals is limited by the amount of monomer bonds available for crystallization in this temperature range.

The master-curve phenomenon for crystallization and melting of homogeneous copolymers can be attributed to the sequence-length segregation in combination with crystallization at different temperatures. On cooling, longer monomer sequences hold stronger crystallization capability and crystallize in a higher priority. They form thicker crystals at higher temperatures. During reheating, the crystals of longer monomer sequences with larger lamellar thickness formed at higher temperatures also melt at higher temperatures. Therefore, any monomer sequences with specific lengths crystallize and melt in a narrow temperature range, and a wide distribution of sequence lengths results in the master crystallization and melting curves over a broad temperature range. The average lengths of monomer sequences in crystals reflect this kind of partitioning or monomer-sequence segregation during crystallization and melting processes [40, 41]. A simulation example of a slightly alternating EO copolymer with comonomer content of 0.24 during cooling is shown in Fig. 21 [75], demonstrating lower average sequence lengths joining the crystal-line phase at lower temperatures on cooling.

The local crystallization and on-the-spot melting for separation sequence lengths can also be observed from the snapshots shown in Fig. 22 [75]. One can see that the crystallinity obtained at lower temperatures can be mainly attributed to the edges of existing lamellar crystals, instead of forming new individual lamellae. This kind of inserting crystal growth in copolymers has been related to the sequence-length selection in random copolymers [76, 77]. When the temperature is modulated instead of linearly decreasing or increasing, the formation and melting of the crystals at the lamellar edge are reversible, which lead to a high value for the



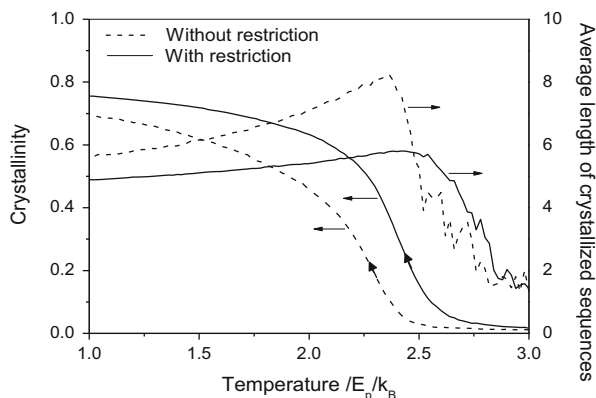
**Fig. 21** The average sequence length in crystals for a slightly alternating ethylene-1-octene copolymer with comonomer content of 0.24 and a hard sliding diffusion restriction during the cooling and reheating process. The sequence length was calculated when more than half of the crystallizable bonds become crystalline (each containing more than five parallel neighbors of the same species). The absolute crystallinity curves on cooling and heating are also shown for parallel simulations [75]. Courtesy of W-B Hu



**Fig. 22** Snapshots of an alternating copolymer with comonomer content of 0.24 during cooling when (a)  $T = 2.3$  and (b)  $T = 1$ ; and followed by heating back to (c)  $T = 2.8$ . The red circles denote the places of crystal growth and melting of short sequences [75]. Courtesy of W-B Hu

reversing heat capacity of random copolymers over a wide temperature range. The high reversing heat capacity has been treated as evidence of reversible melting at the lateral surface of copolymer lamellar crystals by Wunderlich and collaborators [74, 78, 79]. By contrast, for linear polyethylene (LPE) reversible melting was found at the longitudinal surface of the lamellar crystallites, which is facilitated by sliding diffusion occurring smoothly in LPE [80, 81].

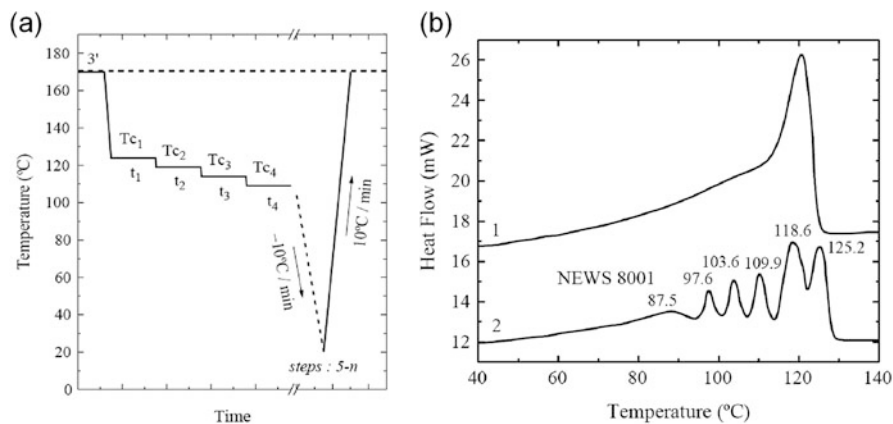
For homogeneous copolymers, a sliding diffusion restriction of comonomers stabilizes the crystal interface slightly, resulting in a slight increase in the melting point of crystallites. By decreasing or removing the comonomer sliding diffusion



**Fig. 23** Crystallinity and average sequence lengths in crystals as a function of temperature on cooling for homogeneous random copolymers with/without (*solid/dashed lines*) comonomer sliding restrictions in the crystalline regions made up of crystallizable monomers. More details can be found in [71]. Courtesy of W-B Hu

restriction and allowing comonomer inclusion into the crystalline phase, the monomer-sequence segregation upon crystallization on cooling can be enhanced, as demonstrated in Fig. 23 [71]. However, at the same time, the crystallization temperature and the obtained crystallinity both decrease. This result is not obvious for the weakened chemical confinement along polymer chains in this case. Probably, allowing the comonomers to slide into crystallites significantly increases the amount of defects in the crystalline region, but it is a relatively time-consuming process that delays crystallization.

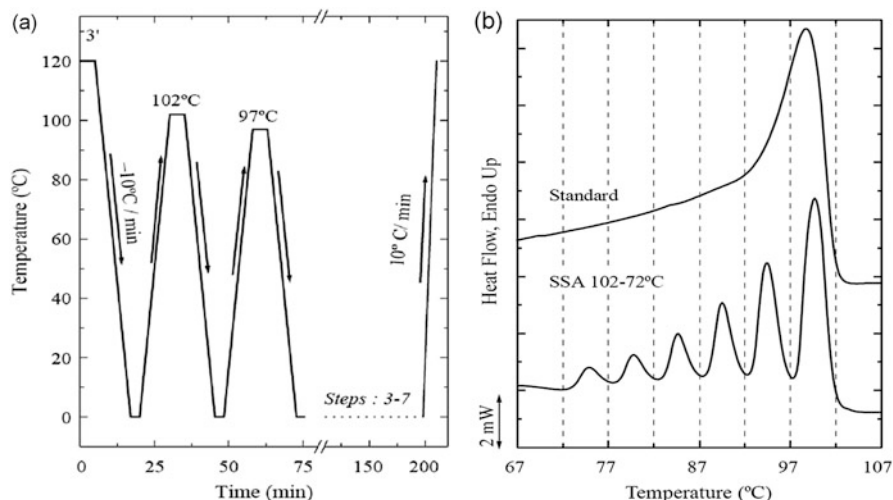
Based on the nature of sequence-length segregation for the master-curve phenomenon of random copolymer crystallization, various fractionation DSC methods have been proposed for characterization of the sequence-length distribution of copolymers [82–84]. The step crystallization method (SC) [85, 86] divides the sample into fractions obtained by isothermal crystallization during stepwise cooling from high to low temperatures, as illustrated in Fig. 24. The fractions differ according to their crystallizability and thus chains are separated according to the presence of segments with those monomer sequence lengths that are capable of crystallization at the isothermal temperature set. The only way to produce high quality thermal fractions by SC is to employ a very long fractionation time (over 1 week), which can induce sample degradation. A much faster and more efficient way to obtain thermally fractionated samples is provided by the successive self-nucleation and annealing method (SSA) [83]. In this thermal fractionation method, successive heating and cooling cycles are applied to promote faster molecular segregation and annealing at each selected fractionation temperature. As a result, ethylene- $\alpha$ -olefin copolymers, for instance, can be fractionated in minutes, depending on the heating/cooling rates employed, and the fractions have better resolution than those obtained by SC (see Fig. 25 and a recent review on SSA [84]). Speeding up of measurement has also been explored and up to 50°C/min have been



**Fig. 24** Illustration of step-crystallization fractionation method that collects the particular sequence length fractions by isothermal crystallization at a series of step-down temperatures. (a) The temperature program for step-crystallization fractionation. (b) Comparison of DSC heating curves for ethylene-1-octene copolymers (4.2% comonomer mole fraction) resulting from step crystallization (2) and from conventional continuous cooling at  $10^{\circ}\text{C}/\text{min}$  (1) [83]. Reprinted with permission from Wiley Publisher

obtained, and even higher rates with HPer DSC and Flash DSC. These fractionation methods are based on the crystallization capabilities of sequence lengths and can also be applied to compare differences in comonomer distributions of heterogeneous copolymers.

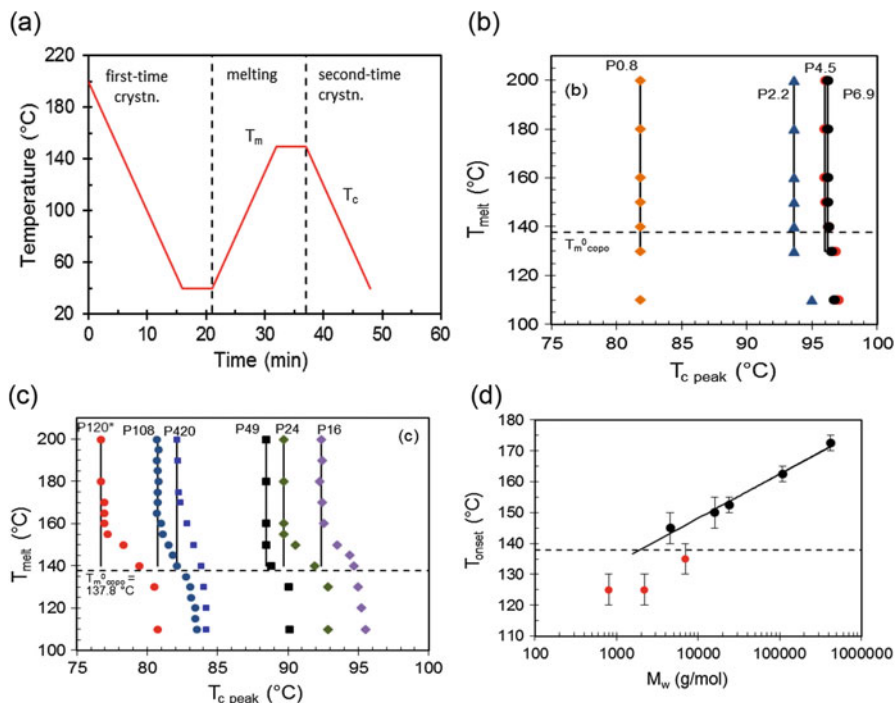
Crystallization temperatures of polymers on cooling usually depend on their thermal history, such as the presence of crystalline residues, foreign surfaces for nucleation, oriented segments, or less entangled melt [87–91]. Memory of crystallization in the melt can raise the subsequent crystallization temperature, increase the crystallization rate, decrease the crystal sizes, and even change the crystalline lattice [92–95]. Such memory effects are typically erased by annealing of polymers above their equilibrium melting points. Recently, the strong memory effects of crystallization in homogeneous copolymers with relatively low comonomer content were observed, even when the annealing temperature was above the equilibrium melting point of the copolymers [96]. Illustrated in Fig. 26 are data for HPBDs that are models for random ethylene–1-butene (EB) copolymers. A series of HPBDs with a fixed content of ethyl branches of  $\sim 2.2$  mol% and molar masses ranging from 800 to 420,000 g/mol were studied [96]. These samples were first cooled from  $200^{\circ}\text{C}$  to  $40^{\circ}\text{C}$  at a rate of  $10^{\circ}\text{C}/\text{min}$  to develop a standard crystalline state. Then, the samples were heated to different annealing temperatures ( $T_{\text{melt}}$ ) for 5 min. The second-round crystallization temperatures ( $T_{\text{c,peak}}$ ) on DSC cooling curves were compared to test for the memory effect of crystallization (see Fig. 26a). For low molar mass samples,  $T_{\text{c,peak}}$  is independent of  $T_{\text{melt}}$ ; hence, no memory effect can be observed above the equilibrium melting point (Fig. 26b). However, as shown in Fig. 26c, a strong memory effect is observed for copolymers of high molar mass,



**Fig. 25** Illustration of successive self-nucleation and annealing (SSA) fractionation method that collects the particular sequence-length fractions by avoiding primary nucleation upon isothermal crystallization of that sequence length. (a) The temperature program for successive self-nucleation and annealing fractionations. (b) Comparison of DSC heating curves for hydrogenated 1,4-butadiene polymer resulting from the SSA method and conventional continuous cooling [83]. Reprinted with permission from Wiley Publisher

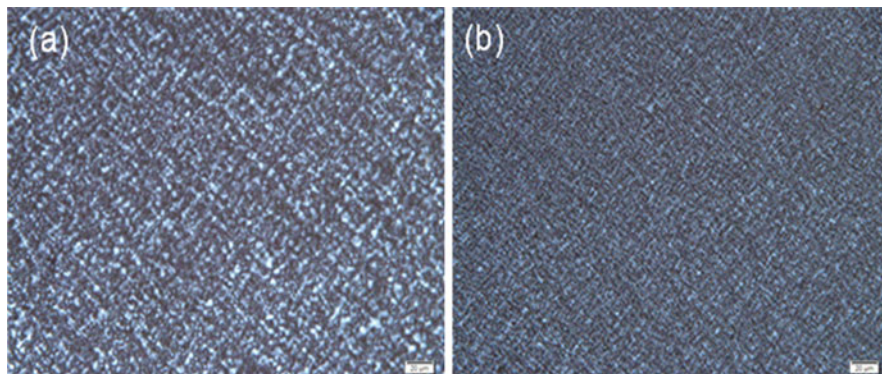
even when the annealing temperatures are above the equilibrium melting point. The onset of melt memory ( $T_{\text{onset}}$ ) is the highest annealing temperature for which a subsequent crystallization is enhanced. The strength of the melt memory of ethylene copolymers is measured by the difference between  $T_{\text{onset}}$  and the equilibrium melting temperature of the copolymer. The latter can be calculated according to Eq. (6).  $T_{\text{onset}}$  is plotted versus the weight-average molar mass in Fig. 26d, giving a critical molar mass of about 1,311 g/mol for such a strong memory effect. This threshold length for preventing strong melt memory is coincidentally the critical entanglement molecular weight for polyethylene [97–99].

The strong crystallization memory in the melt observed in model HPBDs is a general feature of random ethylene copolymers. Ethylene–1-alkene copolymers synthesized with a single-site metallocene catalyst display the same self-nucleation features as observed in HPBDs. The increase in nucleation density as a result of melt memory is dramatic, as illustrated by the polarized optical micrographs in Fig. 27. As seen in Fig. 28, a plot of the difference between  $T_{\text{onset}}$  and the equilibrium melting point against branching content of the copolymer shows a parabolic-shaped curve with a maximum at ~2 mol%. The seeds that speed up the crystallization disappear at temperatures about or below the equilibrium melting point for copolymers with low branching and for copolymers with comonomer contents above ~4.5 mol% [96, 100].

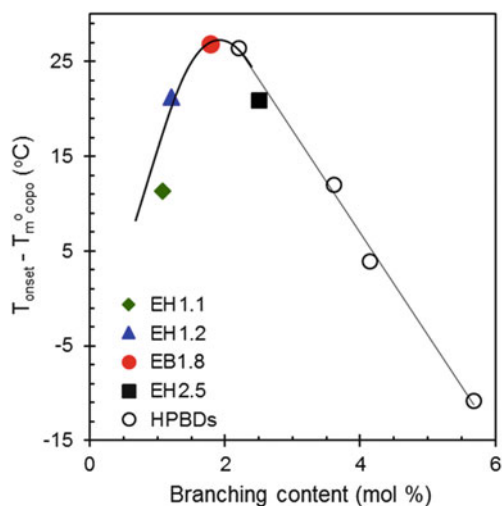


**Fig. 26** (a) Temperature program for study of the memory effect of crystallization in homogeneous random copolymers. (b) Crystallization temperature ( $T_{c\ peak}$ ) versus annealing temperature ( $T_{melt}$ ) for low molar mass hydrogenated polybutadienes with 2.2 mol% ethyl branches in the second-time crystallization. (c) Same as (b) for high molar mass samples. (d) Plot of upper-limit annealing temperatures ( $T_{onset}$ ) for the memory effect of crystallization in hydrogenated polybutadienes of differing molar mass (weight-averaged). The dashed line indicates the equilibrium melting point of these copolymers following Eq. (6) (137.8°C) [96]. Courtesy of RG Alamo

The strong molar mass effect for melt memory, and the weakening of melt memory with increasing comonomer content, eventually vanishing for copolymers that develop low levels of crystallinity, point to a self-nucleation phenomenon, as shown schematically in Fig. 29. For annealing temperatures between the equilibrium melting point and  $T_{onset}$ , the copolymer melt is heterogeneous. Here, seeds remain as a memory of the crystalline sequence partitioning to form the initial crystallites. Because residues of ordered structures are not observed by polarized optical microscopy or in the X-ray diffraction patterns of melts between  $T_{onset}$  and  $T_{m\ copo}^0$ , the seeds are associated with long ethylene sequences that, albeit molten, remain in close proximity and are unable to diffuse quickly to the randomized melt. These seeds speed up subsequent crystallization from such heterogeneous melts because the critical initial step of monomer sequence partitioning is partially bypassed.



**Fig. 27** Polarized optical micrographs of model ethylene 1-butene copolymer P108: (a) Morphology from a homogeneous melt,  $T_{\text{melt}} = 200^\circ\text{C}$ , (b) morphology from a heterogeneous melt,  $T_{\text{melt}} = 150^\circ\text{C}$ . The scale bars represent  $20\ \mu\text{m}$  [100]. Courtesy of RG Alamo

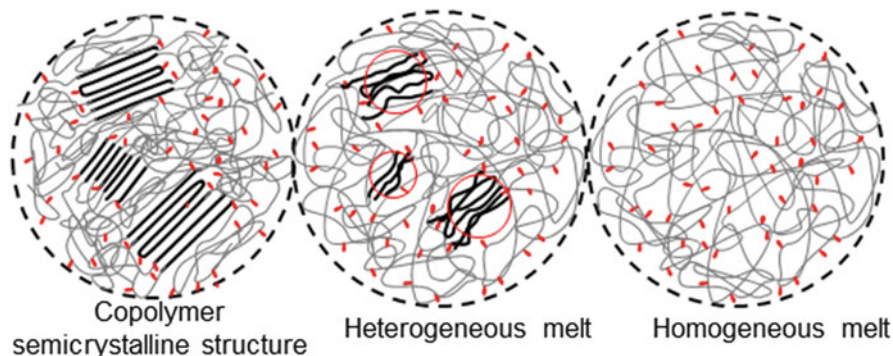


**Fig. 28** Plot of difference between onset temperature for melt memory and equilibrium melting temperature against branching content of narrow ethylene-1-alkene copolymers and hydrogenated polybutadienes (HPBDs) [100]. Courtesy of RG Alamo

Conversely, the melts above  $T_{\text{onset}}$  are homogeneous because all crystalline sequences randomize quickly when reaching these annealing temperatures. Crystallization from homogeneous melts is independent of the annealing temperature and is relatively slow as a result of the much lower number of nuclei.  $T_{\text{onset}}$ , the critical temperature for melt memory, is well defined and easy to obtain experimentally, as shown in Fig. 26.

The stability and extent of melt memory above the equilibrium melting point has been proven to be a function of the initial level of crystallinity, and is explained by a





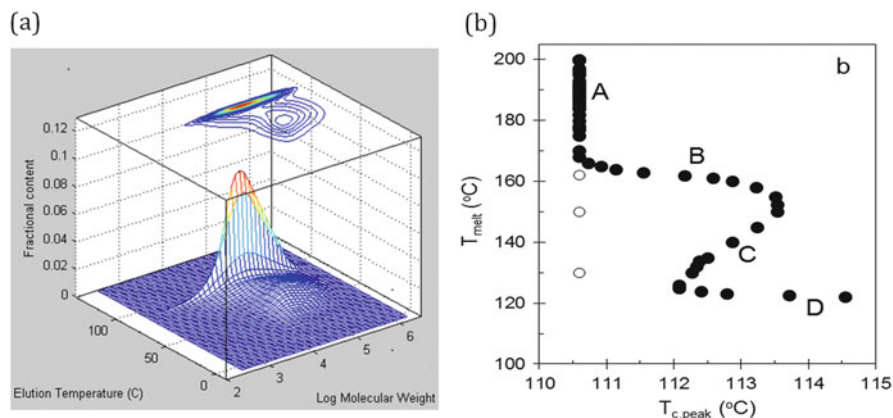
**Fig. 29** Schematics of the copolymer crystalline structure (*left*), the heterogeneous melt with self-seeds (*center*), and homogeneous melt free of self-seeds (*right*) [96]. Courtesy of RG Alamo

progressive increase in the entangled topology of the intercrystalline regions of the copolymer during evolution of the semicrystalline structure [101]. There is a threshold level of crystallinity for which melt memory can be observed. This is explained as the need to develop sufficient constraints in the intercrystalline regions in the process of dragging crystalline sequences to the crystal front. These constraints may slow down diffusion of long ethylene sequences, thus preventing dissolution of self-seeds [101].

The strong memory effects of crystallization in homogeneous random copolymers were confirmed by dynamic Monte Carlo simulations under parallel temperature programs [44]. De Gennes once pointed out that homogeneous random copolymers may undergo weak segregation in the case of very large Flory–Huggins interaction parameters [102]. In principle, owing to the sequence-length segregation, the melting of large crystals of homogeneous random copolymers generates local regions rich in long monomer sequences, as evidenced in molecular simulations [44]. In consequence, the local equilibrium melting point is increased, which brings a larger supercooling for the initiation of crystallization on cooling, appearing as a strong memory effect above the equilibrium melting points of the original homogeneous melts. Short copolymer chains do not hold sufficient long monomer sequences for such a crystallization-enhanced segregation as well as the strong memory effect. The same is true for high comonomer contents.

## 5 Crystallization with Macromolecular Segregation

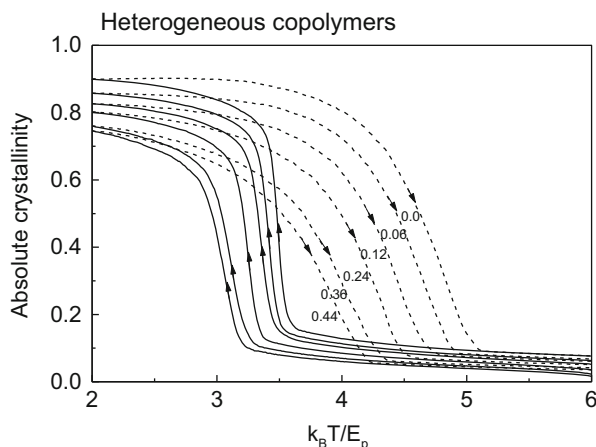
In comparison with homogeneous random copolymers, where only the molar mass distribution is a factor in changing properties at a fixed comonomer content, heterogeneous copolymers exhibit two parallel distributions: molar mass distribution and comonomer content across the molar mass distribution (termed bivariate distribution). The crystallization of heterogeneous copolymers depends on the



**Fig. 30** (a) Three-dimensional bivariate distribution for commercial broad ethylene–1-hexene copolymer with average branching content of 1.66 mol%. (b) Temperature of the initial melt ( $T_{\text{melt}}$ ) versus crystallization peak temperature ( $T_{\text{c,peak}}$ ). *Closed circles* correspond to  $T_{\text{melt}}$  approached from below. *Open circles*,  $T_{\text{melt}}$  is approached from above. Regions A, B, C, and D correspond to regions of different melt structures. The melt undergoes liquid–liquid phase separation in region C [100]. Courtesy of RG Alamo

breadth of the comonomer distribution and the nature of the bivariate (i.e., whether mono- or bimodal) [25, 26]. It has been experimentally demonstrated that ethylene copolymers with broad bimodal distributions and with contents of 1-hexene comonomer changing from 1 to 14 mol% across the molar mass distribution display an interplay between the strong memory effect of crystallization and liquid–liquid phase separation (LLPS) at relatively high temperatures [100, 103]. This phenomenon is illustrated in Fig. 30 for a commercial broad ethylene–1-hexene copolymer. Bringing the reference crystalline structure to temperatures of 170 °C or higher, subsequent crystallization gives constant  $T_{\text{c,peak}}$  because the crystallization takes place from a one-phase homogeneous melt that is free of self-seeds. For  $T_{\text{melt}}$  of 170 °C to ~150 °C, the crystallization peak increases as a result of remaining self-seeds, akin to the behavior of narrowly distributed copolymers. For  $T_{\text{melt}}$  of 150 °C down to 125 °C,  $T_{\text{c,peak}}$  decreases, denoting an inversion in the crystallization rate. The inversion in the rate demarcates the onset of a self-seed-assisted LLPS between comonomer-rich and comonomer-poor macromolecules. The crystallization rate decreases in this range of  $T_{\text{melt}}$  because the number of self-seeds decreases. A fraction of the seeds dissolve as a result of the strong thermodynamic driving force to diffuse macromolecules to each liquid phase domain in order to equilibrate the composition of the two phases. The overall crystalline morphology changes accordingly, as documented by polarized optical microscopy in samples cooled from different melt structures [100]. The comonomer-rich domains that develop when cooling from a two-phase melt structure were identified by TEM as having a diameter of about 0.5  $\mu\text{m}$  [100].

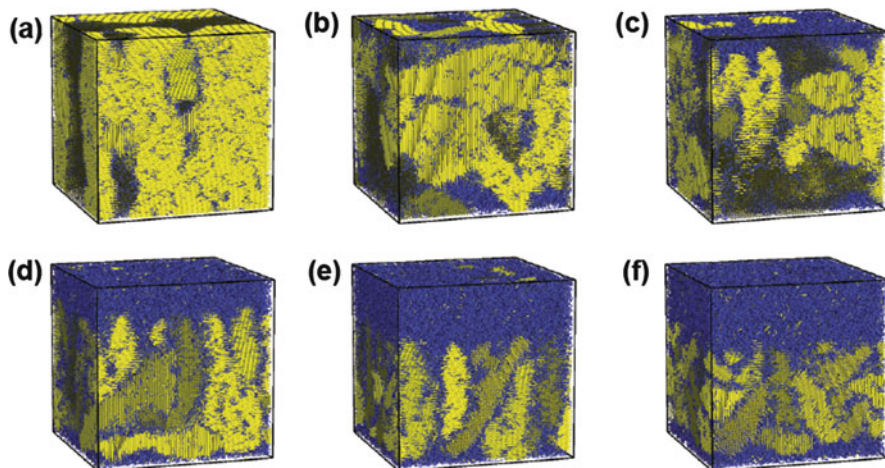
The low branching of the high molar mass molecules present in classical Ziegler–Natta heterogeneous copolymers means that their crystallization and



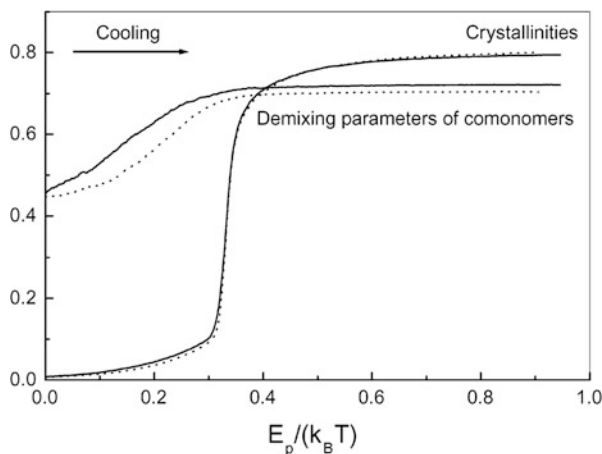
**Fig. 31** Absolute crystallinity curves for a set of heterogeneous copolymers with various comonomer mole fractions, as labeled, during cooling (*solid lines*) and reheating (*dashed lines*) processes. The *arrows* show the direction of temperature scanning [67]. Courtesy of W-B Hu

melting temperatures do not appear to be very sensitive to the average comonomer content [24, 104]. This insensitivity of crystallization rate to the average comonomer content in heterogeneous copolymers has been observed in both experiments [105–108] and simulations [67], as demonstrated in Fig. 31 for the simulation results of temperature scans in comparison to the parallel results for homogeneous copolymers in Fig. 14. In addition, one can see that with the increase in comonomer content, heterogeneous copolymers display lower absolute crystallinity.

These features of heterogeneous copolymers – in contrast to those of homogeneous random copolymers – can be attributed to macromolecular segregation prior to crystallization. In simulations, the preparation of heterogeneous copolymers results in extreme diversity of comonomer content among the molecules present, much like a binary blend with one component containing few comonomers with high crystallization capability and another containing many comonomers with very limited crystallization capability. Figure 32 demonstrates the prior phase separation that results in crystals accumulated in a local region [67]. More clearly, the temperature evolution of demixing parameters of comonomers (average occupation fraction of monomers around each comonomer) demonstrates prior phase separation at high temperatures before crystallization, as shown in Fig. 33. Because crystallization of heterogeneous copolymer takes place in the separated phase, the crystallization and melting temperatures as well as the crystal morphologies of a heterogeneous copolymer are less sensitive to comonomer content than those of homogeneous random and slightly alternating copolymers. Prior phase separation has also been observed by small-angle neutron-scattering experiments on heterogeneous LLDPE samples and blends [109–111]. Transmission electron microscopy (TEM) has made distinct semicrystalline domains (CSDs) visible [112], composed

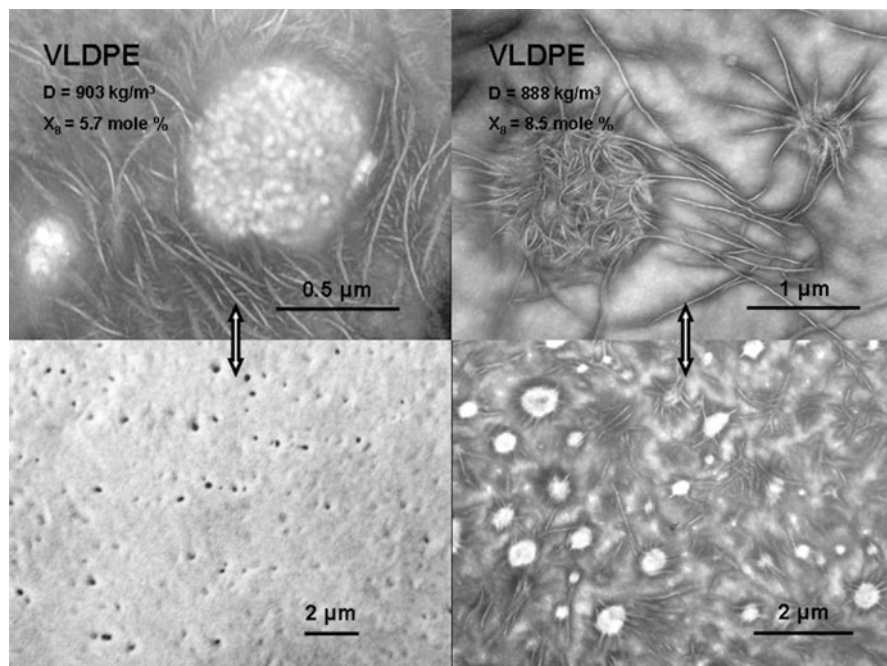


**Fig. 32** Snapshots of a set of heterogeneous random copolymers with various comonomer contents when cooled to  $T=2$  in Fig. 31 of simulations. The comonomer mole fractions are separately (a) 0, (b) 0.06, (c) 0.12, (d) 0.24, (e) 0.36, and (f) 0.44. The amorphous bonds are represented by *blue cylinders*, and the crystalline bonds are represented by *yellow cylinders* [67]. Courtesy of W-B Hu



**Fig. 33** Cooling curves of absolute crystallinity and demixing parameters of comonomers for a heterogeneous copolymer with comonomer mole fraction of 0.36 with (*solid lines*) and without (*dotted lines*) the hard restriction of sliding diffusion of comonomers in the crystalline regions [67]. Courtesy of W-B Hu

of the least branched molecules in heterogeneous VLDPEs, irrespective of whether the most branched molecules form a matrix (Fig. 34, right) or are dispersed (Fig. 34, left). This implies a (massive) segregation on a macromolecular scale. It is striking that when the CSDs are made up of the least branched molecules (see Fig. 34 right),



**Fig. 34** *Bottom left*: SEM image of a VLDPE (5.7 mol% of 1-octene) after extraction with xylene at room temperature to remove the most branched molecules, revealing their dispersed, low-crystalline or amorphous nature within the matrix of mainly the least branched (well-crystallized, up to HDPE type) molecules. *Top left*: TEM image of (bulked-fixed/stained by means of chlorosulfonation in the vapor phase) ultrathin sections of the same VLDPE showing the dispersed phase and surrounding long and thick lamellae with shorter and thinner lamellae crystallized on the longer ones. *Bottom right*: Compact semicrystalline domains (CSDs) of another VLDPE (8.5 mol% of 1-octene) made up of the least-branched molecules (up to HDPE-type) in a low-crystalline matrix of the most-branched molecules. *Top right*: CSDs made visible by a more severe fixation/staining treatment are connected by single lamellae. From [112]. SciTe\_DSM-R. Deblieck ©. Courtesy of VBF Mathot

they are connected by single lamellae – segregation on a much smaller scale – and thus a network is established. Heterogeneous copolymers therefore provide us with a good model of polymer blends to study the interplay between polymer crystallization and LLPS [113].

Even if the mixing interactions between monomers and comonomers are athermal, the different crystallizability of comonomer-rich and comonomer-poor macromolecules alone results in phase separation prior to crystallization. This conclusion was achieved by the development of classical lattice thermodynamic theory of polymer solutions to include the consideration of polymer crystallization [114]. The mixing free energy of binary polymer blends is given by [115]:

$$\begin{aligned} \frac{\Delta F_{\text{mix}}}{kT} &= n_1 \ln \varphi_1 + n_2 \ln \varphi_2 \\ &+ \varphi_1 r_2 n_2 \left[ (q-2) \frac{B_{12}}{kT} + \left(1 - \frac{2}{q}\right) \left(1 - \frac{1}{r_2}\right)^2 \frac{E_p}{kT} \right], \end{aligned} \quad (12)$$

where  $n_1$  and  $n_2$  are the number of moles of two component polymers,  $\varphi_1$  and  $\varphi_2$  are their corresponding volume fractions,  $r_2$  is the chain length of crystallizable polymers,  $q$  is the coordination number of the regular lattice, and  $B_{12}$  is the mixing interaction of two component monomers. One can see that because the mixing entropy of the two polymers in the first two terms is relatively small, even with  $B_{12} = 0$ , the crystallizability of the second component holding  $E_p$  still makes the mixing free energy remain positive (i.e., the polymers are immiscible). In practice, this principle explains the incompatibility of isotactic polypropylene (PP) with either atactic or syndiotactic PP in the melt. Near the equilibrium melting point, the strong thermal fluctuations of crystalline ordering also enhance LLPS in the binary blends [116]. On the other hand, the interfaces of two incompatible polymers facilitate crystal nucleation [117]. The interplay between LLPS and polymer crystallization brings us rich information to understand better the complex phase transition behaviors of multicomponent polymer systems [2].

In heterogeneous copolymers, besides the two components with extreme high and low comonomer contents, the intermediate component with intermediate comonomer content also plays an important role in tuning the mechanical performance of copolymer materials [101]. One commercial example is high-impact polypropylene, as PP toughened by in-situ blending with ethylene-propylene copolymers and HDPE [118–120]. The intermediate component can be analyzed and extracted by methods such as temperature rising elution fractionation (TREF) and crystallization analysis fractionation (CRYSTAF) [121, 122] but is best achieved through cross-fractionation schemes [123, 124]. These fractionation methods are based on the differences in molar mass and/or crystallizability in solvents of the various components present. Interactive liquid chromatography has been recently developed to characterize the crystalline and noncrystalline components of homogeneous and heterogeneous copolymers [124–127].

In simulations [128], the reactivity ratios can be changed to generate heterogeneous copolymers containing a significant amount of intermediate components. The intermediate component mainly acts as an amphiphile between the two extreme components, which enhances their compatibility at the interfaces, because of its richness in both monomers and comonomers in sequences. With prior phase separation, crystallization of copolymers takes place in the monomer-rich domain surrounded by the matrix of more comonomers. The presence of intermediate components allows networking of crystallites in the amorphous matrix, which provides toughness for such types of heterogeneous copolymers [119, 121]. Unlike traditional amphiphiles, that contain only two blocks, the intermediate component contains many short sequences of monomers or comonomers, which is more similar to multiblock amphiphilic copolymers.

For the extreme case of intramolecular-heterogeneous but homogeneous copolymers (e.g., diblock copolymers), microphase separation on the length scale of monomer sequences competes with crystallization on cooling [129]. The pre-existing microdomains of diblock copolymers bring a spatial nanoconfinement effect to the crystallization behavior of monomer sequences, which is another interesting issue, and whose simulation progress has been recently reviewed [130].

## 6 Summary

An overview is presented of our current understanding of the complex crystallization and melting behaviors of both homogeneous and heterogeneous statistical copolymers, in combination with possible segregation of components. The statistical nature of copolymerization and related distributions of monomers and comonomers and their sequence lengths (as determined by modeling of the complete  $^{13}\text{C}$  NMR spectrum) is the starting point of the discussion. These parameters are missing links in the understanding of crystallization behavior, which is why they are a necessary input for subsequent extensive Monte Carlo simulations of the crystallization, melting, and component-segregation phenomena of statistical copolymers. The impact of (co)monomer segregation on copolymer crystallization can be classified into three length scales for chain microstructures: monomer segregation, monomer-sequence segregation, and macromolecular segregation. The former two mainly occur in homogeneous copolymers and the latter mainly in heterogeneous copolymers. Such segregations are of direct relevance for crystallization because they can give rise to unique phenomena such as strong memory effects on copolymer crystallization. In addition, we have briefly discussed (cross) fractionation using methods such as TREF, CRYSTAF, and (TREF-)SEC-HPer DSC to characterize the microstructure features of heterogeneous copolymers, and thermal fractionation methods such as step-crystallization and SSA to characterize the microstructure features of homogeneous copolymers. The interplay between polymer crystallization and component segregation at various length scales provides us with a clear clue to understanding the complex phase transition behaviors of both intramolecular and intermolecular multicomponent copolymer systems.

**Acknowledgement** We appreciated the helpful discussion with Professor Alejandro J. Müller at the University of the Basque Country UPV/EHU, Spain. Financial support from the National Natural Science Foundation of China (NO. 21274061 and 21474050) and the Program for Changjiang Scholars and Innovative Research Team in University is appreciated. RGA acknowledges funding from the USA National Science Foundation under grant No. DMR1105129.

## References

1. Karssenberg FG (2005) Chain microstructures of homogeneous olefin copolymers and characteristics of single site catalysis. Thesis Technische Universiteit Eindhoven. doi:10.6100/IR591592
2. Hu W-B (2013) Polymer physics: a molecular approach. Springer, Wien
3. Mathot VBF (1994) Chapter 5: Thermal characterization of states of matter, pp. 105-167; Chapter 9: The crystallization and melting region, pp. 231-299. In: Mathot VBF (ed) Calorimetry and thermal analysis of polymers. Hanser, Munich, pp 231-299
4. Mathot VBF, Scherrenberg RL, Pijpers TFJ, Engelen YMT (1996) New trends in polyolefin science and technology. Research Signpost, Trivandrum, pp 71-95
5. Mathot VBF, Scherrenberg RL, Pijpers TFJ (1998) Polymer 39:4541-4559
6. Vanden Eynde S. (1999) Homogeneous ethylene-1-alkene copolymers: a study of the crystallization and melting behavior at ambient and elevated pressures. Thesis Katholieke Universiteit Leuven, pp 1-178
7. Alamo RG, Mandelkern L (1994) Thermochim Acta 238:155-201
8. Ring W, Mita I, Jenkins AD, Bikales NM (1985) Pure Appl Chem 57:1427-1440
9. Coote ML, Davis TP (1999) Prog Polym Sci 24:1217-1251
10. Mathot VBF (1984) Molecular structure of LLDPE. In: Polycon '84-LDPE Papers and Proceedings, The Plastics and Rubber Institute, Chameleon, London, pp 1-15
11. Mathot VBF, Fabrie CM, Tiemersma-Thoone GPJM, van der Velden GPM (1985) In: Proceedings of the international rubber conference, Kyoto, Japan, pp 334-340
12. Mathot VBF, Fabrie CM (1990) J Polym Sci Part B Polym Phys 28:2487-2507
13. Mathot VBF, Fabrie CM, Tiemersma-Thoone GPJM, van der Velden GPM (1990) J Polym Sci Part B Polym Phys 28:1-15
14. Karssenberg FG, Mathot VBF, Zwartkruis TJG (2006) J Polym Sci Part B Polym Phys 44:722-737
15. Randall JC (1977) Polymer sequence determination, carbon-13 NMR method. Academic, New York
16. Wunderlich B (1980) Macromolecular physics, vol. 3: crystal melting. Academic, New York, p 225
17. Adriaensens PJ, Gelan FG, Karssenberg JM, Mathot VBF (2003) Polymer 44:3483-3489
18. Karssenberg FG, Karssenberg FG, Joubert DJ, Assumption HJ, Mathot VBF (2005) Reactivity ratios of metallocene catalysts in copolymerizations of propene and 1-pentene, Chapter 8. In: Karssenberg FG (ed) Chain microstructures of homogeneous olefin copolymers and characteristics of single site catalysis. Thesis Technische Universiteit Eindhoven. doi: 10.6100/IR591592
19. Piel C, Karssenberg FG, Kaminski W, Mathot VBF (2005) Macromolecules 38:6789-6795
20. Karssenberg FG, Mathot VBF (2006) J Polym Sci Part B Polym Phys 44:738-746
21. Hopf A, Kaminsky W, Karssenberg FG, Mathot VBF, Piel C (2005) Macromol Theory Simul 14:289-290
22. Karssenberg FG, Piel C, Hopf A, Mathot VBF, Kaminsky W (2005) Macromol Theory Simul 14:295-299
23. Karssenberg FG, Piel C, Hopf A, Mathot VBF, Kaminsky W (2006) J Polym Sci Part B Polym Phys 44:747-755
24. Alamo RG, Blanco JA, Agarwal P, Randall JC (2003) Macromolecules 36:1559-1571
25. Vadlamudi M, Subramanian G, Shanbhag S, Alamo RG, Varma-Nair M, Fiscus DM, Brown GM, Lu C, Ruff CJ (2009) Macromol Symp 282:1-13
26. Vadlamudi M, Alamo RG, Fiscus DM, Varma-Nair M (2009) J Therm Anal Calorim 96:697-704
27. Flory PJ (1947) J Chem Phys 15:684
28. Flory PJ (1949) J Chem Phys 17:223-240
29. Flory PJ (1955) Trans Faraday Soc 51:848-857



30. Baker CH, Mandelkern L (1966) *Polymer* 7:7–21
31. Casey HK, Elston CT, Phibbs MK (1964) *J Polym Sci Polym Lett Ed* 2:1053–1056
32. Bastien IJ, Ford RW, Mark HD (1966) *J Polym Sci Polym Lett Ed* 4:147–150
33. Alamo RG, Domszy K, Mandelkern L (1984) *J Phys Chem* 88:6587–6595
34. Hosoda KS (1988) *Polym J* 20:383–397
35. Coleman BD (1958) *J Polym Sci* 31:155–164
36. Allegra LG, Marchessault RH, Bloembergen S (1992) *J Polym Sci Polym Phys Ed* 30:809–815
37. Isasi JR, Haigh JA, Graham JT, Mandelkern L, Alamo RG (2000) *Polymer* 41:8813–8823
38. Chen H-Y, Chum SP, Hiltner A, Baer E (2001) *J Polym Sci Polym Phys Ed* 39:1578–1593
39. Alamo RG, Mandelkern L (1989) *Macromolecules* 22:1273–1277
40. Alamo RG, Chan EKM, Mandelkern L, Voigt-Martin IG (1992) *Macromolecules* 25:6381
41. Alamo RG, Viers BD, Mandelkern L (1993) *Macromolecules* 26:5740–5747
42. Bensason S, Minick J, Moet A, Chum SP, Hiltner A, Baer E (1996) *J Polym Sci* 34:1301–1315
43. Alizadeh A, Richardson L, Xu J, McCartney S, Marand H, Cheung YW, Chum S (1999) *Macromolecules* 32:6221–6235
44. Gao H-H, Vadlamudi M, Alamo RG, Hu W-B (2013) *Macromolecules* 46:6498–6506
45. Flory PJ (1947) *J Chem Phys* 15:397–408
46. Nie Y-J, Gao H-H, Wu Y-X, Hu W-B (2014) *Soft Matter* 10:343–347
47. Richardson MJ, Flory PJ, Jackson JB (1963) *Polymer* 4:221–236
48. Baker CH, Mandelkern L (1966) *Polymer* 7:71–83
49. Ver Strate G, Wilchinsky ZW (1971) *J Polym Sci Part A-2* 9:127–142
50. Ruiz de Ballesteros O, Auriemma F, Guerra G, Corradini P (1996) *Macromolecules* 29:7141–7148
51. Colson JP, Eby RK (1966) *J Appl Phys* 37:3511–3514
52. Helfand E, Lauritzen JI (1973) *Macromolecules* 6:631–638
53. Sanchez IC, Eby RK (1973) *J Res Nat Bur Stand Sec A* 73:353
54. Sanchez IC, Eby RK (1975) *Macromolecules* 8:638–641
55. Hu W-B (2000) *J Chem Phys* 113:3901–3908
56. Vander Hart DL, Alamo RG, Nyden MR, Kim MH, Mandelkern L (2000) *Macromolecules* 33:6078–6093
57. Alamo RG, VanderHart DL, Nyden MR, Mandelkern L (2000) *Macromolecules* 33:6094–6105
58. Clas S-D, McFaddin DC, Russell KE, Scammel-Bullock MV, Peat IR (1987) *J Polym Sci Polym Chem* 25:3105
59. Jeon K, Palza H, Quijada R, Alamo RG (2009) *Polymer* 50:832–844
60. Poon B, Rogunova M, Hiltner A, Baer E, Chum SP, Galeski A, Piorowska E (2005) *Macromolecules* 38:1232–1243
61. De Rosa C, Dello Iacono S, Auriemma F (2006) *Macromolecules* 39:6098–6109
62. De Rosa C, Auriemma F, Ruiz de Ballesteros O, Resconi L, Camurati I (2007) *Macromolecules* 40:6600–6616
63. De Rosa C, Auriemma F, Ruiz de Ballesteros O, Resconi L, Camurati I (2007) *Chem Mater* 19:5122–5130
64. Ruiz-Orta C, Alamo RG (2012) *Polymer* 53:810–822
65. Ruiz-Orta C, Fernandez-Blazquez JP, Pereira EJ, Alamo RG (2011) *Polymer* 52:2856–2868
66. Vanden Eynde S, Mathot VBF, Koch MHJ, Reynaers H (2000) *Polymer* 41:4889–4900
67. Hu W-B, Mathot VBF, Frenkel D (2003) *Macromolecules* 36:2165–2175
68. Madkour TM, Goderis B, Mathot VBF, Reynaers H (2002) *Polymer* 43:2897–2908
69. Litvinov VM, Mathot VBF (2002) *Solid State Nucl Magn Reson* 22:218–234
70. Bensason S, Stephanov EV, Chum S, Hiltner A, Baer E (1997) *Macromolecules* 30:2436–2444
71. Hu W-B, Karssenbergh FG, Mathot VBF (2006) *Polymer* 47:5582–5587
72. Vanden Eynde S, Rastogi S, Mathot VBF (2000) *Macromolecules* 33:9696–9704

73. Vanden Eynde S, Mathot VBF, Hoehne GWH, Schawe JWK, Reynaers H (2000) *Polymer* 41:3411–3423
74. Androsch R, Wunderlich B (1999) *Macromolecules* 32:7238–7247
75. Hu W-B, Mathot VBF (2004) *Macromolecules* 37:673–675
76. Strobl GR, Engelke T, Meier H, Urban G, Zachmann HG, Hosemann R, Mathot VBF (1982) *Colloid Polym Sci* 260:394–403
77. Strobl G (2007) *The physics of polymers*. Springer, Berlin/Hedelberg, p 208
78. Androsch R, Wunderlich B (2000) *Macromolecules* 33:9076–9089
79. Wunderlich B (2003) *Thermochim Acta* 396:33–41
80. Hu W-B, Albrecht T, Strobl G (1999) *Macromolecules* 32:7548–7554
81. Goderis B, Reynaers H, Scherrenberg R, Mathot VBF, Koch MHJ (2001) *Macromolecules* 34:1779–1787
82. Starck P (1996) *Polym Int* 40:111–122
83. Müller AJ, Arnal ML (2005) *Prog Polym Sci* 30:559–603
84. Müller AJ, Michell RM, Pérez RA, Lorenzo AT (2015) *Eur Polym J* 65:132–154
85. Chen F, Shanks RA, Amarasinghe G (2004) *Polym Int* 53:1795–1805
86. Keating MY, McCord EF (1994) *Thermochim Acta* 243:129–145
87. Mamun A, Umemoto S, Okui N, Ishihara N (2007) *Macromolecules* 40:6296–6303
88. Xu J-J, Ma Y, Hu W-B, Rehahn M, Reiter G (2009) *Nat Mater* 8:348–353
89. Martins JA, Zhang W, Brito AM (2010) *Polymer* 51:4185–4194
90. Lorenzo AT, Arnal ML, Sanchez JJ, Muller AJ (2006) *J Polym Sci Part B Polym Phys* 44:1738–1750
91. Zhang Y-S, Zhong L-W, Yang S, Liang D-H, Chen E-Q (2012) *Polymer* 53:3621–3628
92. Maus A, Hempel E, Thurn-Albrecht T, Saalwaechter K (2007) *Eur Phys J E Soft Matter Biol Phys* 23:91–101
93. Khanna YP, Kumar R, Reimschuessel AC (1988) *Polym Eng Sci* 28:1607–1611
94. Cho K, Saheb DN, Choi J, Yang H (2002) *Polymer* 43:1407–1416
95. Cho K, Saheb DN, Yang HC, Kang BI, Kim J, Lee SS (2003) *Polymer* 44:4053–4059
96. Reid BO, Vadlamudi M, Mamun A, Janani H, Gao H-H, Hu W-B, Alamo RG (2013) *Macromolecules* 46:6485–6497
97. Litvinov VM, Ries ME, Baughman TW, Henke A, Matloka PP (2013) *Macromolecules* 46:541–547
98. Ries ME, Brereton MG, Ward IM, Cail JI, Stepto RFT (2002) *Macromolecules* 35:5665–5669
99. Graessley WW (1982) *Adv Polym Sci* 47:67–117
100. Mamun A, Chen X, Alamo RG (2014) *Macromolecules* 47:7958–7970
101. Chen X, Mamun A, Alamo RG (2015) *Macromol Chem Phys* 216:1220–1226
102. de Gennes PG (2003) *Macromol Symp* 191:7–10
103. Ren M, Chen X, Sang Y, Alamo RG (2015) *Macromolecular Symposia* 356:131–141
104. Alamo RG (2004) *Macromol Symp* 213:303
105. Krigas T, Carella J, Struglinski M, Crist B, Graessley WW, Schilling FC (1985) *J Polym Sci Polym Phys Ed* 23:509–520
106. Mirabella FM, Westphal SP, Fernando PL, Ford EA, Williams JG (2005) *J Polym Sci Part B Polym Phys* 26:1995–2005
107. Kim MH, Phillips PJ (1998) *J Appl Polym Sci* 70:1893–1905
108. Gelfer MY, Winter HH (1999) *Macromolecules* 32:8974–8981
109. Wignall GD, Alamo RG, Ritchson EJ, Mandelkern L, Schwahn D (2001) *Macromolecules* 34:8160–8165
110. Alamo RG, Londono JD, Mandelkern L, Stehling FC, Wignall GD (1994) *Macromolecules* 27:411–417
111. Alamo RG, Graessley WW, Krishnamoorti R, Lohse DJ, Londono JD, Mandelkern L, Stehling FC, Wignall GD (1997) *Macromolecules* 30:561–566
112. Deblieck RAC, Mathot VBF (2001) *J Mater Sci Lett* 34:1779–1787

113. Wang H, Shimizu K, Kim H, Hobbie EK, Wang Z-G, Han CC (2002) *J Chem Phys* 116:7311–7315
114. Hu W-B, Frenkel D (2005) *Adv Polym Sci* 191:1–35
115. Hu W-B, Mathot VBF (2003) *J Chem Phys* 119:10953
116. Ma Y, Hu W-B, Wang H (2007) *Phys Rev E* 76:031801
117. Ma Y, Zha L-Y, Hu W-B, Reiter G, Han CC (2008) *Phys Rev E* 77:061801
118. Fu Z, Fan Z, Zhang Y, Feng L (2003) *Eur Polym J* 39:795–804
119. Chen R-F, Shangguan Y-G, Zhang C-H, Chen F, Harkin-Jone E, Zheng Q (2011) *Polymer* 52:2956–2963
120. Zhang CH, Chen RF, Shangguan YG, Zheng Q (2011) *Chinese J Polym Sci* 29:497–505
121. Wild L (1990) *Adv Polym Sci* 98:1–47
122. Xu J-T, Feng L-X (2000) *Eur Polym J* 36:867–878
123. Cheruthazhekatt S, Pijpers TFJ, Harding GW, Mathot VBF, Pasch H (2012) *Macromolecules* 45:5866–5880
124. Cheruthazhekatt S, Pijpers TFJ, Harding GW, Mathot VBF, Pasch H (2012) *Macromolecules* 45:2025–2034
125. Macko T, Brüll R, Alamo RG, Thomann Y, Grumel V (2009) *Polymer* 50:5443–5448
126. Macko T, Brüll R, Alamo RG, Stadler FJ, Losio S (2011) *Anal Bioanal Chem* 399:1547–1556
127. Lee D, Shan CLP, Meunier DM, Lyons JW, Cong R, de Groot AW (2014) *Anal Chem* 86:8649–8656
128. Yang F, Gao H-H, Hu W-B (2012) *J Mat Res* 27:1383–1388
129. Ma Y, Li C, Cai T, Li J, Hu W-B (2011) *J Phys Chem B* 115:8853–8857
130. Zha L-Y, Hu W-B (2016) *Prog Polym Sci* 54–55:232–258

# Molecular View of Properties of Random Copolymers of Isotactic Polypropylene

**Finizia Auriemma, Claudio De Rosa, Rocco Di Girolamo, Anna Malafronte, Miriam Scoti, and Claudia Cioce**

**Abstract** The yield behavior during uniaxial drawing of isotactic random copolymers of propene with ethylene (iPPeEt), 1-butene (iPPBu), 1-pentene (iPPPe), 1-hexene (iPPHe), and 1-octadecene (iPPOc) is analyzed within the framework of our current understanding of deformation properties of semicrystalline polymers, that is, the intrinsic stability of lamellar crystals and related polymorphism phenomena, along with the ability of entangled amorphous chains to transmit stress. The samples selected for analysis were synthesized using single-site metalorganic catalysts, are highly stereoregular, and contain small amounts of regiodefects caused by secondary 2,1 erythro units. Moreover, the interchain and intrachain distribution of comonomeric units is uniform. In the case of iPPeEt copolymers, samples containing  $\approx 3.5$  mol% stereodefects were also studied. The yield behavior of these samples depends on the kind and concentration of defects, and is directly related to the level of inclusion in and exclusion from crystals of the comonomeric units. Apart from iPPBu copolymer samples with high butene content, the yield stress of all samples increases with the thickness of lamellar crystals according to a common trend, regardless of comonomer. In the case of iPPBu copolymers containing a high concentration of butene units, the yield stress decreases with increasing lamellar thickness. The increase in yield stress with lamellar thickness is rationalized in terms of the micromechanical model of crystallographic slips, based on thermal activation of screw dislocations. The parameters of the model describing the yield behavior are the critical free energy required to form a screw dislocation and the shear modulus associated with the slip planes of the dislocations. These were set as identical to those deduced for isotactic polypropylene homopolymer samples (iPP) crystallized under different conditions. Study of the yield behavior of

---

F. Auriemma (✉), C. De Rosa, R. Di Girolamo, A. Malafronte, M. Scoti, and C. Cioce  
Dipartimento di Scienze Chimiche, Complesso Monte Sant' Angelo, via Cintia, 80126 Naples,  
Italy  
e-mail: [finizia.auriemma@unina.it](mailto:finizia.auriemma@unina.it)

these copolymers extends the use of the dislocation model to a set of samples crystallized under similar conditions but characterized by differences in comonomeric unit, degree of crystallinity, lamellar thickness, polymorphism, and intrinsic flexibility of the chain backbone. The results indicate that for a homogeneous class of propene-based copolymers, namely crystallized in the  $\alpha$ -form of iPP under similar conditions, lamellar thickness controls the level of plastic resistance provided that the concentration of structural irregularities in the crystals is not too high. iPPBu copolymers with high comonomer concentration do not obey this rule because of the high level of inclusion of comonomers in the crystals, which induces an increase in lamellar thickness but also a decrease in crystal stability.

**Keywords** Random copolymers • Yield behavior • Crystallographic slip process • Dislocation model • Polymorphism

## Contents

1	Introduction .....	46
2	Experimental Details .....	53
3	Structural Analysis and Thermal Behavior .....	59
4	Mechanical Properties .....	73
5	Concluding Remarks .....	84
	References .....	85

## 1 Introduction

The uniaxial deformation of semicrystalline polymers having spherulitic or lamellar morphology transforms an initially isotropic material into oriented fibers. In semicrystalline polymers, the complex interwoven structure of amorphous and crystalline phases that are tightly intermingled [1] entails that the deformation process is complex [2, 3, 4, 5–9]. Deformation involves movement of atoms or groups of atoms, both in the crystalline and amorphous phase, in a cascade of events over different length scales. These range from the length scale of monomeric units, unit cells, and coils to the thickness of lamellar crystals, assembly of lamellae in stacks separated by amorphous phase, and spherulites [5, 7, 10–19]. The movements follow a common scheme during uniaxial stretching and involve both elastic (reversible) deformation and plastic (permanent) deformation as a result of viscous flow activated by the stress field [3, 5–7, 20, 21].

At low strains, the stress increases linearly and the polymer sample responds to the applied strain elastically, obeying Hooke's law [22]. The main mechanisms behind the Hooke regime of deformation occurring at the subnanometric length scale are the deformation of covalent bonds and valence angles, librational motion of internal rotation angles, and reversible deformation of unit cell axes [22, 25]. By

releasing the tension, the sample recovers its initial shape and dimensions. The proportionality constant between stress and strain is the Young's modulus, which depends mainly on the intrinsic flexibility of the chains and the volume fraction of the crystalline phase [22–24].

With further increase in strain, the stress within the polymer increases to reach the yield point. The high mobility achieved at the yield point initiates plastic (irreversible) deformation in the material, at a rate equal to the applied strain rate. After yielding, strain softening takes place, leading to strain localization and subsequent necking. From now on, plastic deformation dominates until break [5, 7, 26, 27].

The molecular mechanisms involved at yield and during plastic deformation up to the break point depend on the deformation rate, temperature, and crystallization conditions of the sample [5, 7, 27, 28]. Possible mechanisms associated with yielding behavior and plastic deformation of a polymer are partial melting and recrystallization [29, 30], thermal activation of screw dislocations with the Burgers vector parallel to the chain axis [6, 8, 14–19, 25, 31, 32], cavitation, and micronecking [3, 20, 21].

The concept that yielding and successive plastic deformation are the result of strain-induced melting of crystals followed by recrystallization into new crystals in adiabatic conditions (mechanical melting) was suggested by Yoon and Flory [29] on the basis of speculative considerations and not on experiments. According to this concept, the melting of initially unoriented crystals followed by recrystallization of the molten material into new crystals with a predominant chain orientation induced by strain is the thermodynamic driving force for plastic deformation, because it would allow reduction of the local stress level during drawing. Although this mechanism can explain the decrease in thickness and lateral dimensions of lamellar crystals during drawing, and the high degree of orientation achieved in a fiber, it does not account for the yielding process. Indeed, only after yielding does the stress-induced melting–recrystallization mechanism play some role in the plastic flow of a polymer [5–7]. The new crystals may either correspond to the same polymorph initially present in the sample or to a completely different polymorph [33–44]. It has been shown that occurrence of stress-induced polymorphic transitions during stretching produces a neat increase in ductility, because this provides a mechanism for conversion of mechanical energy into latent heat of fusion, which induces local melting of the crystals followed by recrystallization into a new phase [40–43].

By contrast, the crystallographic model based on thermal activation of screw dislocations is the most general and important micromechanical model of plastic deformation in polymers [23, 24, 31, 32, 35–37]. The mechanism of thermal activation of screw dislocations becomes effective from the yield point through occurrence of crystal slip processes, assisted by interlamellar slip in the amorphous layers. Moreover, for some polymers, additional twinning modes or stress-induced polymorphic transformations can also occur at high deformations [45–52]. Stress-induced phase transition, in turn, may occur not only through mechanical melting followed by recrystallization [29, 40, 41, 43, 44, 53], but can also be first-order as in martensitic (displacive) processes [35–45, 54–59]. The crystallographic

approach correctly predicts the dependence of the yield stress on the stem length of lamellae, temperature, and strain-rate [16, 60–67].

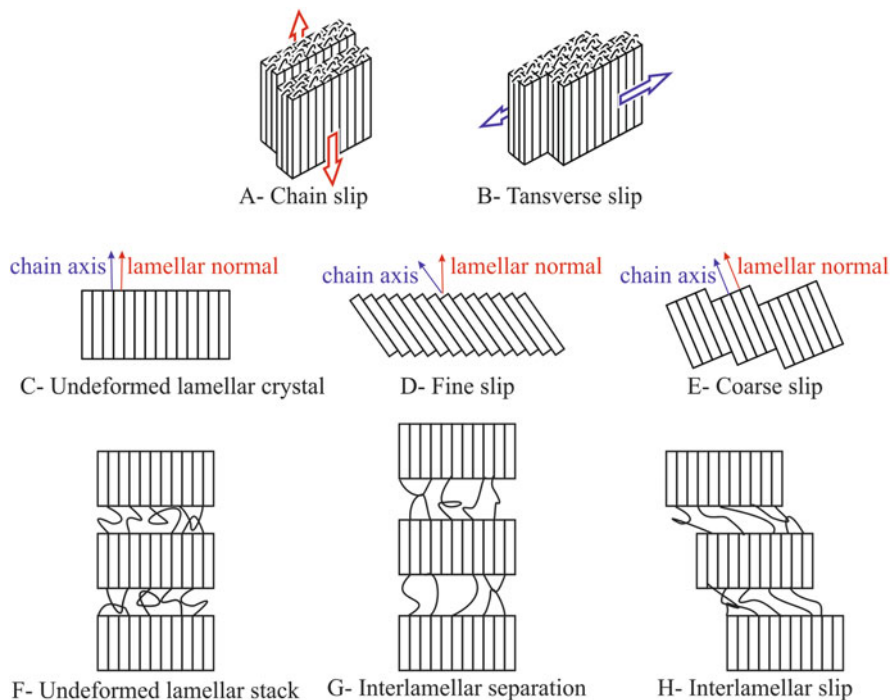
More precisely, the crystallographic approach to plastic deformation of semicrystalline polymers originates from basic ideas borrowed from the classical theory of crystal plasticity, that is, that the yield stress is governed by the energy required to nucleate a dislocation within a lamellar crystal [68–72]. Bowden and Young [25] adopted this idea and demonstrated that the picture based on classical concepts of nucleation of dislocations and their glide along the crystal lattice agrees well with the behavior of semicrystalline polymers [6, 8, 12–19, 25, 31, 32, 73–76].

According to this approach, the plastic deformation of polymer crystals is, in essence, of crystallographic origin and takes place without destroying the crystalline order. It occurs by crystallographic slips in the planes of closest packing (slip planes), generally corresponding to large interplanar distances, in directions coinciding with the direction of the closest packing located in the slip plane [25]. The slip mechanism is produced by the glide of a linear defect, namely a screw dislocation, along the slip plane. It can therefore accommodate plastic strains much more easily than other mechanisms such as twinning or martensitic transitions. The slip begins when the shear stress in the slip direction  $\tau$  reaches a value higher than a threshold level that is critical for the given slip system. Such a stress level  $\tau_0$  corresponds to the critical resolved shear stress [5–7, 14–19, 25]. Thus, yielding starts when the critical resolved shear stress is reached in any family of lattice planes with low  $\tau_0$ .

For polymer crystals, the slip systems need to operate in planes parallel to the chain axes. The most typical modes are chain slip involving a glide parallel to chain axes and transverse slip involving a glide perpendicular to chain axes (Fig. 1A, B). Additional constraints to the crystallographic deformation process are imposed by chain folds [5]. Chain folds should not be destroyed during deformation. Therefore, slip processes parallel to planes containing chain folds are generally preferred.

The slip process during deformation may occur in two different ways, producing either fine slips (Fig. 1D) or coarse slips (Fig. 1E) [7, 14–19, 49–52, 77–79]. Fine slips consist of displacements by one or two lattice vectors on every other lattice plane of a crystal [77–79]. With increased slip processes, the global effect results in a progressive increase in chain tilting with respect to the lamellar normal and a decrease in lamellar thickness (Fig. 1D). Coarse slips consist of significant shear displacements of crystal blocks on well-separated crystal planes. In general, coarse slips take place in lamellae containing a high concentration of defects or having a block fine-structure and in the late stages of deformation, when the crystals are already thinned as a result of advanced fine slip processes [77–79]. Eventually, at this stage of deformation, lamellae become so weak that they undergo slip instabilities, that is, complete fragmentation, orientation, destruction [32], and recrystallization in oriented crystals of fibrillar morphology.

The third micromechanical model of plastic deformation in semicrystalline polymers is based on the role of cavitation and micronecking [3, 4, 20, 21, 80]. This model was elaborated by Peterlin and coworkers and assumes that plastic



**Fig. 1** (A, B) Two types of crystallographic slip in macromolecular crystals: chain slip (longitudinal) (A) and transverse slip (B) [6, 25]. Regular chain folds connect adjacent stems in the crystal. Arrows denote the direction of the chain translation. Slip occurs parallel to chain fold. (C–E) Deformation modes of lamellar crystals [32]: undeformed crystal (C), models of fine chain slip (D), and coarse chain slip (E). The orientation of chain axes and the vector normal to lamellar surface are indicated. (F–H) Deformation modes of the amorphous phase: undeformed stack (F), interlamellar separation mode (G), and interlamellar slip (shear) (H). In G, H only the chains bridging adjacent lamellar crystals are drawn

yielding is a result of the shearing of crystalline lamellae followed by their simultaneous fragmentation into crystal blocks [20, 21, 81]. In practice, the initial lamellar stacks inside the initial isotropic spherulites transform into fibrillar entities during stretching through formation of micronecks, which are generated at microcrack boundaries. Upon fragmentation of the lamellar blocks through chain unfolding, the blocks become oriented with chain axes in the stretching direction, originating microfibrils that are characterized by alternation of crystalline and amorphous regions [20, 21]. The basic mechanism for formation of micronecks is cavitation, because cavities remove mechanical constraints on block rotations. Therefore, cavitation and micronecking constitute the basic steps of Peterlin's micromechanical model [20, 21]. Successive studies have shown that morphological transformation from initial isotropic structures into microfibrils by plastic deformation can also take place without formation of cavities or microvoids [7, 32, 82, 83]. This, for instance, occurs in the regime of plane-strain or uniaxial



compression [84]. Therefore, cavitation is merely a side effect produced by particular deformation modes and is not essential for the plastic deformation process and related transformation of polymer morphology [84]. Moreover, Peterlin's model completely neglects crystallographic slip processes, and although it describes well the effect of tensile drawing, it fails completely for other deformation modes such as compression or plane-strain [7, 84]. By contrast, the crystallographic approach is more general and can explain the full deformation sequence in any deformation mode, without invoking any catastrophic events such as micronecking, melting–recrystallization transformation, or cavitation [1, 2, 5–8].

According to a generalized view, the mechanisms that govern the process of tensile deformation of semicrystalline polymers at low and moderate deformations appear strain controlled, rather than stress controlled [33, 34, 66, 67, 85–88]. Within this scheme, the amorphous phase also plays a key role because it participates in the plastic flow of a polymer at any deformation, starting from the yield point, as a result of the high degree of interconnection between crystals and amorphous phase. This connectivity is ensured by chains crossing the crystal–amorphous interphase and bridging adjacent lamellae, either through tie chains or entanglements created by chains emanating from a crystal that re-enter into the same crystal, after passage through a portion of the adjoining amorphous layer (Fig. 1F) [46, 85]. The principal deformation modes of the amorphous phase are interlamellar shear and interlamellar separation (Fig. 1G, H).

In general, the contribution of the amorphous phase to plastic deformation at yield is small and the contribution of the amorphous phase becomes predominant only at large deformations, that is, at deformations corresponding to almost complete lamellar fragmentation and consequent transformation of the spherulitic morphology into fibrillar morphology. In principle, deformation of the intralamellar amorphous regions at temperatures higher than the glass transition is largely recoverable, especially at low deformation. This is a result of the rubbery state of the amorphous phase and the high degree of connectivity of the amorphous phase with the crystalline scaffold, which hampers viscous flow. Moreover, because of this connectivity and the intrinsic incompressibility of the amorphous phase, there is an intrinsic difficulty for the amorphous phase to compensate the deformation along a given direction with shape distortions in the transversal section, as required for volume conservation of the rubbery state [5–7, 14–19]. A direct consequence of this difficulty is that, after yielding, there can be formation of microvoids, lamellar bending (kinking), and consequent stack rotation because these modes cause relaxation of the local strain and prevent scission of the tie chains [85–88]. In all cases, at both large and small deformations, the chains involved in the bridges between adjacent crystals act as efficient stress transmitters [5, 7, 10, 89, 90] that facilitate macroscopic deformation of the sample, up to breaking at large deformations.

More precisely, for deformation temperatures  $T_{\text{def}}$  higher than the glass transition  $T_g$  and immediately after the elastic regime, the plastic deformation of a semicrystalline polymer starts with small distortions of the amorphous portions of the chains located between crystals. The compliant amorphous regions are expected

to deform more easily than the crystals, according to the modes depicted in Fig. 1D, E [2–7]. However, this deformation is quickly exhausted because of the high increase in local stress. This stress is transferred to adjacent crystals. Yield starts as soon as local stress reaches the level of critical resolved shear stress for the easiest slip system, so that the crystals become involved in plastic flow [2–7, 25–28]. From this point on, the plastic deformation of crystals begins to control the whole deformation kinetics of the sample, whereas the amorphous layers respond through continuous adjustments of their conformation [2–7, 25, 27, 62–65]. With increased deformation, the conformation of amorphous chains eventually becomes so taut that collective movements of the crystals are induced, including fragmentation of lamellae into blocks, complete destruction of the initial morphology, and rotation of the stacks [62–65, 85–88]. Therefore, the entire deformation process involves the simultaneous, combined deformation of amorphous and crystalline components. Crystallographic control dominates until the breakdown of crystallites [32–34, 66, 67, 83, 91]. Afterwards, strain hardening may intervene at large deformations prior to breaking [5–7, 26]. Strain hardening is related to the orientational hardening of the amorphous phase and, to a lesser extent, to reorientation of crystals as a result of crystal slip in the late stages of the deformation process. Along the true stress–true strain curves of polymeric materials, the compliance changes at well-defined points corresponding to changes in crystalline morphology and in the relative response of a material in terms of plastic versus elastic deformation [33, 34, 66, 67, 85–87]. These critical points correspond to:

- (A) The onset of isolated inter- and intralamellar slip processes after the initial Hooke's elastic range
- (B) Change into a collective activity of slip motions of crystal blocks at the point of maximum curvature of the true stress–strain curve
- (C) The beginning of destruction of crystal blocks followed by re-crystallization with formation of fibrils
- (D) The beginning of disentanglement of the amorphous network or strain hardening as a result of stretching of the amorphous entangled network at high deformations

The values of the strains at critical points A, B, and C are invariant, for each class of polymer, with variation in crystallinity, temperature, strain rate, and crystal thickness [33, 34, 66, 67, 85–87]. In contrast to the strain, stresses at the critical points vary with deformation rate, and present larger values for higher crystallinities and lower values for higher temperatures. These observations comply well with the general assumption that the strain is homogeneously distributed in semi-crystalline polymers, whereas the stress is not [48–52, 68, 69]. At low stresses or strains, the forces transmitted by the interconnected crystallites dominate, whereas at high strains the rubber-like network forces are superior [68, 69].

The yield point in engineering stretching experiments is always located a little above point B [85–87]. The position of the critical strain at point C, at which the critical stress that starts destruction of the crystal blocks is achieved, depends on the interplay between the entanglement density of the amorphous phase and the

intrinsic stability of crystals [33, 34, 49–52, 66, 67, 85–87]. A higher entanglement density implies that a higher stress is generated when the sample is stretched. The more stable the crystallites, the higher the stress needed for their destruction [49–52].

Within the framework of the crystallographic approach, models for quantitative predictions of the yield stress of semicrystalline polymers have been developed, based on the assumption that yielding involves thermal activation of screw dislocation with the Burgers vector parallel to the chain axis (vide infra) [25, 31, 68, 69, 82, 92–94]. In the resultant model of thermal activation of dislocation, the free energy required to nucleate a dislocation within the crystalline region has been correlated with considerable success to the measured yield stress of various samples of polyethylene (PE) and isotactic polypropylene (iPP) at temperatures higher than  $T_g$  [14–19, 60, 67, 71, 92–96]. In particular, it has been found that at a given temperature the stress required to initiate these dislocations depends on the thickness of the crystals, which accounts quite well for the observed dependence of yield stress on crystal thickness for various samples of PE and iPP, regardless of crystallization conditions, degree of crystallinity, and molecular mass. In particular, the critical free energy required to form a screw dislocation and the shear modulus associated with the slip planes of the dislocation can be extracted from this analysis and correlated with crystallographic features of the material [14–19, 60, 67, 71, 92–96].

In this chapter, the yield behaviors of isotactic copolymers of propene with ethylene, 1-butene, 1-pentene, 1-hexene, and 1-octadecene, prepared with different metallocene catalysts [97–106], are analyzed in terms of the crystallographic approach using the dislocation model. The catalysts allow synthesis of copolymers with compositionally uniform chains, uniform distribution of comonomers along the chain, and tailored microstructure [107–110]. Samples with a very small concentration of stereodefects or regiodefects and variable amounts of comonomeric units, or similar concentration of comonomeric units but different concentration of stereo- and regiodefects, have been prepared. Stereodefects (namely, isolated *rr* triads), regiodefects, and different types and concentrations of comonomeric units have different effects on the crystallization of  $\alpha$ - and  $\gamma$ -forms of iPP, and on crystallization properties in general. The differences in polymorphism and crystallization properties, in turn, induce differences in mechanical properties. The polymorphism and crystallization properties of these systems depend not only on the concentration of comonomers, which in a random copolymer regulates the average length of the fully (crystallizable) propylene sequences, but also on the different degree of inclusion of these defects (stereo- and regio-irregularities, comonomeric units) in the crystals of  $\alpha$ - and  $\gamma$ -forms of iPP. The inclusion of stereo- and regio-irregularities and comonomeric units in the crystal produces point-like defects and an increase in entropy and/or decrease in internal energy and, consequently, influences the relative stability of the crystals [97–106, 111–117]. Therefore, study of the yield behavior of these copolymers allows use of the dislocation model to be extended to a set of samples crystallized under similar conditions but characterized by differences in the degree of crystallinity, lamellar

thickness, polymorphism, and intrinsic flexibility of the chain backbone. The values of these parameters can be finely tailored independently of each other by the type and concentration of defects by simply selecting a different catalyst system. In particular, the present investigation aims at establishing the influence of different degrees of inclusion of point-like defects inside crystals on the parameters of the dislocation model, namely the critical free energy required to form a screw dislocation and the shear modulus associated with the slip planes of the dislocation [25, 92–94]. The final goal is to understand the macroscopic properties of materials at the molecular scale.

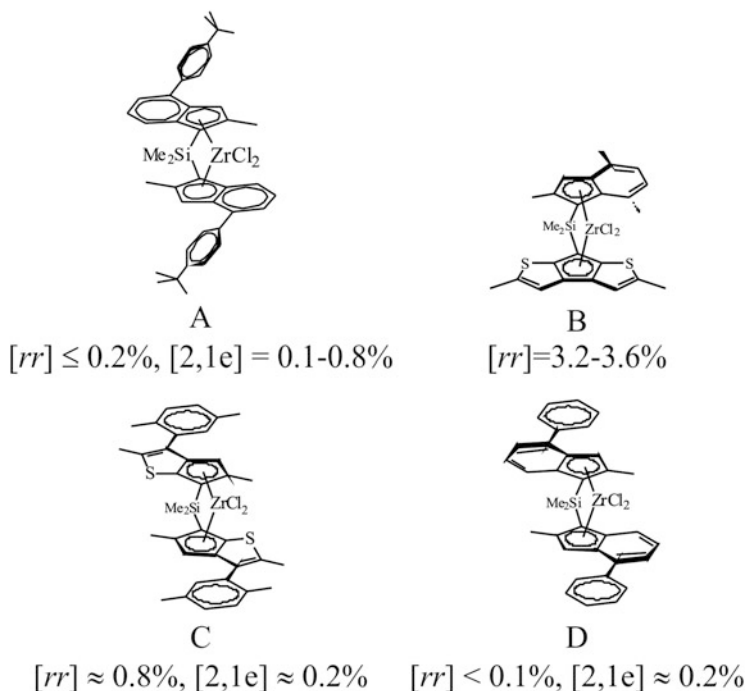
## 2 Experimental Details

The samples selected for this study were iPP homopolymers and propylene-ethylene (iPPe) [97, 98], propylene-(1-butene) (iPPBu) [97–99], and propylene-(1-hexene) (iPPHe) [98, 105, 106] copolymers prepared at temperatures between 60°C and 70°C with the metallocene catalysts A–C shown in Scheme 1, activated with methylalumoxane (MAO). Samples of propylene-(1-pentene) (iPPPe) [103, 104] and propylene-(1-octadecene) (iPPOc) [102] were prepared at 25°C with catalyst D (see Scheme 1). The three C<sub>2</sub>-symmetric metallocenes A, C, and D are not completely regioselective, but highly isoselective [107, 108, 110]. The C<sub>1</sub>-symmetric metallocene B is fully regioselective but not perfectly isoselective [109]. The MAO-activated metallocenes A and B for the synthesis of iPPe and iPPBu copolymers were supported on spherical SiO<sub>2</sub> particles, or on porous polyethylene or polypropylene particles, following a Basell proprietary technology [118].

All samples are listed in Table 1. The copolymers are designated YZ<sub>x</sub>, where Y is the catalyst (A, B, C, or D) and *x* is the concentration of the comonomeric unit Z (where Z=E, B, P, H, and O stands for ethylene, 1-butene, 1-pentene, 1-hexene, and 1-octadecene, respectively).

The microstructural data of all samples were obtained from <sup>13</sup>C NMR analysis (see [97–106] for details). The samples of iPP homopolymer prepared with the catalysts A (iPPA), C, and D (iPPD) are similar. They are highly stereoregular and contain only small amounts of stereoerrors (0.2 and <0.1 mol% of *rr* triad defects in iPPA and iPPD, respectively) and regiodeflects caused by secondary 2,1 erythro units (2,1e) (0.8 and 0.2 mol% of 2,1e units in iPPA and iPPD, respectively). The iPP sample prepared with catalyst B is highly regioregular (no 2,1 regiodeflects detectable) but less stereoregular, and contains 3.5 mol% *rr* triads [119].

All catalysts produce copolymer samples with microstructures similar to those of the homopolymer samples prepared with the same catalyst, with small oscillations in the concentration of *rr* stereoerrors and 2,1e regiodeflects around those of the corresponding iPP (Table 1). In particular, for iPPBu copolymers prepared with the catalyst A the concentration of 2,1e regiodeflects decreases with increasing butene



**Scheme 1** Structures of metallocene catalysts A–D used for synthesis of the samples listed in Table 1

content (Table 1) [97, 98]. For iPPEt and iPPHe copolymers prepared with catalyst A, the content of stereoerrors is not determinable and is assumed to be the same as that found in the corresponding homopolymer iPPA (Table 1) [97, 98, 100, 101]. All the copolymers have a random distribution of comonomers and narrow molecular mass distributions. Details of the NMR analysis are described in the literature [97–106].

The films used for structural and thermal characterization and for mechanical tests were prepared by compression molding. Powder samples were heated at temperatures 20–30°C higher than the melting temperatures between flat brass plates under a press at low pressure and slowly cooled to room temperature by fluxing water in the refrigerating circuit of the press plates. Special care was taken to obtain films of uniform thickness (0.3 mm) and to minimize surface roughness, according to the recommendation of the standard ASTM D-2292-85.

Calorimetric data were collected with a differential scanning calorimeter (DSC) Mettler DSC-30 in a flowing N<sub>2</sub> atmosphere at heating rate of 10°C/min. All samples showed a  $T_g$  lower than  $\approx 0^\circ\text{C}$ , which decreased with increasing comonomer concentration and length of the side chains [97–106].

**Table 1** Details of iPP homopolymers and various copolymers prepared using different MAO-activated metallocene catalysts

Sample <sup>a</sup>	Catalyst/cocatalyst/ carrier <sup>b</sup>	$M_w$ (kg/mol) <sup>c</sup>	$M_w/M_n^d$	$M_v^e$ (kg/mol)	$T_m^f$ (°C)	Comonomer	Comonomer conc. <sup>g</sup> (mol%)	$[\eta]^h$ (mol%)	$[2,1e]^i$ (mol%)	$\epsilon_{tot}^j$ (mol%)
<i>Homopolymers iPP [97, 103]</i>										
iPPA	A/MAO/PE	237	2.2	–	151	–	0	0.2	0.8	1.00
iPPB	B/MAO/PP	247	2.3	–	135	–	0	3.5	0	3.5
iPPD (iPPC)	D/MAO/PP	–	–	680	151	–	0	<0.1	0.2	0.2
<i>Propene-ethylene copolymers iPPEt [97, 98]</i>										
AE0.6	A/MAO/PE	–	–	–	146	Ethylene	0.6	0.2 <sup>k</sup>	0.7	1.5
AE4.0	A/MAO/PE	293	2.1	–	130	Ethylene	4.0	0.2 <sup>k</sup>	0.6	4.8
AE7.4	A/MAO/PE	289	2.1	–	117	Ethylene	7.4	0.2 <sup>k</sup>	0.4	8.0
BE3.6	B/MAO	–	–	–	121	Ethylene	3.6	3.6	0	7.2
BE13.1	B/MAO	193	2.0	–	47, (113) <sup>l</sup>	Ethylene	13.1	3.2	0	16.3
<i>Propene-1-butene copolymers iPPBu [97–99]</i>										
AB1.9	A/MAO/SiO <sub>2</sub>	316	2.2	–	144	1-Butene	1.9	<0.1	0.5	2.4
AB4.3	A/MAO/PE	229	2.1	–	137	1-Butene	4.3	<0.1	0.4	4.7
AB8.3	A/MAO/SiO <sub>2</sub>	200	2.1	–	130	1-Butene	8.3	<0.1	0.3	8.6
AB13.6	A/MAO/SiO <sub>2</sub>	161	2.4	–	115	1-Butene	13.6	<0.1	0.1	13.7
CB12	C/MAO	–	–	165	119	1-Butene	12.0	0.2	0.8	13.0
CB27.6	C/MAO	–	–	182	88	1-Butene	27.6	0.2	0.8	28.6
CB37.3	C/MAO	–	–	177	76	1-Butene	37.3	0.2	0.8	38.3

(continued)

Table 1 (continued)

Sample <sup>a</sup>	Catalyst/cocatalyst/ carrier <sup>b</sup>	$M_w$ (kg/mol) <sup>c</sup>	$M_w/M_n^d$	$M_v^e$ (kg/mol)	$T_m^f$ (°C)	Comonomer	Comonomer conc. <sup>g</sup> (mol%)	$[\eta]^h$ (mol%)	$[2,1e]^i$ (mol%)	$\epsilon_{tot}^j$ (mol%)
<i>Propene-1-pentene copolymers iPPe</i> [103, 104]										
DP3.2	D/MAO	428	1.8	–	126	1-Pentene	3.2	<0.1	0.2	3.4
DP5.3	D/MAO	347	2	–	105, (51) <sup>l</sup>	1-Pentene	5.3	<0.1	0.2	5.5
DP8.8	D/MAO	279	2	–	85, (51) <sup>l</sup>	1-Pentene	8.8	<0.1	0.2	9.0
DP11.0	D/MAO	–	–	–	68, (50) <sup>l</sup>	1-Pentene	11.0	<0.1	0.2	11.2
<i>Propene-1-hexene copolymers iPPh</i> [100, 101, 105, 106]										
AH2.0	A/MAO	122	2.4	–	127	1-Hexene	2.0	0.2	0.2	2.4
AH3.7	A/MAO	333	2.0	–	116	1-Hexene	3.7	0.2	0.2	4.1
AH6.8	A/MAO	239	2.2	–	96	1-Hexene	6.8	0.2	0.1	7.1
AH11.2	A/MAO	266	1.9	–	70	1-Hexene	11.2	0.2	0.1	11.5
<i>Propene-1-octadecene copolymers iPPOc</i> [102] <sup>m</sup>										
DO1	D/MAO	–	–	–	139	1- Octadecene	1	<0.1	0.2	1.2
DO2.2	D/MAO	–	–	–	117	1- Octadecene	2.2	<0.1	0.2	2.4
DO4.8	D/MAO	–	–	–	93	1- Octadecene	4.8	<0.1	0.2	5.0

DO6.0	D/MAO	–	–	85	1- Octadecene	6.0	<0.1	0.2	6.2
DO7.5	D/MAO	–	–	55, 69 <sup>b</sup>	1- Octadecene	7.5	<0.1	0.2	7.7

<sup>a</sup>iPP homopolymers (iPPA, iPPB, and iPPD) and iPPEt, iPPBu, iPPHe, and iPPOc copolymers were prepared with the MAO-activated metallocenes A–D shown in Scheme 1. Sample designations are of the form YZx, where Y is the catalyst (A, B, C, or D) and x is the concentration of the comonomeric unit Z (where Z=E, B, P, H, and O stands for ethylene, 1-butene, 1-pentene, 1-hexene, and 1-octadecene, respectively)

<sup>b</sup>PE polyethylene, PP polypropylene

<sup>c</sup>Mass-average molecular mass ( $M_w$ ) was obtained by GPC

<sup>d</sup>Polydispersity  $M_w/M_n$ . SEC curves show molecular mass distributions for all samples of around 2.0

<sup>e</sup>Values of viscosity average-molecular masses ( $M_v$ ) were obtained from values of the intrinsic viscosities  $[\eta]$

<sup>f</sup>Melting temperature ( $T_m$ ) of compression-molded samples crystallized from the melt by slow cooling to room temperature while fluxing cold water in the refrigerating circuit of the press plates

<sup>g</sup>Concentration of comonomeric units (mol%) determined from solution <sup>13</sup>C NMR analysis

<sup>h</sup>Percentage content of primary stereoregions over all monomer units,  $[rr] = [mrrm] + [mrrr]$ . For copolymers samples prepared with A, C, or D where the content of stereoregions is not determinable, the quantity  $[rr]$  is assumed to be the same as that found in the homopolymers iPPA and iPPD

<sup>i</sup>Concentration of secondary 2,1-erythro units [2,1e]. Secondary insertions 2,1 are only of the erythro type, and their amount is normalized over all monomer units. For iPPEt copolymers, [2,1e] is the sole concentration of isolated secondary 2,1-erythro units (PSP, P = propylene, S = secondary 2,1 propylene unit)

<sup>j</sup>Total concentration of defects ( $\epsilon_{tot}$ )

<sup>k</sup>Content of stereoregions was not determinable and was assumed to be the same as that found in the corresponding homopolymer iPPA

<sup>l</sup>Temperature of a low melting endothermic peak

<sup>m</sup>Samples were fractioned with boiling ethoxyethane to remove unreacted 1-octadecene comonomer

<sup>n</sup>Sample shows a double melting endotherm



X-ray diffraction patterns (WAXS) were obtained at room temperature with Ni-filtered  $\text{CuK}\alpha$  radiation ( $\lambda = 1.5418 \text{ \AA}$ ). The powder profiles were obtained using a Philips diffractometer with continuous scans of the  $2\theta$  angle and scanning rate of  $0.02^\circ/\text{s}$ .

The indices of crystallinity ( $x_c$ , relative error 10%) were evaluated from the X-ray powder diffraction profiles from the ratio between the crystalline diffraction area ( $A_c$ ) and the total area of the diffraction profile ( $A_T$ ),  $x_c = A_c/A_T$ . The crystalline diffraction area was obtained from the total area of the diffraction profile by subtracting the amorphous halo. The procedure used for evaluation of the amorphous halo for each sample and for the subtraction is the same as previously published [97–106].

Small angle X-ray scattering (SAXS) data for compression-molded films were collected at room temperature using a Kratky compact camera SAXSess (Anton Paar, Graz, Austria) in the slit collimation configuration, attached to a conventional X-ray source ( $\text{CuK}\alpha$ , wavelength  $1.5418 \text{ \AA}$ ). The scattered radiation was recorded on a BAS-MS imaging plate (Fujifilm) and processed with a digital imaging reader (Fujibas 1800). The range of scattering vector modulus,  $0.1 \text{ nm}^{-1} \leq q \leq 2 \text{ nm}^{-1}$ , where  $q = (4\pi\sin\theta/\lambda)$  and  $2\theta$  is the scattering angle, was analyzed. After subtraction for dark current, the empty sample holder, and a constant background caused by thermal density fluctuations, the slit smeared data were de-convoluted with the primary-beam intensity distribution using the SAXSquant 2.0 software to obtain the corresponding pinhole scattering (desmeared) intensity distribution. The constant value of intensity approximating the background  $I_{\text{back}}$  was found by fitting the smeared SAXS intensity curve in the range  $2 < q < 4 \text{ nm}^{-1}$  [ $I(q_{\text{high}})$ ] with the function [120, 121]:

$$I(q_{\text{high}}) = I_{\text{back}} + bq^{-3} \quad (1)$$

where  $I_{\text{back}}$  and  $b$  are fitting parameters. The average value of the long period  $L$  was calculated as  $L \approx 2\pi/q^*$ , where  $q^*$  is the  $q$  value corresponding to the maximum in the Lorentz-corrected intensity (i.e., the SAXS intensity multiplied by  $q^2/\pi$ ). Crystal thickness  $l_c$  was then calculated by  $l_c \approx x_c L$ , where  $x_c$  corresponds to the degree of crystallinity, as evaluated from WAXS profiles. The thickness of amorphous layers,  $l_a$ , was evaluated as  $l_a = L - l_c$ . In practice, we used the mass fraction of the crystalline phase derived from WAXS analysis instead of the volume fraction, because the density of amorphous copolymers was not directly determined. Therefore, even though the calculated values of  $l_a$  and  $l_c$  are affected by an absolute error, they are of significance in comparing the properties of the different samples. It is worth noting that the average values of the long period and lamellar thickness (and thickness of amorphous layers) evaluated using the one-dimensional correlation function [120] or the interface distribution function [121] would give similar results to those evaluated directly from the  $q$  values at the maximum of the Lorentz-corrected scattering intensity.

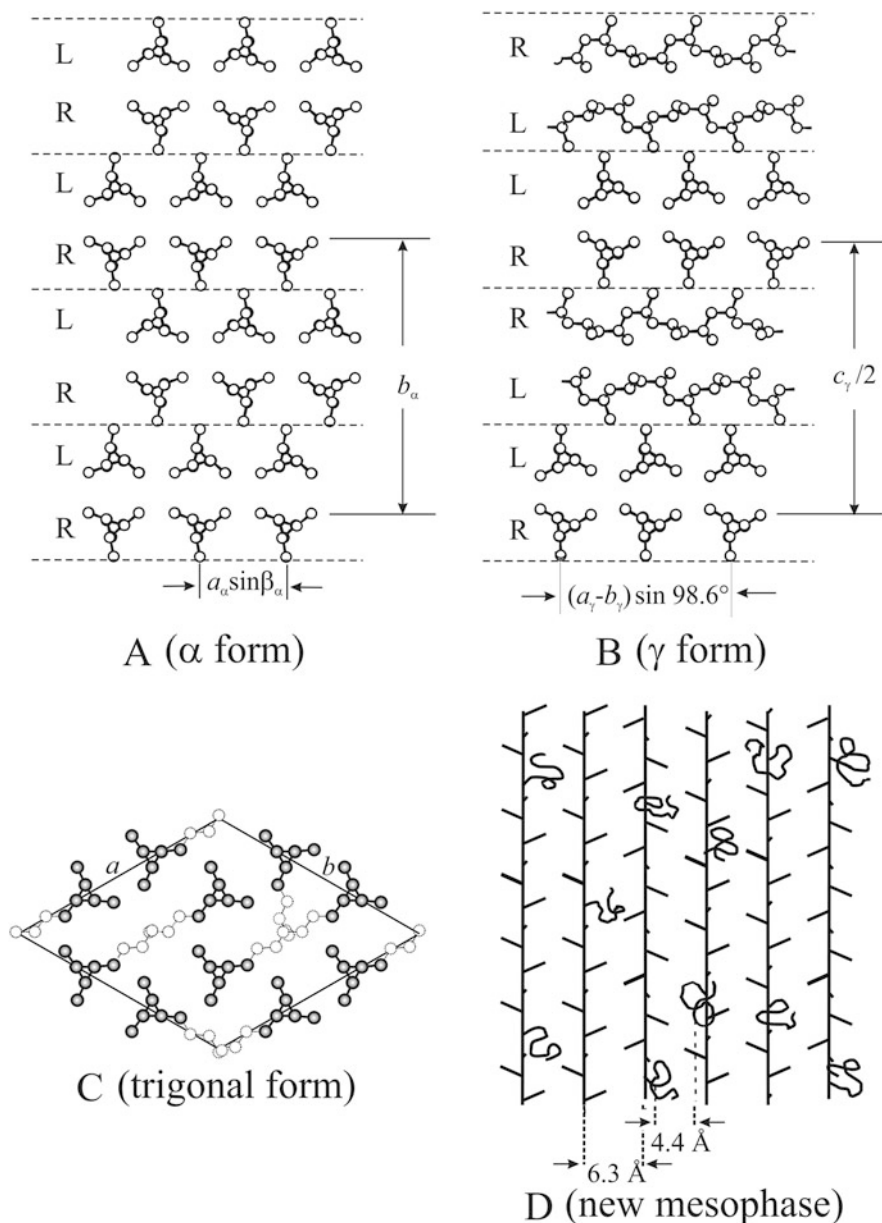
Mechanical tests were performed at room temperature on compression-molded films with a universal testing machine Zwicki (Zwick/Roell), following the standard test method for tensile properties of thin plastic sheeting (ASTM D882-83). Rectangular specimens 10 mm long, 5 mm wide, and 0.3 mm thick were stretched to the break point or to a given deformation  $\varepsilon = [(L_f - L_0)/L_0]100$ , where  $L_0$  and  $L_f$  are the initial and final lengths of the specimen, respectively. Two benchmarks were placed on the test specimens and used to check the local elongation versus the nominal elongation measured from the grip-to-grip distance. In mechanical tests, the ratio between the drawing rate and the initial length was fixed at 10 mm/(mm min). The stress–strain curves and the reported values of the mechanical parameters were averaged over at least five independent experiments.

### 3 Structural Analysis and Thermal Behavior

The crystallization behavior of isotactic copolymers of propene with ethylene, butene, pentene, hexene, and octadecene synthesized with single-center metallocene catalysts has been extensively studied [97–106, 111–117], and compared with that of the corresponding homopolymer iPP produced with the same catalyst system. Single-center metallocene catalysts allow perfect control over the chain microstructure [122]. Thus, iPP-based homo- and copolymer samples characterized by different kinds and amounts of defects along the chain can be produced while maintaining tight control over molecular mass, molecular mass distribution (with polydispersity index close to two), and uniform inter- and intrachain distributions of the defects. Study of these systems has allowed isolation of the different influences of each kind of defect, namely stereodeflects (isolated *rr* triads), regiodeflects (e.g., secondary 2,1 insertions of monomeric units), and comonomeric units, on the crystallization of  $\alpha$ - and  $\gamma$ -forms of iPP.

In particular, it has been shown that chain microstructure strongly influences the polymorphic behavior and physical properties of iPP [40, 41, 97, 100, 111, 114, 119, 123–130]. Samples characterized by chains containing microstructural defects (stereodeflects and regiodeflects) and/or comonomeric units, generated by different catalysts, crystallize as a mixture of the  $\alpha$ - and  $\gamma$ -forms (Fig. 2A, B) [40, 41, 97, 100, 111, 114, 119, 123–130]. In general, formation of the  $\gamma$ -form seems favored by the presence of these defects [40, 41, 97, 100, 111, 114, 119, 123–130]. However, each kind of defect influences the crystallization of  $\alpha$ - and/or  $\gamma$ -forms in a different way according to different mechanisms. A rational and unified picture of the complex polymorphism of these systems [97, 100, 102] has been achieved and the general rules controlling the polymorphism of iPP in defective samples have been identified.

The first important parameter that influences the crystallization of  $\alpha$ - and  $\gamma$ -forms of iPP corresponds to the average length of the regular isotactic propylene sequences [40, 41, 119, 123–130]. Short regular isotactic sequences generally favor



**Fig. 2** Structural models of  $\alpha$ -form (**A**) and  $\gamma$ -form (**B**) of isotactic polypropylene. (**C**) Trigonal form of isotactic copolymers of propene with 1-pentene and 1-hexene containing pentene concentrations higher than 10 mol% and hexene concentrations higher than 15–16 mol% [100, 101, 103, 104]. The structural model of iPPHe copolymers in the trigonal form is shown as an example. The lateral butyl groups of 1-hexene units are statistically included in the unit cell with occupancy factor close to the average content of comonomers in the copolymer chain. (**D**) New mesomorphic form of isotactic copolymers of propene with long 1-alkene [102].

crystallization of the  $\gamma$ -form. For metallocene-made homo- and copolymers of propene characterized by random distribution of defects along the chains, the average length of propene crystallizable sequences scales with the reciprocal concentration of defects. Therefore, even a small number of defects shortens the average length of the regular isotactic sequences, reducing the melting temperature and favoring crystallization of the  $\gamma$ -form [40, 41, 119, 123–130]. Because of the non-parallel arrangement of chains in crystals of the  $\gamma$ -form (Fig. 2B), defects are easily accommodated at the lamellar boundaries, with no need for chain folding. By contrast, in the  $\alpha$ -form (Fig. 2A) defects are rejected at the fold surface because chain folding is a necessary requisite for crystallization in order to avoid overcrowding at the lamellar surface.

A second remarkable effect that drives the crystallization of  $\alpha$ - and/or  $\gamma$ -forms is the possible inclusion of defects in crystals of the two polymorphs [97, 100]. The inclusion effect favors crystallization of the form that better tolerates the defect within its crystalline lattice. Therefore, the two effects can either act synergistically in favoring crystallization in a polymorph, or in competition [97, 100]. In principle, the interruption effect is common to any defect (stereo- and regiodefects and comonomeric units) and always favors crystallization of the  $\gamma$ -form. The inclusion effect produces point-like defects inside the crystals, which may influence the conformational and packing energy of  $\alpha$ - and  $\gamma$ -forms to equal or different extents. The final crystalline form obtained upon crystallization depends on the effective level of disturbance of the defects inside the crystalline lattice, which, in the case of copolymers, is related to the size of the comonomeric units [97, 100, 131].

A third peculiar effect has also been demonstrated in the case of some copolymers that, above a threshold concentration of comonomeric units, tend to crystallize in a polymorphic form that is different to both  $\alpha$ - and  $\gamma$ -forms [100–106]. Crystallization into the new polymorph is driven by the easy inclusion of comonomers inside crystals of the new form. The process is driven by an increase in entropy and density [103–106, 132–140] or by kinetic factors [102]. In other words, crystallization of the new polymorph is competitive with crystallization of the  $\alpha$ -form (expected on the basis of the inclusion effect) and/or the  $\gamma$ -form (expected on the basis of the interruption effect). We call this effect the “competitive crystallization effect.”

It has been shown that iPP homopolymer samples with different concentrations of  $rr$  defects [40, 41, 119, 123–130] and samples of iPPEt and iPPBu copolymers [97, 111] crystallize from the melt as mixtures of the  $\alpha$ - and  $\gamma$ -forms. The amount of  $\gamma$ -form increases with increasing crystallization temperature, ethylene concentration, and content of  $rr$  stereodeflects. By contrast, in iPPBu copolymers, the amount of the  $\gamma$ -form first increases, then decreases for concentrations of butene units higher than 10–14 mol% and is always lower than that crystallized in stereodeflective iPP and iPPEt copolymers [97, 99]. Therefore,  $rr$  stereodeflects and ethylene units favor the crystallization of the  $\gamma$ -form, whereas butene units favor crystallization of the  $\alpha$ - and  $\gamma$ -forms at high and low concentrations, respectively.

These data have been rationalized by resorting to the combined effect of interruption and inclusion [97, 119]. First, it has been shown that in stereodeflective

iPP, iPPeT, and iPPBu copolymers, different proportions of *rr* defects, ethylene, and butene are included in crystals of the  $\alpha$ - and  $\gamma$ -forms [112, 113]. On the one hand, the interruption effect favors crystallization of the  $\gamma$ -form. On the other hand, the inclusion effect also comes into play and the two effects act simultaneously, with one prevailing over the other depending on the compatibility of the different defects within the crystalline lattices of the different polymorphs.

Ethylene and *rr* stereodefects are included in crystals of both  $\alpha$ - and  $\gamma$ -forms but are more easily included in crystals of the  $\gamma$ -form [97]. In iPPeT copolymers and in stereodeficient iPP samples, the effects of crystal inclusion and shortening the regular propylene sequences produce the same result of favoring crystallization of the  $\gamma$ -form [97, 119].

In the case of iPPBu copolymers, butene units are included without differentiation between crystals of the  $\alpha$ - and  $\gamma$ -forms, but are more easily included in the  $\alpha$ -form at high concentrations [97]. At low butene concentrations (< 10 mol%), the effect of shortening the length of regular isotactic propylene sequences prevails and induces crystallization of the  $\gamma$ -form. Hence, at low concentration of butene units (for average propene sequences of 10–100 monomeric units), the relative amount of  $\gamma$ -form increases with increasing butene concentration [97]. For butene concentrations higher than 10 mol%, the effect of inclusion of butene units in crystals of the  $\alpha$ -form prevails over the interruption effect [97]. As a consequence, the relative amount of  $\gamma$ -form decreases and iPPBu samples with butene concentrations higher than 20–30 mol% always crystallize in the pure  $\alpha$ -form, crystallization of the  $\gamma$ -form being completely inhibited.

It has been shown that the crystallization of iPPPe [103, 104] and iPPHe [100, 105, 106] copolymers from the melt produces mixtures of  $\alpha$ - and  $\gamma$ -forms at low pentene or hexene concentrations. For comonomer concentrations higher than a threshold, they crystallize almost completely into the  $\alpha$ -form. Further increase in comonomer content produces crystallization into the trigonal form of iPP [103, 104, 132–140] (Fig. 2C). This is a result of the high inclusion, at high concentrations, of pentene and/or hexene units into crystals of the  $\alpha$ -form, driven by density increase, favoring crystallization of the  $\alpha$ -form instead of the  $\gamma$ -form [100, 103–106]. Therefore, the inclusion effect prevails at these comonomer concentrations. The interruption effect becomes efficient in promoting crystallization of the  $\gamma$ -form only at very low concentrations of pentene and/or hexene (2–3 mol%) [100, 103–106]. The trigonal form does not crystallize by cooling the melt but crystallizes from the amorphous state by cold-crystallization or, for samples with high pentene or hexene concentration, by aging amorphous samples at room temperature [100, 103, 104, 132–140]. The hexene or pentene units are included in crystals of the trigonal form and, at low concentration, also in crystals of the  $\alpha$ -form, producing an increase in the unit cell dimensions. The change in crystallization habit from monoclinic into trigonal, for pentene concentrations higher than 10 mol% and hexene concentrations higher than 15–16 mol%, allows incorporation of higher amounts of monomer in crystals of the trigonal form than in the  $\alpha$ -form, and produces an increase in entropy. Therefore, at high pentene/hexene concentration, competitive crystallization of the trigonal form prevails.

In the case of iPPOc copolymers, octadecene units are completely excluded from the crystals of  $\alpha$ - and  $\gamma$ -forms, and only the interruption effect plays a role [102]. These systems crystallize as mixtures of  $\alpha$ - and  $\gamma$ -forms for low octadecene concentrations, even though the relative amount of  $\gamma$ -form is low, probably because of kinetics factors and/or the intrinsic tendency of long side chains to favor formation of chain-folded lamellae of the  $\alpha$ -form to alleviate steric hindrance. At octadecene concentrations above 7–8 mol%, the  $\alpha$ -form is also destabilized and samples crystallize from the melt into a new mesomorphic form [102] (Fig. 2D). This mesophase is different from the quenched mesomorphic form of iPP homopolymer [141]. It is characterized by parallel chains in 3/1 helical conformation packed at average interchain distances of about 6 Å, defined by self-organization of the flexible side groups and high degree of disorder in the lateral packing of chains [102] (Fig. 2D). Therefore, at high octadecene concentrations, the competitive crystallization effect prevails, leading to formation of the new mesophase instead of  $\alpha$ - and/or  $\gamma$ -forms, probably because the crystallization kinetics of the normal  $\alpha$ - and/or  $\gamma$ -forms become too slow.

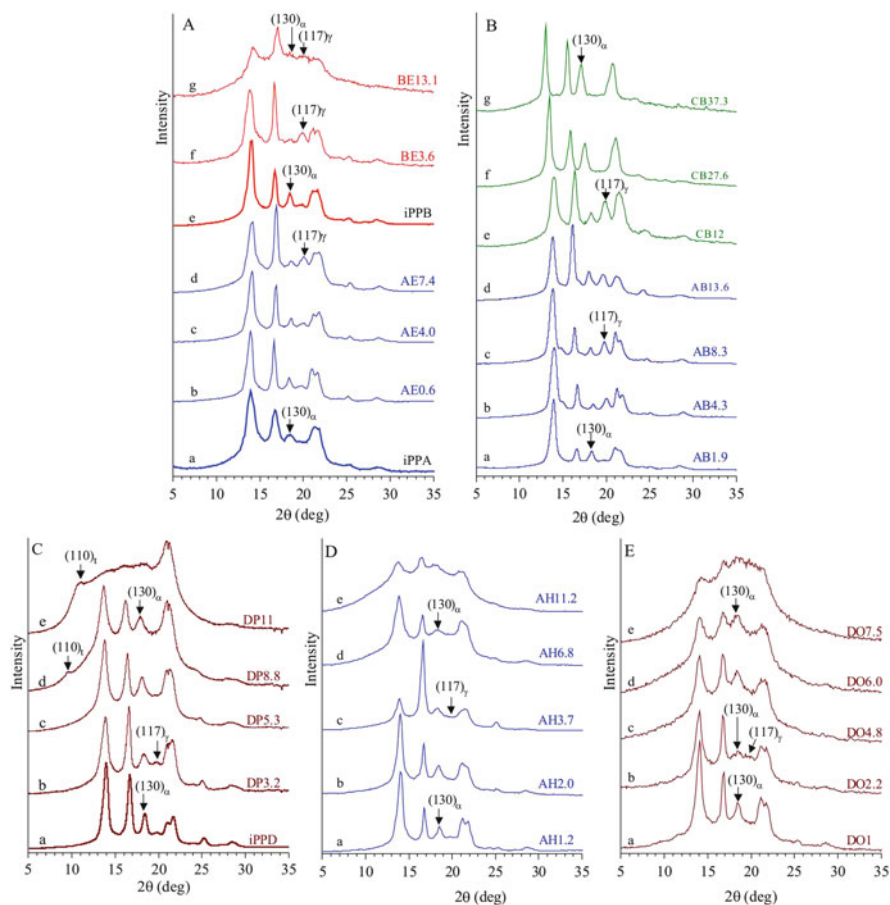
It is worth noting that the crystallization conditions (cooling rate, maximum temperature achieved in the melt, and maximum time that the sample is left at that temperature) can have a strong impact on the resulting structural and morphological features and on the optical and mechanical properties of isotactic copolymers of propene [142–148]. This paper focuses on isotactic copolymers of propene crystallizing from the melt essentially in  $\alpha$ - and/or  $\gamma$ -forms, using identical crystallization conditions, as described in “Experimental Details.” Samples (Table 1) were selected to probe the effect on yield behavior of inclusion/exclusion of comonomeric units in crystals of the two forms. The X-ray powder diffraction profiles of the compression-molded samples are reported in Fig. 3.

All iPP homopolymer samples crystallize from melt in the  $\alpha$ -form. This is indicated by presence of the  $(130)_{\alpha}$  reflection at  $2\theta \approx 18.6^\circ$  of the  $\alpha$ -form [149, 150] and absence or negligible intensity of the  $(117)_{\gamma}$  reflection at  $2\theta \approx 20.1^\circ$  of the  $\gamma$ -form [151, 152], as shown by the X-ray powder diffraction profiles in Fig. 3A (curves a, e) and Fig. 3C (curve a).

The iPPeT copolymers crystallize from the melt as mixtures of  $\alpha$ - and  $\gamma$ -forms of iPP (Fig. 3A). The relative amount of crystals of the  $\gamma$ -form increases with increasing concentration of comonomers, as indicated by the increase in intensity of the  $(117)_{\gamma}$  reflection of the  $\gamma$ -form in the diffraction profiles shown in Fig. 3A.

iPPBu copolymers also crystallize from the melt as mixtures of  $\alpha$ - and  $\gamma$ -forms (Fig. 3B) but, in contrast to iPPeT systems, the relative amount of  $\gamma$ -form first increases with butene concentrations up to 10–15 mol% (Fig. 3C, curves a–e) then decreases. For butene concentrations of 26–40 mol%, the pure  $\alpha$ -form is obtained (Fig. 3B, curves f, g).

In the case of iPPPe and iPPHe samples, small amounts of crystals in the  $\gamma$ -form are obtained only at low concentrations (2–3 mol%) of comonomeric units (Fig. 3C, D, curves b, c). At higher comonomer concentrations, the pure  $\alpha$ -form is obtained (Fig. 3C, D, curve d). Partial inclusion of pentene and hexene units is indicated by



**Fig. 3** X-ray powder diffraction profiles of compression-molded samples of the copolymers iPPeT (A), iPPBu (B), iPPPe (C), iPPHe (D), and iPPOc (E), and of homopolymers iPPA, iPPB, and iPPD prepared with catalysts A–D of Scheme 1. The  $(130)_\alpha$  and  $(117)_\gamma$  reflections at  $2\theta \approx 18.6$  and  $20^\circ$  of the  $\alpha$ - and  $\gamma$ -forms of iPP, respectively, and the  $(110)_t$  reflection at  $2\theta \approx 10^\circ$  of the trigonal form of iPP are indicated

the progressive shift of diffraction peaks toward lower  $2\theta$  values with higher comonomer concentrations. With further increase in pentene units, the iPPPe samples crystallize as mixtures of trigonal (Fig. 2C) and  $\alpha$ -forms (Fig. 2A) of iPP [100, 101, 103–106]. The relative amount of crystals in the trigonal form is small at a pentene concentration of 8.8 mol% (sample DP8.8; Fig. 3C, curve d), as indicated by the low intensity of the diffraction peak at  $2\theta \approx 10^\circ$ , corresponding to  $(110)_t$  reflection of the trigonal form of iPP [103, 104], and increases at higher pentene concentrations (sample DP11; Fig. 3C, curve e).

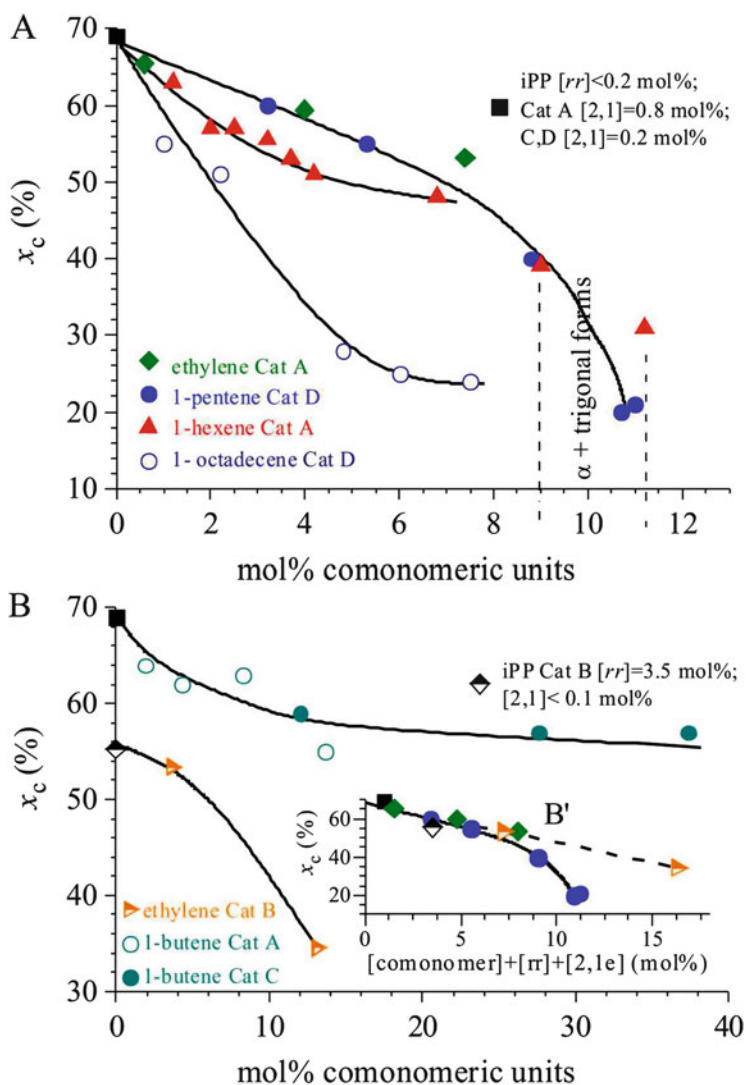
Samples of iPPoc crystallize from the melt in the pure  $\alpha$ -form (Fig. 3E, curves a, c–e). Crystals of both  $\alpha$ - and  $\gamma$ -forms are obtained only for sample DO2.2. However, presence of the new mesophase (Fig. 2D) cannot be excluded [102].

In all cases, the degree of crystallinity (Fig. 4) decreases with comonomer concentration. The decrease is low in the case of iPPBu copolymers and becomes progressively steeper with increasing the size of the comonomeric unit from pentene to octadecene. In particular, in the case of copolymers crystallized with the highly stereoselective but not completely regioselective catalysts A, C, and D it is possible to discern the effect of the presence of comonomeric units on crystallinity and melting temperature. More precisely, the degrees of crystallinity of the copolymers of propene with ethylene (AEx) and pentene (DPx) decrease with the concentration of comonomeric units according to a nearly common trend, in agreement with the fact that ethylene is partially included in the crystals of  $\alpha$ - and  $\gamma$ -forms, and pentene in the crystals the of  $\alpha$ -form (Fig. 4A). In the case of iPPHe copolymers prepared using catalyst A (AHx), hexene units are partially included in the crystals of the  $\alpha$ -form of iPP, and the decrease in crystallinity is only slightly steeper than in iPPPe systems formed using catalyst D (DPx). However, in the case of iPPoc copolymers prepared using catalyst D (DOx), octadecene units are not included at all in the crystals of  $\alpha$ - and/or  $\gamma$ -forms because of the high the size of the lateral side chains. As a consequence, the degree of crystallinity rapidly decreases with the concentration of octadecene units and is always lower than for other copolymers of identical concentration (Fig. 4A). In the case of iPPBu copolymers prepared using catalyst A (ABx), which are crystalline in the whole composition range [97–99], the decrease in degree of crystallinity with butene concentration is low (Fig. 4B), in agreement with the good inclusion of the units in the  $\alpha$ - and  $\gamma$ -forms of iPP.

In the case of the highly regioregular, less stereoregular, iPPet copolymers synthesized with catalyst B (BEx), the degree of crystallinity decreases with increasing concentration of ethylene units more rapidly than in the stereoregular and slightly regiodeficient samples prepared using catalyst A (AEx) of identical composition, in agreement with the presence of a concentration of *rr* stereodeficient of about 3.5 mol%. However, because stereodeficient *rr* are also partially included in the  $\alpha$ - and  $\gamma$ -forms of iPP and these defects play the same role as ethylene co-units, a plot of degree of crystallinity as a function of the total concentration of defects identifies a common trend for iPPet copolymers formed using catalysts A or B (Fig. 4B', inset).

The melting temperature  $T_m$  also decreases with increasing concentration of comonomeric units (Fig. 5) but the slope varies according to the comonomer and/or catalyst. Once again, in the case of the regiodeficient copolymer samples produced with the catalysts A, C, and D (Fig. 5A), the decrease is least for iPPBu copolymers. This diminution increases for iPPet copolymers and becomes steeper with increasing size of comonomeric units, following a common trend for iPPPe and iPPHe copolymers, but then drops rapidly for iPPoc systems. Furthermore, in the case of the highly regioregular but stereodeficient iPPet copolymers synthesized with catalyst B, the decrease in melting temperature with increasing total concentration

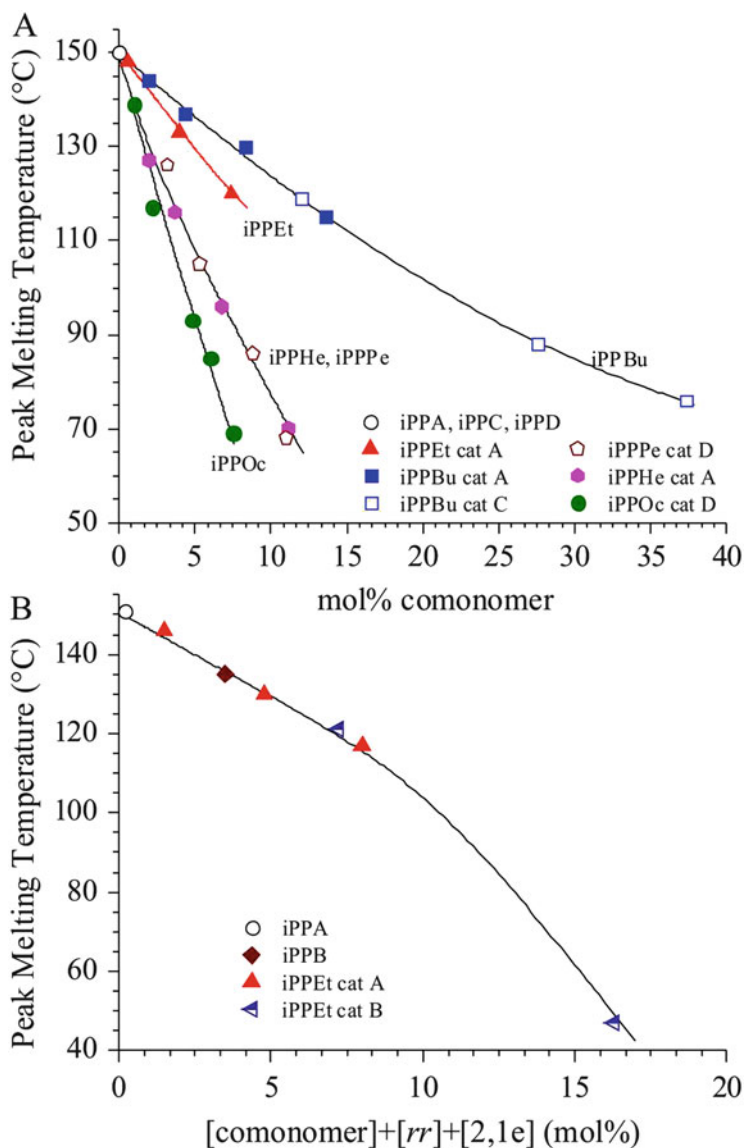




**Fig. 4** Degree of crystallinity of iPP homopolymers and iPPEt, iPPBu, iPPPe, iPPHe, and iPPOc copolymer samples prepared with catalysts A–D of Scheme 1, as a function of the concentration of comonomeric units (A, B) and the total concentration of defects (B', inset)

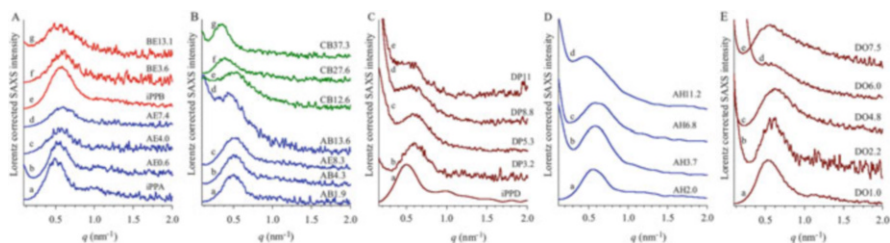
of defects is similar to that for the slightly regioirregular iPPEt copolymers synthesized with catalyst A at similar defect concentration (Fig. 5B).

The Lorentz-corrected SAXS intensity for the compression-molded homo- and copolymer samples listed in Table 1 is shown in Fig. 6. All samples show a broad correlation peak around  $q^* \approx 0.5 \text{ nm}^{-1}$  as a result of lamellar stacking. The broadness of the peak increases with increasing comonomer concentration.



**Fig. 5** Melting temperature of iPP homopolymers iPPA, iPPB, iPPC, and iPPD, and of iPPEt, iPPBu, iPPPe, iPPHe, and iPPOc copolymer samples prepared with the catalysts A–D of Scheme 1, as a function of concentration of comonomeric units (A) and, in the case of iPPA, iPPB and iPPEt samples, as a function of the total concentration of defects (B)

Simultaneously, the SAXS intensity in the background and at low  $q$  regions increases, especially for the highly defective samples AB13.6 (Fig. 6B, curve d), DP5.3, DP8.8, and DP11 (Fig. 6C), AH11.2 (Fig. 6D, curve d), and DO6.0 (Fig. 6E,



**Fig. 6** Lorentz-corrected SAXS intensity of iPP homopolymers and iPPeT (A), iPPBu (B), iPPPE (C), iPPHe (D), and iPPOc (E) copolymer samples prepared with catalysts A–D of Scheme 1

curve d). The SAXS profiles shown in Fig. 6 can be interpreted in terms of a lamellar morphology, which becomes highly imperfect with increasing comonomer content. Imperfections typically correspond to the formation of distorted lamellae having small lateral dimensions, large distributions of the thicknesses of the crystalline and amorphous layers in the lamellar stacks, formation of short lamellar stacks and/or of more than one population of lamellar stacks with different thicknesses, and, especially for copolymers with a higher concentration of comonomeric units, the presence of single lamellar entities together with a population of periodic arrays of parallel lamellae [153].

The average values of the long spacing  $L$ , thickness of the crystalline layer  $l_c$  (lamellar thickness), and thickness of amorphous  $l_a$  layers for the most representative stacks formed in the compression-molded samples, calculated from the position  $q^*$  of the main correlation peak in the SAXS profiles shown in Fig. 5, are compared in Table 2 and Fig. 7. With the exception of iPPBu samples (Fig. 7D), in all cases the lamellar periodicity  $L$  is around 11–13 nm. With increasing concentration,  $L$  first shows a slight decrease up to a monomer content of 6–8 mol%, then tends to increase at higher comonomer concentration (Fig. 7A–C). The thickness of lamellar crystals tends to decrease, whereas that of amorphous layers tends to increase with increasing comonomer concentration.

Three kinds of behavior can be identified, depending on the degree of inclusion of the comonomeric units in  $\alpha$ - and/or  $\gamma$ -forms of iPP. The first kind of behavior corresponds to the case of the isotactic copolymers iPPeT (samples AEx), iPPPe (samples DPx), and iPPHe (samples AHx), produced with the highly stereoselective catalysts A and D, and containing only small amounts of regiodefects. Samples with identical concentrations of comonomeric units develop a lamellar morphology characterized by identical values of the parameters  $L$ ,  $l_c$ , and  $l_a$  (Fig. 7A). In these samples, the ethylene, pentene, and hexene units are partially included in the crystals, the decrease in lamellar thickness  $l_c$  and increase in thickness of amorphous layers  $l_a$  with comonomer concentration are monotonous, whereas the long spacing  $L$  first decreases and, then, at higher comonomer concentration, tends to increase slightly. In the case of copolymers iPPeT synthesized with catalyst B (samples BEx) and containing 3.3–3.6 mol% of  $rr$  stereodefects, the lamellar morphology is characterized by parameters identical to those of samples

**Table 2** Comparison of lamellar parameters for iPP homopolymers and various copolymers prepared using different MAO-activated metallocene catalysts

Sample <sup>a</sup>	$q^{*b}$ (nm <sup>-1</sup> )	$x_c^c$ (%)	$L^d$ (nm)	$l_c^e$ (nm)	$l_a^f$ (nm)	$T_m^g$ (°C)	Comonomer conc. <sup>h</sup> (mol%)	$\epsilon_{tot}^i$ (mol%)	$\sigma_y^j$ (MPa)	$\epsilon_y^k$
<i>Homopolymers iPP</i>										
iPPA	0.51	69	12.32	8.50	3.82	151	0	1.00	—	—
iPPB	0.55	55.3	11.42	6.32	5.11	135	0	3.5	17 ± 2	49 ± 12
iPPD (iPPC)	0.51	69	12.32	8.50	3.82	151	0	0.2	—	—
<i>Propene-ethylene copolymers iPPEt</i>										
AE0.6	0.55	61.4	11.4	7.47	3.95	146	0.6	1.5	—	—
AE4.0	0.57	59.4	11.0	6.55	4.48	130	4.0	4.8	19 ± 5	38 ± 10
AE7.4	0.60	53.1	10.5	5.56	4.91	117	7.4	8.0	17 ± 5	47 ± 10
BE3.6	0.60	53.4	10.5	5.59	4.88	121	3.6	7.2	15 ± 4	49 ± 8
BE13.1	0.56	34.5	11.2	3.87	7.35	47	13.1	16.3	3.9 ± 1	45 ± 9
<i>Propene-1-butene copolymers iPPBu</i>										
AB1.9	0.50	64	12.6	8.04	4.52	144	1.9	2.4	—	—
AB4.3	0.52	62	12.1	7.49	4.59	137	4.3	4.7	18 ± 2	39 ± 4
AB8.3	0.52	63	12.1	7.61	4.47	130	8.3	8.6	17 ± 2	28 ± 3
AB13.6	0.47	55	13.4	7.37	6.03	115	13.6	13.7	14 ± 1	21 ± 2
CB12	0.49	59	12.8	7.56	5.26	119	12.0	13.0	14 ± 1	33 ± 3
CB27.6	0.41	57	15.3	8.74	6.59	88	27.6	28.6	11 ± 1	34 ± 3
CB37.3	0.34	57	18.5	10.5	7.95	76	37.3	38.3	8 ± 1	22 ± 2
<i>Propene-1-pentene copolymers iPPPe</i>										
DP3.2	0.60	60	10.5	6.28	4.19	126	3.2	3.4	22 ± 1	16 ± 2
DP5.3	0.58	55	10.8	5.96	4.88	105	5.3	5.5	13 ± 1	23 ± 2
DP8.8	0.53	40	11.9	4.74	7.11	86	8.8	9.0	8.6 ± 0.5	20 ± 1
DP11	0.52	21	12.1	2.54	9.54	68	11.0	11.2	8.2 ± 0.2	19 ± 1

(continued)

**Table 2** (continued)

Sample <sup>a</sup>	$q^{*b}$ (nm <sup>-1</sup> )	$x_c^c$ (%)	$L^d$ (nm)	$l_c^e$ (nm)	$l_a^f$ (nm)	$T_m^g$ (°C)	Comonomer conc. <sup>h</sup> (mol%)	$\epsilon_{tot}^i$ (mol%)	$\sigma_y^j$ (MPa)	$\epsilon_y^k$
<i>Propene-1-hexene copolymers iPPHe</i>										
AH2.0 <sup>c</sup>	0.57	57	11.0	6.28	4.74	127	2.0	2.4	27 ± 3	16 ± 2
AH3.7 <sup>c</sup>	0.58	53	10.8	5.74	5.09	116	3.7	4.1	19 ± 1	25 ± 6
AH6.8 <sup>c</sup>	0.61	48	10.3	4.94	5.36	96	6.8	7.1	11 ± 1	30 ± 2
AH11.2 <sup>c</sup>	0.45	31	14.0	4.33	9.63	70	11.2	11.5	3 ± 1	32 ± 4
<i>Propene-1-octadecene copolymers iPPOc</i>										
DO1	0.55	54	11.4	6.17	5.25	139	1	1.2	20 ± 2	13 ± 2
DO2.2	0.60	51	10.5	5.34	5.13	117	2.2	2.4	13 ± 1	19 ± 2
DO4.8	0.63	28	9.97	2.79	7.18	93	4.8	5.0	7 ± 1	18 ± 2
DO6.0	0.54	25	11.6	2.91	8.73	85	6.0	6.2	5 ± 0.4	18 ± 2
DO7.5	0.57	24	11.0	2.65	8.38	69	7.5	7.7	2.7 ± 0.2	23 ± 2

<sup>a</sup>iPP homopolymers (iPPA, iPPB, iPPD) and iPPEt, iPPBu, iPPPe, iPPHe, and iPPOc copolymers were prepared with the MAO-activated metallocenes A–D of Scheme 1. Sample designations as in Table 1

<sup>b</sup>Position of the correlation peaks ( $q^*$ ) in the SAXS intensity profiles of Fig. 6

<sup>c</sup>Crystallinity index ( $x_c$ ) determined from X-ray powder diffraction profiles of Fig. 3

<sup>d</sup>Long spacing ( $L$ )

<sup>e</sup>Lamellar thickness ( $l_c$ )

<sup>f</sup>Thickness of amorphous layers ( $l_a$ )

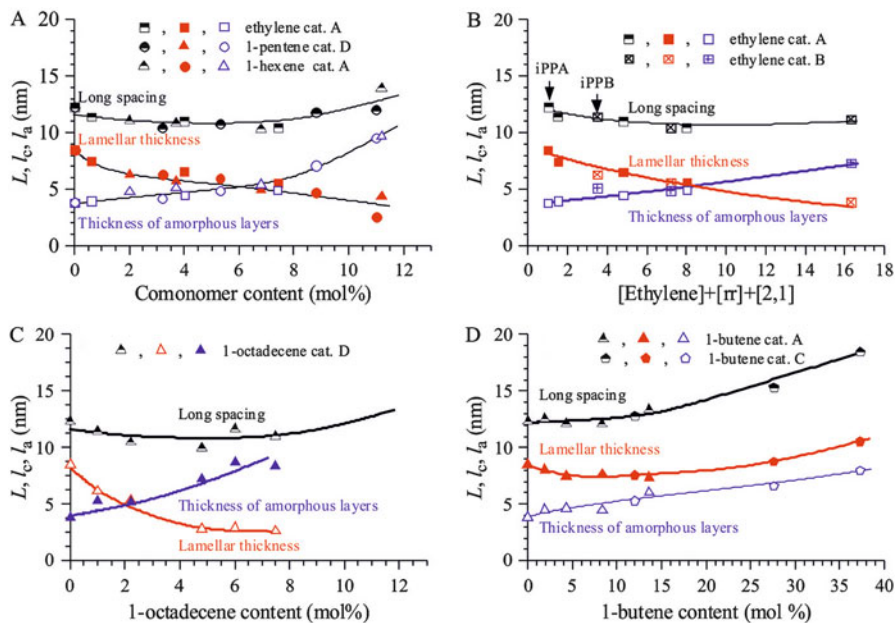
<sup>g</sup>Peak melting temperature ( $T_m$ ) of the compression-molded samples crystallized from the melt by slowly cooling to room temperature while fluxing cold water in the refrigerating circuit of press plates

<sup>h</sup>Concentration of comonomeric units (mol%)

<sup>i</sup>Total concentration of defects ( $\epsilon_{tot}$ )

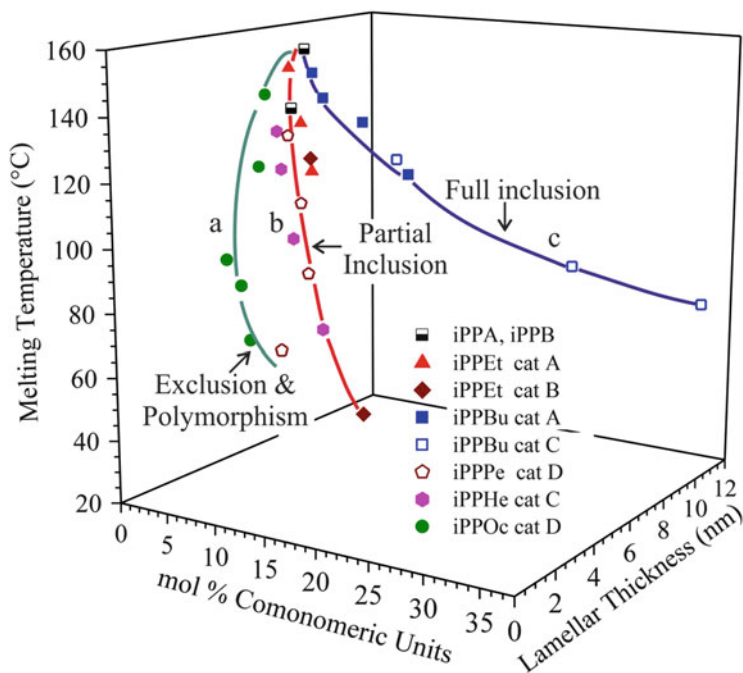
<sup>j</sup>Stress ( $\sigma_y$ ) at yield of compression-molded samples

<sup>k</sup>Strain ( $\epsilon_y$ ) at yield of compression-molded samples



**Fig. 7** Long spacing  $L$  and the thickness of crystalline  $l_c$  and amorphous  $l_a$  layers, as calculated from the SAXS profiles shown in Fig. 6, relative to iPPA, iPPB, and iPPD homopolymers and to iPPeT (A, B), iPPBu (D), iPPPe (A), iPPHe (A) and iPPOc (C) copolymer samples prepared with catalysts A–D of Scheme 1. In B, the lamellar parameters  $L$ ,  $l_c$ , and  $l_a$  of iPPeT copolymers synthesized with catalyst A and containing only 2,1 regiodefects ( $[2,1e] \approx 0.4\text{--}0.8$  mol%) and iPPeT copolymers synthesized with catalyst B and containing only  $rr$  stereodefects ( $[rr] \approx 3.2\text{--}3.6$  mol%) are compared as a function of the total concentration of defects  $\epsilon_{\text{tot}}$

synthesized with catalyst A (samples AEx) and having an equal concentration of defects. In particular, as shown in Fig. 7B, plotting  $L$ ,  $l_c$ , and  $l_a$  versus the total concentration of defects  $\epsilon_{\text{tot}} = [\text{ethylene}] + [rr] + [2,1e]$  for these copolymer samples identifies a unique trend confirming that  $rr$  stereodefects play the same role as ethylene co-units in the crystallization behavior of these systems. Also in this case, with increasing the comonomer concentration, we observe a monotonous decrease in lamellar thickness  $l_c$ , a monotonous increase in the thickness of amorphous layers  $l_a$ , and a slight decrease in the long spacing  $L$ . The second kind of behavior corresponds to total inclusion and occurs for the samples of isotactic copolymers iPPBu (Fig. 7D) synthesized with the highly stereoselective catalysts A and C. The easy inclusion of butene units in the crystals of the  $\alpha$ -form of iPP always produces crystals with lamellar thickness higher than the lamellar thickness of the other copolymers with identical concentration of units and minor degree of inclusion. With increasing comonomer concentration, the lamellar thickness  $l_c$  first decreases, then increases at high butene content, whereas the thickness of the amorphous layers  $l_a$  and the long spacing  $L$  increase monotonously. The third kind of behavior corresponds to total exclusion and occurs for the isotactic copolymers iPPOc



**Fig. 8** Melting temperature of iPP homopolymers and iPPeT, iPPBu, iPPPe, iPPHe, and iPPOc copolymer samples prepared with catalysts A–D of Scheme 1, as a function of lamellar thickness and concentration of comonomeric units. For the iPPeT samples prepared with catalyst B, the concentration of *rr* stereodefects ( $\approx 3.5$  mol%) has been added to the concentration of ethylene units. *Curve a* indicates the trend in the decrease in melting temperature for samples characterized by exclusion of comonomer units from the crystals; *curve b* partial inclusion; *curve c* full inclusion.

(Fig. 7C) synthesized with catalyst D (samples DOx). In this case, the thickness of the lamellar crystals is smaller than that of the copolymers with ethene, butene, pentene, and hexene because the bulky side chains are rejected from the crystals. For the iPPOc copolymers, the decrease in lamellar thickness  $l_c$  and increase in thickness of amorphous layers  $l_a$  with comonomer concentration are monotonous, whereas the long spacing  $L$  decreases only slightly.

From the data of Figs. 5 and 7, it is apparent that parallel to the decrease in melting temperature with comonomer content, the lamellar thickness also decreases. Indeed, the melting temperatures of our copolymers, and semicrystalline polymers in general, depend not only the content of comonomeric units but also on the lamellar thickness [154–158]. A direct correlation between the melting temperature, lamellar thickness, and comonomer content of melt crystallized copolymer samples obtained by compression molding is depicted in Fig. 8. It is apparent that in the case of the copolymers iPPeT, iPPPe, iPPHe, and iPPOc there is a concomitant decrease in melting temperature (Fig. 5) and lamellar thickness (Fig. 7A, B, C and Fig. 8, curves a, b) with increasing the concentration of comonomeric units. By

contrast, in the case of iPPBu copolymers, the melting temperature decreases with increasing butene concentration (Fig. 5), even though the lamellar thickness increases (Fig. 7D and Fig. 8, curve c).

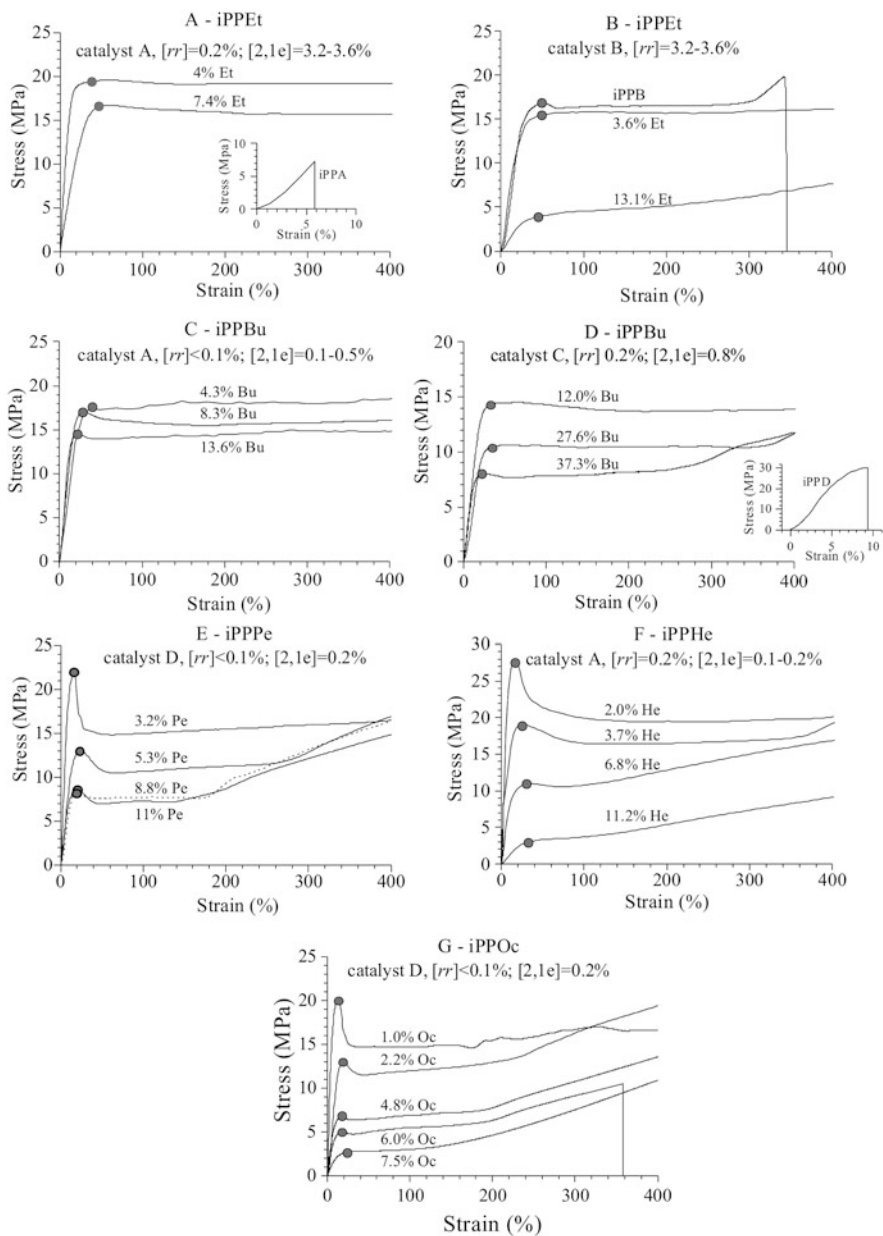
The differences in melting behavior are also common to other systems [154–158] and depend on the different degree of inclusion/exclusion of the comonomeric units in the crystals and/or crystallization into a different polymorph. According to Flory's theory [159] of copolymer crystallization, valid in the limit of strict exclusion, for A/B random copolymers with dilute B units excluded from crystals of A units, the melting temperature of copolymer crystals is lower than that of the A homopolymer exhibiting the same crystal thickness. This is a result of different concentrations of the comonomeric units in the crystals and in the melt in equilibrium. Because the melting temperature  $T_m$  is the ratio of the melting enthalpy  $\Delta H_m$  to the melting entropy  $\Delta S_m$  ( $T_m = \Delta H_m/\Delta S_m$ ), the presence of B units in the melt in equilibrium with crystals, produces a non-zero mixing entropy contribution to the melting entropy. This contribution increases with increasing concentration of B units in the copolymer, producing a decrease in melting temperature. On the other hand, according to the theory of Sanchez and Eby [160, 161], the melting temperature of an A/B random copolymer is lowered, even in the case of inclusion of B units in the crystals. Even in the limit of uniform inclusion of B units in the crystalline and amorphous regions, which corresponds to zero mixing entropy at melting, the enthalpy penalty for incorporation of B units in the crystals produces a decrease in the melting temperature, whereas lamellar thickness does not decrease.

In our case, the decrease in melting temperature with decrease in lamellar thickness follows a common trend in the case of iPPEt, iPPPe, and iPPHe copolymer samples (Fig. 8, curve b), characterized by partial inclusion of the comonomeric units in the crystals of  $\alpha$ - and/or  $\gamma$ -forms of iPP. Moreover, the total exclusion of comonomers from the crystals of  $\alpha$ - and/or  $\gamma$ -forms in the case of iPPOc copolymers produces melting depression associated with a major decrease in lamellar thickness (Fig. 8, curve a). Also, in the case of the iPPPe sample with high pentene concentration (DP11.0 containing 11 mol% pentene units), the comonomers are completely excluded from the crystals of  $\alpha$ - and/or  $\gamma$ -forms and are better included into the trigonal form [105, 106]. The competitive partial crystallization of the trigonal form causes melting point depression and a decrease in lamellar thickness. In the case of iPPBu copolymers, instead, the total inclusion of butene units in the crystals produces melting depression and no decrease in lamellar thickness (Fig. 8, curve c).

## 4 Mechanical Properties

The stress–strain curves of melt-crystallized samples of iPP homopolymers and iPPEt, iPPBu, iPPPe, IPPHe, and iPPOc copolymer samples obtained by compression molding are shown in Fig. 9. Only the first portion of the curves (up to 400% deformation) is reported, to put into evidence the yield behavior. It is worth noting that all copolymer samples show high flexibility, toughness, and ductility, with





**Fig. 9** Stress–strain curves of melt-crystallized films prepared by compression molding of iPP homopolymers iPPA, iPPB, and iPPD and of iPPEt (A, B), iPPBu (C, D), iPPPe (E), iPPHe (F), and iPPOc (G) copolymer samples synthesized with catalysts A–D of Scheme 1

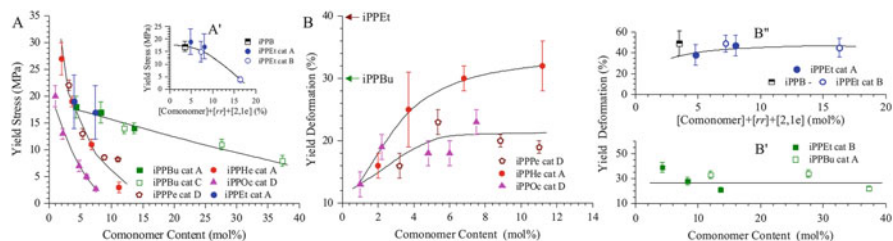
deformation at break higher than 300–400% [98, 101, 103]. By contrast, the highly stereoregular iPP samples prepared with catalyst A, C (data not reported), and D of Scheme 1, (iPPA, iPPC, and iPPD) are stiff and fragile materials, as shown in the insets of Fig. 9A, D [40, 41, 127, 128]. Only the highly regioregular, less stereoregular, iPPB sample containing 3.5 mol% *rr* defects shows high flexibility coupled with high toughness and values of deformation at break of about 350% [40, 41, 127] (Fig. 9B).

In all cases, the stress at any strain decreases with increasing concentration of comonomeric units (Fig. 9). Plastic resistance also decreases, as indicated by the values of the yield stress. The stereodeficient homopolymer sample iPPB, and the copolymer samples iPPeT and iPPBu show uniform deformation and smooth yield behavior regardless of comonomer concentration (Fig. 9A–D) [98]. By contrast, the highly stereoregular copolymer samples with side chains longer than the ethyl group (iPPPe, iPPHe, and iPPOc) show less uniform deformation and sharp yielding behavior at low comonomer concentrations [98, 101–103]. The yielding behavior becomes smoother with increasing comonomer content (Fig. 9E–G), and the deformation becomes uniform. The copolymer samples iPPeT, iPPHe, and iPPOc with the highest comonomer concentrations (BE13.1, AH11.2 and DO7.5, respectively) and the iPPBu sample CB12 with 12 mol% butene units show diffuse yielding behavior and uniform deformation.

The values of stress and deformation at yield are reported in Fig. 10. It is apparent that the decrease in stress at yield with increasing comonomer concentration (Fig. 10A, A') is accomplished with an increase in deformation at yield (Fig. 10B, B' B''). It is also apparent that each kind of comonomer influences the yield behavior of the copolymers differently. In particular, in the case of highly stereoregular, slightly regiodefective copolymer samples iPPeT, iPPBu, iPPPe, iPPHe, and iPPOc prepared with the catalysts A, C, and D, the decrease in  $\sigma_y$  values is smooth and quasilinear for iPPeT and iPPBu systems and becomes steeper with increasing size of comonomeric units. This decrease is similar for iPPPe and iPPHe samples (Fig. 10A). Moreover, as shown in Fig. 10A' (inset), in the case of the stereodeficient iPP homopolymer sample and iPPeT samples prepared with catalyst B, the decrease in the values of stress at yield as a function of the total concentration of defects is similar to that of regiodefective iPPeT samples prepared with catalyst A.

The values of deformation at yield  $\epsilon_y$  for the samples iPPPe, iPPHe, and iPPOc increase with the concentration of pentene, hexene, and octadecene comonomeric units (Fig. 10B), but are nearly constant, or increase only slightly, in the case of iPPeT (Fig. 10B'') and iPPBu (Fig. 10B') copolymers.

The data in Fig. 10 indicate that the decrease in plastic resistance is generally associated with an increase in deformation at yield. The decrease in plastic resistance, in turn, is related to the level of inclusion in and/or exclusion of comonomeric units from crystals, and to the effective level of disturbance of the defects included in the crystals in the case of inclusion. The almost complete inclusion of butene units in the crystals of the  $\alpha$ -form of iPP produces a small decrease in stress at yield (Fig. 10A), and constant values of deformation at yield

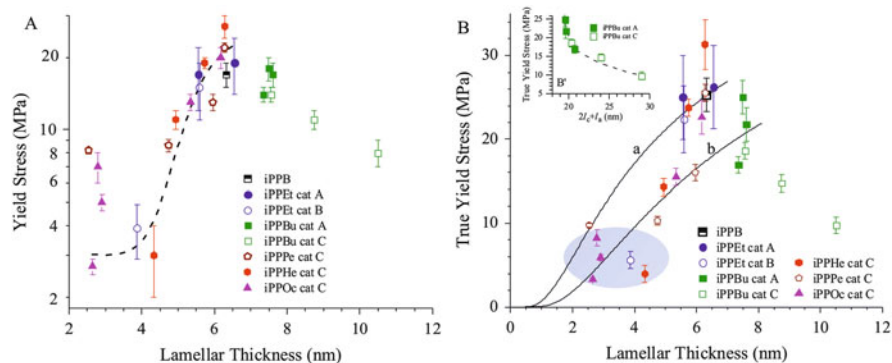


**Fig. 10** Values of stress and strain at yield of melt-crystallized films obtained by compression molding of iPP homopolymer iPPB (A', B'') and iPPeT (A, A', B, B''), iPPBu (A, B, B'), iPPPe (A, B), iPPHe (A, B), and iPPOc (A, B) copolymer samples prepared with catalysts A–D of Scheme 1. Arrows in B indicate the average values of deformation at yield of iPPeT (B'') and iPPBu (B') samples. Samples iPPA, iPPC, and iPPD are not included because they break before yielding

(Fig. 10B') that are not dependent on butene concentration. On the other hand, partial (ethylene, pentene, and hexene) or complete (octadecene) exclusion of comonomeric units from the crystals of  $\alpha$ - or  $\gamma$ -forms of iPP induces a larger decrease in stress at yield (Fig. 10A), coupled with an increase in yield deformation (Fig. 10B, B'').

As analyzed in the preceding section, melt-crystallized films of these copolymers prepared by compression molding are characterized by different lamellar thicknesses. For semicrystalline polymers, the values of yield stress generally increase with lamellar thickness. In fact, thick lamellae generally entail major crystal stability, and therefore also strong plastic resistance [5–7, 14–19]. The values of yield stress shown in Fig. 10A for the compression-molded samples of copolymers crystallized under similar conditions are reported in Fig. 11 as a function of lamellar thickness, as evaluated from the SAXS profiles shown in Fig. 7. A unique correlation line can be established, regardless of comonomer type. In particular, the logarithm of the yield stress increases as a function of the average values of lamellar thickness according to a sigmoidal master curve. Deviation from this correlation is observed for copolymers of iPPBu with butene concentrations higher than 12–13 mol%, where the lamellar thickness increases and the yield stress decreases with increasing butene concentration. For instance, for samples CB12, CB27.6, and CB37.3 (containing 12, 27.6 and 37.3 mol% of butene, respectively) with high lamellar thickness, the yield stress decreases with increasing lamellar thickness. Exceptions occur at low lamellar thickness for the copolymer iPPPe with pentene content of 11 mol% (sample DP11) and the highly defective copolymers iPPOc with octadecene content of 4.8–6 mol% (samples DO4.8 and DO6.0). These samples show yield stress values that are larger than those expected on the basis of the sigmoidal master curve. However, with further increase in octadecene content (sample DO7.5 with 7.5 mol% comonomer), the value of the yield stress suddenly drops, in apparent agreement with expectation.

These results indicate that, on the one hand, for a homogeneous class of propene-based copolymers (crystallizing in  $\alpha$ - and/or  $\gamma$ -forms of iPP under similar conditions) the lamellar thickness controls the level of plastic resistance of the samples.



**Fig. 11** Values of nominal stress (A) and true stress at yield (B) of melt-crystallized films obtained by compression molding of iPP homopolymer iPPB and iPPEt, iPPBu, iPPPe, iPPHe, and iPPOc copolymer samples prepared with catalysts A–D of Scheme 1. *Inset B'* shows values of true stress at yield of melt-crystallized films obtained by compression molding of iPPBu copolymers as a function of  $2l_c + l_a$ . *Solid lines in B* indicate the theoretical predictions of yield stress on the basis of the crystallographic model [25] based on thermal activation of screw dislocations, according to Eq. 5, by setting the value of the Burgers vector  $B = 0.650$  nm, the shear modulus of (040) planes  $K = 0.84$  GPa, and the free energy barrier associated with nucleation of [001] dislocations  $\Delta G^*$  in the range 40–90 kT, namely  $\Delta G^* = 59$  kT (curve a) and 90 kT (curve b) [94]. The shaded area indicates samples with critical dislocation nuclei (calculated using Eq. 3) too large in size to be acceptable

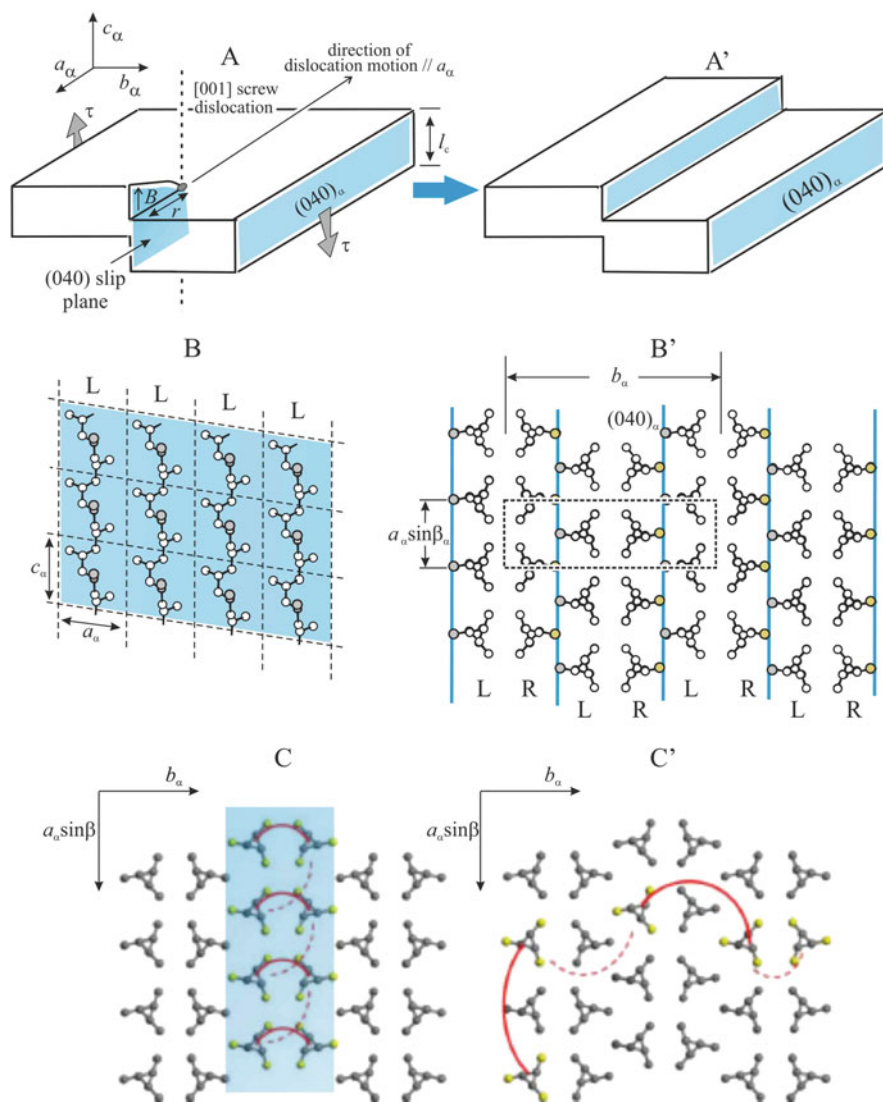
However, because crystal stability also depends on the concentration and distribution of the structural irregularities, in the case of iPPBu copolymers with a high concentration of butene units, the easy inclusion of comonomers in the unit cell of the  $\alpha$ -form of iPP induces formation of lamellar crystals of high thickness but lower plastic resistance (yield stress) than expected for defect-free crystals of homopolymer having identical thickness. This indicates that butene units act as point-like defects in the crystals and, therefore, induce a decrease in plastic resistance. On the other hand, polymorphism and the amorphous phase placed between lamellar crystals could also play a role [5–7, 14–19]. This is evidenced in the case of iPPOc copolymers with 4.8 and 6 mol% of octadecene. For these copolymers, the yield stress is higher than expected on the basis of the low values of lamellar thickness. Because the long branches are rejected from the crystals, their confinement in the amorphous interlamellar layers close to the fold surfaces produces an indirect increase in resistance to plastic deformation of the crystals, probably as a result of topological restraints. Instead, polymorphism is involved for iPPPe and iPPOc copolymer samples DP11 and DO7.5 (with 11 and 7.5 mol% of pentene and octadecene units, respectively). As shown in Fig. 3, the sample DP11 crystallizes in a mixture of crystals of  $\alpha$ -form and trigonal form [103, 104] (Fig. 2C), whereas the sample DO7.5 crystallizes in a mixture of  $\alpha$ -form and the second mesophase of iPP [102] (Fig. 2D). Both the trigonal form and the mesomorphic form that crystallize along with the  $\alpha$ -form are characterized by partial inclusion of comonomers in the crystalline domains. The trigonal form of the iPPPe copolymer is characterized by

long-range order in two dimensions for the positioning of chain axes of the 3/1 helices [162] (Fig. 2C); the new mesomorphic form of the iPPoc sample, instead, presents no lateral order in the position of chain axes, and only an average periodicity parallel to chain axes of 3/1 helices [162] (Fig. 2D). As a consequence, the presence of a second polymorph increases the resistance to plastic deformation in the iPPPe sample partially crystallized in the trigonal form, but decreases the plastic resistance in the iPPoc samples partially crystallized in the new mesophase.

At temperatures higher than the glass transition, the strong dependence of yield stress on lamellar thickness, which is generally observed for semicrystalline polymers and in our copolymers in particular (Fig. 11A), entails a yield behavior possibly controlled by activation of plastic deformation of lamellar crystals through crystallographic slip processes [5–7, 14–19, 25]. Crystallographic slip processes, in turn, are facilitated by nucleation and propagation of dislocations and/or defects [25, 74–76]. According to this mechanism, the stress at yield corresponds to the point of the stress–strain curve at which local stress reaches the level of the critical resolved shear stress for the easiest slip system. This level is, in turn, controlled by nucleation and propagation of dislocations within deforming crystals [5–7, 14–19, 25, 84]. Therefore, the strong dependence of the yield stress of polymer crystals on lamellar thickness (Fig. 11A) can be explained by the fact that the critical stress for activation of chain slip is directly related to the strong dependence of the rate of nucleation of dislocations on the thickness of the crystals.

The minimum stress required for nucleation and activation of a new dislocation at the edges of lamellar crystals and the relationship between this stress to crystal thickness can be predicted using the model of Young [25], successively refined by Shadrake and Guiu [93]. According to this model, any contribution from the chains in the amorphous phase to the yield stress is neglected in a first approximation. The role of amorphous chains is merely as force transmitters, because the modulus of the amorphous phase above  $T_g$  is an order of magnitude lower than the modulus of crystalline phase. The model assumes that deformation occurs by  $\{hk0\} \langle 001 \rangle$  chain direction slip, resulting in the formation of  $[001]$  screw dislocations (i.e., dislocations parallel to the chain axes) [25]. The Burgers vector  $\mathbf{B}$ , parallel to the chain axis (Fig. 12A) at distance  $r$  from the dislocation, has magnitude  $B$  and generally spans only a small integer number  $n$  ( $n = 1, 2$ ) of chain periodicities  $c$ . The nucleation and activation of  $[001]$  dislocations of length  $l_c$  coincident with the lamellar thickness is a thermally activated process requiring a critical level  $\tau^*$  of shear stress. Within the model, only the value of  $\tau^*$  matters because the intrinsic movement of already formed dislocations occur at Peierls–Nabarro stress (i.e., at a stress level much lower than  $\tau^*$ ) (Fig. 11A). According to the crystallographic approach, yielding (i.e., the beginning of plastic deformation) starts when the critical resolved shear stress is reached in any family of planes with low  $\tau^*$ . This corresponds to slip planes coincident with the lattice planes of maximum packing and to slip directions parallel to the lattice directions of maximum packing [5–7, 14–19, 25].

In the simplest approach, the free energy associated with the nucleation of such dislocations can be written as:



**Fig. 12** (A) Model of a  $[001]$  screw dislocation, nucleated at the edge of a lamellar crystal of iPP in the  $\alpha$ -form, that has advanced a distance  $r$  inside the crystal parallel to the  $(040)$  slip planes, along the slip direction. The length of the dislocation is equal to the crystal thickness  $l_c$ , whereas the Burgers vector, parallel to chain axis, has a magnitude equal to the chain periodicity  $c_\alpha$  ( $B = 0.65$  nm). Lamellar crystals (A') obtained through deformation in the  $\{0k0\} \langle 00l \rangle$  chain direction slip leading the dislocation in A to emerge at the opposite edge of the crystal and consequent formation of a step. (B) The  $(040)$  slip planes in two projections parallel (B) and perpendicular (B') to the chain axis. Symbols *L* and *R* stand for left- and right-handed helical chains, respectively. Rows  $a_\alpha - c_\alpha$  of all left-handed helical chains alternate with rows of chains of opposite chirality forming double layers, delimited by traces of the  $(040)$  planes in B'. The lattice planes  $(040)$  are planes of close packing and the slip direction in A is parallel to the lattice direction of maximum packing [149, 150]. (C) Schemes of chain folding with adjacent (C) and non-adjacent re-entry (C') for the limit-ordered [150, 162] and limit-disordered

$$\Delta G = \frac{KB^2l_c}{2\pi} \ln \frac{r}{r_0} - l_c B r \tau \quad (2)$$

In Eq. 2,  $K$  is the shear modulus associated with the  $\{hk0\}\langle 001\rangle$  slip process,  $r_0$  is the core radius of the dislocations (generally assumed to be twice the value of  $B$  [26, 94]), and  $r$  is the distance of the dislocation from the edge of the crystal (Fig. 12A). The first term corresponds to the elastic strain energy and the second term corresponds to the work performed by the external shear stress. In Eq. 2, the core energy contribution as a result of lattice distortions around the dislocation is neglected. Dislocations are activated when the distance of a dislocation from the edge of the crystal reaches a critical value  $r^*$  (size of the critical dislocation nuclei), obtained by setting the derivative of  $\Delta G$  with respect to  $r$  as equal to zero [25]. The obtained value of the critical size of the dislocation  $r^*$ , the critical nucleus, is given by:

$$r^* = \frac{KB}{2\pi\tau} \quad (3)$$

By combining Eqs. 2 and 3, the activation barrier of free energy  $\Delta G^*$  needed to nucleate a dislocation of critical size  $r^*$  is obtained as:

$$\Delta G^* = \frac{KB^2l_c}{2\pi} \left[ \ln \left( \frac{r^*}{r_0} \right) - 1 \right] \quad (4)$$

Finally, introducing Eq. 3 into Eq. 4, the value of tensile stress  $\sigma_y$ , which is twice the critical value of the shear stress  $\tau_y$  (i.e.,  $\sigma_y = 2 \tau_y$ ) according to Tresca's criterion, is obtained as:

$$\sigma_y = \frac{K}{2\pi} \exp \left( - \frac{2\pi\Delta G^*}{l_c KB^2} - 1 \right) \quad (5)$$

Notice that Eq. 5 assumes that the core radius of the dislocation  $r_0$  is equal to twice the length of the Burgers vector  $B$  ( $2r_0$ ) [26, 94].

To compare the yield behavior of our samples with the predictions of the crystallographic model based on thermal activation of dislocations (Eq. 5), the values of true stress at yield are needed. In general, the transverse strain of semicrystalline polymers (perpendicular to the stretching direction under uniaxial elongation) decreases with deformation. For rubbery materials at low deformation, the transverse section  $S$  of the deformed sample is related to the initial section  $S_0$  of the specimen by the relationship  $S = S_0 (l_0/l)$  where  $l_0$  and  $l$  are the initial gauge-

---

**Fig. 12** (continued) [149, 162]  $\alpha$ -forms of iPP, respectively. Deformations in the  $\{010\}\langle 001\rangle$  chain direction slip comply well with the chain folding scheme with adjacent re-entry C. (C and C' are reproduced from [163], with ACS permissions)

length and the gauge-length in the deformed state, respectively. This relationship entails that the sample is incompressible, that is, that Poisson's ratio is equal to 0.5. However, for semicrystalline polymers, Poisson's ratio changes during deformation from the maximum value of 0.5 to values close to zero, as a result of volume expansion caused by crazing, cracks, and voids [164]. We checked that the deformation of our copolymer samples was largely uniform up to the yield point. Therefore, we corrected the nominal values of stress at yield by the factor  $l/l_0$  to obtain the true stress, implicitly assuming a Poisson's ratio close to 0.5. The obtained values of true stress are reported in Fig. 11B as a function of lamellar thickness.

Representative curves describing the change in yield stress with lamellar thickness according to the crystallographic model based on thermal activation of screw dislocations are also given in Fig. 11B. They were generated using Eq. 5 by fixing the parameters of the model according to the values suggested in the literature for modeling the yield behavior of iPP [94]. For the sake of simplicity and without loss of generality, confining attention to the  $\alpha$ -form of iPP, it is assumed that plastic deformation occurs by  $\{0k0\}\langle 00l\rangle$  chain direction slip that is parallel to the (040) planes of maximum packing of the iPP  $\alpha$ -form, with the [001] screw dislocation parallel to the chain axes (Fig. 12A, B, B'). This deformation mechanism complies well with the chain folding scheme for the  $\alpha$ -form of iPP, characterized by adjacent re-entry (Fig. 12C), as proposed by Corradini [165–167] and confirmed by double quantum  $^{13}\text{C}$ – $^{13}\text{C}$  solid state NMR [163]. In particular, the value of the Burgers vector  $B$  is set equal to 0.650 nm, corresponding to the chain periodicity of iPP in the  $\alpha$ -form [149, 150]. The values for the energy barrier  $\Delta G^*$  were selected in the typical range of 40–90  $kT$  [94] associated with the thermal nucleation of dislocation at laboratory time scales, namely  $\Delta G^* = 59$  and 90  $kT$ , respectively. The values of shear modulus for the (040) lattice planes was set at 0.84 GPa, in agreement with values suggested in the literature for iPP (in the range 0.84–1.0 GPa) [94].

A screw dislocation scheme similar to that of Fig. 12 for the  $\alpha$ -form of iPP can also be proposed for the  $\gamma$ -form [151, 152], considering that the chain axes in the  $\gamma$ -form are directed along the diagonal of the  $C$  face of the orthorhombic unit cell (Fig. 2B). This entails that the screw dislocations parallel to the chain axes are parallel to the [110] and/or  $[\bar{1}10]$  lattice directions and that plastic deformation occurs by  $\{00l\}\langle 110\rangle$  chain direction slip (i.e., parallel to the (008) planes of the  $\gamma$ -form). A further adjustment of the crystallographic model entails that the chain axes, and therefore the Burgers vector, lie at a tilted angle of  $\approx 40^\circ$  to the normal of the basal face of the lamellar crystals.

With the exception of iPPBu copolymer samples with high butene content, the results of the model appear to be in good agreement with experimental results in all cases (Fig. 11B). This indicates that, in spite of the simplicity of the model, the crystallographic model describes well (without making any fitting attempt) the yield behavior of our samples, regardless of the kind and concentration of comonomeric units. This result is noteworthy, especially considering that the copolymers are characterized by different degrees of inclusion/exclusion of the



comonomeric units in the crystals. This inclusion generates different concentrations and kinds of structural disorder and, therefore, the crystals are characterized by different intrinsic stabilities. Moreover, the spread of experimental data in Fig. 11B is also the result of measurements being performed in independent experiments, at ambient conditions (room temperature) subject to significant thermal fluctuations ( $\pm 5^\circ\text{C}$ ) and on samples adopting slightly different deformation rates, although the ratio between the deformation rate  $v_{\text{def}}$  and initial gauge length  $l_0$  was fixed at 10 ( $v_{\text{def}}/l_0 = 10$ ). Minor errors also arise from the approximate evaluation of true stress at yield utilizing a Poisson ratio of 0.5 and the approximate evaluation of lamellar thickness  $l_c$ , since the volume fraction of the crystalline phase is slightly lower than the crystallinity index  $x_c$  resultant from WAXS analysis. In fact, using values of the Poisson ratio close to 0.4, typical for semicrystalline polymers at low deformations, and/or values of lamellar thickness evaluated from the one-dimensional correlation function [120, 121], the dislocation model can equally well describe the yield behavior of our samples, using values close to 0.84 GPa for the shear modulus for the (040) planes  $K$  and in the range 59–90  $kT$  for the free energy barrier associated with the nucleation of [001] dislocations  $\Delta G^*$ .

We also checked that the size of the critical dislocation nucleus  $r^*$  calculated using Eq. 2 is in all cases in the range 5–10 nm, that is, less than the typical size of crystal blocks in lamellar crystals (15–30 nm) [100, 101], as estimated from the WAXS profiles using the Scherrer formula (the width at mid-height of the equatorial reflections are all in the range 0.4–0.8°; see Fig. 2). Only in the case of the samples with high comonomer content, having low lamellar thickness and low crystallinity, do the values of  $r^*$  exceed 15 nm. These samples are indicated in Fig. 10B and correspond to samples of iPPoc with octene content higher than 4 mol% (samples DO4.8, DO6.0, and DO7.5), iPPet with ethylene content of 13 mol% (sample BE13.1), and iPPPe and iPPHe with  $\approx 11$  mol% comonomer units (samples DP11 and AH11.2, respectively). Because the value of the critical dislocation nuclei  $r^*$  cannot be greater than the dimensions of a crystal block, the good agreement of the model with experimental data for low values of lamellar thickness should be considered with caution. In fact, the presence of crystals in a different polymorph, namely the  $\gamma$ -form for sample AH11.2, the trigonal form for samples DP11 and AH11.2 (Fig. 2C), and the new mesophase for sample DO7.5 (Fig. 2D), could completely alter the  $\{0k0\} \langle 00l \rangle$  chain direction slip mechanism of [001] dislocation proposed for the  $\alpha$ -form (Fig. 12A, B). Furthermore, the rejection of branches outside the crystals, close to the fold surfaces, increases the plastic resistance of the amorphous phase and overcomes the role of crystals in the yield mechanism [14–19]. This indicates that, for samples with low crystallinity in which the lamellar crystals have a thickness lower than the threshold value of 4–5 nm, the role of the amorphous phase in the yield behavior cannot be neglected.

A further exception occurs at high lamellar thickness for the iPPBu samples with butene concentrations higher than 12 mol%. In particular, the decrease in true stress values with increasing lamellar thickness cannot be explained by resorting to the crystallographic model. The yield behavior of these systems derives from the easy

inclusion of butene units in crystals of the  $\alpha$ -form. This inclusion, on the one hand, increases lamellar thickness while decreasing the stability of crystals and, on the other hand, increases lattice resistance to the gliding of dislocations because point defects act as Peierls barriers. Therefore, the observed values of yield stress achieved in these samples is the resultant of two competitive effects, the decrease in lamellar stability and the simultaneous increment of barriers to the movement of dislocations, because butene units in the crystals act as localized obstacles. An alternative or complementary mechanism subtending the yield behavior of these samples could involve the deformation modes of the amorphous phase, such as interlamellar separation and interlamellar slip (Fig. 1E, F) [5–7, 14–19]. These modes become active whenever the easiest movement at the mesoscale is stretching of the intralamellar amorphous chains connecting adjacent layers instead of crystal slip. To form an efficient tie, a chain emerging from a lamellar crystal (thickness  $l_c$ ) should travel across the amorphous layer (thickness  $l_a$ ) and enter a new crystalline lamella (thickness  $l_c$ ). The higher the number density of tie chains, the higher the yield stress level. Moreover, the higher the degree of separation of adjacent lamellae, the lower the number density of tie chains. Therefore, the probability of formation of a tie chain is expected to decrease with the quantity  $2l_c + l_a$ . The decrease in true stress at yield of these samples with increase in  $2l_c + l_a$  (shown in Fig. 11B', inset), is in agreement with the above argument.

It is worth noting that, using the Eyring formalization of thermally activated processes [168, 169], the temperature and strain rate dependence of yield stress of the iPP homopolymer indicate that two basic processes intervene in the stress response of a semicrystalline polymer [26–28, 62–65]. The first process involves intralamellar deformations or crystal slips, the mechanisms of which have been already detailed. The second process involves interlamellar deformations and is somehow linked to the  $\alpha$ -relaxation mechanism of iPP [170]. This relaxation involves motion of the 3/1 helical chains in the crystals through the combined effect of  $120^\circ$  rotations around the chain axis and  $c/3$  translation parallel to the chain axis [171]. These jumps result in chain diffusion through the crystals and necessarily involve the mobility of repeating units in the constrained amorphous zone surrounding the crystal [171]. In the case of iPP homopolymer, the intralamellar deformation contributes to the yield stress at high temperatures or low strain rates [62–65]. Crystal slip also participates at lower temperatures and/or high strain rates, but the main process contributing to the observed yield stress is the interlamellar process [62–65]. Therefore, in the case of iPP homopolymer, the contribution of  $\alpha$ -relaxation and consequent participation of the amorphous phase to the yield stress should not be neglected at deformation temperatures close to ambient.

In the case of copolymers, the  $\alpha$ -relaxation mechanism is expected to contribute actively to yield stress only at low comonomer concentration. With increasing concentration of comonomeric units, this mechanism becomes less important, regardless of the degree of inclusion/exclusion of comonomers in/from the crystals. In fact, chain diffusion inside the crystals associated with  $\alpha$ -relaxation is prevented by the large steric hindrance caused by comonomers located inside the crystals in

the case of inclusion, and by comonomers located in the amorphous regions close to the fold surfaces in the case of exclusion. The different degrees of participation of the  $\alpha$ -relaxation process to the yielding behavior of our copolymers can explain the bifurcation of the experimental values of yield stress shown in Fig. 11B. For lamellar thicknesses higher than 5 nm, samples with lower content of comonomeric units show values of yield stress close to the curve generated by setting the free energy barrier for nucleation of dislocations  $\Delta G^* = 59 \text{ kT}$  (Fig. 11B, curve a), whereas the samples with higher content of comonomeric units follow the curve generated by setting  $\Delta G^* = 90 \text{ kT}$  (Fig. 11B, curve b). We argue that the lower free energy barrier associated with the thermal nucleation of dislocations observed for the samples of curve a is a result of participation of the  $\alpha$ -relaxation process to their yield behavior. Lack of this participation, for the samples of the curve b, results in an increase in the free energy barrier.

## 5 Concluding Remarks

The yield behavior in tensile experiments of a wide class of semicrystalline polymers is analyzed in the framework of a crystallographic micromechanical model based on the thermal nucleation of dislocations. The samples are isotactic copolymers of propene with ethylene (iPPEt), 1-butene (iPPBu), 1-pentene (iPPPe), 1-hexene (iPPHe), and 1-octadecene (iPPOc) and possess a random distribution of comonomeric units and tailored concentrations of stereo- and regiodefects.

It has been shown that the decrease in plastic resistance depends on the level of inclusion/exclusion of the comonomeric units in/from the crystals and on the effective level of disturbance of the comonomers included in the crystals. Moreover, a remarkable dependence of yield stress on lamellar thickness has been demonstrated. In particular, we have shown that, in all cases, the values of yield stress decrease with lamellar thickness. By contrast, in the case of iPPBu copolymers, the almost complete inclusion of butene units in the crystals of  $\alpha$ -form produces a decrease in stress at yield and simultaneous increase in lamellar thickness.

According to the crystallographic approach, the phenomenon of yielding marks the beginning of plastic flow through occurrence of diffuse crystal slip processes, facilitated by the movement of dislocations, nucleation of new dislocations at the edge of lamellar crystals, and participation of the amorphous component through interlamellar slip or interlamellar rotation. Therefore, the thickness and intrinsic stability of lamellar crystals and the intrinsic mobility of the constrained interlamellar amorphous phase play key roles. Applying these concepts, we have shown that, except for iPPBu copolymers with high butene content, in our copolymers the yield behavior is largely controlled by the activation of plastic deformation of the crystals through crystallographic slip processes, involving, in turn, nucleation of new dislocations. However, for highly defective copolymers of low crystallinity, forming lamellar crystals of low thickness, the role of the deformation

modes of the amorphous phase, such as interlamellar separation and interlamellar slip, should not be neglected. In the case of iPPBu, the beginning of plastic deformation is also controlled by the increase in lattice resistance to glide of dislocations as a result of the butene units in the crystals acting as Peierls barriers.

## References

1. Keller A (1968) Polymer crystals. *Rep Prog Phys* 31:623–704
2. Ward IM, Sweeney J (2004) An introduction to the mechanical properties of solid polymers, 2nd edn. Wiley, Chichester
3. Peterlin A (1977) Plastic deformation of crystalline polymers. *Polym Eng Sci* 17:183–193
4. Peterlin A (1975) Composite structure of fibrous material. *Adv Chem Ser* 142:1–13
5. Oleinik EF, Rudnev SN, Salamatina OB (2007) Evolution in concepts concerning the mechanism of plasticity in solid polymers after the 1950s. *Polym Sci Ser A* 49:1302–1327
6. Haudin JM (1982) Plastic deformation of semi-crystalline polymers. In: Escaig B, G'Sell C (eds) (1982) Plastic deformation of amorphous and semi-crystalline materials. *Les Editions de Physique*, Paris, pp 291–311
7. Bartczak Z, Galeski A (2010) Plasticity of semicrystalline polymers. *Macromol Symp* 294:67–90
8. Lin L, Argon AS (1994) Structure and plastic deformation of polyethylene. *J Mater Sci* 29:294–323
9. Crist B (1993) Plastic deformation in material science and technology. In: Thomas EL (ed) A comprehensive treatment, vol 12. VCH, New York, pp 427–470
10. Lee BJ, Argon AS, Parks DM, Ahzi S, Bartczak Z (1993) Simulation of large strain plastic deformation and texture evolution in high density polyethylene. *Polymer* 34:3555–3575
11. Lee BJ, Argon AS, Ahzi S (1993) Micromechanical modeling of large plastic deformation and texture evolution in semi-crystalline polymers. *J Mech Phys Solids* 41:1651–1687
12. Hay IL, Keller A (1965) Polymer deformation in terms of spherulites. *Kolloid-Zu Z Polymere* 204:43–74
13. Breese DR, Beaucage G (2004) *Curr Opin Solid State Mater Sci* 8:439–448
14. Séguéla R (2007) Plasticity of semi-crystalline polymers: crystal slip versus melting-recrystallization. *e-Polymers* 032:1–20
15. Seguela R (2002) Dislocation approach to the plastic deformation of semicrystalline polymers: kinetic aspects for polyethylene and polypropylene. *J Polym Sci B Polym Phys* 40:593–601
16. Séguéla R (2005) Critical review of the molecular topology of semicrystalline polymers: the origin and assessment of intercrystalline tie molecules and chain entanglements. *J Polym Sci B Polym Phys* 43:1729–1748
17. Liu B, Zhang L, Gao H (2006) Poisson ratio can play a crucial role in mechanical properties of biocomposites. *Mech Mater* 38:1128–1142
18. Liu B, Feng X, Zhang S-M (2009) The effective Young's modulus of composites beyond the Voigt estimation due to the Poisson effect. *Compos Sci Tech* 69:2198–2204
19. Gorbatikh L, Pingle P (2007) On incompressibility of a matrix in naturally occurring composites. *Appl Phys Lett* 91:241913
20. Peterlin A (ed) (1971) Plastic deformation of polymers. Marcel Dekker, New York
21. Peterlin A (1987) In: Mark HF, Bikales NM, Overberger CG, Menges G, Kroschwitz JI (eds) *Encyclopedia of polymer science and engineering*. Wiley, New York, pp 72–94
22. Samuels RJ (1974) Structured polymer properties. Wiley, New York
23. Bueche F (1956) Young's modulus of semicrystalline polymers. *J Polym Sci A Polym Chem* 22:113–122

24. Halpin JC, Kardos JL (1972) Moduli of crystalline polymers employing composite theory. *J Appl Phys* 43:2235–2241
25. Bowden PB, Young RJ (1974) Deformation mechanisms in crystalline polymers. *J Mater Sci* 9:2034–2051
26. Schrauwen BAG, Bernard AG, Janssen RPM, Govaert LE, Meijer HEH (2004) Intrinsic deformation behavior of semicrystalline polymers. *Macromolecules* 37:6069–6078
27. Govaert LE, Meijer HEH (2005) Mechanical performance of polymer systems: the relation between structure and properties. *Prog Polym Sci* 30:915–938
28. Caelers HJM, Govaert LE, Peters GWM (2016) The prediction of mechanical performance of isotactic polypropylene on the basis of processing conditions. *Polymer* 83:116–128
29. Flory PJ, Yoon DY (1978) Molecular morphology in semicrystalline polymers. *Nature* 272:226–229
30. Gent AN, Madan S (1989) Plastic yielding of partially crystalline polymers. *J Polym Sci B Polym Phys* 27:1529–1542
31. Young RJ (1974) A dislocation model for yield in polyethylene. *Philos Mag* 30:85–94
32. Galeski A, Bartczak Z, Argon AS, Cohen RE (1992) Deformation mechanisms and plastic resistance in single-crystal-textured high-density polyethylene. *Macromolecules* 25:5705–5718
33. Hiss R, Hobeika S, Lynn C, Strobl G (1999) Network stretching, slip processes, and fragmentation of crystallites during uniaxial drawing of polyethylene and related copolymers. A comparative study. *Macromolecules* 32:4390–4403
34. Men Y, Strobl GJ (2001) Critical strains determining the yield behavior of s-PP. *J Macromol Sci Phys B40:775–796*
35. Hughes DJ, Mahendrasingam A, Oatway WB, Heeley EL, Martin C, Fuller W (1997) A simultaneous SAXS/WAXS and stress-strain study of polyethylene deformation at high strain rates. *Polymer* 38:6427–6430
36. Yamada M, Miyasaka K, Ishikawa K (1971) Redrawing of oriented polyethylene film. *J Polym Sci B Polym Phys* 9:1083–1096
37. Takahashi Y, Ishida T (1988) *J Polym Sci B Polym Phys* 26:2267–2277
38. Stoclet G, Seguela R, Lefebvre JM, Elkoun S, Vanmansart C (2010) Strain-induced molecular ordering in polylactide upon uniaxial stretching. *Macromolecules* 43:1488–1498
39. Seguela R (2005) On the strain-induced crystalline phase changes in semi-crystalline polymers: mechanisms and incidence on the mechanical properties. *J Macromol Sci C Polym Rev J* 45:263–287
40. De Rosa C, Auriemma F (2007) Stress-induced phase transitions in metallocene-made isotactic polypropylene. *Lect Notes Phys* 714:345–371
41. De Rosa C, Auriemma F (2006) Structural–mechanical phase diagram of isotactic polypropylene. *J Am Chem Soc* 128:11024–11025
42. De Rosa C, Auriemma F, de Ballesteros OR (2006) A microscopic insight into the deformation behavior of semicrystalline polymers: the role of phase transitions. *Phys Rev Lett* 96:167801–167804
43. De Rosa C, Auriemma F (2012) The deformability of polymers: the role of disordered mesomorphic crystals and stress-induced phase transformations. *Angew Chem Int Ed* 124:1233–1237
44. Liu Y, Kennard CHL, Truss RW, Carlos NJ (1997) Characterization of stress-whitening of tensile yielded isotactic polypropylene. *Polymer* 38:2797–2805
45. Hay IL, Keller A (1970) Mechanically induced twinning and phase transformations. *J Polym Sci C Polym Symp* 30:289–295
46. Frank FC, Keller A, O'Connor A (1958) Deformation processes in polyethylene interpreted in terms of crystal plasticity. *Philos Mag* 3:64–74
47. Kiho H, Peterlin A, Geil PH (1964) Polymer deformation. VI. Twinning and phase transformation of polyethylene single crystals as a function of stretching direction. *J Appl Phys* 35:1599–1605

48. Allan P, Crellin EB, Bevis M (1973) Stress-induced twinning and phase transformations in polyethylene single crystals. *Philos Mag* 27:127–145
49. Butler MF, Donald AM, Bras W, Mant GR, Derbyshire GE, Ryan AJ (1995) A real-time simultaneous small- and wide-angle X-ray scattering study of in-situ deformation of isotropic polyethylene. *Macromolecules* 28:6383–6393
50. Butler MF, Donald AM, Ryan AJ (1997) Time resolved simultaneous small- and wide-angle X-ray scattering during polyethylene deformation: 1. Cold drawing of ethylene- $\alpha$ -olefin copolymers. *Polymer* 38:5521–5538
51. Butler MF, Donald AM (1998) A real-time simultaneous small- and wide-angle X-ray scattering study of in situ polyethylene deformation at elevated temperatures. *Macromolecules* 31:6234–6249
52. Butler MF, Donald AM, Ryan AJ (1998) Time resolved simultaneous small- and wide-angle X-ray scattering during polyethylene deformation -- II. Cold drawing of linear polyethylene. *Polymer* 39:39–52
53. Ran S, Zong X, Fang D, Hsiao BS, Chu B, Phillips RA (2001) Structural and morphological studies of isotactic polypropylene fibers during heat/draw deformation by in-situ synchrotron SAXS/WAXD. *Macromolecules* 34:2569–2578
54. Ciferri A (1963) The  $\alpha \leftrightarrow$  transformation in keratin. *Trans Faraday Soc* 59:562–569
55. Ciferri A, Smith KJ Jr (1964) Phase changes in fibrous macromolecular systems and associated elasticity. Model phase diagrams. *J Polym Sci A* 2:731–753
56. Tashiro K, Nakai Y, Kobayashi M, Tadokoro H (1980) Solid-state transition of poly(butylene terephthalate) induced by mechanical deformation. *Macromolecules* 13:137–145
57. Auriemma F, De Rosa C (2003) New concepts in thermoplastic elastomers: the case of syndiotactic polypropylene, an unconventional elastomer with high crystallinity and large modulus. *J Am Chem Soc* 125:13143–13147
58. Auriemma F, De Rosa C (2003) Time-resolved study of the martensitic phase transition in syndiotactic polypropylene. *Macromolecules* 36:9396–9410
59. Auriemma F, De Rosa C, Esposito S, Mitchell GR (2007) Polymorphic superelasticity in semicrystalline polymers. *Angew Chem Int Ed* 46:4325–4328
60. Kazmierczak T, Galeski A, Galeski A, Argon AS (2005) Plastic deformation of polyethylene crystals as a function of crystal thickness and compression rate. *Polymer* 46:8926–8936
61. Argon AS, Galeski A, Kazmierczak T (2005) Rate mechanisms of plasticity in semicrystalline polyethylene. *Polymer* 46:11798–11805
62. Schrauwen BAG, van Breemen LCA, Spoelstra AB, Govaert LE, Peters GWM, Meijer HEH (2004) Structure, deformation, and failure of flow-oriented semicrystalline polymers. *Macromolecules* 37:8618–8633
63. Sedighiamiri A, Govaert LE, Kanters MJW, van Dommelen JAW (2012) Micromechanics of semicrystalline polymers: yield kinetics and long-term failure. *J Polym Sci B Polym Phys* 50:1664–1679
64. van Erp TB, Cavallo D, Peters GWM, Govaert LE (2012) Rate-, temperature-, and structure-dependent yield kinetics of isotactic polypropylene. *J Polym Sci B Polym Phys* 50:1438–1451
65. van Breemen LCA, Engels TAP, Klompen ETJ, Senden DJA, Govaert LE (2012) Rate- and temperature-dependent strain softening in solid polymers. *J Polym Sci B Polym Phys* 50:1757–1771
66. Hobeika S, Men Y, Strobl G (2000) Temperature and strain rate independence of critical strains in polyethylene and poly(ethylene-co-vinyl acetate). *Macromolecules* 33:1827–1833
67. Brooks NWJ, Mukhtar M (2000) Temperature and stem length dependence of the yield stress of polyethylene. *Polymer* 41:1475–1480
68. Peterson JM (1966) Thermal initiation of screw dislocations in polymer crystal platelets. *J Appl Phys* 37:4047–4050
69. Peterson JM (1968) Peierls stress for screw dislocations in polyethylene. *J Appl Phys* 39:4920–4928

70. Crist B, Fisher CJ, Howard P (1989) Mechanical properties of model polyethylenes: tensile elastic modulus and yield stress. *Macromolecules* 22:1709–1718
71. Darras O, Seguela R (1993) Tensile yield of polyethylene in relation to crystal thickness. *J Polym Sci B Polym Phys* 31:759–766
72. O’Kane WJ, Young RJ, Ryan AJ (1995) The effect of annealing on the structure and properties of isotactic polypropylene films. *J Macromol Sci Phys* 34:427–458
73. Bartczak Z, Argon AS, Cohen RE (1992) Deformation mechanisms and plastic resistance in single-crystal-textured high-density polyethylene. *Macromolecules* 25:5036–5053
74. Gleiter H, Argon AS (1971) Plastic deformation of polyethylene crystals. *Philos Mag* 24:71–80
75. Lewis D, Wheeler EJ, Maddams WF, Preedy JE (1972) Comparison of twinning produced by rolling and annealing in high- and low-density polyethylene. *J Polym Sci A-2 Polym Phys* 10:369–373
76. Young RJ, Bowden PB, Ritchie J, Rider RJ (1973) Deformation mechanisms in oriented high-density polyethylene. *J Mater Sci* 8:23–36
77. Gaucher-Miri V, Seguela R (1997) Tensile yield of polyethylene and related copolymers: mechanical and structural evidences of two thermally activated processes. *Macromolecules* 30:1158–1167
78. Seguela R, Gaucher-Miri V, Elkoun S (1998) Plastic deformation of polyethylene and ethylene copolymers. Part I. Homogeneous crystal slip and molecular mobility. *J Mater Sci* 33:1273–1279
79. Seguela R, Elkoun S, Gaucher-Miri V (1998) Plastic deformation of polyethylene and ethylene copolymers. Part II. Heterogeneous crystal slip and strain-induced phase change. *J Mater Sci* 33:1801–1807
80. Peterlin A (1971) Molecular model of drawing polyethylene and polypropylene. *J Mater Sci* 6:490–508
81. Peterlin A (1965) Crystalline character in polymers. *J Polym Sci Part C Polym Symp* 9:61–89
82. Bartczak Z, Cohen RE, Argon AS (1992) Evolution of the crystalline texture of high-density polyethylene during uniaxial compression. *Macromolecules* 25:4692–4704
83. Bartczak Z, Lezak E (2005) Evolution of lamellar orientation and crystalline texture of various polyethylenes and ethylene-based copolymers in plane-strain compression. *Polymer* 46:6050–6063
84. Galeski A (2003) Strength and toughness of crystalline polymer systems. *Prog Polym Sci* 28:1643–1699
85. Men Y, Rieger J, Strobl G (2003) Role of the entangled amorphous network in tensile deformation of semicrystalline polymers. *Phys Lett* 91:95502
86. Al-Hussein M, Strobl G (2002) Strain-controlled tensile deformation behavior of isotactic poly(1-butene) and its ethylene copolymers. *Macromolecules* 35:8515–8520
87. Men Y, Strobl G (2003) Critical strains in poly(*ε*-caprolactone) and blends with poly(vinyl methyl ether) and poly(styrene-co-acrylonitrile). *Macromolecules* 36:1889–1898
88. Hong K, Rastogi A, Strobl G (2004) A model treating tensile deformation of semicrystalline polymers: quasi-static stress–strain relationship and viscous stress determined for a sample of polyethylene. *Macromolecules* 37:10165–10174
89. Brown N, Ward IM (1983) The influence of morphology and molecular weight on ductile–brittle transitions in linear polyethylene. *J Mater Sci* 18:1405–1420
90. Seguela R, Darras O (1994) Phenomenological aspects of the double yield of polyethylene and related copolymers under tensile loading. *J Mater Sci* 29:5342–5347
91. Bartczak Z (2005) Influence of molecular parameters on high-strain deformation of polyethylene in the plane-strain compression. Part II. Strain recovery. *Polymer* 46:10339–10354
92. Bowden B, Young RJ (1971) Critical resolved shear stress for [001] slip in polyethylene. *Nature* 229:23–25
93. Shadrake LG, Guin F (1976) Dislocations in polyethylene crystals: line energies and deformation modes. *Philos Mag* 34:565–581

94. O'Kane WJ, Young RJ (1995) The role of dislocations in the yield of polypropylene. *J Mater Sci Lett* 14:433–435
95. Sirotkin RO, Brooks NW (2001) The effects of morphology on the yield behaviour of polyethylene copolymers. *Polymer* 42:3791–3797
96. Popli R, Mandelkern L (1987) Influence of structural and morphological factors on the mechanical properties of the polyethylenes. *J Polym Sci B Polym Phys* 25:441–483
97. De Rosa C, Auriemma F, de Ballesteros OR, Resconi L, Camurati I (2007) Crystallization behavior of isotactic propylene-ethylene and propylene-butene copolymers: effect of comonomers versus stereodefects on crystallization properties of isotactic polypropylene. *Macromolecules* 40:6600–6616
98. De Rosa C, Auriemma F, de Ballesteros OR, Resconi L, Camurati I (2007) Tailoring the physical properties of isotactic polypropylene through incorporation of comonomers and the precise control of stereo and regioregularity by metallocene catalysts. *Chem Mater* 19:5122–5130
99. De Rosa C, Auriemma F, Vollaro P, Resconi L, Guidotti S, Camurati I (2011) Crystallization behavior of propylene-butene copolymers: the trigonal form of isotactic polypropylene and form I of isotactic poly(1-butene). *Macromolecules* 44:540–549
100. De Rosa C, Auriemma F, Ruiz de Ballesteros O, De Luca D, Resconi L (2008) The double role of comonomers on the crystallization behavior of isotactic polypropylene: propylene-hexene copolymers. *Macromolecules* 41:2172–2177
101. De Rosa C, Auriemma F, Ruiz de Ballesteros O, Dello Iacono S, De Luca D, Resconi L (2009) Stress-induced polymorphic transformations and mechanical properties of isotactic propylene-hexene copolymers. *Cryst Growth Des* 9:165–176
102. De Rosa C, Auriemma F, Di Girolamo R, Romano L, De Luca MR (2010) A new mesophase of isotactic polypropylene in copolymers of propylene with long branched comonomers. *Macromolecules* 43:8559–8569
103. De Rosa C, Auriemma F, Ruiz de Ballesteros O, Di Caprio MR (2012) Crystal structure of the trigonal form of isotactic propylene-pentene copolymers: an example of the principle of entropy-density driven phase formation in polymers. *Macromolecules* 45:2749–2763
104. De Rosa C, Auriemma F, Talarico G, de Ballesteros OR (2007) Structure of isotactic propylene-pentene copolymers. *Macromolecules* 40:88531–88532
105. De Rosa C, Auriemma F, Corradini P, Tarallo O, Dello Iacono S, Ciaccia E, Resconi L (2006) *J Am Chem Soc* 128:80–81
106. De Rosa C, Dello Iacono S, Auriemma F, Ciaccia E, Resconi L (2006) *Macromolecules* 39:6098–6109
107. Bingel C, Goeres M, Fraaije V, Winter A (1998) Preparation of preparing substituted indanones. International patent application WO 1998/040331
108. Resconi L, Ciaccia E, Fait A (2004) Process for preparing porous polymers and polymers thereof. International patent application WO 2004/092230
109. Resconi L, Guidotti S, Camurati I, Frabetti R, Focante F, Nifant'ev IE, Laishevstev IP (2005) C1-symmetric heterocyclic zirconocenes as catalysts for propylene polymerization. 2. ansa-zirconocenes with linked diethienocyclopentadienyl-substituted indenyl ligands. *Macromol Chem Phys* 206:1405–1438
110. Spaleck W, Kueber F, Winter A, Rohrmann J, Bachmann B, Antberg M, Dolle V, Paulus EF (1994) The influence of aromatic substituents on the polymerization behavior of bridged zirconocene catalysts. *Organometallics* 13:954–963
111. Hosier IL, Alamo RG, Estes P, Isasi JR, Mandelkern L (2003) Formation of the  $\alpha$  and  $\gamma$  polymorphs in random metallocene-propylene copolymers. Effect of concentration and type of comonomer. *Macromolecules* 36:623–5636
112. Ruiz-Orta C, Alamo RG (2012) Morphological and kinetic partitioning of comonomer in random propylene 1-butene copolymers. *Polymer* 53:810–822
113. Ruiz-Orta C, Fernandez-Blazquez JP, Pereira EJ, Alamo RG (2011) Time-resolved FTIR spectroscopic study of the evolution of helical structure during isothermal crystallization of



- propylene 1-hexene copolymers. Identification of regularity bands associated with the trigonal polymorph. *Polymer* 52:2856–2868
114. Jeon K, Palza H, Quijada R, Alamo RG (2009) Effect of comonomer type on the crystallization kinetics and crystalline structure of random isotactic propylene 1-alkene copolymers. *Polymer* 50:832–844
  115. Alamo RG, Ghosal A, Chatterjee J, Thompson KL (2005) Linear growth rates of random propylene ethylene copolymers. The changeover from  $\gamma$  dominated growth to mixed ( $\alpha + \gamma$ ) polymorphic growth. *Polymer* 46:8774–8789
  116. Alamo RG, VanderHart DL, Nyden MR, Mandelkern L (2000) Morphological partitioning of ethylene defects in random propylene-ethylene copolymers. *Macromolecules* 33:6094–6105
  117. Alamo RG, Mandelkern L (1991) Crystallization kinetics of random ethylene copolymers. *Macromolecules* 24:6480–6493
  118. Covezzi M, Fait A (2001) Process and apparatus for making supported catalyst systems for olefin polymerisation. International patent application WO 01/44319
  119. De Rosa C, Auriemma F, Di Capua A, Resconi L, Guidotti S, Camurati I, Nifant'ev IE, Laishevsev IP (2004) Structure–property correlations in polypropylene from metallocene catalysts: stereodeficient, regioregular isotactic polypropylene. *J Am Chem Soc* 2004 (126):17040
  120. Roe R-J (2000) *Methods of X-ray and neutron scattering in polymer science*. Oxford University Press, New York
  121. Stribeck N (2007) *X-ray scattering of soft-matter*. Springer, Heidelberg
  122. Resconi L, Cavallo L, Fait A, Piemontesi F (2000) Selectivity in propene polymerization with metallocene catalysts. *Chem Rev* 100:1253–1346
  123. Fischer D, Mulhaupt R (1994) The influence of regio- and stereoirregularities on the crystallization behaviour of isotactic poly(propylene)s prepared with homogeneous group IVa metallocene/methylaluminoxane Ziegler-Natta catalysts. *Macromol Chem Phys* 195:1433–1441
  124. Thomann R, Wang C, Kressler J, Mulhaupt R (1996) On the  $\gamma$ -phase of isotactic polypropylene. *Macromolecules* 29:8425–8434
  125. Alamo RG, Kim MH, Galante MJ, Isasi JR, Mandelkern L (1999) Structural and kinetic factors governing the formation of the  $\gamma$  polymorph of isotactic polypropylene. *Macromolecules* 32:4050–4064
  126. Auriemma F, De Rosa C (2002) Crystallization of metallocene-made isotactic polypropylene: disordered modifications intermediate between the  $\alpha$  and  $\gamma$  forms. *Macromolecules* 35:9057
  127. De Rosa C, Auriemma F, De Lucia G, Resconi L (2005) From stiff plastic to elastic polypropylene: polymorphic transformations during plastic deformation of metallocene-made isotactic polypropylene. *Polymer* 46:9461–9475
  128. De Rosa C, Auriemma F, Paolillo M, Resconi L, Camurati I (2005) Crystallization behavior and mechanical properties of regiodefective, highly stereoregular isotactic polypropylene: effect of regiodefects versus stereodeficient and influence of the molecular mass. *Macromolecules* 38:9143–9154
  129. VanderHart DL, Alamo RG, Nyden MR, Kim MH, Mandelkern L (2000) Observation of resonances associated with stereo and regio defects in the crystalline regions of isotactic polypropylene: toward a determination of morphological partitioning. *Macromolecules* 33:6078–6093
  130. Thomann R, Semke H, Maier RD, Thomann Y, Scherble J, Mulhaupt R, Kressler J (2001) Influence of stereoirregularities on the formation of the  $\gamma$ -phase in isotactic polypropylene. *Polymer* 42:4597–4603
  131. Nyden MR, Vanderhart DL, Alamo RG (2001) The conformational structures of defect-containing chains in the crystalline regions of isotactic polypropylene. *Comput Theor Polym Sci* 11:175–189

132. Poon B, Rogunova M, Hiltner A, Baer E, Chum SP, Galeski A, Piorkowska E (2005) Structure and properties of homogeneous copolymers of propylene and 1-hexene. *Macromolecules* 38:1232–1243
133. Lotz B, Ruan J, Thierry A, Alfonso GC, Hiltner A, Baer E, Piorkowska E, Galeski A (2006) A structure of copolymers of propene and hexene isomorphous to isotactic poly(1-butene) form I. *Macromolecules* 39:5777–5781
134. Stagnaro P, Boragno L, Canetti M, Forlini F, Azzurri F, Alfonso GC (2009) Crystallization and morphology of the trigonal form in random propene/1-pentene copolymers. *Polymer* 50:5242–5249
135. Stagnaro P, Costa G, Trefiletti V, Canetti M, Forlini F, Alfonso GC (2006) Thermal behavior, structure and morphology of propene/higher 1-olefin copolymers. *Macromol Chem Phys* 207:2128–2141
136. Garcia-Penas A, Gomez-Elvira JM, Lorenzo V, Perez E, Cerrada ML (2015) Synthesis, molecular characterization, evaluation of polymorphic behavior and indentation response in isotactic poly(propylene-co-1-heptene) copolymers. *Eur Polym J* 64:52–61
137. Polo-Corpa MJ, Benavente R, Velilla T, Quijada R, Perez E, Cerrada ML (2010) Development of the mesomorphic phase in isotactic propene/higher alpha-olefin copolymers at intermediate comonomer content and its effect on properties. *Eur Polym J* 46:1345–1354
138. Palza H, Lopez-Majada JM, Quijada R, Perena JM, Benavente R, Perez E, Cerrada ML (2008) Comonomer length influence on the structure and mechanical response of metallocenic polypropylenic materials. *Macromol Chem Phys* 209:2259–2267
139. Lopez-Majada JM, Palza H, Guevara JL, Quijada R, Martinez MC, Benavente R, Perena JM, Perez E, Cerrada ML (2006) Metallocene copolymers of propene and 1-hexene: the influence of the comonomer content and thermal history on the structure and mechanical properties. *J Polym Sci B Polym Phys* 44:1253–1267
140. Garcia-Penas A, Cerrada ML, Gomez-Elvira JM, Perez E (2016) Microstructure and thermal stability in metallocene iPP-materials: 1-pentene and 1-hexene copolymers. *Polym Degrad Stab* 124:77–86
141. Natta G, Peraldo M, Corradini P (1959) Modificazione mesomorfa smettica del polipropilene isotattico. *Rend Accad Naz Lincei* 26:14–17
142. Mileva D, Androsch R, Cavallo D, Alfonso GC (2012) Structure formation of random isotactic copolymers of propylene and 1-hexene or 1-octene at rapid cooling. *Eur Polym J* 48:1082–1092
143. Mileva D, Androsch R (2012) Effect of co-unit type in random propylene copolymers on the kinetics of mesophase formation and crystallization. *Colloid Polym Sci* 290:465–471
144. Mileva D, Androsch R, Zhuravlev E, Schick C, Wunderlich B (2011) Formation and reorganization of the mesophase of random copolymers of propylene and 1-butene. *Polymer* 52:1107–1115
145. Mileva D, Cavallo D, Gardella L, Alfonso GC, Portale G, Balzano L, Androsch R (2011) In situ X-Ray analysis of mesophase formation in random copolymers of propylene and 1-butene. *Polym Bull* 67:497–510
146. Mileva D, Zia Q, Androsch R (2010) Tensile properties of random copolymers of propylene with ethylene and 1-butene: effect of crystallinity and crystal habit. *Polym Bull* 65:623–634
147. Mileva D, Androsch R, Zhuravlev E, Schick C (2009) Critical rate of cooling for suppression of crystallization in random copolymers of propylene with ethylene and 1-butene. *Thermochim Acta* 492:67–72
148. Mileva D, Androsch R, Radusch H-J (2008) Effect of cooling rate on melt-crystallization of random propylene-ethylene and propylene-1-butene copolymers. *Polym Bull* 61:643–654
149. Natta G, Corradini P (1960) Structures and properties of isotactic polypropylene. *Nuovo Cimento Suppl* 15:40–51
150. Hikosaka M, Seto T (1973) The order of the molecular chains in isotactic polypropylene crystals. *Polym J* 5:111–127

151. Bruckner S, Meille SV (1989) Non-parallel chains in crystalline  $\gamma$ -isotactic polypropylene. *Nature (London)* 340:455–457
152. Meille SV, Bruckner S, Porzio W (1990)  $\gamma$ -Isotactic polypropylene. A structure with nonparallel chain axes. *Macromolecules* 23:4114–4121
153. Balta-Calleja FJ, Vonk CG (1989) X ray scattering of synthetic polymers. Elsevier, Amsterdam
154. Wunderlich B (1980) *Macromolecular physics*, vol 3. Academic, New York
155. Crist B (2003) Thermodynamics of statistical copolymer melting. *Polymer* 44:4563–4572
156. Crist B, Claudio ES (1999) Isothermal crystallization of random ethylene–butene copolymers: bimodal kinetics. *Macromolecules* 32:8945–8951
157. Crist B, Williams DN (2000) Crystallization and melting of model ethylene-butene random copolymers: thermal studies. *J Macromol Sci Phys B39*:1–13
158. Crist B, Howard PR (1999) Crystallization and melting of model ethylene–butene copolymers. *Macromolecules* 32:3057–3067
159. Flory PJ (1951) Theory of crystallization in copolymers. *Trans Faraday Soc* 55:848–857
160. Sanchez IC, Eby RK (1973) Crystallization of random copolymers. *J Res Natl Bur St A Phys Chem* 77:353–358
161. Sanchez IC, Eby RK (1975) Thermodynamics and crystallization of random copolymers. *Macromolecules* 8:638–641
162. De Rosa C, Auriemma F (2013) *Crystals and crystallinity in polymers: diffraction analysis of ordered and disordered crystals*. Wiley, New York
163. Zhen L, You-lee H, Shichen Y, Jia K, Akihiro K, Akihiro O, Toshikazu M (2015) Determination of chain-folding structure of isotactic polypropylene in melt-grown  $\alpha$  crystals by  $^{13}\text{C}$ – $^{13}\text{C}$  double quantum NMR and selective isotopic labeling. *Macromolecules* 48:5752–5760
164. Nitta KH, Yamana M (2012) Poisson's ratio and mechanical nonlinearity under tensile deformation in crystalline polymers, rheology. In: De Vicente J (ed) *Rheology*. InTech, Rijeka, Croatia, pp 113–132. Available from: <http://www.intechopen.com/books/rheology/poisson-s-ratio-and-mechanical-nonlinearity-undertensile-deformation>
165. Petraccone V, Pirozzi B, Meille SV (1986) Analysis of chain folding in crystalline isotactic polypropylene. The implications of tacticity and crystallographic symmetry. *Polymer* 27:1665–1668
166. Corradini P, Giunchi G, Petraccone V, Pirozzi B, Vidal HM (1980) Structural variations in crystalline isotactic polypropylene ( $\alpha$  form) as a function of thermal treatments. *Gazz Chim Ital* 110:413–418
167. Auriemma F, de Ballesteros OR, De Rosa C, Corradini P (2000) Structural disorder in the  $\alpha$  form of isotactic polypropylene. *Macromolecules* 33:8764–8774
168. Ree T, Eyring H (1955) Theory of non-Newtonian flow. I. Solid plastic system. *J Appl Phys* 26:793–800
169. Ree T, Eyring H (1955) Theory of non-Newtonian flow. I. Solution system of high polymers. *J Appl Phys* 26:800–809
170. Séguéla R, Staniek E, Escaig B, Fillon B (1999) Plastic deformation of polypropylene in relation to crystalline structure. *J Appl Polym Sci* 71:1873–1885
171. Schaefer D, Spiess HW, Suter UW, Fleming WW (1990) Two-dimensional solid-state NMR studies of ultraslow chain motion: glass transition in atactic poly(propylene) versus helical jumps in isotactic poly(propylene). *Macromolecules* 23:3431–3439

# Crystallization of Cyclic Polymers

**Ricardo A. Pérez-Camargo, Agurtzane Mugica, Manuela Zubitur,  
and Alejandro J. Müller**

**Abstract** The effect of chain topology (ring versus linear polymer chains) on polymer crystallization is reviewed. Recent advances in ring closure and ring expansion synthetic techniques have made available a range of well-characterized samples with higher levels of purity than available decades ago. Cyclic molecules are fascinating because the structural difference between them and linear chains is relatively small, yet their behavior can be completely different from that of their linear analogs of identical chain length. The effect of having no chain ends can dramatically change the polymer coil conformation and diffusion rate, as well as the

---

R.A. Pérez-Camargo

POLYMAT and Polymer Science and Technology Department, Faculty of Chemistry,  
University of the Basque Country UPV/EHU, Paseo Manuel de Lardizabal 3, 20018 Donostia/  
San Sebastián, Spain

Grupo de Polímeros USB, Departamento de Ciencia de los Materiales, Universidad Simón  
Bolívar, Apartado 89000, Caracas 1080, Venezuela

A. Mugica

POLYMAT and Polymer Science and Technology Department, Faculty of Chemistry,  
University of the Basque Country UPV/EHU, Paseo Manuel de Lardizabal 3, 20018 Donostia/  
San Sebastián, Spain

M. Zubitur

Chemical Engineering Department, Polytechnic College, University of the Basque Country  
UPV/EHU, Plaza de Europa, 20080 Donostia/San Sebastián, Spain

A.J. Müller (✉)

POLYMAT and Polymer Science and Technology Department, Faculty of Chemistry,  
University of the Basque Country UPV/EHU, Paseo Manuel de Lardizabal 3, 20018 Donostia/  
San Sebastián, Spain

Grupo de Polímeros USB, Departamento de Ciencia de los Materiales, Universidad Simón  
Bolívar, Apartado 89000, Caracas 1080, Venezuela

IKERBASQUE, Basque Foundation for Science, Bilbao, Spain

e-mail: [alejandrojesus.muller@ehu.es](mailto:alejandrojesus.muller@ehu.es)

chain entanglement density in the melt. These changes are reflected in different nucleation and crystallization kinetics for cyclic and linear polymeric chains. However, the results published so far seem to be dependent on the type of polymer employed. Therefore, a careful look at the literature and evidence reported for each group of materials has been assembled and compared. The possible reasons for some of the contradictions in the evidence are also discussed.

**Keywords** Crystallization · Cyclic and linear polymers · Diffusion · Entropic factors · Equilibrium melting temperature

## Contents

1	Introduction .....	94
2	Types of Cyclic Polymers .....	95
3	Crystallization from Solution .....	99
3.1	Single Crystals Obtained from Solution .....	99
4	Crystallization from the Melt State .....	102
4.1	Nucleation and Spherulitic Structures .....	102
4.2	Spherulitic Growth Rate .....	106
4.3	Non-isothermal Differential Scanning Calorimetry .....	108
4.4	Isothermal Overall Crystallization Kinetics .....	111
5	Self-Nucleation and Successive Self-Nucleation and Annealing .....	118
5.1	Self-Nucleation .....	118
5.2	Successive Self-Nucleation and Annealing .....	120
6	Reasons for Different Behavior Reported in the Literature .....	122
7	Conclusions .....	124
	References .....	125

## 1 Introduction

Cyclic polymers are fascinating materials. They only differ from linear analogs in their lack of chain ends; however, this topological difference can have a large impact on their molecular behavior.

Cyclic molecules are present in nature. In fact, the interest in cyclic polymers began in 1958 when Jacob and Wollman [1] concluded that the genetic map of bacterial chromosomes of *Escherichia coli* showed circularity. Additionally, DNA [2–5], peptides [6], and proteins [7] are synthesized in nature with cyclic topologies. Therefore, an open question naturally arises: Do cyclic topologies provide enhanced or unique properties compared with linear structures? [8]. According to Semlyen [9], the absence of chain ends could be an advantage in some applications, and natural structures (e.g., DNA) with circular topologies are designed to prevent any possible reactions or interactions through chain ends.

Cyclic or ring polymers develop fewer entanglements and have more compact molecular conformations than linear chains. As a consequence, properties such as

diffusion rates, melt and solution viscosities, nucleation and crystallization behavior, and degradation kinetics can be dramatically different for chains that have no ends as compared with linear analogs. In this review, we focus on the effect of this difference in chain topology (namely cyclic versus linear) on the morphology, nucleation, and crystallization behavior of polymers.

The crystallization of cyclic polymers is a complex subject that needs investigation in order to understand all relevant factors involved. The synthetic procedures and purification methods employed in the production of ring polymers with high purity have been evolving for decades [10]. Nowadays, new synthetic approaches have allowed the preparation of a wide range of high purity ring polymers, as well as novel and more complex cyclic-based topologies [11–29]. These new synthetic approaches have enabled researchers to study differences between the properties of cyclic and linear polymers, such as the glass transition temperature [9, 30], melt viscosity and diffusion [9, 30–34], morphology [35–37], and crystallization [38–52].

Crystallization studies of several cyclic and linear polymers have been performed and the results obtained have differed substantially from one another. Therefore, a unique interpretation is not always possible and it seems that the crystallization of cyclic chains depends on the specific type of material under study, apart from other factors such as different levels of purity.

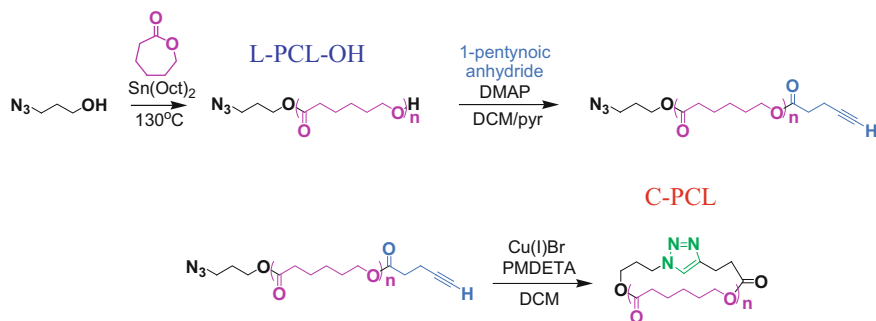
Many different aspects of the morphology and crystallization of cyclic polymers have been reported in the literature, such as solution-grown single crystal morphology, nucleation, spherulitic growth, thermal transition, and overall melt crystallization kinetics. Several arguments have been employed in an effort to explain the obtained findings, leading to the development of models for chain folding of cyclic polymers and taking into account cyclic topology in classical thermodynamic equations. A revision of the most important experimental findings on cyclic and linear polymer crystallization, as well as their interpretation, is presented in this review.

## 2 Types of Cyclic Polymers

The crystallization of several types of cyclic polymers is presented in this work. These polymers are synthesized by two main types of cyclization synthetic methodologies:

- (a) Ring-closure reaction
- (b) Ring-expansion polymerization [53]

Several reviews focus on the synthetic strategies [54–56], which are beyond the scope of the present work. To illustrate the two main types of cyclization synthetic methodologies, poly( $\epsilon$ -caprolactone) (PCL) has been selected as an example because cyclic PCLs have been synthesized by both ring-closure reactions and ring-expansion polymerizations.



**Scheme 1** Synthetic pathway employed to obtain cyclic PCLs (C-PCLs). The precursor linear polymer (L-PCL-OH) can be used as a linear analog that has almost the same molecular weight as the synthesized C-PCL. Reprinted with permission from [48]

Ring-closure reactions are based on traditional coupling routes for cyclization of linear precursor polymers under conditions of high dilution [54]. It is worth noting that ring-closure has been improved thanks to “click” reactions in combination with “living” radical polymerizations and electrostatic self-assembly and covalent fixation (ESA-CF) [56]. An example of one possible synthetic pathway for obtaining cyclic PCLs by ring-closure reactions is shown in Scheme 1.

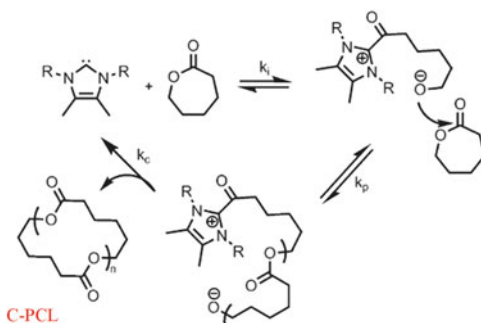
Scheme 1 shows the synthetic pathway employed to obtain a linear PCL precursor (L-PCL-OH) by ring-opening polymerization of  $\epsilon$ -caprolactone. Then, a *bis*-functional cyclization reaction is performed by Cu(I)-catalyzed azide–alkyne cycloaddition, leading to the cyclic polymer (C-PCL in Scheme 1) (more details are given in [47, 48]). Normally, the chemical structure of the resulting linking unit (a triazole ring in this case) is different from the polymer repeating unit, although it is possible in some cases (e.g., for poly(tetrahydrofuran) cyclic materials), to transform the linking unit into a group identical to the repeating unit (see [40]).

Ring-expansion polymerization is a direct method for forming cyclic polymers. For ring-expansion polymerization, the monomer inserts into a cyclic initiator to form larger rings. C-PCL has also been obtained by ring-expansion polymerization. Scheme 2 illustrates the synthetic pathway used by Shin et al. [43] to obtain C-PCL by zwitterionic polymerization, which is a process of enchainment whereby the ionic propagating end and its counterion are contained in the same polymer chain of  $\epsilon$ -caprolactone in the presence of carbene [54].

Tables 1 and 2 show the molecular weight data for selected cyclic polymers obtained by ring-closure reactions (Table 1) and ring-expansion polymerizations (Table 2), and their linear counterparts. They have been chosen because the crystallization of these samples is discussed later in this review (see Sects. 3 and 4).

One of the advantages of ring-closure techniques is that linear analogs have almost identical number-average molecular weight ( $M_n$ ) values (and polydispersity values) as cyclic molecules. This is because the linear molecules are synthesized first, functionalized with clickable groups, and then reacted to form the cyclic chains. Once the cycle is closed, a triazole ring remains within the structure of

**Scheme 2** Proposed mechanism for the zwitterionic ring-opening polymerization of  $\epsilon$ -caprolactone. Reprinted with permission from [43]



**Table 1** Number-average molecular weight ( $M_n$ ) and polydispersity index (PDI) data for ring-closure samples [40, 41, 45, 47–49]

Sample	$M_n$ (g/mol)			PDI <sup>a</sup>			References
	GPC <sup>b</sup>	MALDI	NMR	GPC	MALDI	SEC	
L-PTHF 3.1k	–	–	3,100	–	–	1.10	[45]
L-PTHF 4.9k	–	–	4,900	–	–	1.14	[40]
L-PTHF 5.7k	–	–	5,700	–	–	1.12	[45]
L-PTHF 9.1k	–	–	9,100	–	–	1.09	
C-PTHF 2.9k	–	–	2,900	–	–	1.11	
C-PTHF 4.5k	–	–	4,500	–	–	1.15	
C-PTHF 5.1k	–	–	5,100	–	–	1.14	[40]
C-PTHF 8.2k	–	–	8,200	–	–	1.10	[45]
L-PCL-Acet 2k	2,190	2,360	–	1.11	1.02	–	[41]
L-PCL-OH 2k	2,010	2,040	–	1.17	1.05	–	
L-PCL-OH 3k	3,440	3,140	–	1.15	1.03	–	[48]
L-PCL-Acet 4.9k	4,730	4,900	–	1.16	1.01	–	[47]
L-PCL-OH 7.5k	7,670	7,340	–	1.13	1.02	–	[41]
L-PCL-OH 12k	12,000	12,000	–	1.12	1.03	–	[48, 49]
L-PCL-Acet 22k	20,070	22,000	–	1.15	1.03	–	[48]
C-PCL 2k	1,550	2,320	–	1.17	1.05	–	[41]
C-PCL 3k	2,180	3,200	–	1.15	1.03	–	[48]
C-PCL 4.9k	3,390	5,040	–	1.08	1.02	–	[47]
C-PCL 7.5k	4,800	7,000	–	1.11	1.04	–	[41]
C-PCL 12k	10,580	12,000	–	1.15	1.04	–	[48]
C-PCL 22k	15,140	22,000	–	1.15	1.05	–	[48, 49]

<sup>a</sup>PDI =  $M_w/M_n$

<sup>b</sup>Corrected value for linear PCL [57] using  $M_n(\text{PCL}) = 0.259 \times M_n(\text{PS})^{1.073}$

GPC gel permeation chromatography, MALDI matrix-assisted laser desorption/ionization, NMR nuclear magnetic resonance, SEC size-exclusion chromatography

the cyclic chain (as shown in Scheme 1) that is not present in the linear chains; hence, the slight difference in  $M_n$  values obtained by MALDI-TOF [58]. Table 1 shows two types of linear precursors for PCL (L-PCL-OH and L-PCL-Acet).



**Table 2** Weight- and number-average molecular weights ( $M_w$  and  $M_n$ ) and PDI data for ring-expansion polymerization samples [31, 42–44]

Polymer	$M_w$ (g/mol)	$M_n$ (g/mol)	PDI	References
L-PE 44k	44,000	–	–	[44]
L-PE 200k	200,000	–	2.0	[31]
C-PE 9k	9,300	–	–	[44]
C-PE 43.6k	43,600	–	–	
C-PE 86.5k	86,500	–	–	
C-PE 200k	200,000	–	2.0	[31]
L-PCL 50.6k	–	50,600	1.6	[42]
L-PCL 63.4k	–	63,400	1.6	
L-PCL 69.2k	–	69,200	1.8	
L-PCL 75k	75,000 <sup>a</sup>	103,000	1.38	[43]
L-PCL 77k	77,000	–	2.1	[42]
L-PCL 100k	101,000 <sup>a</sup>	140,000	1.54	[43]
L-PCL 120k	116,000 <sup>a</sup>	168,000	1.29	
C-PCL 45k	–	45,000	1.6	[42]
C-PCL 57.5k	–	57,500	1.6	
C-PCL 64k	–	64,000	1.8	
C-PCL 69k	–	69,000	2.1	
C-PCL 75k	75,000 <sup>a</sup>	66,000	1.91	[43]
C-PCL 110k	109,000 <sup>a</sup>	79,000	1.83	
C-PCL 130k	129,000 <sup>a</sup>	101,000	2.02	
C-PCL 140k	142,000 <sup>a</sup>	114,000	2.03	

<sup>a</sup>Weight-average (absolute) molecular weight determined by gel permeation chromatography using light scattering

The L-PCL-Acet is the product of functionalization of L-PCL-OH to give an acetate group at the end of the molecule. This was originally performed to ascertain whether the OH end groups could affect the diffusion and crystallizability of PCL chains because of their ability to form hydrogen bonds. In fact, it was demonstrated that the behavior of both L-PCL-OH and L-PCL-Acet was identical in terms of crystallization behavior [41]. They can both be considered very similar linear PCL chains.

Ring-closure techniques normally produce high purity samples for oligomers and low to intermediate molecular weights (i.e.,  $M_n$  values in the range 2–22 kg/mol) with very low polydispersities. Ring-expansion techniques, on the other hand, can produce high molecular weight cyclic molecules without any chemically different moiety within the cyclic chain. However, linear analogs must be synthesized separately, with target  $M_n$  values that are similar (but not identical) to those of the cyclic molecules. Also, molecular weight dispersity values can be slightly different between cyclic and linear molecules. Additionally, the polydispersity of samples prepared by ring expansion is much larger than for samples obtained by ring closure (compare Tables 1 and 2).

### 3 Crystallization from Solution

One of the advantages of crystallization from dilute solution is the minimal molecular diffusion hindrance and the lack of isothermal thickening during crystallization. Su et al. [47] studied, for the first time, single crystals obtained from solutions of cyclic PCL samples and their linear counterparts.

#### 3.1 Single Crystals Obtained from Solution

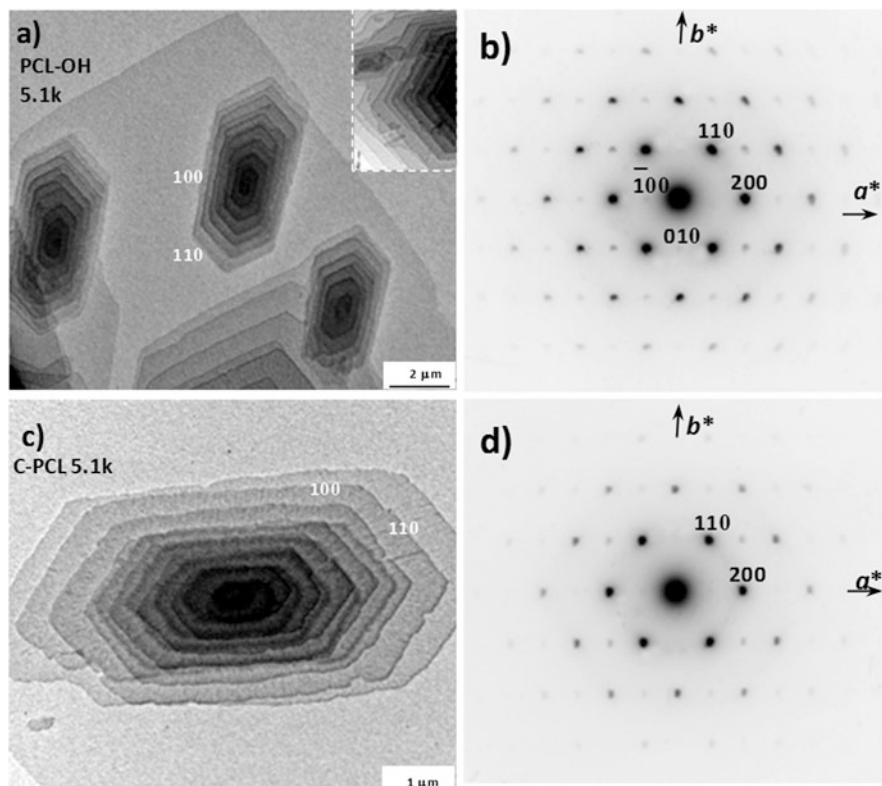
Su et al. [47] prepared single crystals of linear and cyclic PCL samples by isothermal crystallization in dilute *n*-hexanol and *N,N*-dimethylacetamide solutions at temperatures of 40°C and 26°C, respectively. The samples were obtained by ring-closure techniques (see Scheme 1). Identical batches of the parent L-PCL-OH were functionalized with acetic anhydride to provide linear analogs (L-PCL-Acet) without a hydrogen-bond donating hydroxyl end group. No influence of the end group was found in the crystallization behavior of the samples.

The most important findings of Su et al. [47] were that the morphology of C-PCL and L-PCL single crystals was similar [59], but that there were differences in the degree of truncation and in the average lamellar thickness. Figure 1 presents selected TEM micrographs and electron diffraction patterns of linear and cyclic 5.1 kg/mol PCLs [47]. Figure 1a, c shows TEM micrographs in which the distorted hexagonal-shaped morphology of the lamellar crystals is observed.

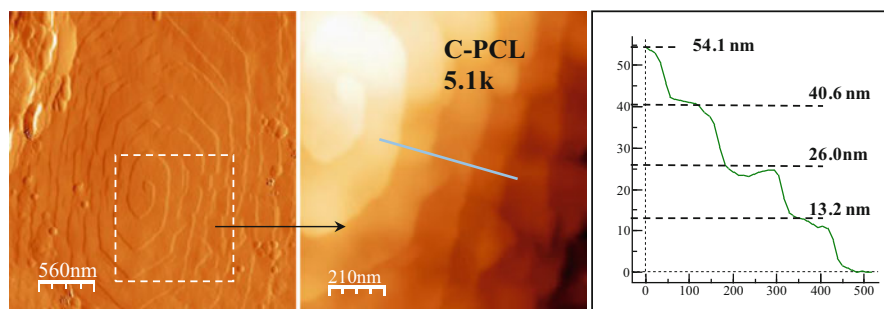
Figure 1a, c shows multilayered crystals with spiral growths of different handedness. Another feature, such as striations is also observed in the micrographs (see [47] for details). These morphological characteristics are also found in the atomic force microscopy (AFM) micrographs shown in Fig. 2. It is worth noting that no major differences between linear and cyclic PCLs were found.

Figure 1b, d shows electron diffraction patterns from selected crystals ( $M_n = 5.1$  kg/mol). These patterns are highly regular and show more than 25 independent reflections, which can be indexed according to the unit cell reported for PCL [60–62] ( $a = 0.747$  nm,  $b = 0.498$  nm and  $c$  (fiber axis) = 1.705–1.729 nm) [47]. Su et al. [47] found that the crystal structures of single crystals of linear and cyclic PCLs are the same. For samples of linear and cyclic PCL [43] and poly(tetrahydrofuran) (PTHF) [45] crystallized from the melt, wide angle X-ray scattering (WAXS) data indicate that their crystal structures are identical at the unit cell level.

According to the correlation of bright field TEM micrographs and selected area electron diffraction patterns (see Fig. 1), single crystals are bounded by four {110} faces, with two truncated {100} faces of variable dimensions. The degree of truncation is defined as the ratio between the length of {100} and {110} faces (see Fig. 1a, c). Su et al. [47] obtained clear differences between the degree of truncation of cyclic (i.e., 1.8–1.9) and linear (i.e., 2.8–2.9) PCL single crystals.



**Fig. 1** TEM micrographs (a, c) and electron diffraction patterns (b, d) of lamellar crystals for linear (a, b) and cyclic (c, d) 5.1 kg/mol PCL samples. Reprinted with permission from [47]



**Fig. 2** AFM topographic (left) and height (middle) images and corresponding height profiles (right) for 5.1 kg/mol C-PCL sample. Crystals were obtained from *N,N*-dimethyl acetamide at 26°C. Reprinted with permission from [47]

**Table 3** Extended chain length values ( $L$ ) and their comparison with lamellar thickness values ( $l$ ) (data extracted from [47])

Sample	$L$ (nm)	$l$ (nm)	$L/l$ (number of chain folds)
PCL-OH 2k <sup>a</sup>	14.2	8.7	1.6
PCL-OH 5.1k <sup>a</sup>	37.4	9.8	3.8
PCL-OH 7.5k <sup>a</sup>	55.3	11.6	4.8
PCL-Acet 5.1k <sup>a</sup>	37.1	7.0	5.3
PCL-Acet 7.5k <sup>b</sup>	55.0	6.73	8.2
PCL-Acet 7.5k <sup>c</sup>	55.0	7.22	7.6
C-PCL 2k <sup>a</sup>	6.8	5.4	1.3
C-PCL 5.1k <sup>a</sup>	18.4	13.2	1.4
C-PCL 7.5k <sup>a</sup>	27.4	13.22	2.1
C-PCL 7.5k <sup>d</sup>	27.4	7.17	3.8

<sup>a</sup>Values determined by AFM for solution-grown crystals at 26°C

<sup>b</sup>Values determined by SAXS for melt-crystallized samples at 20°C

<sup>c</sup>Values determined by SAXS for melt-crystallized samples at 30°C

<sup>d</sup>Values determined by SAXS for melt-crystallized samples at 25°C

The degree of truncation has been correlated with the supercooling applied during crystallization by varying the isothermal crystallization temperature [63–66]. The lower the truncation degree, the higher the supercooling applied during crystal growth (where supercooling is defined as the difference between the equilibrium melting temperature and the crystallization temperature). When the same solvent and the same crystallization temperature are employed, differences in the degree of truncation indicate that the crystals were grown at different supercoolings. The only explanation for this result is that cyclic and linear polymer crystals have different equilibrium melting points. The study of PCL single crystal truncation performed by Su et al. [47] provides direct experimental evidence for the higher supercooling applied during cyclic PCL solution crystallization, hence C-PCLs must have a higher equilibrium melting temperature ( $T_m^0$ ), as corroborated by Su et al. employing the Gibbs–Thomson extrapolation (see below).

The average lamellar thickness of the 5.1 kg/mol C-PCL sample was determined from captured AFM images, as shown in Fig. 2 [47]. Table 3 lists the calculated extended chain values ( $L$ ) together with the lamellar thickness ( $l$ ) determined by AFM. The  $L/l$  ratio represents the number of times that a chain should fold to be a part of a single crystal.

The length of the extended chain was calculated by Su et al. [47] using the following equation:

$$L = nl_{\text{fibre}}, \quad (1)$$

where  $l_{\text{fibre}}$  is the length of two repeating units that are placed in the ideal intracrystalline chain conformation (i.e., 1.705 nm) according to the literature [60, 61] and  $n$  is the number of such distances along the chain:

$$n = \frac{M_n - M_{\text{chainends}}}{2 \times M_{UR}}. \quad (2)$$

Because functional groups at the chain ends (see Scheme 1) and at the center of the C-PCL chains are rejected to the fold surfaces or amorphous zones of the crystals (they cannot be included in the crystal lattice), they were not taken into account in the calculations performed by Su et al. [47].

It should be noted that  $L$  values for cyclic chains are always about one half of those corresponding to the extended chain length of their linear analogs, because they are ring molecules and cannot be completely extended without forming one fold. According to Table 3, most PCL samples undergo folding during crystallization, even cyclic samples. As the molecular weight increases, the number of times that the PCL chain folds also increases, as expected.

It is interesting to note that cyclic chains form thicker lamellae than linear chains, in spite of their half extended chain lengths values. In the cases of 2 and 5.1 kg/mol C-PCLs, the chains crystallize in an almost-once-folded chain conformation (the equivalent of completely stretching the cyclic chains). Some values obtained by small angle X-ray scattering (SAXS) on melt crystallized samples are included in Table 3 for comparison purposes.

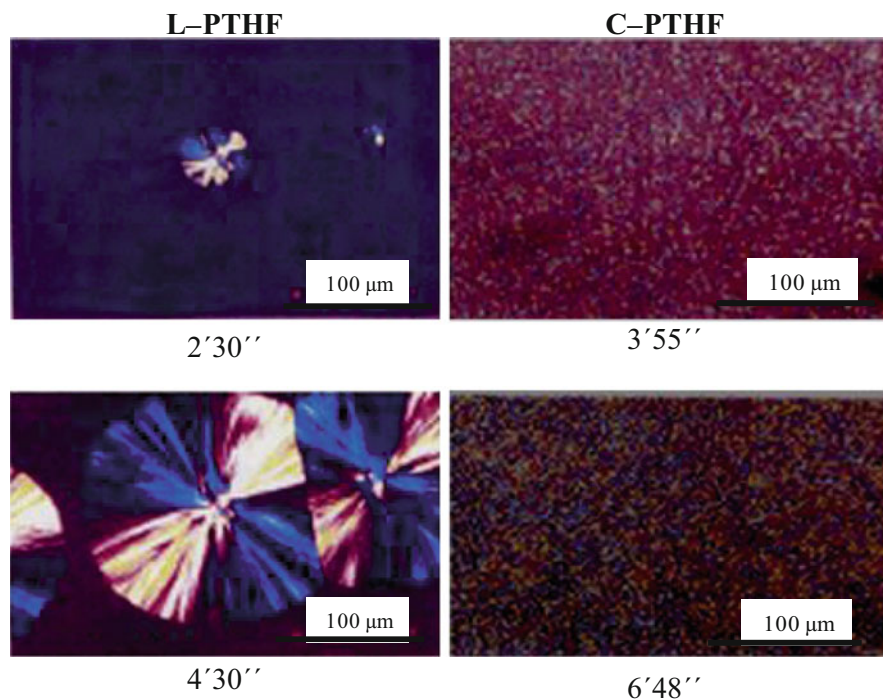
Similar trends were found by Shin et al. [46] for linear and cyclic poly(L-lactide) (PLLA), in which the lamellar thickness and long period of cyclic PLLA lamellae are approximately 20% larger than those of linear PLLA. The authors concluded that their results implied a lack of multiple chain folding in the cyclic PLLA chains, as a consequence of a topological constraint on lamellar folding [37, 67, 68].

In contrast, in a recent work by Sugai et al. [51], cyclic polylactides were found to display long spacing and crystal thickness values that were half of those obtained with their linear counterparts. The authors attributed the results to the more compact and flat conformation of cyclic chains compared with that of linear PLLA chains. The authors indicated that these differences in lamellar thickness and long period could be partly a result of the different thermal history of the samples [69].

## 4 Crystallization from the Melt State

### 4.1 Nucleation and Spherulitic Structures

The nucleation and growth stages of crystallization of cyclic and linear polymers have been studied using polarized light optical microscopy (PLOM) by different authors. There is consensus in the literature on the faster nucleation of cyclic molecules as compared with their linear analogs. Several types of polymers have been used to experimentally determine nucleation kinetics (even with different synthetic procedures and possibly different purity grades), namely PTHF [40, 45], polyethylene (PE) [44], and PCL [48, 49].



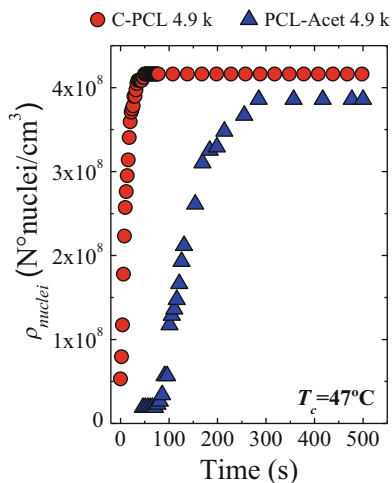
**Fig. 3** PLOM micrographs of spherulites of linear and cyclic PTHF at the indicated crystallization times at  $T_c = 11^\circ\text{C}$ . Reprinted with permission from [45]

Takeshita et al. [45] reported that a higher number of nuclei were generated for cyclic PTHF than for its linear counterpart, as clearly shown in Fig. 3. The authors attributed this behavior to the possibility that C-PTHF has a higher chain density than L-PTHF.

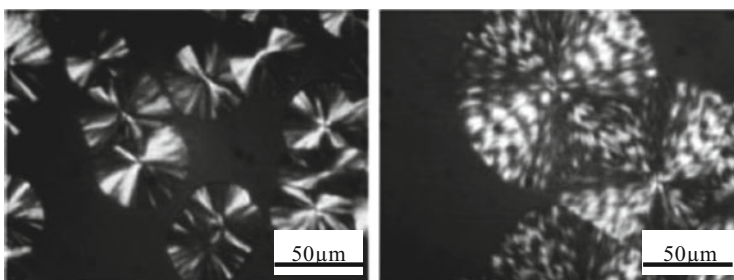
Pérez et al. [48] measured the density of nuclei as a function of time (see Fig. 4) for linear and cyclic 4.9 kg/mol PCL samples. Figure 4 shows a higher nucleation density for C-PCL than for its L-PCL analog. Pérez et al. [48] estimated that nucleation density at saturation is approximately 7% higher for C-PCL than for L-PCL at the same  $T_c$  (i.e.,  $54^\circ\text{C}$ ).

On the other hand, from data obtained at the beginning of nucleation (see Fig. 4), the nucleation rates were determined to be  $1 \times 10^7$  and  $2 \times 10^6 \text{ cm}^{-3} \text{ s}^{-1}$  for cyclic and linear PCL, respectively (4.9 kg/mol samples). Because chains with ring topology are characterized by their lack of chain ends and by their more collapsed coil conformation in the melt state [70–73], it is reasonable to expect that cyclic chains nucleate faster than linear chains.

Tezuka et al. [40] found differences in spherulitic morphology between linear and cyclic PTHF. Figure 5 shows that L-PTHF exhibits classical spherulites with Maltese cross extinction patterns, whereas C-PTHF displays not only Maltese cross extinction but also distorted banding.



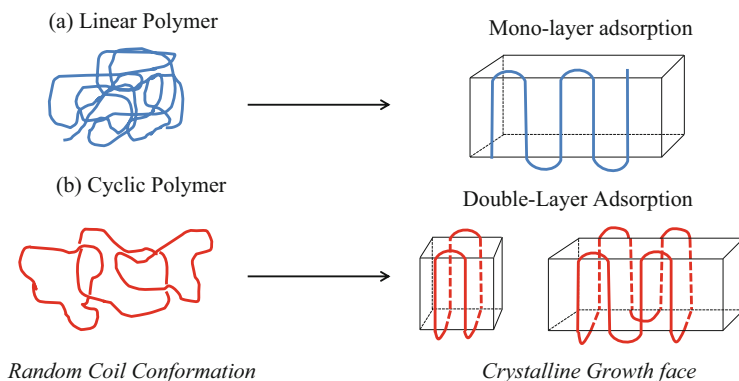
**Fig. 4** Nucleation density determined by PLOM at 47°C for linear and cyclic 4.9 kg/mol PCL samples. Reprinted with permission from [48]



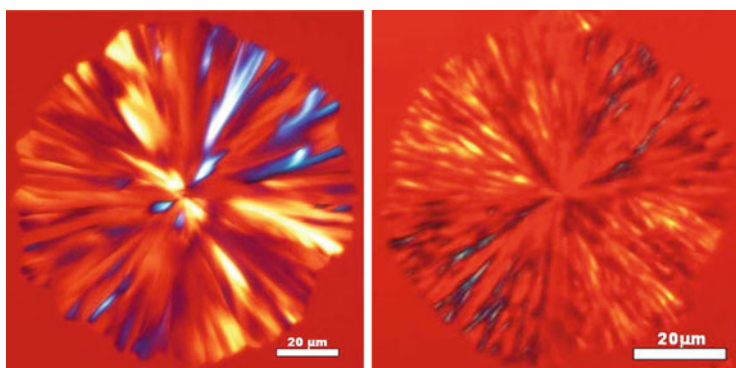
**Fig. 5** PLOM micrographs of spherulites for linear (*left*) and ring (*right*) PTHF crystallized at 10°C from the melt. Reprinted with permission from [40]

Banded spherulites indicate rotation of the optical indicatrix along the radial direction. This rotation is a result of lamellar twisting. Lamellar twisting is a complicated phenomenon that is believed to be caused by (a) cumulative reorientation of lamellae at successive screw dislocation [74, 75] or (b) different surface stresses on opposite fold surfaces of individual lamellae [76, 77]. Tezuka et al. [40] speculated that, in C-PTHF, the banded spherulites are caused by the surface stresses developed by the folded chains, such as uneven fold volume, and that the morphological differences observed between linear and cyclic PTHFs might be caused by the distinctive chain folding structures. To illustrate this, they proposed the model presented in Fig. 6.

The representation of the chain conformation of linear and cyclic PTHF shows that L-PTHF can crystallize with a monolayer adsorption on the crystal growth face



**Fig. 6** Chain folding conformation in (a) linear and (b) ring PTHF crystallized from the melt. Images were extracted from [78]



**Fig. 7** Optical micrographs of spherulites for linear (*left*) and ring (*right*) PCL of 2 kg/mol crystallized at 41°C from the melt. Reprinted with permission from [41]

(see Fig. 6a), whereas C-PTHF is nucleated on the crystal growth face with a double molecular layer (see Fig. 6b) [78].

According to the model, the chain folding surface in C-PTHF is built up by two different chain folding directions, yielding different surface energies at top and bottom lamellar surfaces (see Fig. 6a). Hence, this surface difference, according to Tezuka et al. [40], is the cause of lamellar twisting and banded spherulites in C-PTHF.

In contrast to PTHFs, banded spherulites were not found in linear or cyclic PCLs, as shown in Fig. 7. PLOM images show that both types of spherulites are similar, exhibiting Maltese cross extinction patterns without banding. The spherulites were found to be negative, as expected for PCL [41].



**Table 4** Differences in spherulitic growth rates reported in the literature for cyclic and linear analogs [39–41, 44, 45, 47, 49]

Material	$M_n$ (kg/mol)	$G$ ( $\mu\text{m}/\text{min}$ ) ( $T_c$ ( $^\circ\text{C}$ ))	References
<i>Case 1</i>			
L-PTHF	3.1	13.9–0.86 (12–20)	[45]
	4.9	360 (–20)	[40]
	5.7	8.76–0.64 (11–24)	[45]
	9.1	6.0–0.21 (11–24)	
C-PTHF	2.9	1.5–0.32 (9–17)	[45]
	4.5	3.64–1.07 (5–13)	
	5.1	156 (–20)	[40]
	6.0	3–0.64 (10–20)	[45]
L-PE	44	2.05–0.8 (121–123)	[44]
C-PE	9	1.18–0.36 (117–120)	[44]
	44	0.25–0.1 (113–115)	
	87	1.23–0.28 (112–115)	
<i>Case 2</i>			
L-POE	1.5	44.6 (22)	[39]
C-POE	1.5	100 (22)	
L-PCL-OH	2	18.8–2.8 (40–44)	[41]
C-PCL	2	40.6–14.7 (45–49)	
L-PCL-Acet	2	41.9–6.32 (39–45)	[47]
	4.9	30.2–6.87 (41–47)	
C-PCL	2	25.1–4.99 (47–53)	[47]
	4.9	33.4–4.44 (48–54)	
L-PCL-Acet	22	9.88–1.16 (41–50)	[49]
C-PCL	22	4.94–0.51 (45–54)	[49]

## 4.2 Spherulitic Growth Rate

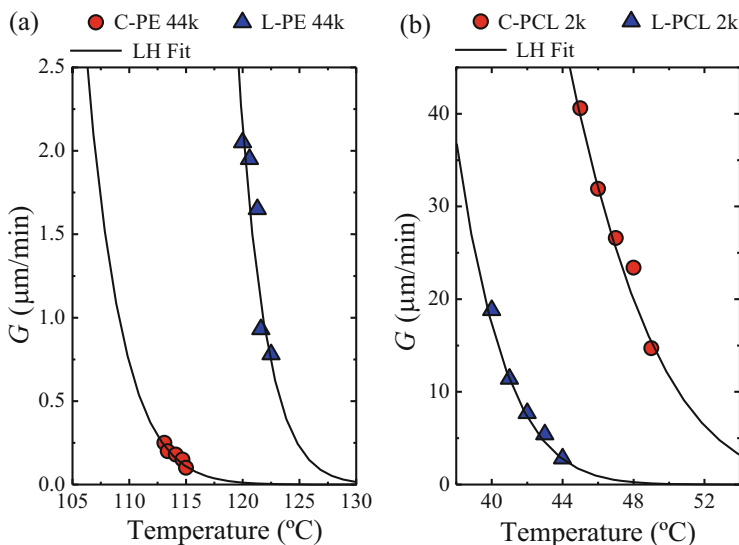
Several works have reported the determination of spherulitic growth rates for cyclic and linear polymers. Two opposite trends have been found:

*Case 1:* Slower spherulitic growth rate for cyclic polymers than for linear polymer analogs. This behavior has been found for PTHF [40, 45] and PE [44].

*Case 2:* Faster spherulitic growth rate for cyclic polymers than for linear polymer analogs. This behavior has been found for poly(oxyethylene) (POE) [39] and PCL [41, 47–49].

The experimental data found in the literature are reported in Table 4 and divided according to the two cases described above. To illustrate these cases, the results of two groups that have found opposite trends are presented here along with the interpretations provided by the authors.

Figure 8 clearly shows opposite trends in spherulitic growth rates between cases 1 and 2 (see Fig. 8a, b). The growth rate is determined by competition between the



**Fig. 8** Spherulitic growth rate ( $G$ ) as a function of isothermal crystallization temperature ( $T_c$ ) for (a) C-PE and L-PE and (b) C-PCL and L-PCL. Lines represent fits to Lauritzen–Hoffman equation. Data points extracted from [44] and [41], respectively. Reprinted with permission from [41] and [44]

free energies associated with chain transport to the growth front and secondary nucleation.

In case 1 (see Fig. 8a), the authors [44] argued that entropic factors cause both transport and secondary nucleation free energies to be higher in cyclic polymers (i.e., PTHF and PE) and, consequently, they exhibit lower  $G$  values than linear polymers of similar  $M_n$ .

According to Tezuka et al. [40], the entropy difference between crystalline and molten states is larger for cyclic polymer chains than for linear chains. This assumption implies that both transport and secondary nucleation require higher free energies in cyclic polymers for the following reasons:

- Cyclic polymer chains are conformationally restricted by the lack of chain ends, especially if the four-folded structure (shown in Fig. 6b) is assumed to be valid [40, 44, 45, 78]. The double-layer molecular arrangement of the cyclic polymers requires more secondary nucleation energy than the monolayer formation of the linear chain [78].
- Under the restricted conformation imposed by the lack of chain ends, the conformational change required in the process of crystallization is hindered in cyclic molecules. This is related to the transport energy involved in processes such as adsorption and chain reel-in on the growth front. On the other hand, the crystal growth rate direction of C-PTHF also changes according to a poisoning or pinning effect [40, 44, 45, 78].

In contrast, in case 2 (see Fig. 8b) both transport and secondary nucleation free energies are claimed to be lower for cyclic polymers than for the linear analogs, leading to higher  $G$  values in cyclic polymers than in linear polymers of similar  $M_n$  values. The authors used molecular diffusion and entropic factors as arguments to explain the higher  $G$  values of cyclic chains:

*Diffusion or kinetic arguments:* The faster diffusion of cyclic molecules has been used as an argument to explain faster spherulitic growth displayed by some cyclic polymers [39, 41]. This faster diffusion has been clearly established in both experiments and simulations [32, 79–82]. Experimental findings indicate that cyclic polymers (both entangled and disentangled) have lower melt viscosities and smaller radii of gyration than linear polymers of equivalent chain lengths [33, 83, 84].

*Entropic or thermodynamic arguments:* Su et al. [47] found a higher  $T_m^0$  value for cyclic PCL than for L-PCL. This finding implies a larger supercooling at the same crystallization temperature for C-PCL as compared with L-PCL (a fact supported by the experimental evidence of single crystal truncation, as presented in Sect. 3.1). Hence, different equilibrium melting points can also partly explain why cyclic PCL molecules crystallize faster than linear molecules. A more detailed explanation of this point is presented in Sect. 4.4.

The contradictory results presented above (case 1 versus case 2) are difficult to explain, especially when some materials (belonging to the group of case 2) change their trends depending on the properties that are being measured, as demonstrated next for non-isothermal and isothermal overall crystallization.

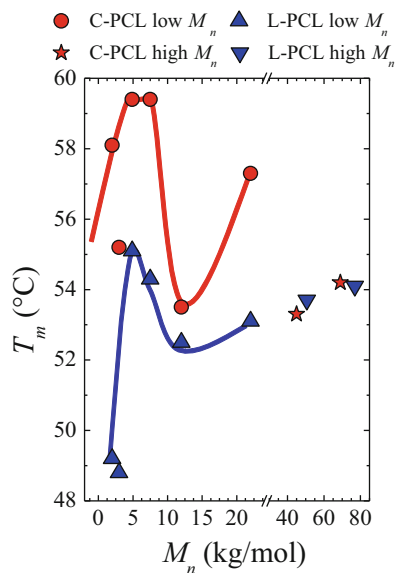
### 4.3 Non-isothermal Differential Scanning Calorimetry

Non-isothermal differential scanning calorimetry (DSC) scans provide important information on the overall crystallization of cyclic and linear polymers. However, the thermal transitions are sometimes only partially reported. For example, the crystallization temperatures ( $T_c$ ) and degrees of crystallinity are not reported in some references for POEs [38, 39], poly(lactic acid)s (PLAs) [46], PLAs with a photocleavable linker [51], PTHFs [40, 45], PE [44], and PCL [18]. In these same studies, cyclic polymers exhibited lower melting temperatures ( $T_m$ ) than their linear analogs. According to Tezuka et al. [40], lower melting points are obtained as a result of the higher entropy of fusion for cyclic chains than for linear chains.

On the other hand, for a large range of oligomeric and polymeric alkanes, PE [31, 85], and PCL [41–43, 47–49], higher values for both crystallization and melting points were found for cyclic molecules compared with their linear analogs.

Su et al. [47] found higher  $T_m$  values in C-PCL single crystals mats prepared by isothermal crystallization from solution than in L-PCL analog samples. Similar results were obtained from the melt state. Müller et al. [41, 47–49] studied cyclic

**Fig. 9** Effect of molecular weight on melting temperatures for low ( $T_m$ , peak) and high ( $T_m$ , onset)  $M_n$ . The solid lines were traced arbitrarily to guide the eye. Data extracted from [48] (for  $M_n$  values lower than 30 kg/mol) and [42] (for  $M_n$  values higher than 30 kg/mol) and re-plotted. Reprinted with permission from [42] and [48]



and linear PCLs of molecular weights ranging from oligomers to intermediate molecular weight values (i.e.,  $M_n$  2–22 kg/mol).

Figure 9 shows a plot of  $T_m$  values obtained during standard DSC experiments as a function of  $M_n$  for the PCL case. The peculiar trend found for the dependence of the melting point on the molecular weight has its origin in competition between diffusion and nucleation, which has also been reported for PE and explained in detail [48].

Table 5 presents results from the literature for PCL samples [41, 47–49]. The general behavior is that C-PCLs always exhibit higher crystallization and melting points than L-PCLs. Shäler et al. [42] performed NMR, Hahn echo, and advanced multiquantum measurements, demonstrating that C-PCLs have a higher segmental mobility in the melt than their linear counterparts.

The enthalpy values determined by DSC and reported in Table 5 indicate that there are no significant differences in crystallinity between cyclic and linear PCLs (Table 5), within the experimental errors involved in measuring enthalpies by DSC (i.e., of the order of 10–15% depending on integration routine, base line fluctuation, and calibration). The NMR data obtained by Shäler et al. [42], also reported in Table 5, show values of similar magnitudes to those obtained by DSC. However, Shäler et al. [42] suggest that, as a result of the enhanced mobility of C-PCL in the melt, higher crystallinity values compared with L-PCL might be obtained.

**Table 5** Non-isothermal differential scanning calorimetry results for L-PCL and C-PCL samples (data extracted from [41, 42, 47–49])

Samples	Cooling scans		Second heating scans			References		
	$T_c$ (°C)	Enthalpy change, $\Delta H_c$ (J/g)	Crystallinity, $X_{c,c}$ (%)	$T_m$ (°C)			Enthalpy change, $\Delta H_m$ (J/g)	Crystallinity, $X_{c,m}$ (%)
				$T_m^1$	$T_m^2$			
L-PCL-OH 2k	29.2	78	57	49.2		83	61	[41]
L-PCL-OH 3k	26.7	74	54	48.8		78	57	[48]
L-PCL-Acet 4.9k	34.6	81	60	55.1		94	69	[47]
L-PCL-OH 7.5k	30.4	69	51	54.3		79	58	[41]
L-PCL-OH 12k	24.1	69	51	52.5		77	57	[48]
L-PCL-Acet 22k	19.9	63	46	53.1	56.1	79	58	[48, 49]
L-PCL 35.9k	35.8	–	–	–	–	–	–	[42]
L-PCL 50.6k	35 <sup>a</sup>	–	–	53.7 <sup>a</sup>	–	–	48	
L-PCL 77k	36.1 <sup>a</sup>	–	–	54.1 <sup>a</sup>	–	–	48	
C-PCL 2k	36.3	79	58	58.1		84	62	[41]
C-PCL 3k	34.0	68	50	55.2		70	51	[48]
C-PCL 4.9k	41.3	75	55	59.4	61.3	93	68	[47]
C-PCL 7.5k	41.5	61	45	59.4	63.4	69	51	[41]
C-PCL 12k	27.3	60	44	53.5		76	56	[48]
C-PCL 22k	26.9	57	42	57.3		73	54	[48, 49]
C-PCL 28.1k	36.5	–	–	–		–	–	[42]
C-PCL 45k	36.4 <sup>a</sup>	–	–	53.3 <sup>a</sup>		–	53	
C-PCL 69k	36.8 <sup>a</sup>	–	–	54.2 <sup>a</sup>		–	54	

<sup>a</sup> $T_c$  and  $T_m$  are onset values taken from [42] whereas all others are peak values are taken from [41, 47–49]

#### 4.4 Isothermal Overall Crystallization Kinetics

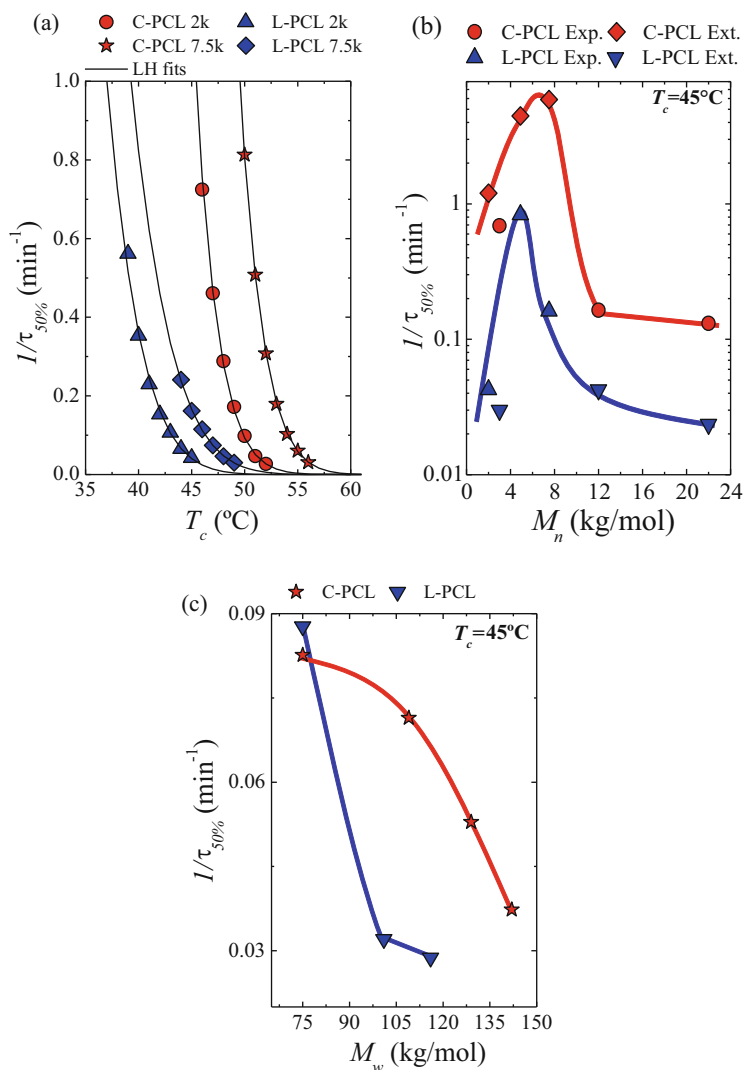
The overall isothermal crystallization kinetics has only been investigated by two groups of researchers in samples of cyclic and linear PCLs with different origins and  $M_n$  ranges. The cyclic samples employed by Müller et al. [41, 47–49] were synthesized by the group of Scott Grayson at Tulane University (New Orleans, LA), employing ring-closure techniques derived from click chemistry, with  $M_n$  range of 2–22 kg/mol and low dispersity indexes. On the other hand, the samples of Shin et al. [43] were prepared at Stanford University (Stanford, CA) by the group of Robert Waymouth using ring-expansion techniques, yielding much higher  $M_n$  values (i.e., 66–114 kg/mol) and larger dispersity indexes (see Tables 1 and 2).

In spite of the differences explained above between the PCL samples obtained by the two synthetic approaches, the results obtained are in agreement with each other. Both groups of authors obtained higher overall crystallization rates (expressed as the inverse of the half-crystallization time,  $1/\tau_{50\%}$ ) for C-PCLs than for L-PCLs. To illustrate this, Fig. 10a shows the overall crystallization rate as a function of isothermal crystallization temperature for samples with  $M_n$  values of 2 and 7.5 kg/mol, whereas Fig. 10b, c shows the overall crystallization rate at 45°C as a function of  $M_n$  and weight-average molecular weight ( $M_w$ ) respectively. C-PCL samples crystallize faster than L-PCL at identical crystallization temperatures.

In Fig. 10a, the solid lines represent linear fits of the Lauritzen–Hoffman theory, employing the equilibrium melting temperature ( $T_m^0$ ) values reported by Su et al. for linear and cyclic PCLs of  $M_n = 7.5$  kg/mol [47] and assuming that these values are independent of molecular weight for the range 2–22 kg/mol. The  $T_m^0$  value has a direct impact on the supercooling, defined as  $\Delta T = T_m^0 - T_c$ . In order to establish the influence of supercooling on the overall crystallization kinetics, Pérez et al. [48] represented the overall crystallization rate ( $1/\tau_{50\%}$ ) as a function of  $\Delta T$ , employing the previously determined values of  $T_m^0$ . Interestingly, the representation of  $1/\tau_{50\%}$  as a function of  $\Delta T$  (for details see [48]) brings the curves of C-PCL and L-PCL closer together. However, the fact that the curves cannot be completely superimposed indicates that other factors also contribute to the differences in overall kinetics. In fact, Su et al. [47] also found differences in fold surface free energies for C-PCL and L-PCL that preclude perfect superposition of the  $1/\tau_{50\%}$  versus  $\Delta T$  curves. The bell-shaped curve presented in Fig. 10b has been discussed in detail previously and has its origin in the existence of an optimum molecular weight value for overall isothermal crystallization [48].

The differences in crystallization rates between C-PCLs and L-PCLs have not only been detected in low and intermediate  $M_n$  samples but also in high molecular weight PCLs. Shin et al. [43] studied the overall crystallization of high molecular weight cyclic and linear PCLs. These authors obtained two different behaviors, depending on the molecular weight. For samples with  $M_w$  of 75–110 kg/mol, both linear and cyclic PCLs crystallize at similar overall rates.

However, when  $M_w$  values are larger than 110 kg/mol, C-PCLs crystallize faster than L-PCLs. The authors explained this peculiar behavior by arguing that C-PCLs



**Fig. 10** Inverse half-crystallization time ( $1/\tau_{50\%}$ ) as a function of (a) crystallization temperature ( $T_c$ ) for the indicated PCL samples, (b)  $M_n$  for ring-closure samples, *solid lines* are included to guide the eye, and (c)  $M_w$  for ring-expansion polymerization samples, *solid lines* are included to guide the eye. *Lines in a* represent fits to Lauritzen–Hoffman equation. Reprinted with permission from [43] and [48]

contain small amounts of L-PCLs as impurities or contaminants. In the lower  $M_w$  range, these impurities might have a dominating influence over the cyclic topology. Thus, cyclic and linear PCL samples crystallize at similar rates, because the linear chains can increase the melt viscosity of cyclic polymers and significantly affect their diffusion to the crystallization front [31, 33, 86–88].

In contrast, for  $M_w > 110$  kg/mol, a dominating influence of cyclic topology on the crystallization kinetics, irrespective of possible contributions from trace amounts of linear polymers, was postulated. Hence, cyclic PCLs crystallize faster than their linear analogs. The reason for the dominating influence of the cyclic topology, according to Shin et al. [43], is that the melt viscosities of the cyclic PCLs are lower than those of linear PCLs, as observed for other cyclic polymers [32, 33, 87]. Additionally, the authors claim that disentanglement in the melt is a crucial feature of polymer crystallization. Therefore, the differences in the entanglement density between linear and cyclic PCLs could be responsible for faster crystallization of the high molecular weight cyclic samples. Evidence for differences in entanglement density have also been obtained by self-nucleation, as described in Sect. 5. The results reported by Shin et al. are shown in Fig. 10c.

Shin et al. [43] performed time-dependent SAXS experiments to study overall isothermal crystallization kinetics of their PCL samples (i.e., samples with  $M_w$  values of 100 kg/mol L-PCL and 130 kg/mol C-PCL). An increase in the scattering density described by the invariant  $Q$  [89] for cyclic PCLs was almost complete within 10 min, whereas for linear PCL it gradually increased over the course of 120–150 min. The Porod coefficient ( $P$ ) [90] was determined as a function of time and used as a means to monitor crystallization kinetics. The Porod coefficient is proportional to the interface area per unit volume ( $O_{ac}$ ):

$$P = \frac{1}{8\pi^3} O_{ac} (\Delta\eta)^2, \quad (3)$$

where  $\Delta\eta$  denotes the difference between the electron densities of the lamellar and amorphous phases. Figure 11 shows that the high molecular weight cyclic PCL crystallizes faster than its linear counterpart at a crystallization temperature ( $T_c$ ) of 45°C. The same trend was found for other crystallization temperatures (30°C, 35°C and 45°C) (for more details see [43]).

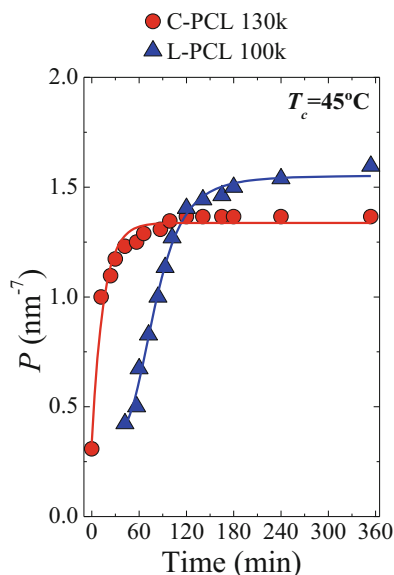
Recently, Wang et al. [50] compared the overall crystallization rates of linear and cyclic oligomeric PCLs with  $M_n = 2$  kg/mol via fast-scanning chip calorimetry measurements (for further details of the specific techniques employed, see [50]).

Figure 12 shows an inverse bell-shaped curve for the overall crystallization time, which can be explained by the classical theory of nucleation and growth. The higher crystallization half-times at temperatures near the glass transition can be assigned to the limited diffusion of molecules, whereas those near to the melting point can be assigned to the limited thermodynamic driving force for nucleation.

Figure 12 shows that at  $T_c$  higher than 20°C, C-PCL crystallizes faster than L-PCL, whereas below 20°C the differences in crystallization half-times are not significant. Qualitatively, both standard and fast-scanning chip calorimetry yield similar results in the high temperature range of Fig. 12. On the other hand, the quantitative differences between the standard DSC data and fast-scanning chip calorimetry are a result of the different equipment involved in the measurements and also in the ways in which the isothermal crystallization experiments were performed [50].



**Fig. 11** Crystal growth rates of cyclic (C-PCL 130k) and linear (L-PCL 100k) PCL during isothermal crystallization at 45°C. Reprinted with permission from [43]



**Fig. 12** Crystallization half-time as a function of isothermal crystallization temperature for both cyclic and linear PCLs with  $M_n = 2$  kg/mol. The crystallization half-times obtained previously [48] by conventional DSC were added for comparison purposes. Reprinted with permission from [50]

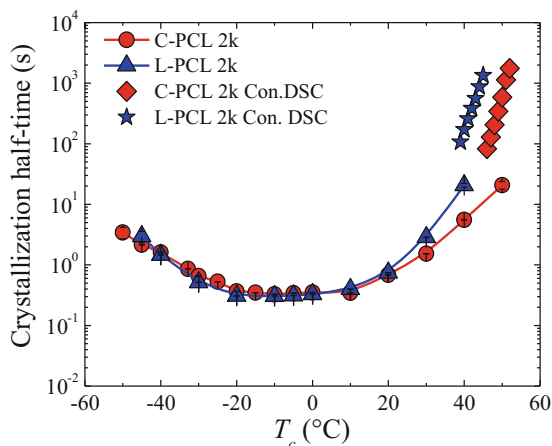
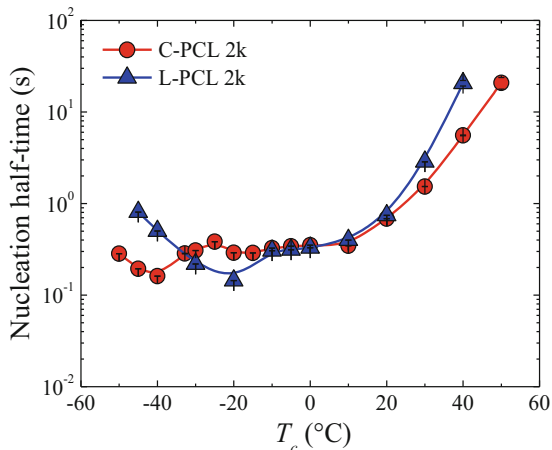


Figure 13 shows the apparent nucleation half-time derived from the data shown in Fig. 12 (see [50] for details on how to derive nucleation half-times from fast-scanning chip calorimetry experiments). The curve of the nucleation half-time as a function of  $T_c$  exhibits two minima: one related to apparent homogeneous nucleation (low-temperature peak) and the other related to heterogeneous nucleation (high-temperature peak).

At higher  $T_c$  values, C-PCL nucleates faster than L-PCL, corroborating the results obtained by PLOM presented above. In contrast, at very low  $T_c$  values, L-PCL exhibits higher onset temperature (around  $-10^\circ\text{C}$ ) than C-PCL (around

**Fig. 13** Nucleation half-time as a function of isothermal crystallization temperature for both cyclic and linear PCLs with  $M_n = 2$  kg/mol. Reprinted with permission from [50]



$-25^{\circ}\text{C}$ ) for the occurrence of apparent homogeneous nucleation. This result was attributed to the free chain ends in L-PCL, which enhance chain mobility and favor diffusion at lower temperatures [50].

According to the results obtained by different techniques, the overall crystallization rates of cyclic PCLs are higher than linear PCLs. This difference can be explained by (a) kinetic factors dominated by diffusion, and (b) thermodynamic factors given by the differences in supercooling, as a result of the different equilibrium melting values for linear and cyclic PCLs.

#### 4.4.1 Difference in Equilibrium Melting Temperature Between Cyclic and Linear Polymers

The equilibrium melting temperature ( $T_m^0$ ) is defined as the transition temperature between the isotropic melt and the 100% crystalline phase, which is given by the ratio of the equilibrium enthalpy of fusion ( $\Delta H^0$ ) to the equilibrium entropy of fusion ( $\Delta S^0$ ):

$$T_m^0 = \frac{\Delta H^0}{\Delta S^0}. \quad (4)$$

There is agreement in the literature that both linear and cyclic polymers have a similar enthalpy of fusion. However, the entropy of fusion is a controversial point, because two interpretations can be found in the literature:

- (a) According to the interpretation of Tezuka et al. [40], the arrangement of the cyclic polymer chains within a lamella, including fold surfaces, is conformationally restricted (see Fig. 6). Hence, they consider that the entropy difference between crystalline and molten states should be larger for cyclic polymers,

**Table 6** Equilibrium melting temperature ( $T_m^0$ ) values reported in the literature for different polymers

Sample	$M_n$ (kg/mol)	$T_m^0$ (°C)	References
L-PTHF	9.1	49.9	[45]
C-PTHF	6.0	32.9	
L-PE	44	145.2	[44]
C-PE	44	139.4	
L-PCL	168	82	[43]
C-PCL	79	84.2	
L-PCL-OH	7.5	80	[41]
C-PCL	7.5	81	
L-PCL-Acet	7.5	80	[47]
C-PCL	7.5	91.2	

even if the conformation in the melt is restricted for rings. If the equilibrium entropy difference between the melt and the crystalline states is larger for cyclic molecules, then  $T_m^0$  would be lower for cyclic polymers in comparison with their linear analogs.

- (b) According to Müller et al. [41, 47–49], because cyclic polymers have a lower configurational entropy in the melt (assuming that the entropy of cyclic and linear polymers within the crystalline state is the same) [37], a higher  $T_m^0$  is predicted. In fact, it is considered that cyclic polymers have a “collapsed” coil conformation in the melt [70–73, 91, 92]. Hence, it is reasonable to expect that in the melt state cyclic polymers have lower configurational entropies than those of linear chains.

The  $T_m^0$  values estimated by the Hoffman–Weeks plot or the Gibbs–Thompson equation are compiled in Table 6. As can be seen, all possible trends have been reported: similar  $T_m^0$  values for cyclic and linear polymers, higher values for cyclic than for linear chains, and lower values for cyclic polymers than for linear analogs.

In order to modify the Hoffman–Weeks and Thomson–Gibbs equations, Su et al. [47] introduced a “cyclization free energy”, as consequence of the difference in free energy in the melt state between cyclic and linear analogs with the same molecular weight. Assuming that the enthalpies of cyclic and linear polymers are the same, the entropy of cyclic chains is smaller than that of linear chains in view of the absence of chain ends and more collapsed conformation.

The modified Thomson–Gibbs and Hoffman–Weeks equations for cyclic polymers explicitly contain an excess free-energy term contributed by the entropic loss upon cyclization. For more details on the derivation of these equations, see [47]. The modified Thomson–Gibbs equation can be expressed as follows:

$$T_m = \frac{T_{mL}^0}{\left(1 + \frac{T_{mL}^0 \Delta S_{cyc}}{\Delta h_f^0}\right)} \left[1 - \frac{2\sigma_e}{\Delta h_f^0 l}\right], \quad (5)$$

where  $T_m$  is the melting point of the lamellar crystal formed by the cyclic polymer,  $T_{mL}^0$  is the equilibrium melting point of the linear polymer,  $\Delta S_{cyc}$  is the cyclization

entropy difference between cyclic and linear polymers in the melt state,  $\Delta h_f^0$  is the equilibrium melting enthalpy difference (being the same for both cyclic and linear polymers),  $\sigma_e$  is the fold surface free energy, and  $l$  is the lamellar thickness. In a plot of  $T_m$  versus  $l^{-1}$ , the intercept can be used to determine the equilibrium melting point of the cyclic polymer ( $T_{mC}^0$ ), defined as:

$$T_{mC}^0 = \frac{T_{mL}^0}{\left(1 + \frac{T_{mL}^0 \Delta S_{cyc}}{\Delta h_f^0}\right)}. \quad (6)$$

On the other hand, the modified Hoffman–Weeks equation for cyclic polymers can be expressed as:

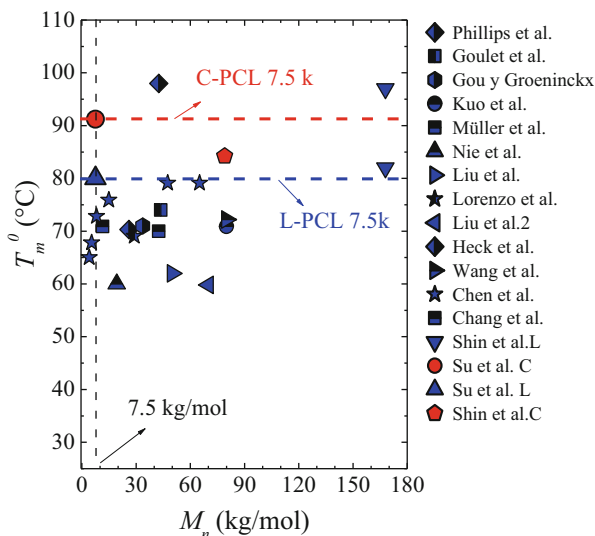
$$T_m = \frac{T_{mL}^0}{\left(1 + \frac{T_{mL}^0 \Delta S_{cyc}}{\Delta h_f^0}\right)} \left(1 - \frac{1}{\gamma}\right) + \frac{T_c}{\gamma} = T_{mC}^0 \left(1 - \frac{1}{\gamma}\right) + \frac{T_c}{\gamma}. \quad (7)$$

Su et al. [47] performed isothermal crystallization experiments from the melt using DSC and SAXS and applied the above equations. In order to estimate  $T_m^0$  for 7.5 kg/mol cyclic and linear PCLs, a  $T_m$  was plotted versus  $l^{-1}$  and the modified Thomson–Gibbs equation employed. As a result (see details in [47]), the value of  $T_{mC}^0$  (i.e., 91.2°C) was found to be higher than that of  $T_{mL}^0$  (i.e., 80°C). This result is in agreement with morphological observations of single crystals, which indicated that C-PCLs are more supercooled than L-PCLs at identical crystallization temperatures.

In Fig. 14, all values reported for the equilibrium melting points of both linear and cyclic PCLs are plotted as a function of  $M_n$  of the samples. The horizontal lines indicate the values obtained by Su et al. for 7.5 kg/mol samples. In the case of the L-PCL sample with 7.5 kg/mol, the  $T_{mL}^0$  value of 80°C is in agreement with other values reported in the literature, including those of Shin et al. [43], which correspond to much higher  $M_n$  values. Many of the values reported in Fig. 14 were obtained by the Hoffman–Weeks extrapolation, which can be unreliable for PCL, depending on the range of  $T_c$  temperatures employed, as demonstrated by Su et al. [47]. This is one of the reasons for the wide spread of  $T_{mL}^0$  values.

In the case of cyclic PCLs, only a few values have been determined. Su et al. [47] estimated a  $\Delta S_{cyc}$  value of  $-12 \text{ J kg}^{-1} \text{ K}^{-1}$ . Additionally, the values for the surface free energy,  $\sigma_e$ , of linear and cyclic PCLs determined from the slopes of the plots were 30.3 and 42.8  $\text{mJ m}^{-2}$ , respectively. The larger  $\sigma_e$  observed for cyclic PCL was attributed to the larger loops formed at the crystal surface when the cyclic chains fold. Another reason for larger values of  $\sigma_e$  in the case of the C-PCLs employed by Su et al. is the presence of the triazole rings (remaining from the click ring-closure reactions) in the amorphous fold planes. In view of the different  $\sigma_e$  values for linear and cyclic PCLs, it is not expected that  $1/\tau_{50\%}$  versus  $\Delta T$  curves

**Fig. 14** Melting equilibrium temperatures reported in the literature. Horizontal lines indicate values obtained by Su et al. [47] for 7.5 kg/mol samples. Data points taken from values reported in the following references [41, 43, 47, 93–106]



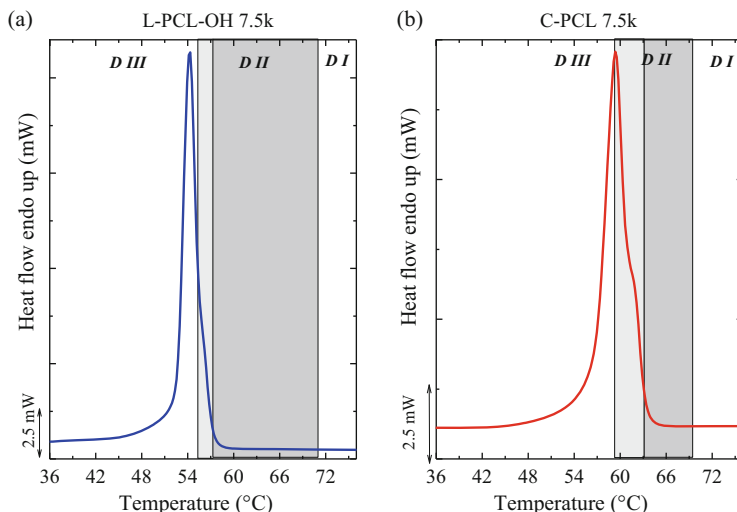
obtained by Pérez et al. [48] can be completely superimposed (see [48] for more details).

Recently, Sugai et al. [51] studied PLLA and poly(D-lactide) (PDLA) with a photocleavable linker and employed an unmodified Thomson–Gibbs equation to determine the equilibrium melting points of their samples. They obtained a smaller  $\sigma_e$  for cyclic PLLA than for its linear analog. According to the authors, this result suggested that cyclic PLLA forms a well-ordered looped structure at the crystal surface that helps stabilize the crystal–amorphous interface, whereas linear PLLA has chains ends that are probably not as organized as cyclic PLLA. Similar results were obtained with PDLA.

## 5 Self-Nucleation and Successive Self-Nucleation and Annealing

### 5.1 Self-Nucleation

The self-nucleation (SN) technique was originally devised by Keller et al. [107] and its use was extended by Fillon et al. [108] by employing DSC [109]. A more detailed explanation of this technique can be found elsewhere [110]. SN consists in performing controlled heating of a sample with a standard thermal history up to a self-seeding temperature called  $T_s$ . If  $T_s$  is high enough to erase thermal history, the sample is in *domain I* (melting domain). If  $T_s$  is high enough to melt the polymer almost completely (or completely) but low enough to leave self-nuclei (crystal fragments or residual segmental orientation in the melt) capable of nucleating the



**Fig. 15** Standard DSC heating scans in the temperature range 36–76°C, where the melting of (a) linear and (b) cyclic PCL samples of 7.5 kg/mol can be observed. The vertical lines indicate the temperatures at which the materials experience self-nucleation domain transition. Domain II (*D II*) is shaded with *two shades of grey*. The temperature range at which the material experiences crystalline memory is shaded *dark grey*. Reprinted with permission from [48]

polymer during cooling, the polymer is in *domain II* (exclusive self-nucleation domain). Finally, if  $T_s$  is so low that the polymer only partially melts, the sample is in *domain III* (self-nucleation and annealing domain), because the unmelted material can anneal.

Use of SN for cyclic and linear polymers revealed novel information regarding crystalline memory, in which a wider domain II was found in L-PCL than in C-PCL (see Fig. 15). The ability to induce self-nucleation when the sample is completely molten is directly related to the crystalline memory of the material [111].

The crystalline memory effect has been explained by considering that the melting process is insufficient to drive the chains back to an isotropic random coil conformation. The chains could have difficulties returning to an isotropic random coil for the following reasons: (a) residual orientation of chain segments or the persistence of metastable or precursor phases [108, 112–129], (b) aligned chains in quasi-crystallographic registers [130–136], or (c) entanglement density [137–145].

Figure 15a shows the capacity of L-PCL to exhibit crystalline memory. This feature has been reported before in commercial L-PCLs by Lorenzo et al., employing similar SN protocols [111]. In contrast, Fig. 15b shows that the crystalline memory of C-PCLs is significantly smaller than that exhibited by its linear analog. A measure of the crystalline memory is given by the width of the self-nucleation domain (i.e., domain II) and, in particular, how far it extends beyond the end melting point of the polymer (after the melting endotherm attains the liquid

baseline). Domain II is shadowed in Fig. 15 with two shades of gray; the darker grey shading corresponds to the crystalline memory range.

Pérez et al. [48] found that the crystalline memory of C-PCL can be erased at lower temperatures than for L-PCLs. According to Pérez et al. [48], C-PCL chains (partially disentangled) reach a pseudo-equilibrium random coil conformation faster than L-PCL as a result of the lower entanglement density of C-PCL. This experimental evidence for the difference in entanglement density is in agreement with the argument employed by Shin et al. [43] to explain the faster overall crystallization of cyclic polymers.

## 5.2 Successive Self-Nucleation and Annealing

Successive self-nucleation and annealing (SSA) is a thermal fractionation protocol designed to deconvolute DSC melting endotherms into elementary components or thermal fractions. This technique was developed by Müller et al. [109, 153]. Recently a review of its correct use and applications has been published [110].

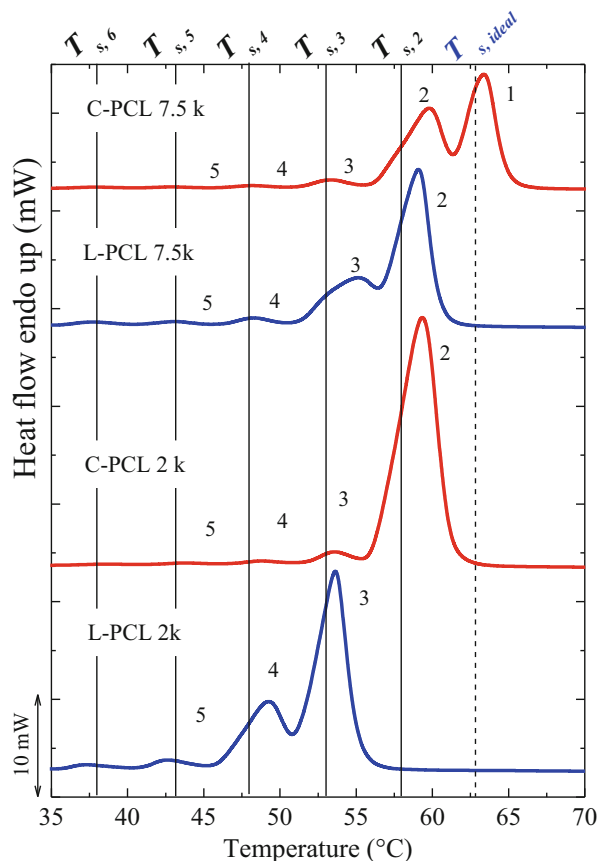
SSA has been employed to study cyclic and linear PCLs by Müller et al. [48, 110], and a novel effect was found. Compared with L-PCLs, a larger annealing capacity of C-PCL lamellar crystals was found. This is remarkable because L-PCL chains can, in theory, be extended to twice the maximum length of C-PCL chains of identical chain length. Hence, L-PCLs have the potential to produce thicker crystals than C-PLCs near equilibrium conditions.

Figure 16 shows the final DSC heating scan after SSA. All samples exhibit some thermal fractionation and, therefore, a distribution of lamellar sizes that melt at distinct temperatures. The melting peaks have been labeled according to their origin (see [48]). Figure 16 also shows vertical lines that indicate the values of the  $T_s$  temperatures employed for the fractionation, and a dashed vertical line that corresponds to the  $T_{s, \text{ideal}}$  for the 7.5 kg/mol C-PCL. This temperature represents the first  $T_s$  employed for all samples.

To illustrate the fractionation exhibited for all the samples, consider melting peak 1 in Fig. 16. Melting peak 1 refers to an annealed population produced mainly during the 5 min holding time at  $T_{s,2}$ , although successive steps might also have some limited influence on the size of the fraction. Melting peak 2 was produced by  $T_{s,3}$  and so on.

If we compare samples with the same molecular weight, it is interesting to note the annealing capacity of the cyclic samples. For instance, the 7.5 kg/mol C-PCL sample had the highest melting fraction (melting peak 1). In contrast, this fraction was not present in other samples, because their melting range was too low. Therefore,  $T_{s,2}$  was only able to produce a thermal fraction (peak 1) for 7.5 kg/mol C-PCL, and for all other samples it caused only self-nucleation but no annealing. Similar behavior was found for C-PCL of 2 kg/mol, in which fraction 2 (melting peak 2) was present, as in almost all samples except for L-PCL of 2 kg/mol. The 2 kg/mol L-PCL was the sample with the lowest melting range.

**Fig. 16** Final heating run after thermal fractionation by successive self-nucleation and annealing. Peaks 1–5 indicate the melting temperatures. Vertical lines indicate the temperatures used for fractionation ( $T_s$ ). Dashed vertical line indicates the ideal  $T_s$  for 7.5 kg/mol C-PCL and was the first fractionation temperature used. See text for full details. Reprinted with permission from [48]

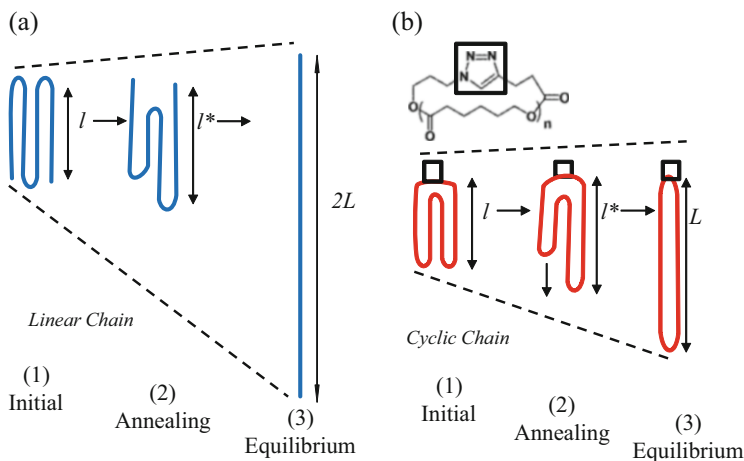


The influence of the molecular weight is reflected in the results. As  $M_n$  increases, the annealing capacity under specific SSA protocol employed also increases, and thermal fractions with higher melting points are produced, as expected.

Figure 16 shows a higher annealing capacity of the cyclic samples, even though the linear samples could be extended, in theory, to twice the maximum length of a C-PCL chain of identical chain length, as represented in the model shown in Fig. 17.

Under equilibrium conditions, linear chains have the potential to produce thicker crystals. However, under the SSA parameters employed by Müller et al. [48, 110] (which are dominated by kinetic factors), cyclic chains anneal and produce thicker crystals than their linear analogs. According to Müller et al. [48, 110], the reasons for the higher annealing capacity of cyclic chains are their lower entanglement density and their ring topology. These characteristics facilitate annealing for cyclic chains, compared with linear chains with a higher entanglement density and lower diffusion coefficients. A collection of stacked lamellar crystals normally thicken at the expense of chains located in the interlamellar regions. Such reel-in processes are





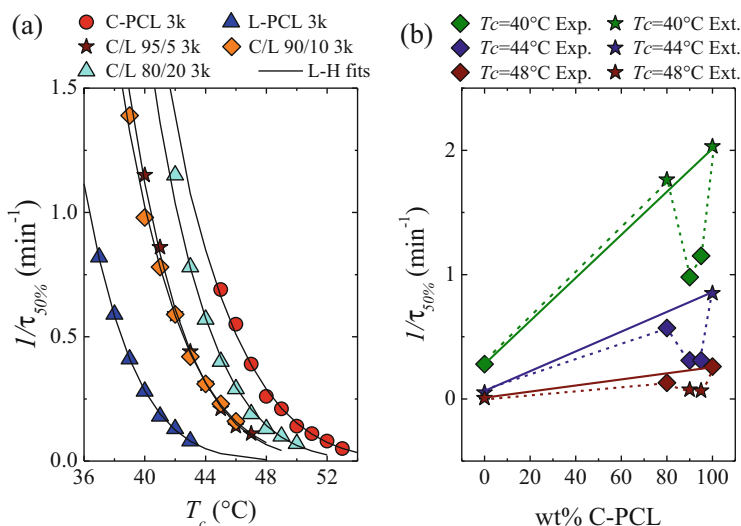
**Fig. 17** A possible way for (a) linear and (b) cyclic chains to thicken during annealing. ( $l$ ) L-PCL and C-PCL with initial lamellar thickness  $l$ . The *square* (not to scale) represents the chemical structure of the triazole group after cyclization, which must be always in the amorphous regions because it cannot enter the crystallographic register of PCL. (2) L-PCL and C-PCL during annealing, in the process of thickening to a larger value,  $l^*$ . (3) L-PCL with an extended chain length of  $2L$  and C-PCL with a once-folded configuration and extended chain length,  $L$ . Reprinted with permission from [48]

facilitated by the lower entanglement densities and higher diffusion coefficients of cyclic chains.

## 6 Reasons for Different Behavior Reported in the Literature

The crystallization of several different cyclic polymers has been studied and in some cases contradictory trends have been found. Experimental evidence indicates that small amounts of linear segments in cyclic polymers have a dramatic impact on their overall crystallization rates. Consequently, sample purity is a crucial issue to be taken into account. On the other hand, it is possible that the conflicting trends found in the literature could be related to the nature of the polymer.

Kapnistos et al. [33] found that the presence of only 0.07 wt% of linear chains can dramatically alter the rheology, diffusion, chain dynamics, and relaxation times of ring polymers. These dramatic changes are related to the bridging or threading effect caused in ring molecules by small amounts of linear chains, which can form a transient network that percolates throughout the material. According to Kapnistos et al. [33], the form of the stress relaxation modulus at intermediate times is affected by this network, producing an entanglement plateau instead of power law behavior.



**Fig. 18** (a) Overall crystallization rate ( $1/\tau_{50\%}$ ) as a function of isothermal crystallization temperature ( $T_c$ ) for 3 kg/mol samples of L-PCL and C-PCL and for their blends at the indicated compositions. *Solid lines* represent fits to the Lauritzen–Hoffman (*L-H*) equation. (b) Values of  $1/\tau_{50\%}$  as a function of C-PCL content at different constant values of  $T_c$ . The plot contains experimental data points (*Exp.*) and values extrapolated (*Ext.*) from the L-H fits to the data shown in a. Reprinted with permission from [49]

Moreover, in blends of linear and cyclic molecules, the trend of cyclic molecules to be threaded by linear chains has been shown by computer simulations [146–151].

The threading effects constitute strong topological interactions capable of slowing down relaxation and chain mobility, because they represent long-lasting entanglements. Therefore, cyclic molecules relax and diffuse more slowly than anticipated by composition effects, as a result of the presence of small amounts of linear chains [146–151].

The threading effects have been shown not only in computer simulations but also experimentally. Gooßen et al. [152] performed small angle neutron scattering (SANS) measurements for mixtures of linear and cyclic polystyrene samples, and their results confirmed the threading of rings by linear chains. Additionally, preliminary results on linear and cyclic PCL blends have been obtained by Müller et al. [49] and are presented in Fig. 18.

Figure 18a shows the overall crystallization rate as a function of  $T_c$  for cyclic and linear PCL samples (with  $M_n$  values of 3 kg/mol). The neat PCL samples display the usual trend (see Fig. 10), in which C-PCL crystallizes faster than L-PCL at identical  $T_c$ . The overall crystallization rates exhibited by the blends are between those of neat C-PCL and L-PCL, as expected. However, a significant reduction in the overall crystallization rate of neat C-PCL is achieved when small amounts of L-PCL (5–10 wt%) are added. Interestingly, the addition of larger amounts (20 wt%) leads to a lower reduction in crystallization rate.

Figure 18b shows the overall crystallization rates at constant  $T_c$  values as a function of composition. The decrease in overall crystallization rate was more pronounced than predicted by a simple mixing law (indicated by the straight lines in Fig. 18b) [49] when small amounts of L-PCL chains were added to C-PCL. Figure 18b shows that the deviation of overall crystallization rate values from a simple rule of mixing is lower as  $T_c$  increases, because the influence of diffusion is smaller. The results shown in Fig. 18 are attributed to the threading effect of linear chains on C-PCL [49]. It is worth noting that more experimental evidence for the threading effect was obtained by Müller et al. [49] during non-isothermal DSC tests and spherulitic growth rates for 3 and 12 kg/mol samples of C-PCLs and their linear analogs (for more details see [49]).

The contradictory trends observed, particularly for PCL and PTHF samples, could be a result of the different nature of each polymer. According to Sugai et al. [51], different crystal systems could cause opposite effects. However, more evidence is needed in this regard.

## 7 Conclusions

The interesting effect of chain topology (ring versus linear) on polymer crystallization has been reviewed. It is well established that chain topology can have an important influence on nucleation, morphology, crystallization kinetics and thermal transitions in general. It is envisaged that such important changes can also modify the mechanical properties, an assumption that needs to be verified in the future. Other properties also depend on chain topology, such as glass transition temperature, visco-elastic and rheological properties, and susceptibility to degradation.

The importance of sample purity cannot be understated, especially in view of recent rheological evidence and the results available on cyclic/linear blends. The purity issue could be relevant when comparing results for polymers produced by different synthetic methods or purification procedures, and it is very difficult to assess its effect because the content of linear chains could vary from sample to sample. Even samples produced by the same technique might have different amounts of linear chains, depending on the molecular weight, for instance.

Although some polymeric systems have been studied extensively (namely PCL and PTHF), the trends observed are sometimes contradictory. If we assume purity issues are not a problem in these cases, from the evidence available in the literature today, it seems that the effect of topology depends on the exact nature of the polymeric structure under consideration (crystal structure and the way the chains fold during lamellae formation). More research efforts are clearly needed to understand the origin of such results.

**Acknowledgements** The POLYMAT/UPV/EHU team would like to acknowledge funding from the following projects: “UPV/EHU Infrastructure: INF 14/38”; “Mineco/FEDER: SINF 130I001726XV1/Ref: UNPV13-4E-1726” and “Mineco MAT2014-53437-C2-P”. R.A.P.-C

gratefully acknowledges the award of a PhD fellowship by POLYMAT Basque Center for Macromolecular Design and Engineering.

## References

1. Jacob F, Wollman EL (1958) Genetic and physical determinations of chromosomal segments in *Escherichia coli*. *Symp Soc Exp Biol* 12:75–92
2. Dulbecco R, Vogt M (1963) Evidence for a ring structure of polynoma virus DNA. *Proc Natl Acad Sci USA* 50(2):236–243
3. Vologodskii A (1998) Exploiting circular DNA. *Proc Natl Acad Sci USA* 95(8):4092–4093
4. Harmon FG, Brockman JP, Kowalczykowski SC (2003) RecQ helicase stimulates both DNA catenation and changes in DNA topology by topoisomerase III. *J Biol Chem* 278:42668–42678
5. Harmon FG, DiGate RJ, Kowalczykowski SC (1999) RecQ helicase and topoisomerase III comprise a novel DNA strand passage function: a conserved mechanism for control DNA recombination. *Mol Cell* 3(5):611–620
6. Saska I, Colgrave ML, Jones A, Anderson MA, Craik DJ (2008) Quantitative analysis of backbone-cyclised peptides in plants. *J Chromatogr B Biomed Sci Appl* 872(1–2):107–114
7. Craik DJ (2009) Circling the enemy: cyclic proteins in plant defence. *Trends Plant Sci* 14(6):328–335
8. Beckham HW (2011) Ring polymers: effective isolation and unique properties. In: Hadjichristidis N, Hirao A, Tezuka Y, Du Prez F (eds) *Complex macromolecular architecture: synthesis and characterization, and self-assembly*. Wiley, Hoboken
9. Semlyen J (2002) *Cyclic polymers*, 2nd edn. Kluwer, Dordrecht
10. Hoskins JN, Grayson SM (2011) Cyclic polyesters: synthetic approaches and potential applications. *Polym Chem* 2:289–299
11. Schappacher M, Deffieux A (1995) Controlled synthesis of bicyclic “eight-shaped” poly(chloroethyl vinyl ether)s. *Macromolecules* 28(8):2629–2636
12. Beinat S, Schappacher M, Deffieux A (1996) Linear and semicyclic amphiphilic diblock copolymers. I. Synthesis and structural characterization of cyclic diblock copolymers of poly(hydroxyethyl vinyl ether) and linear polystyrene and their linear homologues. *Macromolecules* 29(21):6737–6743
13. Kubo M, Hayashi T, Kobayashi H, Itoh T (1998) Syntheses of tadpole- and eight-shaped polystyrenes using cyclic polystyrene as a building block. *Macromolecules* 31(4):1053–1057
14. Oike H, Washizuka M, Tezuka Y (2001) Designing an “a ring-with-branches” polymer topology by electrostatic self-assembly and covalent fixation with interiorly functionalized telechelics having cyclic ammonium groups. *Macromol Rapid Commun* 22(14):1128–1134
15. Oike H, Hamada M, Eguchi S, Danda Y, Tezuka Y (2001) Novel synthesis of single- and double-cyclic polystyrenes by electrostatic self-assembly and covalent fixation with telechelics having cyclic ammonium salt groups. *Macromolecules* 34(9):2776–2782
16. Tezuka Y, Komiya R, Washizuka M (2003) Designing 8-shaped polymer topology by metathesis condensation with cyclic poly(THF) precursors having allyl groups. *Macromolecules* 36(1):12–17
17. Jia Z, Fu Q, Huang J (2006) Synthesis of amphiphilic macrocyclic graft copolymer consisting of poly(ethylene oxide) ring and multi-polystyrene lateral chains. *Macromolecules* 39(16):5190–5193
18. Li H, Jérôme R, Lecomte P (2006) Synthesis of tadpole-shaped copolyesters based on living macrocyclic poly( $\epsilon$ -caprolactone). *Polymer* 47(26):8406–8413

19. Li H, Riva R, Jérôme R, Lecomte P (2007) Combination of ring-opening polymerization and “click” chemistry for the synthesis of an amphiphilic tadpole-shaped poly( $\epsilon$ -Caprolactone) grafted by PEO. *Macromolecules* 40(4):824–831
20. Li H, Jérôme R, Lecomte P (2008) Amphiphilic sun-shaped polymers by grafting macrocyclic copolyesters with PEO. *Macromolecules* 41(3):650–654
21. Pang X, Jing R, Huang J (2008) Synthesis of amphiphilic macrocyclic graft copolymer consisting of a poly(ethylene oxide) ring and multi-poly( $\epsilon$ -caprolactone) lateral chains. *Polymer* 49(4):893–900
22. Shi G-Y, Pan C-Y (2008) Synthesis of well-defined figure-of-eight-shaped polymers by a combination of ATRP and click chemistry. *Macromol Rapid Commun* 29(20):1672–1678
23. Shi GY, Yang LP, Pan CY (2008) Synthesis and characterization of well-defined polystyrene and poly( $\epsilon$ -caprolactone) hetero eight-shaped copolymers. *J Polym Sci Part A Polym Chem* 46(19):6496–6508
24. Dong Y-Q, Tong Y-Y, Dong B-T, Du F-S, Li Z-C (2009) Preparation of tadpole-shaped amphiphilic cyclic PS-*b*-linear PEO via ATRP and click chemistry. *Macromolecules* 42(8):2940–2948
25. Lonsdale DE, Monteiro MJ (2010) Various polystyrene topologies built from tailored cyclic polystyrene via CuAAC reactions. *Chem Commun* 46:7945–7947
26. Fan X, Wang G, Huang J (2011) Synthesis of macrocyclic molecular brushes with amphiphilic block copolymers as side chains. *J Polym Sci Part A Polym Chem* 49(6):1361–1367
27. Laurent BA, Grayson SM (2011) Synthesis of cyclic dendronized polymers via divergent “graft-from” and convergent click “graft-to” routes: preparation of modular toroidal macromolecules. *J Am Chem Soc* 133(34):13421–13429
28. Wang G, Fan X, Hu B, Zhang Y, Huang J (2011) Synthesis of eight-shaped poly(ethylene oxide) by the combination of glaser coupling with ring-opening polymerization. *Macromol Rapid Commun* 32(20):1658–1663
29. Fan X, Huang B, Wang GW, Huang J (2012) Synthesis of amphiphilic heteroeight-shaped polymer *cyclic*-[poly(ethylene oxide)-*b*-polystyrene]<sub>2</sub> via “click” chemistry. *Macromolecules* 45(9):3779–3786
30. Kricheldorf HR (2010) Cyclic polymers: synthetic strategies and physical properties. *J Polym Sci Part A Polym Chem* 48(2):251–284
31. Bielawski CW, Benitez D, Grubbs RH (2002) An “endless” route to cyclic polymers. *Science* 297(5589):2041–2044
32. McKenna GB, Hostetter BJ, Hadjichristidis N, Fetters LJ, Plazek DJ (1989) A study of the linear viscoelastic properties of cyclic polystyrenes using creep and recovery measurements. *Macromolecules* 22(4):1834–1852
33. Kapnistos M, Lang M, Vlassopoulos D, Pyckhout-Hintzen W, Richter D, Cho D, Chang T, Rubinstein M (2008) Unexpected power-law stress relaxation of entanglement ring polymers. *Nat Mater* 7:997–1002
34. Nam S, Leisen J, Breedveld V, Beckham HW (2008) Dynamics of unentangled cyclic and linear poly(oxyethylene) melts. *Polymer* 49(25):5467–5473
35. Lee KS, Wegner G, Hsu SL (1987) Vibrational spectroscopic studies of linear and cyclic alkanes: C<sub>n</sub>H<sub>2n+2</sub>, C<sub>n</sub>H<sub>2n</sub> with 24 ≤ n ≤ 288: chain folding, chain packing and conformations. *Polymer* 28(6):889–896
36. Yang Z, Yu GE, Cooke J, Ali-Adid Z, Viras K, Matsuura H, Ryan AJ, Booth C (1996) Preparation and crystallinity of a large unsubstituted crown ether, cyclic heptacosia(oxyethylene)(*cyclo*-E<sub>27</sub>, 81-crown-27), studied by Raman spectroscopy, X-ray scattering and differential scanning calorimetry. *J Chem Soc Faraday Trans* 92:3173–3182
37. Cooke J, Viras K, Yu GE, Sun T, Yonemitsu T, Ryan AJ, Price C, Booth C (1998) Large cyclic poly(oxyethylene)s: chain folding in the crystalline state studied by Raman spectroscopy, x-ray scattering, and differential scanning calorimetry. *Macromolecules* 31(9):3030–3039

38. Yu GE, Sun T, Yan ZG, Price C, Booth C, Cook J, Ryan AJ, Viras K (1997) Low-molar-mass cyclic poly(oxyethylene)s studied by Raman spectroscopy, X-ray scattering and differential scanning calorimetry. *Polymer* 38(1):35–42
39. Nam S (2006) Dynamics of cyclic and linear poly(oxyethylene), and threading conformation in their blends. Ph.D. dissertation, Georgia Institute of Technology
40. Tezuka Y, Ohtsuka T, Adachi K, Komiya R, Ohno N, Okui N (2008) A defect-free ring polymers: size-controlled cyclic poly(tetrahydrofuran) consisting exclusively of the monomer unit. *Macromol Rapid Commun* 29(14):1237–1241
41. Córdova ME, Lorenzo AT, Müller AJ, Hoskins JN, Grayson SM (2011) A comparative study on the crystallization behavior of analogous linear and cyclic poly( $\epsilon$ -caprolactones). *Macromolecules* 44(7):1742–1746
42. Schäler K, Ostas E, Schröter K, Thurn-Albrecht T, Binder WH, Saalwächter K (2011) Influence of chain topology on polymer dynamics and crystallization. Investigation of linear and cyclic poly( $\epsilon$ -caprolactone)s by  $^1\text{H}$  solid-state NMR methods. *Macromolecules* 44(8):2743–2754
43. Shin EJ, Jeong W, Brown HA, Koo BJ, Hedrick JL, Waymouth RM (2011) Crystallization of cyclic polymers: synthesis and crystallization behavior of high molecular weight cyclic poly( $\epsilon$ -caprolactone)s. *Macromolecules* 44(8):2773–2779
44. Kitahara T, Yamazaki S, Kimura K (2011) Effects of topological constraint and knot entanglement on the crystal growth of polymers proved by growth rate of spherulite of cyclic polyethylene. *Kobunshi Ronbunshu* 68(10):694–701
45. Takeshita H, Poovarodom M, Kiya K, Arai F, Takenaka K, Miya M, Shiomi T (2012) Crystallization behavior and chain folding manner of cyclic, star and linear poly(tetrahydrofuran)s. *Polymer* 53(23):5375–5384
46. Shin EJ, Jones AE, Waymouth RM (2012) Stereocomplexation in cyclic and linear polylactide blends. *Macromolecules* 45(1):595–598
47. Su H-H, Chen H-L, Díaz A, Casas MT, Puiggali J, Hoskins JN, Grayson SM, Pérez RA, Müller AJ (2013) New insights on the crystallization and melting of cyclic PCL chains on the basis of a modified Thomson–Gibbs equation. *Polymer* 54(2):846–859
48. Pérez RA, Córdova ME, López JV, Hoskins JN, Zhang B, Grayson SM, Müller AJ (2014) Nucleation, crystallization, self-nucleation and thermal fractionation of cyclic and linear poly( $\epsilon$ -caprolactone)s. *React Funct Polym* 80:71–82
49. Pérez RA, López JV, Hoskins JN, Zhang B, Grayson SM, Casas MT, Puiggali J, Müller AJ (2014) Nucleation and antinucleation effects of functionalized carbon nanotubes on cyclic and linear poly( $\epsilon$ -caprolactones). *Macromolecules* 47(11):3553–3566
50. Wang J, Li Z, Pérez RA, Müller AJ, Zhang B, Grayson SM, Hu W (2015) Comparing crystallization rates between linear and cyclic poly( $\epsilon$ -caprolactone) via fast-scan chip-calorimeter measurements. *Polymer* 63:34–40
51. Sugai N, Asai S, Tezuka Y, Yamamoto T (2015) Photoinduced topological transformation of cyclized polylactides for switching the properties of homocrystals and stereocomplexes. *Polym Chem* 6:3591–3600. doi:[10.1039/C5PY00158G](https://doi.org/10.1039/C5PY00158G)
52. Takeshita H, Shiomi T (2013) Crystallization of cyclic and branched polymers. In: Tezuka Y (ed) *Topological polymer chemistry: progress of cyclic polymers in synthesis, properties and functions*. World Scientific, Singapore
53. Jia Z, Monteiro MJ (2012) Cyclic polymers: methods and strategies. *J Polym Sci Part A Polym Chem* 50(11):2085–2097
54. Brown HA, Waymouth RM (2013) Zwitterionic ring-opening polymerization for the synthesis of high molecular weight cyclic polymers. *Acc Chem Res* 46(11):2585–2596
55. Elupula R, Laurent BA, Grayson SM (2011) Cyclic polymers. In: Schlüter AD, Hawker CJ, Sawamoto J (eds) *Synthesis of polymers: new structures and methods*. Wiley, Germany
56. Tezuka Y (2012) Topological polymer chemistry for designing multicyclic macromolecular architectures. *Polym J* 44(12):1159–1169

57. Dubois P, Barakat I, Jérôme R, Teyssie P (1993) Macromolecular engineering of polyactones and polyactides. 12. Study of the depolymerization reactions of poly(epsilon-caprolactone) with functional aluminum alkoxide end groups. *Macromolecules* 26(17):4407–4412
58. Li Y, Hoskins JN, Sreerama SG, Grayson SM (2010) MALDI–TOF mass spectral characterization of polymers containing an azide group: evidence of metastable ions. *Macromolecules* 43(14):6225–6228
59. Iwata T, Doi Y (2002) Morphology and enzymatic degradation of poly(epsilon-caprolactone) single crystals: does a polymer single crystal consist of micro-crystals? *Polym Int* 51(10):852–858
60. Chatani Y, Okita Y, Takadoro H, Yamashita Y (1970) Structural studies of polyesters. III. Crystal structure of poly-epsilon-caprolactone. *Polym J* 1(5):555–562
61. Hu H, Dorset DL (1990) Crystal structure of poly(epsilon-caprolactone). *Macromolecules* 23(21):4604–4607
62. Bittiger H, Marchessault RH, Niegish WD (1970) Crystal structure of poly-epsilon-caprolactone. *Acta Crystallogr B* 26(12):1923–1927
63. Gestí S, Almontassir A, Casas MT, Puiggalí J (2004) Molecular packing and crystalline morphologies of biodegradable poly(alkylene dicarboxylate)s derived from 1,6-hexanediol. *Polymer* 45(26):8845–8861
64. Gestí S, Almontassir A, Casas MT, Puiggalí J (2006) Crystalline structure of poly(hexamethylene adipate). Study on the morphology and the enzymatic degradation of single crystals. *Biomacromolecules* 7(3):799–808
65. Gestí S, Casas MT, Puiggalí J (2007) Crystalline structure of poly(hexamethylene succinate) and single crystal degradation studies. *Polymer* 48(17):5088–5097
66. Gestí S, Casas MT, Puiggalí J (2008) Single crystal morphology and structural data of a series of polyesters derived from 1,8-octanediol. *Eur Polym J* 52(7):2295–2307
67. Baratian S, Hall ES, Lin JS, Xu R, Runt J (2001) Crystallization and solid-state structure of random poly(lactide) copolymers: poly(L-lactide-co-D-lactide)s. *Macromolecules* 34(14):4857–4864
68. Huang J, Lisowski MS, Runt J, Hall ES, Kean RT, Buehler N, Lin JS (1998) Crystallization and microstructure of Poly(L-lactide-co-meso-lactide) copolymers. *Macromolecules* 31(8):2593–2599
69. Tsuji H (2005) Poly(lactide) stereocomplexes: formation, structure, properties, degradation, and applications. *Macromol Biosci* 5(7):569–597
70. Obukhov SP, Rubinstein M, Duke T (1994) Dynamics of a ring polymer in a gel. *Phys Rev Lett* 73:1263–1266
71. Arrighi V, Gagliardi S, Dagger AC, Semlyen JA, Higgins JS, Shenton MJ (2004) Conformation of cyclics and linear chains polymer in bulk by SANS. *Macromolecules* 37(21):8057–8065
72. Hur K, Winkler RG, Yoon DY (2006) Comparison of ring and linear polyethylene from molecular dynamics simulations. *Macromolecules* 39(12):3975–3977
73. Suzuki J, Takano A, Matsushita Y (2008) Topological effect in ring polymers investigated with Monte Carlo simulation. *J Chem Phys* 129:034903
74. Bassett DC (2003) Polymer spherulites: a modern assessment. *J Macromol Sci Part B Phys* 42(2):227–256
75. Toda A, Arita T, Hikosaka M, Hobbs JK, Miles MJ (2003) An atomic force microscopy observation of poly(vinylidene fluoride) banded spherulites. *J Macromol Sci Part B Phys* 42(3–4):753–760
76. Keith HD, Padden FJ (1984) Twisting orientation and the role of transient states in polymer crystallization. *Polymer* 25(1):28–42
77. Lotz B, Cheng SZD (2005) A critical assessment of unbalanced surface stresses as the mechanical origin of twisting and scrolling of polymer crystals. *Polymer* 46(3):577–610
78. Okui N, Ohno N, Unemoto S, Tezuka Y (2009) Topological effect on polymer crystallization of linear and ring polymers. *Bussei Kenkyu* 92(1):51–55

79. Roovers J (1985) The melt properties of ring polystyrenes. *Macromolecules* 18 (6):1359–1361
80. Mckenna GB, Hadziioannou G, Lutz P, Hild G, Strazielle C, Straupe C, Rempp P, Kovacs AJ (1987) Dilute solution characterization of cyclic polystyrene molecules and their zero-shear viscosity in the melt. *Macromolecules* 20(3):498–512
81. Orrah DJ, Semlyen JA, Ross-Murphy SB (1988) Studies of cyclic and linear poly(dimethylsiloxanes): 27. Bulk viscosities above the critical molar mass for entanglement. *Polymer* 29 (8):1452–1454
82. Izuka A, Winter HH, Hashimoto T (1992) Molecular weight dependence of viscoelasticity of polycaprolactone critical gels. *Macromolecules* 25(9):2422–2428
83. McLeish T (2002) Polymers without beginning or end. *Science* 297:2005–2006
84. Kawaguchi D, Masuoka K, Takano A, Tanaka K, Nagamura T, Torikai N, Dalglish RM, Langridge S, Matshushita Y (2006) Comparison of interdiffusion behavior between cyclic and linear polystyrenes with high molecular weights. *Macromolecules* 39(16):5180–5182
85. Lee KS, Wegner G (1985) Linear and cyclic alkanes ( $C_nH_{2n+2}$ ,  $C_nH_{2n}$ ) with  $n > 100$ . Synthesis and evidence for chain-folding. *Makromol Chem Rapid Commun* 6(3):203–208
86. Rosen BM, Wilson CJ, Wilson DA, Peterca M, Imam MR, Percec V (2009) Dendron-mediated self-assembly, disassembly, and self-organization of complex systems. *Chem Rev* 109(11):6275–6540
87. Roovers J (1988) Viscoelastic properties of polybutadiene rings. *Macromolecules* 21 (5):1517–1521
88. Nam S, Leisen J, Breedveld V, Beckham HW (2009) Melt dynamics of blended poly(oxyethylene) chains and rings. *Macromolecules* 42(8):3121–3128
89. Porod G (1951) Die Röntgenkleinwinkelstreuung von dichtgepackten kolloiden Systemen I. Teil *Kolloid ZZ Polym* 124(2):83–114
90. Strobl G (2007) *The physics of polymers: concepts for understanding their structures and behavior*, 3rd edn. Springer, Berlin
91. Cates ME, Deutsch JM (1986) Conjectures on the statistics of ring polymers. *J Phys Paris* 47 (12):2121–2128
92. Iyer BVS, Lele AK, Juvekar VA (2006) Flexible ring polymers in an obstacle environment: molecular theory of linear viscoelasticity. *Phys Rev E* 74(2):021805
93. Chen H-L, Li L-J, Yang W-CO, Hwang JC, Wong W-Y (1997) Spherulitic crystallization behavior of poly( $\epsilon$ -caprolactone) with a wide range of molecular weight. *Macromolecules* 30 (6):1718–1722
94. Heck B, Hugel T, Iijima M, Sadiku E, Strobl G (1999) Steps in the transition of an entangled polymer melt to the partially crystalline state. *New J Phys* 1:17.1–17.29
95. Gedde UW (1999) *Polymer physics*, 1st edn. Kluwer, Dordrecht
96. Phillips PJ, Rensch GJ, Taylor KD (1987) Crystallization studies of poly( $\epsilon$ -caprolactone). I. Morphology and kinetics. *J Polym Sci B Polym Phys* 25(8):1725–1740
97. Goulet L, Prud'homme RE (1990) Crystallization kinetics and melting of caprolactone random copolymers. *J Polym Sci B Polym Phys* 28(12):2329–2352
98. Guo Q, Groeninckx G (2001) Crystallization kinetics of poly( $\epsilon$ -caprolactone) in miscible thermosetting polymer blends of epoxy resin and poly( $\epsilon$ -caprolactone). *Polymer* 42 (21):8647–8655
99. Kuo SW, Chan SC, Chang FC (2004) Crystallization kinetics and morphology of binary phenolic/poly( $\epsilon$ -caprolactone) blends. *J Polym Sci B Polym Phys* 42(1):117–128
100. Müller AJ, Albuérne J, Marquez L, Raquez JM, Degée P, Dubois P, Hobbs J, Hamley IW (2005) Self-nucleation and crystallization kinetics of double crystalline poly( $p$ -dioxanone)- $b$ -poly( $\epsilon$ -caprolactone) diblock copolymers. *Faraday Discuss* 128:231–252
101. Nie K, Zheng S, Lu F, Zhu Q (2005) Inorganic–organic hybrids involving poly( $\epsilon$ -caprolactone) and silica network: hydrogen-bonding interactions and isothermal crystallization kinetics. *J Polym Sci B Polym Phys* 43(18):2594–2603



102. Liu Y, Yang X, Zhang W, Zheng S (2006) Star-shaped poly( $\epsilon$ -caprolactone) with polyhedral oligomeric silsesquioxane core. *Polymer* 47(19):6814–6825
103. Lorenzo AT, Müller AJ, Lin MC, Chen HL, Jeng US, Priftis D, Pitsikalis M, Hadjichristidis N (2009) Influence of macromolecular architecture on the crystallization of (PCL<sub>2</sub>)-*b*-(PS<sub>2</sub>) 4-miktoarm star block copolymers in comparison to linear PCL-*b*-PS diblock copolymer analogues. *Macromolecules* 42(21):8353–8364
104. Liu H, Huang Y, Yuan L, He P, Cai Z, Shen Y, Xu Y, Yu Y, Xiong H (2010) Isothermal crystallization kinetics of modified bamboo cellulose/PCL composites. *Carbohydr Polym* 79(3):513–519
105. Wang K, Cai L, Jesse S, Wang S (2012) Poly( $\epsilon$ -caprolactone)-banded spherulites and interaction with MC3T3-E1 Cells. *Langmuir* 28(9):4382–4395
106. Chang H, Zhang J, Li L, Wang Z, Yang C, Takahashi I, Ozaki Y, Yan S (2010) A study on the epitaxial ordering process of the polycaprolactone on the highly oriented polyethylene substrate. *Macromolecules* 43(1):362–366
107. Blundell DJ, Keller A, Kovacs AJ (1966) A new self-nucleation phenomenon and its application to the growing of polymer crystals from solution. *J Polym Sci B Polym Lett* 4(7):481–486
108. Fillon B, Wittmann J, Lotz B, Thierry A (1993) Self-nucleation and recrystallization of isotactic polypropylene ( $\alpha$  phase) investigated by differential scanning calorimetry. *J Polym Sci B Polym Phys* 31(10):1383–1393
109. Müller AJ, Arnal ML (2005) Thermal fractionation of polymers. *Prog Polym Sci* 30(5):559–603
110. Müller AJ, Michell RM, Pérez RA, Lorenzo AT (2015) Successive self-nucleation and annealing (SSA): correct design of thermal protocol and applications. *Eur Polym J* 65:132–154
111. Lorenzo AT, Arnal ML, Sánchez JJ, Müller AJ (2006) Effect of annealing time on the self-nucleation behavior of semicrystalline polymers. *J Polym Sci B Polym Phys* 44(12):1738–1759
112. Fillon B, Thierry A, Wittmann J, Lotz B (1993) Self-nucleation and recrystallization of polymers. Isotactic polypropylene,  $\beta$  phase:  $\beta$ - $\alpha$  conversion and  $\beta$ - $\alpha$  growth transitions. *J Polym Sci B Polym Phys* 31(10):1407–1424
113. Fillon B, Lotz B, Thierry A, Wittman J (1993) Self-nucleation and enhanced nucleation of polymers. Definition of a convenient calorimetric “efficiency scale” and evaluation of nucleating additives in isotactic polypropylene ( $\alpha$  phase). *J Polym Sci B Polym Phys* 31(10):1395–1405
114. Turska E, Gogolewski S (1975) Study on crystallization of nylon 6 (polycapramide). III. Effect of “crystalline memory” on crystallization kinetics. *J Appl Polym Sci* 19(3):637–644
115. Gallez F, Legras R, Mercier JP (1976) Crystallization of bisphenol-A polycarbonate. I. Influence of trimellitic acid tridecyloctyl ester on the kinetics of crystallization. *J Polym Sci Polym Phys Ed* 14(8):1367–1377
116. Di Filippo G, Gonzalez ME, Gasiba MT, Müller AJ (1987) Crystalline memory on polycarbonate. *J Appl Polym Sci* 34(5):1959–1966
117. Khanna YP, Reimschuessel AC (1988) Memory effects in polymers. I. Orientational memory in the molten state; its relationship to polymer structure and influence on recrystallization rate and morphology. *J Appl Polym Sci* 35(8):2259–2268
118. Khanna YP, Kumar R, Reimschuessel AC (1988) Memory effects in polymers. III. Processing history vs crystallization rate of nylon 6—comments on the origin of memory effect. *Polym Eng Sci* 28(24):1607–1611
119. Mehl NA, Rebenfeld L (1992) Effect of melt history on the crystallization kinetics of poly(phenylene sulfide). *Polym Eng Sci* 32(19):1451–1457
120. Kim SP, Kim SC (1993) Crystallization kinetics of poly(ethylene terephthalate): memory effect of shear history. *Polym Eng Sci* 33(2):83–91

121. Khanna YP, Kuhn WP, Macur JE, Messa AF, Murthy NS, Reimshuessel AC, Schneider RL, Sibila JP, Signorelli AJ, Taylor TJ (1995) Memory effects in polymers. V. Processing history versus thermally induced self-orientation of unoriented poly(chlorotrifluoroethylene) films. *J Polym Sci B Polym Phys* 33(7):1023–1030
122. Alfonso GC, Scardigli P (1997) Melt memory effects in polymer crystallization. *Macromol Symp* 118(1):323–328
123. Mendez G, Müller AJ (1997) Evidences of the crystalline memory and recrystallization capacity of bisphenol-A polycarbonate. *J Therm Anal* 50(4):593–602
124. Supaphol P, Spruiell JE (2000) Crystalline memory effects in isothermal crystallization of syndiotactic polypropylene. *J Appl Polym Sci* 75(3):337–346
125. Schneider S, Drujon X, Lotz B, Wittmann JC (2001) Self-nucleation and enhanced nucleation of polyvinylidene fluoride ( $\alpha$ -phase). *Polymer* 42(21):8787–8798
126. Vasanthan N (2003) “Orientation induced memory effect” in polyamides and the relationship to hydrogen bonding. *J Appl Polym Sci* 90(3):772–775
127. Supaphol P, Srimoan P, Sirivat A (2004) Effects of crystalline memory and orientational memory phenomena on the isothermal bulk crystallization and subsequent melting behavior of poly(trimethylene terephthalate). *Polym Int* 53(8):1118–1126
128. Massa MV, Lee MSM, Dalnoki-Veress K (2005) Crystal nucleation of polymers confined to droplets: memory effects. *J Polym Sci B Polym Phys* 43(23):3438–3443
129. Ziabicki A, Alfonso GC (1994) Memory effects in isothermal crystallization. I. Theory. *Colloid Polym Sci* 272(9):1027–1042
130. Isayev AI, Chan TW, Shimojo K, Gmerek M (1995) Injection molding of semicrystalline polymers. I. Material characterization. *J Appl Polym Sci* 55(5):807–819
131. Liedauer S, Eder G, Janeschitz-Kriegl H (1995) On the limitations of shear induced crystallization in polypropylene melts. *Int Polym Process* 10(3):243–250
132. Somani RH, Hsiao BS, Nogales A, Srinivas S, Tsou AH, Sics I, Baltá-Calleja FJ, Ezquerro TA (2000) Structure development during shear flow-induced crystallization of i-PP: in-situ small-angle X-ray scattering study. *Macromolecules* 33(25):9385–9394
133. Somani RH, Hsiao BS, Nogales A, Fruitwala H, Srinivas S, Tsou AH (2001) Structure development during shear flow induced crystallization of i-PP: in situ wide-angle X-ray diffraction study. *Macromolecules* 34(17):5902–5909
134. Nogales A, Hsiao BS, Somani RH, Srinivas S, Tsou AH, Baltá-Calleja FJ, Ezquerro TA (2001) Shear-induced crystallization of isotactic polypropylene with different molecular weight distributions: in situ small- and wide-angle X-ray scattering studies. *Polymer* 42(12):5247–5256
135. Janeschitz-Kriegl H, Ratajski E, Stadlbauer M (2003) Flow as an effective promotor of nucleation in polymer melts: a quantitative evaluation. *Rheol Acta* 42(4):355–364
136. Azurri F, Alfonso GC (2005) Lifetime of shear-induced crystal nucleation precursors. *Macromolecules* 38(5):1723–1728
137. Wunderlich B (1976) Crystal nucleation, growth, annealing, vol 2, *Macromolecular physics*. Academic, New York
138. Alfonso GC, Ziabicki A (1995) Memory effects in isothermal crystallization II. Isotactic polypropylene. *Colloid Polym Sci* 273(4):317–323
139. Zhu X, Li Y, Yan D, Zhu P, Lu Q (2001) Influenced of the order polymer melt on the crystallization behavior: I. Double melting endotherms of isotactic polypropylene. *Colloid Polym Sci* 279(3):292–296
140. Supaphol P, Lin JS (2001) Crystalline memory effect in isothermal crystallization of syndiotactic polypropylenes: effect of fusion temperature on crystallization and melting behavior. *Polymer* 42(23):9617–9626
141. Mamun A, Unemoto S, Okui N, Ishihara N (2007) Self-seeding effect on primary nucleation of isotactic polystyrene. *Macromolecules* 40(17):6296–6303
142. Martins JA, Zhang W, Brito AM (2010) Origin of the melt memory effect in polymer crystallization. *Polymer* 51(18):4185–4194

143. Kawabata J, Matsuba G, Nishida K, Inoe R, Kanaya T (2011) Melt memory effects on recrystallization of polyamide 6 revealed by depolarized light scattering and small-angle X-ray scattering. *J Appl Polym Sci* 122(3):1913–1920
144. Zhang YS, Zhong LW, Yang S, Liang DH, Chen EQ (2012) Memory effect on solution crystallization of high molecular weight poly(ethylene oxide). *Polymer* 53(16):3621–3628
145. Cheng SZD (2008) Phase transitions in polymers: the role of metastable states, 1st edn. Elsevier, Amsterdam
146. Subramanian G, Shanbhag S (2008) Self-diffusion in binary blends of cyclic and linear polymers. *Macromolecules* 41(19):7239–7242
147. Vasquez R, Shanbhag S (2011) Percolation of trace amounts of linear polymers in melt of cyclic polymers. *Macromol Theory Simul* 20(3):205–211
148. Chapman CD, Shanbhag S, Smith DE, Robertson-Anderson RM (2012) Complex effects of molecular topology on diffusion in entangled biopolymer blends. *Soft Matter* 8:9177–9182
149. Halverson JD, Grest GS, Grosberg AY, Kremer K (2012) Rheology of ring polymer melts: from linear contaminants to ring-linear blends. *Phys Rev Lett* 108:038301
150. Henke SF, Shanbhag S (2014) Self-diffusion in asymmetric ring-linear blends. *React Funct Polym* 80:57–60
151. Tsalikis G, Koukoulas T, Mavrantzas VG (2014) Dynamic, conformational and topological properties of ring-linear poly(ethylene oxide) blends from molecular dynamics simulations. *React Funct Polym* 80:61–70
152. Gooßen S, Brás AR, Pyckhout-Hintzen W, Wischniewski A, Richter D, Rubinstein M, Roovers J, Lutz PJ, Jeong Y, Chang T, Vlassopoulos D (2015) Influence of the solvent quality on ring polymer dimensions. *Macromolecules* 48(5):1598–1605
153. Müller AJ, Hernández ZH, Arnal ML, Sánchez JJ (1997) Successive self-nucleation/annealing (SSA): a novel technique to study molecular segregation during crystallization. *Polym Bull* 39(4):465–472

# Crystallization of Precision Ethylene Copolymers

Laura Santonja-Blasco, Xiaoshi Zhang, and Rufina G. Alamo

**Abstract** The crystallization and melting of polyethylene-like copolymer systems with co-units placed at the same equal distance along the backbone are reviewed on the basis of available thermal and structural data for a large variety of pendant and backbone-inserted groups. Data for a series of precision halogen-containing polyethylenes are used to describe the effect of size of the pendant group and the distance between groups along the backbone on crystallization and melting behaviors. The effect of crystallization kinetics on polymorphism observed for systems with co-crystallizable co-units is emphasized with data on polyethylenes containing Cl and Br. The major characterization techniques for identifying different modes of packing are also described. The melting behavior of alkyl-branched precision polyethylenes is analyzed in reference to branch partitioning between crystalline and non-crystalline regions, and also in reference to the behavior of analog polyethylenes containing halogens. Furthermore, the effect of interacting functional groups and tacticity on self-assembly and melting is analyzed using available literature data.

**Keywords** Ethylene copolymers • Polyethylenes • Precision branching • Precision copolymers • Precision substitution

## Contents

1	Introduction .....	134
1.1	Crystallization of Ethylene Copolymers .....	135
2	Crystallization of Polyethylenes with Precision Halogen Substitution .....	139
2.1	Rapid Crystallization .....	140
2.2	Isothermal Crystallization: Polymorphism .....	150

---

L. Santonja-Blasco, X. Zhang, and R.G. Alamo (✉)  
Department of Chemical and Biomedical Engineering, FAMU-FSU College of Engineering,  
2525 Pottsdamer Street, Tallahassee, FL 32310-6046, USA  
e-mail: [alamo@eng.fsu.edu](mailto:alamo@eng.fsu.edu)

3	Crystallization of Precision Alkyl-Branched Polyethylenes .....	157
4	Crystallization of Precision Polyethylenes with Interacting Functional Groups .....	161
4.1	Strength of Pendant Group Interactions .....	162
4.2	Functional Groups Within or Branching from the Methylene Backbone .....	163
4.3	Effect of Tacticity .....	165
5	Concluding Remarks .....	166
	Appendix .....	168
	References .....	176

## 1 Introduction

Studies of novel, model polyolefins and polyolefin-like materials have industrial relevance as well as strong academic interest. Polyolefins, mainly the commodities polyethylenes and polypropylenes, now occupy a leading position among all existing types of materials. High production and versatility of properties account for the relevant position of these polymers over any other polyolefin material. For example, the annual worldwide production of the major polyolefins has increased steadily from 180 BP (billion pounds) in 2000 to over 290 BP in 2013, accounting for >65% of all thermoplastics [1]. The production of polyolefins is expected to increase at an even faster rate in the near future as a result of the exponential expansion of shale gas extraction in the USA and the derived investment in ethylene generation. Consequently, polyolefin research will continue at all levels, as small improvements in the process or in the product can lead to a significant impact on the world economy.

At a fundamental level of research, polyethylene contains the simplest repeating unit,  $(\text{CH}_2)_n$ , yet it can be arranged in a rich variety of architectures. It is now relatively easy and inexpensive to add functional groups, defects, or branches (short or long) to the backbone to enable fine control of molecular structure by simple modification of the process or by copolymerization. Structural changes in the chain modify the level of crystallinity, crystallization rate, and the final semicrystalline morphology, and thus alter the physical and mechanical properties of the material. Polyethylenes have been extensively studied, yet they remain the polymers of choice for model systems to study the fundamental laws that govern the structure–property relations of semicrystalline polymers. The synthesis of models mimicking polyethylenes is still a topic of major interest.

Although incorporation of large comonomer content in polyethylenes while maintaining a uniform comonomer distribution and control of molecular weight is now feasible with metallocene catalysts, a drawback is their inability to incorporate polar groups [2–4]. These constraints make other routes for synthesis of ethylene copolymers with ionic polar groups or halogens attractive, especially as a means to generate model materials for studying the effects of volume of substituent and secondary bonding on the packing behavior of polyethylenes with a controlled content and type of defect. Strategies could then be set to design the next generation of polyolefin materials. Special families of branched and substituted

polyethylene-like systems have been synthesized via acyclic diene metathesis polymerization (ADMET), mainly by Wagener and coworkers [5]. These polyolefins are characterized by the placement of an alkyl branch, a halogen, or a large variety of functional groups at equal distances along the  $\text{CH}_2$  backbone. Structurally, they are a new class of polyolefins with a repeating unit,  $-(\text{CH}_2)_x-\text{CHR}]_n$ , where  $x$  changes from 4 to 74, R is the branch or functional group, and the molar mass is 30–150 K. An alternative route toward precision polyethylene-like structures is via ring-opening metathesis polymerization (ROMP) [6]. Through the latter, the regioregularity of the addition must be maintained in order to generate structures with equidistant control of branch placement [7–9]. Long-spaced polyesters, polyamides, polycarbonates, or polyacetals have also been generated via ROMP, thus providing polyethylene-like models with functional groups directly linked to the backbone [10–13]. The skills of organic chemists in producing these modified model polyethylenes are truly remarkable.

The synthetic route for generation of the acyclic diene, or the cycle if the polymerization is carried out by ROMP, is of paramount importance for further generation of the polyethylene backbone with functional or pendant groups placed at an exact equidistant length or very close to the equidistant length, as in most ROMP avenues [14]. However, synthesis is not the focus of this review; hence, although the source for the synthetic path is cited, we focus our attention on the effect on the crystallization and melting behaviors of the punctuation placed randomly or at a precise distance along the polyethylene backbone. We have chosen halogens as models to establish the effect of size and content on crystallization and to characterize polymorphism in many of these systems. Subsequently, we summarize relevant crystalline behaviors of precision systems with alkyl branches and with other functional groups.

## 1.1 Crystallization of Ethylene Copolymers

The crystallization of statistical ethylene-based copolymers is fairly well understood. The thermodynamic and structural properties of ethylene 1-alkene copolymers have been amply studied and summarized in different reviews [15–19] and the most recent works on statistical ethylene copolymers are covered in a review by Hu et al. in this volume [20]. The decrease in melting temperature with increasing content of 1-alkene is understood on the basis of phase equilibria for a two-component system made of A and B units, and the experimental data are analyzed comparatively with predictions from equilibrium theories. When the crystalline phase remains pure, for example only component A or the backbone  $\text{CH}_2$  units of ethylene/1-alkene random copolymers crystallize, the experimental melting data are analyzed on the basis of Flory's equilibrium theory [21]. Flory's theory was developed for the case where the crystalline phase remains pure. Under this premise, the equilibrium melting temperature of the copolymer ( $T_m^{\circ} \text{copo}$ ), relative to that of the homopolymer ( $T_m^{\circ}$ ), is expressed as:

$$\frac{1}{T_m^o} - \frac{1}{T_{m\text{copo}}^o} = \frac{R}{\Delta H_u} \ln p \quad (1)$$

In this equation,  $\Delta H_u$  is the enthalpy of fusion per mole of crystalline repeating unit, and  $p$  is the crystallizable sequence propagation probability. In statistical copolymers,  $p < 1$  and the equation predicts a large depression of  $T_{m\text{copo}}^o$ . For random copolymers,  $p = X_A$  (the mole fraction of crystallizable units) and  $T_{m\text{copo}}^o$  decreases proportionally to the content of non-crystallizable co-units. For an ordered or block copolymer,  $p$  approaches one, thus predicting a negligible melting point depression in the copolymer.

The concepts embodied by Eq. (1) are amply substantiated by experiments [22–30]. Random ethylene copolymers with 1-butene or longer co-units are known to be rejected from the crystallites. As such, their melting temperature–composition behavior is in full agreement with theoretical predictions [15, 22]. Flory’s theory also puts kinetic limitations on the size and content of crystallites that are formed from a copolymer chain as a function of crystallization temperature [21, 24]. Only crystallizable sequences longer than the critical length for a stable crystallite can participate in the formation of crystallites. This kinetic restraint invariably leads to a sequence length selection process in copolymer crystallization that ultimately determines the morphology and structure of the crystalline (CR) and non-crystalline (NCR) regions of the copolymers. Consequently, on cooling from the melt, the copolymer crystalline morphology is complex because progressively thinner crystallites are expected to develop on cooling. As the branches, or co-units, remain in the intercrystalline regions, the concentration of co-units that surround the copolymer crystallites becomes higher than the chain comonomer concentration during the process of crystallization. On subsequent melting, copolymer crystallites melt over a broad range of temperatures, because thinner crystallites melt first, followed by the thicker crystallites, and because crystals that melt first coexist with a melt that contains the highest content of co-units, or lowest value of  $X_A$ . Even if random copolymers with the co-unit excluded from the crystal develop a relatively narrow distribution of crystal thicknesses, their melting behavior is expected to be broad because of considerations of Eq. (1) and the compositional change in the intercrystalline regions during melting.

When the volume of the branch or pendant group is sufficiently small, some of the co-units can participate in the crystallites. This situation has been found for the methyl branch of random ethylene propylene copolymers [31–37], the halogen of ethylene vinyl halides [38–42], the OH of ethylene vinyl alcohol, and other small pendant or backbone-incorporated groups [43–45]. The thermodynamic predictions for these cases were developed by Sanchez and Eby, considering that the crystallizable co-unit adds an excess free energy  $\varepsilon$  to the crystal free energy of melting [46, 47]. The depression of the copolymer melting point (on equilibrium basis) from the value of the homopolymer is given by:

$$\frac{1}{T_m^o} - \frac{1}{T_{m\text{copo}}^o} = -\frac{R}{\Delta H_u} \left[ \varepsilon \frac{X_C}{RT_{m\text{copo}}^o} + (1 - X_C) \ln \left[ \frac{(1 - X_C)}{(1 - X_B)} \right] + X_C \ln \left( \frac{X_C}{X_B} \right) \right] \quad (2)$$

Here,  $X_B$  is the concentration of co-units B in the chain, and  $X_C$  the concentration of co-units B in the crystallites.

Although the derivations of these equations are rigorous and conceptually viable, their application to distinguish the partitioning of the co-unit between CR and NCR regions from experimental melting temperatures is limited for two major reasons. First, it is impossible to observe the  $T_{m\text{copo}}^o$  predicted by the theoretical equations (1) and (2) under equilibrium conditions. Only crystallites formed with the longest crystalline sequences melt at  $T_{m\text{copo}}^o$ . The content of these sequences is low, and the number of crystallites formed with these sequences even lower because transport limitations reduce the effective number that can diffuse to the crystal front. The small number of crystals from the longest sequences, even if enabled, are not accessible by the usual experimental techniques. As a consequence, the observed copolymer melting temperatures are much lower than theoretically predicted. A second caveat is that both equations predict a decrease in  $T_{m\text{copo}}^o$  with increasing comonomer content, or decreasing  $X_A$ . Hence, from experimental melting point data for random copolymers, which are usually observed to decrease with increasing the co-unit content, one cannot conclude that the co-unit is a defect in the crystallites. Other measurements are needed to discern the partitioning of the copolymer co-units. For example, expansion of the unit cell is often an indication of side branch inclusion in the crystallites, whereas solid state NMR can identify and quantify residues inside the crystallites [48–52].

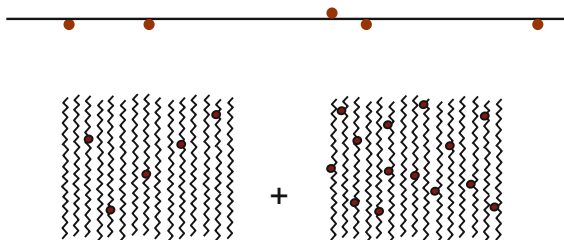
Even for random copolymers with relatively small co-units, such as those that can be partially accommodated in the crystallites, the crystallization path is driven mainly by selection of the most crystallizable sequence lengths. Long ethylene sequences fold back and forth in the early stages, trapping some of the small-sized co-units, and shorter sequences crystallize in subsequent stages with an increased probability of pulling more co-units into the crystals, as schematically shown in Fig. 1a. The final crystalline morphology is a complex mixture of crystallites, with a partitioning of co-units that is difficult to control and a disordered distribution of co-units inside and outside the crystallites.

As a result of the random distribution and the defect-like nature of the co-unit in classical ethylene copolymers, the role of the co-unit has been directed either to decrease the degree of crystallinity in a controlled manner [22–30] or to modify the properties of the interlamellar regions [53–57]. The decrease in the level of crystallinity of random ethylene 1-alkene copolymers with increasing content of 1-alkene is a feature amply exploited by the manufacturers of linear low-density polyethylenes, whereas examples of properties affected by co-unit interactions are found in the families of ionomers and ethylene vinyl alcohol copolymers [43, 54–57].



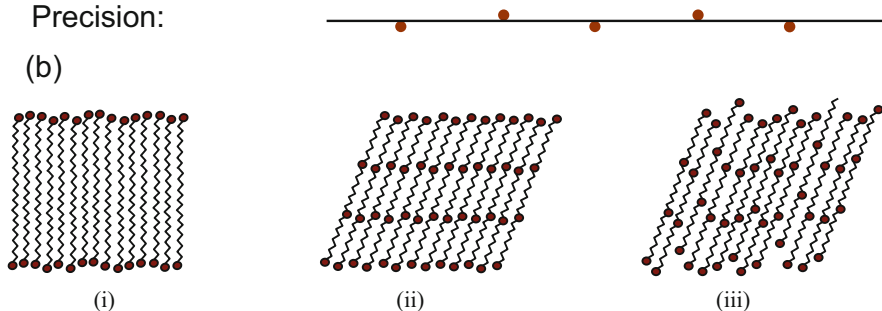
## Random ethylene-based copolymers

(a)



Precision:

(b)



**Fig. 1** Schematic models of crystal chain packing for polyethylenes with pendant groups placed either randomly (a) or at an equidistant spacing along the backbone (b). Three possibilities (*i–iii*) for self-assembly are featured for the latter type

Properties that depend on controlling ordered distributions of co-units in the crystal are not accessible via classical polyolefins with a random distribution of co-units. The present commercial strategy for modifying or enhancing the properties of ethylene-based or propylene-based copolymers is to change the comonomer content and to change the distribution of the comonomer content across the molecular weight distribution while maintaining the statistical intramolecular distribution of the co-unit [2, 18, 58, 59]. This “tuning” of the bivariate distribution can improve material performance, but the type of crystalline structure remains basically unchanged; thus, the basic spectrum of properties is still governed by the level of crystallinity and the molecular mass for most statistical copolymers.

Studies of polyethylenes with co-units placed at the same distance along the backbone serve to address whether copolymers can adopt crystalline structures other than that adapted from the crystallization path of a random copolymer. Depending on the partitioning of the co-unit (excluded or included in the crystalline regions) and the distribution of the co-units in the crystallites, three viable crystalline structures are possible, as shown in Fig. 1b. If the co-unit is too large to be accommodated in the crystal, the only possible packing is obtained by staggering ethylene sequences, leaving the defect at the interface (Fig. 1b, packing scheme i). Crystallites of this nature are thin, because their thickness is limited by the length between co-units, and possibly have large and complex crystal–amorphous

interfaces. Examples of this type of crystal have been described for polyesters [60, 61] and for precision polyethylenes with *n*-hexyl and *n*-butyl pendant groups [62, 63].

When the co-unit finds no discrimination against entering the crystalline regions and folding is preferential (i.e., at the same location along the backbone), the co-units are ordered in layers inside the crystalline lamellae, resulting in unique nanostructures at the lamellar and sub-lamellar level (Fig. 1b, packing scheme ii) that are not feasible in classical branched polyethylenes. The third possible structure for copolymers with equidistant co-units along the backbone is obtained when folding is random along the backbone and the distribution of the co-unit inside the crystal is of a more random nature (Fig. 1b, packing scheme iii). Examples of structures (ii) and (iii) enabled by precision polyethylenes with equidistant pendant units have been found relatively recently [64–67].

Structures such as type (ii) are highly desirable, especially for long-chain macromolecules, because they open the window for design of unique nanostructures with multiple length scales at the lamellar and sub-lamellar levels. Highly symmetric layered systems enable the design of polyolefin-like materials with applications driven by a tunable sub-lamellar crystalline structure.

We summarize here the major works on precision polyolefin-like systems that present clear partitioning of the co-unit inside and outside the crystalline regions and, hence, allow predictions for novel polyolefin-like systems with nanoscale assembly at the lamellar and sub-lamellar level.

## 2 Crystallization of Polyethylenes with Precision Halogen Substitution

Series of polyethylene-like systems with F, Cl, or Br atoms placed on each and every 21st, 19th, 15th, or 9th carbon have been synthesized using ADMET, starting from a common precursor that was further reduced to the alcohol prior to halogenation [68–71]. Exhaustive hydrogenation leads to repeating unit  $-[(\text{CH}_2)_x\text{-CHY}]_n-$ , where Y is the halogen type and  $x$  is the number of groups in the continuous methylene segment between halogens ( $x$  varies between 8 and 20). We term these polymers PE( $x+1$ )Y. For example, PE21F is the polyethylene with a fluorine atom on every 21st backbone carbon. Because the synthetic path does not allow control of tacticity, these polymers are presumed to be atactic.

In spite of their atactic nature, these precision systems are crystalline, and because their molar masses are usually  $>20,000$  g/mol, they have been studied as models to probe the effect of the size and content of halogens on the crystallization of polyethylenes. Capitalizing on the systematic increase in van der Waals radius of the substituent for the series, quantitative data are now available to evaluate the degree to which the orthorhombic polyethylene lattice can tolerate atomic hydrogen substitution. The crystalline properties and thermodynamic data of these systems

under rapid crystallization have been studied in some detail and are reviewed in this section. The formation of different polymorphs, observed under rapid or slow crystallizations, are starting to be reported and are in line with the hypothetical packing modes feasible for systems with equidistant placement of co-units, as mentioned earlier. We review work on each of the crystallization modes in separate sections.

## 2.1 Rapid Crystallization

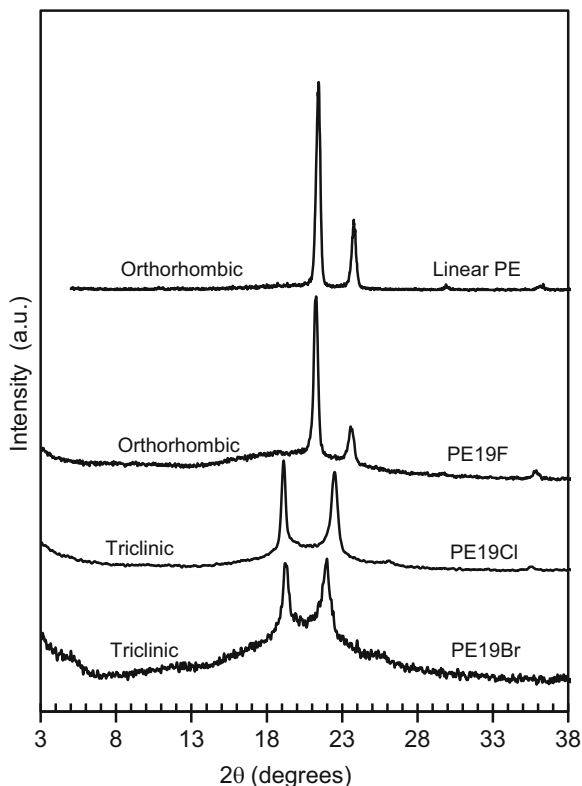
Properties such as melting temperature and heat of fusion are often obtained via differential scanning calorimetry (DSC) and for samples that are crystallized from the melt at 10°C/min. Under these conditions, many precision samples crystallize rapidly in a narrow range of temperatures. Wide-angle X-ray diffraction (WAXD) patterns are also often obtained at room temperature for samples cooled from the melt to infer their crystalline structure.

### 2.1.1 Effect of Halogen Size

The effect of the halogen's van der Waals radius on crystalline packing and melting behavior is extracted from data on precision systems with a F, Cl, or Br atom placed on every 19th backbone carbon ( $x = 18$ ) [68]. To visualize the effect of halogen size at the level of the unit cell, WAXD patterns are shown in Fig. 2, together with the diffractogram of a linear polyethylene with similar molar mass ( $M_n \sim 20,000$  g/mol). In contrast to the broad WAXD patterns of ethylene vinyl halides containing a random distribution of the halogen [39], the X-ray patterns of all precision halogen-substituted samples are sharp, similar in nature to the pattern of the unsubstituted linear polymer. Narrow reflections are a strong indication of a homopolymer-like crystallization for these systems rather than a copolymer-like crystallization. In the latter, the longest ethylene sequences are first selected for crystallization, followed by shorter or less tactic sequences, thus resulting in a mixture of crystallites with different thicknesses. This complexity broadens the X-ray diffraction patterns of randomly distributed copolymers [72].

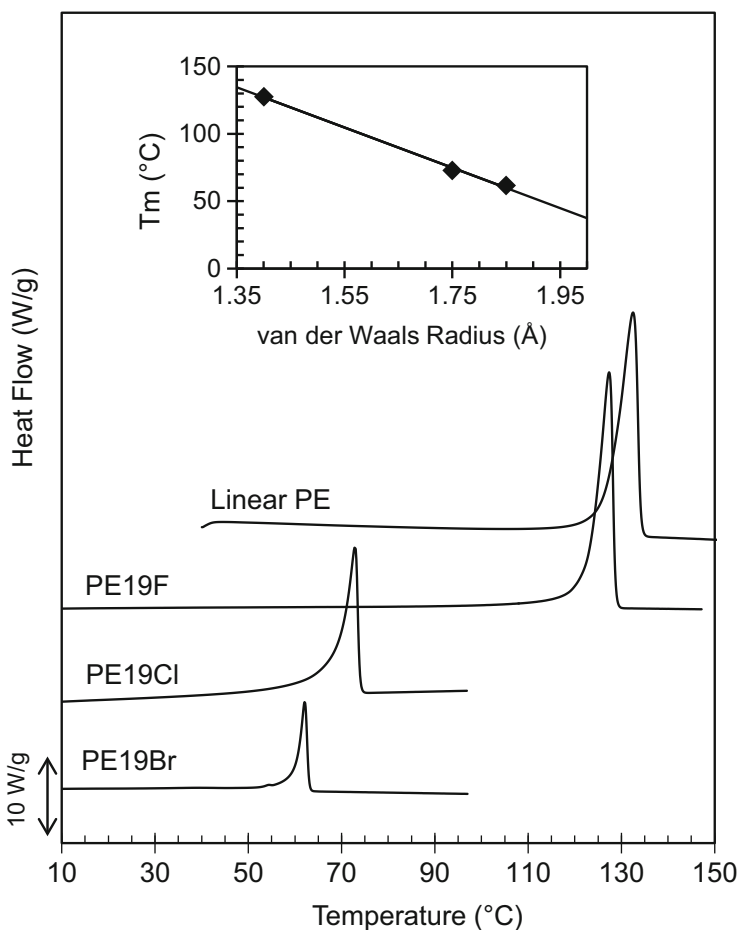
In systems with precision placement of the halogen, sharp WAXD reflections are indicative of relatively thick crystallites that must include the halogen. In fact, atomic force microscopy (AFM) images have demonstrated a lamellar habit with crystal thicknesses  $>100$  Å. As the *all-trans* length between halogens is just 24 Å for all  $-(\text{CH}_2)_{18}\text{-CHY}_n-$  systems, it is evident that the crystal stem length must be a segment of the chain with four or five continuous repeating units. Therefore, these precision systems fold back and forth, accommodating the halogens in the lamellar crystallites.

**Fig. 2** WAXD patterns of rapidly crystallized precision polyethylenes with a halogen placed on each and every 19th backbone carbon. Reprinted with permission from Boz et al. [68]. Copyright 2006 American Chemical Society



The fact that precision polyethylenes develop levels of crystallinity of  $\sim 70\%$ , which are much higher than those for random analogs ( $<30\%$ ), also suggests a crystalline state built on the basis of substitutional solid solutions. In other words, in packing backbone sequences, the substitution of hydrogen for one F, Cl, or Br atom at an equidistant position along the backbone creates lattice distortions at levels proportional to the solute's van der Waals radius. This is readily apparent in the patterns shown in Fig. 2. The small size of the F atom makes insignificant distortions to the crystal lattice, and hence the orthorhombic symmetry of the unbranched system is preserved, as seen by the presence of the (110) and (200) reflections at  $21.5^\circ$  and  $23.5^\circ$ . However, the larger sizes of Cl and Br atoms creates larger lattice strains that promote the formation of a different crystallographic phase, a triclinic cell with reflections at  $2\theta$  of  $\sim 19^\circ$  and  $22^\circ$ , attributed to planes (100) and (010), respectively. Some distortion of the lattice by accommodation of the halogen atom is evident from the shift at lower angles of both reflections in the orthorhombic pattern of PE19F with respect to the X-ray pattern of the unsubstituted polymer. Shifts to lower angles are more pronounced for the reflection at  $\sim 22^\circ$  of the triclinic pattern of PE19Br compared with PE19Cl. Hence, the angular shifts follow expectations for shifts caused by the large number of incorporated side groups in the crystal, in spite of the atactic nature of the halogen substitution for these samples.

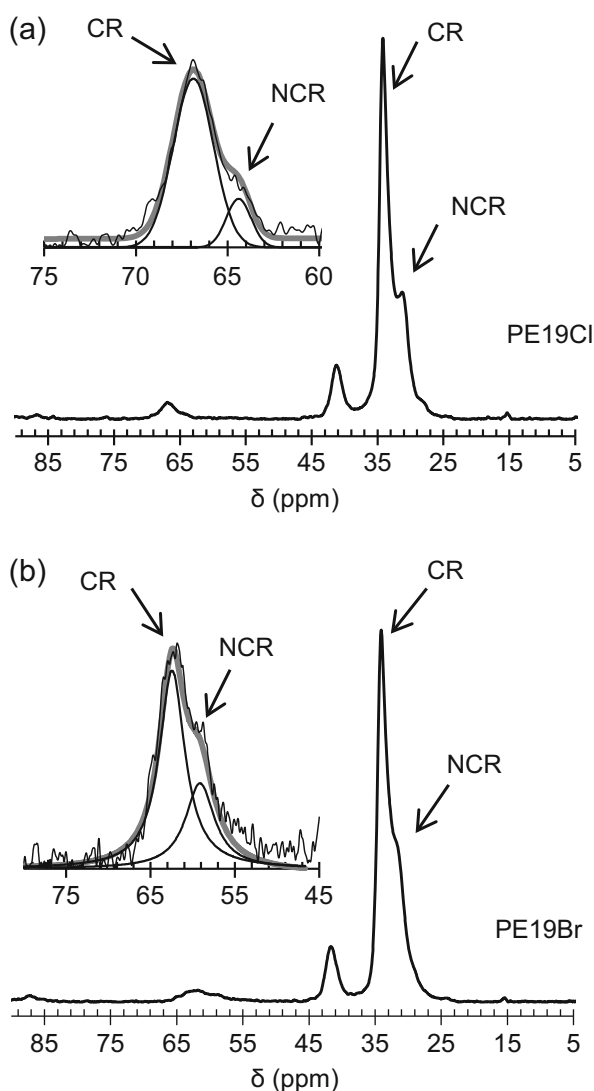
The narrow melting thermograms also reflect a homopolymer-like behavior (as shown in Fig. 3), but the melting temperatures shift at dramatically lower values with increasing van der Waals radius of the halogen [68]. In reference to the 133°C melting of the unsubstituted linear PE, the placement of a fluorine atom on every 19th backbone carbon lowers the melting point to 127.5°C, chlorine brings this value to 72.7°C, and bromine to 61.5°C. Paralleling the decrease in melting temperature, the degree of crystallinity decreases from ~80% to ~40%, indicating that the halogens in the crystallites act as defects that distort the packing structure at levels proportional to their size. This feature is also observed by the linearity of the plot of  $T_m$  versus van der Waals radius, projecting a value of 30°C for the melting temperature of the iodine analog, which is not yet available.



**Fig. 3** Effect of halogen size on melting of rapidly crystallized precision polyethylenes. Melting of a linear unsubstituted polyethylene is shown as reference

Direct evidence of the homopolymer-like crystallization, or lack or preferential partitioning of the halogen between CR and NCR regions, is found by solid-state NMR via direct polarization under MAS [68, 73]. For quantitative data, direct polarization under magic angle spinning (DPMAS) is preferred over cross-polarization (cpMAS) as the latter emphasizes the CR where cross-polarization is most efficient. In  $^{13}\text{C}$  NMR under high power C–H decoupling, the methine resonance is ideal for monitoring the partitioning of Cl and Br atoms between the CR and NCR regions. The CH resonance is also unique and can be used to quantify the content of halogen, or other pendant group, in each region, especially when both phases contain a sufficiently large number of CHY groups and CR and NCR phases display a resolved difference in their chemical shift (as seen in Fig. 4) [68]. CR and

**Fig. 4**  $^{13}\text{C}$  NMR spectra of (a) PE19Cl and (b) PE19Br recorded by direct polarization under magic angle spinning (DP MAS) and high power  $^1\text{H}$  decoupling. Insets show more expanded CH 45–80 ppm regions with fits to crystalline (CR) and non-crystalline (NCR) components. Reprinted with permission from Boz et al. [68]. Copyright 2006 American Chemical Society

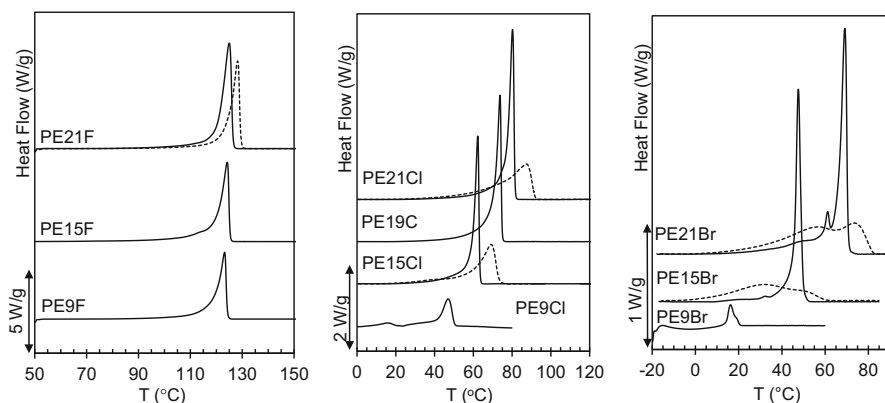


NCR resonances are resolved for  $\text{CH}_2$  at 34.1 and 31.5 ppm, respectively, as well as for CH carbons at 67 and 64 ppm for PE19Cl, respectively. CHBr resonances are centered at 62 ppm (CR) and 59 ppm (NCR). The ratio of intensities between CR and NCR CHY resonances is equivalent to the ratio of CR and NCR  $\text{CH}_2$  resonances in both spectra, thus indicating that  $\text{CH}_2$  and CHY are equally distributed between both phases. In other words, there is no preference for the halogen to be in one particular region, in agreement with the homopolymer-like crystallization behavior extracted from the sharp WAXD and DSC thermograms. In contrast, classical random ethylene vinyl chlorides showed no difference in resonance between both phases in the methine region [38, 72].

## 2.1.2 Effect of Methylene Sequence Length Between Halogens

### Melting Behavior

The effect of F, Cl, or Br substitution placed at equidistant lengths of 9, 15, 19, or 21 backbone carbons is first analyzed by the melting behavior of samples crystallized under relatively rapid conditions. The endotherms are shown in Fig. 5, the dotted lines indicating the behavior of random analogs. All melting peaks of precision samples are sharp, which is characteristic of the fusion of homopolymers. In contrast, the melting of random systems is broad, spreading to final melting temperatures that are higher than those of the precision samples. This is a feature invariably encountered when the melting of semicrystalline precision and random analogs are compared, regardless of the branch moiety, pointing to the effect of the sequence length in the crystallization of random copolymers [72–74]. Long ethylene sequences in random copolymers generate thicker crystallites with little halogen incorporation that melt at higher values. Conversely, shorter sequences

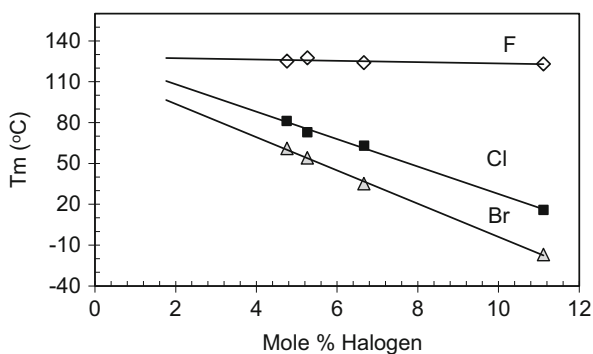


**Fig. 5** DSC endotherms of precision halogen-containing polyethylenes (*solid lines*) and random analogs (*dotted lines*) crystallized at  $10^\circ\text{C}/\text{min}$  from the melt. PE9Cl and PE9Br were quickly quenched from the melt to  $-20^\circ\text{C}$  prior melting. The heating rate was  $10^\circ\text{C}/\text{min}$

generate crystallites with more defects, or generate thinner crystallites that melt at lower temperatures, thus resulting in broad endotherms.

The effect of the halogen, as a defect in the crystal, on melting is substantiated by the shift to lower values of the thermograms with increasing halogen content (as seen in Fig. 5). The peak melting temperatures ( $T_m$ ) are little affected by substitution of a hydrogen of the polyethylene backbone for a fluorine atom on every 9th, 15th, or 21st backbone carbon. This insignificant change in  $T_m$  confirms that the small size of F results in only a small disturbance to the crystal lattice. Nonetheless, the role of F as a defect is made implicit by a decrease in heat of fusion with increasing F content in the series [71]. In contrast, increasing Cl or Br content in precision systems leads to a large depression of the melting point; the larger the size and the higher the content of halogen in the series, the lower the melting point. These trends are emphasized in Fig. 6, where the melting temperature is plotted against halogen content for crystallites of the same structure. As discussed in the following section, these polymers can form two polymorphic structures (forms I and II) depending on crystallization kinetics. When cooled at 10°C/min, most develop form I; however, form I crystallites of PE9Cl and all Br-substituted precision systems undergo fast recrystallization to form II on melting at 10°C/min. The possibility of polymorphism and melt-recrystallization need to be taken into account when comparing melting trends within precision polyethylene series. Hence, to compare the thermal behaviors for the same type of structure, the low melting peak is plotted for PE9Cl and for the bromine series in Fig. 6, instead of the more prominent DSC peaks of Fig. 5. The melting points scale proportionally to size and defect content. When the halogens are largely spaced, for example for the PE21Y series, the content of halogen in the crystal is relatively low; consequently, the depression of melting temperature by the increase in halogen size from F to Br is ~60°C. In shorter spaced precision samples, the crystallites contain larger contents of halogens that, as defects, disturb the crystalline packing to a larger extent; consequently, the melting temperature and heat of fusion are more dramatically depressed by the halogen size. As seen in Fig. 6,  $T_m$  decreases by ~150°C in the PE9Y series.

**Fig. 6** Variation of melting peak temperature with content of halogen (moles of halogen per 100 backbone carbons) for rapidly crystallized precision halogen-substituted polyethylenes. The effect of halogen size on melting temperature is evident in the series

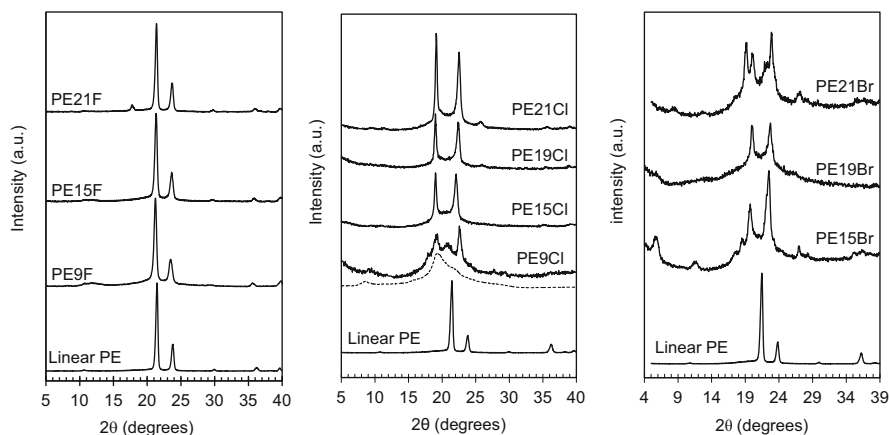




The data sets of Fig. 6 are clear examples of a melting behavior that decreases linearly with co-unit content, but cannot and should not be related to the concepts underlying the basis of Eq. (1), as often encountered in the literature [75]. Even Eq. (2), derived on the basis of co-unit inclusion, might not be a good approach for analysis of the melting behavior of precision polyethylenes. The reason is that the derivation of Eq. (2) assumes a statistical distribution of defects in the crystallites, which is not the case for these precision systems.

## Crystal Structure

The effect of halogen size and content on crystalline packing at the level of the unit cell can be evaluated by the set of diffractograms shown in Fig. 7 for each halogenated series. Clearly, the crystalline state of precision ethylene vinyl fluoride-like copolymers is isomorphous to the crystalline state of linear polyethylene. The orthorhombic symmetry is maintained even at high contents of fluorine, with negligible shifts in angular reflections. In contrast, the unit cell of precision Cl- and Br-containing polyethylenes differs from the orthorhombic packing. Rapidly crystallized precision Cl- and Br-substituted polyethylenes pack in triclinic crystallographic cells characterized by two main reflections at  $\sim 19^\circ$  and  $\sim 22^\circ$ . The change from orthorhombic to a less symmetric triclinic unit cell indicates that a reduced order in the packing is needed to facilitate the spatial requirements for accommodation of Cl and Br atoms between adjacent molecules in the crystallites. The increasing content of Cl and Br inside the crystals expands the lattice to levels proportional to the content of halogen in the chain, as seen for each series by the shift



**Fig. 7** WAXD diffractograms of precision halogen-containing polyethylenes, with halogens placed on every 21st, 19th, 15th, or 9th backbone carbon. Samples were molten and taken to crystallize at room temperature. The *dotted* diffractogram for PE9Cl was collected for a sample quenched quickly to  $10^\circ\text{C}$

to progressively lower angles of the reflection at a  $2\theta$  of  $\sim 22.5^\circ$ , which is characteristic of the (010) plane of the triclinic lattice.

A feature of great interest is the dramatic effect of crystallization kinetics on the packing of Cl- and Br-substituted systems, and on other precision systems with pendant groups able to be accommodated in the crystallites. This feature is observed in the diffractograms of PE9Cl in Fig. 7. PE9Cl crystallizes slowly at room temperature. For this sample to crystallize faster, it needs to be quenched quickly to temperatures below  $23^\circ\text{C}$ . Hence, the pattern of PE9Cl very quickly quenched to  $10^\circ\text{C}$  (given by the dotted line in Fig. 7) displays the two reflections typical of the triclinic lattice, as observed in other precision chlorine members that crystallize quickly above room temperature. Conversely, the pattern of the specimen crystallized at room temperature (continuous line in Fig. 7) displays multiple WAXD reflections, indicating a mixture of polymorphs [73]. This was the first observation revealing that polyethylenes with precise Cl or Br substitution can pack in at least two crystalline polymorphs that can be controlled by crystallization kinetics [64, 65]. Mixed polymorphic behavior is also observed in the WAXD patterns of PE21Br and PE15Br (see Fig. 7). This behavior is discussed further in the next section.

The arrangement of halogens inside the crystallites, whether random or layered, is a feature of extraordinary interest that can be extracted from reflections at low angles of the WAXD patterns, which are characteristic of layered crystallites. These reflections are especially intense for the Br series. In the WAXD patterns shown in Fig. 7, collected under reflection, the reflections at intermediate angles ( $2\theta$  of  $5^\circ$ – $7^\circ$ ) correspond closely to the distance between halogens and reflect a crystalline halogen layered structure in polyethylenes with precise Cl and Br substitution. Intermediate angles are absent in the systems with F substitution, as F is probably randomly dispersed in the crystals and, hence, not layered.

Layered lamellae crystallites are often found when interchain interaction between functional co-units drive the layered packing, as in long alkyl-based aliphatic polyesters [60, 76]. For polyethylenes with halogen substitution, it has been posed that the observed layered packing is likely to be favored by preferential folding at the Cl or Br position [73], a feature also suggested for the crystals of model chlorinated *n*-alkanes [77]. It remains to be elucidated whether the drive to form a layered structure is preferential folding, as pointed out in the Introduction, or halogen–halogen interactions, in spite of the atactic nature of the halogen substitution.

## Degree of Crystallinity and Thermodynamic Properties

The degree of crystallinity can be extracted from the X-ray diffractograms, from the heat of fusion if data for the heat of fusion of the pure crystal is available, from quantitative DPMAS spectra, or from Raman spectroscopic data for orthorhombic crystallites [68, 73]. Degrees of crystallinity obtained from WAXD patterns and the thermodynamic properties for rapidly crystallized precision Cl-containing series

**Table 1** Thermodynamic properties of precision Cl-substituted polyethylenes

Sample	$X_c$ (WAXD) <sup>a</sup>	$\Delta H_m$ (J/g) <sup>a</sup>	$\Delta H^\circ$ (J/mol) <sup>b</sup>	$\Delta H^\circ/\text{bond}$ (J/mol)	$T_m^\circ$ (°C)	$\Delta S^\circ$ (J/mol K) <sup>b</sup>	$\Delta S^\circ/\text{bond}$ (J/mol K)
PE	0.83	238	4,014	4,014	145.5	9.6	9.6
PE21Cl	0.52	120.5	76,777	3,656	83	216	10.3
PE19Cl	0.53	107.6	61,225	3,222	75	176	9.3
PE15Cl	0.46	95.7	51,158	3,411	65	151	10.1
PE9Cl	0.34	38.6	18,397	2,044	54	56	6.2

Data taken with permission from Alamo et al. [73]. Copyright 2008 American Chemical Society

<sup>a</sup>Data for samples cooled at 1°C/min from the melt to room temperature

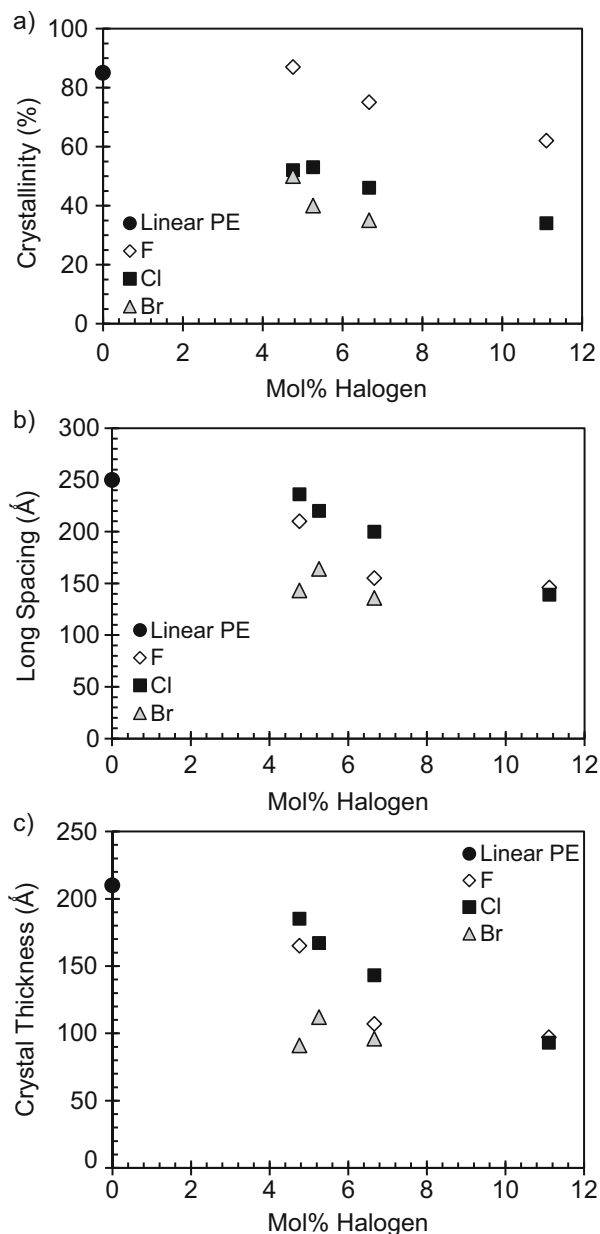
<sup>b</sup>In PE the mole is defined as a CH<sub>2</sub> unit, whereas for the precision EVC series, the mole is the [(CH<sub>2</sub>)<sub>x</sub>-CHCl] unit

(form I) are listed in Table 1 and plotted against Cl content in Fig. 8a. Equilibrium melting temperatures ( $T_m^\circ$ ) were obtained by the Hoffman–Weeks extrapolation method and the level of crystallinity was used to correct the DSC heat of fusion to estimate the value corresponding to the 100% crystalline specimen ( $\Delta H^\circ$ ). Entropy values ( $\Delta S^\circ$ ) are obtained by the ratio between  $\Delta H^\circ$  and  $T_m^\circ$ . Values of  $\Delta H^\circ$  and  $\Delta S^\circ$  are listed per mole of repeating unit and per bond. The level of crystallinity,  $T_m^\circ$ , and  $\Delta H^\circ$  per mole of repeating unit decrease substantially with increasing halogen content, as expected for crystallites that, although layered, become more defective with increasing content of halogen.

### Crystal Thickness and Supermolecular Morphology

Crystallite thickness is an important parameter for correlation with the number of layers in lamellar crystals and with other physical properties of precision systems. Data on crystallite thickness and supermolecular morphology are available for the rapidly crystallized Cl-containing series [73]. For this series, crystal thicknesses were extracted from SAXS profiles and AFM images. Long spacing and crystal thickness decrease with increasing halogen content, as shown in Fig. 8b, c. The data for F-containing polyethylenes fall between the thicknesses of Cl and Br samples, probably as a result of the low molar mass of the precision F samples analyzed ( $M_w < 10,000$ ) [71]. Focusing on the data for Cl-containing samples, a clear trend with halogen size and content is found. At a fixed halogen content, the long spacing and crystal thickness decrease substantially with increasing halogen size. For an *all-trans* conformation, the C–C bond distance is 1.27 Å; hence, crystallites with Cl substitution on every 21st carbon accommodate about eight repeating units in the crystals, whereas the analog with Br substitution accommodates only about four. Hence, although these systems crystallize as homopolymers by folding segments of the chain including the halogen, all properties indicate that as the halogen becomes larger it is more difficult to accommodate it inside the crystallites. As a consequence, the level of crystallinity decreases and crystal thickness also decreases.

**Fig. 8** Effect of halogen content and type on (a) level of crystallinity obtained from WAXD, (b) long spacing from SAXS, and (c) crystal thickness from analysis of the correlation function from SAXS patterns [71, 73]



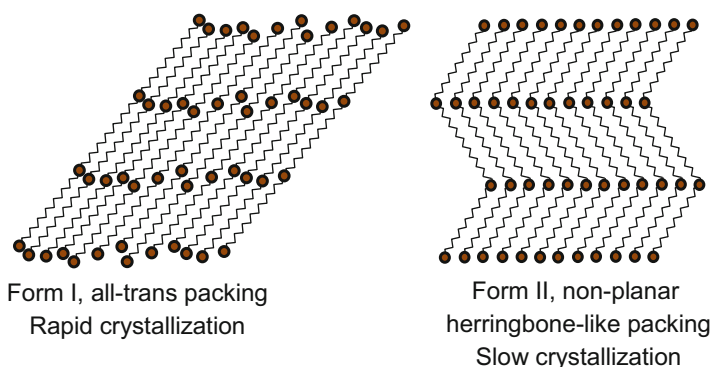
Within a given series, for example Cl-containing samples, the decrease in crystal thickness from 185 Å for PE21Cl to 90 Å for PE9Cl corresponds to nine and eight repeating units, respectively. A similar number of repeats suggests that, in spite of the reduced level of crystallinity, when a higher content of halogen is

accommodated as defects in the crystallites, the lamellae contains about the same number of chain repeating units. All halogen precision systems with  $M_w > 10,000$  display spherulitic morphology [73].

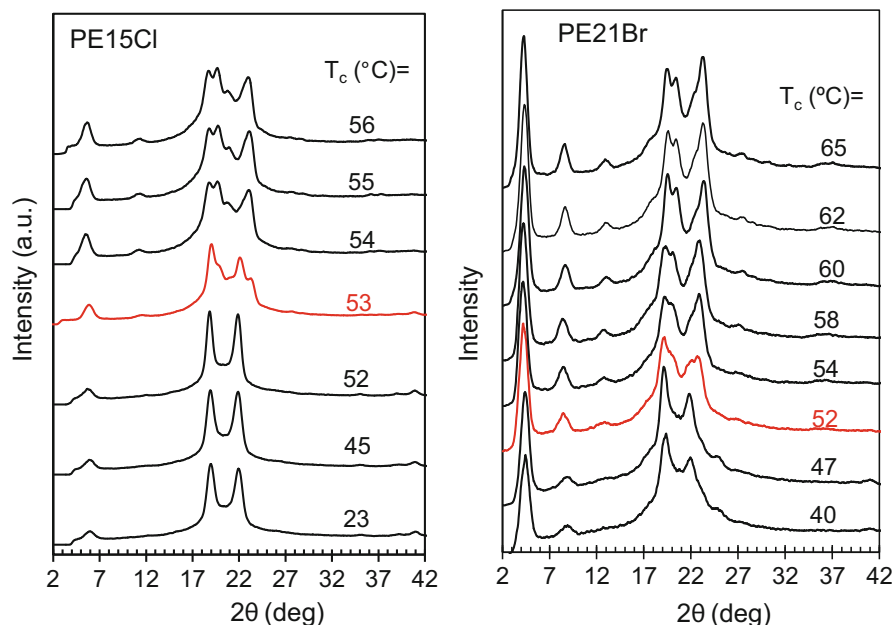
## 2.2 Isothermal Crystallization: Polymorphism

Although most work on the crystalline features of precision polyethylenes has been done under uncontrolled crystallizations, often for samples cooled from the melt to room temperature, it has been recently found that control of crystallization kinetics allows different crystalline structures to be generated for a given precision chain. Polyethylenes with precision halogen substitution have the ability to pack into different polymorphs, depending on the undercooling. Schematics of two major crystalline structures are given in Fig. 9 [64, 65]. At relatively low crystallization temperatures, the lamellae stems pack in the *all-trans* conformation (form I) whereas at relatively high crystallization temperatures, the methylene segment between halogens zig-zags in a herringbone-like structure (form II). In this section we review how this unique polymorphism can be identified spectroscopically or by changes in X-ray patterns or melting behavior.

We start by reviewing X-ray patterns as a function of increasing crystallization temperature. Figure 10 displays a composite of transmission X-ray patterns of PE15Cl and PE21Br that were isothermally crystallized over a wide range of temperatures ( $T_c$ ). There is a clear change in crystallographic packing for  $T_c$  below and above 53°C. At  $T_c < 53^\circ\text{C}$ , the WAXD patterns display the two sharp and strong reflections observed under rapid crystallization (form I). For  $T_c > \sim 53^\circ\text{C}$ , these precision polyethylenes pack in a different polymorph, form II, characterized



**Fig. 9** Major polymorphs (form I and form II) of precision Cl- and Br-containing polyethylenes. Reprinted with permission from Kaner et al. [64]. Copyright 2014 American Chemical Society



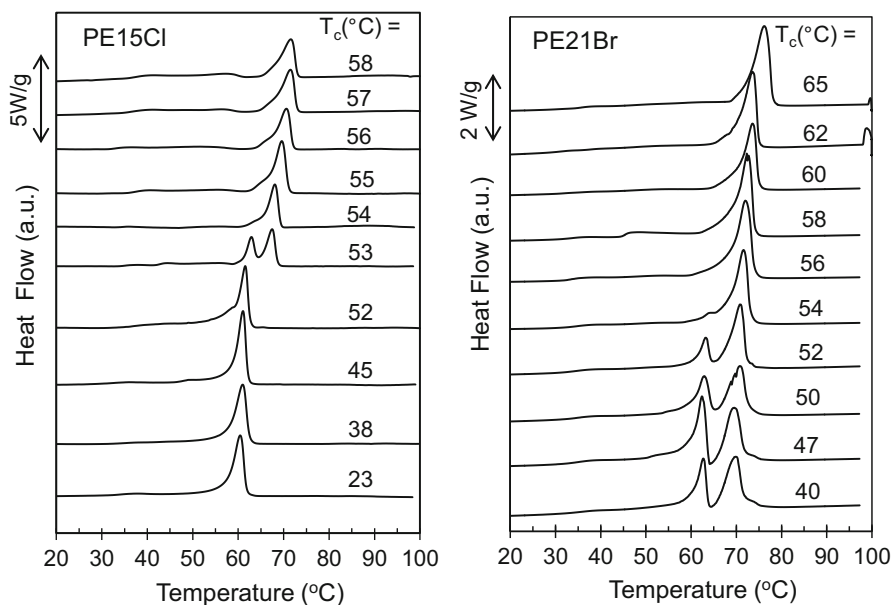
**Fig. 10** WAXD patterns collected at room temperature of PE15Cl and PE21Br isothermally crystallized at the temperatures indicated. Notice the polymorphic change at  $T_c > 52^\circ\text{C}$

by additional reflections. The polymorphic change occurs within one degree of undercooling, a feature that has not yet been reported for any other ADMET precision polyethylene.

The transmission diffractograms also display strong reflections at intermediate angles ( $2\theta < 15^\circ$ ), with periodic diffraction orders that are more relevant for form II. These reflections correspond to spacings of  $\sim 15 \text{ \AA}$  (PE15Cl) and  $\sim 20 \text{ \AA}$  (PE21Br), indicating that in both forms the halogens are arranged inside the crystals in layers and that the chains are tilted at  $35^\circ$  (PE15Cl) or  $41^\circ$  (PE21Br) to the normal of these layers [64, 65]; the larger the halogen, the greater the chain tilt. Crystalline layered structures have been observed for precision polyethylenes with carboxylic acids [78] and polyesters [60, 76], but the polymorphic behavior with increasing crystallization temperature could be a feature related to intermolecular kinks caused by small-volume pendant groups. The fact that PE15Cl and PE21Br display a change from form I to form II at about the same crystallization temperature is only fortuitous. The polymorphic transition for other precision Cl and Br systems is expected at lower or higher crystallization temperatures, depending on their crystallization kinetics; this is ongoing research in our laboratory. Polymorphism has been also observed in precision ethyl-branched polyethylenes [79] and, although yet unreported, it is expected in methyl-branched precision systems as well.

A distinct characteristic distinguishing form I and form II crystallites is the melting point. Form II melts at temperatures 10°C or 15°C higher than form I. Hence, the polymorphic transition is easily identified by DSC experiments. Under controlled isothermal crystallizations and subsequent melting, one notices a sharp increase in melting temperature with increasing crystallization temperature. Examples for PE15Cl and PE21Br are given by the thermograms in Fig. 11, which were obtained for the same isothermally crystallized samples used to record the WAXD patterns shown in Fig. 10. Crystals formed below 52°C (form I) melt at about 61°C whereas crystals formed at  $T_c > 53^\circ\text{C}$  (form II) melt at about 10°C higher. The change in crystallization temperature when crystal packing translates from form I to form II is so sharp (within 1°C) that, in addition to large differences in free energy of nucleation, the development of one or the other polymorph has been associated with the thickness of the critical nucleus in the early stages of crystallization [64]. When the estimated critical nucleus thickness is less than the length between halogens, form I develops. If the thickness is equal to or greater than the length of the methylene sequence between halogens, form II crystallites are formed. Indeed, where the transition between polymorphs is experimentally observed, the estimated thickness of the critical nucleus approaches the ethylene sequence length between halogens.

The double melting at temperatures below the polymorphic transition, such as below 52°C in the thermograms of PE21Br, are caused by melting of form I followed by fast recrystallization in form II and further melting of the latter



**Fig. 11** DSC melting thermograms of PE15Cl and PE21Br isothermally crystallized at the temperatures indicated. Heating rate was 10°C/min

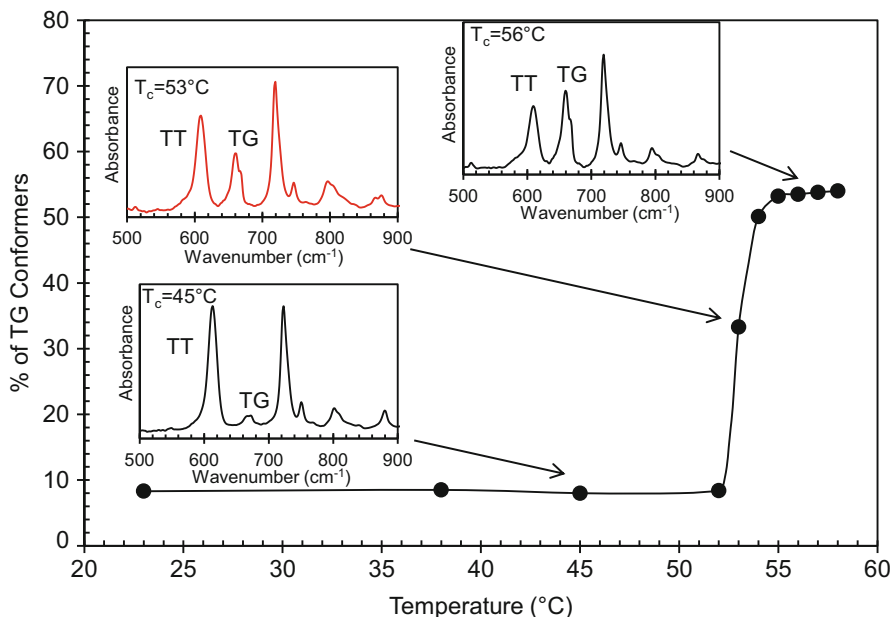
[65]. This melting–recrystallization–melting sequence is absent in the thermograms of precision polyethylenes substituted with the smaller halogen, and the double melting of PE15Cl observed at  $T_c = 53^\circ\text{C}$  represents the simultaneous formation of both forms. Hence, there is a narrow range of crystallization temperatures where both polymorphs coexist. It has also been proven that both form I and form II are stable [64]. For example, form I does not transform to form II when brought to a temperature in the region of formation of form II and below the melting temperature of form I. In other words, form I is not metastable as it needs to fully melt before re-crystallizing into form II.

The structural differences between forms I and II can be extracted by combining the information on layered structures that is obtained from X-ray patterns and FTIR or Raman spectra of isothermally crystallized samples [64, 65]. Vibrational spectroscopy probes the conformation of backbone bonds adjacent to the halogen substitution [80, 81]. This information is crucial in identifying intermolecular kinks along crystalline halogen layers. Using model compounds, it has been shown that in the FTIR stretching region the absorbance of the C–Cl bond depends on the conformation of the adjacent C–C bonds. The absorbance at  $612\text{ cm}^{-1}$  corresponds to C–Cl stretching with vicinal C–C bonding in an *all-trans* conformation. The absorbance at  $665\text{ cm}^{-1}$  corresponds to C–Cl stretching when the side group is adjacent to backbone carbons in the *gauche* conformation [80, 81].

As seen in the FTIR spectra of PE15Cl (Fig. 12, insets), there is a dramatic increase in *gauche* bonding around the halogen substitution when crystallites develop in form II. Indeed, it has been shown quantitatively that all carbons adjacent to the substitution are *gauche*-bonded in the crystalline regions of form II, whereas they are *trans*-bonded in the crystals of form I [64]. The conclusion from this analysis is that the layer structure of form I keeps the *all-trans* conformation, whereas the halogen layers of crystals in form II form a *kink* conformation because the methine is *gauche*-bonded to the adjacent backbone carbons, or out of the plane formed by the long methylene sequence if the conformation of the latter remains *all-trans* (as shown in Fig. 9).

A simple direct way to prove the *all-trans* conformation of the methylene segment between halogens in the crystals of form II is by analyzing the set of progression methylene rocking bands of the FTIR spectral region between 700 and  $1,100\text{ cm}^{-1}$ . These bands can be analyzed in reference to progression modes of *n*-alkanes of equivalent length that are known to pack in an *all-trans* conformation. The *n*-alkane  $\text{CH}_2$  sequence is considered a linear array of *m* identical oscillators, each having one degree of freedom [82, 83]. The oscillator model predicts a frequency mode (*K*) that is only a function of the difference in phase angle between adjacent oscillators ( $\phi_{(K)}$ ), calculated as  $\phi_{(K)} = K\pi/(m+1)$ , with  $K = 1, 3, 5, \dots$ . Even *K* values are forbidden for the ideal model, and *m* is the number of continuous  $\text{CH}_2$  units that adhere most closely to the ideal oscillator. The ends of the *n*-alkane pendant groups and the backbone carbons adjacent to the methine of precision polyolefins all break or affect the oscillator's symmetry. Hence, in calculating  $\phi_{(K)}$  for different *K* values, the length of the ideal oscillator is often shorter than the length between pendant groups [84, 85]. For example, in the *n*-alkane  $\text{C}_{14}\text{H}_{30}$ ,



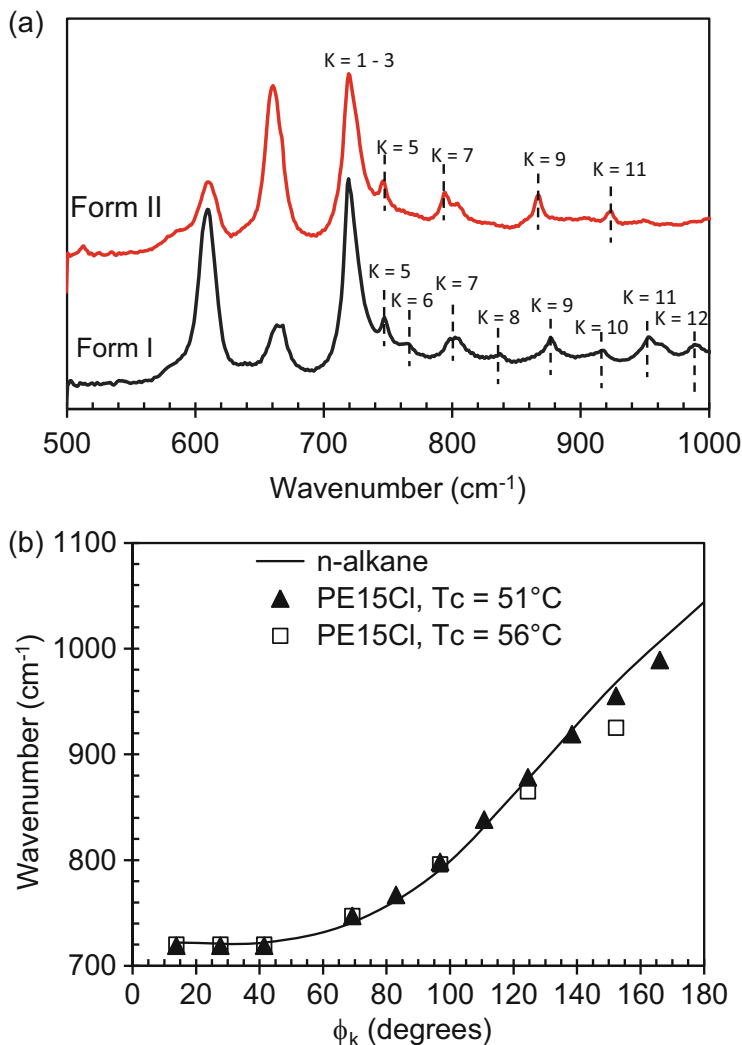


**Fig. 12** Percentage of gauche bonds adjacent to the CH for PE15Cl isothermally crystallized. Notice the steep increase in gauche conformers at  $T_c > 52^\circ\text{C}$ . Insets show FTIR spectra for specimens crystallized at different isothermal temperatures

$m = 12$  (14 backbone carbons minus 2 ends), and in precision PE15Cl,  $m = 12$  (14 methylene backbone carbons minus 2 adjacent to the methine).

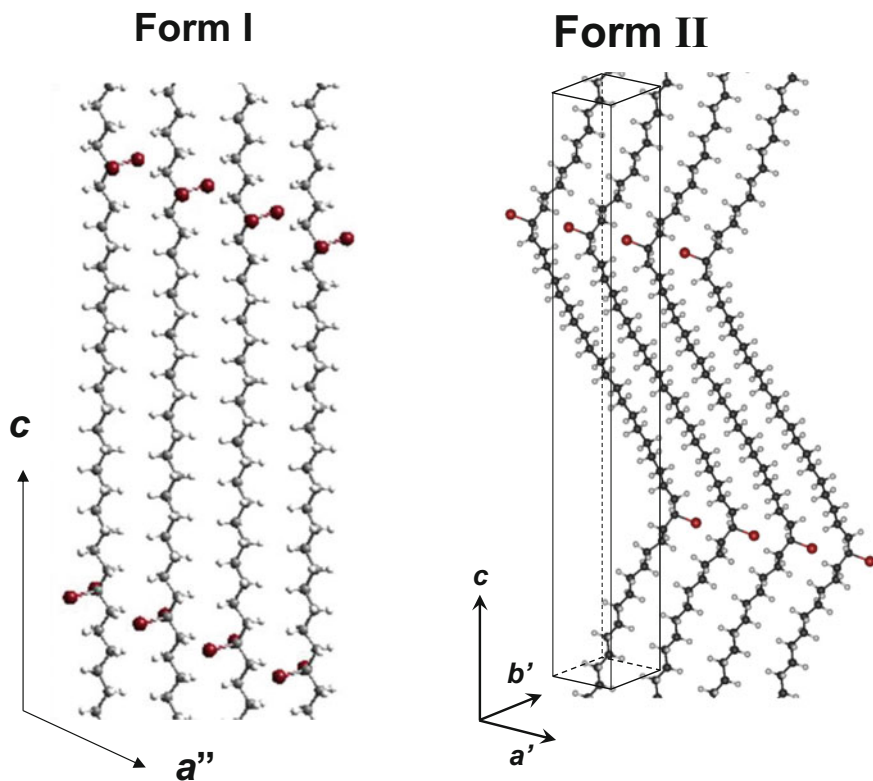
When a progression of absorbance bands in the rocking region of the IR spectra of precision polyethylenes follows the predicted frequency-phase angle dispersion of the  $n$ -alkane of the same segment length, the  $\text{CH}_2$  sequences of both systems must have the same *all-trans* conformation. Hence, proving that the methylene sequences between pendant groups pack in an *all-trans* conformation can be easily tested by evaluating the adherence of the frequency versus phase angle curve to the  $n$ -alkane prediction. This simple model is extremely useful for testing periodic  $n$ -alkane-like packing and has been successfully applied for evaluating the packing of fatty acids [84–86] and aromatic polyesters with different methylene runs [87].

The oscillator model was also successfully applied to the spectra of PE15Cl and PE21Br, giving evidence that the methylene segments between halogens pack in *all-trans* conformation in forms I and II [64, 65]. An example of the progression modes in the rocking-twisting region of FTIR spectra is given in Fig. 13a for forms I and II of PE15Cl. Notice that the calculated  $\phi_{(K)}$  for a sequence of 12 methylenes closely follows the continuous line for the  $n$ -alkanes. The behaviors of form I and form II are basically identical, thus demonstrating that the crystal packing of the methylene run is *all-trans* in both (Fig. 13b). Because the bonding around the substitution point is also *trans* for form I, but *gauche* for form II, the most plausible structural models for crystalline packing that can be extracted from a detailed, yet



**Fig. 13** (a) FTIR spectra of PE15Cl for crystals in forms I and II. Methylene progression bands are indicated for  $K = 1-12$ . (b) Dispersion curve for *n*-alkanes (continuous line) and for PE15Cl (symbols) calculated for form I ( $T_c = 51^\circ\text{C}$ ) and form II ( $T_c = 56^\circ\text{C}$ ), demonstrating that methylene  $\text{CH}_2$  sequences pack in the *all-trans* conformation. Reprinted with permission from Kaner et al. [64]. Copyright 2014 American Chemical Society

simple, analysis of X-ray and FTIR are those of Fig. 9. Subsequent crystallographic analysis of fiber patterns for forms I and II of PE21Br corroborated the planar and nonplanar structures of the two major polymorphs of these precision systems [65]. The triclinic unit cells and lattice parameters are shown in Fig. 14. Whereas the backbone conformation of form I is *all-trans*, the conformation of form II



Crystal form	$a/\text{\AA}$	$b/\text{\AA}$	$c/\text{\AA}$	$\alpha/\text{deg}$	$\beta/\text{deg}$	$\gamma/\text{deg}$
Form I	4.90	5.75	52.7	43.2	109.8	107.9
Form II	5.00	5.65	47	77.5	112	65

**Fig. 14** Crystal unit cell structures extracted from WAXD fiber patterns of PE21Br. Two Br atoms are placed on a methine carbon at a 0.5 statistical probability to account for the atactic nature of the chain [65]. The triclinic lattice parameters for forms I and II are listed

follows the pattern ...TTTTTGGTTTT...TTT'TTG'G'TT... , thus perpetuating lamellar symmetry.

The unique feature that emerges from the currently available studies is that precision halogen-containing polyethylenes pack in at least two different crystalline structures, depending on the undercooling. At large undercooling, form I develops with molecules packing in *all-trans* zig-zag conformation and a layered, albeit a little disordered, intermolecular staggering of chlorines. At relatively low undercooling, the staggering of chlorines or bromines is highly symmetric, leading to intermolecular kinks or a herringbone-like conformation where the long methylene runs zig-zag around the substitution point (Fig. 14). This polymorphism is

obviously related to the size of the halogen and the regularity of the substitution along the backbone. As the halogen inside the crystal must be in layers, the larger the size the stronger is the intermolecular halogen compression. Fluorine is too small to cause any intermolecular effect, whereas chlorine, bromine, and larger halogens have dramatic effects on methylene packing.

One issue that remains is the major driving force for the observed layered crystalline structures. Three possibilities are at play: (a) preferential folding at a given location in the backbone as earlier speculated, and perhaps directed by crystal size; (b) intermolecular  $\text{CH}_2$  van der Waals interactions; and (c) intermolecular halogen–halogen interactions. Interactions between functional groups have been posed to dominate over the other two possibilities in packing aliphatic long methylene polyesters [76], polyethylenes with equidistant sulfite groups [67], and polyethylenes with other strongly interacting moieties [13, 66]. However, the strength of halogen–halogen interactions over the enthalpic drive to assemble intermolecular methylene segments in precision halogen-containing specimens is difficult to quantify. Some works point out ineffective F–F interactions and effective halogen–halogen interactions for Cl- and Br-containing molecules [88]. Moreover, methylene *all-trans* packing may dominate in these systems as the layer symmetry increases at higher temperatures where form II is enabled.

Controlled crystallization of precision polyethylenes with methyl branches can help to discern whether halogen–halogen interactions are the major driving force for formation of layered crystallites in these systems. The size of a methyl group is similar to that of a Br atom, but the interactions between  $\text{CH}_3$  pendant groups are significantly weaker than those between Br atoms. Unfortunately, systematic studies of the melting behavior and crystalline structure of isothermally crystallized samples are not yet available for precision polyethylenes with methyl branches [75, 89–92]. Although deviations from the regular *all-trans* geometry of the backbone carbons near the methyl branch have been already identified in the crystalline regions of deuterated precision systems [92], determination of whether crystallites of precision methyl-branched polyethylenes are also layered requires more detailed thermal, X-ray, and spectroscopic analysis of isothermally crystallized samples. A conclusion from the in-depth crystallization studies of PE15Cl is that understanding all forms of crystalline packing can help clarify the multiple melting that is often observed in many of these precision systems.

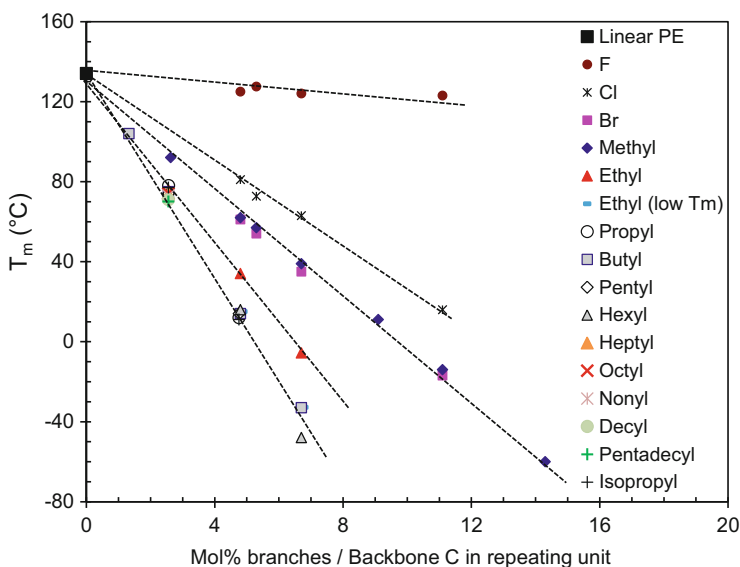
### 3 Crystallization of Precision Alkyl-Branched Polyethylenes

Because of their relevance for the polyethylene industry, considerable effort has been made by Wagener and coworkers to synthesize precision polyethylenes with alkyl branches. Thermal data are available for series with methyl [75, 89–91, 93, 94] ethyl [79, 93–96], propyl [93, 94], butyl [93, 94, 97, 98], pentyl [93, 94], hexyl

[63, 93, 94, 99], and up to pentadecyl [94, 100] branches, and with distances between branches of 7–39 carbons. A polyethylene with butyl branches spaced by 75 carbons was also synthesized [101]. The synthesis of these systems and their thermal and crystalline properties have been summarized in different reviews [5, 102–105]; therefore, only major highlights of their crystallization behavior are covered in this section.

The behavior of this type of precision polyethylene with respect to partitioning of the alkyl branch between crystalline and non-crystalline regions has been deduced from the comparative melting behavior of crystals formed under the usual dynamic cooling from the melt. A compilation of literature data for melting temperatures ( $T_m$ ) as a function of increasing branching is given in Fig. 15. Data on rapidly crystallized (form I) precision halogenated polyethylenes are also included as a reference, representing systems with no discrimination for partitioning of the pendant group. For alkyl-branched systems that display multiple melting peaks, the lowest  $T_m$  is plotted. The only exception is for data on ethyl-branched samples, for which low  $T_m$  for quenched and high  $T_m$  for isothermally crystallized specimens are both included.

The linear variation of  $T_m$  with decreasing length between pendant groups can be extrapolated to the observed melting point of the unbranched chain; the gradient of



**Fig. 15** Melting temperature versus. branching composition of precision halogen-substituted polyethylenes and precision alkyl-branched polyethylenes crystallized from the melt at  $10^\circ\text{C}/\text{min}$ . Included are data of Fig. 6 for precision halogen-substituted polyethylenes and data for precision samples with the following branches: methyl [75, 91, 94], ethyl [94, 95], propyl [93, 94] butyl [93, 98, 101], pentyl [93, 94], hexyl [94, 99], heptyl [94], octyl [94], nonyl [94], decyl [94], pentadecyl [94], and isopropyl [93, 94]. Data for slowly crystallized ethyl-branched samples are also added (*red triangles*)

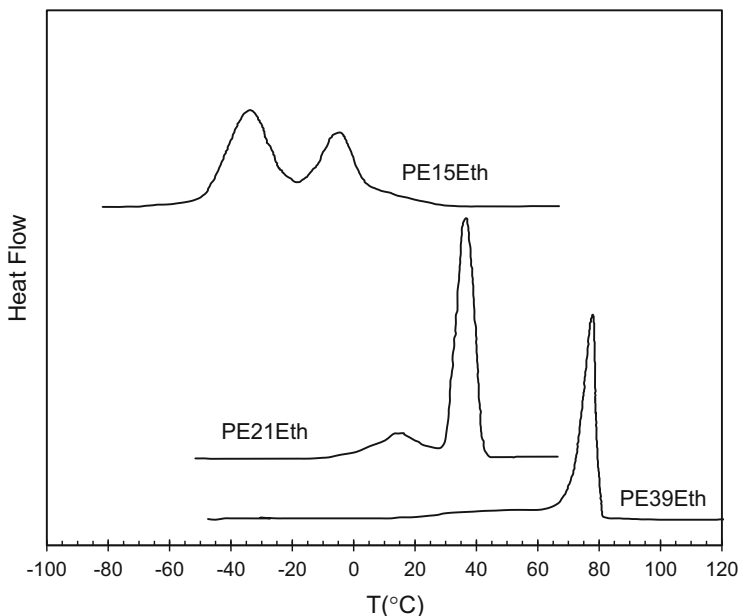
each line is proportional to the size of the pendant group. The trends in Fig. 15 are clear: At a fixed branching content, systems with propyl and longer branches melt at about the same temperature and systems with ethyl and methyl branches melt at progressively higher values. The size and content of the pendant group nicely correlates with the types of crystals formed.

If the pendant group is rejected to the intercrystalline regions, as is likely for propyl and longer branches, the crystalline structure follows model (i) shown in Fig. 1. For a fixed length of the methylene sequence, the lamellae thickness is constant and the branch is preferentially placed at the surface of the crystallites. Hence, the melting temperature is simply a function of the basal surface free energy, following the Gibbs–Thomson relation. Under the assumption of lamellar crystallites with negligible lateral surfaces and large basal surfaces, this relation takes the form:

$$T_m = T_m^o \left( 1 - \frac{2\sigma_e}{l\Delta H_u} \right) \quad (3)$$

Here,  $T_m^o$  is the melting temperature of the infinite thick crystallite,  $T_m$  the observed melting temperature,  $\sigma_e$  the basal surface free energy,  $l$  the lamellae thickness, and  $\Delta H_u$  the heat of fusion per unit volume of pure crystal. Because the basal surface free energy is presumably very similar for alkyl branches that remain uncrystallized, following Eq. (3), the same  $T_m$  is expected for crystals of the same thickness. Indeed, with  $T_m^o = 145.5^\circ\text{C}$ ,  $\Delta H_u = 2.8 \times 10^9 \text{ erg/cm}^3$ , a C–C distance of  $1.27 \text{ \AA}$  for *all-trans* packing, and  $\sigma_e = 110 \text{ erg/cm}^2$  [24], the calculated  $T_m$  values are very close to the observed melting temperatures ( $\pm 4^\circ\text{C}$ ) for systems with propyl and longer branches spaced at a distance  $\geq 15$  methylenes. Hence, the data for propyl and longer branches follow the predictions for model (i) in Fig. 1. The  $T_m$  data for systems with bulkier, non-interacting groups such as cyclohexyl and adamantyl fall below the line, suggesting a more strained basal surface or a higher value of  $\sigma_e$  [93].

Works on ethyl-branched precision systems are among the very few where properties for quenched and isothermally crystallized specimens are reported [79]. Low melting thin crystallites free of branches are formed at the lowest crystallization temperatures or on quenching; their melting behavior is similar to the behavior of precision systems with branches excluded from the crystallites (see plot representing propyl and longer branches in Fig. 15). Conversely, crystallites of ethyl-branched systems that include at least one branch are formed at higher isothermal crystallization temperatures; consequently, they melt at higher values (see red triangles in Fig. 15). Even under rapid cooling, ethyl-branched precision systems spaced every 15th or every 21st carbon develop two different crystalline structures (as seen in Fig. 16 by their dual melting behavior) [94, 95]. Therefore, on dynamic cooling, the development of one or two populations of crystallites with different melting peaks depends on the kinetics of the formation of each polymorph. The ethyl-branched system spaced every 8th carbon was amorphous, an indication



**Fig. 16** DSC melting endotherms for precision polyethylenes with ethyl branches placed on every 15th, 21st or 39th backbone carbons. Thermograms of PE15Eth and PE21Eth extracted from [95], thermogram for PE39Eth from [94]

of incommensurate steric effects in accommodating the ethyl branch in the crystallites at this branching level.

The work of Lieser et al. on precision methyl-branched polyethylenes with the branch placed on every 15th or every 21st backbone carbon was a pioneer contribution to an understanding of the crystallization of precision polyethylenes [90]. From X-ray powder diffraction patterns of melt-crystallized specimens and electron diffraction of solution-crystallized samples, the authors concluded that these polymers form superlattices involving two full repeating units in a triclinic symmetry. The lamellae of the crystallites are 100–200 Å thick, in other words, at least five times the length of the methylene sequence. Such thick crystallites provide the first evidence that long chain segments including multiple repeating units fold back and forth in the crystallites, hence including the branches.

The thermal properties of the series of precision methyl-branched systems indicate that all these atactic models are semicrystalline, even at very high branch content. Only polyethylenes with a methyl branch on each 5th carbon showed no evidence of crystallization, even after annealing [91]. At this short distance, the atactic nature of the substitution obviously prevents the formation of any stable or metastable lattice. Crystal entities do not form because the excess free energy from the methyl defects in the crystal overcomes the free energy of formation of any crystallite from this highly branched structure. The plots of  $T_m$  versus composition for the methyl-branched series (represented by diamonds in Fig. 15) fall closely on

the line of precision Br-substituted samples. This feature emphasizes a similar crystallization path, and that the size of the substituent is a major drive directing the crystallization and melting behavior of precision systems. As the van der Waals radius of the methyl and bromine are the most similar, their distortion effects on the crystal lattice, and thus  $T_m$ , are also very similar.

The melting temperature of the polyethylene with methyl branches on each and every 7th carbon is  $-60^\circ\text{C}$ , but increases by  $\sim 30^\circ\text{C}$  on annealing, a feature also consistent with the formation of different polymorphic structures [91]. It is likely that a highly defective metastable structure that melts at  $-60^\circ\text{C}$  develops on dynamic cooling, whereas annealing or isothermal crystallization favors better interchain staggering of the methylene sequences, thus increasing the symmetry of the crystal packing and hence the melting point, similar to halogen behavior. Other members of the methyl-branched series display single melting peaks on rapid cooling [91]. However, it is quite likely that they would also develop polymorphism and different levels of layered crystalline structures during controlled isothermal crystallization. This issue has yet to be explored.

In summary, the partitioning of linear alkyl branches between crystalline and non-crystalline regions correlates well with the melting behavior of crystals formed under rapid cooling, and scales with the size of the pendant group. Different polymorphic structures are predicted for systems with methyl and ethyl branches that can be incorporated in the crystals. These predictions are based on differences in the melting behavior of crystals formed under fast and slower crystallizations. A compendium of crystalline unit cells that have been suggested in the literature for precision alkyl-branched systems are listed in Table A1 of the Appendix.

## 4 Crystallization of Precision Polyethylenes with Interacting Functional Groups

Interacting pendant groups in precision polyethylenes bring additional complications to the study of their crystallization behavior. The strength of the interaction is often a function of the melt temperature. This feature translates to crystallizations that depend on the structure or entropy of the initial melt state. However, most available crystallization and melting data are for precision systems that were cooled from the same melt temperature. Polymers synthesized with functional groups directly attached to the methylene backbone (such as long spaced aliphatic or aromatic polyesters) or with pendant functional groups placed at an exact distance along a polyethylene-like backbone are too numerous to allow elaboration on suggested crystalline structures and melting behavior of each type in this section. Because of space limitations, the thermal properties of many of these precision polyethylene-like systems are compiled in Table A2 of the Appendix. In this section, we focus on three aspects that drastically affect the packing and melting behavior of these systems, namely, type and strength of interactions, placement



within or branching from the backbone, and configuration with respect to the backbone of the functional punctuation placed at a precise distance along the polyethylene backbone.

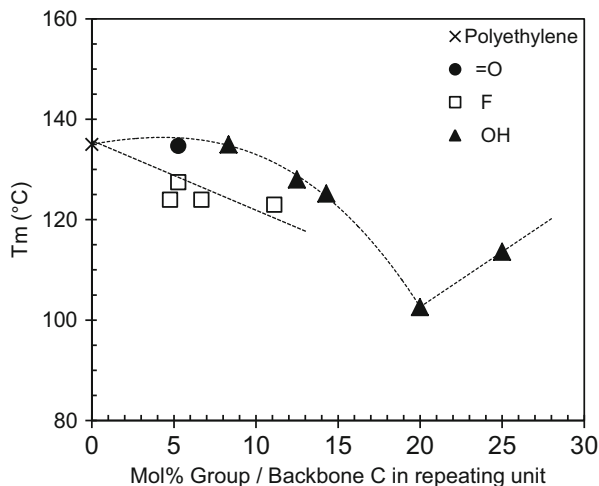
#### 4.1 *Strength of Pendant Group Interactions*

In general, as the strength of the pendant group interaction increases, the melting temperature also increases. This interaction can be ionic [106–112]; via hydrogen bonding between carboxyl [61, 66, 113–115], hydroxyl [116–119], or amine [120, 121] pendant groups; or interactions induced by bond polarity in groups such as ketone [13, 68], ether [122, 123], acetoxy [9, 124], or acrylate [125]. Layered crystalline structures often develop in precision systems with strongly interacting functional groups. Extensive work by Winey and coworkers on acid-containing, and ionomer-like precision systems [106–112] have revealed that interactions between functional or ionic groups exist, even at high melt temperatures, and play a role in self-assembly, which ultimately affects their uniaxial tensile deformation behavior [115]. Moreover, crystallization from a dilute solution of precision polyethylenes with pendant carboxylic acids leads to crystallites with thicknesses corresponding to the length of the methylene sequence [61]. Hence, preferential folding and structures of the type shown in Fig. 1b (model i) may prevail in crystallizations from dilute solution, leaving the carboxylic acid groups accommodated preferentially at the crystal surface.

Examples of increasing interactions between small-sized pendant groups and the effect on melting behavior are given in Fig. 17 for precision systems with fluorine [68, 71], ketone [68, 126], and hydroxyl [116] groups. As the pendant moiety is easily accommodated in the crystal lattice, it is expected that all these systems crystallize as homopolymers. Perturbation of the crystal lattice by the small pendant group is relatively minor; hence, all crystalline structures developed by these long-spaced systems are isomorphous to the orthorhombic polyethylene crystals [68, 71, 116, 118].

The F–F interaction is the weakest of the groups studied in Fig. 17 and, as such, precision F-substituted polyethylenes display the lowest melting temperatures. Dipole–dipole interactions increase in ketone-decorated systems, favoring interchain interactions and resulting in  $\sim 10^\circ\text{C}$  increase in the melting point of ketone-precision systems compared with the fluorine analogs. The highest melting points belong to the systems with hydroxyl pendant groups, which are prone to strong hydrogen bonding [116]. The decrease in melting temperatures with increasing alcohol content again makes it relevant that the  $-\text{OH}$  is primarily a defect in crystallites that maintain the orthorhombic symmetry up to 20 mol% hydroxyls ( $-\text{OH}$  on every 5th backbone carbon). Decreasing the space beyond five methylenes leads to a change in crystallographic packing to one that approaches the monoclinic packing of polyvinyl alcohol, and explains the observed increase in melting temperatures for  $-\text{OH}$  contents  $>20$  mol% (see Fig. 17). Precision random

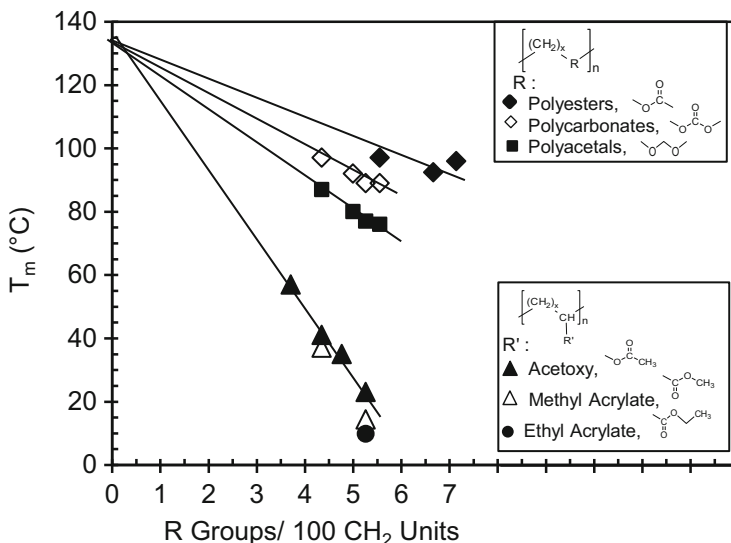
**Fig. 17** Effect of strength of interaction between pendant groups on the melting temperature of polyethylenes with ketone (=O) [68, 126], hydroxyl (-OH) [116], or fluorine [68, 71] groups placed at the same precise distance along the backbone



polyamides show a similar behavior, with a minimum in melting points at much lower content of amide groups [12]. The melting data shown in Fig. 17 for hydroxyl pendant groups were obtained for samples synthesized via ROMP [116]. Melting data for the same hydroxyl-branched structures synthesized via ADMET are lower and basically invariant for systems spaced with 8–20 methylenes ( $T_m \sim 125^\circ\text{C}$ ) [118]. This melting difference is probably a result of differences in tacticity between ROMP- and ADMET-derived specimens, which may affect the strength of hydrogen bonding.

#### 4.2 Functional Groups Within or Branching from the Methylene Backbone

The difference in crystalline packing and melting behavior of a methylene backbone precisely decorated with functional punctuations that are either directly linked to the backbone or branching from the backbone is quite drastic, as shown by the data compiled in Fig. 18. The melting temperatures of precise long-spaced aliphatic polyesters [126–128], aliphatic polycarbonates [11], and aliphatic polyacetals [11] are compared with analogs containing pendant acetoxy [124], and pendant methyl or ethyl acrylates [125]. The melting points of the first type are displaced at much higher values. For the first group, the melting temperatures of polyesters are the highest, followed by polycarbonates and then polyacetals, denoting differences in size of the functional group and in polarity. Polyethylenes with ketone groups (not included in Fig. 18) are expected to melt at even higher temperatures than polyesters as they have stronger dipolar interactions, and the available data for two precise ketone-containing polyethylenes corroborate their higher melting points [13, 68].



**Fig. 18** Effect of placement, as a branch ( $R'$ ) or inserted in backbone ( $R$ ), on the melting temperature of precision polyethylene-like polymers with increasing content of functional groups. Data shown are for long-spaced polyesters [126, 127], polycarbonates [11], polyacetals [11], and precision polyethylenes with acetoxy [124], methyl acrylate [125], and ethyl acrylate [125] pendant groups

As seen in Fig. 18, the polyester spaced every 18 methylenes melts at 97°C, whereas the analog with an acetoxy pendant group melts at 23°C. This is a drastic depression of the melting point that cannot be accounted for simply by polar interactions. The effect of the type of linkage on chain packing is evident. In long-spaced polyesters, polycarbonates, or polyacetals, the functional group is part of the polyethylene backbone; hence, it is an integral part of the crystal lattice, with polar groups of different chains interdigitated in a close packing arrangement [126, 127]. A crystalline layered symmetry is easily set in this precision type, as shown recently in a precision polysulfite system [67]. Conversely, intermolecular packing of a chain with acetoxy or acrylate pendant groups is driven to a large extent by van der Waals interactions between the methylene runs of different chains, with the pendant groups causing large distortions to the *all-trans* methylene packing, or being rejected to the crystal–amorphous interfacial region. Crystallites from precision chains with pendant side groups either have more defects or are thinner than those of the first group; hence, they melt at lower temperatures.

Wagener et al. have published X-ray patterns of polyethylenes with pendant acetoxy groups on every 23rd carbon that display low angle reflections corresponding to the distance between acetoxy groups, suggesting that these groups are also layered and are part of the crystalline symmetry [124]. Hence, layered crystallites are feasible for systems with pendant-interacting functional groups. This is inferred by the high melting points of these systems compared with the melting

temperatures of precision systems with large uncrystallizable pendant groups [63, 124, 125] and by the double melting observed in some of the former type, suggesting polymorphism [124].

### 4.3 Effect of Tacticity

Precision structures generated by ADMET allow unprecedented control over the generation of models of polyethylene-like systems for understanding the effect of defects of different types, sizes, and precise placement along the backbone on chain folding and self-assembly of macromolecules. However, to date, it has not been possible to control the tacticity of ADMET-generated model precision polyethylenes. The question still remains as to whether the crystalline packing and properties of the same structures with control of tacticity will remain the same or change radically. If a higher order of symmetry is found in crystallites from isotactic or syndiotactic precision systems, their melting temperature may also be dramatically higher. Sporadic data for systems with control over both the sequence and stereochemistry appear to point in this direction [7–9].

It is well known that tacticity and regiochemistry can have a dramatic effect on the crystallization, thermal, and mechanical properties of polyolefins. To probe this effect, regio- and stereoselective systems with ethylene backbones and di-hydroxyl, alkyl, phenyl, and acetoxy pendant groups have been synthesized via ROMP by the groups of Grubbs and Hillmyer [7, 9, 129]. Regioregular atactic polyethylene with a methyl branch on every 8th backbone carbon is crystalline with a melting point of 1.7°C, which is about 10°C higher than the atactic ADMET system with a methyl branch on each 9th carbon [91]. Regioregular ROMP systems with an ethyl, hexyl, or phenyl group on each 8th backbone carbon are amorphous under standard DSC cooling at 10°C/min, but annealing procedures were not attempted [7].

Both the atactic and isotactic regioregular systems with acetoxy pendant groups on every 8th carbon are crystalline with melting temperatures of 53°C and 91°C, respectively. These values are also higher than predicted melting points of ADMET systems spaced at a similar distance [124]. Interestingly, the atactic but regioselective system with acetoxy groups on the 7th carbon was amorphous. This drastic loss of crystallinity caused by reducing the methylene length from seven to six carbons was explained as the need for a minimum sequence length of seven methylenes to generate crystallites [9]. Moreover, the loss of crystallinity could also be related to a dramatic effect on melting of an odd versus even backbone placement of the acetoxy group, similar to the odd versus even end-group effect in *n*-alkane packing [130]. The atactic ADMET acetoxy system spaced by 18 methylenes (5.3 mol%) melts at 23°C [124] and, following Fig. 18, a much lower melting temperature was expected for the system with a higher content of branches. The atactic acetoxy-branched system spaced by six methylenes (14.3 mol%) follows this expectation, but the system spaced by seven methylenes (12.5 mol%) does not.

**Table 2** Melting temperatures and heats of fusion for precise ADMET and regioregular and stereoselective ROMP systems

Pendant group	Tacticity	Synthetic route	Number of CH <sub>2</sub> groups between pendant groups	T <sub>m</sub> (°C)	ΔH <sub>m</sub> (J/g)	Reference
CH <sub>3</sub>	Atactic	ADMET	8	-13	39	[91]
CH <sub>3</sub>	Atactic	ROMP	7	1.7	30	[7]
Acetoxy	Atactic	ADMET	18	23	NA <sup>a</sup>	[124]
Acetoxy	Atactic	ROMP	6	Amorphous		
Acetoxy	Atactic	ROMP	7	53	39	[9]
Acetoxy	Isotactic	ROMP	7	91	67	[9]
OH	Atactic	ADMET	8	120	NA <sup>a</sup>	[118]
OH	Atactic	ROMP	7	128	67	[116]
OH	Atactic	ROMP	4	102	15.3	[116]
di-OH	( <i>syn</i> -1,2 diol)	ROMP	6	111, 119	NA <sup>a</sup>	[129]
di-OH	( <i>anti</i> -1,2 diol)	ROMP	6	157	NA <sup>a</sup>	[129]

<sup>a</sup>Not available

It is feasible that, as the methylene spacer becomes shorter, the dipolar interactions between the acetoxy groups prevail over the van der Waals CH<sub>2</sub> interactions. Clearly, more research on regio- and tacticity-controlled samples is needed to elucidate these features. Melting points and heats of fusion of similar structures synthesized by ADMET and regio- and stereoselective ROMP are listed comparatively in Table 2.

From the data in Table 2 one can see that atactic and isotactic acetoxy systems melt at much higher temperatures than the precision analog with methyl substituents, in spite of the larger group size [9, 91, 124]. Higher melting points and higher heats of fusion accentuate the dipolar nature of the acetoxy group. Furthermore, the precision isotactic acetoxy system shows double melting, thus suggesting that the isotactic systems also develop different polymorphic structures [9]. A dramatic difference in melting points was also found between the *syn*- and *anti*-diols for stereoregular precision systems with hydroxyl groups on every 7th and 8th backbone carbon [129], again suggesting that the relative stereochemistry has a remarkable effect on packing of the side groups and, hence, on the properties of the material.

## 5 Concluding Remarks

Precision polyethylenes with co-units placed at a periodic equal distance along the backbone are excellent models for analyzing the effect of co-unit size, type, and content or the distance between co-units on their crystallization and melting

behaviors. These are novel polyolefin-like systems with crystallization mechanisms and crystalline properties that diverge from the most common random ethylene copolymer systems. In this review, we focus on the crystalline properties of the precision polyethylenes that are available via ADMET or ROMP synthetic paths.

Data on a series of precision halogen-substituted polyethylenes serve to establish the effect of size and content of a relatively small pendant group on crystallization. Even with the atactic configuration, if the co-unit is relatively small, all precision systems crystallize as homopolymers. Crystalline structure and melting are affected by the level of strain that the co-unit asserts on the crystal lattice. The crystallization behavior under rapid and slow crystallization is contrasted for Cl- and Br-containing systems, as the precise nature of the substitution enables unprecedented herringbone-like layered crystalline structures controlled by changing the undercooling. Planar and nonplanar polymorphic structures can be identified by X-ray diffraction, vibrational spectroscopy, and thermal analysis of isothermally crystallized specimens.

This review also analyzes the melting behavior of alkyl-branched precision polyethylenes, specifically branch partitioning between crystalline and non-crystalline regions and the behavior of analog polyethylenes containing halogens. Precision systems with propyl branches and longer, which are rejected from the crystal, display the same melting temperature-branching composition relation and their crystal thicknesses are close to the *all-trans* methylene sequence length. Conversely, smaller ethyl and methyl branches are accommodated in the crystallites and thus melt at higher temperatures. Different polymorphs are also enabled in the latter by changing the undercooling.

The effects of interacting functional groups and tacticity on self-assembly and melting are analyzed using available literature data. Strongly interacting functional groups lead to layered crystalline structures and high melting temperatures, as seen for polyketones, polyesters, and polysulfites. It is also demonstrated that, for the same methylene spacer, the melting temperatures of polyethylenes with functional groups inserted in the backbone are much higher than if the same group is added as a side branch. Similarly, stereoregular precision systems enable formation of crystallites with more symmetry, as they melt at higher temperatures than their atactic counterparts.

In summary, the potential for precision polyethylene-like copolymers to generate crystalline structures not accessible by the present state-of-the-art linear low-density polyethylenes is now becoming apparent. However, control of crystallization kinetics is of paramount importance in developing multiple polymorphic structures driven by different modes of staggering co-units in the crystallites.

**Acknowledgements** This material is based upon work supported by the National Science Foundation under grant no. DMR1105129. Any opinions, findings, conclusions, or recommendations expressed in this material are those of the author(s) and do not necessarily reflect the views of the National Science Foundation. We remain grateful to Prof. Wagener and E. Boz who kindly gave us the precision halogenated systems for study of their crystallization behavior. LSB acknowledges a postdoctoral fellowship APOSTD/2013/036 supported by the Generalitat Valenciana and the Universitat Politècnica de Valencia, Spain.

## Appendix

**Table A1** Suggested crystallographic packing for alkyl-branched precision ADMET polyethylenes

Branch type	Number of CH <sub>2</sub> groups between pendant groups	Inclusion of the branch in the crystal	$T_m$ (°C)	$\Delta H_m$ (J/g)	Suggested crystalline packing	References
Methyl	14	Yes	39	82	Triclinic unit with hexagonal sub lattice	Lieser et al. [90]
Methyl	20	Yes	62	103	Triclinic unit (18.75° and 21.75°) with hexagonal sub lattice	Lieser et al. [90]
					Monoclinic structure (19.1° and 22.1°)	Qiu et al. [131]
Methyl	38	Yes	92	137	Expanded orthorhombic unit cell (21.1° and 23°)	Inci et al. [94]
Ethyl	20	Yes	15/ 34	58.5	Triclinic (18° and 21°)	Rojas et al. [93]
					Triclinic (20.1° and 22.5°) Sample crystallized at 10°C for 4 days	Hosoda et al. [63]
Ethyl	38	No	76	93	Orthorhombic coexisting with a metastable monoclinic structure (~19.6°, 21.4° and 23.4°)	Inci et al. [94]
Propyl	20	No	12	60	Triclinic (broader and asymmetric peaks suggesting more than one crystalline lattice) (~19.5° and 22.5°)	Rojas et al. [93]
Propyl	38	No	78	71	Orthorhombic coexisting with a metastable monoclinic structure (~19.6°, 21.4° and 23.4°)	Inci et al. [94]
Butyl	20	No	12	57	Triclinic (broader and asymmetric peaks suggesting more than one crystalline lattice) (~19.5° and 22.5°)	Rojas et al. [93]
Butyl	38	No	75	66	Orthorhombic coexisting with a metastable monoclinic structure (~19.7°, 21.4° and 23.5°)	Zuluaga et al. [97], Inci et al. [94]

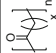
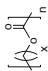
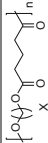
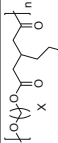
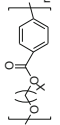
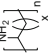
(continued)

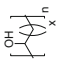
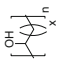

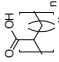

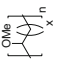
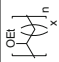
**Table A1** (continued)

Branch type	Number of CH <sub>2</sub> groups between pendant groups	Inclusion of the branch in the crystal	$T_m$ (°C)	$\Delta H_m$ (J/g)	Suggested crystalline packing	References
Pentyl	20	No	14	58	Triclinic (broader and asymmetric peaks suggesting more than one crystalline lattice) (~19.5° and 22.5°)	Rojas et al. [93]
Pentyl	38	No	74	88	Orthorhombic coexisting with a metastable monoclinic structure (~19.6°, 21.4° and 23.4°)	Inci et al. [94]
Hexyl	20	No	16	53	Monoclinic (~19.6° and 23.1°) Sample crystallized at 0°C for 4 days	Hosoda et al. [63]
Hexyl	38	No	73	85	Orthorhombic coexisting with a metastable monoclinic structure (19.6°, 21.4° and 23.4°)	Inci et al. [94]
Gem-dimethyl	20	No	45	61	Reflections of hexagonal, monoclinic and triclinic packing, pointing towards polymorphism	Qiu et al. [131], Rojas et al. [103]
Isopropyl	38	No	77	74	Orthorhombic coexisting with a metastable monoclinic structure (~19.6°, 21.4° and 23.4°)	Inci et al. [94]
Sec-butyl	20	No	9	43	Triclinic (broader and asymmetric peaks suggesting more than one crystalline lattice) (~19.5° and 22.5°)	Rojas et al. [93]
Iso-butyl	38	No	73	51	Orthorhombic coexisting with a metastable monoclinic structure (~19.6°, 21.4° and 23.4°)	Inci et al. [94]



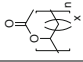
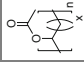
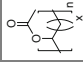
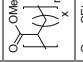
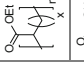
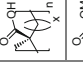
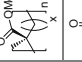
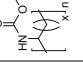
Table A2 Thermal properties of precision polyethylene-like polymers with functional groups

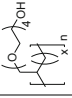

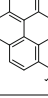
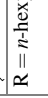

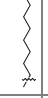
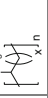
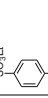
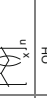
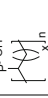
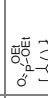
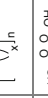
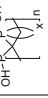
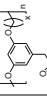
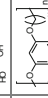
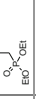

Group	Structure	CH <sub>2</sub> sequence (x)	T <sub>m</sub> (°C)	T <sub>c</sub> (°C)	ΔH <sub>m</sub> (J/g)	T <sub>g</sub> (°C)	References	
Ketone		18	134		127		Watson and Wagener [126]	
			134.7	120	106		Boz et al. [68]	
Aliphatic ester		14	95.9	78.2	125.6		Meulen et al. [127]	
			15	92.4	76.6	145.5		
			18 <sup>a</sup>	97		122		
Diester		22	85–88				Watson and Wagener [126] Hove et al. [60]	
			44	91–93, 100–102				
Diester with propyl branches		22	46–48					
			44	87–92				
Aromatic ester		9	92.8				Tasaki et al. [87]	
			10	120.3, 125.5				
			11	89.8, 96.5				
			12	119.1, 122.7				
			15	99.7, 101.9				
Amine		20	115.2				Leonard et al. [120]	
			20	117.1				
			8	42 <sup>b</sup>				10
			14	49				
		20	44					

Hydroxyl		8	120					Thompson et al. [118]	
		14	128			86			
		20	125			52		Valenti and Wagener [117]	
ADMET		3	113.6			36	48.5	Ramakrishnan [116]	
		4	102.6			15	45.4		
		6	125.2			59	37.8		
		7	128			67	35.1		
		11	135			92	31.6		
ROMP		18	76, 82	64	147			Ortmann et al. [11]	
		19	77, 83	67	158				
		23	87	72	167				
		18	89	67	116				
		19	89	61	143				
Carboxyl		23	97	77	156				
		8					22		Baughman et al. [78]
		14					-4		
		20	45	42					
		20	49	33	52				Ortmann et al. [61]
Gem-dimethyl		44	79, 99	85	100				
		8					-47		Schwendeman et al. [132]
		14	32	-39	40	-42			
		20	45	8.5	61	-22			
		10	-40, -30	-58	35	-62			Baughman et al. [123]
Methoxy		14	-10	-22	62				
		20	40	22	78				
		20	40	23	80				Baughman et al. [122]
		10	-4	-35	33	-65			Baughman et al. [123]
		14	-33	-40	36				
Ethoxy		20	28	10	79				

(continued)

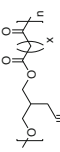
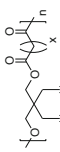
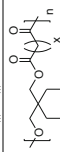
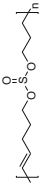


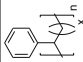
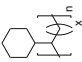
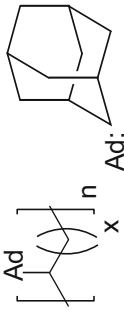
Table A2 (continued)

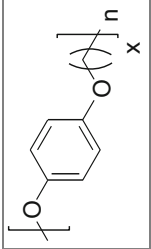
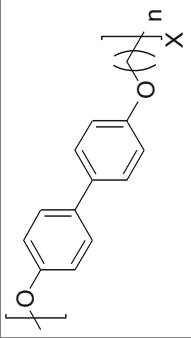
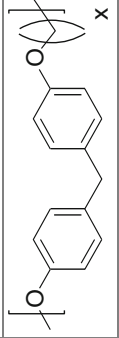
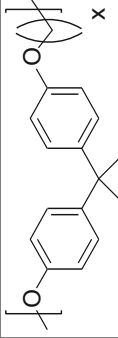
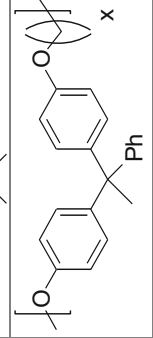
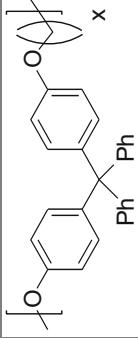
Group	Structure	CH <sub>2</sub> sequence (x)	T <sub>m</sub> (°C)	T <sub>c</sub> (°C)	ΔH <sub>m</sub> (J/g)	T <sub>g</sub> (°C)	References	
Acetoxy		18	23				Watson and Wagener [124]	
		20	35					
		22	41					
		26	57					
ADMET atactic		7	53	9	39	-36	Zhang et al. [9]	
		8				-46		
ROMP atactic		7	91	59	67	-30		
Methyl acrylate		18	14.4				Watson and Wagener [125]	
		22	37					
		18	9.8, 15.1					
Ethyl acrylate		18						
Methacrylic		20	13	4.5	21		Schwendeman et al. [133]	
Methacrylate		20	7	-1.3	49		Schwendeman et al. [133]	
Tert-butyl oxycarbonyl (Boc) amine		8				4	Leonard et al. [120]	
		14				2		
		18						-8
		20						2

Amphiphilic Tetra(ethylene glycol)		8										Berda et al. [134]	
Amphiphilic branches: Tetra(ethylene glycol) with different hydrophobic segments		20	-3	-34	19	-65							
	R = Pyrene group	20	29	20	36	-63							
		20	9	-12	25	-21							Berda et al. [135]
	R = <i>n</i> -hexyl group	20	4, 11, -37, -48	-4, 0	28								
		20	23	17	72								
	R = <i>n</i> -tetradecyl	20											
Sulfonic acid ethyl ester		20	29	24	34								Opper et al. [136]
Aromatic sulfonic ethyl acid ester		20											Opper et al. [136]
Phosphonic acid		8				44							Opper et al. [137]
Single phosphonic ester		14				45							
		20	48, 67		23, 22								
Geminal phosphonic acid		8				-57							
		14				-61							
Benzyl phosphonic acid		20	11, 13	3	55								
		14				32							
Benzyl phosphonic ester		20	87		120								
		14				43							
Benzyl phosphonic ester		20	46		42								
		14				-25							
		20	2		47								

(continued)

Table A2 (continued)

Group	Structure	CH <sub>2</sub> sequence (x)	T <sub>m</sub> (°C)	T <sub>c</sub> (°C)	ΔH <sub>m</sub> (J/g)	T <sub>g</sub> (°C)	References
Esters with perfluoroalkyl segments		18	98, 108	90, 103	99.8, 12.3		Mandal et al. [138]
		18	110, 128	104, 121	57, 14.1		
		18	71	66, 68.4	98.76		
Sulfite		8	–	–	–	–	Gaines et al. [67]
		14	7	–	49	–	
		20	37	–	63	–	
Phenyl		18	–1.5, –22.5	–23.6	–	–	Watson and Wagener [125]
Cyclohexyl		20	9	–	37	–	Rojas et al. [93]
Adamantyl		20	–8, 17	–	2, 8	–	Rojas et al. [93]

Aryl ether units		20	123.3, 134.9	120.1		Song et al. [139]
		20	128.2, 133.1	119.9		
		20	127.2, 132.4			
		20	77.6, 90.4			
		20	-		-6	
		20	-		20	

Available data for melting temperature ( $T_m$ ), crystallization temperature ( $T_c$ ), heat of melting ( $\Delta H_m$ ) and glass transition temperature ( $T_g$ ) are listed

<sup>a</sup>Polyesters with possible head-head, head-tail, and tail-tail orientation (1:2:1 ratio)

<sup>b</sup>A melting peak is not apparent in the endotherm shown for this sample

## References

1. Markets and Markets (2013) Polyolefins market by types, applications & geography – Global trends & forecasts to 2018. Markets and Markets, Dallas. [www.marketsandmarkets.com](http://www.marketsandmarkets.com)
2. Brintzinger HH, Fischer D, Mulhaupt R, Rieger B, Waymouth RM (1995) Stereospecific olefin polymerization with chiral metallocene catalysts. *Angew Chem Int Ed Engl* 34:1143–1170
3. Scheirs J, Kaminsky W (eds) (2000) Metallocene-based polyolefin, vol 2. Wiley, Chichester
4. Carrow BP, Nozaki K (2014) Transition-metal-catalyzed functional polyolefin synthesis: effecting control through chelating ancillary ligand design and mechanistic insights. *Macromolecules* 47:2541–2555
5. Berda EB, Wagener KB (2011) Precision polyolefins. In: Hadjichristidis N, Hirao A, Tezuka Y, Du Prez F (eds) *Complex macromolecular architectures: synthesis, characterization and self-assembly*, chap 10. Wiley, Singapore, p 317
6. Bielawski CW, Grubbs RH (2007) Living ring-opening metathesis polymerization. *Prog Polym Sci* 32:1–29
7. Kobayashi S, Pitet LM, Hillmyer MA (2011) Regio- and stereoselective ring-opening metathesis polymerization of 3-substituted cyclooctenes. *J Am Chem Soc* 133:5794–5797
8. Zhang J, Matta ME, Hillmyer MA (2012) Synthesis of sequence-specific vinyl copolymers by regioselective ROMP of multiply substituted cyclooctenes. *ACS Macro Lett* 1:1383–1387
9. Zhang J, Matta ME, Martinez H, Hillmyer MA (2013) Precision vinyl acetate/ethylene (VAE) copolymers by ROMP of acetoxy-substituted cyclic alkenes. *Macromolecules* 46:2535–2543
10. Ortmann P, Mecking S (2013) Long-spaced aliphatic polyesters. *Macromolecules* 46:7213–7218
11. Ortmann P, Heckler I, Mecking S (2014) Physical properties and hydrolytic degradability of polyethylene-like polyacetals and polycarbonates. *Green Chem* 16:1816–1827
12. Ortmann P, Lemke TA, Mecking S (2015) Long-spaced polyamides: elucidating the gap between polyethylene crystallinity and hydrogen bonding. *Macromolecules* 48:1463–1472
13. Ortmann P, Wimmer FP, Mecking S (2015) Long-spaced polyketones from ADMET copolymerizations as ideal models for ethylene/CO copolymers. *ACS Macro Lett* 4:704–707
14. Hillmyer MA, Laredo WR, Grubbs RH (1995) Ring-opening metathesis polymerization of functionalized cyclooctenes by a ruthenium-based metathesis catalyst. *Macromolecules* 28:6311–6316
15. Alamo RG, Mandelkern L (1994) The crystallization behavior of random copolymers of ethylene. *Thermochim Acta* 238:155–201
16. Crist B (2003) Thermodynamics of statistical copolymer melting. *Polymer* 44:4563–4572
17. Mandelkern L (2002) *Crystallization of polymers*, vol 1. Cambridge University Press, Cambridge, Chap 5
18. Mathot VBF, Reynaers H (2002) Crystallization, melting and morphology of homogeneous ethylene copolymers. In: Cheng SZD (ed) *Handbook of thermal analysis and calorimetry*, vol 3. Applications to polymers and plastics. Elsevier, Amsterdam, p 197
19. Li S, Register RA (2013) Crystallization in copolymers. In: Piorkowska E, Rutledge GC (eds) *Handbook of polymer crystallization*, 1st edn. Wiley, Hoboken, pp 327–346
20. Hu W, Gao H, Mathot V, Chen X, Alamo RG (2015) Crystallization of Statistical Copolymers. *Adv Polym Sci* (this issue)
21. Flory PJ (1955) Theory of crystallization in copolymers. *Trans Faraday Soc* 51:848–857
22. Alamo R, Domszy R, Mandelkern L (1984) Thermodynamic and structural properties of copolymers of ethylene. *J Phys Chem* 88:6587–6595
23. Alamo RG, Mandelkern L (1989) Thermodynamic and structural properties of ethylene copolymers. *Macromolecules* 22:1273–1277
24. Alamo RG, Mandelkern L (1991) Crystallization kinetics of ethylene copolymers. *Macromolecules* 24:6480–6493

25. Alamo RG, Chan EKM, Mandelkern L, Voigt-Martin IG (1992) The influence of molecular weight on the melting and phase structure of random copolymers of ethylene. *Macromolecules* 25:6381–6394
26. Alamo RG, Viers BD, Mandelkern L (1993) Phase structure of random ethylene copolymers: a study of the comonomer content and molecular weight as independent variables. *Macromolecules* 26:5740–5747
27. Isasi JR, Haigh JA, Graham JT, Mandelkern L, Alamo RG (2000) Some aspects of the crystallization of ethylene copolymers. *Polymer* 41:8813–8823
28. Alizadeh A, Richardson L, Xu J, McCartney S, Marand H, Cheung YW, Chum S (1999) Influence of structural and topological constraints on the crystallization and melting behavior of polymers. 1. Ethylene/1-octene copolymers. *Macromolecules* 32:6221–6235
29. Defoor F, Groeninckx G, Reynaers H, Schouterden P, Van der Heijden B (1993) Molecular, thermal, and morphological characterization of narrowly branched fractions of 1-octene linear low-density polyethylene. 3. Lamellar and spherulitic morphology. *Macromolecules* 26:2575–2582
30. Bensason S, Minick J, Moet A, Chum S, Hiltner A, Baer E (1996) Classification of homogeneous ethylene-octene copolymers based on comonomer content. *J Polym Sci B Polym Phys* 34:1301–1315
31. Walter ER, Reding FP (1956) Variations in unit cell dimensions in polyethylene. *J Polym Sci* 21:561–562
32. Cole EA, Holmes DR (1960) Crystal lattice parameters and the thermal expansion of linear paraffin hydrocarbons, including polyethylenes. *J Polym Sci* 46:245–256
33. Swan PR (1962) Polyethylene unit cell variations with branching. *J Polym Sci* 56:409–416
34. Ruiz de Ballesteros O, Auriemma F, Guerra G, Corradini P (1996) Molecular organization in the pseudo-hexagonal crystalline phase of ethylene–propylene copolymers. *Macromolecules* 29:7141–7148
35. Baker CH, Mandelkern L (1965) The crystallization and melting of copolymers II—variation in unit-cell dimensions in polymethylene copolymers. *Polymer* 7:71–83
36. Richardson MJ, Flory PJ, Jackson JB (1963) Crystallization and melting of copolymers of polymethylene. *Polymer* 4:221–236
37. Ver Strate G, Wilchinsky ZW (1971) Ethylene-propylene copolymers: degree of crystallinity and composition. *J Polym Sci Part A-2*(9):127–142
38. Stephens CH, Yang H, Islam M, Chum SP, Rowan SJ, Hiltner A, Baer E (2003) Characterization of polyethylene with partially random chlorine substitution. *J Polym Sci Part B Polym Phys* 41:2062–2070
39. Gomez MA, Tonelli AE, Lovinger AJ, Schilling FC, Cozine MH, Davis DD (1989) Structure and morphology of ethylene-vinyl chloride copolymers. *Macromolecules* 22:4441–4451
40. Stoeva S, Popov A, Rodriguez R (2004) Wide angle X-ray diffraction study of the solid-phase chlorinated poly(ethylene). *Polymer* 45:6341–6348
41. Kalepky U, Fischer EW, Herchenroder P, Schelten J, Lieser G, Wegner G (1979) Characterization of semicrystalline random copolymers by small-angle neutron scattering. *J Polym Sci Part B Polym Phys* 17:2117–2131
42. Landes BG, Harrison IR (1987) The location of comonomer units in crystallizable copolymers: brominated polyethylene. *Polymer* 28:911–917
43. Bunn CW, Peiser HS (1947) Mixed crystal formation in high polymers. *Nature* 159:161–162
44. Chatani Y, Takizawa T, Murahashi S (1962) Crystal structures of polyketones (ethylene/carbon monoxide copolymers). *J Polym Sci* 62:S27–S30
45. Wunderlich B (1976) *Macromolecular physics*, vol 1. Academic Press, New York
46. Sanchez IC, Eby RK (1975) Thermodynamics and crystallization of random copolymers. *Macromolecules* 8:638–641
47. Helfand E, Lauritzen JJ Jr (1973) Theory of copolymer crystallization. *Macromolecules* 6: 631–638



48. Alamo RG, VanderHart DL, Nyden MR, Mandelkern L (2000) Morphological partitioning of ethylene defects in random propylene-ethylene copolymers. *Macromolecules* 33:6094–6105
49. VanderHart DL, Alamo RG, Nyden MR, Kim MH, Mandelkern L (2000) Observation of resonances associated with stereo and regio defects in the crystalline regions of isotactic polypropylene: towards a determination of morphological partitioning. *Macromolecules* 33: 6078–6093
50. Nyden MR, VanderHart DL, Alamo RG (2001) The conformational structures of defect-containing chains in the crystalline regions of isotactic polypropylenes. *Comput Theor Polym S* 11:175–189
51. De Rosa C, Auriemma F, Capitani D, Caporaso L, Talarico G (2000) Solid state  $^{13}\text{C}$  NMR analysis of syndiotactic copolymers of propene with 1-butene. *Polymer* 41:2141–2148
52. Ruiz-Orta C, Alamo RG (2012) Morphological and kinetic comonomer partitioning in random propylene 1-butene copolymers. *Polymer* 53:810–822
53. Otocka EP, Kwei TK (1968) Properties of ethylene-acrylic acid copolymers. *Macromolecules* 1:244–249
54. Eisenberg A, Hird B, Moore RB (1990) A new multiplet-cluster model for the morphology of random ionomers. *Macromolecules* 23:4098–4107
55. Ding YS, Hubbard SR, Hodgson KO, Register RA, Cooper SL (1988) Anomalous small-angle X-ray scattering from a sulfonated polystyrene ionomer. *Macromolecules* 21: 1698–1703
56. Laurer JH, Winey KI (1998) Direct imaging of ionic aggregates in Zn-neutralized poly(ethylene-co-methacrylic acid) copolymers. *Macromolecules* 31:9106–9108
57. Voigt-Martin IG, Mandelkern L (1989) In: Cheremisinoff NP (ed) *Handbook of polymer science and technology*, vol. 3. Marcel Dekker, New York, p 99
58. Vadlamudi M, Subramanian G, Shanbhag S, Alamo RG, Varma-Nair M, Fiscus DM, Brown GM, Lu C, Ruff CJ (2009) Molecular weight and branching distribution of a high performance metallocene ethylene 1-hexene copolymer film-grade resin. *Macromol Symp* 282:1–13
59. Mamun A, Chen X, Alamo RG (2014) Interplay between a strong memory effect of crystallization and liquid-liquid phase separation in melts of broadly distributed ethylene-1-alkene copolymers. *Macromolecules* 47:7958–7970
60. Le Fevere De Ten Hove C, Penelle J, Ivanov DA, Jonas AM (2004) Encoding crystal microstructure and chain folding in the chemical structure of synthetic polymers. *Nat Mater* 3: 33–37
61. Ortmann P, Trzaskowski J, Krumova M, Mecking S (2013) Precise microstructure self-stabilized polymer nanocrystals. *ACS MacroLett* 2:125–127
62. Hosoda S, Nozue Y, Kawashima Y, Suita K, Seno S, Nagamatsu T, Wagener KB, Inci B, Zuluaga F, Rojas G, Leonard JK (2011) Effect of the sequence length distribution on the lamellar crystal thickness and thickness distribution of polyethylene: perfectly equisequential ADMET polyethylene vs ethylene/ $\alpha$ -olefin copolymer. *Macromolecules* 44:313–319
63. Hosoda S, Nozue Y, Kawashima Y, Utsumi S, Nagamatsu T, Wagener K, Berda E, Rojas G, Baughman T, Leonard J (2009) Perfectly controlled lamella thickness and thickness distribution: a morphological study on ADMET polyolefins. *Macromol Symp* 282:50–64
64. Kaner P, Ruiz-Orta C, Boz E, Wagener KB, Tasaki M, Tashiro K, Alamo RG (2014) Kinetic control of chlorine packing in crystals of a precisely substituted polyethylene. Toward advanced polyolefin materials. *Macromolecules* 47:236–245
65. Tasaki M, Yamamoto H, Hanesaka M, Tashiro K, Boz E, Wagener KB, Ruiz-Orta C, Alamo RG (2014) Polymorphism and phase transitions of precisely halogen-substituted polyethylene. (1) Crystal structures of various crystalline modifications of bromine-substituted polyethylene on every 21st backbone carbon. *Macromolecules* 47:4738–4749
66. Seitz ME, Chan CD, Opper KL, Baughman TW, Wagener KB, Winey KI (2010) Nanoscale morphology in precisely sequenced poly(ethylene-co-acrylic acid) zinc ionomers. *J Am Chem Soc* 132:8165–8174

67. Gaines TW, Nakano T, Chujo Y, Trigg EB, Winey KI, Wagener KB (2015) Precise sulfite functionalization of polyolefins via ADMET polymerization. *ACS Macro Lett* 4:624–627
68. Boz E, Wagener KB, Ghosal A, Fu R, Alamo RG (2006) Synthesis and crystallization of precision ADMET polyolefins containing halogens. *Macromolecules* 39:4437–4447
69. Boz E, Nemeth AJ, Alamo RG, Wagener KB (2007) Precision ethylene vinyl bromide polymers. *Adv Synth Catal* 349:137–141
70. Boz E, Nemeth AJ, Ghiviriga I, Jeon K, Alamo RG, Wagener KB (2007) Precision ethylene/vinyl chloride polymers via condensation polymerization. *Macromolecules* 40:6545–6551
71. Boz E, Nemeth AJ, Wagener KB, Jeon K, Smith R, Nazirov F, Bockstaller MR, Alamo RG (2008) Well-defined precision ethylene/vinyl fluoride polymers: synthesis and crystalline properties. *Macromolecules* 41:1647–1653
72. Boz E, Ghiviriga I, Nemeth AJ, Jeon K, Alamo RG, Wagener KB (2008) Random, defect-free ethylene/vinyl halide model copolymers via condensation polymerization. *Macromolecules* 41:25–30
73. Alamo RG, Jeon K, Smith RL, Boz E, Wagener KB, Bockstaller MR (2008) Crystallization of polyethylenes containing chlorines: precise vs random placement. *Macromolecules* 41:7141–7151
74. Schulz MD, Wagener KB (2014) Precision polymers through ADMET polymerization. *Macromol Chem Phys* 215:1936–1945
75. Smith JA, Brzezinska KR, Valenti DJ, Wagener KB (2000) Precisely controlled methyl branching in polyethylene via acyclic diene metathesis (ADMET) polymerization. *Macromolecules* 33:3781–3794
76. Pepels MPF, Hansen MR, Goossens H, Duchateau R (2013) From polyethylene to polyester: influence of ester groups on the physical properties. *Macromolecules* 46:7668–7677
77. Gutzler F, Wegner G (1980) Synthesis and melting behavior of poly(ethylene) copolymers obtained by polymeranalogous reaction. *Colloid Polym Sci* 258:776–786
78. Baughman TW, Chan CD, Winey KI, Wagener KB (2007) Synthesis and morphology of well-defined poly(ethylene-co-acrylic acid) copolymers. *Macromolecules* 40:6564–6571
79. Matsui K, Seno S, Nozue Y, Shinohara Y, Amemiya Y, Berda EB, Rojas G, Wagener KB (2013) Influence of branch incorporation into the lamella crystal on the crystallization behavior of polyethylene with precisely spaced branches. *Macromolecules* 46:4438–4446
80. Bowner TN, Tonelli AE (1986) Infrared spectroscopy of ethylene–vinyl chloride copolymers. *J Polym Sci Part B Polym Phys* 24:1631–1650
81. Tonelli AE, Bowner TN (1987) C–Cl stretching vibrations in ethylene–vinyl chloride copolymers. *J Polym Sci Part B Polym Phys* 25:1153–1156
82. Snyder RG, Schachtschneider JH (1963) Vibrational analysis of the n-paraffins I: assignments of infrared bands in the spectra of C<sub>3</sub>H<sub>8</sub> through n-C<sub>19</sub>H<sub>40</sub>. *Spectrochim Acta* 19:85–116
83. Snyder RG (1960) Vibrational spectra of crystalline n-paraffins: part I. Methylene rocking and wagging modes. *J Mol Spectrosc* 4:411–434
84. Yu GS, Li HW, Hollander F, Snyder RG, Strauss HL (1999) Comparison of the structures of ammonium myristate, palmitate, and stearate by X-ray diffraction, infrared spectroscopy, and infrared hole burning. *J Phys Chem B* 103:10461–10468
85. Yan WH, Strauss HL, Snyder RG (2000) Conformation of the acyl chains in diacylphospholipid gels by IR spectroscopy. *J Phys Chem B* 104:4229–4238
86. Venkataraman NV, Vasudevan S (2001) Interdigitation of an intercalated surfactant bilayer. *J Phys Chem B* 105:7639–7650
87. Tasaki M, Yamamoto H, Yoshioka T, Hanesaka M, Ninh TH, Tashiro K, Jeon HJ, Choi KB, Jeong HS, Song HH, Ree MH (2014) Microscopically-viewed relationship between the chain conformation and ultimate Young's modulus of a series of arylate polyesters with long methylene segments. *Polymer* 55:1799–1808

88. Desiraju GR, Parthasarathy R (1989) The nature of halogen-halogen interactions: are short halogen contacts due to specific attractive forces or due to close packing of nonspherical atoms? *J Am Chem Soc* 111:8725–8726
89. Wagener KB, Valenti D, Hahn SF (1997) ADMET modeling of branching in polyethylene. The effect of a perfectly-spaced methyl group. *Macromolecules* 30:6688–6690
90. Lieser G, Wegner G, Smith JA, Wagener KB (2004) Morphology and packing behavior of model ethylene/propylene copolymers with precise methyl branch placement. *Colloid Polym Sci* 282: 773–781
91. Baughman TW, Sworen JC, Wagener KB (2006) Sequenced ethylene-propylene copolymers: effects of short ethylene run lengths. *Macromolecules* 39:5028–5036
92. Wei Y, Graf R, Sworen JC, Cheng C-Y, Bowers CR, Wagener KB, Spiess HW (2009) Local and collective motions in precise polyolefins with alkyl branches: A combination of  $^2\text{H}$  and  $^{13}\text{C}$  solid-state NMR spectroscopy. *Angew Chem Int Ed* 48:4617–4620
93. Rojas G, Inci B, Wei Y, Wagener KB (2009) Precision polyethylene: changes in morphology as a function of alkyl branch size. *J Am Chem Soc* 131:17376–17386
94. Inci B, Lieberwirth I, Steffen W, Mezger M, Graf R, Landfester K, Wagener KB (2012) Decreasing the alkyl branch frequency in precision polyethylene: effect of alkyl branch size on nanoscale morphology. *Macromolecules* 45:3367–3376
95. Sworen JC, Smith JA, Berg JM, Wagener KB (2004) Modeling branched polyethylene: copolymers possessing precisely placed ethyl branches. *J Am Chem Soc* 126:11238–11246
96. Nozue Y, Seno S, Nagamatsu T, Hosoda S, Shinohara Y, Amemiya T, Berda EB, Rojas G, Wagener KB (2012) Cross nucleation in polyethylene with precisely spaced ethyl branches. *ACS Macro Lett* 1:772–775
97. Zuluaga F, Inci B, Nozue Y, Hosoda S, Wagener KB (2009) Reducing branch frequency in precision polyethylene. *Macromolecules* 42:4953–4955
98. Rojas G, Wagener KB (2009) Precisely and irregularly sequenced ethylene/1-hexene copolymers: a synthesis and thermal study. *Macromolecules* 42:1934–1947
99. Sworen JC, Wagener KB (2007) Linear low-density polyethylene containing precisely placed hexyl branches. *Macromolecules* 40:4414–4423
100. Few CS, Wagener KB, Thompson DL (2014) Systematic studies of morphological changes of precision polyethylene. *Macromol Rapid Commun* 35:123–132
101. Inci B, Wagener KB (2011) Decreasing the alkyl branch frequency in precision polyethylene: pushing the limits toward longer run lengths. *J Am Chem Soc* 133:11872–11875
102. Berda EB, Baughman TW, Wagener KB (2006) Precision branching in ethylene copolymers: synthesis and thermal behavior. *J Polym Sci Part A Polym Chem* 44:4981–4989
103. Rojas G, Berda EB, Wagener KB (2008) Precision polyolefin structure: modeling polyethylene containing alkyl branches. *Polymer* 49:2985–2995
104. Schulz MD, Sauty NF, Wagener KB (2015) Morphology control in precision polyolefins. *Appl Petrochem Res* 5:3–8
105. Mutlu H, Montero De Espinosa L, Meier MAR (2011) Acyclic diene metathesis: a versatile tool for the construction of defined polymer architectures. *Chem Soc Rev* 40:1404–1445
106. Hall LM, Stevens MJ, Frischknecht AL (2012) Dynamics of model ionomer melts of various architectures. *Macromolecules* 45:8097–8108
107. Alam TM, Jenkins JE, Bolintineanu DS, Stevens MJ, Frischknecht AL, Buitrago CF, Winey KI, Opper KL, Wagener KB (2012) Heterogeneous coordination environments in lithium-neutralized ionomers identified using  $^1\text{H}$  and  $^7\text{Li}$  MAS NMR. *Materials* 5:1508–1527
108. Hall LM, Seitz ME, Winey KI, Opper KL, Wagener KB, Stevens MJ, Frischknecht AL (2012) Ionic aggregate structure in ionomer melts: effect of molecular architecture on aggregates and the ionomer peak. *J Am Chem Soc* 134:574–587
109. Aitken BS, Buitrago CF, Heffley JD, Lee M, Gibson HW, Winey KI, Wagener KB (2012) Precise ionomers: synthesis and thermal/mechanical characterization. *Macromolecules* 45: 681–687

110. Buitrago CF, Alam TM, Opper KL, Aitken BS, Wagener KB, Winey KI (2013) Morphological trends in precise acid- and ion-containing polyethylenes at elevated temperature. *Macromolecules* 46:8995–9002
111. Buitrago CF, Jenkins JE, Opper KL, Aitken BS, Wagener KB, Alam TM, Winey KI (2013) Room temperature morphologies of precise acid- and ion-containing polyethylenes. *Macromolecules* 46:9003–9012
112. Choi UH, Middleton LR, Soccio M, Buitrago CF, Aitken BS, Masser H, Wagener KB, Winey KI, Runt J (2015) Dynamics of precise ethylene ionomers containing ionic liquid functionality. *Macromolecules* 48:410–420
113. Buitrago CF, Opper KL, Wagener KB, Winey KI (2012) Precise acid copolymer exhibits a face-centered cubic structure. *ACS Macro Lett* 1:71–74
114. Buitrago CF, Bolintineanu DS, Seitz ME, Opper KL, Wagener KB, Stevens MJ, Frischknecht AL, Winey KI (2015) Direct comparisons of X-ray scattering and atomistic molecular dynamics simulations for precise acid copolymers and ionomers. *Macromolecules* 48:1210–1220
115. Middleton LR, Szewczyk S, Azoulay J, Murtagh D, Rojas G, Wagener KB, Cordaro J, Winey KI (2015) Hierarchical acrylic acid aggregate morphologies produce strain-hardening in precise polyethylene-based copolymers. *Macromolecules* 48:3713–3724
116. Ramakrishnan S (1991) Well-defined ethylene-vinyl alcohol copolymers via hydroboration: control of composition and distribution of the hydroxyl groups on the polymer backbone. *Macromolecules* 24:3753–3759
117. Valenti DJ, Wagener KB (1998) Direct synthesis of well-defined alcohol-functionalized polymers via acyclic diene metathesis (ADMET) polymerization. *Macromolecules* 31:2764–2773
118. Thompson D, Yamakado R, Wagener KB (2014) Extending the methylene spacer length of ADMET hydroxy-functionalized polymers. *Macromol Chem Phys* 215:1212–1217
119. Thompson DL, Wagener KB, Schulze U, Voit B, Jehnichen D, Malanin M (2015) Spectroscopic examinations of hydrogen bonding in hydroxy-functionalized ADMET chemistry. *Macromol Rapid Comm* 36:60–64
120. Leonard JK, Wei Y, Wagener KB (2012) Synthesis and thermal characterization of precision poly(ethylene-co-vinyl amine) copolymers. *Macromolecules* 45:671–680
121. German I, D'Agosto F, Boisson C, Tencé-Girault S, Soulié-Ziakovic C (2015) Microphase separation and crystallization in H-bonding end-functionalized polyethylenes. *Macromolecules* 48:3257–3268
122. Baughman TW, van der Aa E, Lehman SE, Wagener KB (2005) Circumventing the reactivity ratio dilemma: synthesis of ethylene-co-methyl vinyl ether copolymer. *Macromolecules* 38:2550–2551
123. Baughman TW, van der Aa E, Wagener KB (2006) Linear ethylene-vinyl ether copolymers: synthesis and thermal characterization. *Macromolecules* 39:7015–7021
124. Watson MD, Wagener KB (2000) Ethylene/vinyl acetate copolymers via acyclic diene metathesis polymerization. Examining the effect of “long” precise ethylene run lengths. *Macromolecules* 33:5411–5417
125. Watson MD, Wagener KB (2000) Functionalized polyethylene via acyclic diene metathesis polymerization: effect of precise placement of functional groups. *Macromolecules* 33:8963–8970
126. Watson MD, Wagener KB (2000) Tandem homogeneous metathesis/heterogeneous hydrogenation: preparing model ethylene/CO<sub>2</sub> and ethylene/CO copolymers. *Macromolecules* 33:3196–3201
127. van der Meulen I, de Geus M, Antheunis H, Deumens R, Joosten EA, Koning CE, Heise A (2008) Polymers from functional macrolactones as potential biomaterials: enzymatic ring opening polymerization, biodegradation, and biocompatibility. *Biomacromolecules* 9:3404–3410

128. Pepels MPF, Govaert LE, Duchateau R (2015) Influence of the main-chain configuration on the mechanical properties of linear aliphatic polyesters. *Macromolecules* 48:5845–5854
129. Scherman OA, Walker R, Grubbs RH (2005) Synthesis and characterization of stereoregular ethylene-vinyl alcohol copolymers made by ring-opening metathesis polymerization. *Macromolecules* 38:9009–9014
130. Broadhurst MG (1962) An analysis of the solid phase behavior of the normal paraffins. *J Res Nat Bur St A Phys Chem* 66A:241–249
131. Qiu W, Sworen J, Pyda M, Nowak-Pyda E, Habenschuss A, Wagener KB, Wunderlich B (2006) Effect of the precise branching of polyethylene at each 21st CH<sub>2</sub> group on its phase transitions, crystal structure, and morphology. *Macromolecules* 39:204–217
132. Schwendeman JE, Wagener KB (2005) gem-Dimethyl effects in the thermal behavior of polyethylene. *Macromol Chem Phys* 206:1461–1471
133. Schwendeman JE, Wagener KB (2004) Modeling ethylene/methyl methacrylate and ethylene/methacrylic acid copolymers using acyclic diene metathesis chemistry. *Macromolecules* 37:4031–4037
134. Berda EB, Lande RE, Wagener KB (2007) Precisely defined amphiphilic graft copolymers. *Macromolecules* 40:8547–8552
135. Berda EB, Wagener KB (2008) Inducing pendant group interactions in precision polyolefins: synthesis and thermal behavior. *Macromolecules* 41:5116–5122
136. Opper KL, Wagener KB (2009) Precision sulfonic acid ester copolymers. *Macromol Rapid Commun* 30:915–919
137. Opper KL, Markova D, Klapper M, Mullen K, Wagener KB (2010) Precision phosphonic acid functionalized polyolefin architectures. *Macromolecules* 43:3690–3698
138. Mandal J, Prasad SK, Rao DSS, Ramakrishnan S (2014) Periodically clickable polyesters: study of intrachain self-segregation induced folding, crystallization, and mesophase formation. *J Am Chem Soc* 136:2538–2545
139. Song S, Miao W, Wang Z, Gong D, Chen ZR (2015) Synthesis and characterization of precisely-defined ethylene-co-aryl ether polymers via ADMET polymerization. *Polymer* 64:76–83

# Supramolecular Crystals and Crystallization with Nanosized Motifs of Giant Molecules

**Xue-Hui Dong, Chih-Hao Hsu, Yiwen Li, Hao Liu, Jing Wang, Mingjun Huang, Kan Yue, Hao-Jan Sun, Chien-Lung Wang, Xinfei Yu, Wen-Bin Zhang, Bernard Lotz, and Stephen Z.D. Cheng**

**Abstract** Supramolecular crystals and crystallization are general concepts used to describe broader aspects of ordered structures and their formation in the three-dimensional (3D) bulk and solution and in 2D thin film states at length scales ranging from sub-nanometers to sub-micrometers. Although the fundamental crystallographic principles are still held in these structures, starting from their basic repeating units (motifs), it is not necessary that each atomic position within their motifs possesses translational symmetry in long range order, but could have quasi-long range or short range order. As a result, the motif becomes the smallest unit for constructing 3D or 2D ordered structures that maintain the long range translational order. The formation of these supramolecular ordered structures essentially follows the physical principle of phase transformations, involving either nucleation and

---

Xue-Hui Dong and Chih-Hao Hsu are equally contributed.

X.-H. Dong, C.-H. Hsu, Y. Li, H. Liu, J. Wang, M. Huang, K. Yue, H.-J. Sun, C.-L. Wang, X. Yu, and S.Z.D. Cheng (✉)

Department of Polymer Science, College of Polymer Science and Polymer Engineering,  
The University of Akron, Akron, OH 44325-3909, USA  
e-mail: [scheng@uakron.edu](mailto:scheng@uakron.edu)

W.-B. Zhang (✉)

Department of Polymer Science, College of Polymer Science and Polymer Engineering,  
The University of Akron, Akron, OH 44325-3909, USA

Key Laboratory of Polymer Chemistry and Physics of Ministry of Education, College of  
Chemistry and Molecular Engineering, Center for Soft Matter Science and Engineering,  
Peking University, Beijing 100871, China

e-mail: [wenbin@pku.edu.cn](mailto:wenbin@pku.edu.cn)

B. Lotz (✉)

Institut Charles Sadron (CNRS-Université de Strasbourg), 23, Rue du Loess, 67034  
Strasbourg, France

e-mail: [bernard.lotz@ics-cnrs.unistra.fr](mailto:bernard.lotz@ics-cnrs.unistra.fr)

growth or spinodal decomposition mechanisms. However, larger ordered structures require stronger and more cooperative interactions to sustain their structures in equilibrium or stable states. We propose utilization of collective secondary interactions, similar to those found in biological and living systems, to generate sufficient interactions and stabilize these structures. Furthermore, when the basic unit of the structure becomes increasingly larger and heavier, thermal (density) fluctuations during the phase transitions may not be sufficiently large to overcome transition barriers of the basic unit. In these cases, external fields might be required to stimulate the magnitude of thermal (density) fluctuation and/or redistribute (thus, decrease) a single transition barrier into several stepwise transition sequences with lower barriers for each transition, and thus increase the speed of phase transformations.

**Keywords** Crystallization • Giant molecules • Molecular nanoparticles • Nanoatoms • Supramolecular crystal

## Contents

1	Concept of Giant Molecules .....	184
2	Supramolecular Crystals and Crystallization .....	187
3	Giant Shape Amphiphiles .....	190
4	Giant Janus Particles .....	194
5	Giant Surfactants .....	198
6	Giant Tetrahedra .....	203
7	Thin Films of Giant Molecules .....	206
8	Concluding Remarks .....	209
	References .....	210

## 1 Concept of Giant Molecules

Rapid developments in polymer materials since Staudinger's macromolecular hypothesis [1] have revolutionized the whole field of science and engineering, and generated significant impact on human society. These materials are now popularly beneficial to our daily life. However, precise control of chemical primary structure and composition and accurate construction of hierarchal physical structures in synthetic polymers (similar to natural polymers such as nuclei acids and proteins) remain grand challenges. Traditional approaches in designing and synthesizing polymers usually start from currently available or newly synthesized monomer units as building blocks, within which covalent links are established between different atoms using chemical principles. Utilizing various polymerization reactions such as anionic, cationic, condensation, free radical, and coordination, the monomers are connected in different ways to generate polymers with linear, branched, or other architectures [2]. This type of approach intrinsically leads to an understanding that polymer properties are evidently associated with molecular weight (MW) and its distribution, tacticity, and topology, but less appreciated are the effects of controlling supramolecular structure across different length scales.

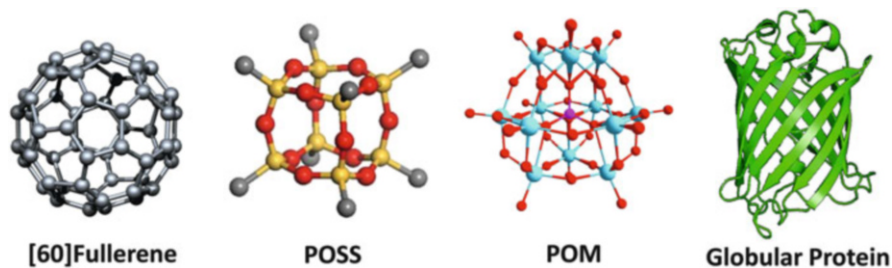
Nevertheless, these supramolecular structures at different mesoscales are crucially important for transferring and amplifying microscopic functions to macroscopic properties.

About 60 years ago a great physicist, R. Feynman, asked a fundamental question: “What would the properties of materials be if we could really arrange the atoms the way we want them?” [3]. To fully address Feynman’s question, we are required not only to know the primary chemical structures of materials, but also to control sequential and hierarchical secondary, tertiary, and quaternary structures so that we can completely understand how each structure at different length scales affects the final properties of the material. To seek solutions to Feynman’s inquiry in the context of macromolecular science, precision syntheses of primary chemical structures and accurate control over higher level supramolecular structures are prerequisites. In other words, simply connecting monomers in a desired sequence is not sufficient to achieve a desired property for a specific polymer.

What we need to do is to follow the principles of chemistry and physics and integrate them into an ever-increasing sophistication of molecular, supramolecular, and structural design to direct development of new functional macromolecules. Yet, the unique features of polymers (large size, large number of functional groups, difficulties associated with purification, large degrees of conformational freedom, and so on) have made precision synthesis of polymers yet to be demonstrated [4]. An approach we have adopted to possibly overcome these difficulties is the modular construction of macromolecules (a word taken in the present context to have a broader meaning than “polymers”) using precisely defined molecular nanoscale building blocks [5–7]. Example of precisely synthesized macromolecules are dendrimers with a cascade topology, which are regularly branched and monodisperse, yet without shape persistence [8–10]. Many investigations have been carried out on dendron–polymer conjugates [11–13] and Janus dendrimers [14–16]. When we think of macromolecular precision syntheses, nanoscale building blocks must possess relatively independent, modular, and well-defined three-dimensional (3D) structure and shape so that further assembly into a variety of hierarchal structures at different length scales is predictable and robust.

As modular building blocks, we propose the use of molecular nanoparticles (MNPs), which are shape- and volume-persistent nano-objects with well-defined molecular structure and specific symmetry [5]. Typical MNPs under consideration include cage-like compounds and folded globular proteins (Fig. 1) with compact and rigid nature as well as precisely defined symmetry and surface functionality. In this article, we focus on the cage-like compounds. Generally speaking, the overall molecular shape of cage-like compounds can be held either by noncovalent bonds, as demonstrated in the “molecular flasks” reported by Fujita and coworkers [17, 18] and the “tennis ball” reported by Rebek and colleagues [19], or by covalent bonds as in [60]fullerene ( $C_{60}$ ) [16], polyhedral oligomeric silsesquioxane (POSS) [20], and polyoxometalate (POM) [21–23]. To construct stable supramolecular structures, “collective physical secondary interactions” are necessary, which are generated by the functional groups on the periphery of MNPs. These interactions constitute the enthalpic driving force for further assembly of MNPs into hierarchal structures under the packing constraints imposed by the overall molecular shape





**Fig. 1** Typical examples of molecular nanoparticles

(entropic effect), leading to a variety of unconventional structures and phase behaviors, as predicted by computer simulation [24–27].

A large variety of MNPs with different sizes, symmetries, and surface functional groups can be used as versatile nanoscale building blocks. In view of their incompressible and impenetrable features, we describe them as “nanoatoms.” This term is evocative of the term “artificial atoms” that has been used to describe quantum dots [28] and even metal nanoparticles [29, 30]. It is also similar to “nanoscale atoms,” as used recently by Nukolls and coworkers to refer to pseudo-spherical molecular clusters employed as “atoms” in constructing binary crystalline solids with unique electronic and magnetic properties [31]. We use “giant molecules” to describe the macromolecules built from MNP nanoatoms or their conjugates with other macromolecules such as polymers and dendrimers [5]. Although the term “giant molecules” has been used interchangeably with “macromolecules” or more generally to describe structures with a large number of atoms, we attempt to distinguish it from traditional macromolecules. Giant molecules can be viewed as large-sized analogs of small molecules modularly constructed from MNP nanoatom building blocks, and emphasize that giant molecules are monodisperse and precisely defined macromolecules [5].

We have designed, synthesized, and investigated the supramolecular lattices of several categories of giant molecules, including giant surfactants, giant shape amphiphiles, giant Janus particles, and giant polyhedra [5, 6]. It is certain that many more types of giant molecules will appear in the future. However, even in these few giant molecule categories, highly diverse, thermodynamically stable or metastable phase structures and assembly processes in the bulk, thin film, and solution have been recognized [6, 32–40]. Giant surfactants, simulating small molecular surfactants, are polymer tail-tethered nanoatoms in which the head and tail components are chemically very different, generating amphiphilicity [6, 32, 33, 35–37, 39–45]. Giant shape amphiphiles and giant Janus particles consist of covalently bonded MNPs with distinct shapes, where self-assembly is not only driven by chemical interactions but is also largely influenced by the packing constraints of each individual shape [46, 47]. Giant polyhedra are synthesized either by large MNPs with polyhedral shape or by deliberately placing nanoatoms at the vertices of a polyhedron [38]. These giant molecules capture the fundamental

structural and functional features of their small-molecule counterparts but are about a thousand times bigger in volume; they are recognized to be size-amplified versions of their smaller counterparts [5].

In this article, we focus on how these giant molecules are modularly assembled together via collective secondary interactions to form various ordered supramolecular structures with identified lattices. We call this type of ordered structure “supramolecular crystals,” and their formation process “supramolecular crystallization.”

## 2 Supramolecular Crystals and Crystallization

Before we describe supramolecular crystals and crystallization in detail, we need to briefly review what crystals are and how they form. A crystal is a homogenous solid whose constituents (such as atoms, molecules, or ions) are arranged in a highly ordered microscopic structure, forming a crystal lattice that periodically extends in exactly the same arrangement over three directions in a real space [48]. The smallest building block that repeats itself in the crystal lattice is called the motif, which can be constructed of atoms, ions, parts of a molecule, a whole molecule, or even several molecules. A crystal must possess long-range positional, bond-orientational, and molecular-orientational orders. These orders are based on the motif, in which every atom must be located at a specific space position that can be orderly repeated. There exist 7 Lattice system and 14 Bravais lattices. To determine a crystal structure, X-ray and/or electron diffraction experiments are required to obtain diffraction patterns based on the Bragg equation in its reciprocal lattice. Note that a reciprocal lattice is a Fourier transformation of its corresponding lattice in real space. In most cases, the length scale associated with the determination is in the range of a fraction of nanometer to one nanometer [49].

Compared with crystallization of simple, small molecules, polymer crystallization takes place even in supercooled liquids far from thermodynamic equilibrium (crystallization temperatures are far below the equilibrium melting temperature at a constant pressure). In the case of a crystallizable polymer, the Gibbs free energy of the isotropic liquid in undercooling is always higher than that of the crystal solid. The traditional crystallization concept is that the crystal nucleus is small in volume and large in surface. The volume free energy term is negative towards the overall Gibbs free energy and stabilizes the nucleus, whereas the surface free energy term is positive in Gibbs free energy and destabilizes the nucleus. In the initial stage of crystallization, the surface free energy wins the competition between these two free energy terms, leading to a free energy barrier. The driving force to overcome the free energy barrier and trigger the nucleation process (either primary or surface nucleation) originates from the thermal (density) fluctuations of the liquid [50].

Beyond the general thermodynamics of a crystallization process, detailed descriptions of polymer crystallization are based on two different approaches, as

deduced from experimental observation of structural and morphological data or scattering data. These two viewpoints have led to dissimilar models for detailed microscopic descriptions of polymer crystallization, although all of these theoretical models are kinetic in nature. In the past half century, tremendous development in this research area has been achieved. If we look back, those exciting events include the discovery of polymer single crystals, lamellae, and chain folding. Explosive growth followed, based on detailed studies of crystallization, annealing, and melting; determination and control of molecular conformations, crystal structures, and morphologies; heated debates over crystal-growth models and the validity and extent of chain folding; elucidation and exploitation of mechanical, optical, electrical, and other physical properties; crystallization under various confined environments having low dimensions in space; and many others. In addition, new syntheses provided a number of macromolecules with different chemical and topological structures. Their crystallization behaviors have also stimulated many new observations and discoveries such as molecularly double-twisted helical single crystals [51–53].

However, major issues and questions still remain in polymer crystallization and are yet to be resolved: (1) Understanding of the microscopic structure and dynamics of supercooled liquids is still not complete (e.g., are supercooled liquids homogeneous?). (2) Current theoretical models in analytical forms all adopt mean-field approaches and, thus, lose the details of molecular dynamic pathways during crystallization; the specific trajectory of the pathway of one individual chain molecule during crystallization can be very different from others. Although the models can provide reasonable explanations for major, but not all, experimental results observed and reported so far, they cannot predict the crystallization behavior. (3) What is the nucleation barrier? This free energy barrier must have both enthalpic and entropic origins, which are crucially associated with the molecular structure and chain dynamics at microscopic length scales; namely, how does a chain molecule that starts out in a 3D random coil conformation convert into predominately chain-folded lamellar crystals? [50, 54, 55]

We now introduce the concept of “supramolecular crystals and crystallization.” First and by far the most important notion is that they are crystals and must be in a highly ordered microscopic, supramolecular lattice that periodically extends over three directions in real space. The building block (motif), which repeats itself in the lattice, contains many molecules and/or clusters within the motif, and those molecules and/or clusters often do not have specific space positions at the atomic and/or molecular scales to generate a repetition scheme in the motif. In a supramolecular crystal, although the positional, bond-orientational, and molecular-orientational long-range orders are retained at the length scale of motif repetition (we have to replace the bond-orientational order to be motif-orientational order at this length scale), these long-range orders are not necessary for the structures within the motifs at smaller length scales. In essence, molecules and/or clusters within the motif can either have long-range, quasi-long-range, or short-range order. In such a way, supramolecular lattices are constructed on the basis of the repeatability of motifs to describe the ordered structures and are called “supramolecular crystals.” This

concept is different from the protein crystallography often used to deal with large crystal structures. In protein crystals, each ordered atomic position in the crystal is perfectly retained. A simple example of supramolecular lattice formation is the nanophase separation process as a result of immiscibility between components. Flexible diblock copolymers with two immiscible blocks in the strong phase separation region can form various supramolecular crystals (e.g., double gyroid and body-centered cubic lattices) based on the composition of the blocks. The length scale of supramolecular crystals ranges from nanophase-separated, ordered structures at a length scale of below 10 nm to “colloidal crystals” that are usually micrometers in length.

In general, secondary interactions play an important role in ordered phase structural formation processes. However, these secondary interactions often do not possess sufficiently strong interaction to hold supramolecular lattices with a size of up to hundreds of nanometers [6]. To stabilize these lattice structures, stronger interactions are necessary. It is possible to introduce collective secondary interactions, as found in biological and living systems, to strengthen the stability of the lattice. For example, a single hydrogen bond energy is relatively weak (~20–40 kJ/mol) and much lower than that of a chemical bond (a single carbon–carbon bond energy is ~145 kJ/mol). However, combination of 14 hydrogen bonds at a single location simultaneously generates an interaction energy of 280–560 kJ/mol, which is strong enough to stabilize the supramolecular lattice. In principle, for the formation of supramolecular crystals, a balance of both enthalpic and entropic terms must be achieved to establish a thermodynamically stable or metastable system with a minimum free energy.

Supramolecular crystallization mechanisms are usually identical to, but broader in scope than, crystallization of small molecules and polymers. Classic phase transition processes involve either nucleation and growth, which illustrate a phase transition from a metastable state to an equilibrium state with a free energy barrier, or spinodal decomposition, which describes a phase transition from an unstable state to an equilibrium state without overcoming a free energy barrier [49–51]. In addition, supramolecular crystallization processes also take place in hierarchal structures at different length scales. In many cases, the overall supramolecular lattice formation requires several stages of sequential ordering structure formation to complete. The overall barrier of the phase transformation could thus be separated into several steps to speed up the transition kinetics (Ostwald’s stage rule) [50]. When the size of building blocks becomes increasingly large with heavier masses, the dynamics of these building blocks is more sluggish. Overcoming a free energy barrier or simply diffusing/moving to an equilibrium state through thermal (density) fluctuations becomes more difficult and time consuming. External force fields (such as mechanical, electric, or magnetic) are helpful in providing assistance for the building blocks to move and/or overcome the barriers.

More complicated pathways for structural formation may exist in giant molecules. In many cases, the supramolecular crystallization ends at a state that is not thermodynamically the most stable but, rather, the molecules are trapped in a metastable state. This probably occurs for kinetic reasons. Generally speaking, a

metastable phase possesses a local free energy minimum, but not a global minimum as in thermodynamic equilibrium states [50]. Whether this metastable state can be experimentally observed during its phase transition process relies on the height of transition free energy barrier leading to this metastable state. Once a metastable state exists, its lifetime is determined by the height of the transition free energy barrier that prevents it from transferring to a more stable state. One example is the polymorphism observed in supramolecular crystals, which is very similar to that in common crystals. Another example is the observation of various kinetically trapped, metastable morphologies in micelles. To judge whether a supramolecular crystal is in a metastable or a thermodynamically equilibrium state is, however, difficult in most cases for giant molecules. This is because, unless the metastable phase can be transferred to a more stable or a final equilibrium state in the experimentally accessible time period, obtaining the thermodynamic properties of these metastable and stable phases is extremely challenging.

In the following sections, we focus on this interesting topic and describe various aspects of supramolecular crystals and crystallizations based on our recently obtained experimental results with giant molecules. Understanding of this topic is certainly just beginning. It requires many further scientific efforts to make this concept fruitful.

### 3 Giant Shape Amphiphiles

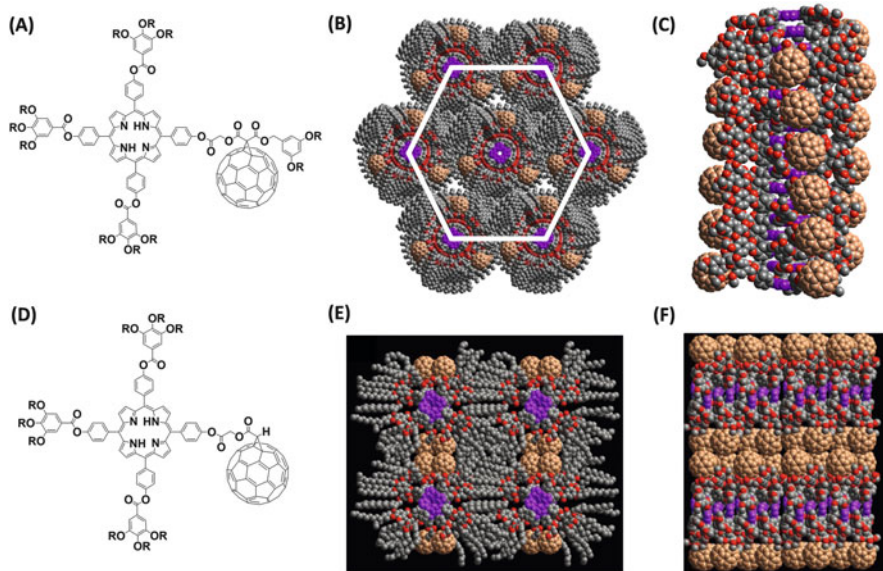
When the motif increases in size, its shape starts to play an increasingly important role in determining the self-assembly behavior and characteristics of the supramolecular structure. This is even more significant when the motifs have rigid conformations that pose specific packing constraints. Recently, Glotzer and coworkers outlined a roadmap for predicting the phase formations from well-defined rigid Archimedean polyhedra [24]. These polyhedra could not only form crystals, liquid crystals, and amorphous glasses, but they also self-assemble into plastic crystals and quasicrystals which are relatively more restricted regarding the shape of components for building the motifs. There is good reason to expect that, when components of distinct shapes are coupled together, the packing constraints of each shaped component imposes an additional dimension for controlling their self-assembled structure besides the differences in their compositions and chemical interactions. These compounds are termed “shape amphiphiles,” with emphasis on the role of shape in assembly [26]. Shape could be the single driving force for self-assembly. If we put a plane–cube shape amphiphile to assemble, we anticipate that in the condensed state, planes would preferentially stack together as long as the cube arrangement allows. In combination with designed chemical interactions, shape amphiphiles exhibit rich and versatile phase structures. It is also noteworthy that in order for shape to take an important role in assembly, the component should have a relatively rigid conformation and large size. Therefore, most shape amphiphiles form supramolecular crystals whose supramolecular lattice is well defined

even though detailed atomic order may be absent. Over the past decade, researchers have developed a sizable family of shape amphiphiles [26, 27, 56, 57]. We now look briefly at their structures and self-assembly principles.

The first example of shape amphiphiles was reported in 2003 when a disc-like columnar mesogen was linked with a rod-like mesogen [56]. The former prefers to stack one on top of another as a result of  $\pi$ - $\pi$  interactions, whereas the latter align with each other as a result of dipole-dipole interactions. Consequently, the disc-rod amphiphiles promote the mixing of disc liquid crystal and rod liquid crystals. However, the structure of such an amphiphile has not yet been revealed. Years later, Glotzer and colleagues used computer simulations to predict the self-assembly of various shape amphiphiles, including polymer-tethered nanoparticles and nanorods. [26, 27]. Many novel and intriguing hierarchical structures were predicted, which stimulated further research in this direction. Our group was among the first of several groups to look into the crystallization of such amphiphiles. For accurate control of the chemical structure, we first applied the concept of “click” chemistry [58–60] to the synthesis of this class of shape amphiphiles. It is believed that precise chemical structure is the basis for study of the physical behavior of these novel materials.  $C_{60}$  and POSS were identified as the prototype molecular nanoparticles because of their well-defined structure and the ease of their functionalization [5]. Various shape amphiphiles were then designed and synthesized.

Fullerene is one type of carbon allotrope with wide-ranging applications [61, 62]. It is known to be very hydrophobic and tends to aggregate randomly. One often needs to chemically modify it to improve its compatibility with other materials, but the formation of ordered structures is difficult [63]. To drive the formation of ordered structures, the following aspects must be recognized: (1)  $C_{60}$  is a conformationally rigid, incompressible sphere; (2) when closed, it is impenetrable to most atoms and functional groups and thus the structure is relatively independent; and (3) it is likely to form aggregates as a result of strong  $\pi$ - $\pi$  interactions. Therefore, we realized that we could either take advantage of the strong aggregation of  $C_{60}$  to interplay with other interactions to guide the formation of ordered structures, or use even stronger interactions of other components to override that of  $C_{60}$  and serve as template for the arrangement of  $C_{60}$ . Alternatively, we could use a conformationally rigid, incompressible, impenetrable counterpart of  $C_{60}$  to assist the formation of an ordered structure.

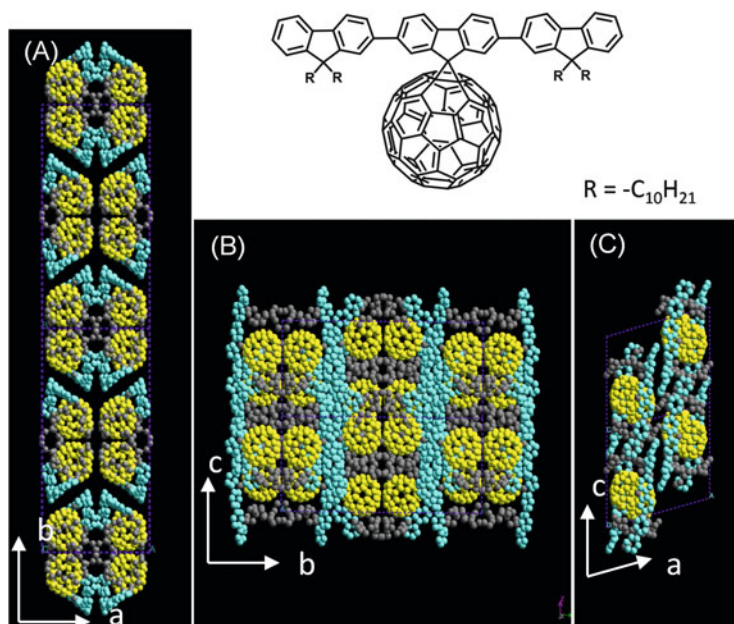
We first investigated a class of plane-sphere shape amphiphiles [64–67]. Porphyrin is a known discotic mesogen when functionalized with multiple alkyl chains of varying lengths. By linking donor porphyrin with acceptor  $C_{60}$ , we hoped that columnar liquid crystals would still be preferred. There are a variety of ways to connect the two components with varying side chain lengths, linkages, and number of  $C_{60}$  molecules. The molecules shown in Fig. 2a, d differ by the presence of two long alkyl chains modification and were studied in detail. The results indicate that the  $\pi$ - $\pi$  stacking of porphyrin overrides the aggregation of  $C_{60}$  molecules, and the formation of columnar liquid crystals persists in both cases [64–67]. The former gives a hexagonal columnar phase with an unusual  $129_{44}$  helical structure for each column [67]. The  $C_{60}$ s were found to interact within each column to form three



**Fig. 2** Self assembly of plane–sphere shape amphiphiles: (A, D) chemical structures and (B, C and E, F) corresponding supramolecular structures [64]

pendant, continuous helical channels along the column (Fig. 2). This is a typical supramolecular double cable structure that contains parallel arrays of hole- and electron-transporting channels. Upon removal of the alkyl groups on  $C_{60}$ , intercolumnar  $C_{60}$ – $C_{60}$  interactions take over and, hence, a rectangular columnar liquid crystal phase in an orthorhombic unit cell forms (Fig. 2d–f) [64]. Nevertheless, in this case, the  $C_{60}$ s form separate continuous domains parallel to the column of porphyrin, which is still one type of supramolecular double cable structure. Although their performances have yet to be optimized, preliminary device tests have shown higher photovoltaic conversion efficiency than their phenyl- $C_{61}$ -butyric acid methyl ester (PCBM) counterpart. Therefore, even for the same type of shape amphiphiles, the self-assembled structures can be very different, depending on the detailed primary structure. It should also be recognized that, although precise prediction of physical structure is not possible, the key structural features apparently do not change, as reflected in the supramolecular double cable structure in both cases. It is anticipated that cycles of iteration are required to understand the structure–property relationship and optimize the properties of the material [68].

The strategy was also extended to other shape amphiphiles. For example, a series of rod–sphere shape amphiphiles,  $C_{60}$ -oligofluorene (OF) conjugates, were prepared [69]. This time, the framework was held constant for the rod–sphere shape amphiphile owing to a rigid spiro linkage. The only thing that changed was the length of the alkyl side chains. Interestingly, all three crystal structures exhibit very similar molecular packing schemes with alternating layers of the  $C_{60}$  and OF



**Fig. 3** Crystal structure of a rod-sphere shape amphiphile, OFn-C<sub>60</sub>: molecular packing model projection on *ab* plane (A), *bc* plane (B), and *ac* plane (C) [69]

components (Fig. 3), although their symmetry is very different. It seems that, although the interaction are both  $\pi$ - $\pi$  interactions, their geometry is very different, with spherical C<sub>60</sub> being isotropic and rod-like OF being anisotropic. This imposes different packing constraints, which leads to maximum contact between C<sub>60</sub> molecules, but not OF conjugates. The alkyl chains fill in the gaps between C<sub>60</sub> spheres, thereby leaving more space for close packing of the rod-like planar OF components. In the above examples, C<sub>60</sub> acts as a 3D sphere and interacts with the rest of the molecule as a relatively independent unit. We anticipate that this is also true for other molecular nanoparticles.

Polyhedral oligomeric silsesquioxanes are perhaps the smallest of silicon nanoparticles. Of these, T<sub>8</sub> POSS possesses the highest O<sub>h</sub> symmetry and is cube-like. With a shape-persistent cage (diameter ~ 1.0 nm), it is an ideal inorganic counterpart of C<sub>60</sub> [70–74]. A cube-sphere shape amphiphile, POSS-C<sub>60</sub>, can be easily designed and prepared by covalently linking POSS and C<sub>60</sub> together via a simple ester bond [34, 46, 47]. Upon crystallization, it exhibits polymorphism, forming hexagonal and orthorhombic crystals [46]. In both cases, the double-layered structure can be observed, because POSS and C<sub>60</sub> are chemically incompatible but geometrically complementary to each other. Phase separation between POSS and C<sub>60</sub> is the very first step, after which the molecular nanoparticles in each layer start to further organize into intriguing hierarchical structures. Interestingly, because POSS is generally considered as insulating and C<sub>60</sub> is regarded as



conducting or even superconducting upon doping, this unique structure can be proposed as an as-assembled “nanocapacitor” [68]. Moreover, changing the molar ratio of the components to two POSS to one  $C_{60}$  creates an asymmetric shape amphiphile, which packs into a three-layered structure with interdigitated  $C_{60}$  as the center sandwiched layer [47].

Replacing  $C_{60}$  with another POSS molecule and linking both POSS molecules by a rigid ribbon creates interesting packing, as shown in a novel cube–plane–cube shape amphiphile POSS-PDI-POSS [75]. There are two competing interactions, the  $\pi$ - $\pi$  stacking interaction and the close-packing of POSS. Because the POSS has a larger volume and the steric hindrance is considerable, the stacking is frustrated beyond dimer formation. As a balance, the two perylene diimide (PDI) molecules are packed face-to-face to maximize the contact and the POSS cages bend away from the plane and block the opposite side of the PDI. Finally, the dimer serves as the basic building block for crystal construction. The principles hold true no matter whether the linker between POSS and PDI is a rigid phenylene linkage or a relatively flexible propylene linkage. It should be noted that in all of these crystals, although the basic structural features are evident, the atomic order may not be as precise as in small-molecule crystals. This is reflected in the relatively diffuse diffraction spots of these crystals and, sometimes, by streaks caused by crystal defects. Within these supramolecular crystals, the molecular nanoparticles are relatively independent of the rest of the molecule. They interact with the rest basically through the collective physical interactions from the functional groups on the surface. Their inner structures and compositions are kept identical, which allows us to at least qualitatively predict the molecular packing using the coarse-grained model. This, in our opinion, is a valuable direction of research on supramolecular crystals.

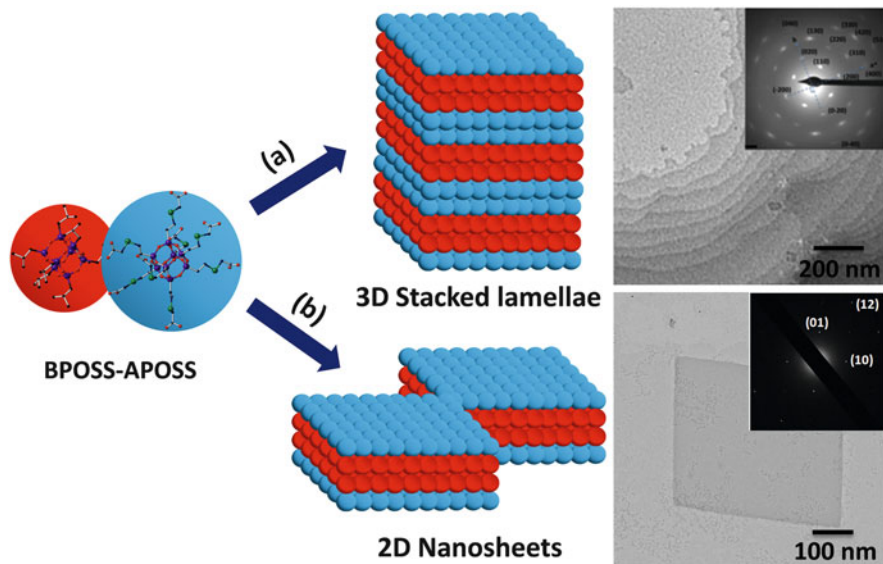
## 4 Giant Janus Particles

Molecular nanoparticle (MNP)-based Janus molecules represent the simplest two-component model systems in giant molecules. The word “Janus” comes from the double-faced Roman god and reflects the asymmetric nature of particles with two regions of distinct surface chemistry, polarity, and/or interactions [76–78]; the name was first proposed by de Gennes in his 1991 Nobel lecture [79]. As a new class of nano-Janus grains that bridge the gap between conventional inorganic/polymeric colloidal Janus particles [80–82] and molecular Janus entities (i.e., amphiphilic dendrimers [16] or polymer brushes [83]), MNP-based Janus particles (or so-called molecular Janus nanoparticles) usually possess 3D volume and shape-persistent nanostructure with molecular precision and high uniformity. Fine tuning of the molecular symmetry and surface chemistry of each MNP could efficiently manipulate the hierarchical structure formation of the whole molecular Janus particle in the solid state.

The Janus feature requires breaks in both geometrical and chemical symmetry, which serve as the driving force to mediate the self-assembly and hierarchical structure formation of the molecule. The geometric sense describes the decrease in overall molecular symmetry during the mono- and multifunctionalization of MNPs [84]. The chemical sense refers to the incorporation of surface functionalities with different interactions into the other part of the molecule to generate amphiphilicity. In the family of molecular Janus nanoparticles, one of the simplest ways to achieve symmetry breaking is to connect two or more immiscible MNPs together via short covalent linkage(s).

Following this premise, a dumbbell-shaped molecular Janus particle was designed and synthesized by closely coupling together two MNP units with similar structure but distinct surface functional groups: carboxylic acid-functionalized POSS (APOSS) and isobutyl-functionalized POSS (BPOSS) [85]. Because a short linkage is used to connect these two immiscible POSS molecules together (hydrophilic versus hydrophobic), the  $O_h$  symmetry of the  $T_8$  cage is reduced to  $C_{3v}$  symmetry along the long axis of the molecule. The amphiphilic feature of the whole particle (APOSS-BPOSS) is thus created, allowing the formation of a solid-state bilayered structure with a head-to-head, tail-to-tail type of packing arrangement (Fig. 4). Moreover, the supramolecular crystalline packing of BPOSS particles within each layer is also formed at low temperatures, further generating a hierarchical structure with an orthorhombic unit cell and a symmetry group of  $P2_12_12$ . This can be confirmed by selected area electron diffraction (SAED) patterns from stacked single lamellar crystals with a flat-on arrangement (Fig. 4) and further illustrated by computer simulation. Each atomic position of the motif does not possess 3D translational symmetry, yet the unit cell does. This structure is thus a typical supramolecular crystal. Furthermore, the ordered crystal structure in the layers disappears upon heating as a typical first-order transition, whereas the bilayered structure persists throughout as a supramolecular liquid crystal phase.

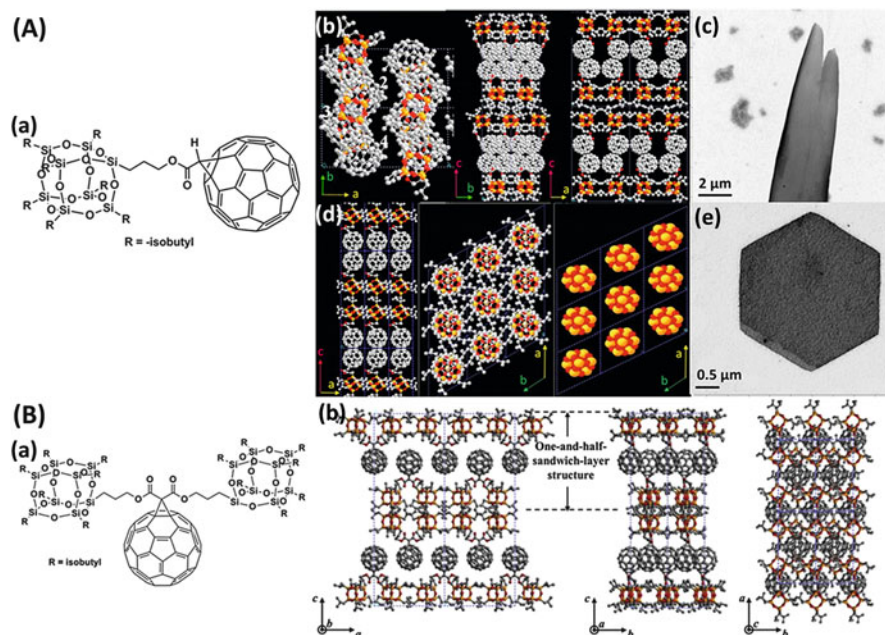
Notably, the formation of such a bilayered structure with possible supramolecular ordering at the *meso*-length scale is highly favored for the 3D packing of Janus particles, provided the volume/shape and the coverage of surface functionalities are commensurate. Introducing incommensurate factors into the Janus particle system can offer opportunities for construction of new frustrated supramolecular structures beyond the bulk supramolecular crystals [86]. For example, introduction of a strong electrostatic repulsive force between the amphiphilic layers, which prevents crystal growth along the lamellar normal direction in a polar solvent (i.e., dimethylformamide, methanol, and acetonitrile), can result in the final formation of ultrathin 2D supramolecular crystals with extra-large specific area ratio (Fig. 4). Specifically, the collective hydrogen bonding within the APOSS layers is partially suppressed by titrating with tetraalkylammonium hydroxide (TBAOH) to a certain molar ratio. Well-defined 2D supramolecular crystals with definite and uniform thickness can be formed by slow evaporation of the resulting solution. Atomic force microscopy (AFM) shows an average thickness that is nearly equal to the *c*-axes of the unit cell of BPOSS-APOSS bulk crystals without counterions. The structure of 2D supramolecular crystals of BPOSS-APOSS has been revealed by SAED. They consist of



**Fig. 4** Self-assembly of APOSS-BPOSS molecular Janus particles into 3D stacked lamellae crystal or 2D nanosheets under different conditions: (a) in the solid state or in melt [85] and (b) in polar solvent or mixing with tetraalkylammonium hydroxide [86]

two inner BPOSS crystalline layers that are sandwiched by two outer APOSS layers covered by counterions. In polar solvents, solvation of the counterions creates partially charged 2D supramolecular crystals and, thus, generates electrostatic repulsive interactions that block supramolecular crystal growth along the layer normal direction. The role of counterions has been illustrated by tuning both their number and size. Only a certain degree of neutralization of carboxylic groups can result in well-defined 2D supramolecular crystals.

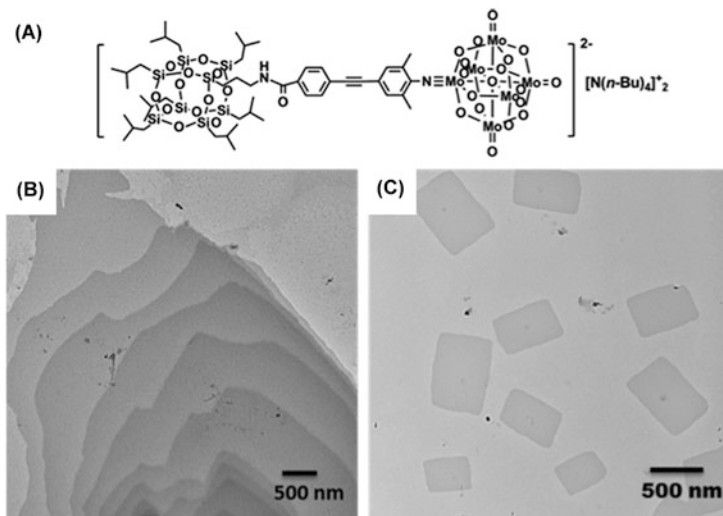
BPOSS- $C_{60}$  conjugates, another typical molecular Janus nanoparticle, self-assembles into a double-layered lamellar supramolecular crystal as a result of the immiscible nature of BPOSS and  $C_{60}$  with similar sizes [46]. Interestingly, depending on growth conditions, polymorphism with two different crystal structures was observed as a result of the distinct packing ordering sequence of those two MNPs at the initial stage. For example, an orthorhombic unit cell is formed when BPOSS cages initiate the crystallization process, whereas a hexagonal unit cell is generated when  $C_{60}$  packs into the first layer and dominates the supramolecular structure formation (Fig. 5A). The self-assembled alternating  $C_{60}$  and POSS layers along the  $c$ -axis of the crystals with  $d$ -spacing of several nanometers finally induce the bilayered structure in both crystal forms. The hexagonal lattice is the thermodynamically more stable phase, based on the supramolecular crystal packed structure and density difference.



**Fig. 5** (A) Self-assembled structures of BPOSS-C<sub>60</sub> [46]: (a) chemical structure of BPOSS-C<sub>60</sub>; (b) molecular packing in orthorhombic crystal and (c) the corresponding morphology; (d) molecular packing in crystal hexagonal crystal and (e) the corresponding morphology. (B) Self-assembled structures of diBPOSS-C<sub>60</sub> [47]: (a) chemical structure of diBPOSS-C<sub>60</sub> and (b) molecular packing in orthorhombic crystal

We further extended the dumbbell-like Janus grains into “Mickey Mouse”-like molecular Janus particles via the development of a diBPOSS-C<sub>60</sub> shape amphiphile that consists of one C<sub>60</sub> covalently linked with two BPOSS MNPs [47]. Considering the incommensurate volume of two immiscible domains (two BPOSS versus one C<sub>60</sub>), the formation of a conventional bilayered structure is not possible. Alternatively, the unbalanced volume of two BPOSS domains and one C<sub>60</sub> domain could induce the formation of a “one-and-half-layered” supramolecular packing scheme, whereby one single layer of interdigitated C<sub>60</sub> molecules is sandwiched between two layers of BPOSS cages (Fig. 5B). Such a packing scheme along the *c*-axis could generate a 3D orthorhombic supramolecular crystal lattice with *Pnmm* symmetry.

Another group of MNPs, POMs, are also utilized to build up molecular Janus particles as a result of their intrinsic electrostatic interactions and size comparable with other preceding MNPs. POMs are defined as discrete metal-oxygen anionic clusters and are composed of transition and/or actinide metals in their high oxidation states with oxygen atoms to be shared. A simple example is BPOSS-Lindqvist POM (see Fig. 6a), where Lindqvist POM is a molybdenum-oxygen cluster with two negative charges and covalently bonded to BPOSS via the Sonogashira coupling reaction [86]. When slowly evaporated from low polarity solvent (e.g., acetone), the molecular dyad crystallizes into a 3D triclinic supramolecular lattice

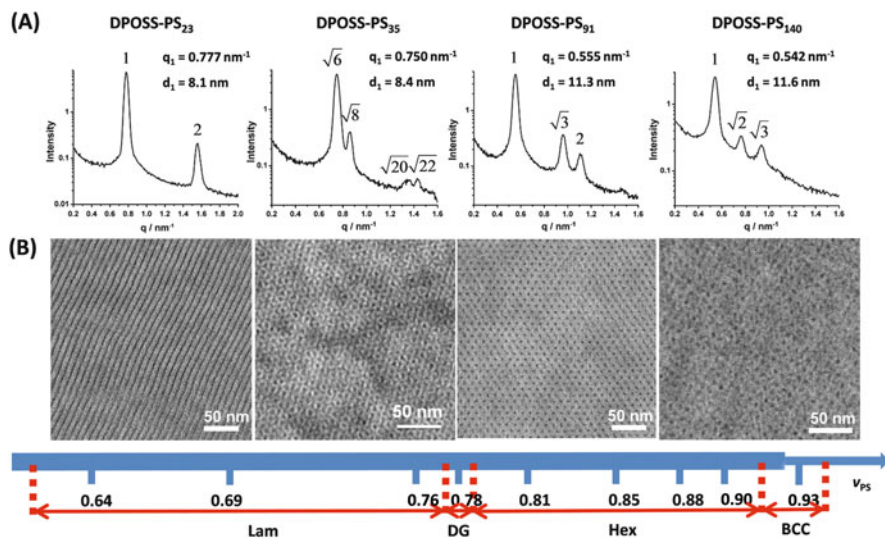


**Fig. 6** (A) Chemical structure of BPOSS-Lindqvist POM. (B) Stacked 3D crystals grown from acetone solution. (C) Well-defined 2D nanocrystals grown from acetonitrile solution [86]

that is dictated by the BPOSS cages. However, when crystallized from polar solvents (e.g., acetonitrile, DMF, and methanol), the counterions of Lindqvist POMs are solvated and prevent 3D crystal growth (see Fig. 6b). As a result, 2D supramolecular crystals with definite and uniform size of several nanometers are generated (Fig. 6c).

## 5 Giant Surfactants

Giant surfactants are a subcategory of giant molecules and consist of MNPs as head (s) and polymer chains as tail(s). Thus, they contain the essential geometrical features of small-molecule surfactants yet with amplified size [5, 6]. In contrast to giant shape amphiphiles and Janus particles, the conformational entropy originating from the flexible nature of polymeric tails plays an important role in the system. In this sense, giant surfactants possess the duality of both small molecule surfactants and block polymers [5]. Although the general principles of phase separation and crystallization of (block) polymers are beyond the scope of this review, giant surfactants possess their own unique characteristics during the formation of supramolecular crystals. First, clustering of functional groups at the periphery of the MNPs generates collective secondary interactions that act cumulatively and cooperatively and are indispensable for the construction and stabilization of the supramolecular crystals. Second, the presence of shape-persistent MNPs imposes external constraints on the polymer tails during supramolecular



**Fig. 7** (A) SAXS pattern and (B) bright field TEM images of ordered phases (from left to right: Lam, DG, Hex, and BCC) from DPOSS-PS. The phase diagram shown at the bottom [36]

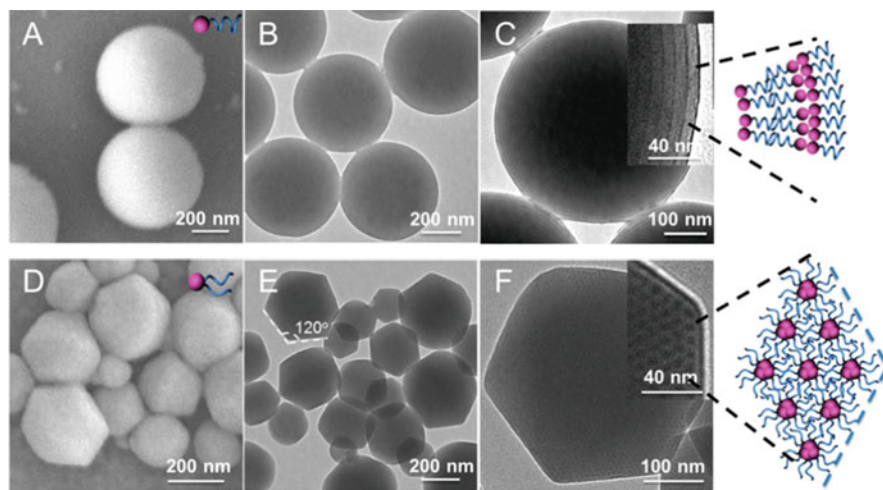
crystallization, which alters the pathway of Gibbs free energy minimization and leads to unconventional structures with varied metastabilities. Third, the flexible polymer tails provide more packing freedom than available in giant shape amphiphiles and Janus particles, resulting in highly diverse, thermodynamically stable/metastable ordered structures that behave similarly to block polymers.

These unique characteristics are illustrated by a representative giant surfactant with a hydroxyl-functionalized POSS (DPOSS) head and a polystyrene (PS) tail (DPOSS-PS) [36]. In the bulk, diverse supramolecular ordered structures, including lamellae (Lam), bicontinuous double gyroids (DG), hexagonally packed cylinders (Hex), and body-centered cubic packed spheres (BCC), are observed with increasing volume fraction of the PS tail, as evidenced by small-angle X-ray scattering (SAXS) patterns and transmission electron microscopy (TEM) images (Fig. 7). The structures are analogous to the classic phases of block copolymers, yet with much smaller domain spacings. The collective hydrogen bonding between DPOSS molecules enhances the interaction parameters, which provides a versatile platform for engineering technologically relevant nanostructures with feature sizes of less than 10 nm. It is worth noting that, although the molecular structure of DPOSS-PS prohibits access to the phase diagram for a volume fraction of PS less than 0.64 as a result of the fixed size of one block, new molecular designs with multiple heads could be applied to explore the other half of the phase diagram [36].

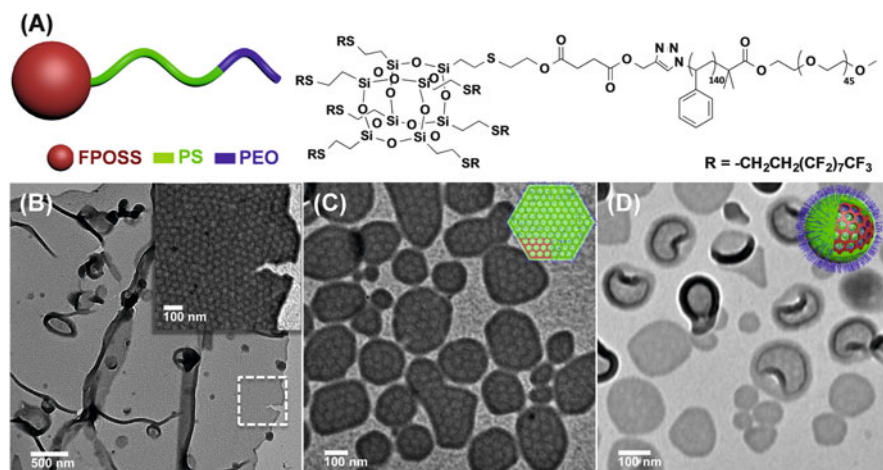
Another remarkable feature is that the supramolecular structures constructed by giant surfactants are very sensitive to the molecular architecture, which is significantly weakened in the case of block copolymers as a result of the elasticity and compressibility of random coils [36, 40]. We compared the phase behaviors of

topological isomer pairs with identical chemical composition but different architectures to highlight this sensitivity. For example, a bicontinuous DG supramolecular structure was observed in DPOSS-PS<sub>35</sub> with a single PS tail, but a Hex phase was seen for the corresponding topological isomer with the same PS volume fraction but two tails (DPOSS-2PS<sub>17</sub>) [36]. It is thus not sufficient to use a single order parameter (volume fraction) to describe the phase behavior of giant surfactants. Additional parameters associated with the molecular architecture should also be considered.

Interestingly, the sensitivity of molecular architecture is also observed in solution self-assembly. Unusual nanostructured colloidal particles have been observed in a topological isomer pair consisting of a carboxylic acid-functionalized C<sub>60</sub> (AC<sub>60</sub>) head and PS tail(s) (AC<sub>60</sub>-PS<sub>44</sub> and AC<sub>60</sub>-2PS<sub>23</sub>) by slow addition of a selective solvent into their solution in 1,4-dioxane [36]. Spherical colloidal particles were observed for AC<sub>60</sub>-PS<sub>44</sub>, but double truncated conical particles for AC<sub>60</sub>-2PS<sub>23</sub> (Fig. 8). Both showed unimodal narrow size distribution, as confirmed by dynamic light scattering (DLS). A zoom-in characterization by TEM showed that the spherical particles have an onion-like inner structure, whereas the double truncated conical particles exhibit a hexagonal inner structure (Fig. 8c, f), which is in good agreement with their corresponding bulk structures (Lam for AC<sub>60</sub>-PS<sub>44</sub> and Hex for AC<sub>60</sub>-2PS<sub>23</sub>). The surface of these particles is covered mainly by anionic AC<sub>60</sub>, and the inner part undergoes further self-organization into different finer nanostructures through phase separation between AC<sub>60</sub> and PS tails. The formation of these colloidal particles is a result of strong collective interactions and conformational rigidity of MNPs, which is not observed in traditional block copolymer self-assembly.



**Fig. 8** SEM and TEM images of colloidal nanoparticles of (A–C) AC<sub>60</sub>-PS<sub>44</sub> and (D–F) AC<sub>60</sub>-2PS<sub>23</sub> under similar conditions [36]

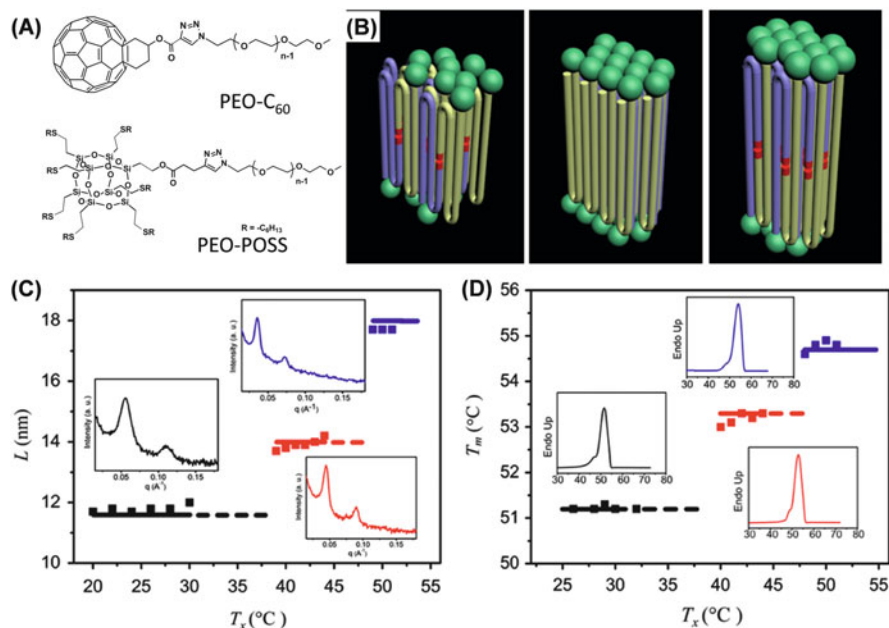


**Fig. 9** (A) Illustration and chemical structure of the FPOSS-based giant surfactant. (B–D) The resultant nanostructures in solution: 2D hexagonally patterned nanosheets (B, C) and laterally structured vesicles (D) [35]

Large 2D hexagonally patterned colloidal nanosheets with a size of tens of micrometers were observed in solution assembly of a giant surfactant with a fluorinated polyhedral oligomeric silsesquioxane (FPOSS) head and a polystyrene-*block*-poly(ethylene oxide) (PS-*b*-PEO) diblock copolymer tail (FPOSS-PS-*b*-PEO) (Fig. 9) [35]. With vigorous stirring, the strong shear force interrupts the formation of large sheets, resulting in small debris with faceted or hexagonal shapes (Fig. 9c). According to the relative hydrophobicity of the three components, the nanosheets are 2D layers with hexagonally connected FPOSS domains embedded inside a continuous PS matrix that is further covered by the PEO corona. The nanosheets have a thicker boundary than the interior, which partially releases the excess rim-cap energy and stabilizes this unusual structure. Further increasing the water content induces the formation of vesicles with hexagonally patterned walls (Fig. 9d).

The rigid conformation of MNPs imposes packing constraints on the polymer tails, leads to intriguing unconventional supramolecular structures that are usually inaccessible for free polymers. A typical example is the observation of exactly defined half-stemmed polymer lamellar supramolecular crystals with polymer chain-ends remaining trapped in the middle of the lamellar crystal as defects. These structures have been obtained using giant surfactants having a crystalline PEO tail (PEO-POSS and PEO-C<sub>60</sub>) (Fig. 10) [32]. Upon crystallization from the melt, PEO is sandwiched between two layers of MNPs. To balance the cross-sectional areas of the MNPs and the PEO stems, half-stemmed crystals with precisely controlled defects were formed, as evidenced by lamellar thickness and melting temperature (Fig. 10c, d). Note that the half-stemmed crystals are





**Fig. 10** (A) Chemical structure of PEO-C<sub>60</sub> and PEO-POSS. (B) Illustration of integral folding and half-stemmed crystals. (C) Relationship between lamellar thickness,  $L$ , and crystallization temperature  $T_x$ ; insets show the corresponding SAXS pattern. (D) Relationship between melting temperature,  $T_m$ , and crystallization temperature  $T_x$ ; insets show ultrafast heating chip DSC thermograms [32]

thermodynamically unstable and further reorganize into integral folded crystals. With the geometric restrictions imposed by MNPs, these half-stemmed PEO crystals are settled in free-energy minima and experimentally accessible.

Furthermore, the geometric constraints and selective affinities of MNPs could promote phase separation between two tail blocks in giant surfactants with block copolymer tails. Giant surfactants with a low molecular weight PS-*b*-PEO diblock copolymer tail (FPOSS-PS-*b*-PEO and AC<sub>60</sub>-PS-*b*-PEO) could self-assemble into a library of diverse ordered structures in the bulk [87, 88]. The FPOSS-based giant surfactants form lamellae with alternating MNP domain and block polymer domain [87]. We found that the fixed volume and shape of FPOSS generates a spatially confined environment for tethered PS-*b*-PEO tails. The incommensurate cross-sectional area between the MNP head and polymer tail results in chain overcrowding and stretching, which provides additional entropic driving force to facilitate the phase separation of block copolymer tails. The chain stretching leads to unexpected phase separation between low molecular weight PS and PEO blocks, and subsequent formation of hierarchical lamellar structures among the three immiscible components. On the other hand, the hydrogen bonding between the AC<sub>60</sub> and the PEO blocks also facilitates nanophase separation of originally disordered low molecular weight PS-*b*-PEO block copolymers, affording the

formation of various ordered nanostructures, including Lam, DG, and Hex phases [88]. In these ordered structures, the  $AC_{60}$  and PEO blocks are associated with each other in one domain and the PS blocks segregate into another. These examples provide an efficient and practical strategy for the design and preparation of giant surfactants for the construction of ordered nanostructures for technologically relevant applications.

## 6 Giant Tetrahedra

For the concept of supramolecular crystals, there is no example more convincing than the case of giant tetrahedral molecules. The assembly/packing of building blocks with specific shape and symmetry in 3D space is a long-lasting topic in scientific research. Typical polyhedra are among the most intriguing 3D structures. Figure 11 shows three different types of tetrahedra as examples.

The first type includes classic tetrahedra (type I in Fig. 11), which have closed structures with flat faces, straight edges, and sharp corners or vertices. Glotzer and coworkers simulated hundreds of convex polyhedra whose assembly arises solely from their anisotropic shape, and developed simple criteria to predict how polyhedra pack into ordered structures such as crystals, liquid crystals, and quasicrystals, or remain amorphous [24, 89]. Meanwhile, the synthetic advances in generation of inorganic polyhedral nanocrystals (e.g., tetrahedra, cubes, truncated cubes, cuboctahedra, octahedra, and rhombic dodecahedra) with good control of size, shape, and surface chemistry have provided some simple illustrations of the entropy-driven packing of polyhedra [90–94].

The second type of polyhedra includes closed framework structures, which have straight edges and sharp corners or vertices but are without flat faces (type II in Fig. 11). With the aid of coordination interactions using transition metals as “nodes” and organic ligands as “spaces,” many complex 3D topologies possessing polyhedral geometries or symmetries have been revealed. The development of elaborate design principles during the last few decades has led to diverse polyhedral structures, ranging from simple Platonic solids including tetrahedron, octahedron,

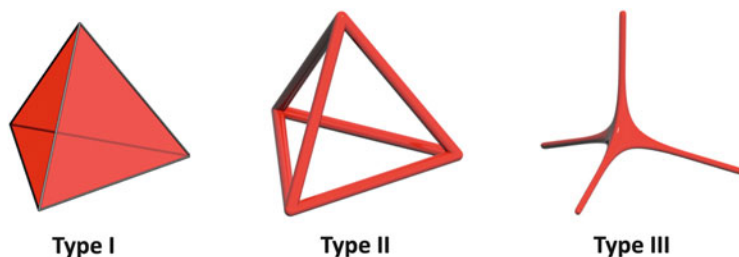
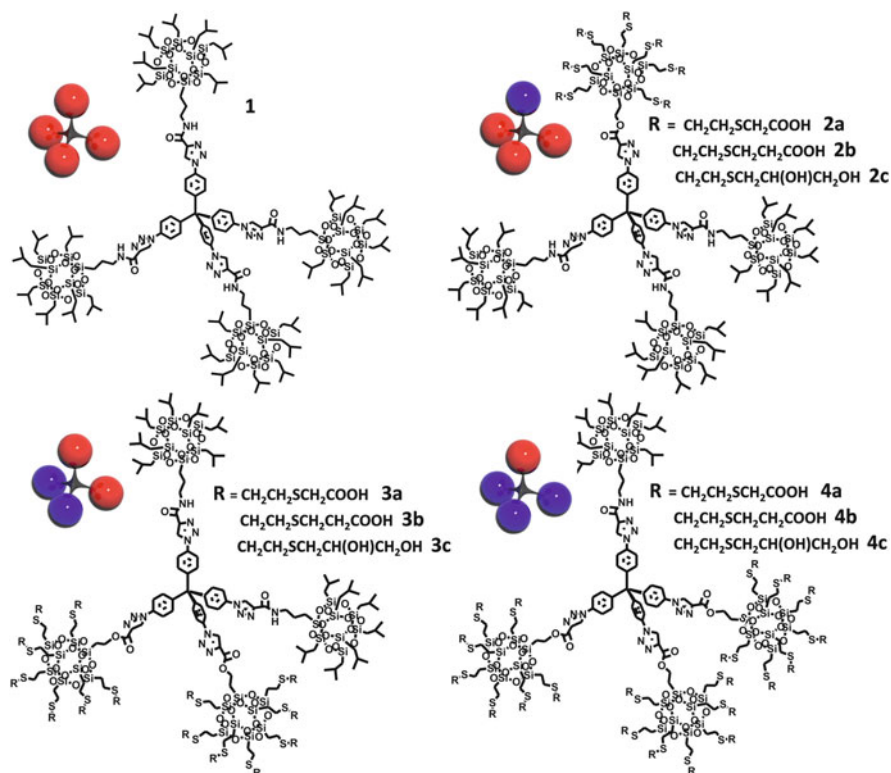


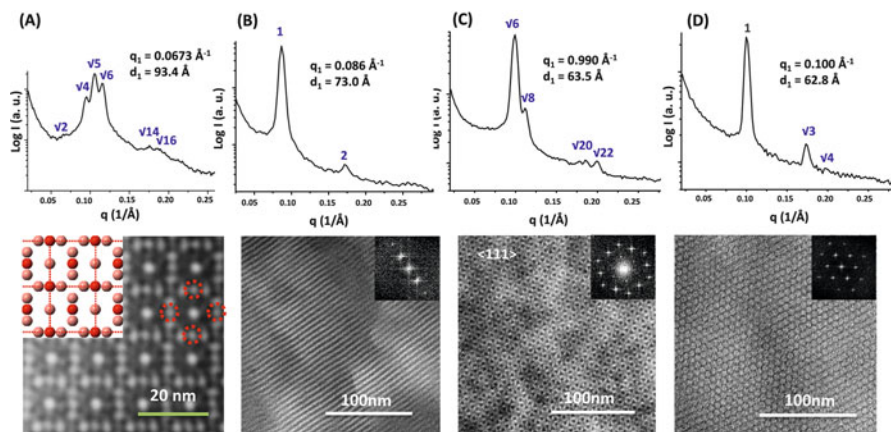
Fig. 11 Three different types of tetrahedra building blocks



**Fig. 12** Chemical structures of giant tetrahedra 1–4. The *cartoons* in the *top left* are the corresponding simplified schemes [38]

cube, dodecahedron, and icosahedron, to more complex Archimedean solids [95–97].

The third type of polyhedral structure possesses polyhedral symmetry with only sharp corners or vertices, all connected to one center (type III in Fig. 11). The best example of this type of polyhedra is the methane,  $\text{CH}_4$ , structure with a tetrahedral shape. The colloidal nanotetrapods or nano-octapods also belong to this type [98, 99]. This type of polyhedra can be easily constructed starting from nanoatoms. If nanoatoms are placed on the apexes of a rigid polyhedron linker to form a larger faceted giant molecule, the molecules amplify the symmetry of the linkers and result in giant polyhedra, reminiscent of the classic small-molecule valence shell electron pair repulsion structures. Of all the polyhedra, the tetrahedron is the simplest to start with. Recently, we presented an experimental approximation of giant tetrahedra by coupling four POSS MNPs with different surface functionalities to a rigid tetrahedral core [38]. These giant tetrahedra have precise and uniform molecular weights. By introducing different numbers of hydrophilic and hydrophobic POSS NMPs, it was possible to achieve symmetry breaking of the positional interactions in giant tetrahedra generated by the collective (multiple) hydrogen

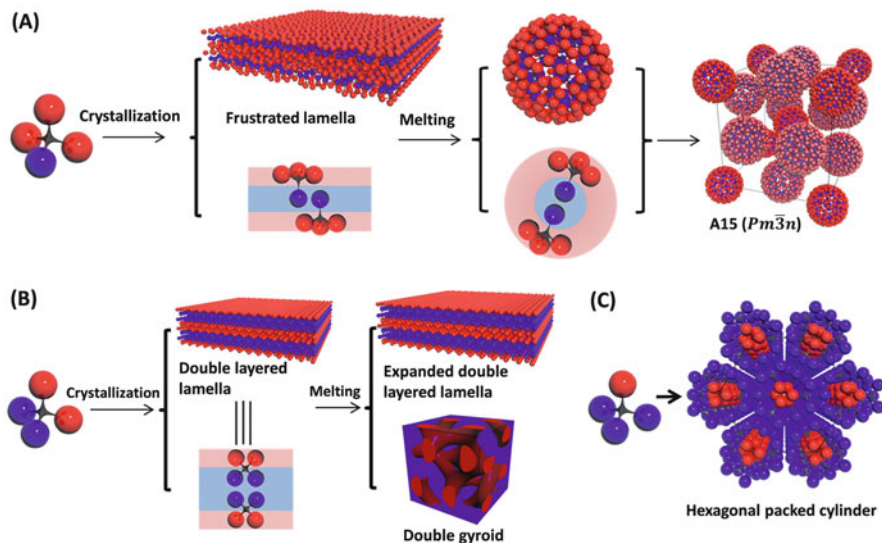


**Fig. 13** SAXS patterns of structures **2a** (A), **3c** (B), **3a** (C), and **4b** (D) after corresponding thermal treatments. The corresponding BF TEM images of thin-sectioned samples are shown below; insets show the corresponding fast Fourier transform patterns [38]

bonding between the hydrophilic POSS MNPs and crystallization of the hydrophobic POSS MNPs. Detailed chemical structures of these giant tetrahedra are shown in Fig. 12 (structures **1–4**).

In the giant tetrahedron **1** with four hydrophobic POSS MNPs, tetrahedral cores adopt an interpenetrated stacking manner to form geometrically locked columns along the *c*-axis, surrounded by a shell of crystalline BPOSS cages. When one hydrophobic BPOSS is replaced by a hydrophilic POSS in giant tetrahedra **2**, there exist the two competing interactions of collective hydrogen bonding between the hydrophilic POSS MNPs and crystallization of the hydrophobic BPOSS MNPs. At room temperature, the latter dominates and forces the giant tetrahedra into a frustrated three-layer packing mode, as crystallization of BPOSS MNPs always prefers to create flat interfaces. After melting the crystals, the hydrophilic DPOSS MNPs aggregate via collective hydrogen bonding to form the spherical core. The hydrophobic BPOSS MNPs undergo a 2D scrolling and construct shells of the spheres located on the surfaces to fit into an A15 supramolecular crystal lattice, as demonstrated by both SAXS and bright field (BF) TEM observations (see Fig. 13A). Figure 14a illustrates the assembly mechanism. It is surprising that two types of supramolecular spheres with different coordination environments can be resolved clearly under TEM (Fig. 13A). It is speculated the Frank–Kasper A15 supramolecular lattice formation must be associated with the deformability of the selectively assembled spheres and shape polydispersity.

The giant tetrahedra of series **3** are more symmetric in terms of both volume fractions and interactions. Above the melting temperature of crystalline BPOSS, double layered Lam (see Fig. 13B for the SAXS and TEM analyses, and Fig. 14b for a schematic illustration of the mechanism) or DG (Fig. 13C and Fig. 14b) supramolecular structures could be identified. However, in giant tetrahedra **4**,



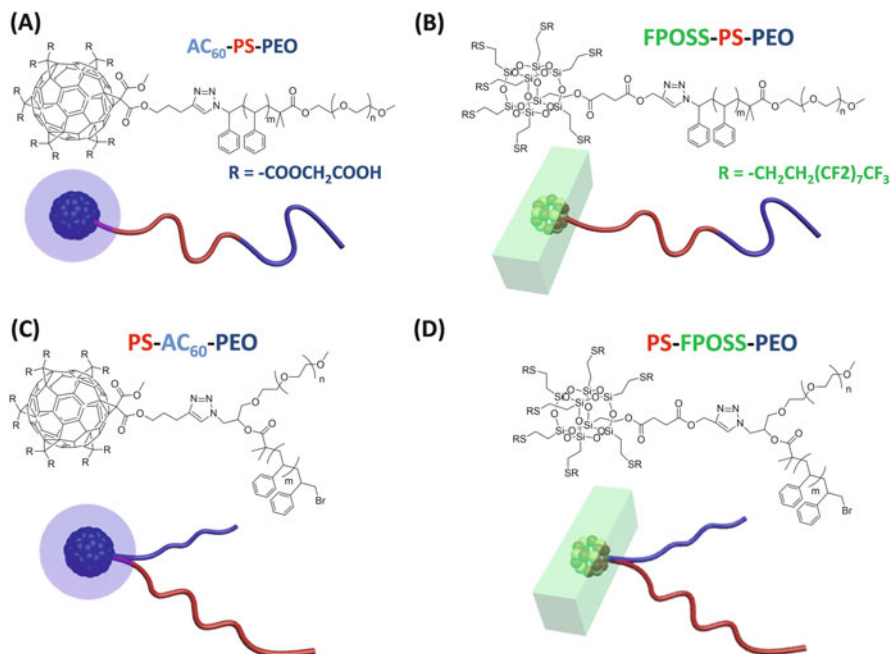
**Fig. 14** Selective assembly mechanisms and packing models for giant tetrahedra **2** (A), **3** (B), and **4** (C) [38]

BPOSS MNPs fail to crystallize at room temperature as a result of the low BPOSS volume fraction. After annealing, an inverse Hex structure (Fig. 13D and Fig. 14c) having hydrophilic POSS MNPs in the continuous matrix and hydrophobic BPOSS MNPs in the core domain appears, rather than a spherical supramolecular structure as in the giant tetrahedra **2**. This use of rigid giant polyhedra as building blocks to construct diverse supramolecular crystal lattices including the “metal alloy”-like Frank–Kasper structure opens up a wide field of supramolecular crystals with unexpected structures and properties.

## 7 Thin Films of Giant Molecules

The diverse self-assembly and crystallization behaviors of giant molecules in the bulk state have been described extensively in the previous sections. Similar to the concept that adding nanoatoms to a macromolecular system imposes an additional dimension for controlling supramolecular structure, factors such as surface tension and substrate interactions could further enrich the self-assembled structures of giant molecules in thin films.

Self-assembly in thin films with only a few repeating motifs of supramolecular lattices along the film normal is greatly affected by surface conditions [100–102]. To minimize the free energy, the components with low surface energy preferentially emerge to the free surface, whereas components with affinity for substrates wet the substrate [103]. The subtle balance of enthalpy and entropy that determines the lowest free energy state can be manipulated in thin films by tuning

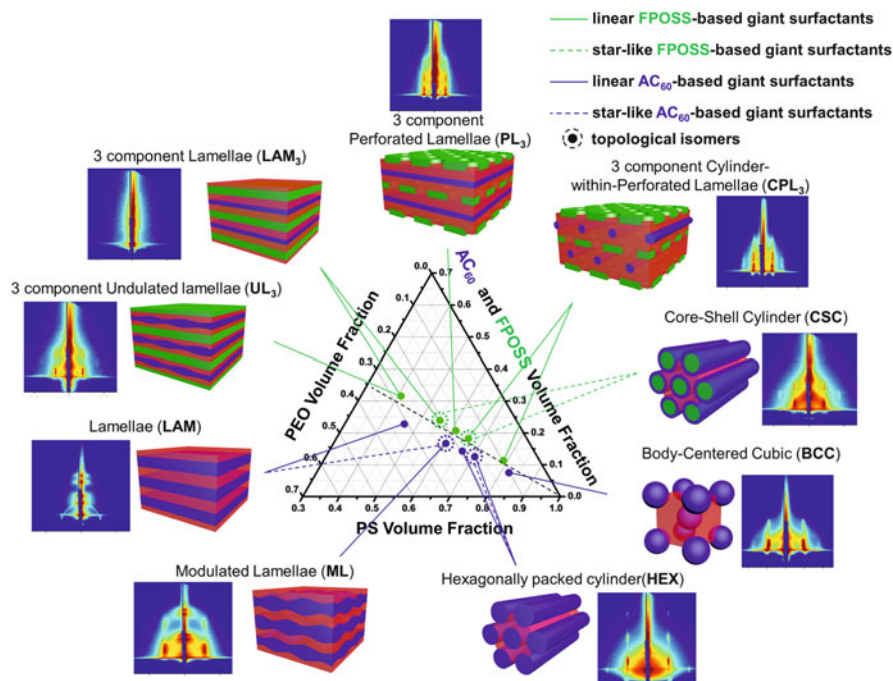


**Fig. 15** Molecular structures of giant surfactants (A) AC<sub>60</sub>-PS-PEO, (B) FPOSS-PS-PEO, (C) PS-AC<sub>60</sub>-PEO, and (D) PS-FPOSS-PEO. Hydrophilic components are labeled in blue, hydrophobic components in red, and omniphobic components in green (C.-H. Hsu et al., unpublished work)

the secondary interactions between molecules and substrate and the molecular confinement close to surfaces.

Supramolecular crystallization of giant surfactants with a PS-*b*-PEO block copolymer have been studied in thin films (Fig. 15) (C.-H. Hsu et al., unpublished work). Using rational molecular design, four categories of giant surfactants with distinct molecular topologies and different MNP surface functionalities were constructed as a comprehensive model system. Two MNPs with different affinities to the tail blocks (i.e., hydrophilic AC<sub>60</sub> and omniphobic FPOSS) are utilized as heads of the giant surfactants. The MNP is tethered to a PS-*b*-PEO block copolymer at two specific positions, the end of the PS block (MNP-PS-PEO) and the junction point [PS-(MNP)-PEO], resulting in topological isomer pairs with almost identical chemical compositions but different architectures. The molecular weights of PS-*b*-PEO were controlled within the weak segregation region to highlight the enhanced immiscibility between polymer blocks in the presence of MNPs.

The self-assembly behaviors of specifically designed giant surfactants are systematically studied in thin films using grazing incidence X-ray scattering and TEM, focusing on the effects of head surface functionalities and molecular architectures on nanostructure formation. With fixed length of the PEO block, changing the molecular weight of the PS block leads to phase formation and transition. As a result of the distinct affinity, the AC<sub>60</sub>-based giant surfactants form two-component



**Fig. 16** Ternary phase diagram of three-component giant surfactant self-assembly in thin films. Self-assemblies of  $AC_{60}$ -based and FPOSS-based giant surfactants are depicted by blue and green lines, respectively. Each self-assembled phase is represented by the colored model and supported by the corresponding grazing incidence X-ray diffraction pattern. Solid lines represent the linear giant surfactants and dashed lines represent star-like surfactants. The black dashed line indicates compositions with equal volume fraction of MNP and PEO (C.-H. Hsu et al., unpublished work)

morphologies, whereas three-component morphologies are found in the FPOSS-based surfactants. A library of interesting morphologies is observed. For linear giant surfactants, the  $AC_{60}$ -based giant surfactants show a transition sequence of LAM, modulated lamellae (ML), HEX, and BCC structures, whereas three-component undulated lamellae ( $UL_3$ ), three-component lamellae ( $LAM_3$ ), perforated lamellae ( $PL_3$ ), and cylinder-*within*-perforated lamellae ( $CPL_3$ ) structures are sequentially observed in the FPOSS-based samples, with increasing the molecular weight of the PS block (Fig. 16) (C.-H. Hsu et al., unpublished work). Within these structures,  $AC_{60}$ s are distributed in the PEO domain without long range positional order, whereas FPOSS forms separated domains with mesomorphic packing. The topological isomers of  $AC_{60}$ -based surfactants exhibit different dimensions yet similar or identical morphologies; however, those FPOSS-based giant surfactants show strong topological dependence on the stable morphologies. A stretching parameter of the PS block has been utilized to interpret and characterize the phase transitions (C.-H. Hsu et al., unpublished work). The versatile self-assembled morphologies suggest that giant surfactants are an excellent platform for producing well-controlled supramolecular structures, and that topology can serve as an additional crucial factor for finely tuning the size and the geometry of structures.

## 8 Concluding Remarks

In summary, we have collected as many experimental observations of ordered supramolecular structures via self-assembly processes as possible and introduced the concept of supramolecular crystals and crystallization. This concept extends conventional crystals and crystallization to a broader research field and includes ordered structures with crystallographic building blocks within which atoms in motifs might not possess classic positional, bond-orientational, and molecular-orientational long-range order. Various examples are given of different types of giant molecules, including giant shape amphiphiles, Janus particles, giant surfactants, and giant tetrahedra self-assembled (“crystallized”) in bulk, solution, and film states. Although they undergo different assembly processes in forming ordered structures (supramolecular crystallization), the classic phase transformation theory and concepts are still the guiding principles for these formation mechanisms. The central issue is the following: What are the features of the packing scheme in these supramolecular crystals of giant molecules with nanosized motifs? First, within their motifs, long-range ordered atomic positions with translational symmetry are not required. The motifs are the smallest repeating building blocks in the crystals. Second, topologies of the giant molecules are crucially important in the formation of these supramolecular crystals as a result of their relatively rigid molecular shape persistency as individual packing units. Third, the design and introduction of collective secondary interactions can stabilize crystal structures with nanosized motifs and ordered structures. Fourth, the selective assembly process leads to stepwise structure formation and makes modular self-organization possible at different length scales. It is expected that the investigation of ordered supramolecular structures can also be extended from supramolecular crystals to supramolecular liquid crystals, plastic crystals, and quasicrystals. For a broader perspective, in parallel with finding new phase structures, there must be further developments in many research fields in chemistry and physics. For example, in chemistry, we need to improve synthetic ability from “well-defined” to “precisely defined” chemistry. Traditionally, one starts to construct a material on the basis of an atomic platform. How do we think of a modular approach using building blocks (nanoatoms) to construct our materials at the nanoscale or even higher length scales, in addition to the classic random-coil polymers? How do we design structural and functional synthons to transfer and amplify molecular functions to macroscopic properties? In physics, how do we describe a non-equilibrium state during the phase transitions? How do we deal with an entropy-dominated transformation? When we describe a phase transition, we always think that it is in an infinitely large space. If the space becomes limited and even smaller than the lower limit for application of statistical mechanics, what could we do? Finally, we are at present studying the structure and properties of materials at one length and time scale. How could we expand our understanding to multiple lengths, space and time scales? All of these questions need to be answered through the joint efforts of chemists, physicists, bioscientists, life scientists, and engineers.



**Acknowledgments** This work was supported by the National Science Foundation (DMR-1408872). Use of the Advanced Photon Source at Argonne National Laboratory was supported by the U.S. Department of Energy, Office of Science, Office of Basic Energy Sciences, under contract DE-AC02-06CH11357.

## References

1. Staudinger H (1920) *Ber Dtsch Chem Ges* 53:1073
2. Odian G (2004) *Principles of polymerization*, 4th edn. Wiley-Interscience, New York
3. Feynman RP (1960) *Eng Sci* 23:22
4. Ober CK, Cheng SZD, Hammond PT, Muthukumar M, Reichmanis E, Wooley KL, Lodge TP (2009) *Macromolecules* 42:465
5. Zhang W-B, Yu X, Wang C-L, Sun H-J, Hsieh I-F, Li Y, Dong X-H, Yue K, van Horn RM, Cheng SZD (2014) *Macromolecules* 47:1221
6. Yu X, Li Y, Dong X-H, Yue K, Lin Z, Feng X, Huang M, Zhang W-B, Cheng SZD (2014) *J Polym Sci B Polym Phys* 52:1309
7. Zhang W-B, Cheng SZD (2015) *Chin J Polym Sci* 33:797
8. Tomalia DA, Christensen JB, Boas U (2012) *Dendrimers, dendrons, and dendritic polymers: discovery, applications, and the future*. Cambridge University Press, Cambridge
9. Newkome GR, Moorefield CN, Vogtle F (2001) *Dendrimers and dendrons: concepts, syntheses, applications*. Wiley, Weinheim
10. Fréchet JMJ, Tomalia DA (2001) *Dendrimer and other dendritic polymers*. Wiley, West Sussex
11. Roovers J, Comanita B (1999) *Dendrimers and dendrimer-polymer hybrids*. In: Roovers J (ed) *Branched polymers I*, vol 142, *Adv. Polym. Sci.* Springer, Berlin, pp 179–228
12. del Barrio J, Oriol L, Sanchez C, Serrano JL, Di Cicco A, Keller P, Li MH (2010) *J Am Chem Soc* 132:3762
13. Dong X-H, Lu X, Ni B, Chen Z, Yue K, Li Y, Rong L, Koga T, Hsiao BS, Newkome GR, Shi A-C, Zhang W-B, Cheng SZD (2014) *Soft Matter* 10:3200
14. Percec V, Imam MR, Peterca M, Leowanawat P (2012) *J Am Chem Soc* 134:4408
15. Rosen BM, Wilson CJ, Wilson DA, Peterca M, Imam MR, Percec V (2009) *Chem Rev* 109:6275
16. Percec V, Wilson DA, Leowanawat P, Wilson CJ, Hughes AD, Kaucher MS, Hammer DA, Levine DH, Kim AJ, Bates FS, Davis KP, Lodge TP, Klein ML, DeVane RH, Aqad E, Rosen BM, Argintaru AO, Sienkowska MJ, Rissanen K, Nummelin S, Ropponen J (2010) *Science* 328:1009
17. Fujita M, Oguro D, Miyazawa M, Oka H, Yamaguchi K, Ogura K (1995) *Nature* 378:469
18. Tominaga M, Suzuki K, Kawano M, Kusakawa T, Ozeki T, Sakamoto S, Yamaguchi K, Fujita M (2004) *Angew Chem Int Ed* 43:5621
19. Branda N, Wyler R, Rebek J (1994) *Science* 263:1267
20. Hartmann-Thompson C (2011) *Applications of polyhedral oligomeric silsesquioxanes*. Springer, Dordrecht
21. Coronado E, Gomez-Garcia CJ (1998) *Chem Rev* 98:273
22. Katsoulis DE (1998) *Chem Rev* 98:359
23. Dolbecq A, Dumas E, Mayer CR, Mialane P (2010) *Chem Rev* 110:6009
24. Damasceno PF, Engel M, Glotzer SC (2012) *Science* 337:453
25. Horsch M, Zhang Z, Glotzer S (2005) *Phys Rev Lett* 95:056105
26. Glotzer SC, Horsch MA, Iacovella CR, Zhang Z, Chan ER, Zhang X (2005) *Curr Opin Colloid Interface Sci* 10:287
27. Glotzer SC, Solomon MJ (2007) *Nat Mater* 6:557

28. Bratschitsch R, Leitenstorfer A (2006) *Nat Mater* 5:855
29. Kastner MA (1993) *Phys Today* 46:24
30. Dmitrii F, Rosei F (2007) *Angew Chem Int Ed* 46:6006
31. Roy X, Lee C-H, Crowther AC, Schenck CL, Besara T, Lalancette RA, Siegrist T, Stephens PW, Brus LE, Kim P, Steigerwald ML, Nuckolls C (2013) *Science* 341:157
32. Dong X-H, van Horn R, Chen Z, Ni B, Yu X, Wurm A, Schick C, Lotz B, Zhang W-B, Cheng SZD (2013) *J Phys Chem Lett* 4:2356
33. Su H, Zheng J, Wang Z, Lin F, Feng X, Dong X-H, Becker ML, Cheng SZD, Zhang W-B, Li Y (2013) *ACS Macro Lett* 2:645
34. Lin Z, Lu P, Hsu CH, Yue K, Dong XH, Liu H, Guo K, Wesdemiotis C, Zhang WB, Yu X, Cheng SZD (2014) *Chem Eur J* 10:11630
35. Ni B, Huang M, Chen Z, Chen Y, Hsu CH, Li Y, Pochan D, Zhang WB, Cheng SZD, Dong XH (2015) *J Am Chem Soc* 137:1392
36. Yu X, Yue K, Hsieh IF, Li Y, Dong XH, Liu C, Xin Y, Wang HF, Shi AC, Newkome GR, Ho RM, Chen EQ, Zhang WB, Cheng SZD (2013) *Proc Natl Acad Sci USA* 110:10078
37. Wang Z, Li Y, Dong X-H, Yu X, Guo K, Su H, Yue K, Wesdemiotis C, Cheng SZD, Zhang W-B (2013) *Chem Sci* 4:1345
38. Huang M, Hsu C-H, Wang J, Mei S, Dong X, Li Y, Li M, Liu H, Zhang W, Aida T, Zhang W-B, Yue K, Cheng SZD (2015) *Science* 348:424
39. Yu X, Zhong S, Li X, Tu Y, Yang S, van Horn RM, Ni C, Pochan DJ, Quirk RP, Wesdemiotis C, Zhang W-B, Cheng SZD (2010) *J Am Chem Soc* 132:16741
40. Yu X, Zhang WB, Yue K, Li X, Liu H, Xin Y, Wang CL, Wesdemiotis C, Cheng SZD (2012) *J Am Chem Soc* 134:7780
41. Dong X-H, Zhang W-B, Li Y, Huang M, Zhang S, Quirk RP, Cheng SZD (2012) *Polym Chem* 3:124
42. Li Y, Dong X-H, Guo K, Wang Z, Chen Z, Wesdemiotis C, Quirk RP, Zhang W-B, Cheng SZD (2012) *ACS Macro Lett* 1:834
43. Zhang W-B, Li Y, Li X, Dong X, Yu X, Wang C-L, Wesdemiotis C, Quirk RP, Cheng SZD (2011) *Macromolecules* 44:2589
44. Ni B, Dong X-H, Chen Z, Lin Z, Li Y, Huang M, Fu Q, Cheng SZD, Zhang W-B (2014) *Polym Chem* 5:3588
45. Yue K, Liu C, Guo K, Wu K, Dong X-H, Liu H, Huang MJ, Wesdemiotis C, Cheng SZD, Zhang W-B (2013) *Polym Chem* 4:1056
46. Sun H-J, Tu Y, Wang C-L, van Horn RM, Tsai C-C, Graham MJ, Sun B, Lotz B, Zhang W-B, Cheng SZD (2011) *J Mater Chem* 21:14240
47. Lin M-C, Hsu C-H, Sun H-J, Wang C-L, Zhang W-B, Li Y, Chen H-L, Cheng SZD (2014) *Polymer* 55:4514
48. Benz K-W, Neumann W (2014) *Introduction to crystal growth and characterization*. Wiley, Weinheim
49. De Graef M, Mcherry ME (2012) *Structure of materials*. Cambridge University Press, Cambridge
50. Cheng SZD (2008) *Phase transitions in polymers the role of metastable states*. Elsevier, Amsterdam
51. Li CY, Cheng SZD, Ge JJ, Bai F, Zhang JZ, Mann IK, Harris FW, Chien L-C, Yan D, He T, Lotz B (1999) *Phys Rev Lett* 83:4558
52. Li CY, Cheng SZD, Ge JJ, Bai F, Zhang JZ, Mann IK, Chien L-C, Harris FW, Lotz B (2000) *J Am Chem Soc* 122:72
53. Lotz B, Cheng SZD (2005) *Polymer* 46:577
54. Cheng SZD, Lotz B (2003) *Philos Transact A Math Phys Eng Sci* 361:517
55. Cheng SZD, Lotz B (2005) *Polymer* 46:8662
56. Date RW, Bruce DW (2003) *J Am Chem Soc* 125:9012
57. Yang Y, Zimmt MB (2015) *J Phys Chem B* 119:7740
58. Hoyle CE, Bowman CN (2010) *Angew Chem Int Ed* 49:1540

59. Kolb HC, Finn MG, Sharpless KB (2001) *Angew Chem Int Ed* 40:2004
60. Meldal M, Tornøe CW (2008) *Chem Rev* 108:2953
61. Kadish KM, Ruoff RS (2000) *Fullerenes: chemistry, physics, and technology*. Wiley-Interscience, New York
62. Martin N, Giacalone F (2009) *Fullerene polymers: synthesis, properties and applications*. Wiley-VCH, Weinheim
63. Hirsch A, Brettreich M (2005) *Fullerenes: chemistry and reactions*. Wiley-VCH, Weinheim
64. Wang CL, Zhang WB, van Horn RM, Tu Y, Gong X, Cheng SZD, Sun Y, Tong M, Seo J, Hsu BB, Heeger AJ (2011) *Adv Mater* 23:2951
65. Wang CL, Zhang WB, Yu X, Yue K, Sun HJ, Hsu CH, Hsu CS, Joseph J, Modarelli DA, Cheng SZD (2013) *Chem Asian J* 8:947
66. Wang C-L, Zhang W-B, Hsu C-H, Sun H-J, van Horn RM, Tu Y, Anokhin DV, Ivanov DA, Cheng SZD (2011) *Soft Matter* 7:6135
67. Wang C-L, Zhang W-B, Sun H-J, van Horn RM, Kulkarni RR, Tsai C-C, Hsu C-S, Lotz B, Gong X, Cheng SZD (2012) *Adv Energy Mater* 2:1375
68. Zhang W-B, Wang X-M, Wang X-W, Liu D, Han S-Y, Cheng SZD (2015) *Prog in Chem* 27:1333
69. Teng FA, Cao Y, Qi YJ, Huang M, Han ZW, Cheng SZD, Zhang WB, Li H (2013) *Chem Asian J* 8:1223
70. Cordes DB, Lickiss PD, Rataboul F (2010) *Chem Rev* 110:2081
71. Pielichowski K, Njuguna J, Janowski B, Pielichowski J (2006) *Adv Polym Sci* 201:225
72. Roll MF, Asuncion MZ, Kampf J, Laine RM (2008) *ACS Nano* 2:320
73. Tanaka K, Chujo Y (2012) *J Mater Chem* 22:1733
74. Kuo S-W, Chang F-C (2011) *Prog Polym Sci* 36:1649
75. Ren X, Sun B, Tsai C-C, Tu Y, Leng S, Li K, Kang Z, van Horn RM, Li X, Zhu M, Wesdemiotis C, Zhang W-B, Cheng SZD (2010) *J Phys Chem B* 114:4802
76. Jiang S, Chen Q, Tripathy M, Luijten E, Schweizer KS, Granick S (2010) *Adv Mater* 22:1060
77. Cleland AN (2009) *Phys Today* 62:68
78. Walther A, Müller AHE (2008) *Soft Matter* 4:663
79. de Gennes P (1992) *Angew Chem Int Ed* 31:842
80. Dendukuri D, Pregibon DC, Collins J, Hatton TA, Doyle PS (2006) *Nat Mater* 5:365
81. Nie Z, Li W, Seo M, Xu S, Kumacheva E (2006) *J Am Chem Soc* 128:9408
82. Nisisako T, Torii T, Takahashi T, Takizawa Y (2006) *Adv Mater* 18:1152
83. Walther A, Andre X, Drechsler M, Abetz V, Muller AHE (2007) *J Am Chem Soc* 129:6187
84. Li Y, Guo K, Su H, Li X, Feng X, Wang Z, Zhang W, Zhu S, Wesdemiotis C, Cheng SZD, Zhang W-B (2014) *Chem Sci* 5:1046
85. Li Y, Zhang WB, Hsieh IF, Zhang G, Cao Y, Li X, Wesdemiotis C, Lotz B, Xiong H, Cheng SZD (2011) *J Am Chem Soc* 133:10712
86. Liu H, Hsu CH, Lin Z, Shan W, Wang J, Jiang J, Huang M, Lotz B, Yu X, Zhang WB, Yue K, Cheng SZD (2014) *J Am Chem Soc* 136:10691
87. Dong X-H, Ni B, Huang M, Hsu C-H, Chen Z, Lin Z, Zhang W-B, Shi A-C, Cheng SZD (2015) *Macromolecules* 48:7171. doi:[10.1021/acs.macromol.5b01661](https://doi.org/10.1021/acs.macromol.5b01661)
88. Lin Z, Lu P, Hsu C-H, Sun J, Zhou Y, Huang M, Yue K, Ni B, Dong X-H, Li X, Zhang W-B, Yu X, Cheng SZD (2015) *Macromolecules* 48:5496
89. Haji-Akbari A, Engel M, Keys AS, Zheng X, Petschek RG, Palfy-Muhoray P, Glotzer SC (2009) *Nature* 462:773
90. Henzie J, Grünwald M, Widmer-Cooper A, Geissler PL, Yang P (2012) *Nat Mater* 11:131
91. Greyson EC, Barton JE, Odom TW (2006) *Small* 2:368
92. Boles MA, Talapin DV (2014) *J Am Chem Soc* 136:5868
93. Quan Z, Fang J (2010) *Nano Today* 5:390
94. Liao C-W, Lin Y-S, Chanda K, Song Y-F, Huang MH (2013) *J Am Chem Soc* 135:2684
95. Chakrabarty R, Mukherjee PS, Stang PJ (2011) *Chem Rev* 111:6810
96. Furukawa H, Cordova KE, O'Keeffe M, Yaghi OM (2013) *Science* 341:1230444

97. Guillerme V, Kim D, Eubank JF, Luebke R, Liu X, Adil K, Lah MS, Eddaoudi M (2014) *Chem Soc Rev* 43:6141
98. Miszta K, de Graaf J, Bertoni G, Dorfs D, Brescia R, Marras S, Ceseracciu L, Cingolani R, van Roij R, Dijkstra M, Manna L (2011) *Nat Mater* 10:872
99. Manna L, Milliron DJ, Meisel A, Scher EC, Alivisatos AP (2003) *Nat Mater* 2:382
100. Park I, Park S, Park HW, Chang T, Yang HC, Ryu CY (2006) *Macromolecules* 39:315
101. Ludwigs S, Boker A, Voronov A, Rehse N, Magerle R, Krausch G (2003) *Nat Mater* 2:744
102. Knoll A, Horvat A, Lyakhova KS, Krausch G, Sevink GJA, Zvelindovsky AV, Magerle R (2002) *Phys Rev Lett* 89:035501
103. Yin Y, Sun P, Jiang R, Li B, Chen T, Jin Q, Ding D, Shi A-C (2006) *J Chem Phys* 124:184708

# Self-Nucleation of Crystalline Phases Within Homopolymers, Polymer Blends, Copolymers, and Nanocomposites

R.M. Michell, A. Mugica, M. Zubitur, and A.J. Müller

**Abstract** Self-nucleation (SN) is a special nucleation process triggered by self-seeds or self-nuclei that are generated in a given polymeric material by specific thermal protocols or by inducing chain orientation in the molten or partially molten state. SN increases the nucleation density of polymers by several orders of magnitude, producing significant modifications to their morphology and overall crystallization kinetics. In fact, SN can be used as a tool for investigating the overall isothermal crystallization kinetics of slow-crystallizing materials by accelerating the primary nucleation stage in a previous SN step. Additionally, SN can facilitate the formation of one particular crystalline phase in polymorphic materials. The SN behavior of a given polymer is influenced by its molecular weight, molecular topology, and chemical structure, among other intrinsic and extrinsic characteristics. This review paper focuses on the applications of DSC-based SN techniques to study the nucleation, crystallization, and morphology of different types of polymers, blends, copolymers, and nanocomposites.

---

R.M. Michell

Grupo de Polímeros USB, Departamento de Ciencia de los Materiales, Universidad Simón Bolívar, Apartado 89000, Caracas 1080-A, Venezuela

A. Mugica and M. Zubitur

Faculty of Chemistry, POLYMAT and Polymer Science and Technology Department, University of the Basque Country UPV/EHU, Paseo Manuel de Lardizabal 3, 20018 Donostia/San Sebastián, Spain

A.J. Müller (✉)

Grupo de Polímeros USB, Departamento de Ciencia de los Materiales, Universidad Simón Bolívar, Apartado 89000, Caracas 1080-A, Venezuela

Faculty of Chemistry, POLYMAT and Polymer Science and Technology Department, University of the Basque Country UPV/EHU, Paseo Manuel de Lardizabal 3, 20018 Donostia/San Sebastián, Spain

IKERBASQUE, Basque Foundation for Science, Bilbao, Spain

e-mail: [alejandrojesus.muller@ehu.es](mailto:alejandrojesus.muller@ehu.es)

**Keywords** Crystallization rate · Melt memory · Self-nucleation

## Contents

1	Introduction .....	216
2	Brief Description of the DSC Experimental Protocol Required for Study of Self-Nucleation .....	217
3	Crystalline Memory .....	222
4	Self-Nucleation as a Tool for Ascertaining the Origin of Fractionated Crystallization .....	227
5	Influence of Confinement on Self-Nucleation Behavior .....	231
6	Effect of Chain Topology on Self-Nucleation Behavior .....	237
7	Self-Nucleation and Preferential Polymorphism .....	239
8	Self-Nucleation Before Isothermal Crystallization .....	240
9	Molecular Weight .....	244
10	Self-Nucleation and Nucleating Agents Efficiency Determination .....	245
11	Conclusions .....	247
	References .....	247

## 1 Introduction

The understanding and control of polymer crystallization is an important goal for both academy and industry. The solidification of a semicrystalline polymer from the melt usually involves overall crystallization, a process that includes primary nucleation and crystal growth. Primary nucleation can have a dominating influence on overall crystallization and in the resulting morphology. Self-nucleation (SN) provides a way to enhance primary crystal nucleation in polymers. SN in polymeric materials has attracted much attention since 1966, when Keller et al. [1] employed it for the first time to produce single crystals crystallized from solution with similar sizes. Fillon et al. [2] in 1993 studied SN of melt-crystallized isotactic polypropylene (PP), establishing a simple experimental protocol employing differential scanning calorimetry (DSC).

SN can be defined as a thermal protocol for the production of self-nuclei within a polymer melt. As a consequence, nucleation density increases significantly as self-nuclei are produced. For any given polymer, self-nuclei should in theory be its best nucleating agent. If self-nuclei are composed of crystal fragments remaining from partial melting experiments, such crystal fragments have the capacity to produce epitaxial nucleation because they have the same crystal structure as the polymer being crystallized. On the other hand, self-nuclei can also be constituted by regions of the melt where segmental orientation has not been erased. Such regions produce crystalline memory effects that can induce nucleation upon cooling from non-isotropic melts [1–4]

In this paper, the application of the DSC SN technique is reviewed since its inception in 1993. Results obtained from study of fractionated crystallization,

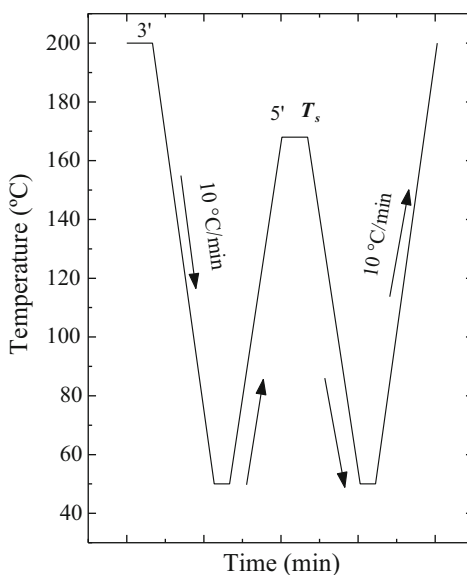
confinement, nucleation efficiency, or crystalline memory in homopolymers, blends, copolymers, and nanocomposites are presented.

## 2 Brief Description of the DSC Experimental Protocol Required for Study of Self-Nucleation

The typical SN experimental procedure can be described as follows [2, 3] (see Fig. 1):

1. Erasure of crystalline thermal history. The sample is heated to a temperature of approximately 25–30°C above the DSC melting temperature peak and kept in the melt for 3 min. The exact temperature can vary from polymer to polymer because crystalline memory is a function of molecular weight, thermal history, and intermolecular interactions. The objective is to erase all crystalline memory and obtain an isotropic melt. All thermally sensitive nuclei are destroyed, leaving only the temperature-resistant heterogeneous nuclei of unknown nature, such as catalyst residues or impurities.
2. Creation of a standard semicrystalline state. The sample is cooled from the homogeneous melt at a constant rate (usually 10 or 20°C/min) down to a temperature low enough to allow the sample to crystallize until saturation. The crystallization temperature peak recorded during this cooling scan is defined as the *standard crystallization temperature* (or standard  $T_c$ ), because it is only a function of the density of thermally stable nuclei in the sample. The sample is held at the minimum temperature for 3 min.

**Fig. 1** Scheme of a self-nucleation (SN) experiment [2]



3. Thermal conditioning at a temperature denoted  $T_s$ . At this temperature, the sample could melt, self-nucleate, or self-nucleate and anneal. The sample is heated at a constant rate (the same rate employed in step 2) from the chosen minimum temperature up to a selected self-seeding or self-nucleation temperature (frequently denoted  $T_s$ ), and then held at this  $T_s$  temperature for 5 min.
4. Cooling at a constant rate from  $T_s$  down to the minimum temperature chosen in step 2. During cooling, the sample crystallizes at a temperature that depends on the previous treatment (step 3) at  $T_s$ .
5. Final melting. Subsequent heating at a constant rate (the same rate as in steps 2–4) from the minimum temperature chosen in step 2 up to the maximum melting temperature established in step 1.

For this experimental protocol, the most important parameters are [2, 4]:

- (a) Heating and cooling rates. Typically the heating and cooling scans employed are 10 or 20°C/min; however, the SN protocol can also be performed employing higher rates [5–7]
- (b)  $T_s$  temperature
- (c) Time spent at  $T_s$

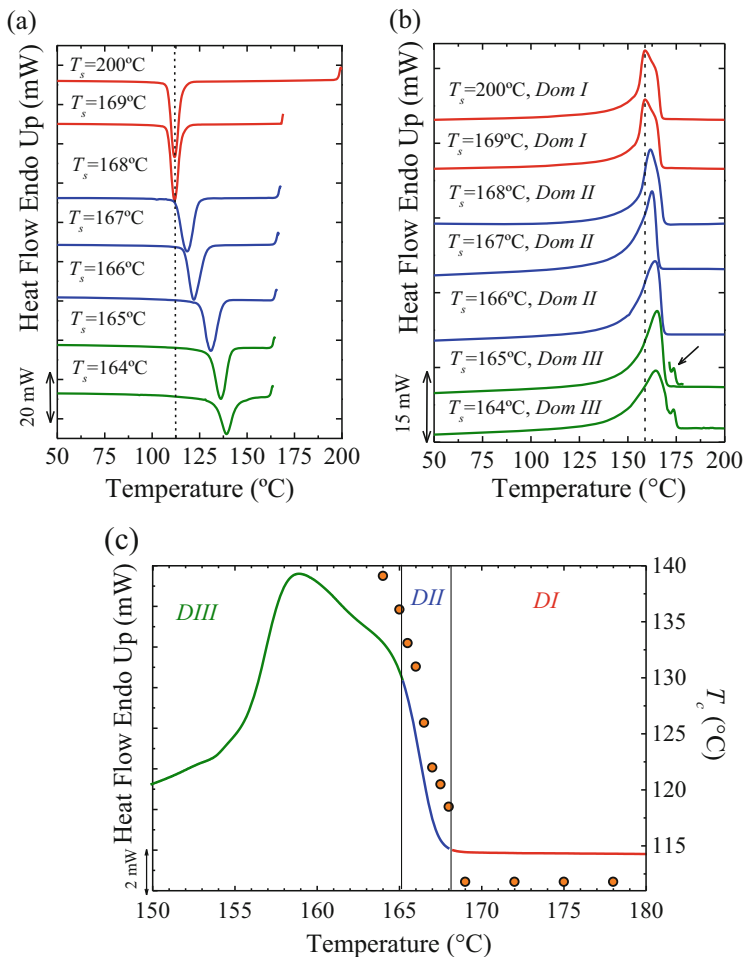
An example of the experimental data obtained during SN is shown in Fig. 2. The cooling scans after the isothermal step at  $T_s$  are presented in Fig. 2a and the subsequent heating scans are shown in Fig. 2b. Finally, the standard heating scan, with the domains indicated, is shown in Fig. 2c. The SN domains were defined by Fillon et al. [2] for isotactic PP. The three SN domains are described below (see Fig. 2):

*Domain I or melting domain.* The polymer is under domain I when complete melting occurs and the crystalline history of the material is erased. Therefore, all crystalline memory is erased and the melt is isotropic. For the PP studied in Fig. 2, complete melting is found at 169°C. At this  $T_s$  and above, no change is detected in peak crystallization temperature ( $T_c$ ), as compared with the standard crystallization temperature obtained with  $T_s = 200^\circ\text{C}$ . The PP in Fig. 2 is under domain I at any  $T_s$  temperature larger or equal to 169°C. In this domain, the nucleation density for the PP sample employed in Fig. 2 is constant and its value is approximately  $10^6$  nuclei/cm<sup>3</sup>. Both crystallization and melting DSC scans are identical within domain I (see red curves in Fig. 2).

*Domain II or self-nucleation domain.* In domain II, the  $T_s$  range employed is low enough to produce self-nuclei, but high enough to avoid annealing. Therefore, domain II is easily identified when after 5 min at a given  $T_s$ , the peak crystallization temperature of the sample increases in comparison with the standard value. According to Fig. 2a, the start of domain II for the PP sample employed occurs at a  $T_s = 168^\circ\text{C}$ . Additionally, the subsequent melting trace in Fig. 2b does not reveal any sign of annealing. This is the distinctive behavior of domain II or exclusive SN domain.

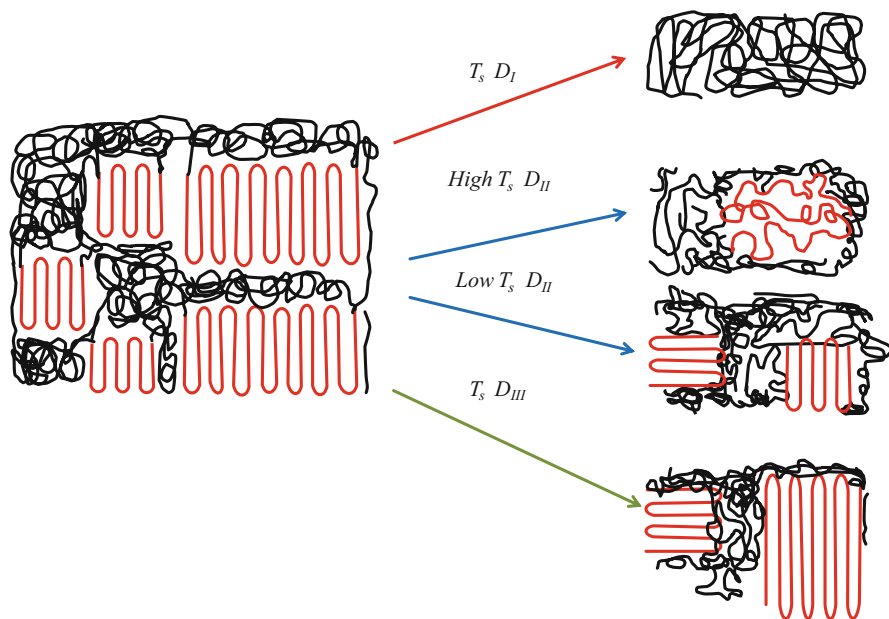
The nature of the self-nuclei generated in domain II has been the subject of debate. Fillon et al. [2] considered that small crystal fragments remain in domain





**Fig. 2** (a) DSC cooling scans (at 10°C/min) for PP after 5 min at the indicated  $T_s$ . (b) Subsequent heating scans (at 10°C/min) after the cooling runs shown in (a). The arrow points to a close-up of a small high temperature peak. (c) Representation of the self-nucleation domains for PP homopolymer superimposed on top of the standard DSC melting trace. Data points represent crystallization temperature peaks (plotted using the right-hand y-axis) as a function of  $T_s$  values (on the x-axis). Reprinted from Müller et al. [6], Copyright (2015), with permission from Elsevier

II, or in other words, that  $T_s$  is high enough to melt almost all of the polymer crystals, but low enough to leave “small” crystal fragments that can act as self-nuclei. This explanation is probably true for the lowest temperatures of domain II. Lorenzo et al. [4] considered that the presence of residual segmentation orientation in the melt is enough to produce self-nuclei by inducing the so-called memory effect, especially in the highest temperature range within domain II. Further discussion of the nature of the self-nuclei and the importance of the crystalline memory is addressed in the next sections.



**Fig. 3** Molecular representation of the three different self-nucleation domains ( $D_I$ ,  $D_{II}$ , and  $D_{III}$ ). Reprinted from Müller et al. [6], Copyright (2015), with permission from Elsevier

The generation of self-nuclei increases the number of nuclei in PP from about  $10^6$  nuclei/cm<sup>3</sup> (in domain I) to  $10^{12}$ – $10^{13}$  nuclei/cm<sup>3</sup>, with a concomitant reduction in spherulitic size (see Fig. 3).

The SN effect within domain II can slightly alter the subsequent melting trace after crystallization. Small increases in peak melting temperature can be observed, as well as the disappearance of partial melting and recrystallization effects that may have been present in the standard melting scan within domain I. In Fig. 2, the polypropylene standard melting behavior in domain I is characterized by a bimodal melting peak, or a main melting peak with a right-hand side high temperature shoulder, easily appreciated in Fig. 2c. This bimodality is a result of reorganization processes experienced by PP during the heating scan (i.e., by a process of partial melting of thinner crystals, which re-crystallize into thicker crystals). The first melting peak is a result of fusion of the crystals formed during the standard cooling scan, whereas the second (or high temperature shoulder) is a result of fusion of re-crystallized PP during the scan. Figure 2b clearly shows that, after SN, the melting peak bimodality within domain II disappears. This behavior is caused by the enhanced nucleation density, which makes possible the crystallization of PP at higher temperatures with thicker crystals that do not need to reorganize during the heating scan.

*Domain III or self-nucleation and annealing domain.* When  $T_s$  is too low, partial melting is produced and the unmolten crystals anneal during the 5 min at  $T_s$ . Figure 2b shows that, at  $T_s = 165^\circ\text{C}$ , the melting endotherm exhibits a small high

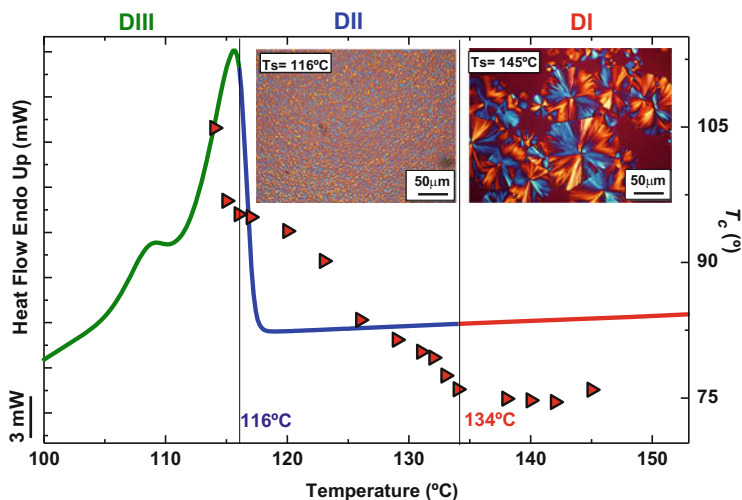
temperature sharp peak (shown in a close up and indicated with an arrow) that is a result of the melting of annealed crystals. Careful inspection reveals that, at  $T_s = 164^\circ\text{C}$ , the crystallization exotherm shows a high temperature tail (indicating immediate recrystallization when the material is cooled from  $T_s$ ), which is also a sign that the sample is in domain III.

Figure 2c shows the transition temperatures between SN domains on top of the standard PP melting endotherm. The same figure also shows the variation in the peak crystallization temperature ( $T_c$ ) with  $T_s$  ( $T_c$  data is associated with the right-hand y-axis, and the x-axis with  $T_s$  temperature). This plot represents the typical  $T_c$  variations during SN behavior [2].  $T_c$  values remain constant in domain I, whereas in domain II they increase sharply, as peak  $T_c$  values are proportional to nucleation density.

Figure 3 illustrates the different SN domains at a molecular level. In domain I the polymer chains are completely molten, forming isotropic random coils or a homogeneous melt. When  $T_s$  decreases to domain II, the melt is no longer uniform and two possible representations are considered in Fig. 3. At higher temperatures within domain II, the melt retains some residual segmental orientation, or crystalline memory, which produces SN. On the other hand, at lower temperatures within domain II, small fragments of crystals are found, as postulated by Fillon et al. [2]. In domain III, the temperature is low enough to partially melt the polymer, while the unmolten crystals anneal into thicker crystals.

Figure 4 illustrates the SN behavior of poly(butylene succinate) (PBS) [8]. Two polarized optical micrographs show the typical morphology after cooling the sample from the melt in domain I (after the melt memory is erased) or from domain II (after SN). The dramatic increase in nucleation density causes an exponential increase in the number of spherulites being nucleated and, therefore, their size is reduced, because they impinge on one another before they can grow. This illustrates how the morphology of a semicrystalline sample can be significantly altered by SN.

Figure 4 additionally shows how PBS possesses a remarkable crystalline memory. Note that the melting process is completely over by  $120^\circ\text{C}$ . Nevertheless, the material experiences significant SN until  $133^\circ\text{C}$ , as judged by the increase in  $T_c$  values ( $T_c$  data is associated with the right-hand y-axis). In the case of PBS, Fig. 3 can be used to illustrate a strong crystalline memory effect. It is clear that crystalline memory is the only explanation for the behavior of the material in the high  $T_s$  region within domain II, because full melting had been attained, as judged by the return of the DSC trace to the base line after melting at temperatures above  $120^\circ\text{C}$ . Wide-angle X-ray scattering (WAXS) experiments also indicate complete melting at temperatures above  $120^\circ\text{C}$  [8].



**Fig. 4** Self-nucleation domains for PBS homopolymer, superimposed on top of its standard DSC melting trace. *Insets* show polarized light optical micrographs taken during cooling from  $T_s = 145^\circ\text{C}$  (domain I) and  $T_s = 116^\circ\text{C}$  (domain II). The *data points* represent peak crystallization temperatures (plotted using the *right handy-axis*) as a function of  $T_s$  values (on the *x-axis*). Reprinted with permission from Arandia et al. [8]. Copyright (2015) American Chemical Society

### 3 Crystalline Memory

The controversial idea that polymer crystallization from the melt could start from some kind of initial transient state, precursor, or mesophase has been discussed in several works [4, 9–63]. Such precursors could be correlated with the nucleation density and also with melt memory.

“Melt memory” is a term employed to describe the phenomenon that occurs when a semicrystalline polymer melt retains a partial memory of its previous crystalline structure [2, 4, 27, 45, 47, 56, 64–76] and it could be related to the existence of precursors, according to some authors [4, 77].

Self-nuclei could also originate from crystalline memory. Lorenzo et al. [4] have argued that crystalline memory is observed in semicrystalline polymers in the quiescent state as a consequence of their high molecular weight and the availability of multiple chain conformations (from random coil in the melt to linear segments within crystals). The transition from a semicrystalline morphology to homogeneous melt is not instantaneous, and it requires high temperatures and finite times.

The melt must be heated to high temperatures (typically, 25–30°C above the peak melting temperature; however, the exact temperature depends on the polymer under study) for a short time (typically ~3–5 min) or to lower temperatures (always above the melting temperature) for longer times. This process erases the memory of previous processing and thermal treatments. The memory effect could originate from some embryos (molecular clusters) that survive the thermal treatment and then

become active nuclei once the temperature is lowered [26, 44]. However, it is not clear why some embryos could survive the high temperatures applied. Another explanation given in the literature for the memory effect is the presence of precursor structures, which are analogous to embryos because they could eventually transform into nuclei. The origin of precursors differs for any given polymer. According to some authors, some precursors are formed by shear flow in the melt [44, 78–86]. Shear flow is the origin of polymer chain orientation and their partial alignment. These precursors can be destroyed by thermal treatment if the temperature is high enough and the time sufficient. Crystalline precursors can also be produced if the temperature and/or time are not sufficient to erase the crystalline memory of the previous chain conformational state in the crystal [4].

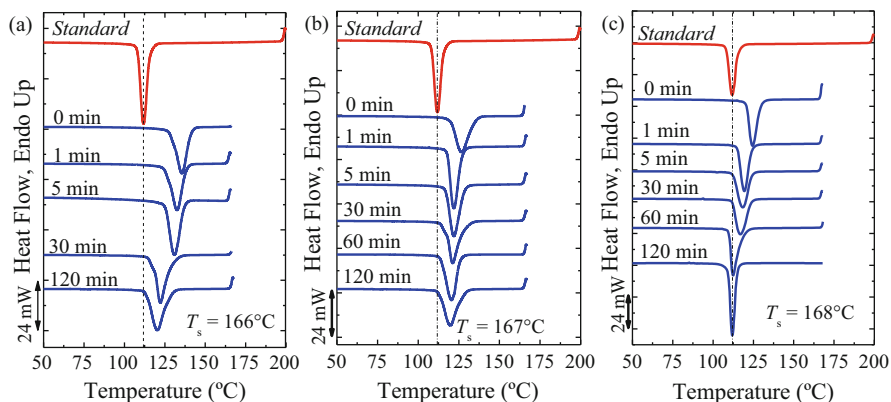
According to Somani et al. [79], precursors do not have crystallographic order, can survive for a long time after the shear stops (more than 2 h), and are layer-like superstructures [79].

Strobl and coworkers [18, 34, 35] explained memory effects by considering that a precursor is a conceptual object that contains crystallites. During crystallization, the object volume is filled with crystals and grows with crystallization time. During melting, the object is progressively emptied. At low melting temperatures, some crystals remain inside the object (causing melt memory effects upon cooling). However, at high temperatures, when the memory effect is erased, the object is completely empty. Additionally, the authors postulate that the melt memory effect is related to the creation rate of the crystals within the precursor. These objects or precursors have never been observed without the presence of crystals, but Häfele et al. [34, 35] consider that indirect experimental evidence points towards their presence before crystallites are formed.

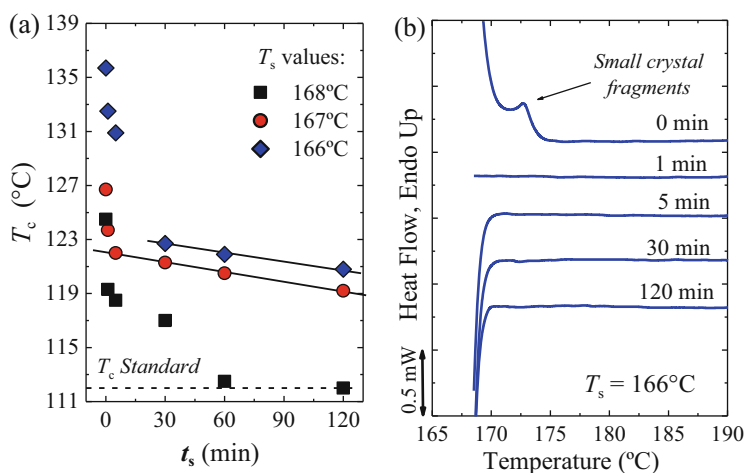
Lorenzo et al. [4] studied the origin of isotactic polypropylene (PP) self-nuclei produced in domain II and the influence of SN time at specific  $T_s$  values. Figure 5 shows cooling scans after partial melting at three different  $T_s$  values and for different annealing times. The standard cooling scan is also shown for comparison.

Figure 5 demonstrates that the existence of self-nuclei not only depends on  $T_s$ , but also depends on the time spent at  $T_s$  ( $t_s$ ). For all  $T_s$  values employed, when  $t_s$  increases the nucleating effect decreases or completely disappears, and the exothermic peak is progressively shifted to lower values until it reaches the equilibrium at the same  $T_c$  displayed by the material during the standard cooling run. Another interesting effect found by Lorenzo et al. [4] is that the time needed to reach the standard  $T_c$  is lower for the higher  $T_s$  temperatures (see Fig. 5a). At  $T_s = 168^\circ\text{C}$ , only 60 min are needed to decrease nucleation density to values similar to those of the standard sample. However, when lower  $T_s$  values (within domain II) are employed (Fig. 5a), an isotropic melt is not achieved at the times employed (120 min).

According to Fillon et al. [2], domain II originates from the presence of residual crystalline fragments; however, Lorenzo et al. [4] considered the possibility of the existence of noncrystalline structures that could act as self-nuclei, especially in the high  $T_s$  range within domain II.



**Fig. 5** (a–c) DSC cooling scans (at  $10^\circ\text{C}/\text{min}$ ) after the indicated annealing times for three different  $T_s$  temperatures (within domain II) for PP. The standard cooling scan is also included in each figure. Reprinted with permission from Lorenzo et al. [4]. Copyright (2006) John Wiley and Sons



**Fig. 6** (a) Variation in peak crystallization temperature ( $T_c$ ) for PP as a function of the annealing time ( $t_s$ ) at the given  $T_s$  temperatures. (b) Heating DSC scans (at  $10^\circ\text{C}/\text{min}$ ) after the indicated annealing times at  $T_s = 166^\circ\text{C}$ . Reprinted with permission from Lorenzo et al. [4]. Copyright (2006) John Wiley and Sons

Lorenzo et al. [4] performed a special thermal protocol to explore the nature of self-nuclei. They ran the conventional protocol for SN, but instead of cooling the sample after the time spend at  $T_s$ , they immediately heated the sample until melting. Any crystals remaining in the sample should melt in the subsequent heating run. Figure 6b shows the result for the lowest  $T_s$  temperature within domain II.

Lorenzo et al. [4] performed the experiments reported in Fig. 6b at  $T_s = 166^\circ\text{C}$ , because it gives the largest probability of survival of crystalline fragments. The presence of a crystalline phase in the sample partially molten at  $166^\circ\text{C}$  was

detectable only at  $t_s = 0$  min. When the annealing time was increased, the signal disappeared. As a consequence, no crystalline fragments were present, or at least not in the necessary quantities to produce a signal in the DSC.

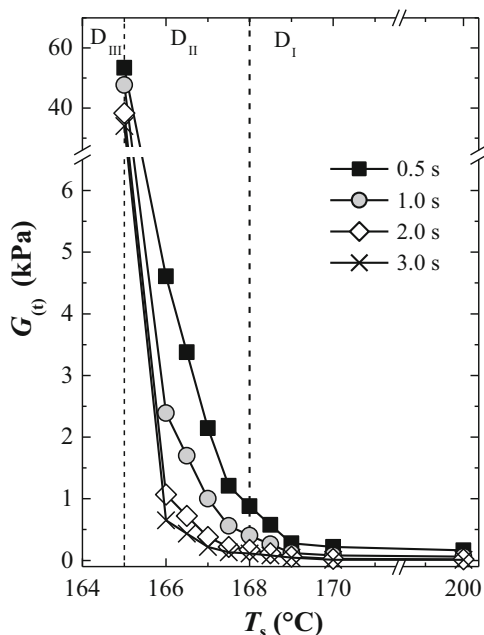
The previous results show that the SN experimental protocol is very sensitive to annealing time and to cooling and heating rates, therefore it is a nonequilibrium procedure. Also, self-nuclei are more likely to arise from a pre-order phase in the melt than from residual crystalline fragments. Figure 5 shows that SN persists at  $T_s = 166^\circ\text{C}$ , even after 120 min of annealing. However, in Fig. 6b it seems evident that after only 1 min there are no traces of crystalline fragments.

According to Lorenzo et al. [4], application of the SN thermal protocol involves the presence of some pre-order state (or precursor) in domain II. Such precursors (or residual orientation in melt regions of the sample) are produced by incomplete erasing of the crystalline order. Lorenzo et al. [4] also studied the influence of SN in shear modulus relaxation experiments.

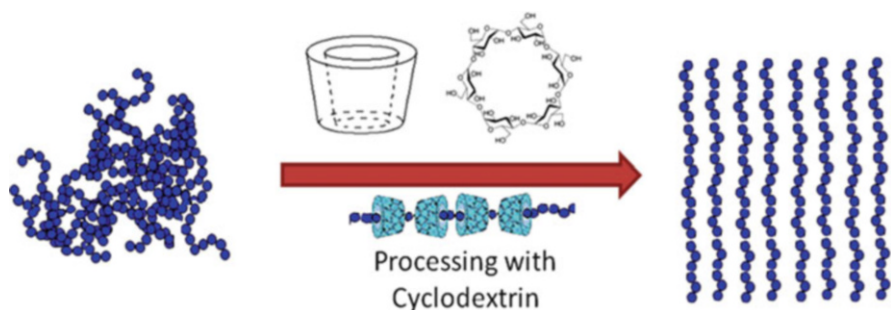
Figure 7 shows shear modulus ( $G_{(t)}$ ) values extracted at constant times plotted as a function of the  $T_s$  employed. The vertical lines are drawn to illustrate the limits between domains, according to parallel DSC experiments. Figure 7 shows differences in the relaxation behavior of the shear modulus in the melt depending on its crystalline memory. The curves show three ranges at low, intermediate, and high values of  $G_{(t)}$ . The transition between the different values corresponds to the three different SN domains. At higher temperatures within domain I ( $200\text{--}169^\circ\text{C}$ ), the values of  $G_{(t)}$  are very similar and exhibit small increments as the temperature decreases. On the other hand, at temperatures belonging to domain II, small increases in temperature produce a large increase in  $G_{(t)}$ . This fact could be related to the existence of residual segmental orientation in the melt. Finally, when the temperature decreases to  $165^\circ\text{C}$  (within domain III), the values of  $G_{(t)}$  increase remarkably as a result of unmolten crystals present in the melt.

Gurarslan et al. [33] developed a method to produce highly oriented polymer melts, employing cyclodextrins (CDs). These water-soluble polysaccharides are nanometric in size and have internal hydrophobic cavities and external hydrophilic groups. The cavities can be filled with polymer chains and produce crystalline compounds, originating an arrangement of extended polymer chains (see Fig. 8). The authors employed poly(L-lactic acid), poly( $\epsilon$ -caprolactone), and nylon-6 in conjunction with CDs in order to form crystalline compounds. Water was used to remove CDs and obtain coalesced polymeric samples of each material.

The coalesced samples were amorphous, but they had a strong pre-orientation. The influence of the previous state in the subsequent crystallization was studied by DSC. Figure 9 shows the first cooling scan for two PCL samples, one as-received and the other as a coalesced sample. The difference in the crystallization temperature was more than  $25^\circ\text{C}$ , resembling the changes produced by the SN process. An interesting fact of this system is that chain orientation remained in the sample, even after days of exposure to temperatures above the melting temperature. It is possible that the orientation given during this particular treatment is even larger than that produced by the crystallization process. The process for production of a homogeneous random melt for these structures takes much longer times than for a conventional crystalline sample. According to Gurarslan et al. [33], the proximity of the



**Fig. 7** Shear modulus ( $G_{(t)}$ ) values at constant time intervals plotted versus  $T_s$  (see text for details). Vertical lines indicate the limits between domains. Reprinted with permission from Lorenzo et al. [4]. Copyright (2006) John Wiley and Sons



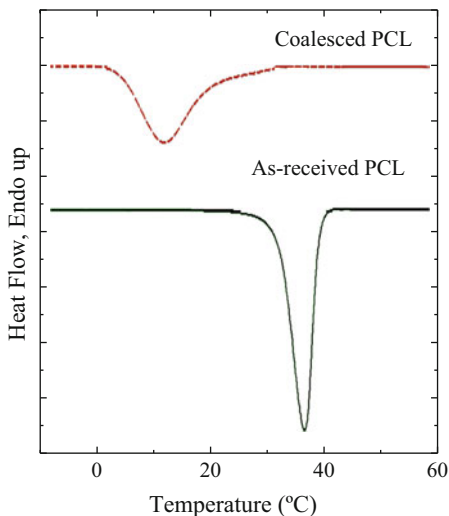
**Fig. 8** Extended unentangled polymer chains in a coalesced sample (*right*) and the randomly coiling entangled chains in polymer solution or melt (*left*). Reprinted with permission from Gurarslan et al. [33]. Copyright (2012) John Wiley and Sons

crystals to the amorphous zone, in an as-received sample, facilitates chain mobility and allows the formation of a homogeneous melt. However, the coalesced sample exhibits uniform order throughout, making the creation of random coiled chains in the melt more difficult.

Gurarslan et al. [33] employed 2 wt% of the coalesced sample as self-nucleating agent in the as-received PCL sample and found that the crystallization temperature



**Fig. 9** DSC cooling curves of as-received and coalesced PCL samples determined at 20°C/min. Adapted with permission from Gurarslan et al. [33]. Copyright (2012) John Wiley and Sons



of the self-nucleated sample was the same as that of the coalesced sample. This experiment demonstrates that a small quantity of pre-order structure is able to self-nucleate a polymeric sample and that there is no need for crystalline fragments.

Melt memory effects are also viewed by Luo and Sommer as responsible for SN [43]. The authors performed molecular dynamic simulations and primitive path analysis to study the process of crystallization from the melt state. According to their predictions, the disentanglement process necessary for crystallization occurs from locally unentangled chains and their posterior folding. On the other hand, they also found that re-entanglement is a slow process and could originate memory effects during the heating–recooling process (i.e., self-nucleation).

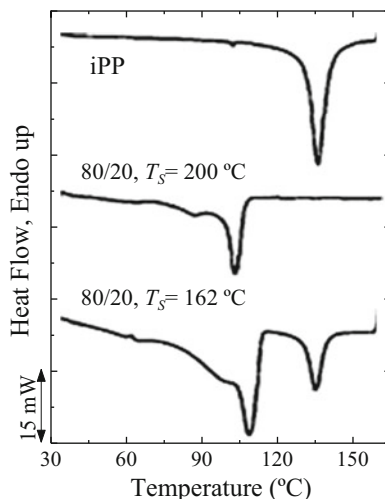
#### 4 Self-Nucleation as a Tool for Ascertaining the Origin of Fractionated Crystallization

Self-nucleation has many useful applications in polymer characterization. Coincident and fractionated crystallization phenomena are frequently observed in blends and copolymers, and SN can be employed to investigate the origin of the crystallization process [3, 8, 87–100]. The work performed by Morales et al. [93] has been chosen as an example of the application of SN to a polymer blend.

Morales et al. [93] studied the crystallization of PP and LLDPE blends employing different melt mixing techniques. The minor component was PP, and it was dispersed as small isolated particles in the LLDPE matrix. The crystallization process of the PP microdomains (MDs) occurs at lower temperatures (see Fig. 10) than those typical for bulk PP.

Once PP is divided into many small and isolated droplets, the heterogeneities responsible for PP nucleation are also divided among the different droplets,

**Fig. 10** DSC cooling scans at  $10^\circ\text{C}/\text{min}$  for 80/20 LLDPE/PP blends after complete melting at  $T_s = 200^\circ\text{C}$  and partial melting at  $T_s = 162^\circ\text{C}$ . Data taken from Morales et al. [93]



whereas some heterogeneities can migrate to the LLDPE matrix component during processing. When the number of droplets is of the same order of magnitude (or larger) than the number of heterogeneities originally present in bulk PP, many droplets are free of highly active heterogeneities and nucleate at lower temperatures (higher supercooling). The average number of PP particles in the blends is about  $10^{11}$  particles/ $\text{cm}^3$  [93], which is much greater than typically present in commercial PP (approximately  $10^6$  heterogeneities/ $\text{cm}^3$  [2]). Such a large difference normally leads to statistically clean droplets and a large depression in their crystallization temperature. For more details on the process of fractionated crystallization, the reader is referred to the literature [3, 101–105].

The PP/LLDPE blends studied by Morales et al. [93] experienced coincident crystallization for both PP droplets and LLDPE matrix when the blend was cooled from the melt. Therefore, a single main crystallization peak is observed in the DSC cooling run, corresponding to the 80/20 blend where crystalline memory has been erased or is in domain I (see the DSC cooling curve corresponding to  $T_s = 200^\circ\text{C}$  in Fig. 10). On the other hand, the subsequent heating scan shows two separate melting peaks (not shown in Fig. 10) associated with the fusion of PP and LLDPE, indicating that both components were able to crystallize during the previous cooling from the melt. The difference between the melting temperatures of LLDPE and PP is large enough to apply SN to the PP phase while the LLDPE phase is in the melt.

Morales et al. [93] applied SN to the PP component of the blend with the purpose of injecting self-nuclei into every PP droplet. The blend sample was molten at  $200^\circ\text{C}$  for 3 min to erase any previous thermal history, then it was cooled at  $10^\circ\text{C}/\text{min}$  to room temperature to create a standard crystalline state. Subsequently, the sample was heated at  $10^\circ\text{C}/\text{min}$  up to the SN temperature ( $T_s = 162^\circ\text{C}$ ), which belongs to domain II, for 5 min. As PP is self-nucleated, the increase in the crystallization temperature produces total separation from the crystallizing peak

of the LLDPE phase, as shown in the cooling curve corresponding to  $T_s = 162^\circ\text{C}$  in Fig. 10. Therefore, the coincident crystallization process is a result of the lack of highly active heterogeneities in most PP droplets. The self-nucleated blend (where only the PP phase was self-nucleated) shows two crystallization peaks, the self-nucleated PP at  $T_c = 135^\circ\text{C}$  and the LLDPE matrix at  $T_c = 108\text{--}109^\circ\text{C}$ . It should be noted that the crystallization temperature of the LLDPE matrix also increased in comparison with the original blend. This increment is associated with the nucleating effect of the self-nucleated PP on LLDPE [93].

Another typical case observed for immiscible blends is the occurrence of fractionated crystallization. In these blends, the crystallization process of the dispersed phase can be fractionated into several exothermic processes upon cooling from the melt. Arnal et al. [87] studied the crystallization of an 80/20 PS/PP blend, and found that the PP phase within the blend exhibits fractionated crystallization (see Fig. 11). The blend has the typical sea-island morphology, with PP droplets within a PS matrix (see Fig. 11a). The number of droplets for this blend is reported by Arnal et al. [87] to be in the order of  $10^{11}$  particles/cm<sup>3</sup> and the PP employed contains approximately  $10^7$  heterogeneities/cm<sup>3</sup>. According to Fig. 11, the single exotherm ( $109\text{--}111^\circ\text{C}$ ) present in bulk PP is fractionated into four peaks (labeled A, B, C and D) after blending.

Fractionated crystallization is a result of the presence of different types of heterogeneities in the PP phase (dispersed as droplets) within the 80/20 PS/PP blend, each one with a different activation energy. The most active heterogeneity originates crystallization peak A in Fig. 11 (at the highest  $T_c$ ) and it is the same type of heterogeneity as that responsible for the nucleation of bulk PP. When PP is in the bulk state, the heterogeneity with the lowest specific interfacial energy difference is activated at lower supercooling (high  $T_c$ ) and dominates the crystallization of the polymer via secondary nucleation.

The crystallization peaks labeled B and C for the 80/20 PS/PP blend in Fig. 11 were attributed by Arnal et al. to crystallization processes originating from different types of less active heterogeneities, which need larger undercoolings to be activated. In the case of peak D, the largest undercooling is required for a small fraction of the material to crystallize. It is likely that it corresponds to the crystallization of a fraction of heterogeneity-free PP droplets. Its exact origin is debatable because it could correspond to the crystallization of a group of clean droplets whose nucleation either starts from the surface of the droplets (or the interface between PP and PS) or by homogeneous nucleation inside the PP droplets (see [3, 101–105]).

Fractionated crystallization in immiscible blends with sea-island morphologies has been explained by the lack of highly active heterogeneities in every dispersed phase droplet. The different peaks at lower crystallization temperatures than for the bulk polymer can be attributed to nucleation triggered by less active heterogeneities and, eventually, to surface or homogeneous nucleation. One way to demonstrate the validity of this explanation is to inject nuclei in every droplet by adding a nucleating agent [106] or by SN [87]. Then, all the low temperature crystallization peaks should disappear and the dispersed phase should crystallize in a single peak at low undercoolings [87, 93, 106, 107].

**Fig. 11** (a) SEM image of the 80/20 PS/PP blend. (b) DSC cooling scans at  $10^\circ\text{C}/\text{min}$  for the samples indicated at  $T_s = 162^\circ\text{C}$  (blue) and  $T_s = 161^\circ\text{C}$  (red). The single exotherm (A) present in bulk iPP is fractionated into peaks A, B, C, and D after blending. Adapted with permission from Arnal et al. [87]. Copyright (1998) John Wiley and Sons

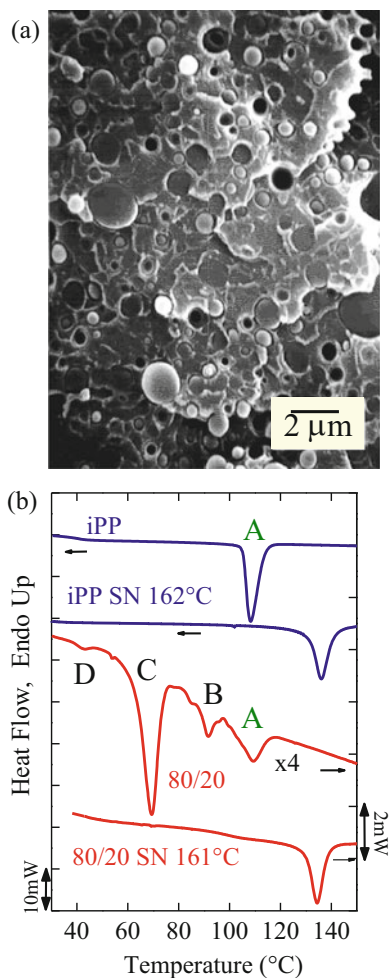


Figure 11b shows the DSC cooling scan of bulk PP after SN at  $162^\circ\text{C}$ . The  $T_s$  employed belongs to domain II and it is the lowest temperature in this domain or the ideal SN temperature (because it produces maximum SN without annealing). This  $T_s$  temperature was employed to generate the maximum quantity of self-nuclei and, hence, produce the largest shift in  $T_c$ . The introduction of self-nuclei (the most active nuclei theoretically possible) in PP produces an increase of  $28^\circ\text{C}$  in its peak crystallization temperature. A similar SN procedure was employed in the blend (with  $T_s = 161^\circ\text{C}$ , as the ideal SN temperature is  $1^\circ\text{C}$  lower in the blend). In Fig. 11, the cooling scan after SN shows that the four exothermic peaks present in the untreated blend disappear and that there is only one crystallization peak at  $134.5^\circ\text{C}$  ( $2^\circ\text{C}$  lower than in self-nucleated bulk PP). This result confirms that SN generates at least one self-nuclei in each MD.

## 5 Influence of Confinement on Self-Nucleation Behavior

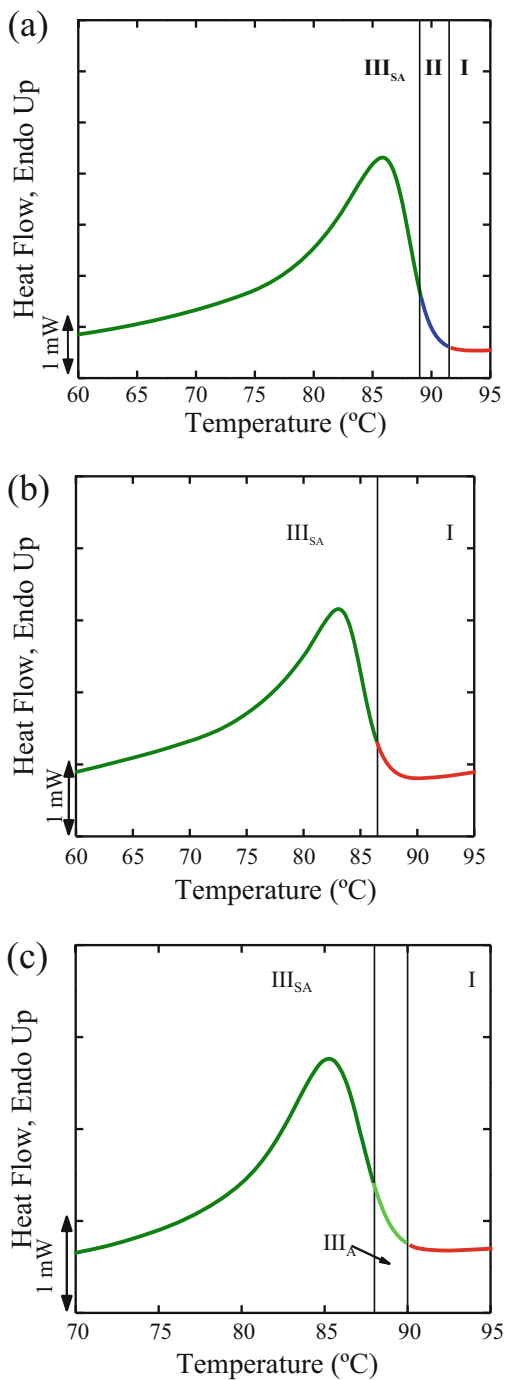
The SN technique has been employed to study the nucleation and crystallization of block copolymer components. In block copolymers, factors such as the volumetric fraction and the degree of segregation affect the type of confinement and, as a consequence, influence the SN behavior. Several works dealing with the crystallization of semicrystalline block copolymers have reported the SN of crystallizable block(s) [3, 94–98, 108–119]. In these studies, three kinds of behavior have been reported:

1. *Presence of three self-nucleation domains.* The classical behavior described by Fillon et al. [2], with three SN domains, has been observed for strongly segregated block copolymers, when the studied blocks are continuous phases or percolated MDs and the nucleation is induced by heterogeneous nucleation. The classical behavior has also been observed in miscible or weakly segregated block copolymers that crystallize from a homogeneous or weakly segregated melt [3]. Figure 12a shows the SN domains for the PE block within a strongly segregated PS-*b*-PE-*b*-PCL triblock terpolymer with weight percent ratio of 27/37/36 (denoted  $S_{27}E_{37}C_{36}$ ). In this case, the PE phase is percolated and crystallization can easily spread by secondary nucleation. The material exhibits three SN domains.
2. *Absence of domain II.* Several block copolymer systems only exhibit domains I and III. The absence of the SN domain (domain II) occurs within isolated MDs and its disappearance has been linked to confinement [3]. Figure 12b shows the SN domains for the PE block within  $S_{57}E_{27}C_{16}$ , a strongly segregated PS-*b*-PE-*b*-PCL triblock terpolymer. PE forms isolated MDs in this case. The material exhibits only domains I and III.
3. *Absence of domain II and partition of domain III into two subdomains.* In cases where the injection of self-nuclei into every MD is difficult, in view of the very large number of MDs, domain III is split into two domains [3]:
  - (a) Domain  $III_A$ , where annealing without SN occurs
  - (b) Domain  $III_{SA}$ , where SN and annealing are simultaneously observed; domain  $III_{SA}$  is the exact equivalent of the standard domain III established by Fillon et al. [2]

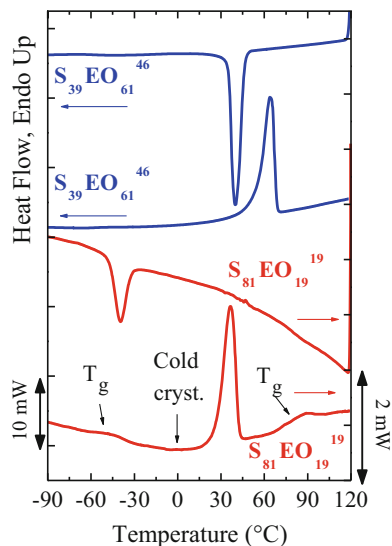
Figure 12c shows the SN domains for the PE block within  $S_{50}E_{15}C_{35}$ , a strongly segregated PS-*b*-PE-*b*-PCL triblock terpolymer with only 15% PE. The PE block forms isolated MDs that are strongly confined by the other two blocks. The material exhibits only domains I and III; additionally, domain III is split into two domains,  $III_A$  and  $III_{SA}$  [98, 109].

By changing the composition of a block copolymer, it is possible to switch from one behavior to another. Müller et al. [98] studied a series of different block copolymers to establish the influence of the composition, molecular weight, and chemical structure on homogeneous nucleation, fractionated crystallization, and self nucleation behavior. One of the systems studied was PS-*b*-PEO diblock

**Fig. 12** Self-nucleation domains for the PE block within the following strongly segregated triblock terpolymers: (a)  $S_{27}E_{37}C_{36}$ , (b)  $S_{57}E_{27}C_{16}$ , and (c)  $S_{35}E_{15}C_{50}$ .  $III_A$  domain where annealing without self-nucleation occurs,  $III_{SA}$  domain where annealing and self-nucleation occur simultaneously. Adapted with permission from Balsamo et al. [109]. Copyright (2000) John Wiley and Sons



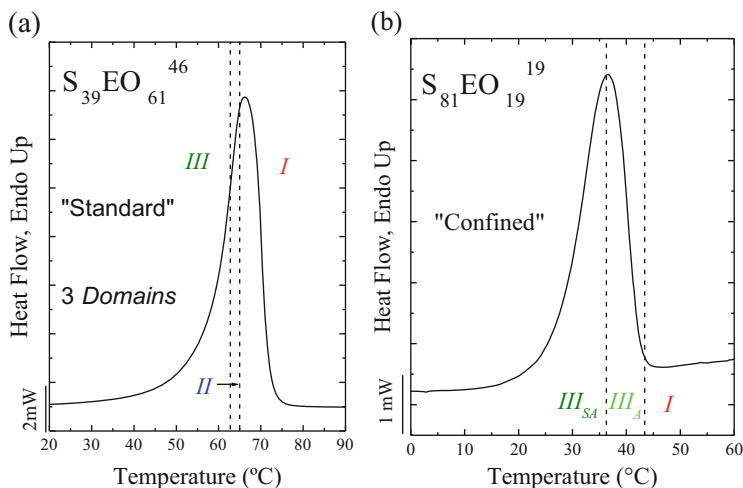
**Fig. 13** Cooling and heating DSC scans ( $10^\circ\text{C}/\text{min}$ ) for two PS-*b*-PEO diblock copolymers. Adapted with permission from Müller et al. [98]. Copyright (2002) American Chemical Society



copolymers with two different compositions:  $S_{39}EO_{61}^{45}$  and  $S_{81}EO_{19}^{19}$  (the subscripts indicate the weight composition and the superscripts the molecular weight of the entire copolymer in kilograms per mole). In the first copolymer, the PEO block constitutes the continuous phase (i.e., PS forms cylinders in a PEO matrix). In the second copolymer, PEO is dispersed as nanodroplets in a PS matrix. Figure 13 shows the DSC cooling and heating scans for these copolymers.

As expected, the DSC cooling scan of the  $S_{39}EO_{61}^{46}$  diblock copolymer exhibits a single crystallization peak at  $37^\circ\text{C}$  (see Fig. 13), as PEO constitutes the continuous phase and the crystallization starts from heterogeneous nucleation. On the other hand, for the  $S_{81}EO_{19}^{19}$  diblock copolymer, PEO is dispersed as nanodroplets [98, 108, 120, 121] and crystallization develops inside isolated MDs. This copolymer is strongly segregated, and the crystallization of the PEO nanodroplets occurs under rigid confinement (no break-out is possible), as PS vitrifies at around  $75^\circ\text{C}$  (because of the low molecular weight of the PS block). Additionally, the typical number of heterogeneities for the PEO block is several orders of magnitude (i.e., approximately seven orders of magnitude) lower than the number of PEO nanodroplets. Therefore, the majority of these MDs are free of heterogeneities, and the crystallization can start by surface (or interphase) nucleation or by homogeneous nucleation. The extremely low crystallization temperature (from  $-30$  to  $-50^\circ\text{C}$ ) suggests that the nucleation is more likely to be homogeneous for this copolymer, because  $T_c$  is very close to the glass transition temperature ( $T_g$ ) of the PEO block. The SN behavior of these copolymers is shown in Fig. 14.

The  $S_{39}EO_{61}^{46}$  diblock copolymer exhibits classical SN behavior, as shown in Fig. 14a, where the three domains can be detected. This is the expected behavior



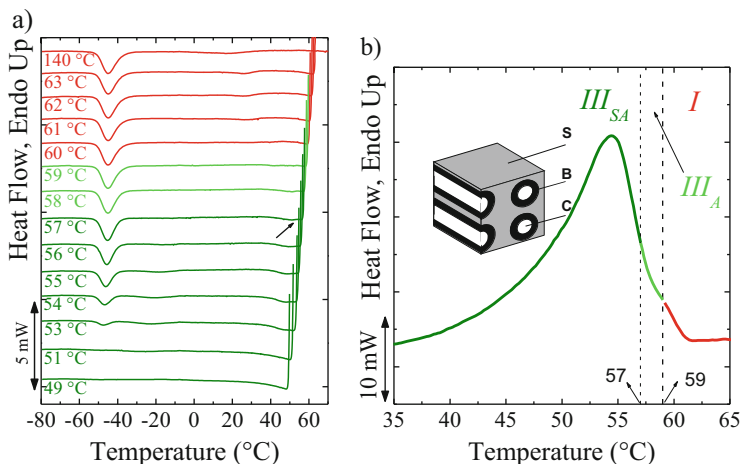
**Fig. 14** Self-nucleation domains corresponding to the PEO block for (a)  $S_{39}EO_{61}^{46}$  diblock copolymer and (b)  $S_{81}EO_{19}^{8.5}$  diblock copolymer (see text for details)

because PEO constitutes the matrix phase. However, for the  $S_{81}EO_{19}^{8.5}$  diblock copolymer, PEO is dispersed as weakly confined nanodroplets surrounded by vitrified PS phase at the temperatures where PEO can crystallize (as discussed above). In the case of highly confined polymeric phases, domain II disappears and domain III splits into two. In addition, annealing occurs before SN, making it impossible to detect domain II [98].

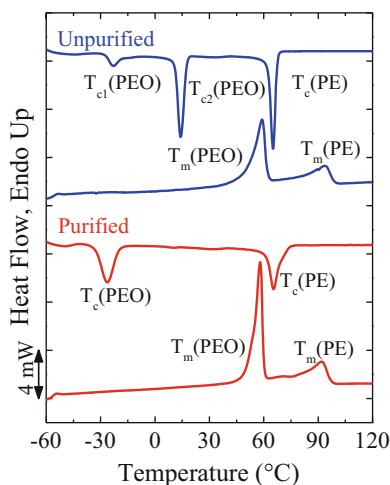
The triblock terpolymer  $S_{62}B_{27}C_{11}^{62}$  (PS-*b*-PB-*b*-PCL) has a peculiar morphology consisting of a PS matrix in which core-shell cylinders (where PCL is the core and PB the shell) are dispersed (see cartoon in Fig. 15b). In this case, the isolated PCL cylindrical cores are surrounded by PB soft shells. The copolymer is strongly segregated, but PCL is only weakly confined. Even so, the segregation strength is large enough to prevent any break-out and the PCL has to crystallize within the confinements of the cylindrical cores. Figure 15 shows how the crystallization temperature changes during the process of SN at different  $T_s$  temperatures. The crystallization temperature of the PCL block is extremely low ( $-40$  to  $-50^\circ\text{C}$ ), indicating that homogenous nucleation probably triggers crystallization, as  $T_c$  is very close to the vitrification temperature of PCL. The transition between domain I and domain  $III_A$  can be clearly seen in Fig. 15a, as well as the subsequent transition to domain  $III_{SA}$ . Domain II is absent as a consequence of the confinement.

Müller et al. [98] also studied the crystallization of PE and PEO blocks within  $E_{24}EP_{57}EO_{19}^{69}$  triblock terpolymer. It should be noted that the poly(ethylene-*alt*-propylene) (PEP) block cannot crystallize. This copolymer was synthesized via hydrogenation of the  $B_{24}EP_{56}EO_{20}^{67}$  precursor employing the Wilkinson catalyst. Wilkinson catalysis provides active heterogeneities to the PEO block. Figure 16 shows the cooling scan of the unpurified  $E_{24}EP_{57}EO_{19}^{69}$  sample. Upon





**Fig. 15** (a) Cooling scans at  $10^\circ\text{C}/\text{min}$  after partial melting at the indicated  $T_s$ . (b) Self-nucleation domains for  $S_{62}B_{27}C_{11}$  triblock terpolymer. *Inset* shows core-shell structure of the terpolymer; C PCL core, B PB shell, S PS matrix. Adapted with permission from Müller et al. [98]. Copyright (2002) American Chemical Society



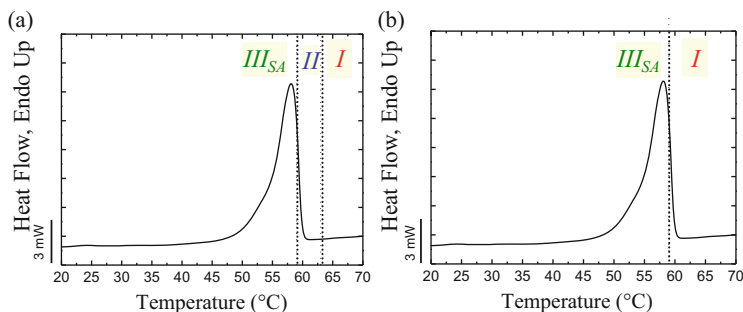
**Fig. 16** Cooling and heating DSC scans of original and purified  $E_{24}EP_{57}EO_{19}$  triblock copolymer. Adapted with permission from Müller et al. [98]. Copyright (2002) American Chemical Society

cooling from the melt, the PE block crystallizes first (at high temperatures) and then, at lower temperatures, crystallization of the PEO block takes place in two peaks, exhibiting fractionated crystallization. A large part of the PEO block crystallizes close to  $20^\circ\text{C}$ , whereas a smaller fraction crystallizes at lower

temperatures ( $-20^{\circ}\text{C}$  and below). To investigate the origin of the fractionated crystallization and whether or not the Wilkinson catalyst provided impurities for the heterogeneous nucleation of a fraction of PEO MDs, the sample was purified to remove as much of the Wilkinson catalyst as possible. The sample was refluxed in a toluene solution with concentrated HCl and all the catalyst was successfully removed.

Crystallization of the PEO block in purified  $\text{E}_{24}\text{EP}_{57}\text{EO}_{19}^{69}$  triblock copolymer is different from crystallization in the unpurified sample. In the purified sample, the exotherm that was present at around room temperature completely disappears. Therefore, this exotherm can be assigned to the nucleating effect of the Wilkinson catalyst. The purified PEO block crystallizes in two lower temperature peaks, the largest exotherm being located around  $-27^{\circ}\text{C}$  and a very small exotherm at  $-47^{\circ}\text{C}$ . The first exotherm could originate from crystallization of the PEO block after heterogeneous nucleation from a weakly nucleating heterogeneity or surface nucleation. The lowest crystallization exotherm clearly originates from crystallization after homogeneous nucleation of the PEO block.

The purification process also affects the self nucleation behavior. Figure 17 shows the SN domains of the PEO block within the original and purified  $\text{E}_{24}\text{EP}_{57}\text{EO}_{19}^{69}$  triblock terpolymer. The PEO block in the unpurified version of  $\text{E}_{24}\text{EP}_{57}\text{EO}_{19}^{69}$  exhibits classical behavior, with three domains. This is interesting because PEO in this block copolymer forms isolated MDs (i.e., a mixture of spheres and cylinders). Therefore, the presence of the Wilkinson catalyst is probably responsible for the observation of domain II. On the other hand, the PEO block within the purified  $\text{E}_{24}\text{EP}_{57}\text{EO}_{19}^{69}$  exhibits the expected behavior of a largely confined phase and domain II disappears. This is shown in Fig. 17, where a direct transition from domain I to III can be observed [98].



**Fig. 17** (a) Self-nucleation domains for unpurified  $\text{E}_{24}\text{EP}_{57}\text{EO}_{19}^{69}$ . (b) Self-nucleation domains for purified  $\text{E}_{24}\text{EP}_{57}\text{EO}_{19}^{69}$

## 6 Effect of Chain Topology on Self-Nucleation Behavior

Pérez et al. [119] studied the crystallization of linear (L-PCL) and cyclic (C-PCL) PCL chains of almost identical molecular weights. They found that the transition temperatures between domains are affected by chain topology (see Table 1). In fact, domain II is much wider in L-PCLs than in C-PCLs. In addition, the transition temperature between domain I and domain II ( $T_s^{I-II}$ ) occurs in L-PCLs at higher values than the final melting temperature of the sample, as compared with C-PCLs. In other words, L-PCL samples have a much higher crystalline memory than C-PCLs of similar molecular lengths. Crystalline memory effects are a function of entanglement density [26, 40, 44, 63, 122–126], and the entanglement density in L-PCLs is significantly higher than in C-PCL as a result of its free chain ends. Therefore, partially disentangled PCL cyclic chains can reach a random coil conformation, or a uniform melt, faster than more entangled linear chains. As a consequence, the crystalline memory of C-PCLs can be erased at lower temperatures than for L-PCLs.

Another parameter that influences SN behavior is the branch content in PE [50, 127, 128]. Reid et al. [50] studied the crystallization of a series of PE-*co*-1-butene copolymers with different amounts of 1-butene (ethylene branches). They found that when the branch content increases, the transition temperature between domain I and domain II decreases. They attributed this tendency to the reduced crystallinity and thinner lamellae formed by highly branched copolymers. The process of producing a homogeneous random melt is facilitated if the quantities of crystals are reduced and if they are thinner. As a consequence, domain I can occur at lower temperatures [50].

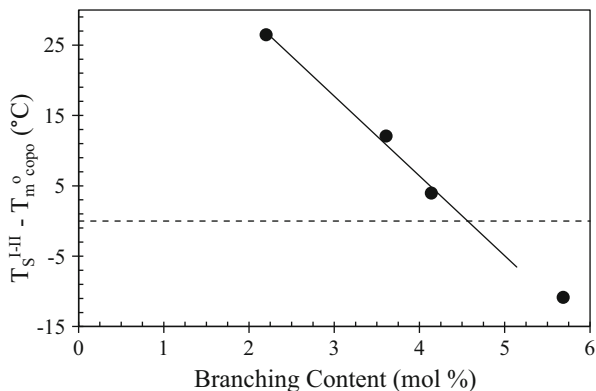
Reid et al. [50] calculated the equilibrium melting temperatures ( $T_m^0$ ) for the PE-*co*-1-butene copolymers, and found that the value of  $T_s^{I-II}$  was higher than  $T_m^0$  for the copolymers with low branch content. However, when the branch content reached 4.53 mol% the  $T_s^{I-II}$  was similar or lower than  $T_m^0$  (see Fig. 18). This unique behavior was present only in the copolymers; the linear PE studied by Reid et al. showed the expected behavior; that is, for any temperature above  $T_m^0$  the melt was always homogeneous and no evidence of self nucleation was reported (see Fig. 19) [4, 20, 31, 69, 124, 125].

Reid et al. attributed the presence of crystalline memory above  $T_m^0$  to residual sequence segregations in the melt, originating from diffusion restriction of the crystalline sequences in reaching the homogeneous random melt. The restricted

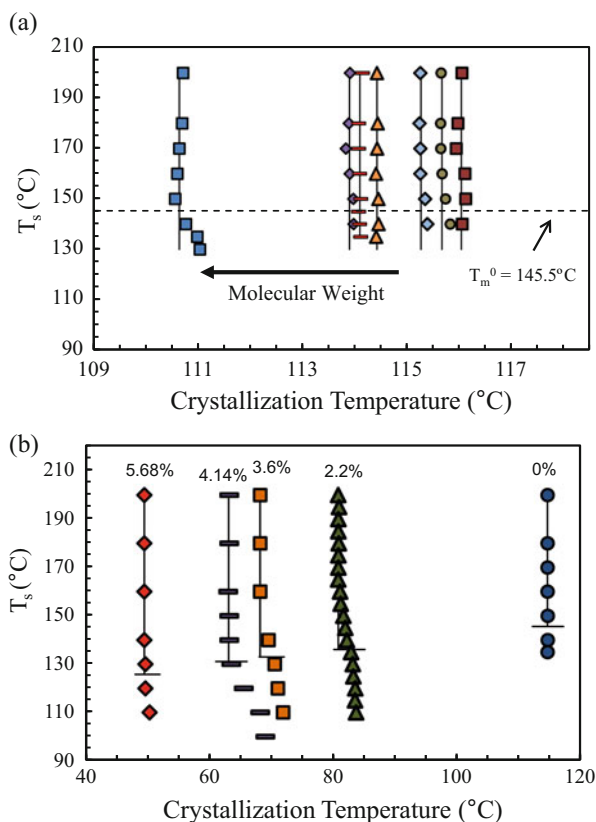
**Table 1** Transition temperatures for the self-nucleation domains, for the samples indicated [119]

Material	DI to DII (°C)	DII to DIII (°C)
C-PCL (2,000 g/mol)	64	60
C-PCL (7,500 g/mol)	69	61
L-PCL-OH (2,000 g/mol)	60	51
L-PCL-OH (7,500 g/mol)	67	56

**Fig. 18** Plot of the difference between the temperature of transition from domain I to domain II ( $T_s^{I-II}$ ) and the final melting temperature of the copolymer ( $T_m^0$ ) versus ethyl branching content. Adapted with permission from Reid et al. [50]. Copyright (2013) American Chemical Society



**Fig. 19**  $T_s$  versus peak crystallization temperature after partial melting for (a) linear polyethylene fractions with different molecular weights and (b) polyethylene with fixed molecular weight and varying branching content. The horizontal lines indicate  $T_m^0$  for each sample. Adapted with permission from Reid et al. [50]. Copyright (2013) American Chemical Society



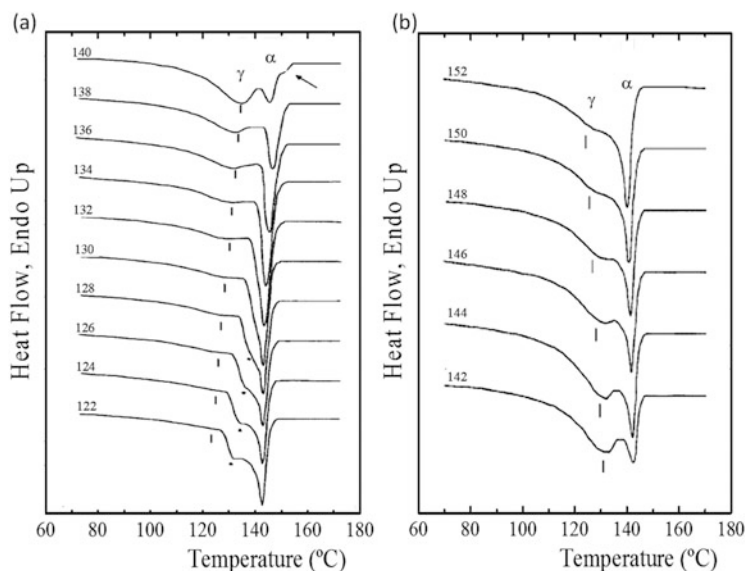
diffusion of ethylene linear sequences is caused by the branches, since there are no other differences between the homopolymers and copolymers. Ethyl or longer branches do not participate in the crystalline regions and during the crystallization process they are segregated to the amorphous phase surrounding the crystals. The

authors argue that when the melting process begins, the diffusion of linear sequences is hindered by chain branches. As a consequence, the melt needs a longer time and/or higher temperatures to allow diffusion and subsequent homogenization of the melt.

## 7 Self-Nucleation and Preferential Polymorphism

Self-nucleation can be employed to trigger specific crystallization of a polymorphic polymer sample. Increasing the number of crystals using a specific polymorphic modification is a practical option for improving the performance of a polymeric material [129–138].

Dai et al. [132] studied the effect of SN treatment on the thermal properties and structure of PP. The PP employed was synthesized using a metallocene catalyst. The standard cooling scan shows the formation of equal amounts of  $\alpha$ - and  $\gamma$ -polymorphism. The authors studied the SN behavior from 122 to 160°C. The relative amount of  $\alpha$ - and  $\gamma$ -crystals was determined by WAXS. In the DSC heating scans, the lower temperature melting peak corresponds to the fusion of  $\gamma$ -crystals, whereas the high temperature peak corresponds to the fusion of  $\alpha$ -crystals. Dai et al. established the following series of regions with specific combinations of polymorphs (see Fig. 20) [132]:



**Fig. 20** DSC heating scans at 5°C/min of m-PP after self-nucleation at the temperatures indicated followed by cooling at (a) low  $T_s$  (122–140°C) and (b) high  $T_s$  (142–152°C). Dai et al. [132]. Copyright (2002) John Wiley and Sons

*Region I:*  $T_s = 122\text{--}130^\circ\text{C}$ , and  $T_s$  values are lower than the melting temperature of the  $\gamma$ -phase. At these temperatures, the  $\gamma$ -crystals are annealed and the  $\alpha$ -phase remains unaffected. The amount of  $\alpha$ -crystals increases in the subsequent cooling scans as a result of the epitaxial recrystallization within existing  $\alpha$ -lamellae as substrates.

*Region II:*  $T_s = 122\text{--}130^\circ\text{C}$ , and  $T_s$  values are higher than the melting temperature of the  $\gamma$ -phase, but lower than the melting temperature of  $\alpha$ -crystals. In this region,  $\alpha$ -crystals anneal and the  $\gamma$ -phase is melted. As in region I, the amount of  $\alpha$ -crystals increases in the subsequent cooling scans.

*Region III:*  $T_s = 140\text{--}148^\circ\text{C}$ , and  $T_s$  values are higher than the melting temperature of the  $\alpha$ -phase, but not high enough for complete melting. Therefore, in this region, complete melting of  $\gamma$ -crystals takes place but  $\alpha$ -crystals are partially melted. When  $T_s$  increase, the nucleation of  $\alpha$ -crystals decreases, originating a depression in the crystallization and melting temperatures on subsequent DSC scans. The amount of  $\gamma$ -phase increases and exceeds the amount of  $\alpha$ -crystals as a result of the effective nucleation of  $\gamma$ -crystals by the  $\alpha$ -phase.

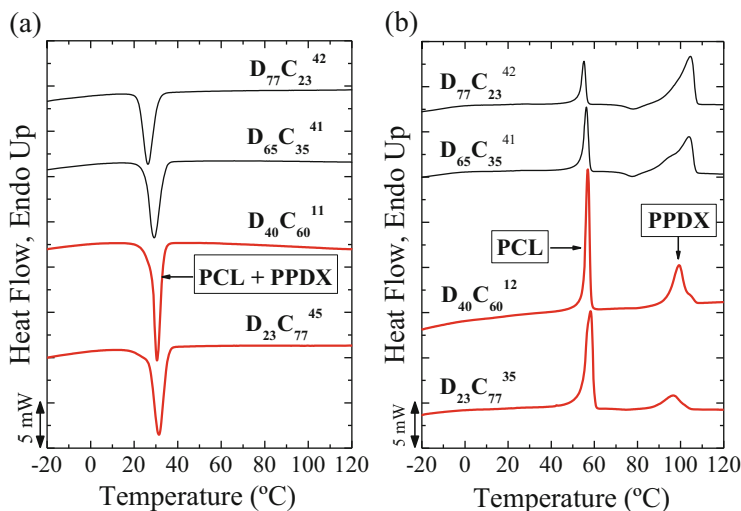
*Region IV:*  $T_s = 150\text{--}160^\circ\text{C}$ , and  $T_s$  values are higher than those employed in region III. Only a small amount of self-nuclei remain. Subsequent cooling originates recrystallization at lower temperatures. As in region III, the relative amount of  $\gamma$ -crystals is higher than that of  $\alpha$ -crystals.

Kang et al. [133, 134] studied  $\alpha$ - and  $\beta$ -PP crystals. They identified three regions where the relative amount of each polymorphic form changes according to the  $T_s$  employed during partial melting.

On the other hand, Cavallo et al. [129, 130] studied in detail the self-nucleation and cross-crystallization between the polymorphic phases of poly(1-butene). Other studies based on the SN and control of polymorphism were performed for polyamide 11 [131], poly(vinylidene fluoride) [135, 136], poly(butylene adipate) [138], and chocolate [137].

## 8 Self-Nucleation Before Isothermal Crystallization

It is well known that some polymers or crystallizable blocks within block copolymers have slow crystallization kinetics. In some cases, the overall crystallization kinetics is so slow that isothermal DSC experiments cannot be performed. Acceleration of the nucleation step can be accomplished by previous SN of the polymer. Under these conditions, the crystallization rate of self-nucleated material increases such that isothermal DSC can be performed [4, 69, 76, 96, 123, 139–152]. It is well known that overall crystallization kinetics obtained by isothermal DSC experiments contains both nucleation and growth components. If the isothermal crystallization starts from an ideally self-nucleated material, the experimental data may correspond exclusively to crystal growth [142].

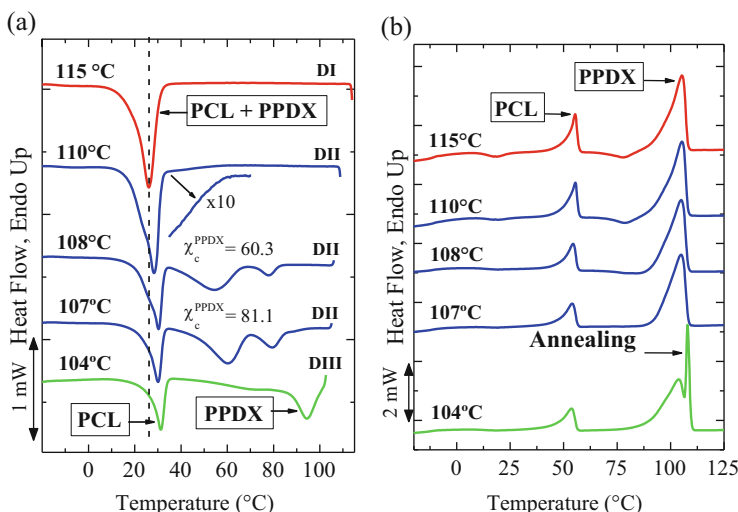


**Fig. 21** (a) DSC cooling scans ( $10^\circ\text{C}/\text{min}$ ) for PPDX-*b*-PCL diblock copolymers. (b) Subsequent heating scans ( $10^\circ\text{C}/\text{min}$ ). Reproduced from Müller et al. [96] with permission of The Royal Society of Chemistry

Müller et al. [96] studied the isothermal crystallization and SN of PPDX-*b*-PCL diblock copolymers. The cooling and subsequent heating scans for the PPDX-*b*-PCL samples are shown in Fig. 21. The nomenclature employed is the same as that employed above, where subscripts indicate the composition (in wt%) and the superscripts the molecular weight of the block copolymer in kilograms per mole.

Figure 21a shows that only one crystallization exotherm is observed for all copolymers. This single crystallization peak corresponds to the coincident crystallization of both PCL and PPDX blocks [153]. Parallel real-time WAXS experiments demonstrated that both phases crystallize in the same temperature range. It was shown that the PPDX block crystallization occurs at lower temperatures than neat PPDX because of the topological restrictions induced by covalent bonding with the highly flexible PCL block. The depression in the PPDX temperature is large enough to overlap with crystallization of the PCL block, which is triggered almost immediately when the PPDX block starts to crystallize. The subsequent heating scans demonstrate the separate melting of the crystals of each block.

Figure 22 shows how the SN of the PPDX block within the  $D_{77}C_{23}^{42}$  block copolymer can separate the crystallization of each component. In Fig. 22a, evolution of the separation of the two blocks is evident. When the number of self-nuclei increases (as  $T_s$  decreases), the coincident crystallization peak splits into two ( $T_s = 110^\circ\text{C}$ ) and, finally, into three exotherms ( $T_s = 108^\circ\text{C}$ ). For  $T_s = 108^\circ\text{C}$ , the PPDX block crystallization is self-nucleated and crystallizes at higher temperatures in a complex bimodal exotherm. The annealing of PPDX crystals begins when  $T_s = 104^\circ\text{C}$ , and in the subsequent heating scan the presence of a second higher temperature peak is evident. On the other hand, the exothermic peak around  $30^\circ\text{C}$  is



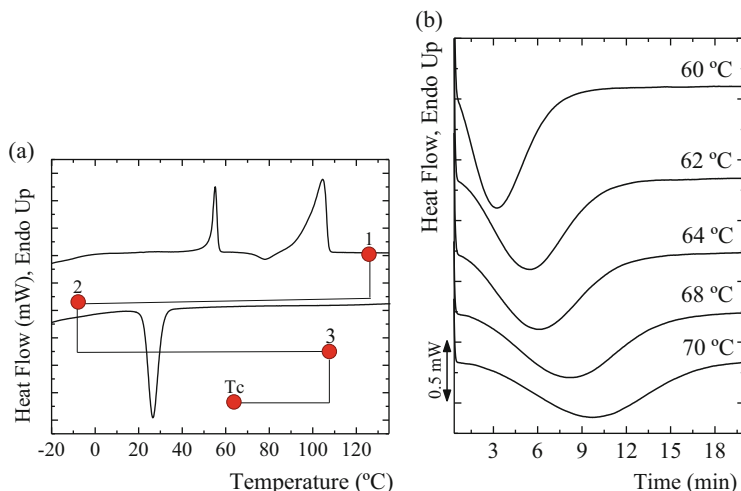
**Fig. 22** Self-nucleation of the PPDX block within  $D_{77}C_{23}^{42}$ . (a) DSC cooling scans from the indicated  $T_s$  temperatures;  $\chi_c^{PPDX}$  represents the amount of PPDX that has been self-nucleated. (b) Subsequent heating scans. The arrow points to the melting endotherm of annealed crystals during treatment at  $T_s = 104^\circ\text{C}$ . Reproduced from Müller et al. [96] with permission of The Royal Society of Chemistry

associated with crystallization of the PCL block, whereas all the PPDX crystallizes at much higher temperatures. Figure 22a also shows that the self-nucleated PPDX block crystals can nucleate the PCL block crystals (as the crystallization temperature of the PCL block increases).

Employing the conventional method to determine the overall isothermal crystallization kinetics by DSC, the crystallization rate of the PPDX block was extremely low so no significant exothermic signal was possible. Müller et al. [96] developed a different methodology to study the crystallization kinetics of the PPDX block. The samples were first self-nucleated (steps 1–3 in Fig. 23a) and then quenched (at  $80^\circ\text{C}/\text{min}$ ) to their isothermal crystallization temperature ( $T_c$ , indicated in Fig. 23b). Self-nucleation accelerates the overall kinetics as a result of an increase in the number of active nuclei in the sample. The effect is equivalent to starting the isothermal DSC measurements shown in Fig. 23b with samples whose nucleation process had already finished. Self-nucleation should provide all the necessary nuclei for crystallization; as a consequence, only secondary nucleation or growth is measured during the isothermal DSC runs shown in Fig. 23b.

For comparison, Müller et al. [96] also applied the same procedure indicated in Fig. 23a for a PPDX homopolymer. The experimental data was analyzed employing Lauritzen–Hoffman theory (LH). The value obtained for  $K_g^\tau$  (a value proportional to the energy barrier for primary and secondary nucleation) was lower than that obtained for the same sample employing conventional isothermal crystallization from the melt without SN. The value of  $K_g^\tau$  shifts from  $31.0 \times 10^4 \text{ K}^2$  for the





**Fig. 23** Examples of DSC isothermal crystallization scans for the PPDX block within  $D_{77}C_{23}^{42}$  diblock copolymer. The measurements were performed after the PPDX block had been previously self-nucleated at  $T_s = 110^\circ\text{C}$  and then quenched ( $80^\circ\text{C}/\text{min}$ ) to the indicated  $T_c$  temperatures. (a) Thermal protocol applied to the sample: the sample is first heated to a completely molten state (at  $130^\circ\text{C}$ ), indicated by *point 1*. Then, the sample is cooled at  $10^\circ\text{C}/\text{min}$  to obtain a “standard” crystalline state (*point 2*). The sample is then ideally self-nucleated by heating to *point 3*. Finally, the sample is quenched (at  $80^\circ\text{C}/\text{min}$ ) to the isothermal crystallization temperature desired ( $T_c$ ). (b) Isothermal DSC curves recorded after applying the procedure indicated in (a). Reproduced from Müller et al. [96] with permission of The Royal Society of Chemistry

conventional method to  $17.0 \times 10^4 \text{ K}^2$  after SN.  $K_g^r$  is proportional to the energy barrier for overall crystallization. This result indicates that the energy barrier for nucleation and growth is reduced by performing the nucleation in the previous SN step.

On the other hand, the same LH analysis was performed on spherulitic growth data for neat PPDX homopolymer. The value obtained for the secondary nucleation constant for PPDX spherulitic growth was  $K_g^G = 17.2 \times 10^4 \text{ K}^2$ , a value in remarkable agreement with the  $K_g^r$  value obtained by DSC after SN. This result shows that SN saturated the polymer with active nuclei such that the DSC measurements correspond to growth only. The same analysis was performed for PPDX-*b*-PCL block copolymers. The obtained values of  $K_g^r$  were higher than for neat PPDX, indicating that presence of the PCL block hinders secondary nucleation. Such hindrance is responsible for the coincident crystallization of both blocks during non-isothermal crystallization.

This technique of performing SN just before isothermal DSC measurements has been applied to segmented copolymers of poly(ether ester), based on poly(ethylene glycol) and poly(ethylene terephthalate) [139], PP [63, 133, 141, 151], PCL[142], PPDX [142], poly( $\epsilon$ -caprolactone)-*block*-poly(propylene adipate) [143], poly(ethylene naphthalate) [144], poly(propylene suberate) [145], poly(propylene

terephthalate)/SiO<sub>2</sub>nanocomposites [146], poly(propylene azelate) [147], poly(propylene sebacate) [147], poly(ethylene azelate) [148], syndiotactic poly(propylene) (sPP) [69, 123], poly(propylene terephthalate) [149], poly(trimethylene terephthalate) [76], and poly(lactic acid) [150].

Additionally, non-isothermal crystallization kinetics has also been performed after SN. In all cases, the crystallization rate was accelerated for the SN system compared with crystallization from the isotropic melt [154, 155].

Self-nucleation can be used as a tool for tailoring the morphology of block copolymers in thin films. The nanostructure of thin films has an influence on their surface properties, which could be of great interest for the fabrication of photonic crystals and bioanalytical devices. Shultze et al. [156] studied the SN behavior and its influence on the surface morphology of polybutadiene-*b*-poly(ethylene oxide). According to their results, it is possible to modify the periodicity of the block copolymer phase separation using SN treatment [156].

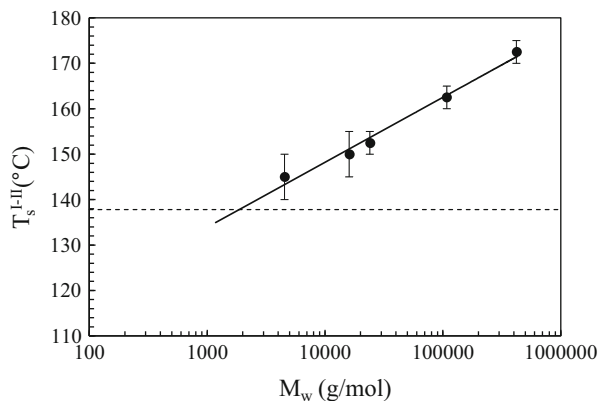
## 9 Molecular Weight

Another molecular parameter that influences SN behavior is molecular weight. Melt memory depends on entanglement density, which increases with molecular weight. Self-nucleation behavior is closely related to melt memory effects, as discussed above. As a consequence, it is expected that the temperature of transition between domains is dependent on molecular weight [50, 134, 157, 158].

Reid et al. [50] reported the effect of molecular weight on the crystallization of random ethylene-*co*-1-butene copolymers and linear PE samples. They performed a series of crystallization experiments after partial melting and found that, for low molecular weight samples ( $M < 4,500$  g/mol), the crystallization temperature upon subsequent cooling does not depend on the  $T_s$  employed, at least in the range studied. However, when the molecular weight was higher, a shift in  $T_c$  to higher temperatures was observed, indicating SN effects.

The process of erasing previous crystalline memory needs high temperatures. Reid et al. [50] have shown (see Fig. 24) that the critical melting temperature ( $T_s^{I-II}$ ) needed to reach homogeneous copolymer melts depends on the molecular weight (for an ethylene-*co*-1-butene copolymer with 2.2 mol% of ethyl branches). They found that the transition between domains I and II strongly depends on molar mass. They concluded that the origin of the SN process is associated with the entangled melt dynamics. The partial melting at  $T_s$  involves the movement of chains, which are constrained by a series of obstacles such as entanglements, loops, ties, and knots. To accomplish a homogeneous melt, the original crystalline structure must be completely destroyed, and this process needs chain movements to overcome obstacles that prevent chain relaxation. When the molecular weight increases, the number of obstacles also increases, making the chain movements needed to achieve a fully homogeneous random melt more difficult.

**Fig. 24** Critical melting temperature ( $T_s^{I-II}$ ) plotted as a function of molar mass of random ethylene 1-butene copolymers with 2.2 mol% ethyl branches. The *dashed line* represents the equilibrium melting temperature. Adapted with permission from Reid et al. [50]. Copyright (2013) American Chemical Society



For the ethylene-*co*-1-butene copolymer with 2.2 mol% of ethyl branches,  $T_s^{I-II}$  increases linearly with the logarithm of molar mass (Fig. 24). One particular finding of Reid et al. is that the value of  $T_s^{I-II}$  is always higher than the calculated equilibrium melting temperature ( $T_m^0$ ) of the copolymer as long as the molecular weight is higher than 1,300 g/mol. For molecular weights below this value, the copolymer exhibits a  $T_s^{I-II}$  that is equal to or lower than  $T_m^0$ . Additionally, 1,300 g/mol also corresponds to the critical molecular weight for the development of entanglements in polyethylene. Hence, ethylene/ $\alpha$ -olefin copolymer samples that are free of entanglements do not have memory effects above  $T_m^0$ .

## 10 Self-Nucleation and Nucleating Agents Efficiency Determination

Fillon et al. [159] developed a method for evaluating the efficiency of a nucleating agent employing SN. Self-nuclei are commonly considered to be the best nuclei for the polymer under study because they have the ideal crystallography for epitaxial nucleation. Also, the number of self-nuclei increases with a decrease of  $T_s$  within domain II. Therefore, the minimum temperature within domain II is the ideal SN temperature, because it causes maximum production of self-nuclei without any annealing of unmolten crystal fragments (if present). The peak  $T_c$  value reached after SN at the ideal  $T_s$  is therefore the maximum value of the crystallization temperature induced by SN without the influence of annealing.

The above facts are the basis of Eq. (1), where calculation of the nucleation efficiency (NE) is related to the shift in crystallization temperature produced by the nucleating agent under consideration, in comparison with the shift produced by the maximum quantity of self-nuclei generated in the process of ideal SN [159]. NE can be calculated by the following simple expression:

$$NE = \frac{T_{CNA} - T_{CP}}{T_{CMP} - T_{CP}}, \quad (1)$$

where  $T_{CNA}$  is the peak crystallization temperature of the polymer with the nucleating agent,  $T_{CP}$  is the peak crystallization temperature of the neat polymer (without any nucleating agent and with a standard thermal history), and  $T_{CMP}$  is the maximum crystallization temperature of the ideally self-nucleated neat polymer sample (i.e., SN is performed with the minimum  $T_s$  value within domain II).

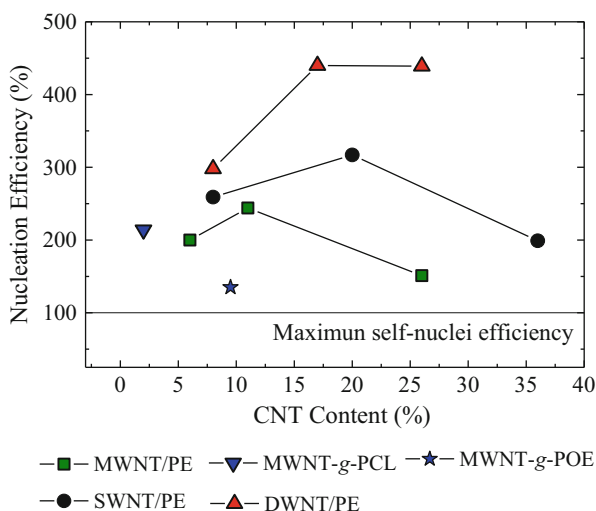
NE is a convenient parameter for comparing the efficiencies of different nucleating agents in a quantitative way and with respect to a unique property of every polymer (i.e., its SN ability).

Equation (1) has been recently used to determine nucleation efficiency in several publications that deal with the use of nucleating agents to increase factors such as the crystallinity degree, mechanical properties, optical properties, and processing window [75, 160–183].

A typical nucleating agent never reaches an NE value higher than 100%, because a value higher than 100% in Eq. (1) implies that the nucleating agent is better than self-nuclei. However, Müller et al. [168, 175, 184] found that, in some cases, the NE of carbon nanotubes (CNTs) yields values above 100%, referring to this phenomenon as “supernucleation.”

Figure 25 shows CNT nucleation efficiency for PE, PCL, and PEO. Values well above 100% were found, demonstrating that CNTs are better nucleating agents than the corresponding homopolymer self-nuclei in these specific cases. The reasons for supernucleation are still being studied. It is not clear what are the exact conditions needed to achieve such high levels of nucleating efficiency. Two factors are believed to be important: the interactions between the polymer and the nucleating agent and excellent dispersion of the nanofiller [168, 175, 184].

**Fig. 25** Efficiency of CNTs as nucleating agent for the indicated samples. Reprinted from Müller et al. [168], Copyright (2011), with permission from Elsevier



## 11 Conclusions

The self-nucleation technique (SN), applied using a simple thermal protocol performed with a standard differential scanning calorimeter, is a powerful and convenient tool for studying polymer nucleation and crystallization. SN increases nucleation density by orders of magnitude, thus affecting the morphology, crystallinity degree, and (potentially) the mechanical properties of the polymer under study. SN can accelerate the overall crystallization of polymeric materials (by exponentially enhancing the primary nucleation step) and can be used as a tool for investigating crystallization in slow-crystallizing materials.

SN is affected by the architecture (e.g., homopolymer versus copolymer) and topology (e.g., ring versus linear, or branched versus linear) of polymer chains, molecular weight, chemical structure, and molecular orientation, among other factors. Additionally, SN provides a mean to quantify the nucleation efficiency (NE) of additives such as nucleating agents and nanofillers, establishing a relative scale that allows meaningful comparisons between the NE of different additives. The SN technique is now well established and, as shown in this review, has been applied to the study of homopolymers, random and graft copolymers, polymer blends, polymorphic polymers, and nanocomposites.

**Acknowledgments** The POLYMAT/UPV/EHU team would like to acknowledge funding from the following projects: “UPV/EHU Infrastructure: INF 14/38”; “MINECO/FEDER: SINFI30I001726XV1/Ref.: UNPV13-4E-1726” and “MINECO MAT2014-53437-C2-2-P”.

## References

1. Blundell DJ, Keller A, Kovacs AJ (1966) A new self-nucleation phenomenon and its application to the growing of polymer crystals from solution. *J Polym Sci B Polym Lett* 4:481–486
2. Fillon B, Wittmann JC, Lotz B, Thierry A (1993) Self-nucleation and recrystallization of isotactic polypropylene ( $\alpha$  phase) investigated by differential scanning calorimetry. *J Polym Sci B* 31:1383–1393
3. Müller AJ, Balsamo V, Arnal ML (2005) Nucleation and crystallization in diblock and triblock copolymers. *Adv Polym Sci* 190:1–63
4. Lorenzo AT, Arnal ML, Sánchez JJ, Müller AJ (2006) Effect of annealing time on the self-nucleation behavior of semicrystalline polymers. *J Polym Sci Polym Phys* 44:1738–1750
5. Vanden Poel G, Mathot VBF (2007) High performance differential scanning calorimetry (HPer DSC): a powerful analytical tool for the study of the metastability of polymers. *Thermochim Acta* 461:107–121
6. Müller AJ, Michell RM, Pérez RA, Lorenzo AT (2015) Successive self-nucleation and annealing (SSA): correct design of thermal protocol and applications. *Eur Polym J* 65:132–154
7. Müller AJ, Arnal ML (2005) Thermal fractionation of polymers. *Prog Polym Sci* 30:559–603
8. Arandia I, Mugica A, Zubitur M et al (2015) How composition determines the properties of isodimorphic poly(butylene succinate-ran-butylene azelate) random biobased copolymers: from single to double crystalline random copolymers. *Macromolecules* 48:43–57

9. Allegra G (ed) (2005) *Advances in polymer science series: interphases and mesophases in polymer crystallization*, vol I–III. Springer, Berlin
10. Bassett DC, Turner B (1974) On the phenomenology of chain-extended crystallization in PE. *Philos Mag* 29:925–955
11. Rastogi S, Hikosaka M, Kawabata H, Keller A (1991) Role of mobile phases in the crystallization of polyethylene. Part 1. Metastability and lateral growth. *Macromolecules* 24:6384–6391
12. Okada T, Saito H, Inoue T (1992) Time-resolved light scattering studies on the early stage of crystallization in isotactic polypropylene. *Macromolecules* 25:1908–1911
13. Imai M, Mori K, Mizukami T, Kaji K, Kanaya Y (1992) Structural formation of poly(ethylene terephthalate) during the induction period of crystallization: 2. Kinetic analysis based on the theories of phase separation. *Polymer* 33:4457–4462
14. Ezquerro TA, López-Cabarcos E, Hsiao BS, Balta-Calleja FJ (1996) Precursors of crystallization via density fluctuations in stiff-chain polymers. *Phys Rev E Stat Phys Plasmas Fluids Relat Interdiscip Topics* 54:989–992
15. Terrill NJ, Fairclough PA, Towns-Andrews E, Komanshek BU, Young RJ, Ryan AJ (1998) Density fluctuations: the nucleation event in isotactic polypropylene crystallization. *Polymer* 39:2381–2385
16. Olmsted PD, Poon WCK, McLeish TCB, Terrill NJ, Ryan AJ (1998) Spinodal-assisted crystallization in polymer melts. *Phys Rev Lett* 81:373–376
17. Matsuba G, Kaji K, Nishida K, Kanaya T, Imai M (1999) Conformational change and orientation fluctuations of isotactic polystyrene prior to crystallization. *Polym J* 31:722–727
18. Strobl G (2000) From the melt via mesomorphic and granular crystalline layers to lamellar crystallites: a major route followed in polymer crystallization. *Eur Phys J E* 3:165–183
19. Lotz B (2000) What can polymer crystal structure tell about polymer crystallization processes. *Eur Phys J E* 3:185–194
20. Cho K, Saheb DN, Choi J, Yang H (2002) Real time in situ X-ray diffraction studies on the melting memory effect in the crystallization of  $\beta$ -isotactic polypropylene. *Polymer* 43:1407–1416
21. Lotz B (2005) Analysis and observation of polymer crystal structures at the individual stem level. *Adv Polym Sci* 180:17–44
22. Li L, De Jeu WH (2005) Flow-induced mesophases in crystallizable polymers. *Adv Polym Sci* 181:75–120
23. Allegra G, Meille SV (2005) Pre-crystalline, high-entropy aggregates: a role in polymer crystallization. *Adv Polym Sci* 191:87–135
24. Kaji K, Nishida K, Kanaya T, Matsuba G, Konishi T, Imai M (2005) Spinodal crystallization of polymers: crystallization from the unstable melt. *Adv Polym Sci* 191:187–240
25. Muthukumar M (2005) Modeling polymer crystallization. *Adv Polym Sci* 191:241–274
26. Alfonso GC, Ziabicki A (1995) Memory effects in isothermal crystallization II. Isotactic polypropylene. *Colloid Polym Sci* 273:317–323
27. Alfonso GC, Scardigli P (1997) Melt memory effects in polymer crystallization. *Macromol Symp* 118:323–328
28. Balzano L, Rastogi S, Peters G (2011) Self-nucleation of polymers with flow: the case of bimodal polyethylene. *Macromolecules* 44:2926–2933
29. Bastiaansen CWM, Meyer HEH, Lemstra PJ (1990) Memory effects in polyethylenes: influence of processing and crystallization history. *Polymer* 31:1435–1440
30. Cavallo D, Zhang L, Portale G, Alfonso GC, Janani H, Alamo RG (2014) Unusual crystallization behavior of isotactic polypropylene and propene/1-alkene copolymers at large undercoolings. *Polymer* 55:3234–3241
31. Cho K, Saheb DN, Yanga H, Kanga BI, Kim J, Lee SS (2003) Memory effect of locally ordered  $\alpha$ -phase in the melting and phase transformation behavior of  $\beta$ -isotactic polypropylene. *Polymer* 44:4053–4059

32. Di Lorenzo ML, Righet MC (2004) Morphological analysis of poly(butylene terephthalate) spherulites during fusion. *Polym Bull* 53:53–62
33. Gurarlan A, Jojjode AS, Tonelli AE (2012) Polymers coalesced from their cyclodextrin inclusion complexes: what can they tell us about the morphology of melt-crystallized polymers. *J Polym Sci B Polym Phys* 50:813–823
34. Häfele A, Heck B, Kawai T, Kohn P, Strobl G (2005) Crystallization of a poly(ethylene-co-octene): I. A precursor structure and two competing mechanisms. *Eur Phys J E* 16:207–216
35. Häfele A, Heck B, Hippler T, Kawai T, Kohn P, Strobl G (2005) Crystallization of poly(ethylene-co-octene): II. Melt memory effects on first order kinetics. *Eur Phys J E* 16:217–224
36. Horst RH, Winter HH (2000) Stable critical gels of a copolymer of ethene and 1-butene achieved by partial melting and recrystallization. *Macromolecules* 33:7538–7543
37. Gao H, Vadlamudi M, Alamo RG, Hu W (2013) Monte Carlo simulations of strong memory effect of crystallization in random copolymers. *Macromolecules* 46:6498–6506
38. He Y, Xu Y, Wei J, Fan Z, Li S (2008) Unique crystallization behavior of poly(l-lactide)/poly(d-lactide) stereocomplex depending on initial melt states. *Polymer* 49:5670–5675
39. Jorda R, Wilkes GL (1988) Rapid recrystallization of freshly melted spherulites. *Polym Bull* 19:409–415
40. Kawabata J, Matsuba G, Nishida K, Inoue R, Kanaya T (2011) Melt memory effects on recrystallization of polyamide 6 revealed by depolarized light scattering and small-angle X-ray scattering. *J Appl Polym Sci* 122:1913–1920
41. Li X, Su F, Ji Y et al (2013) Influence of the memory effect of a mesomorphic isotactic polypropylene melt on crystallization behavior. *Soft Matter* 9:8579–8588
42. Li X, Ma Z, Su F et al (2014) New understanding on the memory effect of crystallized iPP. *Chin J Polym Sci* 32:1224–1233
43. Luo C, Sommer JU (2013) Disentanglement of linear polymer chains toward unentangled crystals. *ACS Macro Lett* 2:31–34
44. Martins JA, Zhang W, Brito AM (2010) Origin of the melt memory effect in polymer crystallization. *Polymer* 51:4185–4194
45. Massa MV, Lee MSM, Dalnoki-Veress K (2005) Crystal nucleation of polymers confined to droplets: memory effects. *J Polym Sci B Polym Phys* 43:3438–3443
46. Maus A, Hempel E, Thurn-Albrecht T, Saalwächter K (2007) Memory effect in isothermal crystallization of syndiotactic polypropylene - role of melt structure and dynamics. *Eur Phys J E* 23:91–101
47. Mendez G, Müller AJ (1997) Evidences of the crystalline memory and recrystallisation capacity of bisphenol-A polycarbonate. *J Therm Anal* 50:593–602
48. Prox M, Pommnimit B, Yarga J, Ehrenstein GW (1990) Thermoanalytical investigations of self-reinforced polyethylene. *J Therm Anal* 36:1675–1684
49. Rault J, Robelin E (1980) Memory effect in liquid polyolefine. *Polym Bull* 2:373–381
50. Reid BO, Vadlamudi M, Mamun A et al (2013) Strong memory effect of crystallization above the equilibrium melting point of random copolymers. *Macromolecules* 46:6485–6497
51. Stribeck N, Bösecke P, Bayer R, Camarillo AA (2005) Structure transfer between a polymer melt and the solid state. Investigation of the nanostructure evolution in oriented polyethylene by means of continuous X-ray scattering. *Progr Colloid Polym Sci* 130:127–139
52. Varga J, Menczel J, Solti A (1976) Memory effect of low-density polyethylene crystallized in a stepwise manner. *J Therm Anal* 10:433–440
53. Varga J, Menczel J, Solti A (1979) The melting of high-pressure polyethylene subjected to stepwise heat treatment. *J Therm Anal* 17:333–342
54. Varga J, Schulek-Tóth F, Ille A (1991) Effect of fusion conditions of  $\beta$ -polypropylene on the new crystallization. *Colloid Polym Sci* 269:655–666
55. Varga J, Schulek-Tóth E (1996) Crystallization, melting and spherulitic structure of B-nucleated random propylene copolymers. *J Therm Anal* 47:941–955

56. Vasanthan N (2003) "Orientation induced memory effect" in polyamides and the relationship to hydrogen bonding. *J Appl Polym Sci* 90:772–775
57. Wang M, Hu W, Ma Y, Ma Y (2005) Orientational relaxation together with polydispersity decides precursor formation in polymer melt crystallization. *Macromolecules* 38:2806–2812
58. Xu J, Ma Y, Hu W, Rehahn M, Reiter G (2009) Cloning polymer single crystals through self-seeding. *Nat Mater* 8:348–353
59. Yamato M, Kimura T (2006) Relationship between magnetic alignment and the crystallization condition of isotactic polystyrene. *Sci Technol Adv Mater* 7:337–341
60. Zheng C, Zhang X, Dong X et al (2006) Variations of regular conformation structures in melt of syndiotactic polypropylene. *Polymer* 47:7813–7820
61. Zhou T, Yang H, Ning N, Xiang Y, Du R, Fu Q (2010) Partial melting and recrystallization of isotactic polypropylene. *Chin J Polym Sci* 28:77–83
62. Zhu H, Yang H, Zhao Y, Wang D (2011) The dynamic crystallization and multiple melting behavior of polypropylene in the in-reactor alloy: a differential scanning calorimetry study. *J Appl Polym Sci* 121:1372–1383
63. Zhu X, Li Y, Yan D, Zhu P, Lu Q (2001) Influence of the order of polymer melt on the crystallization behavior: I. Double melting endotherms of isotactic polypropylene. *Colloid Polym Sci* 279:292–296
64. Turska E, Gogolewski S (1975) Study on crystallization of nylon 6 (polycapramide). III. Effect of "crystalline memory" on crystallization kinetics. *J Appl Polym Sci* 19:637–644
65. Di Filippo G, Gonzalez ME, Gasiba MT, Müller AJ (1987) Crystalline memory on polycarbonate. *J Appl Polym Sci* 34:1959–1966
66. Mehl NA, Rebenfeld L (1992) Effect of melt history on the crystallization kinetics of poly(phenylene sulfide). *Polym Eng Sci* 32:1451–1457
67. Fillon B, Lotz B, Thierry A, Wittman JC (1993) Self-nucleation and enhanced nucleation of polymers. Definition of a convenient calorimetric "efficiency scale" and evaluation of nucleating additives in isotactic polypropylene ( $\alpha$  phase). *J Polym Sci B Polym Phys* 31:1395–1405
68. Fillon B, Thierry A, Wittman JC, Lotz B (1993) Self-nucleation and recrystallization of polymers. Isotactic polypropylene,  $\beta$  phase:  $\beta$ - $\alpha$  conversion and  $\beta$ - $\alpha$  growth transitions. *J Polym Sci B Polym Phys* 31:1407–1424
69. Supaphol P, Spruiell JE (2000) Crystalline memory effects in isothermal crystallization of syndiotactic polypropylene. *J Appl Polym Sci* 75:337–346
70. Gallez F, Legras R, Mercier JP (1976) Crystallization of bisphenol-A polycarbonate. I. Influence of trimellitic acid tridecyloctyl ester on the kinetics of crystallization. *J Polym Sci Polym Phys Ed* 14:1367–1377
71. Khanna YP, Reimschuessel AC (1988) Memory effects in polymers. I. Orientational memory in the molten state; its relationship to polymer structure and influence on recrystallization rate and morphology. *J Appl Polym Sci* 35:2259–2268
72. Khanna YP, Kumar R, Reimschuessel AC (1988) Memory effects in polymers. III. Processing history vs. crystallization rate of nylon 6—comments on the origin of memory effect. *Polym Eng Sci* 28:1607–1611
73. Kim SP, Kim SC (1993) Crystallization kinetics of poly(ethylene terephthalate): memory effect of shear history. *Polym Eng Sci* 33:83–91
74. Khanna YP, Kuhn WP, Macur JE et al (1995) Memory effects in polymers. V. Processing history versus thermally induced self-orientation of unoriented poly(chlorotrifluoroethylene) films. *J Polym Sci B Polym Phys* 33:1023–1030
75. Schneider S, Drujon X, Lotz B, Wittmann JC (2001) Self-nucleation and enhanced nucleation of polyvinylidene fluoride ( $\alpha$ -phase). *Polymer* 42:8787–8798
76. Supaphol P, Srimoan P, Sirivat A (2004) Effects of crystalline and orientational memory phenomena on the isothermal bulk crystallization and subsequent melting behavior of poly(trimethylene terephthalate). *Polym Int* 53:1118–1126



77. Rieger J (2003) Polymer crystallization viewed in the general context of particle formation and crystallization. In: Sommer JU, Reiter G (eds) *Polymer crystallization: observations, concepts and interpretations*. Springer, Berlin, pp 7–16
78. Azzurri F, Alfonso GC (2008) Insights into formation and relaxation of shear-induced nucleation precursors in isotactic polystyrene. *Macromolecules* 41:1377–1383
79. Somani RH, Yang L, Hsiao BS (2002) Precursors of primary nucleation induced by flow in isotactic polypropylene. *Physica A* 304:145–157
80. Azzurri F, Alfonso GC (2005) Lifetime of shear-induced crystal nucleation precursors. *Macromolecules* 38:1723–1728
81. Cavallo D, Azzurri F, Balzano L, Funari SS, Alfonso GC (2010) Flow memory and stability of shear-induced nucleation precursors in isotactic polypropylene. *Macromolecules* 43:9394–9400
82. Gai JG, Cao Y (2013) Structure memory effects and rheological behaviors of polyethylenes in processing temperature window. *J Appl Polym Sci* 129:354–361
83. Janeschitz-Kriegl H, Ratajski E (2005) Kinetics of polymer crystallization under processing conditions: transformation of dormant nuclei by the action of flow. *Polymer* 46:3856–3870
84. Somani RH, Sics I, Hsiao BS (2006) Thermal stability of shear-induced precursor structures in isotactic polypropylene by rheo-X-ray techniques with couette flow geometry. *J Polym Sci B Polym Phys* 44:3553–3570
85. Tao F, Bonnaud L, Auhl D, Struth B, Dubois P, Bailly C (2012) Influence of shear-induced crystallization on the electrical conductivity of high density polyethylene carbon nanotube nanocomposites. *Polymer* 53:5909–5916
86. Zhang W, Martins JA (2006) Evaluation of the effect of melt memory on shear-induced crystallization of low-density polyethylene. *Macromol Rapid Commun* 27:1067–1072
87. Arnal ML, Matos ME, Morales RA, Santana O, Müller AJ (1998) Evaluation of the fractionated crystallization of dispersed polyolefins in a polystyrene matrix. *Macromol Chem Phys* 199:2275–2288
88. Arnal ML, Müller AJ, Maiti P, Hikosaka M (2000) Nucleation and crystallization of isotactic poly(propylene) droplets in an immiscible polystyrene matrix. *Macromol Chem Phys* 201:2493–2504
89. Córdova ME, Lorenzo AT, Müller AJ, Gani L, Tence-Girault S, Leibler L (2011) The influence of blend morphology (co-continuous or sub-micrometer droplets dispersions) on the nucleation and crystallization kinetics of double crystalline polyethylene/polyamide blends prepared by reactive extrusion. *Macromol Chem Phys* 212:1335–1350
90. Gao Y, Liu H (2007) Crystallization behavior of dry-brush PEO-PS block copolymer and PEO homopolymer blend. *J Appl Polym Sci* 106:2718–2723
91. Ibarretxe J, Groeninckx G, Bremer L, Mathot VBF (2009) Quantitative evaluation of fractionated and homogeneous nucleation of polydisperse distributions of water-dispersed maleic anhydride-grafted polypropylene. *Polymer* 50:4584–4595
92. Luo C, Han X, Gao Y, Liu H, Hu Y (2009) Crystallization behavior of “wet brush” and “dry brush” blends of PS-b-PEO-b-PS/h-PEO. *J Appl Polym Sci* 113:907–915
93. Morales RA, Arnal ML, Müller AJ (1995) The evaluation of the state of dispersion in immiscible blends where the minor phase exhibits fractionated crystallization. *Polym Bull* 35:379–386
94. Müller AJ, Arnal ML, López-Carrasquero F (2002) Nucleation and crystallization of PS-b-PEO-b-PCL triblock copolymers. *Macromol Symp* 183:199–204
95. Müller AJ, Albuérne J, Esteves LM et al (2004) Confinement effects on the crystallization kinetics and self-nucleation of double crystalline poly(p-dioxanone)-b-poly( $\epsilon$ -caprolactone) diblock copolymers. *Macromol Symp* 215:369–382
96. Müller AJ, Albuérne JML, Raquez JM et al (2005) Self-nucleation and crystallization kinetics of double crystalline poly(p-dioxanone)-b-poly( $\epsilon$ -caprolactone) diblock copolymers. *Faraday Discuss* 128:231–252

97. Arnal ML, López-Carrasquero F, Laredo E, Müller AJ (2004) Coincident or sequential crystallization of PCL and PEO blocks within polystyrene-*b*-poly(ethylene oxide)-*b*-poly( $\epsilon$ -caprolactone) linear triblock copolymers. *Eur Polym J* 40:1461–1476
98. Müller AJ, Balsamo V, Arnal ML, Jakob T, Schmalz H, Abetz V (2002) Homogeneous nucleation and fractionated crystallization in block copolymers. *Macromolecules* 35:3048–3058
99. Manaure AC, Müller AJ (2000) Nucleation and crystallization of blends of poly(propylene) and ethylene/ $\alpha$ -olefin copolymers. *Macromol Chem Phys* 201:958–972
100. Molinuevo CH, Mendez GA, Müller AJ (1998) Nucleation and crystallization of PET droplets dispersed in an amorphous PC matrix. *J Appl Polym Sci* 70:1725–1735
101. Castillo RV, Müller AJ (2009) Crystallization and morphology of biodegradable or biostable single and double crystalline block copolymers. *Prog Polym Sci* 34:519–560
102. Müller AJ, Balsamo V, Arnal ML (2007) Crystallization in block copolymers with more than one crystallizable block. In: Reiter G, Strobl G (eds) *Lecture notes in physics: progress in understanding of polymer crystallization*, vol 714. Springer, Berlin, pp 229–259
103. Müller AJ, Arnal ML, Lorenzo AT (2013) Crystallization in nano-confined polymeric systems. In: Piorkowska E, Rutledge G (eds) *Handbook of polymer crystallization*. Wiley, New York, pp 347–378
104. Michell RM, Blaszczyk-Lezak I, Mijangos C, Müller AJ (2013) Confinement effects on polymer crystallization: from droplets to alumina nanopores. *Polymer* 54:4059–4077
105. Michell RM, Blaszczyk-Lezak I, Mijangos C, Müller AJ (2014) Confined crystallization of polymers within anodic aluminum oxide templates. *J Polym Sci B Polym Phys* 52:1179–1194
106. Santana OO, Müller AJ (1994) Homogeneous nucleation of the dispersed crystallisable component of immiscible polymer blends. *Polym Bull* 32:471–477
107. Manaure AC, Morales RA, Sánchez JJ, Müller AJ (1997) Rheological and calorimetric evidences of the fractionated crystallization of iPP dispersed in ethylene/ $\alpha$ -olefin copolymers. *J Appl Polym Sci* 66:2481–2493
108. Chen HL, Wu JC, Lin TL, Lin JS (2001) Crystallization kinetics in microphase-separated poly(ethylene oxide)-block-poly(1,4-butadiene). *Macromolecules* 34:6936–6944
109. Balsamo V, Paolini Y, Ronca G, Müller AJ (2000) Crystallization of the polyethylene block in polystyrene-*b*-polyethylene-*b*-polycaprolactone triblock copolymers, 1. Self-nucleation behavior. *Macromol Chem Phys* 201:2711–2720
110. Schmalz H, Müller AJ, Abetz V (2003) Crystallization in ABC triblock copolymers with two different crystalline end blocks: influence of confinement on self-nucleation behavior. *Macromol Chem Phys* 204:111–124
111. Boschetti-de-Fierro A, Lorenzo AT, Müller AJ, Schmalz H, Abetz V (2008) Crystallization kinetics of PEO and PE in different triblock terpolymers: effect of microdomain geometry and confinement. *Macromol Chem Phys* 209:476–487
112. Huang CL, Jiao L, Zeng JB, Zhang JJ, Yang KK, Wang YZ (2013) Fractional crystallization and homogeneous nucleation of confined PEG microdomains in PBS-PEG multiblock copolymers. *J Phys Chem B* 117:10665–10676
113. Castillo RV, Müller AJ, Lin MC, Chen HL, Jeng US, Hillmyer MA (2008) Confined crystallization and morphology of melt segregated PLLA-*b*-PE and PLDA-*b*-PE diblock copolymers. *Macromolecules* 41:6154–6164
114. Lin MC, Chen HL, Lin WF, Huang PS, Tsai JC (2012) Crystallization of isotactic polypropylene under the spatial confinement templated by block copolymer microdomains. *J Phys Chem B* 116(40):12357–12371
115. Müller AJ, Lorenzo AT, Arnal ML, Boschetti de Fierro A, Abetz V (2006) Self-nucleation behavior of the polyethylene block as function of the confinement degree in polyethylene-block-polystyrene diblock copolymers. *Macromol Symp* 240:114–122
116. Lorenzo AT, Arnal ML, Müller AJ, Boschetti-de-Fierro A, Abetz V (2007) Nucleation and isothermal crystallization of the polyethylene block within diblock copolymers containing polystyrene and poly(ethylene-alt-propylene). *Macromolecules* 40:5023–5037

117. Lorenzo AT, Müller AJ, Lin MC et al (2009) Influence of macromolecular architecture on the crystallization of (PCL<sub>2</sub>)-b-(PCL<sub>2</sub>) 4-miktoarm star block copolymers in comparison to linear PCL-b-PS diblock copolymer analogues. *Macromolecules* 42:8353–8364
118. Pan Y, Yu X, Shi T, An L (2010) Nucleation and crystallization of H-shaped (PS)<sub>2</sub>PEG(PS)<sub>2</sub> block copolymers. *Chin J Polym Sci* 28:347–355
119. Pérez RA, Córdova ME, López JV et al (2014) Nucleation, crystallization, self-nucleation and thermal fractionation of cyclic and linear poly( $\epsilon$ -caprolactone)s. *React Funct Polym* 80:71–82
120. Chen H, Hsiao S, Lin T, Yamauchi K, Hasegawa H, Hashimoto T (2001) Microdomain-tailored crystallization kinetics of block copolymers. *Macromolecules* 34:671–674
121. Hamley IW (1998) *The physics of block copolymers*. Oxford University Press, London
122. Wunderlich B (1976) *Macromolecular physics. Crystal nucleation, growth, annealing*, vol 2. Academic, New York
123. Supaphol P, Lin JS (2001) Crystalline memory effect in isothermal crystallization of syndiotactic polypropylenes: effect of fusion temperature on crystallization and melting behavior. *Polymer* 42:9617–9626
124. Mamun A, Unemoto S, Okui N, Ishihara N (2007) Microdomain-tailored crystallization kinetics of block copolymers. *Macromolecules* 40:6296–6303
125. Zhang YS, Zhong LW, Yang S, Liang DH, Chen EQ (2012) Memory effect on solution crystallization of high molecular weight poly(ethylene oxide). *Polymer* 53:3621–3628
126. Cheng SZD (2008) *Phase transitions in polymers: the role of metastable states*, 1st edn. Elsevier Science, Amsterdam
127. Mamun A, Chen X, Alamo RG (2014) Interplay between a strong memory effect of crystallization and liquid-liquid phase separation in melts of broadly distributed ethylene-1-alkene copolymers. *Macromolecules* 47:7958–7970
128. Wang Y, Lu Y, Zhao J, Jiang Z, Men Y (2014) Direct formation of different crystalline forms in butene-1/ethylene copolymer via manipulating melt temperature. *Macromolecules* 47:8653–8662
129. Cavallo D, Gardella L, Portale G, Müller AJ, Alfonso GC (2013) On cross- and self-nucleation in seeded crystallization of isotactic poly(1-butene). *Polymer* 54:4637–4644
130. Cavallo D, Gardella L, Portale G, Müller AJ, Alfonso GC (2014) Self-nucleation of isotactic poly(1-butene) in the trigonal modification. *Polymer* 55:137–142
131. Chocinski-Arnault L, Gaudefroy V, Gacougnolle JL, Rivière A (2002) Memory effect and crystalline structure in polyamide 11. *J Macromol Sci B* 41:777–785
132. Dai PS, Cebe P, Capel M (2002) Thermal analysis and X-ray scattering study of metallocene isotactic polypropylene prepared by partial melting. *J Polym Sci B Polym Phys* 40:1644–1660
133. Kang J, Zhang J, Chen Z et al (2014) Isothermal crystallization behavior of  $\beta$ -nucleated isotactic polypropylene with different melt structures. *J Polym Res* 21:506
134. Kang J, Chen Z, Chen J et al (2015) Crystallization and melting behaviors of the  $\beta$ -nucleated isotactic polypropylene with different melt structures - the role of molecular weight. *Thermochim Acta* 599:42–51
135. Na B, Pan H, Lv R, Zhu J, Li C (2012) A facile route to ordered  $\gamma$  phase in poly(vinylidene fluoride) via melt annealing and re-crystallization. *Mater Lett* 85:37–39
136. Pan H, Na B, Lv R, Li C, Zhu J, Yu Z (2012) Polar phase formation in poly(vinylidene fluoride) induced by melt annealing. *J Polym Sci B Polym Phys* 50:1433–1437
137. Schenk H, Peschar R (2004) Understanding the structure of chocolate. *Radiat Phys Chem* 71:829–835
138. Wu MC, Woo EM (2005) Effects of  $\alpha$ -form or  $\beta$ -form nuclei on polymorphic crystalline morphology of poly(butylene adipate). *Polym Int* 54:1681–1688
139. Gu Q, Wu L, Wu D, Shen D (2001) Effect of self-nucleation on the crystallization of segmented copolymer poly(ether ester). *J Appl Polym Sci* 81:498–504

140. Kang J, Li J, Chen S et al (2013) Investigation of the crystallization behavior of isotactic polypropylene polymerized with different Ziegler-Natta catalysts. *J Appl Polym Sci* 129:2663–2670
141. Kang J, Li J, Chen S et al (2013) Hydrogenated petroleum resin effect on the crystallization of isotactic polypropylene. *J Appl Polym Sci* 130:25–38
142. Lorenzo AT, Müller AJ (2008) Estimation of the nucleation and crystal growth contributions to overall crystallization energy barrier. *J Polym Sci B Polym Phys* 46:1478–1487
143. Nanaki SG, Papageorgiou GZ, Bikiaris DN (2012) Crystallization of novel poly( $\epsilon$ -caprolactone)-block-poly(propylene adipate) copolymers. *J Therm Anal Calorim* 108:633–645
144. Papageorgiou GZ, Achilias DS, Karayannidis GP (2010) Estimation of thermal transitions in poly(ethylene naphthalate): experiments and modeling using isoconversional methods. *Polymer* 51:2565–2575
145. Papageorgiou GZ, Panayiotou C (2011) Crystallization and melting of biodegradable poly(propylene suberate). *Thermochim Acta* 523:187–199
146. Papageorgiou ZG, Bikiaris DN, Achilias DS (2012) Spherulite growth rates of in situ prepared poly(propylene terephthalate)/SiO<sub>2</sub> nanocomposites. *J Therm Anal Calorim* 114:431–440
147. Papageorgiou GZ, Achilias DS, Bikiaris DN (2009) Crystallization kinetics and melting behaviour of the novel biodegradable polyesters poly(propylene azelate) and poly(propylene sebacate). *Macromol Chem Phys* 210:90–107
148. Papageorgiou GZ, Bikiaris DN, Achilias DS, Karagiannidis N (2010) Synthesis, crystallization, and enzymatic degradation of the biodegradable polyester poly(ethylene azelate). *Macromol Chem Phys* 211:2585–2595
149. Sisti L, Finelli L, Lotti N, Berti C, Munari A (2003) Memory effect in melting behaviour, crystallization kinetics and morphology of poly(propylene terephthalate). *ePolymers* 54:1–19
150. Xu Y, Wang Y, Xu T, Jingjing Z, Liu C, Shen C (2014) Crystallization kinetics and morphology of partially melted poly(lactic acid). *Polym Test* 37:179–185
151. Zhu X, Li Y, Yan D, Fang Y (2001) Crystallization behavior of partially melting isotactic polypropylene. *Polymer* 42:9217–9222
152. Zhao Y, Vaughan AS, Sutton SJ, Swingler SG (2001) On nucleation and the evolution of morphology in a propylene/ethylene copolymer. *Polymer* 42:6599–6608
153. Albuera J, Marquez L, Müller AJ et al (2003) Nucleation and crystallization in double crystalline poly(p-dioxanone)-b-poly( $\epsilon$ -caprolactone) diblock copolymers. *Macromolecules* 36:1633–1644
154. Cai J, Li T, Han Y, Zhuang Y, Zhang X (2006) Nonisothermal crystallization kinetics and morphology of self-seeded syndiotactic 1,2-polybutadiene. *J Appl Polym Sci* 100:1479–1491
155. Zheng H, Wang B, Zheng G, Wang Z, Dai K, Liu C (2014) Study on crystallization kinetics of partially melting polyethylene aiming to improve mechanical properties. *Ind Eng Chem Res* 53:6211–6220
156. Schulze R, Arras MML, Helbing C et al (2014) How the calorimetric properties of a crystalline copolymer correlate to its surface nanostructures. *Macromolecules* 47:1705–1714
157. Kanga J, Penga H, Wanga B et al (2015) Investigation on the self-nucleation behavior of controlled-rheology polypropylene. *J Macromol Sci B* 54:127–142
158. Tidick P, Fakirov S, Avramova N, Zachmann HG (1984) Effect of the melt annealing time on the crystallization of nylon-6 with various molecular weights. *Colloid Polym Sci* 262:445–449
159. Fillon B, Lotz B, Thierry A, Wittmann JC (1993) Self-nucleation and enhanced nucleation of polymers. Definition of a convenient calorimetric “efficiency scale” and evaluation of nucleating additives in isotactic polypropylene ( $\alpha$  phase). *J Polym Sci B* 31:1395–1405
160. Abraham F, Schmidt HW (2010) 1,3,5-Benzenetrisamide based nucleating agents for poly(vinylidene fluoride). *Polymer* 51:913–921
161. Anderson KS, Hillmyer MA (2006) Melt preparation and nucleation efficiency of polylactide stereocomplex crystallites. *Polymer* 47:2030–2035

162. Bouza R, Marco C, Naffakh M, Barral L, Ellis G (2011) Effect of particle size and a processing aid on the crystallization and melting behavior of iPP/red pine wood flour composites. *Compos Part A* 42:935–949
163. Dai J, Shen Y, Yang J, Huang T, Zhang N, Wang Y (2014) Crystallization and melting behaviors of polypropylene admixed by graphene and  $\beta$ -phase nucleating agent. *Colloid Polym Sci* 292:923–933
164. Fanegas N, Gómez MA, Marco C, Jiménez I, Ellis G (2007) Influence of a nucleating agent on the crystallization behaviour of isotactic polypropylene and elastomer blends. *Polymer* 48:5324–5331
165. Gahleitner M, Kheirandish GS, Wolfschwenger J (2011) Nucleation of polypropylene homo and copolymers. *Int Polym Proc* 26:2–20
166. Laoutid F, Estrada E, Michell RM, Bonnaud L, Müller AJ, Dubois P (2013) The influence of nanosilica on the nucleation, crystallization and tensile properties of PP-PC and PP-PA blends. *Polymer* 54:3982–3993
167. Libster D, Aserin A, Garti N (2007) Advanced nucleating agents for polypropylene. *Polym Adv Technol* 18:685–695
168. Müller AJ, Arnal ML, Trujillo M, Lorenzo AT (2011) Super-nucleation in nanocomposites and confinement effects on the crystallizable components within block copolymers, Miktoarm star copolymers and nanocomposites. *Eur Polym J* 47:614–629
169. Patil N, Invigorito C, Gahleitner M, Rastogi S (2013) Influence of a particulate nucleating agent on the quiescent and flow-induced crystallization of isotactic polypropylene. *Polymer* 54:5883–5891
170. Pérez RA, López JV, Hoskins JN et al (2014) Macromolecules nucleation and antinucleation effects of functionalized carbon nanotubes on cyclic and linear poly( $\epsilon$ -caprolactones). *Macromolecules* 47:3553–3566
171. Priftis D, Sakellariou G, Hadjichristidis N, Penott E, Lorenzo AT, Müller AJ (2009) Surface modification of multiwalled carbon nanotubes with biocompatible polymers via ring opening and living anionic surface initiated polymerization. Kinetics and crystallization behavior. *J Polym Sci A Polym Chem* 47:4379–4390
172. Pucciariello R, Villani V, Giammarino G (2011) Thermal behaviour of nanocomposites based on linear-low-density poly(ethylene) and carbon nanotubes prepared by high energy ball milling. *J Polym Res* 18:949–956
173. Song P, Wei Z, Liang J, Chen G, Zhang W (2012) Crystallization behavior and nucleation analysis of poly(L-lactic acid) with a multiamide nucleating agent. *Polym Eng Sci* 52:1058–1068
174. Trujillo M, Arnal ML, Müller AJ et al (2007) Thermal and morphological characterization of nanocomposites prepared by in-situ polymerization of high-density polyethylene on carbon nanotubes. *Macromolecules* 40:6268–6276
175. Trujillo M, Arnal ML, Müller AJ et al (2012) Supernucleation and crystallization regime change provoked by MWNT addition to poly( $\epsilon$ -caprolactone). *Polymer* 53:832–841
176. Wu Y, Ling HS (2012) The role of surface charge of nucleation agents on the crystallization behavior of poly(vinylidene fluoride). *J Phys Chem B* 116:7379–7388
177. Xu S, Zhao X, Ye L (2013) Mechanical and crystalline properties of monomer casting Nylon-6/SiO<sub>2</sub> composites prepared via in situ polymerization. *Polym Eng Sci* 53:1809–1822
178. Xu Y, Wu L (2013) Synthesis of organic bisurea compounds and their roles as crystallization nucleating agents of poly(L-lactic acid). *Eur Polym J* 49:865–872
179. Yang Z, Zhang Z, Tao Y, Mai K (2008) Effects of polyamide 6 on the crystallization and melting behavior of  $\beta$ -nucleated polypropylene. *Eur Polym J* 44:3754–3763
180. Zhang Q, Chen Z, Wang B, Chen J, Yang F, Kang J (2015) Effects of melt structure on crystallization behavior of isotactic polypropylene nucleated with  $\alpha/\beta$  compounded nucleating agents. *J Appl Polym Sci* 132:41355

181. Zhuravlev E, Wurma A, Pötschke P, Androsch R, Schmelzer JWP, Schick C (2014) Kinetics of nucleation and crystallization of poly( $\epsilon$ -caprolactone) - multiwalled carbon nanotube composites. *Eur Polym J* 52:1–11
182. Sabino MA, Ronca G, Müller AJ (2000) Heterogeneous nucleation and self-nucleation of poly(p-dioxanone). *J Mater Sci* 35:5071–5084
183. Wang K, Mai K, Han Z, Ze H (2001) Interaction of self-nucleation and the addition of a nucleating agent on the crystallization behavior of isotactic polypropylene. *J Appl Polym Sci* 81:78–84
184. Trujillo M, Arnal ML, Müller AJ et al (2008) Thermal fractionation and isothermal crystallization of polyethylene nanocomposites prepared by in situ polymerization. *Macromolecules* 41:2087–2095

# Crystal Nucleation of Polymers at High Supercooling of the Melt

René Androsch and Christoph Schick

**Abstract** Analysis of the crystallization kinetics of numerous polymers has revealed a bimodal dependence of the gross crystallization rate on temperature, often leading to the occurrence of two crystallization-rate maxima at widely different temperatures. This review discusses possible reasons for this observation, including temperature-controlled changes in the mechanism of primary crystal nucleation, activation of growth at different crystal faces, and formation of different crystal polymorphs as a result of variation of the supercooling. It is suggested that crystallization proceeds via homogeneous crystal nucleation at high supercooling of the melt, which is supported by estimation of the nucleation density from morphological analyses, crystallization experiments performed on heterogeneity-free droplets, and a link between the time scales of molecular relaxations in the glassy state and primary crystal nucleation. The final part of this review presents an example of the application of Tammann's nuclei development method to obtain nucleation rates in polymer glasses.

**Keywords** Crystal morphology · Homogenous crystal nucleation · Nucleation density · Nucleation rate · Tammann's nuclei development method

## Contents

1	Introduction .....	258
2	Gross Crystallization Rate of Polymers at Widely Different Supercooling .....	261

---

R. Androsch (✉)  
Martin-Luther-University Halle-Wittenberg, Center of Engineering Sciences, 06099 Halle/  
Saale, Germany  
e-mail: [rene.androsch@iw.uni-halle.de](mailto:rene.androsch@iw.uni-halle.de)

C. Schick  
University of Rostock, Institute of Physics, Wismarsche Strasse 43-45, 18051 Rostock,  
Germany

3	Nuclei Density by Analysis of the Semicrystalline Morphology .....	263
4	Homogeneous Nucleation at High Supercooling: Evidence from Droplet Experiments .	266
5	Sequence of Enthalpy Relaxation, Homogeneous Crystal Nucleation, and Crystal Growth in the Glassy Amorphous Phase .....	268
6	Mesophase Formation During Crystallization at High Supercooling .....	272
7	Crystallization of Poly(L-lactic acid) at High Supercooling: Application of Tammann's Nuclei Development Method to Obtain Nucleation Rates .....	274
8	Summary .....	279
	References .....	281

## 1 Introduction

Melt-crystallization of macromolecules is restricted to the temperature range between the equilibrium melting temperature ( $T_{m,0}$ ) and a temperature  $T_{\infty}$ , which is assumed to be 30–50 K below the glass transition temperature ( $T_g$ ). Whereas the high-temperature limit of the temperature range of crystallization is thermodynamically controlled, the low-temperature limit is related to the decreasing mobility of molecular segments, with  $T_{\infty}$  interpreted as the temperature at which no transport across the liquid–crystal phase boundary can be expected. Superposition of the effects of increasing thermodynamic driving force for the liquid–crystal phase transition and decreasing mobility of molecular segments with increasing supercooling (where supercooling is defined as the difference between  $T_{m,0}$  and the crystallization temperature) typically leads, first, to an increase in the crystallization rate in response to a lower crystallization temperature and, subsequently, to a decrease as the temperature approaches  $T_g$  [1, 2].

Crystallization proceeds via the stages of primary crystal nucleation and crystal growth. Primary nucleation involves the formation of a nucleus of supercritical size (i.e., a small crystal that does not disappear with time). Nucleation is controlled by the interplay between the gain and loss of free enthalpy as a result of the liquid–crystal phase transformation and the formation of a liquid–crystal interface, respectively. In general, with increasing size of the nucleus at a given temperature, the total free-enthalpy change goes through a maximum, which defines the critical size of the nucleus and the free-enthalpy barrier required to allow growth of the nucleus, connected with a lowering of the free enthalpy. The formation of such a nucleus can occur in the bulk phase (homogeneous crystal nucleation) or on pre-existing surfaces/heterogeneities (heterogeneous crystal nucleation) [3–6]. In the latter case (i.e., in the presence of active sites at surfaces), the total interfacial stress at the nucleus surface is considered lower than in the case of homogeneous nucleation, and for this reason heterogeneous nucleation is often thermodynamically favored, particularly in the temperature range of low supercooling. The critical size of the nucleus and the free-enthalpy barrier both decrease with increased supercooling (i.e., with increased thermodynamic driving force for the phase transformation). From thermodynamic considerations, it is expected that the nucleation frequency



for a given nucleation mechanism increases exponentially with the supercooling of the melt; however, this is opposed by kinetic restraints (i.e., increasing characteristic time of transport of motifs) [1–6]. As a function of temperature, the dominating mechanism of nucleation can change because it is controlled by the critical size of the nucleus and the work required for creation of the surfaces of the crystal nuclei, both of which depend on the supercooling.

Formation of primary nuclei is followed by their growth to crystals at faces that are often parallel or nearly parallel to the chain axis. The kinetics of lateral crystal growth is often modeled by the Hoffman–Lauritzen (HL) approach, in which different growth regimes are based on the relationship between the crystal surface nucleation rate and the rate of lateral spreading of such secondary crystal nuclei across the growth face [7–9]. To account for the large entropic barrier for attaching a molecular stem at the growth face, several alternative models have been introduced. However, all these models assume that crystals grow directly into the melt; examples include the model of molecular nucleation by Wunderlich [10] and, more recently introduced, the model of Strobl proposing that molecular segments at the crystal growth front pass a transient mesomorphic stage [11–13]. This notwithstanding, the temperature dependence of the crystal growth rate qualitatively obeys similar rules as in case of the temperature dependence of the nucleation rate. The crystal growth rate increases with decreasing temperature as a result of the increasing thermodynamic driving force for the phase transformation, passes through a maximum, and then decreases as a result of the reduced mobility of amorphous molecular segments at the growth faces.

If the rates of both primary crystal nucleation and crystal growth are not too high, they can be measured separately by optical microscopy [14]. The number of spherulites forming at a given crystallization temperature provides information about the nucleation density, whereas the crystal growth rate is evaluated by the time evolution of the spherulite radius. Such analyses, however, can only be performed if the nucleation density is relatively low, that is, at low supercooling when the distance between nuclei is of the order of several micrometers. Alternatively, in such a case, the nucleation density can be evaluated using high-resolution imaging techniques for analysis of the submicron spherulite or crystal density after complete crystallization.

A different, although frequently applied, technique for gaining information about the crystallization rate is calorimetry, which is based on analysis of the time-dependence of the release of exothermic heat flow during the crystallization process [14–16]. Although it is impossible to identify the absolute number of simultaneously growing entities contributing to the increase in crystallinity, it has been shown that application of the Avrami model can give information about nucleation and growth mechanisms [17–20]. Also, analysis of the temperature dependence of the gross crystallization rate allows detection of changes in both growth regimes [21] and nucleation mechanisms with temperature, because the activation energies for the different processes change. This has been shown with the recent introduction of fast scanning chip calorimetry (FSC) for analysis of polymer crystallization at any supercooling of the melt [22–24]. FSC allows not only

adjustment of well-defined states of amorphous structure prior to crystal nucleation and growth, but also analysis of the kinetics of crystallization even at the temperatures of maximum crystallization rate, related to both the short FSC instrumental time constant and high cooling capacity. It is worth noting that the maximum cooling rate in conventional differential scanning calorimeters (DSC) is of the order of only a few hundred degrees Kelvin per minute [25–27], similar to that for commercial hot-stage microscopy systems, although efforts have been made to widen the cooling-rate range [28–30]. However, such a low cooling rate does not often allow large supercooling of the melt because crystallization may begin before the analysis temperature has been reached [31]. This is particularly true for polymers containing heterogeneous nucleators, regardless of whether they are present by chance or added purposely. FSC, in contrast, depending on the particular device, allows cooling of the samples at rates up to  $10^3$ – $10^6$  K s<sup>-1</sup> [32, 33], which for most polymers is sufficiently fast to completely suppress crystallization of the melt when cooling to below  $T_\infty$ . This gives the possibility of studying crystallization not only at low supercooling but in the entire temperature range between  $T_{m,0}$  and  $T_\infty$ , so that supercooling-controlled changes in nucleation and growth mechanisms can be easily recognized. Although not the focus of this review, variation of the cooling scheme permits (a) controlled generation and freezing of nuclei populations, which then can be grown to crystals on re-heating or at elevated temperature in order to obtain information about their density, or (b) to obtain glasses of different instabilities, allowing sub- $T_g$  crystal nucleation and even growth. In addition to the fast-cooling capacity, FSC also allows analysis of the kinetics of crystallization at temperatures of maximum crystallization rate. In many cases, the characteristic crystallization time is less than a second, which does not permit its quantification by conventional DSC, because of the high instrument time constant and low cooling capacity. Note that the FSC time constant, depending on the particular sensor and device employed, is of the order of milliseconds or faster [32, 33].

FSC analysis of the crystallization kinetics of numerous polymers has revealed a bimodal dependence of the gross crystallization rate on temperature, often leading to the occurrence of two crystallization-rate maxima at different temperatures, or to a distinctly broadened crystallization-rate maximum as a result of superposition of contributions from two different crystallization mechanisms [34–45]. This experimental observation has been explained by a change in the mechanism of primary crystal nucleation, although without further knowledge and structural analyses such interpretation is unjustified. The occurrence of two crystallization-rate maxima at different temperatures can be caused by many reasons, including a change in the mechanism of growth, activation of growth at different crystal faces, or formation of different equilibrium or nonequilibrium crystal polymorphs as a function of the supercooling. Thus, the initial assumption of a qualitative change in the nucleation mechanism requires further research. This paper is structured to first provide examples of the bimodal temperature dependence of gross crystallization rate for different polymers. This is followed by presentation of research supporting the assumption that crystallization at different supercooling of the melt is governed by different mechanisms of nucleation. It includes (a) using imaging techniques for

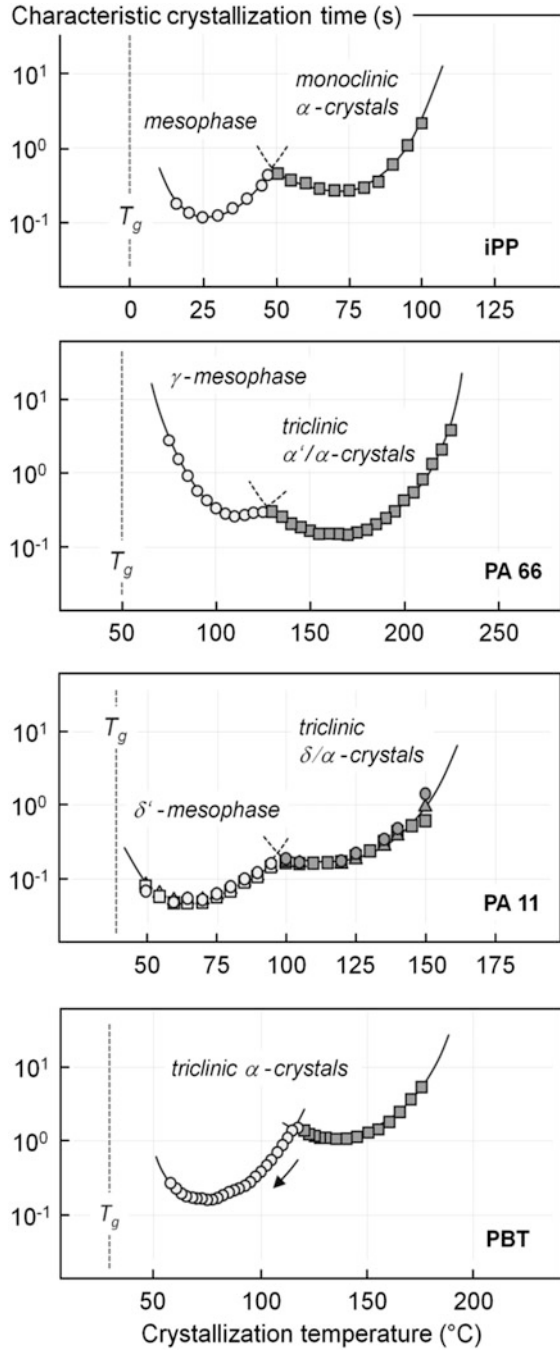
analysis of the semicrystalline morphology of various polymers, each crystallized at different supercooling, to yield conclusions about the nucleation density; (b) discussion of the crystallization behavior of heterogeneity-free polymer phases; and (c) linking the time scale of the molecular relaxations in the glassy state to the time scale of primary nucleation. In the two final parts of this review, mesophase formation during crystallization at high supercooling is discussed, and an example of the application of Tammann's nuclei development method to obtain nucleation rates in polymer glasses is presented.

## 2 Gross Crystallization Rate of Polymers at Widely Different Supercooling

FSC has been applied to study the gross crystallization rate of several polymers in a wide range of different supercooling of the melt [34–47]. Samples were heated to above the melting temperature and after equilibration of the melt cooled to the crystallization temperature at a rate high enough to avoid crystallization during cooling, typically with a rate of the order of magnitude of  $10^3 \text{ K s}^{-1}$ . Isothermal crystallization leads to observation of an exothermic peak, which often is analyzed to obtain the so-called peak-time of crystallization, that is, the time of maximum heat-flow rate during crystallization or the half-transition time, both being measures of the crystallization rate. Figure 1 shows typical examples of the temperature-dependence of the characteristic crystallization time obtained for isotactic polypropylene (iPP) [34, 35], polyamide 66 (PA 66) [37], polyamide 11 (PA 11) [38], and poly(butylene terephthalate) (PBT) [39–41]. Note that in all of the presented experiments, data sets are shown so as to emphasize the occurrence of two distinct crystallization-rate maxima or crystallization-time minima. In particular, for all of the examples, there were numerous data collected from DSC experiments at low supercooling showing characteristic crystallization times exceeding  $10^2 \text{ s}$ . Moreover, the observation of a bimodal dependence of the crystallization rate on supercooling is not restricted to the example polymers shown in Fig. 1 as similar data were reported in the literature for polyamide 6 (PA 6) [36], poly( $\epsilon$ -caprolactone) (PCL) [42, 43], a variety of random copolymers of propylene with 1-alkenes [44, 45], and syndiotactic polypropylene [46].

The data shown in Fig. 1 demonstrate that, with increasing supercooling, the characteristic time of crystallization decreases as a result of increasing thermodynamic driving force for the crystallization, presumably leading to a continuous increase in both the rate of crystal nucleation and growth. It is important to note that, as a result of the recording of an integrated exothermic heat-flow rate signal, distinction between these contributions a priori and without modeling is impossible. The characteristic time of crystallization passes through a first minimum and begins to increase, probably because the decreasing mobility of chain segments hinders growth. However, at even larger supercooling there is further increase in the

**Fig. 1** Characteristic time of crystallization of iPP [34, 35], PA 66 [37], PA 11 [38], and PBT [41] (from top to bottom) as a function of the crystallization temperature. The approximate position of  $T_g$  is indicated in each plot. The squares and circles indicate crystallization processes of different kinetics. The arrow in the PBT plot indicates increasing crystallization rate. Furthermore, the plots contain information about crystal polymorphs forming at different supercooling. The lines connecting data points are drawn to guide the eye

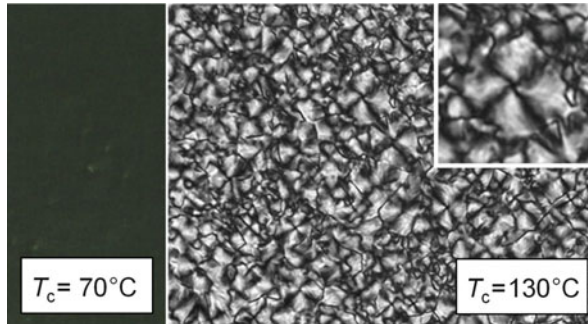


crystallization rate, as indicated by the arrow in the PBT data plot shown in Fig. 1. Possible reasons have been outlined above and include a sudden increase in the nucleation density, as a result of changes in the nucleation mechanism, and an increase in the crystal growth rate. The latter could be the result of a change in the mechanism of secondary nucleation, activation of crystal growth at faces of lower surface free energy, or growth of different crystal polymorphs.

In Fig. 1, in addition to the crystallization-rate data, information is provided about the structure of the ordered phase formed at different supercooling. For iPP, PA 66, PA 11, and PA 6 (not shown), it is proven that during crystallization at low and high supercooling there is formation of crystals and mesophases, respectively. For PBT and poly(ethylene terephthalate) (PET; not shown) such supercooling-controlled crystal/mesophase polymorphism was not detected. As such, at least for some of the examples shown, it cannot be excluded that the low- and high-temperature crystallization-rate maxima are the result of formation of different crystal polymorphs. Detailed information and further discussion on this subject are given in Sect. 6.

### 3 Nuclei Density by Analysis of the Semicrystalline Morphology

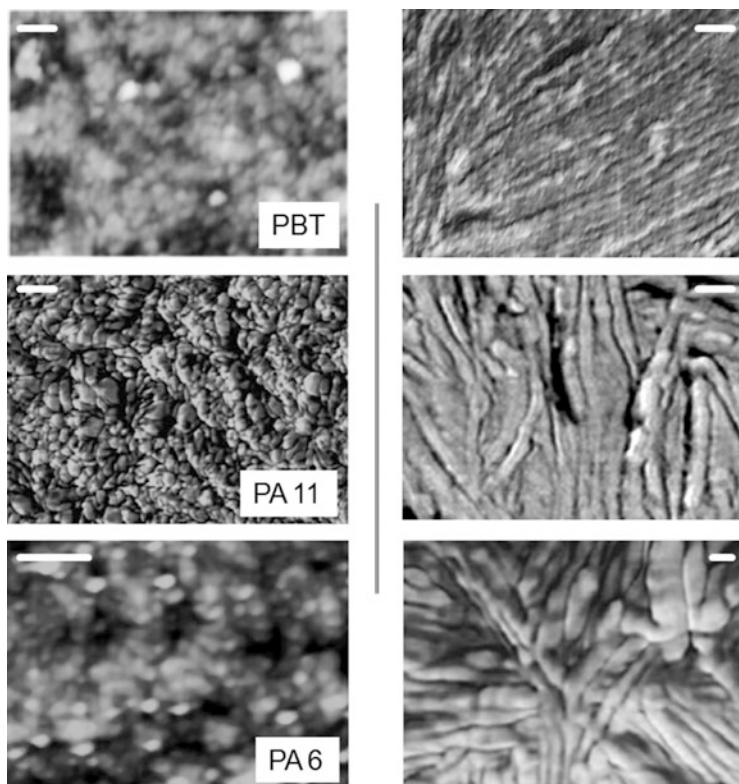
To obtain at least semiquantitative information about nucleation densities at temperatures associated with high- and low-temperature crystallization processes for all the examples shown in Fig. 1, detailed morphological analyses were performed at both the nanometer and micrometer length scales. Figure 2 shows, as a typical example, polarizing optical microscopy (POM) micrographs of PBT crystallized at 130°C and 70°C, that is, at the temperatures of the high- and low-temperature crystallization rate maxima, respectively. Crystallization at the higher temperature reveals a space-filling spherulitic superstructure, with the size of spherulites being 5–20  $\mu\text{m}$ . Observation of spherulites formed during crystallization at low supercooling, in general, indicates the presence of lamellae, which began to grow from a former primary crystal nucleus to yield a birefringence pattern with radial symmetry [48–51]. In the case of the sample crystallized at 70°C, a spherulitic superstructure was not observed, because the sample appeared black and featureless between crossed polarizers. It was concluded that in this case crystals are irregularly arranged in the amorphous phase when forming at high supercooling of the melt. The inset in the right-hand image of Fig. 2 is a soft zoom of a spherulite, illustrating rotation of the Maltese cross to 45° off the polarizer axes (parallel to the image borders), indicating formation of so-called abnormal spherulites, which are a specific feature of PBT crystallization [52, 53]. Qualitatively similar POM images showing spherulites formed during crystallization at low supercooling and a featureless birefringence pattern after crystallization at high supercooling or cold-crystallization (implying nucleation at high supercooling) have also been obtained for iPP and its random copolymers with 1-alkenes [54–58], for PA 6 [59], and for PA 11 [38].



**Fig. 2** POM images of PBT crystallized at 70°C (*left*) and 130°C (*right*), that is, at the temperatures of maximum rate of the low- and high-temperature crystallization processes, respectively (see Fig. 1). The *inset* is a soft zoom of a spherulite, illustrating rotation of the Maltese cross 45° off the polarizer axes (parallel to the image borders) and indicating formation of so-called abnormal spherulites, which are a specific feature of PBT crystallization. Reprinted from [41], Copyright (2015), with permission from Elsevier

Further details of the semicrystalline morphology and nucleation density were collected by atomic force microscopy (AFM) and transmission electron microscopy (TEM). Figure 3 shows AFM images of the nanometer length scale surface structure of PBT [41], PA 11 [38], and PA 6 [60] of different crystallization histories. The images in the left- and right-hand columns of Fig. 3 were obtained from samples crystallized at high and low supercooling, respectively (i.e., at temperatures related to the low- and high-temperature crystallization-rate maximum in Fig. 1). In all the examples presented in Fig. 3, there was formation of laterally extended lamellae during crystallization at low supercooling of the melt, as concluded from the observation of spherulitic birefringence patterns (see Fig. 2, right). In contrast, during crystallization at temperatures related to the low-temperature crystallization rate maxima shown in Fig. 1, formation of lamellae was not detected. Instead, the AFM images reveal the presence of small and apparently isometric nodular domains with a size in the order of 10 nm. It is furthermore visible that these domains do not form a higher-order superstructure at the micrometer length scale, which is in accord with the featureless POM structure.

Although the observation of lamellae and spherulites after crystallization at low supercooling is well described in the literature [61], the nanometer-scale morphology of polymers crystallized at high supercooling has been less investigated. However, earlier reports in this field of research are consistent with the images shown in Fig. 3 (left-hand column), such that there is formation of nodular domains with a size of less than about 10 nm. Pioneering work in this area has been performed by Geil [62–64] using an ultraquenching technique and electron microscopy to identify nanoscale granular structures in a large number of polymers after quenching. These observations of a nodular morphology in quenched samples were initially doubted as being possibly related to instrumental artifacts of electron microscopy [65, 66]. However, the observations were then confirmed in many



**Fig. 3** AFM images of PBT [41], PA 11 [38], and PA 6 [60] (from *top* to *bottom*). Images in the *left* and *right* columns are of samples crystallized at high and low supercooling, respectively, that is, at temperatures related to the low- and high-temperature crystallization-rate maximum in Fig. 1. *Scale bars*: 50 nm. Images in the *top* and *center* rows were adapted from [41], Copyright (2015), with permission from Elsevier, and from [38], Copyright (2013) American Chemical Society, respectively. The *bottom left* image was adapted from [60], Copyright (2012), with permission from Elsevier

independent studies using a wide variety of different preparation techniques and instrumentation [67–74].

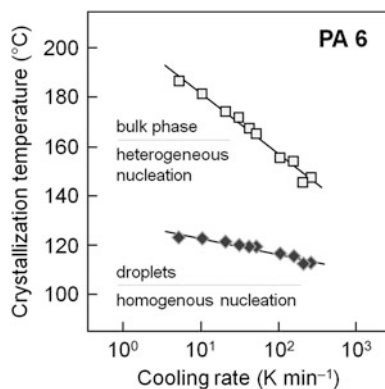
Most important in the context of this review is the observation that, on crystallization at comparatively high temperature, the distance between former crystal nuclei is of the order of several micrometers. It cannot be shorter than the lateral size of lamellae and can be safely quantified by the diameter of spherulites formed during radial growth of lamellae. In the case of crystallization at high supercooling, the nucleation density is several orders of magnitude higher, as the distance between neighboring crystals, and therefore former nuclei, is only 10–20 nm. A rough estimation of the number of independently grown crystals, that is, formed via primary nucleation (as shown in the top left image in Fig. 3, representing the structure of PBT crystallized at 70°C), yields a value of about  $10^{15}$  nuclei  $\text{mm}^{-3}$ .

In the case of crystallization at 130°C, spherulites with a diameter of about 10 μm were detected (see right image in Fig. 2), indicating a nucleation density of only about 10<sup>6</sup> nuclei mm<sup>-3</sup> [41]. In other words, the nucleation density for crystallization at temperatures close to the low-temperature crystallization-rate maximum is at least nine orders of magnitude higher than for crystallization at temperatures close to the high-temperature crystallization-rate maximum.

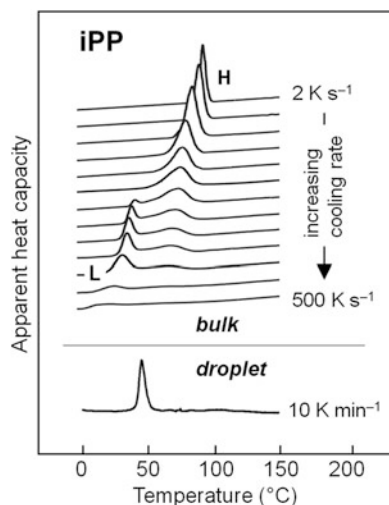
#### 4 Homogeneous Nucleation at High Supercooling: Evidence from Droplet Experiments

Both the increase in the gross crystallization rate and the change in semicrystalline morphology during crystallization of the melt at high supercooling consistently indicate a distinct increase in the nucleation density. Assuming that the high-temperature crystallization process occurs via heterogeneous nucleation, the increase in nucleation rate at high supercooling could be the result of activation of a different kind of heterogeneous nuclei or formation of homogeneous nuclei. In order to prove or disprove the hypothesis of homogeneous nucleation experimentally, nucleation/crystallization experiments in droplets of sufficiently small size were performed, as suggested long ago by Turnbull [75–79]. In more recent investigations, submicron-sized heterogeneity-free droplets of iPP [80–82] and PA 6 [83] were slowly cooled from the melt, revealing crystallization only at high supercooling in the temperature range of the low-temperature maximum of the crystallization rate. As an example, Figure 4 shows the temperatures of crystallization of bulk PA 6 and dispersed PA 6 droplets, both as a function of the cooling rate. Crystallization in PA 6 droplets, regardless of the rate of cooling of the melt in the investigated range of 5–300 K min<sup>-1</sup>, occurred only at temperatures of 110–120°C (i.e., at high supercooling) and at distinctly lower temperatures than in bulk PA 6. Because of the absence of heterogeneous nuclei in droplets, it was

**Fig. 4** Temperature of crystallization of bulk PA 6 (*squares*) and dispersed PA 6 droplets (*diamonds*) as a function of the cooling rate [83]. Adapted with permission from [83]. Copyright (2006) Wiley





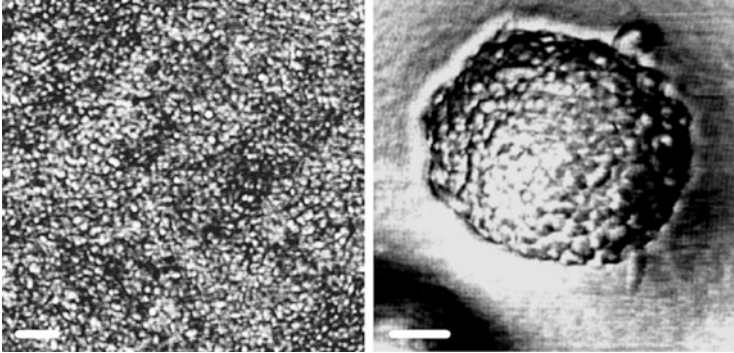


**Fig. 5** FSC (*top*) and DSC (*bottom*) cooling scans of iPP, demonstrating the occurrence of high- and low-temperature crystallization processes, labeled *H* and *L*, respectively, measured during cooling at different rates [80, 84]. The *top set of curves* was obtained for bulk iPP containing heterogeneous nuclei, whereas the *bottom curve* was obtained for heterogeneity-free droplets. Adapted from [84], Copyright (2012), with permission from Elsevier (*top part*), and from [80], Copyright (2011) Wiley (*bottom part*)

concluded that crystallization at low temperatures proceeds via homogeneous nucleation.

Similar observation of the drastically reduced temperature of crystallization during slow cooling has been reported for iPP droplets. Whereas crystallization of the bulk phase of iPP (containing impurities) typically occurs at 110–120°C, when cooling at rates usually applied in DSC, crystallization in droplets was only observed well below 50°C (i.e., at temperatures corresponding to the low-temperature crystallization-rate maximum).

Figure 5 shows FSC cooling scans for bulk and heterogeneity-free droplet iPP [84]. The top curve in Fig. 5 was measured on cooling at 2 K s<sup>-1</sup> and reveals crystallization at about 90°C. This crystallization event (labeled ‘H’) is associated with the high-temperature crystallization process initiated by heterogeneous nucleation. With increasing cooling rate, the high-temperature crystallization process becomes less intense, and is almost completely suppressed during cooling at about 200 K s<sup>-1</sup>. The decrease in the enthalpy of crystallization of the high-temperature crystallization process (indicated by the decreasing peak area in Fig. 5) is paralleled by the evolution of a low-temperature crystallization event (labeled ‘L’ in Fig. 5) below 50°C. It was concluded that if the high-temperature crystallization process is suppressed as a result of fast cooling, then crystallization continues by a different nucleation mechanism at lower temperatures. Fast cooling, in order to avoid crystallization via heterogeneous nucleation at high temperature, is not required if heterogeneous nuclei are absent, as shown by droplet-crystallization experiments.



**Fig. 6** AFM images of iPP. The *left image* was obtained from a rapidly cooled sample annealed at ambient temperature containing heterogeneous nuclei/impurities [85]. The *right image* shows the nanometer scale structure of a heterogeneity-free droplet [80]. *Scale bars*: 100 nm. Adapted with permission from [85], Copyright (2009) IOP publishing (*left image*) and from [80], Copyright (2011) Wiley (*right image*)

Analysis of the crystallization kinetics of heterogeneity-free droplets of iPP revealed a crystallization peak at 44°C, although cooling was performed at a low rate of 10 K min<sup>-1</sup> (Fig. 5, bottom curve) [80]. Comparison of the temperature of crystallization of iPP droplets with the temperature of the low-temperature crystallization event in bulk iPP indicates an identical mechanism of crystallization (i.e., prevalence of homogenous nucleation).

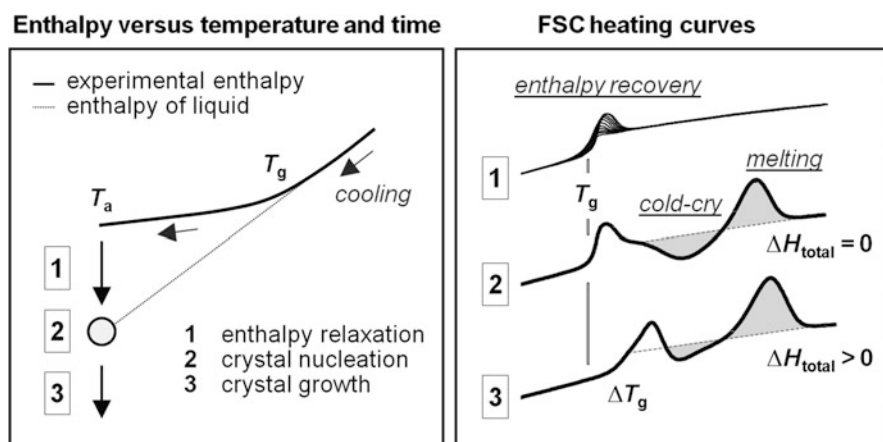
Further striking evidence for identical mechanisms of nucleation in heterogeneity-free droplets and the bulk phase of polymers when crystallizing at high supercooling is provided by analysis of the nucleation density using microscopy. Figure 6 shows the AFM surface structures of two different samples of iPP. The left image was obtained on an iPP that contained heterogeneous nuclei/impurities and which was rapidly cooled from the melt to avoid the high-temperature crystallization, before annealing at ambient temperature [85]. The right image in Fig. 6 shows the nanometer-scale structure of a heterogeneity-free droplet with a size of about 500 nm [80, 81]. In both cases, the same nodular morphology of the ordered phase and nucleation density were detected, as discussed for the left-hand images in Fig. 3, obtained for PA 6, PA 11, and PBT after crystallization at temperatures related to the low-temperature crystallization rate maximum shown in Fig. 1.

## 5 Sequence of Enthalpy Relaxation, Homogeneous Crystal Nucleation, and Crystal Growth in the Glassy Amorphous Phase

Formation of crystal nuclei and crystal growth of polymers is predicted to cease at a temperature 30–50 K below  $T_g$  (i.e., at a temperature where no further transport across the liquid–crystal phase boundary is expected) [1, 2]. In the context of

investigating the nucleation and crystallization behaviors of polymers at high supercooling of the melt, nucleation rates have also been measured in the glassy state for PCL [42, 43], iPP [86], iPB-1 [47], poly(L-lactic acid) (PLLA) [87, 88], PET [89], and PA 6 [90] by both calorimetry and microscopy. It was found experimentally that the rate of nuclei formation of the low-temperature crystallization process is fastest in the temperature range between  $T_g$  and  $(T_g + 50)$  K and that the nucleation rate decreases monotonically with decreasing temperature. These results point to predominance of a single nucleation mechanism in the analyzed temperature range, regardless of whether nucleation occurs in the glassy or devitrified amorphous phase.

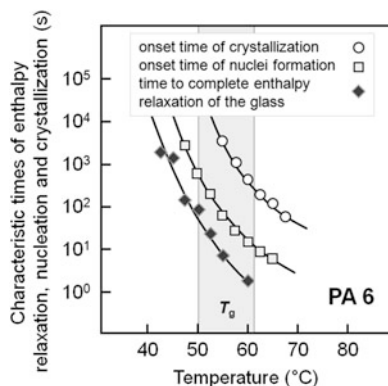
Specific nucleation experiments have been performed to quantitatively describe homogeneous nucleation of polymers in the glassy state, aiming to identify a link between the rate of nuclei formation and the structure of the glass, with the latter being controlled by the conditions of its formation and by the temperature and time of annealing. Figure 7 shows the change in enthalpy of a polymer during fast cooling followed by isothermal annealing at the temperature  $T_a$ . At high temperature, the enthalpy of the polymer melt decreases during cooling, as expected from the short relaxation time of the system. With reference to the enthalpy of the liquid phase (Fig. 7, left), the experimentally observed enthalpy remains at a higher level after vitrification of the melt at  $T_g$ . It is known that, for a given polymer, the difference between the enthalpy of the glass and the liquid depends on both the cooling rate (which controls  $T_g$ ) and the annealing temperature (which controls the enthalpy values of the liquid and glass) [91–93]. The enthalpy decreases during



**Fig. 7** *Left:* Plot of the enthalpy of an initially fully amorphous and liquid polymer as a function of temperature during cooling to the glassy state, and during subsequent isothermal annealing at the annealing temperature  $T_a$ . Vertical arrows indicate the enthalpy decrease during annealing and then again during crystal growth. Arrows on the *experimental curve* indicate cooling. *Right:* FSC heating scans showing enthalpy relaxation (1), crystal nucleation (2), and crystal growth (3) during annealing, with these processes identified in their exact time sequence (see text for detailed description)

annealing such that, at first, the enthalpy relaxes to the value of the liquid state. This is followed by a further decrease towards the enthalpy of the crystal phase as a result of crystal growth (vertical arrows in Fig. 7, left). Prior to crystal growth, formation of nuclei is required which, however, does not lead to a measurable change in enthalpy. The exact time sequence of the various processes (enthalpy relaxation, crystal nucleation, and crystal growth) has been evaluated by analysis of FSC heating scans, recorded after annealing for different times (Fig. 7, right). The top set of curves in Fig. 7 demonstrate that only enthalpy relaxation occurs on annealing of an amorphous sample in the glassy state for short periods of time, as it causes an enthalpy-recovery peak at  $T_g$  on subsequent heating. Note that the heating rate selected for recording the heating scan and the previous cooling rate were sufficiently high to suppress nuclei formation. Otherwise, there would have been detected an exothermic cold-crystallization peak followed by endothermic melting, which was not the case. If annealing is continued after complete relaxation of the glass, then cold-crystallization and melting are observed (Fig. 7, curve 2). The areas of both peaks increase with annealing time; however, they are always identical in area but of opposite sign. In other words, the total change in enthalpy during this annealing-time period is close to zero, indicating absence of crystallization. Eventually, on extended annealing, the area of the endothermic melting peak exceeds the area of the exothermic cold-crystallization peak (Fig. 7, curve 3), which proves that the enthalpy of the sample decreases further as a result of the formation of crystals at the annealing temperature. Note that the endothermic low-temperature peak in curve 3, close to the glass transition, is a result of both enthalpy recovery and melting of the small crystals formed at  $T_a$ . Melting, however, overlaps with exothermic reorganization and cold-crystallization, leading to observation of the high-temperature melting peak. Simultaneously, as a result of the formation of small crystals, there is a significant shift of  $T_g$  towards a higher temperature, indicating immobilization of the amorphous phase, probably as a result of the formation of a rigid amorphous fraction (RAF). Note that, as a result of the covalent linkage of crystals and the amorphous structure in partially crystallized polymers, the mobility of amorphous chain segments in regions near the crystals is reduced. This often leads to an increase in  $T_g$  and the formation of fractions of amorphous structure with different properties [94–100].

Analysis of FSC curves (Fig. 7, right) allows determination of the time required to complete the process of enthalpy relaxation, and of characteristic times for formation of crystal nuclei and crystals. These times are shown in Fig. 8 as a function of the annealing temperature for the specific case of PA 6, focusing on the temperature range close to  $T_g$ . The temperature range of the glass transition on cooling at  $10^3 \text{ K s}^{-1}$ , applied in this particular investigation of PA 6, is indicated in Fig. 8 by the shaded area. It was concluded from visual inspection of the various data sets that formation of crystal nuclei in glassy PA 6 only occurred if the process of enthalpy relaxation of the glass is complete. The experimentally assessable decrease in enthalpy of the glass to the value of the liquid state at identical temperature corresponds to a densification of the glass, involving cooperative rearrangement of molecular segments on a length scale of a few nanometers.



**Fig. 8** Time to complete enthalpy relaxation (*diamonds*), onset time of formation of crystal nuclei (*squares*), and onset time of crystallization (*circles*) as a function of the temperature of annealing initially fully amorphous PA 6 [90]. The *shaded area* indicates the temperature range of the glass transition on cooling at a rate of  $10^3 \text{ K s}^{-1}$ . Adapted with permission from [90], Copyright (2014) Elsevier

The data in Fig. 8 suggest that densification of the glass and disappearance of the relatively large scale motions connected to enthalpy relaxation are complete prior to formation of crystal nuclei. In other words, completion of the enthalpy relaxation of the glass is considered a pre-requisite for the formation of crystal nuclei in the glass. The experimentally evidenced link between the processes of enthalpy relaxation and crystal nucleation suggests that the latter occurs homogeneously in the bulk by rearrangement of molecular segments, but is not initiated on heterogeneities for which such a delay in nucleation is not expected.

The interpretation of a bimodal temperature dependence of the gross crystallization rate and crystallization in heterogeneity-free droplets in terms of bulk homogeneous crystal nucleation is still controversial and not yet unequivocally agreed upon [101, 102]. In a recent review of confinement effects on polymer crystallization it was suggested that the ordering process in droplets is initiated by surface nucleation, because it requires a lower supercooling than homogeneous nucleation in the bulk of the droplets [102]. Surface nucleation, however, is excluded as an explanation for the experimental results presented above because it has been proven that the surface morphology of samples crystallized at high supercooling is indifferent to the structure in the bulk. TEM and small-angle X-ray scattering (SAXS) analyses, in particular for the specific case of iPP, provide similar information as the AFM surface analysis with respect to the higher nucleation density than that obtained on crystallization at low supercooling. In the case of surface nucleation, different nucleation densities at the surface and in the bulk are expected, but have not been proven. A link between enthalpy relaxation of the glass (occurring in the bulk) and crystal nucleation has been confirmed for PCL [42, 43], iPB-1 [47], and PA 6 [90], and favors a bulk nucleation process. However, surface nucleation, regardless of whether at the surface of droplets or in bulk samples, cannot always be excluded as contributing to the crystallization process of

polymers at high supercooling as there is little evidence described in the literature [102, 103]. For example, there are several reports that crystallization of PET at high supercooling is faster in the regions near the surface than in the bulk [104–107], with the results explained in terms of higher mobility of chain segments located near the surface. In a more recent study, the morphology/habit of crystals of cold-crystallized PET was evaluated using electron microscopy and AFM [108]. It was found that crystals formed on heating the amorphous glass to a temperature higher than  $T_g$  are of lamellar shape in the bulk and almost isometric in habit at the surface. This is consistent with the notion that the nucleation density in the bulk is lower than at the surface, probably related to the relatively low bulk nucleation rate. PET, like PLLA, belongs to a small group of polymers that reveal formation of spherulites during cold-crystallization (i.e., after nuclei formation at high supercooling or in the glassy state). For the polymers discussed above, including iPP, PA 6, PA 66, PA 11, and PBT, such a result has not yet been reported, nor different surface and bulk crystal morphologies. In other words, there is a lack of evidence for surface nucleation as a dominant nucleation mechanism during crystallization at high supercooling.

## 6 Mesophase Formation During Crystallization at High Supercooling

In addition to the change in the nucleation mechanism/density, the low-temperature crystallization-rate maximum could be caused by an increase in the crystal growth rate. Such an increase could be a result of activation of growth at different crystal faces when lowering the crystallization temperature, or a result of the formation of a different crystal polymorph. In fact, for iPP, PA 6, PA 66, PA 11, and PLLA, crystal formation at high temperature is replaced by formation of conformationally disordered crystals or mesophases at low temperature, with the latter being metastable at the condition of their formation. In all cases, the conformationally disordered crystals or mesophases convert irreversibly into the stable crystal polymorph with heating. The exact mechanism of the transformation, that is, whether it occurs via melting and melt-recrystallization or within a solid–solid phase transition, has not yet been fully investigated. Important in the context of the discussion of the crystallization kinetics, the temperature ranges of formation of crystals and mesophases coincide with the high- and low-temperature crystallization-rate maxima in Fig. 1, respectively.

Detailed information on the crystal/mesophase polymorphism is available for iPP, with major findings summarized in several reviews [109–114]. It was found [112–114] that crystallization at low supercooling results in formation of monoclinic  $\alpha$ -crystals, in which left- and right-handed helices are arranged in layers to achieve high lateral packing density. Quenching in ice water followed by annealing at ambient temperature led to formation of the mesophase with a pseudohexagonal

symmetry and helix reversals as the main conformational defects. Quantitative thermal analysis of the specific heat capacity of semi-mesomorphic iPP revealed almost no increase beyond the level of the vibrational heat capacity of solid iPP, which suggests that the mesophase co-exists with rigid amorphous structure and only contains immobilized chain segments; therefore, it is termed conformationally disordered glass [115]. The mesophase is metastable and can only be annealed at temperatures lower than the stability limit of about 80°C [115, 116]. At higher temperatures, connected with the onset of helix mobility [117], the mesophase becomes unstable and converts to monoclinic  $\alpha$ -crystals with a latent heat of 7% of the heat of fusion of monoclinic crystals. It is worth noting that the mesophase–crystal phase transition at temperatures higher than 80°C can be suppressed by heating at rates faster than 30,000 K s<sup>-1</sup> to a temperature higher than the melting temperature of the  $\alpha$ -phase. Although it has been suggested that the mesophase–crystal phase transition occurs in the solid state, such a transition relies on slow heating, which allows fast local melting and immediate but slower recrystallization.

Fewer details are available regarding the mesophase/crystal polymorphism of polyamides, which is controlled by the crystallization temperature, as in the case of iPP. Although the structure (and thermodynamic properties) of crystals forming from the quiescent melt at low supercooling are known for PA 6, PA 66, and PA 11 [118–123], little information has been reported on the mesophases forming at low temperature. Melt-crystallization at low supercooling typically leads to formation of  $\alpha$ -crystals, in which a planar/sheet-like orientation of hydrogen bonding between the amide groups of neighboring chain segments is achieved after cooling to room temperature. In contrast, crystallization at high supercooling of the melt leads to formation of a pseudohexagonal mesophase in which the molecular stems exhibit rotational symmetry, leading to an arbitrary orientation of hydrogen bonds between neighboring chains [38, 124–127]. It is important to note that the pseudohexagonal mesophase forming at high supercooling is different from the high-temperature modification of the  $\alpha$ -form. Crystals formed from the melt at low supercooling show a Brill transition [128, 129]. At temperatures lower than the Brill transition temperature, depending on the particular polyamide, crystals exhibit monoclinic or triclinic symmetry. At higher temperatures, the anisotropy of lateral chain packing is lost, leading to the observation of a pseudohexagonal unit cell. Regarding the stability of the mesophase that forms at high supercooling of the melt, it is known that on heating it converts irreversibly into stable crystals [38, 130, 131], but the exact mechanism has not yet been investigated. In other words, it is unknown whether and under what conditions, with respect to heating rate or transformation temperature, the mesophase converts to crystals via melting and melt-recrystallization, or within a solid–solid phase transformation.

For iPP, PA 6, PA 66, and PA 11 it has been shown that the low-temperature crystallization-rate maximum in the curves of Fig. 1 is connected with both a tremendous increase in the nucleation rate/density and the growth of a different crystal polymorph. Unfortunately, for all these polymers, data on the growth rate of the low-temperature polymorph are not yet available, and therefore it cannot be excluded that the low-temperature crystallization-rate maximum in Fig. 1 is a result

of both an increase in the nucleation density and an increase in growth rate. This notwithstanding, it is also true for all these polymers that the mesophase is at best metastable at the temperature of its formation with respect to the crystal phase that forms from the melt at low supercooling. It must be assumed that formation of the mesophase at high supercooling is kinetically controlled, but the exact thermodynamics are unknown. The mesophase can be considered to represent an intermediate phase, with a local minimum of the free enthalpy along the path from the unstable melt to the stable crystal phase in accord with Ostwald's rule of stages [132], or even as a frozen-in. It can be speculated that, as a result of the extremely high nucleation density of perhaps one nucleus in a cube with a side length of 5–10 nm, the mobility of internuclei amorphous chain segments is reduced by mesophase formation at high supercooling. Thus, conformational defects are entrapped in the ordered phase without the possibility of their removal due to vitrification of the whole system, with the latter proven (e.g., for PCL) by observation of a distinct increase in  $T_g$  proportional to the crystalline content [42, 43].

Of the example polymers shown in Fig. 1 (employed for demonstration of the bimodal temperature dependence of the crystallization rate), PBT does not exhibit supercooling-controlled crystal/mesophase polymorphism as shown by iPP and polyamides. It has recently been demonstrated that the structures of crystals forming at temperatures associated with the low- and high-temperature crystallization-rate maxima in Fig. 1 are identical [41]. PBT can form two different crystal structures [133] and a mesophase [134], with the latter only being observed on stretching the amorphous phase. Crystallization of the quiescent melt leads to formation of triclinic  $\alpha$ -crystals, which are characterized by a non-extended chain conformation of the butylene unit between the planar phenylene rings. The  $\alpha$ -structure can reversibly transform into the  $\beta$ -structure under tension, with the butylene units then adopting an extended all-*trans* conformation, causing a slight change in the unit cell parameters with respect to those of the  $\alpha$ -phase. However, analysis of the X-ray structure of samples of different cooling/crystallization history led to the conclusion that observation of the two crystallization-rate maxima at different temperatures (as shown in Fig. 1) is not related to the formation of different crystal polymorphs of different growth rate [41, 135] but related to the large increase in nucleation density.

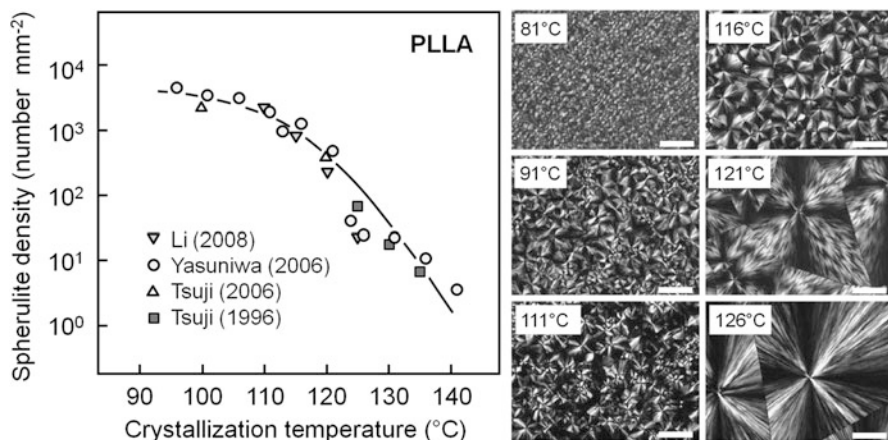
## 7 Crystallization of Poly(L-lactic acid) at High Supercooling: Application of Tammann's Nuclei Development Method to Obtain Nucleation Rates

A further example of a polymer showing a distinct crystal/mesophase polymorphism controlled by the crystallization temperature is poly(L-lactic acid) (PLLA). The crystallization behavior of PLLA is discussed separately because there has not yet been proven a change in the nucleation mechanism with variation in



temperature. Instead, there is evidence that the nucleation kinetics is decoupled from the kinetics of crystal growth and the formation of different crystal polymorphs. PLLA forms different ordered structures as a function of the conditions of crystallization [136, 137]. Crystallization of the quiescent melt at temperatures higher than about 110°C leads to formation of  $\alpha$ -crystals with two antiparallel aligned helical chain segments packed in an orthorhombic unit cell [138–140]. Formation of  $\alpha$ -crystals is replaced by formation of pseudo-hexagonal  $\alpha'$ -crystals at temperatures lower than about 110°C. The  $\alpha'$ -form is considered to be a conformationally disordered  $\alpha$ -crystal with slightly increased lattice spacings. It irreversibly transforms upon heating into the stable  $\alpha$ -form [141–145], either within a solid–solid state transformation [143–145] or via melting followed by melt-recrystallization [146, 147].

Typically, the density of primary crystal nuclei forming in a supercooled melt is assessed by hot-stage microscopy. This allows counting the number of spherulites per unit volume at a given analysis temperature, either after complete crystallization or during the isothermal crystallization process. In the latter case, information about the kinetics of nuclei formation can also be obtained. As a general rule, for a given nucleation scheme (i.e., both homogeneous nucleation or nucleation on a substrate/impurity), the nucleation density increases with decreasing temperature as a result of the decreasing work required to produce a critical-sized nucleus from the melt. Using optical microscopy, it can be observed that the number of spherulites increases and their size decreases. An example of such analysis is presented in Fig. 9 (right), which shows POM micrographs obtained for PLLA, isothermally crystallized at different temperatures between 126°C and 81°C. As expected, with decreasing crystallization temperature, the number of spherulites (i.e., the number



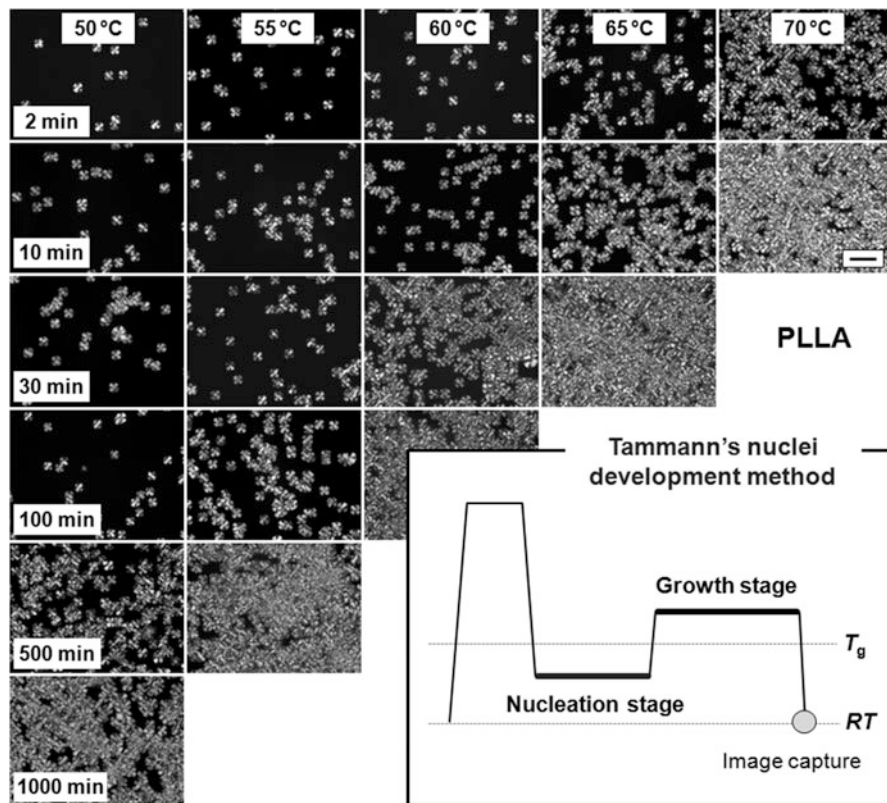
**Fig. 9** Right: POM images of PLLA isothermally crystallized at different temperatures between 81°C and 126°C [148]. Left: Spherulite density of PLLA as a function of crystallization temperature [136]. Scale bars: 50  $\mu\text{m}$ . The POM images were adapted from [148], Copyright (2013), with permission from Elsevier. The graph on the left was adapted from [136], Copyright (2013), with permission from Elsevier

of nucleation sites) increases, leading to a reduction in spherulite size. Quantitative information about the temperature-dependence of the nucleation density is given in the graph shown in Fig. 9 (left), which indicates the spherulite number of PLLA per square millimeter as a function of the crystallization temperature [136, 148–151]. The data suggest increasing nucleation density with decreasing temperature in the analyzed temperature range between 95°C and 140°C, reaching a plateau value at around 90°C. At temperatures lower than 95°C, which is 30–40 K above  $T_g$ , such analysis of the nucleation density via measurement of the spherulite density fails because their number then is too high to be reliably analyzed.

To obtain data on the nucleation kinetics/density at higher supercooling of the melt, specifically designed nucleation experiments can be performed, as described by Tammann over a century ago [152]. Tammann's two-stage crystal nuclei development method implies formation of nuclei at large supercooling and follows their isothermal growth at higher temperatures, utilizing the often widely different temperatures of maximum rate of primary crystal nucleation and crystal growth. In other words, this method allows detection of nuclei that were formed at low temperature by growing them at a higher temperature to experimentally detectable sizes. In the specific case of PLLA, such experiments have been performed using both POM and FSC [87, 88].

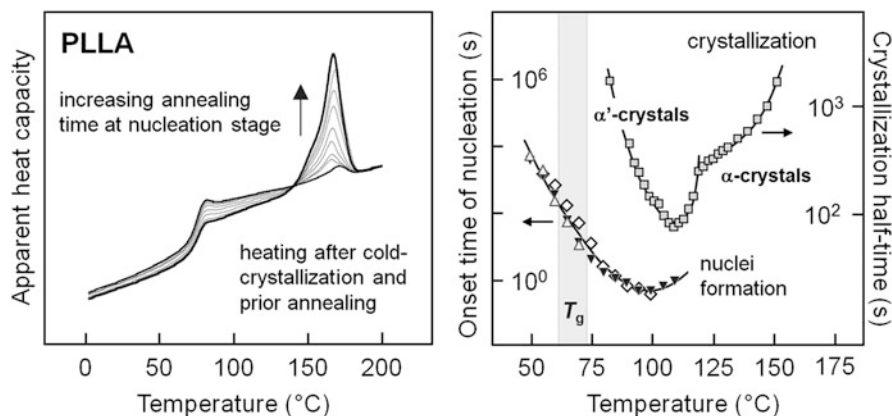
For demonstration, Fig. 10 shows POM images of initially amorphous samples of PLLA, annealed for different times between 2 and 1,000 min at temperatures between 50°C and 70°C (i.e., slightly below  $T_g$ ) and then cold-crystallized at an elevated temperature of 120°C for 10 min. The temperature–time profile is also shown in Fig. 10. Annealing at 50°C for less than 100 min is not connected with nuclei formation, as concluded from the constant low number of spherulites growing at 120°C. However, if the annealing time exceeds 100 min then there is an increase in spherulite density as a result of formation of additional nuclei at 50°C. With increasing annealing temperature, an increased spherulite number is observed on annealing for a shorter time, ultimately providing information about the temperature dependence of the nucleation rate.

It is worth noting that application of Tammann's two-stage crystal nuclei development method is not restricted to analysis of the nucleation rate at temperatures below  $T_g$ . Rather, it is required that the growth of nuclei in the nucleation stage is either completely absent or at least distinctly slower than the nucleation rate. This is particularly true at temperatures below  $T_g$ , although it has been shown that crystal growth can also be observed under such conditions [42, 43, 86, 90]. However, for the specific case of PLLA, Tammann's two-stage crystal nuclei development method has also been applied for the temperature range between  $T_g$  and 110°C (using FSC) in order to complete the analysis of the nucleation behavior presented in Fig. 9. Figure 11 (left) shows FSC heating curves recorded using a rate of 200 K s<sup>-1</sup>, which is sufficiently fast to suppress cold-crystallization of PLLA on heating. The set of curves was obtained for initially fully amorphous samples, which were annealed at 70°C for different times between 0 and 10,000 s, to allow nuclei formation, and then heated to 120°C to allow growth of nuclei for 300 s. Afterwards, the samples were rapidly cooled to -60°C and heated to 200°C to gain



**Fig. 10** POM images of initially amorphous PLLA, annealed in the glassy state at different temperatures for different times (as indicated), and then cold-crystallized at 120°C for 10 min [87]. Scale bar: 100  $\mu\text{m}$ . Also shown is the time–temperature profile for Tammann's nuclei development method. Adapted with permission from [87], Copyright (2013) American Chemical Society

information about the crystal fraction formed in the growth stage. It can be seen that, with increasing annealing time in the nucleation stage, the area of the endothermic peak increases, indicating an increase in the crystal fraction during the 300 s growth step. Analysis of the peak area or enthalpy of melting as a function of the time of annealing in the nucleation stage provides information about the nucleation kinetics, quantified, for example, as the onset-time of nuclei formation (shown in Fig. 11, right). The data reveal that the rate of nuclei formation is fastest at about 95°C, which is in agreement with studies of the temperature dependence of nucleation density (shown in Fig. 9). In extension of earlier work on the nucleation density of PLLA (performed by microscopy), it was not only shown that on lowering the temperature to values below 95°C the nucleation rate decreases progressively in the investigated temperature range, but also that the temperature dependence of the nucleation rate in the high-supercooling temperature range does

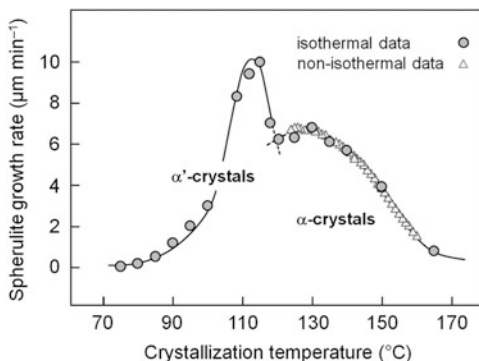


**Fig. 11** *Left*: Apparent heat capacity of PLLA as a function of temperature, obtained on heating at  $200 \text{ K s}^{-1}$  after prior annealing in the nucleation stage at  $70^\circ\text{C}$  for different times between 0 and 10,000 s, followed by cold-crystallization in the growth stage at  $120^\circ\text{C}$  for 300 s. *Right*: The diamonds and triangles indicate the onset time of crystal nucleation, obtained by plotting the enthalpy of melting determined from the FSC curves in the left plot as a function of the annealing time in the nucleation stage. For comparison, the squares show half-times of crystallization of PLLA as a function of temperature, as obtained from the literature [153]. Adapted from [88], Copyright (2013), with permission from Elsevier

not seem to be affected by the glass transition. The data shown in Fig. 11 also reveal, by extrapolation, that annealing glassy PLLA at ambient temperature, (i.e., about 30 K below  $T_g$ ) leads to formation of crystal nuclei after  $10^7$ – $10^8$  s. Note that this observation might be of importance from an application point of view because such ordering is perhaps connected with changes in the mechanical behavior, at least if nucleation is followed by growth.

Figure 11 (right) shows that the gross crystallization rate is about three orders of magnitude slower than the nucleation rate at the same temperature. The crystallization half-time data were adapted from the literature [153], and are scaled with the right axis to emphasize the occurrence of two qualitatively different crystallization processes, with the crossover observed at around  $120^\circ\text{C}$ . Crystallization at temperatures higher than about  $120^\circ\text{C}$  is connected with formation of  $\alpha$ -crystals, whereas at lower temperatures conformationally disordered  $\alpha'$ -crystals form. Inspection of the gross crystallization rate (Fig. 11, right) indicates that the maximum crystallization rate of  $\alpha'$ -crystals is almost one order of magnitude higher than that of  $\alpha$ -crystals. However, the data in Fig. 9 prove that the  $\alpha/\alpha'$  polymorphism is not connected with a change in the mechanism of crystal nucleation. Rather, it has been shown in numerous studies that the rates of growth of  $\alpha'$ - and  $\alpha$ -crystals are very different [153–155]. The growth rate of the different crystal polymorphs has been measured by analysis of spherulite growth rates using hot-stage microscopy, and a typical finding reported in the literature is presented in Fig. 12. The data suggest that the temperature of maximum growth rate of  $\alpha$ -crystals/spherulites is about

**Fig. 12** Spherulite growth rate for PLLA as a function of the crystallization temperature. Adapted from [155], Copyright (2005), with permission from Elsevier



130°C, whereas that of  $\alpha'$ -crystals/spherulites is at 110–115°C, with the maximum growth rate of the latter being almost twice that of  $\alpha$ -crystals/spherulites.

Regarding nucleation of the crystallization process of PLLA at high supercooling of the melt, there exist a few further independent studies [156–159]. In particular, it has been shown that cold-crystallization is faster than melt-crystallization at identical temperatures, with the observed results being explained by formation of additional crystal nuclei on the thermal pathway to the crystallization temperature. Parameters in such nucleation experiments were the rate of cooling to, and the residence time at, various minimum temperatures before heating of the sample to the cold-crystallization temperature. In a further work [159], melt-quenched PLLA was aged below  $T_g$ , and changes in the structure of the initially fully amorphous specimen were monitored in situ by time-resolved infrared spectroscopy. The data provided evidence for local ordering and the formation of a mesophase. It has been suggested that the formed mesophase becomes disordered in conjunction with the physical aging peak at the glass transition temperature, while simultaneously enhancing cold-crystallization on continuation of heating. The discussed reports [156–159] all prove that nuclei/locally ordered structures develop at low temperatures and that these structures increase the crystallization kinetics at elevated temperatures.

## 8 Summary

Analysis of the temperature-dependence of the gross crystallization rate of a large number of polymers, including PCL, iPP, PA 6, PA 66, PA 11, and PBT, has revealed qualitatively different crystallization behaviors at temperatures below and above about  $(T_g + 30)$  K. In several cases, two distinct crystallization-rate maxima are observed at low and high supercooling. Possible reasons for this observation could be a change in the mechanism of primary crystal nucleation, in the forming crystal structure/polymorph, or of the crystal morphology/growth face in response to variation of the supercooling, all of which are discussed in this review.

Recent research supports the notion that the low-temperature crystallization-rate maximum is caused by a drastic increase in the number of primary crystal nuclei. For iPP, PA 6, PA 11, and PBT it has been shown that crystallization at low supercooling proceeds via spherulitic growth of lamellae, whereas at high supercooling the formation of lamellae and spherulites is often not observed. Instead, there is formation of small ordered domains or crystals, which do not form a higher-order superstructure, indicating their independent growth. A rough estimation of the nucleation density on crystallization at low and high supercooling gave values of  $10^6$  and  $10^{15}$  nuclei  $\text{mm}^{-3}$ , respectively, with the increase occurring in a relatively narrow temperature interval. Although the exact mechanism of nucleation is not known for either of these temperature ranges, it is speculated that crystallization at low and high supercooling is related to heterogeneous and homogeneous nucleation, respectively. Heterogeneous nucleation is assumed for the low supercooling temperature range, because purposely added nucleation agents are active in just this temperature range [160, 161], increasing the crystallization rate only at those temperatures. In contrast, the low-temperature crystallization-rate maximum is not affected by the addition of heterogeneous nuclei, suggesting that it is related to formation of homogeneous nuclei.

A homogeneous nucleation mechanism for crystallization at high supercooling is supported by analysis of the crystallization behavior of heterogeneity-free droplets. In such cases, crystallization at low supercooling is not detected but only occurs in exactly the same temperature range for which the low-temperature crystallization-rate maximum is observed in samples containing heterogeneous nucleators. Moreover, the density of primary crystal nuclei in such heterogeneity-free droplets and in bulk samples containing impurities when crystallized at high supercooling is seemingly identical. Further evidence favoring homogeneous nucleation at high supercooling is provided by establishment of a link between the time scales of the densification/relaxation of the glass and the formation of nuclei. It has been shown that nuclei are able to form only after completion of the relaxation of the glass by cooperative rearrangement of molecular segments on a length scale of a few nanometers. Nuclei formation is then assumed to occur without cooperative displacement of segments, but only with local changes of conformations.

Final conclusions cannot be drawn about the effect of crystal/mesophase polymorphism on the gross crystallization rate and its bimodal temperature-dependence in the cases of iPP, PA 6, PA 66, and PA 11, because the growth rates for mesophase formation at high supercooling are unknown. It might be possible that the low-temperature crystallization-rate maximum is also caused by an increased growth rate, which, however, does not contradict the above conclusions about the effect of a change in the nucleation mechanism.

In contrast to iPP, PA 6, PA 66, and PA 11, which show a distinct supercooling-controlled crystal/mesophase polymorphism that is paralleled by observation of a large difference in nucleation densities, the  $\alpha/\alpha'$ -crystal polymorphism of PLLA seems completely decoupled from the primary crystal-nucleation step, including its kinetics. For PLLA, crystal growth rates have also been measured at high

supercooling, suggesting that formation of the low-temperature  $\alpha'$ -phase has a higher growth rate than the high-temperature  $\alpha$ -crystal polymorph. The transition of formation of  $\alpha$ -crystals at low supercooling to formation of  $\alpha'$ -crystals at high supercooling, occurring around 110°C, however, is not connected with a drastic increase in the nucleation density.

For PBT, in contrast, it has been proven that crystallization at low and high supercooling leads to formation of the same crystal polymorph. For PCL, information on the formation of different crystal polymorphs during crystallization at different supercooling is not yet available.

## References

1. Hoffmann JD, Davis GT, Lauritzen JI Jr (1976) The rate of crystallization of linear polymers with chain folding. In: Hannay HB (ed) Treatise on solid state chemistry, crystalline and noncrystalline solids, vol 3. Plenum, New York
2. Wunderlich B (1976) Crystal nucleation, growth, annealing, vol 2, Macromolecular physics. Academic, New York
3. Becker R (1938) Die Keimbildung bei der Ausscheidung von metallischen Mischkristallen. *Ann Phys* 32:128–140
4. Turnbull D, Fisher JC (1949) Rate of nucleation in condensed systems. *J Chem Phys* 17:71–73
5. Turnbull D (1950) Kinetics of heterogeneous nucleation. *J Chem Phys* 18:198–203
6. Binsbergen FL (1977) Natural and artificial heterogeneous nucleation in polymer crystallization. *J Polym Sci Polym Symp* 59:11–27
7. Hoffman JD, Lauritzen JI Jr (1961) Crystallization of bulk polymers with chain folding: theory of growth of lamellar spherulites. *J Res Natl Bur Stand* 65A:297–336
8. Hoffman JD (1964) Theoretical aspects of polymer crystallization with chain folds: bulk polymers. *SPE Trans* 4:315–362
9. Lauritzen JI Jr, Hoffman JD (1973) Extension of theory of growth of chain-folded polymer crystals to large undercoolings. *J Appl Phys* 44:297–336
10. Wunderlich B, Mehta A (1974) Macromolecular nucleation. *J Polym Sci Polym Phys* 12:255–263
11. Strobl G (2000) From the melt via mesomorphic and granular crystalline layers to lamellar crystallites: a major route followed in polymer crystallization? *Eur Phys J E3*:165–183
12. Strobl G (2005) A thermodynamic multiphase scheme treating polymer crystallization and melting. *Eur Phys J E18*:295–309
13. Strobl G (2006) Crystallization and melting of bulk polymers: new observations, conclusions and a thermodynamic scheme. *Prog Polym Sci* 31:398–442
14. Long Y, Shanks RA, Stachurski ZH (1995) Kinetics of polymer crystallization. *Prog Polym Sci* 20:651–701
15. Booth A, Hay JN (1969) The use of differential scanning calorimetry to study polymer crystallization kinetics. *Polymer* 10:95–104
16. Chan TW, Isayev AI (1994) Quiescent polymer crystallization: modeling and measurements. *Polym Eng Sci* 34:461–471
17. Lorenzo AT, Arnal ML, Albuerno J, Müller AJ (2007) DSC isothermal polymer crystallization kinetics measurements and the use of the Avrami equation to fit the data: guidelines to avoid common problems. *Polym Test* 26:222–231
18. Avrami M (1939) Kinetics of phase change. I General theory. *J Chem Phys* 7:1103–1112

19. Avrami M (1940) Kinetics of phase change. II Transformation-time relations for random distribution of nuclei. *J Chem Phys* 8:212–224
20. Avrami M (1941) Granulation, phase change, and microstructure kinetics of phase change III. *J Chem Phys* 9:177–183
21. Vyazovkin S, Sbirrazzuoli N (2004) Isoconversional approach to evaluating the Hoffman–Lauritzen parameters ( $U^*$  and  $K_g$ ) from the overall rates of nonisothermal crystallization. *Macromol Rapid Commun* 25:733–738
22. Adamovsky SA, Minakov AA, Schick C (2003) Scanning microcalorimetry at high cooling rate. *Thermochim Acta* 403:55–63
23. Adamovsky S, Schick C (2004) Ultra-fast isothermal calorimetry using thin film sensors. *Thermochim Acta* 415:1–7
24. Minakov AA, Adamovsky SA, Schick C (2005) Non adiabatic thin-film (chip) nanocalorimetry. *Thermochim Acta* 432:177–185
25. Wunderlich B (2005) Thermal analysis of polymeric materials. Springer, Berlin
26. Pijpers TFI, Mathot VBF, Goderis B, Scherrenberg RL, van der Vegte EW (2002) High-speed calorimetry for the study of the kinetics of (de)vitrification, crystallization, and melting of macromolecules. *Macromolecules* 35:3601–3613
27. Kolesov IS, Androsch R, Radosch HJ (2004) Non-isothermal crystallization of polyethylenes as function of cooling rate and concentration of short chain branching. *J Therm Anal Calorim* 78:885–895
28. Ding Z, Spruiell JE (1996) An experimental method for studying nonisothermal crystallization of polymers at very high cooling rates. *J Polym Sci Polym Phys* 34:2783–2804
29. Boyer SAE, Haudin JM (2010) Crystallization of polymers at constant and high cooling rates: a new hot-stage microscopy set-up. *Polym Test* 29:445–452
30. Mårtson T, Ots A, Krumme A, Lohmus A (2010) Development of a faster hot-stage for microscopy studies of polymer crystallization. *Polym Test* 29:127–131
31. Kamal MR, Chu E (1983) Isothermal and non-isothermal crystallization of polyethylene. *Polym Eng Sci* 23:27–31
32. van Herwaarden S, Iervolino E, van Herwaarden F, Wijffels T, Leenaers A, Mathot V (2011) Design, performance and analysis of thermal lag of the UFS1 twin-calorimeter chip for fast scanning calorimetry using the Mettler-Toledo Flash DSC 1. *Thermochim Acta* 522:46–52
33. Minakov AA, Schick C (2007) Ultrafast thermal processing and nanocalorimetry at heating and cooling rates up to 1 MK/s. *Rev Sci Instrum* 78:073902
34. De Santis S, Adamovsky S, Titomanlio G, Schick C (2007) Isothermal nanocalorimetry of isotactic polypropylene. *Macromolecules* 40:9026–9031
35. Silvestre C, Cimmino S, Duraccio D, Schick C (2007) Isothermal crystallization of isotactic poly(propylene) studied by superfast calorimetry. *Macromol Rapid Commun* 28:875–881
36. van Drongelen M, Meijer-Vissers T, Cavallo D, Portale G, Vanden Poel G, Androsch R (2013) Microfocus wide-angle X-ray scattering of polymers crystallized in a fast scanning chip calorimeter. *Thermochim Acta* 563:33–37
37. Rhoades AM, Williams JL, Androsch R (2015) Crystallization of polyamide 66 at processing-relevant cooling conditions and at high supercooling. *Thermochim Acta* 603:103–109
38. Mollova A, Androsch R, Mileva D, Schick C, Benhamida A (2013) Effect of supercooling on crystallization of polyamide 11. *Macromolecules* 46:828–835
39. Pyda M, Nowak-Pyda E, Heeg J, Huth H, Minakov AA, Di Lorenzo ML et al (2006) Melting and crystallization of poly(butylene terephthalate) by temperature-modulated and superfast calorimetry. *J Polym Sci Polym Phys* 44:1364–1377
40. Schawe JEK (2014) Influence of processing conditions on polymer crystallization measured by fast scanning DSC. *J Therm Anal Calorim* 116:1165–1173
41. Androsch R, Rhoades AM, Stolte I, Schick C (2015) Density of heterogeneous and homogeneous crystal nuclei in poly(butylene terephthalate). *Eur Polym J* 66:180–189



42. Zhuravlev E, Schmelzer JWP, Wunderlich B, Schick C (2011) Kinetics of nucleation and crystallization in poly( $\epsilon$ -caprolactone). *Polymer* 52:1983–1997
43. Wurm A, Zhuravlev E, Eckstein K, Jehnichen D, Pospiech D, Androsch R, Wunderlich B, Schick C (2012) Crystallization and homogeneous nucleation kinetics of poly( $\epsilon$ -caprolactone) (PCL) with different molar masses. *Macromolecules* 45:3816–3828
44. Mileva D, Androsch R (2012) Effect of co-unit type in random propylene copolymers on the kinetics of mesophase formation and crystallization. *Colloid Polym Sci* 290:465–471
45. Cavallo D, Gardella L, Alfonso GC, Mileva D, Androsch R (2012) Effect of comonomer partitioning on the kinetics of mesophase formation in random copolymers of propene and higher  $\alpha$ -olefins. *Polymer* 53:4429–4437
46. Supaphol P, Spruiell JE (2001) Isothermal melt- and cold-crystallization kinetics and subsequent melting behavior in syndiotactic polypropylene: a differential scanning calorimetry study. *Polymer* 42:699–712
47. Stolte I, Androsch R, Di Lorenzo ML, Schick C (2013) Effect of aging the glass of isotactic polybutene-1 on Form II nucleation and cold-crystallization. *J Phys Chem B* 117:15196–15203
48. Keller A (1955) The spherulitic structure of crystalline polymers. Part I. Investigations with the polarizing microscope. *J Polym Sci* 17:291–308
49. Keller A (1955) The spherulitic structure of crystalline polymers. Part II. The problem of molecular orientation in polymer spherulites. *J Polym Sci* 17:351–364
50. Keller A, Waring JRS (1955) The spherulitic structure of crystalline polymers. Part III. Geometrical factors in spherulitic growth and the fine-structure. *J Polym Sci* 17:447–472
51. Magill JH (2001) Review spherulites: a personal perspective. *J Mater Sci* 36:3143–3164
52. Roche EJ, Stein RS, Thomas EL (1980) Electron microscopy study of the structure of normal and abnormal poly(butylene terephthalate) spherulites. *J Polym Sci Polym Phys* 18:1145–1158
53. Stein RS, Misra A (1980) Morphological studies on poly(butylene terephthalate). *J Polym Sci Polym Phys* 18:327–342
54. Piccarolo S (1992) Morphological changes in isotactic polypropylene as a function of cooling rate. *J Macromol Sci Phys B* 31:501–511
55. Zia Q, Androsch R, Radusch HJ, Piccarolo S (2006) Morphology, reorganization, and stability of mesomorphic nanocrystals in isotactic polypropylene. *Polymer* 47:8163–8172
56. Zia Q, Androsch R, Radusch HJ (2010) Effect of structure at the micrometer and nanometer length scales on the light transmission of isotactic polypropylene. *J Appl Polym Sci* 117:1013–1020
57. Mileva D, Zia Q, Androsch R, Radusch HJ, Piccarolo S (2009) Mesophase formation in poly(propylene-ran-1-butene) by rapid cooling. *Polymer* 50:5482–5489
58. Mileva D, Androsch R, Radusch HJ (2009) Effect of structure on light transmission in isotactic polypropylene and random propylene-1-butene copolymers. *Polym Bull* 62:561–571
59. Mileva D, Kolesov I, Androsch R (2012) Morphology of cold-ordered polyamide 6. *Colloid Polym Sci* 290:971–978
60. Mileva D, Androsch R, Zhuravlev E, Schick C (2012) Morphology of mesophase and crystals of polyamide 6 prepared in a fast scanning chip calorimeter. *Polymer* 53:3994–4001
61. Wunderlich B (1973) Crystal structure, morphology defects, vol 1, *Macromolecular physics*. Academic, New York
62. Gezovich DM, Geil PH (1968) Morphology of quenched polypropylene. *Polym Eng Sci* 8:202–209
63. Hsu CC, Geil PH, Miyaji H, Asai K (1983) Structure and properties of polybutylene crystallized from the glassy state. II. Electron microscopy. *J Macromol Sci Phys B* 22:489–496
64. Yeh GSY, Geil PH (1967) Crystallization of polyethylene terephthalate from the glassy state. *J Macromol Sci Phys B* 1:235–249

65. Meyer M, Van der Sande J, Uhlmann DR (1978) On the structure of glassy polymers. VI. Electron microscopy of polycarbonate, poly(ethylene terephthalate), poly(vinyl chloride), and polystyrene. *J Polym Sci Polym Phys* 16:2005–2014
66. Kanig G (1983) Application of the short-time staining for the electron microscopic investigation of the crystallization of polyethylene. *Colloid Polym Sci* 261:373–374
67. Caldas V, Brown GR, Nohr RS, MacDonald JG, Raboin LE (1994) The structure of the mesomorphic phase of quenched isotactic polypropylene. *Polymer* 35:899–907
68. Ogawa T, Miyaji M, Asai K (1985) Nodular structure of polypropylene. *J Phys Soc Jpn* 54:3668–3670
69. Wang ZG, Hsiao BS, Srinivas S, Brown GM, Tsou AH, Cheng SZD et al (2001) Phase transformation in quenched mesomorphic isotactic polypropylene. *Polymer* 42:7561–7566
70. Grubb DT, Yoon DY (1986) Morphology of quenched and annealed isotactic polypropylene. *Polym Commun* 27:84–88
71. Zia Q, Androsch R, Radusch HJ, Ingolič E (2008) Crystal morphology of rapidly cooled isotactic polypropylene: a comparative study by TEM and AFM. *Polym Bull* 60:791–798
72. Miyamoto Y, Fukao K, Yoshida T, Tsurutani N, Miyaji H (2000) Structure formation of isotactic polypropylene from the glass. *J Phys Soc Jpn* 69:1735–1740
73. Manabe N, Yokota Y, Minami H, Uegomori Y, Komoto T (2002) A TEM study on melt-crystallized poly(butylene terephthalate). *J Electron Microsc* 51:11–19
74. Schaper A, Hirte R, Ruscher C, Hillebrand R, Walenta E (1986) The electron microscope characterization of the fine structure of nylon 6: I. The supermolecular structure in melt-cast, isotropic bulk material. *Colloid Polym Sci* 264:649–658
75. Cormia RL, Price FP, Turnbull D (1962) Kinetics of crystal nucleation in polyethylene. *J Chem Phys* 37:1333–1340
76. Cormia RL, Turnbull D (1961) Kinetics of crystal nucleation in some normal alkane liquids. *J Chem Phys* 34:820–827
77. Burns JR, Turnbull D (1966) Kinetics of crystal nucleation in molten isotactic polypropylene. *J Appl Phys* 37:4021–4026
78. Koutsky JA, Walton AG, Baer E (1967) Nucleation of polymer droplets. *J Appl Phys* 38:1832–1839
79. Gornick F, Ross GS, Frolen LJ (1967) Crystal nucleation in polyethylene: the droplet experiment. *J Polym Sci Polym Symp* 18:79–91
80. Langhe DS, Hiltner A, Baer E (2011) Transformation of isotactic polypropylene droplets from the mesophase into the  $\alpha$ -Phase. *J Polym Sci Polym Phys* 49:1672–1682
81. Jin Y, Hiltner A, Baer E, Masirek R, Piorkowska E, Galeski A (2006) Formation and transformation of smectic polypropylene nanodroplets. *J Polym Sci Polym Phys* 44:1795–1803
82. Ibarretxe J, Groeninckx G, Bremer L, Mathot VBF (2009) Quantitative evaluation of fractionated and homogeneous nucleation of polydisperse distributions of water-dispersed maleic anhydride-grafted-polypropylene micro- and nano-sized droplets. *Polymer* 50:4584–4595
83. Salmerón Sánchez M, Mathot V, Vanden Poel G, Groeninckx G, Bruls W (2006) Crystallization of polyamide confined in sub-micrometer droplets dispersed in a molten polyethylene matrix. *J Polym Sci Polym Phys* 44:815–825
84. Mileva D, Androsch R, Cavallo D, Alfonso GC (2012) Structure formation of random isotactic copolymers of propylene and 1-hexene or 1-octene at rapid cooling. *Eur Polym J* 48:1082–1092
85. Zia Q, Androsch R (2009) Effect of atomic force microscope tip geometry on the evaluation of the crystal size of semicrystalline polymers. *Meas Sci Technol* 20:097003 (4pp)
86. Mileva D, Androsch R, Zhuravlev E, Schick C, Wunderlich B (2012) Homogeneous nucleation and mesophase formation in glassy isotactic polypropylene. *Polymer* 53:277–282
87. Androsch R, Di Lorenzo ML (2013) Crystal nucleation in glassy poly(L-lactic acid). *Macromolecules* 46:6048–6056

88. Androsch R, Di Lorenzo ML (2013) Kinetics of crystal nucleation of poly(L-lactic acid). *Polymer* 54:6882–6885
89. Illers KH (1971) Geordnete Strukturen in “amorphem” Polyäthylenterephthalat. *Kolloid Z Z Polym* 245:393–398
90. Androsch R, Schick C, Schmelzer JWP (2014) Sequence of enthalpy relaxation, homogeneous crystal nucleation and crystal growth in glassy polyamide 6. *Eur Polym J* 53:100–108
91. Hodge IM (1994) Enthalpy relaxation and recovery in amorphous materials. *J Non-Cryst Solids* 169:211–266
92. Moynihan CT, Eastale AJ, De Bolt MA, Tucker J (1976) Dependence of the fictive temperature of glass on cooling rate. *J Am Ceram Soc* 59:12–16
93. Moynihan CT, Eastale AJ, Wilder J, Tucker J (1974) Dependence of the glass transition temperature on heating and cooling rate. *J Phys Chem* 78:2673–2677
94. Wunderlich B (2003) Reversible crystallization and the rigid–amorphous phase in semicrystalline macromolecules. *Prog Polym Sci* 28:383–450
95. Schick C, Krämer L, Mischok W (1985) Der Einfluß struktureller Veränderungen auf den Glasübergang in teilkristallinem Polyethylenterephthalat I. Isotherme Kristallisation. *Acta Polym* 36:47–53
96. Schick C, Fabry F, Schnell U, Stoll G, Deutschbein L, Mischok W (1988) Der Einfluß struktureller Veränderungen auf den Glasübergang in teilkristallinem Poly(ethylenterephthalat) 2. Charakterisierung der übermolekularen Struktur. *Acta Polym* 39:705–710
97. Schick C, Wigger J, Mischok W (1990) Der Einfluß struktureller Veränderungen auf den Glasübergang in teilkristallinem Poly(ethylenterephthalat) 3. Der Glasübergang in den zwischenlamellaren Bereichen. *Acta Polym* 41:137–142
98. Androsch R, Wunderlich B (2005) The link between rigid amorphous fraction and crystal perfection in cold-crystallized poly(ethylene terephthalate). *Polymer* 46:12556–12566
99. Zia Q, Mileva D, Androsch R (2008) The rigid amorphous fraction in isotactic polypropylene. *Macromolecules* 41:8095–8102
100. Kolesov I, Androsch R (2012) The rigid amorphous fraction of cold-crystallized polyamide 6. *Polymer* 53:4070–4077
101. 12th Laehnwitz Seminar on Calorimetry: Interplay between nucleation, crystallization, and the glass transition, 10–15 June 2012, Rostock, Germany.
102. Michell RM, Blaszczyk-Lezak I, Mijangos C, Müller AJ (2013) Confinement effects on polymer crystallization: from droplets to alumina nanopores. *Polymer* 54:4059–4077
103. Carvalho JL, Dalnoki-Veress K (2010) Homogeneous bulk, surface, and edge nucleation in crystalline nanodroplets. *Phys Rev Lett* 105:237801
104. Hayes NW, Beamson G, Clark DT, Law DSL, Raval R (1996) Crystallization of PET from the amorphous state: observation of different rates for surface and bulk using XPS and FTIR. *Surf Interface Anal* 24:723–728
105. De Cupere VM, Rouxhet PG (2002) Surface crystallization of poly(ethylene terephthalate) studied by atomic force microscopy. *Polymer* 43:5571–5576
106. Jukes PC, Das A, Durell M, Trolley D, Higgins AM, Geoghegan M, MacDonald JE, Jones RAL, Brown S, Thompson P (2005) Kinetics of surface crystallization in thin films of poly(ethylene terephthalate). *Macromolecules* 38:2315–2320
107. Durell M, MacDonald JE, Trolley D, Wehrum A, Jukes PC, Jones RAL, Walker CJ, Brown S (2002) The role of surface-induced ordering in the crystallization of PET films. *Europhys Lett* 58:844–850
108. Zia Q, Ingolič E, Androsch R (2010) Surface and bulk morphology of cold-crystallized poly(ethylene terephthalate). *Colloid Polym Sci* 288:819–825
109. Wunderlich B, Grebowicz J (1984) Thermotropic mesophases and mesophase transitions of linear, flexible macromolecules. *Adv Polym Sci* 60(61):1–59
110. Auriemma F, De Rosa C, Corradini P (2005) Solid mesophases in semicrystalline polymers: structural analysis by diffraction techniques. *Adv Polym Sci* 181:1–74

111. Androsch R, Di Lorenzo ML, Schick C, Wunderlich B (2010) Mesophases in polyethylene, polypropylene, and poly(1-butene). *Polymer* 51:4639–4662
112. Natta G, Peraldo M, Corradini P (1959) Smectic mesomorphic form of isotactic polypropylene. *Rend Accad Naz Lincei* 26:14–17
113. Natta G, Corradini P (1960) Structure and properties of isotactic polypropylene. *Nuovo Cimento* 15(Suppl):40–51
114. Natta G (1960) Progress in the stereospecific polymerization. *Makromol Chem* 35:94–131
115. Grebowicz J, Lau SF, Wunderlich B (1984) The thermal properties of polypropylene. *J Polym Sci Polym Symp* 71:19–37
116. Mileva D, Androsch R, Zhuravlev E, Schick C (2009) The temperature of melting of the mesophase of isotactic polypropylene. *Macromolecules* 42:7275–7278
117. Schaefer D, Spiess HW, Suter UW, Fleming WW (1990) Two-dimensional solid-state NMR studies of ultraslow chain motion: glass transition in atactic poly(propylene) versus helical jumps in isotactic poly(propylene). *Macromolecules* 23:3431–3439
118. Bunn CW, Garner EV (1947) The crystal structures of two polyamides ('nylons'). *Proc R Soc Lond A Math Phys Sci* 18:39–68
119. Aelion R (1948) Preparation and structure of some new types of polyamides. *Ann Chim Appl* 3:5–61
120. Slichter WP (1959) Crystal structures in polyamides made from  $\omega$ -amino acids. *J Polym Sci* 36:259–266
121. Little K (1959) Investigation of Nylon "texture" by X-ray diffraction. *Br J Appl Phys* 10:225–230
122. Advanced Thermal Analysis System (ATHAS) Data Base. Implemented into Springer-Materials, available at [materials.springer.com](http://materials.springer.com)
123. Wunderlich B (2008) Thermal properties of aliphatic Nylons and their link to crystal structure and molecular motion. *J Therm Anal Calorim* 93:7–17
124. Schmidt GF, Stuart HA (1958) Gitterstrukturen mit räumlichen Wasserstoffbrückensystemen und Gitterumwandlungen bei Polyamiden. *Z Naturforsch A* 13:222–225
125. Ziabicki A (1959) Über die mesomorphe  $\beta$ -Form von Polycapronamid und ihre Umwandlung in die kristalline Form  $\alpha$ . *Kolloid Z* 167:132–141
126. Cavallo D, Gardella L, Alfonso GC, Portale G, Balzano L, Androsch R (2011) Effect of cooling rate on the crystal/mesophase polymorphism of polyamide 6. *Colloid Polym Sci* 289:1073–1079
127. Haberkorn H, Illers KH, Simak P (1979) Molekülordnung und Kristallinität in Polyhexamethylenadipamid. *Colloid Polym Sci* 257:820–840
128. Brill R (1942) Über das Verhalten von Polyamiden beim Erhitzen. *J Prakt Chem* 161:49–64
129. Brill R (1956) Beziehungen zwischen Wasserstoffbindung und einigen Eigenschaften von Polyamiden. *Makromol Chem* 18:294–309
130. Androsch R, Stolp M, Radusch HJ (1996) Crystallization of amorphous polyamides from the glassy state. *Acta Polym* 47:99–104
131. Fichera A, Malta V, Marega C, Zannetti R (1988) Temperature dependence of the polymorphic phases of nylon 6. *Makromol Chem* 189:1561–1567
132. Threlfall T (2003) Structural and thermodynamic explanations of Ostwald's rule. *Org Process Res Dev* 7:1017–1027
133. Yokouchi M, Sakakibara Y, Chatani Y, Tadokori H, Tanaka T, Yoda K (1976) Structures of two crystalline forms of poly(butylene terephthalate) and reversible transition between them by mechanical deformation. *Macromolecules* 9:266–273
134. Son K (2000) Formation of polymorphic structure and its influences on properties in uniaxially stretched polybutylene terephthalate films. *J Appl Polym Sci* 78:412–423
135. Bornschlegl E, Bonart R (1980) Small angle X-ray scattering studies of poly(ethylene terephthalate) and poly(butylene terephthalate). *Colloid Polym Sci* 258:319–331
136. Saeidlou S, Huneault MA, Li H, Park CB (2012) Poly(lactic acid) crystallization. *Prog Polym Sci* 37:1657–1677

137. Cocca M, Androsch R, Righetti MC, Malinconico M, Di Lorenzo ML (2014) Conformationally disordered crystals and their influence on material properties: the cases of isotactic polypropylene, isotactic poly(1-butene), and poly(L-lactic acid). *J Mol Struct* 1078:114–132
138. De Santis P, Kovacs AJ (1968) Molecular conformation of poly(S-lactic acid). *Biopolymers* 6:299–306
139. Kalb B, Pennings AJ (1980) General crystallization behaviour of poly(L-lactic acid). *Polymer* 21:607–612
140. Hoogsteen W, Postema AR, Pennings AJ, Ten Brinke G, Zugenmaier P (1990) Crystal structure, conformation, and morphology of solution-spun poly(L-lactide) fibers. *Macromolecules* 23:634–642
141. Pan P, Zhu B, Kai W, Dong T, Inoue Y (2008) Effect of crystallization temperature on crystal modifications and crystallization kinetics of poly(L-lactide). *J Appl Polym Sci* 107:54–62
142. Pan P, Kai W, Zhu B, Dong T, Inoue Y (2007) Polymorphous crystallization and multiple melting behavior of poly(L-lactide): molecular weight dependence. *Macromolecules* 40:6898–6905
143. Zhang J, Tashiro K, Domb AJ, Tsuji H (2006) Confirmation of disorder  $\alpha$  form of poly(L-lactic acid) by the X-ray fiber pattern and polarized IR/Raman spectra measured for uniaxially-oriented samples. *Macromol Symp* 242:274–278
144. Zhang J, Duan Y, Sato H, Tsuji H, Noda I, Yan S, Ozaki Y (2005) Crystal modifications and thermal behavior of poly(L-lactic acid) revealed by infrared spectroscopy. *Macromolecules* 38:8012–8021
145. Kawai T, Rahman N, Matsuba G, Nishida K, Kanaya T, Nakano M, Okamoto H, Kawada J, Usuki A, Honma N, Nakajima K, Matsuda M (2007) Crystallization and melting behavior of poly(L-lactic acid). *Macromolecules* 40:9463–9469
146. Androsch R, Schick C, Di Lorenzo ML (2014) Melting of conformationally disordered crystals ( $\alpha'$ -phase) of poly(L-lactic acid). *Macromol Chem Phys* 215:1134–1139
147. Androsch R, Zhuravlev E, Schick C (2014) Solid-state reorganization, melting and melt-recrystallization of conformationally disordered crystals ( $\alpha'$ -phase) of poly(L-lactic acid). *Polymer* 55:4932–4941
148. Yasuniwa M, Tsubakihara S, Iura K, Ono Y, Dan Y, Takahashi K (2006) Crystallization behavior of poly(L-lactic acid). *Polymer* 47:7554–7563
149. Tsuji H, Takai H, Saha SK (2006) Isothermal and non-isothermal crystallization behavior of poly(L-lactic acid): effects of stereocomplex as nucleating agents. *Polymer* 47:3826–3837
150. Tsuji H, Ikada Y (1996) Crystallization from the melt of poly(lactide)s with different optical purities and their blends. *Macromol Chem Phys* 197:3483–3499
151. Li X, Li Z, Zhong G, Li L (2008) Steady – shear-induced isothermal crystallization of poly(L-lactide) (PLLA). *J Macromol Sci Phys* 47:511–522
152. Tammann G (1898) Number of nuclei in supercooled liquids. *Z Phys Chem* 25:41–479
153. Di Lorenzo ML (2006) The crystallization and melting processes of poly(L-lactic acid). *Macromol Symp* 234:176–183
154. Di Lorenzo ML (2001) Determination of spherulite growth rates of poly(L-lactic acid) using combined isothermal and non-isothermal procedures. *Polymer* 42:9441–9446
155. Di Lorenzo ML (2005) Crystallization behavior of poly(L-lactic acid). *Eur Polym J* 41:569–575
156. De Santis F, Pantani R, Titomanlio G (2011) Nucleation and crystallization kinetics of poly(lactic acid). *Thermochim Acta* 522:128–134
157. Sánchez MS, Mathot VBF, Vanden Poel G, Ribelles JLG (2007) Effect of cooling rate on the nucleation kinetics of poly(L-lactic acid) and its influence on morphology. *Macromolecules* 40:7989–7997
158. Hernández Sánchez F, Molina Mateo J, Romero Colomer FJ, Salmerón Sánchez M, Gómez Ribelles JL, Mano JF (2005) Influence of low-temperature nucleation on the crystallization process of poly(L-lactide). *Biomacromolecules* 6:3283–3290

159. Zhang T, Hu J, Duan Y, Pi F, Zhang J (2011) Physical aging enhanced mesomorphic structure in melt-quenched poly(L-lactic acid). *J Phys Chem B* 115:13835–13841
160. Androsch R, Monami A, Kucera J (2014) Effect of an alpha-phase nucleating agent on the crystallization kinetics of a propylene/ethylene random copolymer at largely different supercooling. *J Cryst Growth* 408:91–96
161. Zhuravlev E, Wurm A, Pötschke P, Androsch R, Schmelzer JWP, Schick C (2014) Kinetics of nucleation and crystallization of poly( $\epsilon$ -caprolactone) – multiwalled carbon nanotube composites. *Eur Polym J* 52:1–11

# Index

## A

Anisotropy, strain-induced, 173  
Anthracene, 59–62  
Arrhenius shift factor, 158  
Atomic force microscopy (AFM), 69, 75, 83,  
97, 99, 110, 114, 120, 131  
Autoepitaxy, 62

## B

Ballistic cooling, 129, 145, 148  
Banded–nonbanded transition (BNB), 114  
Banded polymer spherulite, 95  
Bifurcation of growth, 26  
Biomorphs, 98  
Borax, 96

## C

Chain tilt, 95  
Chirality, 102, 121  
Clapeyron equation, 154, 249, 261, 275  
Compressibility, 243, 257, 265  
Concomitant crystallization, 1  
Continuous-cooling-transformation (CCT)  
diagrams, 148  
Cooling, fast, 212  
undercooling, 4, 16, 24, 31, 40, 49, 147,  
152, 209, 275, 282  
Couette cell, 249  
Cross-nucleation, 1  
Crystallization, 55  
flow-induced, 243  
kinetics, 167, 207, 261  
shear-induced, 127

strain-induced, 167, 177  
Crystal modification, control, 78  
Cyclic voltammetry (CV), 83

## D

Dicyclohexylterephthalamide, 57  
Differential radial distribution function  
(DRDF), 170  
Dilatometry, 218, 243  
extended, 249  
Discrete elastic-viscoelastic stress split  
(DEVSS), 253

## E

Entanglements, 128, 197  
Epitaxy, 23, 32, 46, 55, 58, 87  
Ewald sphere, 102, 106, 107, 145  
Extended-chain crystals (shishs), 62  
Extended pom-pom (XPP) model, 248

## F

Fast scanning calorimetry (FSC), 216  
Flow-induced crystallization (FIC), 244  
Flow instabilities, 271  
Folded-chain lamellar crystals (kebabs), 62  
Fourier transform infrared spectroscopy  
(FTIR), 67–69, 129

## G

Gibbs–Thomson relation, 6  
Growth, bifurcation, 26

Growth (*cont.*)

- transformation, 26
- transition, 26, 48, 79

Guinier approximation, 142

**H**

- Halos, amorphous, 170
- Heat balance, 221, 231, 233, 257
- Hencky strain rate, 159
- Hermans' orientation factor, 251, 270, 274
- Heteroepitaxy, 64
- Hexamethyleneadipate (HA), 18
- High-density polyethylene (HDPE), 95, 97, 102, 107
- High shear rates, 252
- Hoffman–Lauritzen theory, 28, 100, 275
- Homoepitaxy, 62

**I**

Impingement, 281

**K**

- Keabs, 62, 142, 160, 245, 270, 279
- Kolmogoroff–Avrami expression, 210, 247
- KP-model, 100

**L**

- Lamellae, 44, 62, 95
  - branching, 243
  - chirality, 95, 106–108
  - daughters, 245, 263, 270, 287
  - edge-on, 74
  - handedness, 107
  - nanoscale, 31
  - thickness, 5, 6, 71, 118, 154, 226
  - twisted, 99–106, 119
- Lauritzen–Hoffman theory, 28, 100, 275
- Lennard–Jones potential, 24
- Linear low density polyethylene (LLDPE), 130, 152
- Linear viscoelastic envelope (LVE), 158
- Log-conformation representation (LCR), 253

**M**

- Mannitol, 23
- Mechanical cycling, 189
- 5-methyl-2-[(2-nitrophenyl)amino]-3-thiophenecarbonitrile, 23

- Millisecond time resolution, 127
- Modelling, 207
- Molecular vibration spectroscopy, 68
- Momentum balance, 254
- Monte Carlo simulations, 68

**N**

- Nanocalorimetry, 95
- Nanofocus X-ray scattering, 95
- Natural rubber, 167, 168
- Nucleation, 1, 4
  - cross-nucleation, 1
  - density, 208
  - point-like, 264, 282
  - shish-kebab, 279

**O**

- Organic field-effect transistors (OFETs), 56, 76
- Orientation factor, 251, 270
- Ostwald's rule, 1, 3–6, 24, 42

**P**

- Parameter sensitivity analysis, 267
- Photoswitchers, 79, 81
- Pirouette dilatometer, 218, 249
- Polanyi sphere, 107
- Polarized optical microscopy (POM), 11, 43, 110, 130, 151, 271
- Poly(1,3-dioxolan) (PDOL), 19, 24
- Poly(3-hexylthiophene) (P3HT), 69
- Poly(3-hydroxybutyrate) (PHB), 74, 95, 120
- Poly(3-hydroxypropionate) (PHP), 17
- Poly(3-hydroxyvalerate) (PHV), 120
- Poly(3-methylthiophene) (P3MT), 83
- Poly(butylene adipate) (PBA), 5, 17
- Poly(butylene terephthalate) (PBT), 113
- Poly(butylene-2,6-naphthalate) (PBN), 18
- Poly(caprolactone) (PCL), 66, 77, 102
- Poly(*di-n*-hexylsilane), 74
- Poly(ethylene adipate) (PEA), 72
- Poly(ethylene oxide) (PEO), 19
- Poly(ethylene sebacate), 77
- Poly(ethylene terephthalate) (PET), 113, 208
- Poly(heptamethylene terephthalate) (PHepT), 18
- Poly(hexamethylene terephthalate) (PHexT), 11, 18, 32
- Poly(lactic acid) (PLA), 97, 246
- Poly(L-lactic acid) (PLLA), 21, 33, 102
- Poly(methylmethacrylate) (PMMA), 74



- Poly(pivalolactone) (PPVL), 3, 30, 35  
 Poly(propylene adipate) (PPA), 95, 97, 110  
 Poly(tetrafluoroethylene) (PTFE), 76, 77, 86  
 Poly(trimethylene terephthalate) (PTT), 95, 97, 102, 113  
 Poly(vinylidene fluoride) (PVDF), 2, 15, 57, 95, 97, 99  
 Poly(vinylpyrrolidone), 23  
 Polyethylene, 25, 59, 95, 207  
   high-density (HDPE), 97, 102, 107  
   linear low density (LLDPE), 130, 152, 209, 224  
   shish-kebab, 131  
 Poly(1-butene), isotactic (i-PBu), 3, 13, 42, 102, 246  
 Poly(4-methyl-1-pentene), isotactic (i-P4M1P), 2, 14  
 Polymorphic self-poisoning, 20  
 Polymorphism, 1, 72, 78, 208, 243  
 Polymorphs, 1, 98, 157, 209, 275, 282  
   concomitant crystallization, 7  
   cross-nucleation, 22  
   ROY, 23  
 Polyoctamer, 77  
 Polyoxymethylene, 77  
 Poly(*p*-phenylene ethynylene)s, 79  
 Polypropylene, 2, 207, 243  
   isotactic (iPP), 2, 11, 57, 148, 208, 246  
   syndiotactic (sPP), 2, 71  
 Polystyrene, isotactic, 75, 76, 102  
   syndiotactic, 11, 14, 21  
 Pressure, 217  
 Processing, 127, 243  
 Propene/ethylene, ballistic cooling, 145
- Q**
- Quiescent state, 169, 176, 180  
 Quinacridone, 57
- R**
- Real-time fast structuring, 127  
 Recovery, 113, 191–194, 199, 201  
 Rheo-SAXS/WAXD, 156  
 ROY polymorphs, 23  
 Rubber elasticity, 178
- S**
- Schneider rate equations, 210, 230, 247, 262, 275, 278, 288  
 Screw dislocation, 100, 109, 116  
 Selected-area electron diffraction (SAED), 113
- Self-poisoning, polymorphic, 20  
 Semicrystalline polymers, 2, 7, 55, 57, 68, 74, 79, 111, 128–138, 158, 170, 244  
   cross-nucleation, 24  
   non-isothermal crystallization, 207  
   polymorphs, 2  
   Porod behavior, 141  
 Sentmanat extension rheometer (SER), 156  
 Shear layer thickness, 271  
 Shish, 62, 243, 248, 273  
 Shish-kebab, 62, 131–159, 243, 245, 280  
 Slit flow, 149–152, 217, 250  
 Small-angle light scattering (SALS), 228  
 Small-angle oscillatory shear (SAOS), 255  
 Small-angle X-ray scattering (SAXS), 104, 107, 127, 135, 264  
 Spherulites, 11, 16, 18, 62, 96, 130, 260  
   banding, 97, 116  
   bandwidth, 115  
   branches, 38  
   crystallization kinetics, 247, 278  
   flow-induced, 287  
   isotropic, 262  
   nucleated, 30, 36, 243  
 Strain-induced anisotropy, 173  
 Strain-induced crystallization, 167, 177  
 Strain rate, Hencky, 159  
 Strain-regulation process, 196  
 Strain relaxation, 167  
 Streamers, 259  
 Streamline-upwind Petrov–Galerkin (SUPG), 253  
 Stretching, 57, 167, 195, 253  
   uniaxial, 127, 142  
 Structure regulation, 74  
 Synchrotron radiation, 95
- T**
- Tazofelone (TZF), 33  
 Temperature-induced crystallization (TIC), 169  
 Terphenyl, 59, 61, 72  
 Thompson scattering, 135
- U**
- Undercooling, 4, 16, 24, 31, 40, 49, 147, 152, 209, 275, 282
- V**
- Viscoelastic fluid model, 255  
 Viscoelasticity, nonlinear, 243, 253, 260, 269

**W**

- Wide-angle X-ray diffraction (WAXD), 12, 18,  
34, 43, 67, 129, 131, 213, 250  
Wide-angle X-ray scattering (WAXS), 104,  
127, 129, 161

**X**

- X-ray diffraction, 12, 15, 25, 43, 69, 85,  
167–175, 202, 213, 247, 250  
X-ray photoelectron spectrum (XPS), 84  
X-ray scattering, nanofocus, 95, 102